



**University of
Nottingham**

UK | CHINA | MALAYSIA

Thermomechanical Forming Simulation for Fibre Reinforced Thermoplastic Laminates

By

George Edward Street

MEng (Hons.)

Thesis submitted to the
University of Nottingham
for the degree of
Doctor of Philosophy

Abstract

The use of fibre reinforced composite (FRC) materials has grown exponentially in recent years, due mainly to the attractive properties that they exhibit compared with conventional isotropic materials. While they pose an attractive proposition, challenges to the composite industry stem from long manufacturing time, poor recyclability and difficult joinability. Fibre reinforced thermoplastic (FRTP) composites aim to meet the challenges posed by thermoset FRCs. The increase in demand for FRTP components has driven the need for improved continuous sheet forming processes allowing for viable production of high-performance components at a range of manufacturing scales. This includes improved process modelling, with the objective to reduce the reliance on costly and time-consuming trial-and-error methods and optimise process control.

The aim of this work was to produce a functional FRTP thermomechanical forming simulation for the attractive double-diaphragm forming (DDF) process, identified as a gap in literature where current FRTP models are limited to just the matched-tool processes. It was envisaged that the model would allow for accurate defect prediction at a range of forming conditions, subsequently allowing for optimisation of the FRTP DDF process. To achieve this aim, the thesis was broken down into four key areas:

(i) FRTP DDF Experimental Study

A FRTP DDF rig was produced to conduct forming at a range of conditions. The objective was to identify the parameters for successful forming, such as materials and forming conditions, and also provide validation for the subsequent numerical model. Successful isothermal forming was conducted with single-ply carbon fibre (CF) / Polyamide 6 (PA6) organosheets, utilising silicone diaphragms over a double-dome tool geometry. For this purpose, preheating of the diaphragms to 200 °C was necessary to mitigate issues resulting from the significant thermal expansion of silicone. It was shown that both reducing the laminate temperature and/or increasing the forming rate results in increased defect formation in the formed component. For example, bridging (tool-laminate conformity) and wrinkle lengths increased by 110% and 490% respectively with forming at 200 °C compared to that at 250 °C. High-rate forming

resulted in a 58% increase in wrinkle amplitude. It was found that using an infrared (IR) lamp resulted in significant in-plane thermal distributions of up to 18 °C, and that the solid organosheet did not permit airflow, thus inhibiting vacuum propagation at the start of the forming process. A maximum diaphragm strain of 80% was noted, highlighting that both laminate and diaphragm deformation are critical to the success of the DDF process.

Experimental repeatability was analysed and found to be high at higher temperatures, with variations in bridging and shear generally limited to 8%. This repeatability degraded at lower temperatures, especially concerning wrinkle propagation, both between repeats and intra-test between two sides of a symmetrical tool. This highlighted the instability of wrinkles and the variability that can occur owing to errors with specimen alignment and heating.

(ii) Material Behaviour Characterisation

It was necessary to characterise the significant deformation mechanisms, associated with both the laminate and diaphragms, which allowed mould conformity to be achieved in the experimental DDF routine. The significant laminate deformation mechanisms that were analysed were deconsolidation, intra-ply shear, out-of-plane bending (intra-ply mechanisms) and finally the interaction between the laminate and the silicone diaphragms. Deconsolidation was found to be limited to 9% upon heating, owing to the single-ply laminates utilised in this work. A critical reconsolidation pressure of 0.4 bar was also identified, therefore indicating that full reconsolidation is achieved in the DDF process. Intra-ply shear characterisation was conducted predominately utilising the bias extension test due to the poor repeatability (45% variations) of the picture frame test. This was caused by poor specimen alignment (non-orthogonality in the organosheets) and localised effects from the clamping arrangement. Shear forces were shown to increase by approximately 440% and 240% with a temperature reduction from 270 °C to 210 °C and 25x forming-rate increase, respectively. This behaviour was parameterised using an overstress-law and an Arrhenius-type relation respectively. A similar parameterisation process was utilised for out-of-plane bending, with experimental tests conducted with the cantilever bending test. It was found, however, that the influence of bending-rate could not be analysed with this technique. The diaphragm-laminate friction was characterised with

the pull-through method, and parameterised with a Stribeck analysis, showing the friction condition to lie within the hydrodynamic regime. Regarding the diaphragms, hyperelastic behaviour was characterised with the uniaxial, biaxial and pure-shear methods. Silicone was found to not exhibit significant directionality or rate-dependence (within 6%), but did exhibit temperature-dependence and was influenced by the loading history. To remove the influence of loading history, a novel technique was utilised where the samples were pre-compressed before testing. This also resulted in an approximately 25% reduction in material stiffness.

(iii) FRTP DDF Thermomechanical Simulation

Following the successful characterisation of the material behaviour, it was implemented within a DDF numerical routine. The model itself was based on a continuous hypoelastic formulation with decoupled membrane and bending behaviour. Initially, each deformation mechanism was validated using Abaqus/Explicit to ensure that it was captured accurately. Intra-ply shear viscoelasticity was well captured, although a gradually increasing error of 20% - 100% was present due to the normalisation procedure adopted. Diaphragm-ply friction behaviour was captured within 16% of the experimental pull-through forces and included a novel method for incorporating the initial 'static' friction within the model. The validity of the bending input could not be validated due to buckling that was identified on the experimental samples, however a sensitivity study showed it was captured sufficiently within defined bounds for accurate wrinkle prediction. Finally, the Ogden hyperelastic material model for the silicone diaphragm was shown to accurately capture the elastomeric behaviour within 10% of the experimental forces. The isothermal DDF model was subsequently produced to replicate the experimental forming process, run at the different process conditions adopted and then validated against did, nonetheless, predict the experimental forms. At higher temperatures ($210\text{ }^{\circ}\text{C} \leq$), the model was able to capture bridging within 0.5 mm, wrinkle amplitudes within 20% and maximum shear angles within 1° . The accuracy of the model was also shown to not degrade with an alternative $-45/45^{\circ}$ fibre orientation. At a higher forming rate, wrinkling was still well predicted, although a slight (0.9 mm) overestimation of bridging was identified. The model nonetheless predicted the occurrence of secondary wrinkling in the high shear regions at this rate, and also predicted this behaviour well for the lowest tested

temperature of 200 °C. Bridging was significantly underestimated at this temperature, however, caused by the inhomogeneous in-plane thermal profile in the experimental tests. This profile was subsequently incorporated, resulting in a 44% and 62% improvement in bridging and shear prediction respectively, at lower temperatures.

(iv) FRTP DDF Optimisation

Having produced a functional FRTP DDF simulation that could predict forming behaviour with a good degree of accuracy, the model was subsequently adapted to allow for optimisation of the process conditions. Initially, the heat transfer mechanisms of conduction, radiation and convection were obtained through numerical, experimental and analytical methods respectively. Each of these methods was subsequently validated within an Abaqus/Explicit numerical model, with laminate cooling captured within 3% accuracy. This was coupled in parallel with modelling of laminate crystallinity, identified in the initial numerical model as an important consideration for low-temperature forming. This was twinned with crystallisation-dependent specific heat capacity, such that the crystallisation exotherm was captured in the model. The influence of crystallisation was implemented utilising a rule of mixtures approach between the molten and solid material states. Non-isothermal simulations were run at different forming rates, and it was found that including transient effects results in a slight bridging reduction (0.3 mm) at higher forming rates, as opposed to the increase (0.1 mm) noted in the isothermal study. Wrinkle amplitudes were also more aligned (within 4%) between the two non-isothermal forming rates, compared to the isothermal equivalent (72% differential). This was followed by a tool temperature optimisation process where the tool temperature was minimised for the lowest demoulding time, yet still forming within acceptable defect limits. A minimum tool temperature of 200 °C was identified, resulting in bridging of less than 5 mm and reduced wrinkling behaviour, with a demoulding time of 38 seconds. Finally, a novel ‘zoned’ tool heating strategy was implemented, allowing for equivalent forming quality but resulting in a 42% reduction in the demoulding time.

In summary, this work provides the foundations for accurate FRTP forming simulation of alternative manufacturing techniques to conventional matched-tool methods, with the possibility for increased process monitoring, control and optimisation.

Acknowledgements

First and foremost, I would like to express my deepest gratitude to my supervisor, Prof. Michael Johnson, for his invaluable guidance, patience, and support throughout the past four years. His expertise and encouragement have been instrumental in shaping my research and academic development.

I am also incredibly grateful for my colleagues who have provided invaluable guidance and support along the way, particularly Dr Albert Gibbs, Dr Ángela Lendínez Torres, Dr George Spackman, Dr Guy Lawrence, Dr Matthew Thompson, Mr Michael Causon Mrs Monika Lingemann, Mr James Mortimer, Mr Joseph Humphries and Miss Phoebe Rylatt. A special mention goes to Mr Liam Sprake, the composites lab manager, whose expertise and dedication made it possible for me to achieve my research aims.

I acknowledge the financial support provided by the Engineering and Physical Sciences Research Council (EPSRC) through the EPSRC Future Composites Manufacturing Research Hub (Grant number: EP/P006701/1).

Beyond academia, I am deeply thankful for the support of my family and friends who have been by my side over the past four years. While this list is by no means exhaustive, I would like to express my gratitude to Miss Beatriz Sardinha, Dr Charlotte Moss, Miss Elizabeth Taaffe, Miss Emma Branston, Miss Hannah Blamire, Miss Lucy Rostron, Miss Sophie Greenfield, Mr Alexander Court, Mr Daniel Wickes, Mr Edward Court, Mr George Waring, Mr Harry Plaistowe, Mr James Wheeler, Mr Joe Batchelor, Mr Joshua Barraclough, Mr Miles Pemberton, Mr Oliver Gamble, Mr Oliver Parr and Mr Sainath Sivakumar. Their friendship and encouragement have been invaluable throughout this journey. Special thanks to my brother, Mr William Street, and sister-in-law, Mrs Megan Street whose humour, warmth, and endless encouragement have been a welcome source of balance and perspective throughout.

Finally, there are no words to fully express my gratitude to my parents, Mrs Helen Street and Mr Graham Street. Their unwavering belief in me, their constant support, and their boundless love have been the foundation of everything I have achieved. Through every challenge and success, they have been my greatest source of strength, and for that, I am forever grateful.

Publication List

Journal Papers

Street, G.E.; Johnson, M.S. The Intra-Ply Shear Behaviour of Non-Isothermal Thermoplastic Composite Laminates. *J. Compos. Sci.* 2023, 7, 432.

<https://doi.org/10.3390/jcs7100432>

Street, G.E.; Mistry, P.J.; Johnson, M.S. Impact Resistance of Fibre Reinforced Composite Railway Freight Tank Wagons. *J. Compos. Sci.* 2021, 5, 152.

<https://doi.org/10.3390/jcs5060152>

Conference Papers

Street, G.E.; Johnson, M.S. Characterising the Thermo-viscoelastic Bending Behaviour of Carbon Fibre Reinforced PA6 Laminates via the Cantilever Test.

ECCM21 Proceedings, 2024.

Street, G.E.; Johnson, M.S. Investigating the Shear Behaviour of Multi-Ply Woven Carbon Fibre Reinforced PA6 Composite Laminates. *ICCM23 Proceedings*, 2023.

Table of Contents

Chapter 1. Introduction.....	1
1.1 Background and Motivation	2
1.2 Aim and Objectives.....	6
1.3 Thesis Outline	6
1.4 Chapter Summary	9
Chapter 2. Literature Review	11
2.1 Introduction.....	12
2.2 Fabric Reinforced Composites.....	13
2.2.1 Fabric Reinforcements	13
2.2.2 Matrix Materials.....	16
2.3 FRTP Forming Processes.....	20
2.3.1 Matched-Tool Processes	22
2.3.2 Diaphragm Processes	24
2.4 Fabric Forming Mechanisms	26
2.4.1 In-Plane Shear	27
2.4.2 In-Plane Tension	28
2.4.3 Out-of-Plane Bending	30
2.4.4 Friction	31
2.5 Fabric Behaviour Characterisation	34
2.5.1 In-Plane Shear	35
2.5.2 In-Plane Tension	37
2.5.3 Out-of-Plane Bending	38
2.5.4 Friction	41
2.6 FRTP Forming Defects	42
2.6.1 Wrinkling	43
2.6.2 Bridging	44

2.6.3	Deconsolidation.....	45
2.7	Forming Simulation	47
2.7.1	Simulation Approaches	48
2.7.1.1	Kinematic Models.....	48
2.7.1.2	Finite Element Models.....	49
2.7.1.2.1	Implicit versus Explicit FE Methods.....	50
2.7.1.2.2	FE Modelling Scales	51
2.7.1.2.3	Continuous FE Method Formulations.....	55
2.7.2	Process Modelling.....	57
2.7.2.1	Finite Element Simulation Tools.....	57
2.7.2.2	Element Formulation	58
2.7.2.3	Forming Processes	60
2.7.3	F RTP Forming Simulation	61
2.7.3.1	Isothermal Forming Simulation.....	62
2.7.3.2	Non-Isothermal Forming Simulation.....	66
2.7.3.3	Proposed Modelling Framework	72
2.8	Chapter Conclusions	74
Chapter 3. Experimental Double Diaphragm Forming.....		77
3.1	Introduction.....	78
3.2	F RTP Selection and Property Validation.....	78
3.2.1	Laminate Thickness Validation.....	79
3.2.2	Laminate Density Validation	79
3.2.3	Laminate Volume Fraction Validation.....	79
3.2.4	Laminate Thermal Response	80
3.3	Apparatus Production.....	81
3.4	F RTP Experimental DDF Forming Trial	86
3.4.1	Setup Optimisation.....	87
3.4.2	Thermoforming	88
3.4.3	Forming Validation	92

3.4.3.1	Laminate Thermal Validation.....	93
3.4.3.2	Pressure Validation.....	95
3.4.3.3	Diaphragm Strain Validation.....	97
3.5	F RTP Experimental DDF Results.....	99
3.5.1	Variable Forming Temperature.....	101
3.5.2	Variable Forming Rate.....	104
3.5.3	Variable Laminate Orientation.....	106
3.6	Chapter Conclusions	107
Chapter 4. Laminate Thermomechanical Characterisation.....		109
4.1	Introduction.....	110
4.2	Methodology.....	110
4.2.1	Deconsolidation.....	111
4.2.2	Intra-ply shear	112
4.2.2.1	Experimental Setup	112
4.2.2.2	Data Normalisation.....	114
4.2.3	Diaphragm-Ply Friction	118
4.2.4	Out-of-plane bending	121
4.2.4.1	Experimental Setup	121
4.2.4.2	Data Normalisation.....	123
4.3	Deconsolidation Characterisation Results	124
4.3.1	Laminate Deconsolidation	124
4.3.2	Laminate Reconsolidation.....	125
4.4	Intra-ply Shear Characterisation Results	126
4.4.1	Bias Extension Test Results.....	127
4.4.2	Picture Frame Test Results	129
4.4.3	Data Parameterisation	130
4.5	Diaphragm-Ply Friction Characterisation Results	133
4.5.1	Pull-through Test Results.....	133
4.5.2	Data Parameterisation	136

4.6	Out-of-plane Bending Characterisation Results	141
4.6.1	Experimental Results.....	141
4.6.2	Data Parameterisation	146
4.7	Chapter Conclusions	149
Chapter 5. Diaphragm Thermomechanical Characterisation ...		151
5.1	Introduction.....	152
5.2	Methodology	152
5.2.1	Hyperelastic Characterisation	152
5.2.2	Uniaxial Testing	154
5.2.2.1	Biaxial and Pure-Shear Testing	156
5.2.2.2	Strain Energy Density Function	157
5.2.3	Friction Characterisation	159
5.3	Results.....	160
5.3.1	Hyperelastic Characterisation Results	160
5.3.1.1	Uniaxial Testing Results.....	160
5.3.1.2	Biaxial and Pure-Shear Testing Results	165
5.3.1.3	Strain Energy Density Function	168
5.3.2	Diaphragm-Tool Friction Characterisation Results	169
5.4	Chapter Conclusions	170
Chapter 6. Isothermal Thermomechanical Simulation		171
6.1	Introduction.....	172
6.2	Methodology	172
6.2.1	Algorithm for Stress Computation	173
6.2.2	CF/PA6 Material Input Validation.....	175
6.2.2.1	Intra-Ply Shear Input Validation.....	176
6.2.2.1.1	Intra-Ply Shear Behaviour Implementation	176
6.2.2.1.2	BET Finite Element Model	178
6.2.2.2	Diaphragm-Ply Friction Input Validation.....	179

6.2.2.2.1	Inter-ply Friction Behaviour Implementation	179
6.2.2.2.2	Diaphragm-Ply Friction Finite Element Model	181
6.2.2.3	Out-of-Plane Bending Input Validation	183
6.2.2.4	Diaphragm Hyperelastic Validation	183
6.2.3	Isothermal DDF Thermomechanical Model	184
6.2.3.1	Part Geometry and Mesh	184
6.2.3.2	Material and Section Controls	186
6.2.3.3	Contact Definition	186
6.2.3.4	Step Properties	186
6.2.3.5	Boundary Conditions	187
6.2.3.6	Model Implementation	188
6.3	Numerical Validation Results	189
6.3.1	Intra-ply Shear Input Validation	189
6.3.2	Diaphragm-ply Friction Input Validation	193
6.3.3	Out-of-plane Bending Input Validation	195
6.3.4	Diaphragm Input Validation Results	198
6.4	DDF Thermomechanical Simulation Results	199
6.4.1	Initial Model Validation	199
6.4.2	Variable Temperatures	203
6.4.3	Variable Rate and Orientation	209
6.4.4	Inhomogeneous Thermal Profile	212
6.5	Chapter Conclusions	218
Chapter 7. Transient Thermal Characterisation		221
7.1	Introduction	222
7.2	Methodology	222
7.3	Transient Crystallisation Kinetics	223
7.3.1	Cooling-Rate-dependent Crystallisation	223
7.3.2	Specific Heat Capacity	228
7.4	Convective and Radiative Heat Transfer	230

7.4.1	Convection	230
7.4.2	Radiation	237
7.5	Intra-Laminate Conductivity	239
7.6	Heat Transfer Input Validation	244
7.6.1	Experimental Benchmark	245
7.6.2	Analytical Validation	248
7.6.3	Silicone Heat Transfer	252
7.7	Tool-ply Conductivity	255
7.7.1	Experimental Benchmark	255
7.7.2	Numerical Study	257
7.8	Chapter Conclusions	258
Chapter 8. Numerical Forming Optimisation		260
8.1	Introduction	261
8.2	Methodology	261
8.2.1	Bending Behaviour Modification	262
8.2.2	Implementing Transient Thermal Effects	265
8.2.2.1	Intra-ply Conduction	266
8.2.2.2	Convection and Radiation	266
8.2.2.3	Diaphragm-Tool Conduction	267
8.2.2.4	Laminate Specific Heat Capacity	267
8.2.3	Crystallised Material Behaviour	267
8.2.4	Non-Isothermal Thermomechanical Model	269
8.3	Results	270
8.3.1	Bending Validation Results	270
8.3.2	Non-Isothermal Thermomechanical Simulation	271
8.3.2.1	Forming Rate Study	273
8.3.2.2	Tool Temperature Optimisation	275
8.3.2.3	Zonal Tooling	279
8.4	Chapter Conclusions	282

Chapter 9. Conclusions	284
9.1 Summary of Thesis	285
9.2 Reflection and Implications	285
9.2.1 Objective 1: Experimental DDF study	285
9.2.2 Objective 2: Thermomechanical Characterisation	286
9.2.3 Objective 3: Creation of a Thermomechanical Simulation	286
9.2.4 Objective 4: DDF Process Conditions Optimisation	287
9.3 Overall Impact and Contribution	288
9.4 Recommendations for Future Work	288
9.5 Final Remarks	289
Appendix A.	291
Appendix B.	293
Appendix C.	300
Appendix D.	301
D.1 Hypoplastic Law	301
D.2 Bending Formulation	305
D.3 Curvature Updating	307
Appendix E.	311
Appendix F.	315
References	317

Nomenclature

Acronym	Definition
AOI	Area of interest
ABS	Acrylonitrile butadiene styrene
BET	Bias extension test
CAGR	Compound annual growth rate
CF	Carbon fibre
CFRTP	carbon fibre reinforced thermoplastic
COF	Coefficient of friction
DDF	Double diaphragm forming
DOF	Degrees of freedom
DSC	differential scanning calorimetry
FE	Finite element
FRC	Fibre reinforced composite
FRTTP	Fibre reinforced thermoplastic
FST	Fire smoke and toxicity
GF	Glass fibre
GN	Green-Naghdi
ICP	Iterative Closest Point
IR	Infrared
KES	Kawabata Evaluation System
LE	Logarithmic strain
NCF	Non-crimp fabric
NTS	Not to scale
PA	Polyamide
PC	Polycarbonate
PEEK	Polyetheretherketone

PEKK	Polyetherketoneketone
PEI	Polyetherimide
PET	Polyethylene terephthalate
PFT	Picture frame test
PID	Proportional iterative derivative
PP	Polypropylene
PPA	Parts per annum
PPS	Polyphenylene sulphide
SDF	Single diaphragm forming
UD	Unidirectional

Chapter 1.

Introduction

1.1 Background and Motivation

The demand for advanced materials in engineering applications has seen an exponential increase over recent years, driven by the need for lightweight, high-strength, and durable materials across various industries. Composite materials have been at the forefront of this development. The uptake of composite materials has been particularly pronounced in sectors such as aerospace, automotive, marine, and renewable energy. For example, Boeing's 787 Dreamliner and Airbus's A350 feature extensive use of carbon fibre-reinforced composites, accounting for more than 50% of their structural weight [1, 2]. Moreover, in the automotive industry, companies such as BMW [3], Jaguar Land Rover [4] and Toyota [5] have invested heavily in composites research in recent years. Similarly, wind turbine blades, which require high stiffness and fatigue resistance, commonly use glass fibre-reinforced composites [6]. Furthermore, marine applications benefit from composites in hull construction for their corrosion resistance and reduced weight [7].

The global composites industry reached a production volume of approximately 11.8 million tonnes in 2019 [8]. Projections suggest continued growth, with the market expected to reach 163.97 billion USD by 2030, driven by a compound annual growth rate (CAGR) of 7.2% from 2023 to 2030 [9]. This growth will be fuelled by significant contributions from key sectors such as aerospace, renewable energy, and automotive applications. In the UK alone, the 2035 zero-vehicle-emissions target [10] has led to a surge in electric vehicle sales which are expected to approach 600,000 units annually in 2025, representing 24% of new car sales [11].

While much of the early focus in composites has centred on thermosetting matrices, the shift toward thermoplastic composites has been gaining momentum due to several key advantages. This includes enhanced recyclability [12], faster processing times [13], improved impact resistance [14], superior fire, smoke and toxicity (FST) performance [15] and easier storage and shelf life [16]. These advantages have led to thermoplastic composites being adopted in a wide range of applications. In the aerospace sector, for example, the Airbus A380 incorporates thermoplastic composites for a range of leading edge-structures due to the enhanced impact performance, with glass fibre (GF) reinforced polyphenylene sulphide (PPS) utilised for components like the J-nose [17].

More recently, the Boeing 787 ‘Dreamliner’ has utilised carbon fibre (CF) PPS thermoplastic composites for structural components such as the elevators and tailplane, as opposed to just body panels [18]. Figure 1.1 shows how the utilisation of fibre reinforced thermoplastic (FRTP) composites has evolved in the aerospace and defence industry, from simple flat rib sections through to primary structures with high performance polyetheretherketone (PEEK) matrices [19, 20]. Between 2024 and 2030, the aerospace and defence industry is projected to generate a cumulative demand of approximately 12,000 tonnes for thermoplastic composites alone [20].

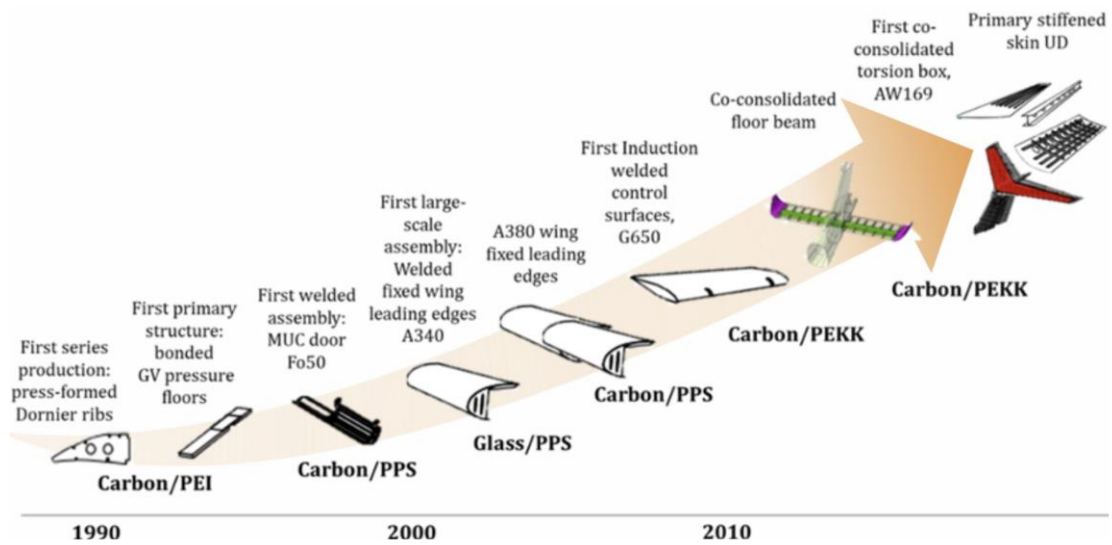


Figure 1.1: Utilisation of fibre reinforced thermoplastics within the aerospace sector [20].

It is not just the aerospace industry that has benefitted from the advancements in FRTP technology. The automotive industry integrates them in structural and non-structural components to achieve high production rates and reduced assembly times [21]. This has included brake pedals (Bentley Continental GT, Porsche Panamera NF) [22], seatback structures (GAC ENO.146 concept) [23], engine undertrays (Bentley Bentayga, Audi Q7) [24] and floor modules [25]. Additionally, thermoplastic composites are utilised in sports and recreation for lightweight and high-performance equipment such as bicycle frames [26] and high performance footwear [27], owing to their superior strength-to-weight ratio and durability. Consumer electronics benefit from thermoplastics with protective casings and internal components, such as with the HP Spectre 13 Ultrabook, the world’s thinnest laptop, comprising of a chassis made from a polycarbonate (PC) and acrylonitrile butadiene styrene (ABS) blend reinforced with CF [28]. In these applications, impact resistance, heat dissipation and FST

requirements are critical, making FRTPs an ideal selection. FRTPs are increasingly utilised in medical devices, including prosthetics and surgical instruments, due to their biocompatibility, chemical resistance and sterilization capabilities [29]. Finally, in infrastructure and construction, FRTPs can be used in bridge reinforcements, panels and barriers due to their toughness and environmental resistance [30]. The increase in FRTP uptake is clearly not limited to a single industry, owing to the multitude of desirable properties they exhibit compared to conventional thermosets.

Despite the advantages of thermoplastic composites, their adoption in high-volume applications is often constrained by manufacturing costs and the complexities involved in the high-temperature processing [31]. Traditional FRTP manufacturing methods, such as matched-tool forming processes, have been proven viable for high-volume production. However, the high tooling costs make these methods less cost-effective for low-to-mid volume production [32]. Consequently, industries are exploring alternative low-cost FRTP forming techniques that offer greater economic efficiency and improved flexibility. Processes such as the double-diaphragm forming (DDF) method present viable alternatives, where flexible diaphragms are utilised to form composite sheets. This allows for lower capital investment and enables more economical production [33, 34]. Additionally, the DDF process is more suitable for the production of large parts, as it is not constrained by fixed tooling sizes [35]. By adopting alternative forming methods, manufacturers can achieve a more balanced approach to production, optimising both cost and efficiency across varying production volumes.

For these thermoplastic composite manufacturing techniques to be effective and competitive, accurate simulations are essential [36]. Traditional trial-and-error approaches commonly used in the industry are both time-consuming and costly, leading to inefficiencies in process optimisation and material utilisation [37]. Simulation-driven design, on the other hand, enables the prediction of material behaviour under different forming conditions, allowing engineers to optimise process parameters, minimise defects, and improve overall production efficiency [36]. Therefore, by leveraging these simulations, manufacturers can reduce their reliance on costly experimental trials, shorten development cycles, and enhance product performance. In order to fuel the momentum behind the implementation of FRTPs, it

is therefore crucial to combine the various aforementioned manufacturing techniques with these advanced numerical models for a synergistic approach to composite manufacturing.

Accordingly, this thesis presents the first comprehensive thermomechanical simulation of the DDF process for FRTP composites. This marks a significant advancement in a field where no prior simulations have specifically addressed FRTP manufacturing using the DDF method. Uniquely, this work goes beyond replicating observed forming behaviour by introducing an optimisation strategy for the DDF process through simulation, something not previously attempted. Moreover, it is the first publication to incorporate the full spectrum of material characterisation, both mechanical and thermal, for all relevant constituents involved in the DDF process. This characterisation spans from initial experimental testing through to implementation within the simulation framework, ensuring consistency and traceability across the workflow. Notably, several of the characterisation methods employed were novel or adapted specifically for this work, enabling accurate capture of critical deformation and thermal mechanisms under realistic forming conditions. This integrated approach provides a level of detail and rigour not previously demonstrated in the literature and makes the study one of the most complete and well-rounded contributions to the field of thermoplastic composite forming to date.

The development of these simulation tools has formed a section of the work produced within an arm of the Future Composites Manufacturing Research Hub (CIMComp) [38], specifically within the Composites Research Group, at The University of Nottingham [39]. Works such as those by Yu *et al.* [40-45] and Chen *et al.* [33, 46-50] have pioneered dry fibre forming simulations. A key focus has been on the DDF process, including advanced material characterisation techniques, allowing numerical models to accurately capture fabric deformation behaviour. The work presented in this thesis aims to build on the foundations from these previous studies, representing another spoke in improving the modelling of composite forming processes, specifically focussing on FRTP materials.

1.2 Aim and Objectives

It was envisaged that the current knowledge regarding thermoplastic composite forming simulation could be expanded. Therefore, the aim of this thesis is:

To produce a bespoke, fully-coupled FRTP thermomechanical simulation for defect prediction and optimisation of the DDF process.

To meet this aim, four primary objectives must be met:

1. To evaluate the manufacturing viability of the FRTP DDF process, at a range of processing conditions, through an experimental study.
2. To accurately characterise the viscoelastic FRTP and diaphragm material behaviour at expected 'in-process' conditions.
3. To produce a thermomechanical simulation capable of predicting FRTP DDF behaviour, subsequently validated with the experimental DDF exercise.
4. To optimise the FRTP DDF processing conditions through the use of the numerical model.

This work therefore outlines the process that can be followed for creation of a complete FRTP DDF model, from initial material selection and behaviour characterisation, through to numerical model creation, validation and subsequent forming optimisation. It is anticipated that the thesis will provide the foundations for viable low-to-mid volume production of FRTP components, where conventional matched-tool processes are not suitable. The aim and objectives are further elaborated on in Chapter 2, where the critical gap in current research is identified, demonstrating the need for this work.

1.3 Thesis Outline

To achieve the aim and objectives outlined in Section 1.2, this thesis is divided into a series of chapters. These chapters are outlined below, and Figure 1.2 is included which illustrates how each results chapter correlates with a specific objective, thus meeting the overall thesis aim.

- **Chapter 2 – Literature Review:** This chapter outlines the current knowledge regarding FRTP composite processing. The initial sections (2.1-2.6) are focused on informing the reader of the various considerations required for FRTP forming, including: material selection, forming processes, fabric deformation methods (and ensuing characterisation exercises) and forming defects. This is then followed by Section 2.7, an in-depth review of current publications regarding forming simulations. This includes analysis of different simulation approaches and modelling techniques, followed by a complete review of all FRTP forming simulations that have been published to date.
- **Chapter 3 – Experimental Double Diaphragm Forming:** This chapter focuses on meeting Objective #1, by conducting experimental DDF operations to identify critical forming parameters and provide validation for the subsequent numerical model. This includes material selection and creation of a FRTP DDF cell, followed by an FRTP forming validation exercise and finishing with forming at a range of different processing conditions.
- **Chapter 4 – Laminate Thermomechanical Characterisation:** The key laminate deformation mechanisms that are necessary for mould conformity to be achieved are characterised in this chapter (Objective #2). This includes laminate deconsolidation, intra-ply shear, out-of-plane bending and diaphragm-laminate friction behaviour, all of which were identified within Chapter 2 as being critical to the success of a forming operation. For each of these mechanisms, the viscoelastic response of the FRTP is evaluated and subsequent input for a numerical model considered.
- **Chapter 5 – Diaphragm Thermomechanical Characterisation:** This chapter follows that of the previous chapter, focussing on Objective #2, now characterising the thermomechanical behaviour of the diaphragm material used in this work. The hyperelastic diaphragm analysis is therefore outlined in which the important behaviour-dependencies are identified. This is followed by an evaluation of diaphragm-tool friction behaviour, with the input for a numerical model considered throughout.

- **Chapter 6 – Isothermal Thermomechanical Simulation:** This chapter implements the numerical characterisation exercises of Chapters 4 and 5 within a finite element (FE) model to accurately predict deformation behaviour, thereby focussing on Objective #3. This includes an in-depth description of the algorithm for stress computation, followed by validation of each individual characterised input. Finally, an isothermal thermomechanical model is produced capable of simulating the FRTP DDF process. This allows for a thorough comparison between simulation and experiment to be conducted, validating the simulation accuracy.
- **Chapter 7 – Transient Thermal Characterisation:** For optimisation of the FRTP DDF process (Objective #4), it was required that the transient thermal behaviour of the laminate during the DDF process be evaluated. This chapter therefore focuses on analysing all thermal processes that occur during the DDF process, including both the crystallisation behaviour and the heat transfer processes (conduction, convection, radiation) relevant to the DDF operation.
- **Chapter 8 – Non-Isothermal Thermomechanical Simulation:** This chapter brings together the validated isothermal simulation (Chapter 6) and the transient thermal analysis (Chapter 7) for the production of a fully-coupled non-isothermal DDF thermomechanical simulation. The primary focus is on meeting Objective #4, where the DDF process is optimised with regards to processing conditions. This includes analysis of an ideal forming rate and minimum mould temperature for a balance between defect development and demoulding time.
- **Chapter 9 – Conclusions:** This chapter evaluates the success of the work presented in this thesis, specifically referring to the aim and individual objectives set out in Section 1.2. The key contributions of the work are outlined and areas for potential future work are discussed.

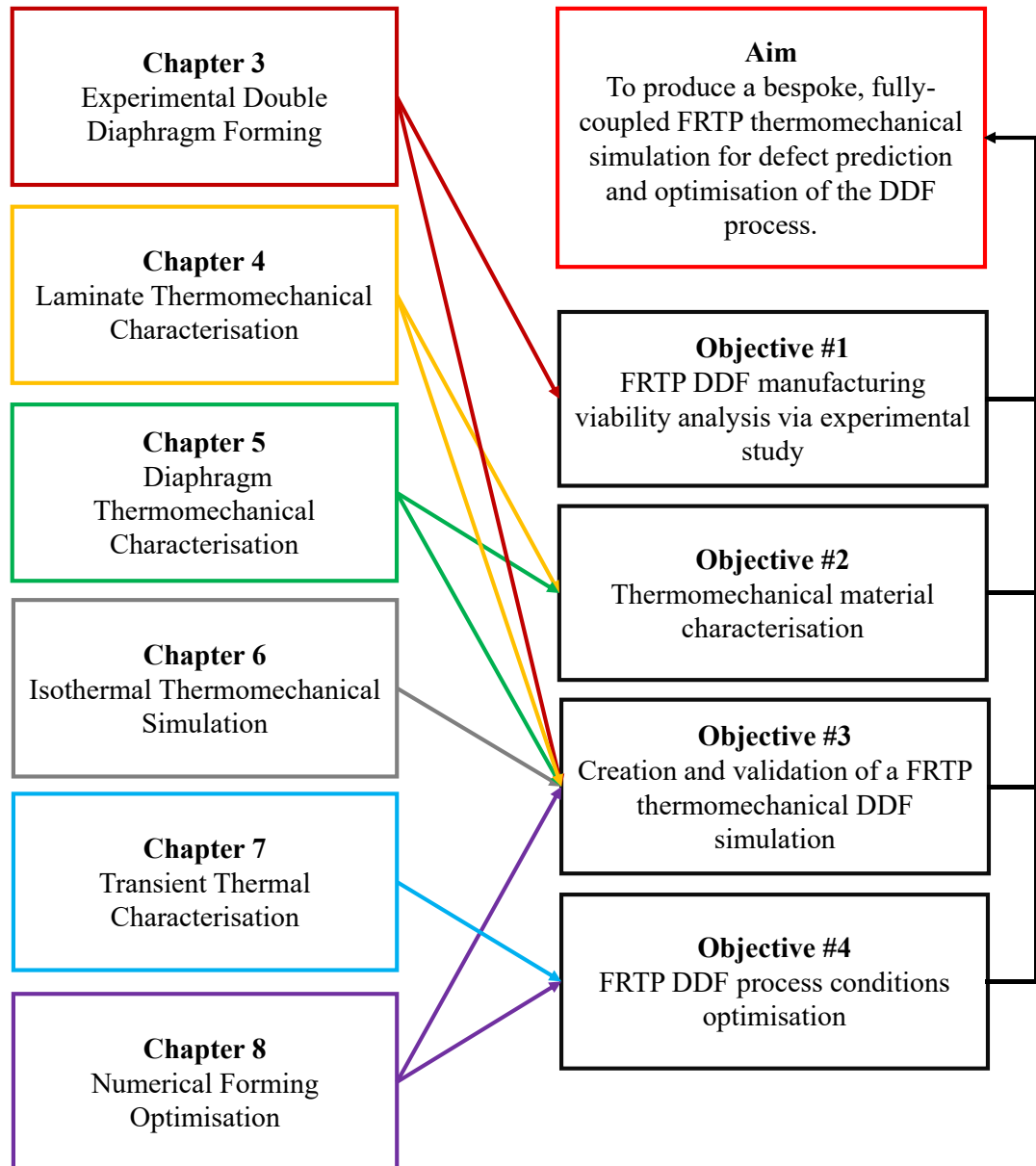


Figure 1.2: Overview of thesis structure.

1.4 Chapter Summary

This introductory chapter has provided an overview of the thesis, establishing the broader aims and objectives while offering a concise introduction to the background of the problem. The organisation of the work is outlined, with a discussion on how each chapter aligns with the research objectives.

Chapter 2.

Literature Review

2.1 Introduction

A composite material is formed by combining two or more distinct materials. Typically, one constituent serves as the reinforcement, characterised by high strength and stiffness but lacking structural cohesion. This reinforcing material is embedded within a matrix, which generally has a lower density but provides structural integrity and supports the reinforcement. By integrating these materials, the resulting composite exhibits a balance of high stiffness and strength along with low density, making it an ideal substitute for heavier structural materials. These properties have propelled the use of composite materials significantly in recent times. Figure 2.1a illustrates the significant increase in composite material usage in just the aerospace sector between 1980 – 2010 [51], with a specific breakdown of the Boeing 787 material usage illustrated in Figure 2.1b [52].

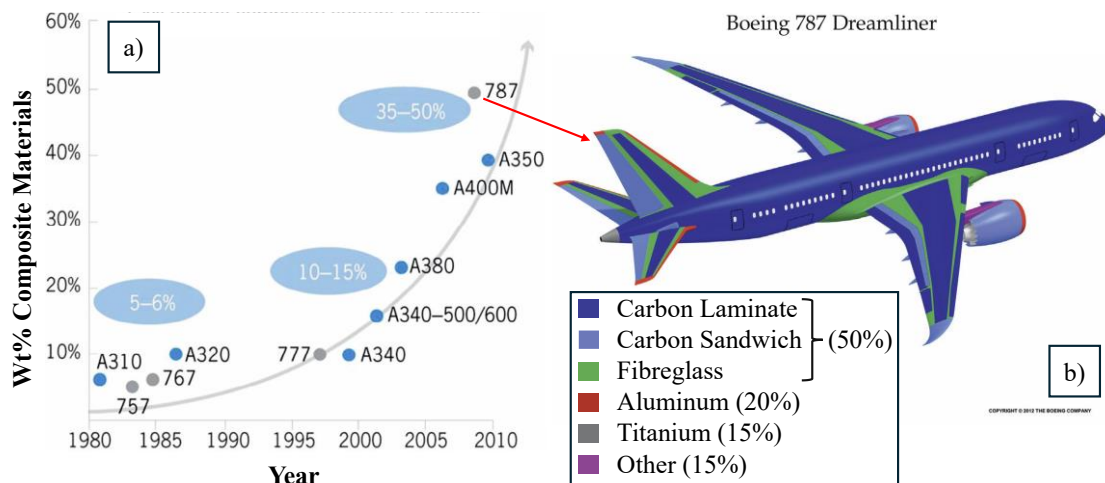


Figure 2.1: a) Weight percentage usage of composite materials in the civil aviation industry between 1980-2010 [51], b) Material usage breakdown for the Boeing 787 Dreamliner [52].

This chapter provides a brief overview of composite materials, regarding the fibre architecture and the matrix properties. This is followed by analysis of thermoplastic composite manufacturing (thermoforming) techniques with a key focus on the DDF process. This includes analysis of the forming mechanisms that take place allowing mould conformity to be achieved (shear, friction, bending) and the subsequent characterisation exercises to quantify these deformation behaviours. Furthermore, the defects that can be expected during forming are outlined. Finally, a holistic overview of the current knowledge regarding composite forming simulation is presented leading

up to the current state-of-the-art in FRTP thermomechanical simulation. From this review, the gap in current research is identified, providing the subsequent motivations for this work.

2.2 Fabric Reinforced Composites

This section focuses on the very make-up of composite materials, regarding both the fibres (material selection and architecture) and the supporting matrix, introducing thermoplastic fibre-reinforced composite materials.

2.2.1 Fabric Reinforcements

Fabric reinforcements are the structural backbone that define many of the mechanical properties and performance characteristics of the final composite material. This work focuses on the use of carbon fibres, renowned for their high strength-to-weight ratio, stiffness, and excellent fatigue resistance [53]. Alternatives to carbon fibres, however, include the use of glass fibres which exhibit high strength and affordability [54], and aramid fibres such as Kevlar which exhibits high toughness and impact resistance [55].

Individual carbon fibres, which are typically 5-50 μm in diameter, are typically bundled together into a “tow”. A tow consists of thousands of continuous filaments, grouped and held together by surface sizing, which enhances handling and compatibility with the matrix material [56]. The number of filaments per tow (e.g. 3k, 6k, or 12k) determines the thickness and strength of the bundle, influencing its suitability for specific applications [55]. These tows are then processed into various fabric architectures. The hierarchy from the individual fibre, to the fibre tow and finally to the fabric is known as the multi-scale, with each level defined by an approximate characteristic length [57-59]. Figure 2.2 illustrates the multi-scale for a woven fabric [58].

- **Microscopic scale:** 1-10 μm for fibre diameters.
- **Mesosopic scale:** 0.5-10 mm for tow diameters and repeating unit cells.
- **Macroscopic scale:** 0.1-10 m and above for textiles and textile structures.

Fabric architectures refer to the specific configurations in which fibres are arranged within the reinforcement. The principal composite architectures used in engineering applications are woven fabrics, non-crimp fabrics (NCFs) and unidirectional (UD) fabrics [60]. This work focuses on the use of a woven fabric architecture, however the reader is referred to the works of Long [57], Lomov [61] and Akkerman *et al.* [62] for a detailed overview of both NCFs and UD fabrics, the latter authors specifically focussing on FRTP composite implementation.

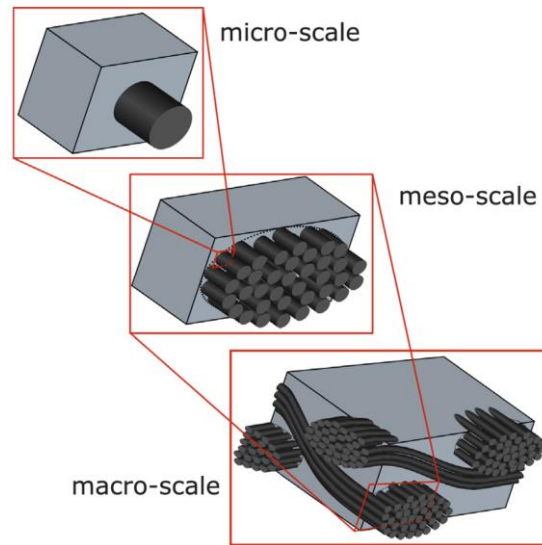


Figure 2.2: Multi-scale for a woven fibre reinforced fabric [58].

Woven reinforcements are among the most traditional and widely used fabric architectures in composite materials. They are created by interlacing warp (longitudinal) and weft (transverse) fibres at right angles to form a stable two-dimensional fabric. This interlacing pattern facilitates deformation of the fabric through shearing, by allowing each tow-intersection to function as a friction-dependent pivot point around which the tows can rotate [63]. The interlacing patterns can be classified into various types, including plain weave, twill weave, and satin weave, each exhibiting a trade-off between formability (shearing) and stability [60]. Figure 2.3 illustrates these weaving patterns, with twill weave being the most common occurring weave in the composite industry due to it sitting in-between the relatively unstable satin weave, and the less-formable plain weave.

The formability and stability of a fabric is also influenced by the size of the tow. For a fixed tow spacing, larger tow widths typically result in smaller gaps within the woven

structure. This leads to lower “shear locking” angles, as the tows compact more readily at lower shear angles [64]. Similarly, an increase in tow thickness reduces gap width while increasing the undulation of the tows. This greater undulation decreases formability and causes earlier shear locking in woven fabrics [64]. These out-of-plane undulations at each tow-intersection are known as crimps. Crimps introduce normal forces due to tow bending, which generates frictional resistance. This resistance is essential for maintaining the positional stability of the tows, preventing unwanted sliding, and preserving the structural integrity of the fabric [65]. Even with these crimps, instabilities are common at the boundaries of a woven fabric where tension in the interlaced tows is minimal, allowing for free movement of transverse tows (tow slippage).

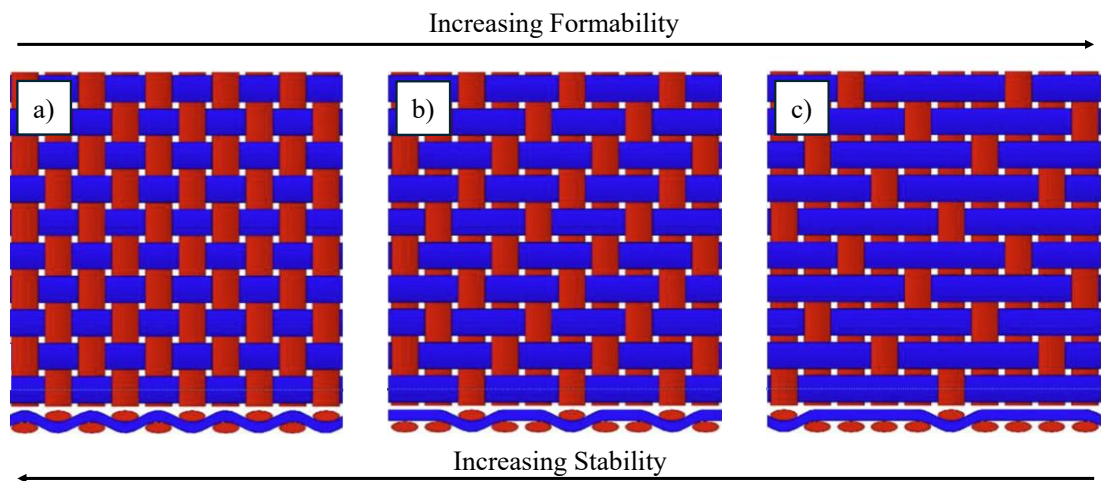


Figure 2.3: Common weave patterns, generated using TexGen software [66]: a) Plain weave, b) Twill weave, c) Satin weave.

Woven composites, compared to unidirectional reinforcements, offer greater damage tolerance, dimensional stability, and ease of manufacturing [67]. One distinct advantage of woven fabrics over other textile structures is their ability to conform to double-curved surfaces due to their low shear resistance [68]. This adaptability arises from the varying angles between the warp and weft yarns, allowing the fabric to align closely with the tool surface during forming [69]. The biggest drawback of woven architectures is attributed to the crimping, resulting in localised stress concentrations [67], decreasing the in-plane mechanical performance of the fabric (by up to 50% for 3D weaves) [70, 71].

2.2.2 Matrix Materials

In composite materials, the matrix serves several essential functions [72]. It binds the reinforcing fibres together, maintaining their alignment and enabling effective load transfer [73]. By surrounding and supporting the fibres, the matrix protects them from environmental damage such as moisture, chemicals, and ultraviolet radiation [54]. Additionally, it provides the composite with its overall shape and structural integrity, filling the spaces between fibres and contributing to the material stiffness and toughness [72]. The matrix also plays a critical role in absorbing energy, reducing vibrations, and enhancing the composites fatigue resistance [53].

Most commercially produced composites use a polymer as the matrix material. Polymers are composed of small molecular units called monomers and can be categorised into two main types based on their thermal behaviour: thermosets and thermoplastics [74]. Thermosets, such as epoxies and polyesters, are characterised by their irreversible curing process, which forms a rigid, cross-linked structure [57]. This results in excellent thermal stability, chemical resistance, and dimensional integrity [75]. However, thermosets have notable disadvantages, including their inability to be reshaped or recycled after curing, making them less environmentally friendly [76]. Additionally, thermoset composites often require longer processing times and specific curing conditions, which can increase manufacturing complexity and cost [77]. In contrast, thermoplastics can be reheated and reshaped multiple times without significant degradation [55]. They offer greater toughness, impact resistance, and ease of recyclability, which make them suitable for applications requiring durability and sustainability, often at a lower manufacturing cost compared to thermosets [14]. Figure 2.4 illustrates a comparison in the stiffness behaviour between both thermoplastics and thermosets [78], where T_g , T_m and T_d represent the glass transition, melting and degradation temperatures, respectively. This work focuses on the use of thermoplastic matrices in particular, so they are further introduced below.

Thermoplastics, as a class of matrix materials, can be further divided into amorphous and semi-crystalline polymers, each defined by their molecular arrangements and physical behaviour [79]. Amorphous thermoplastics, such as polycarbonate and polystyrene, have a random molecular structure with no long-range order [80]. This lack of crystallinity limits their resistance to solvents and thermal degradation [81]. In

contrast, semi-crystalline thermoplastics, such as polyethylene and polypropylene, exhibit regions of highly ordered molecular chains called lamella, interspersed with amorphous areas [82]. This partial crystallinity enhances their mechanical strength, thermal stability and chemical resistance, making them a favourable choice during matrix selection for a thermoplastic composite laminate [83]. Figure 2.5 illustrates the molecular structure of amorphous and semi-crystalline polymers.

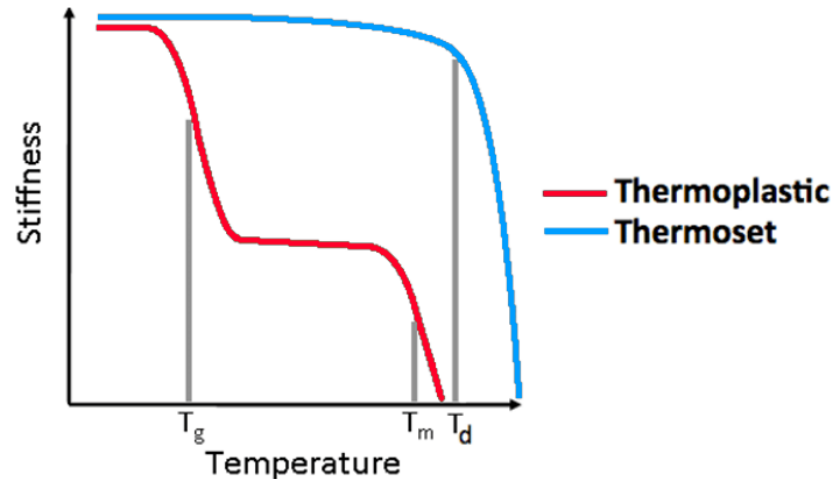


Figure 2.4: Temperature dependent stiffness of thermoset and thermoplastic polymers [84].

Regarding semi-crystalline polymers, molecular interactions are generally dominated by chain entanglements and van der Waals forces [85, 86]. In some cases, such as with polyamides, hydrogen bonding also exists between chains at low temperatures [79, 81, 87]. These physical interactions can however be overcome with the presence of thermal energy. Increasing the temperature of a semi-crystalline polymer initially results in an increase in the rotational frequency and therefore relaxation of the amorphous regions, where the van der Waals forces are easily broken above a given T_g , resulting in a drop in polymer stiffness [88]. Crystalline regions, however, remain largely unaffected until T_m is approached, where the vibration of the molecules becomes great enough to cause a large degree of molecular disentanglement and overcome any present hydrogen bonding [82]. This allows the polymer chains to move freely and the material to transition into a liquid state, but only after T_m is exceeded. During cooling, the crystalline regions and physical bonds re-form, however the degree of crystallinity is intrinsically linked to the cooling profile of the polymer. No semi-crystalline polymer ever reaches 100% crystallinity [89].

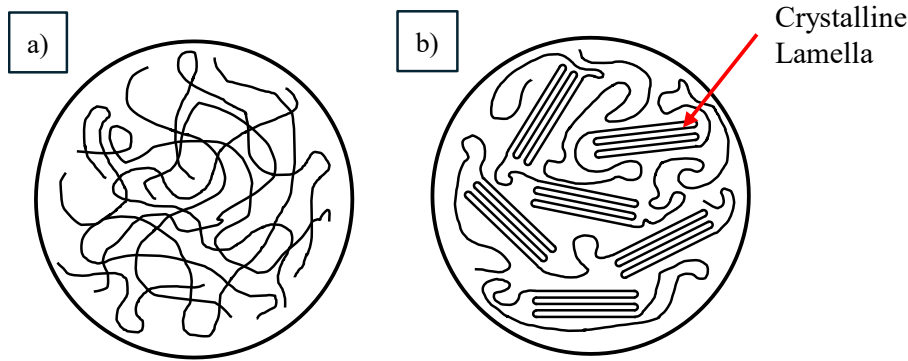


Figure 2.5: Molecular structure of a) amorphous polymers, b) semi-crystalline polymers.

Among many, the most commonly used semi-crystalline polymers in FRTP laminates include polypropylene (PP), polyethylene terephthalate (PET), polyamide (PA) and polyetheretherketone (PEEK) [55, 90]. Their versatility makes them integral to the production of lightweight, durable, and high-performance composite laminates. PP is widely used due to its low density, good chemical resistance, and cost-effectiveness, although it has relatively moderate mechanical properties when compared to other semi-crystalline polymers [91]. PET offers excellent stiffness and dimensional stability, making it suitable for high-strength applications [81]. Similarly, PA exhibits good mechanical properties, wear resistance and hydrogen bonding in its crystalline regions, further enhancing its thermal and impact resistance [90]. Finally, PEEK, a high-performance thermoplastic, provides outstanding thermal stability, chemical resistance, and mechanical strength [92]. Deciding upon the specific thermoplastic matrix depends on the requirements of the final composite part, alongside limitations imposed by different manufacturing processes (Section 2.3). Table 2.1 illustrates a comparison between these four popular semi-crystalline matrices [55, 81, 90, 92].

In this work, limitations regarding the DDF manufacturing process (Section 2.3.2) placed restrictions on the polymer that could be selected regarding the maximum melting temperature. Therefore, to ensure an adequate thermal window existed, a PA matrix was deemed to be the best option; maintaining strong mechanical performance and versatility at a moderate cost (Table 2.1). Polyamides are characterised by the presence of amide groups (-CONH-) in their backbone, which enable strong hydrogen bonding between molecular chains [79, 81, 92, 93]. The most common polyamides available (specifically for use in a FRTP) are PA-6 and PA-6,6, each possessing unique mechanical and thermal properties owing to the different chemical structures [94].

Figure 2.6 illustrates the chemical makeup of these two PA-X polymers, where X represents the number of carbon atoms in each monomer unit that makes up the polyamides molecular structure [95].

Table 2.1: Table comparing various properties of four common thermoplastic matrix materials [55, 81, 90, 92].

	PP	PET	PA	PEEK
Density (g/cm³)	0.9	1.38	1.13-1.15	1.3
Melting Temperature (°C)	160-170	250-260	215-265	343
Thermal Stability	Moderate	High	Moderate to High	Very High
Chemical Resistance	Very High	High	Moderate	Very High
Mechanical Strength	Low	Moderate	High	Very High
Toughness	Moderate	Moderate	High	High
Cost	Low	Moderate	Moderate	Very High

In the quest to minimise the melting temperature, PA-6 (Nylon) was utilised as the FRTP matrix material in this work, identified in particular as having the lowest melting point of these two common polyamides. This can be explained by PA-6 being synthesised from a single monomer, caprolactam, which leads to a repeating unit with a relatively simple structure [92]. This results in a lower degree of crystallinity compared to Nylon 6,6, such that less thermal energy is required to disrupt the less tightly packed crystalline regions. One of the drawbacks with PA-6, however, is the water absorption. This is due to the highly repetitive -CONH- chains in PA-6 coupled with their high polarity, creating a strong affinity for hydrogen bonding with water molecules [92]. This absorptivity is therefore considered in this work.

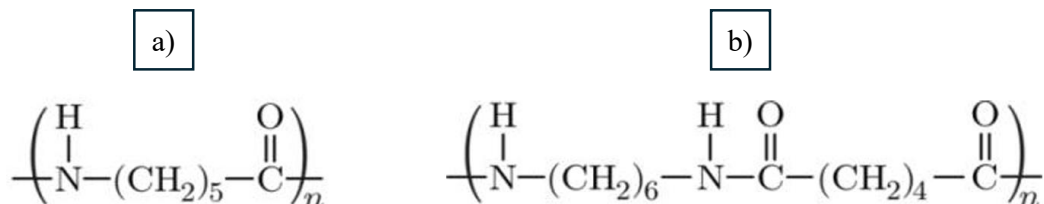


Figure 2.6: Chemical composition of a) PA-6, b) PA-6,6 [95].

2.3 FRTP Forming Processes

This section focuses on the different processes utilised to transform 2D FRTP composite preforms, with the architecture and materials discussed in Section 2.2, into 3D shapes. Since this work is focussed on FRTPs, traditional processes commonly used with dry fabrics of pre-impregnated thermosets, such as hand-layup, are not discussed here. Furthermore, this section only focuses on continuous preform processes including those with architectures illustrated in Figure 2.3, rather than processes suitable for use with short (discontinuous) fibres (injection moulding, compression moulding etc.). These continuous preforms deform into complex 3D shapes via specific forming mechanisms, discussed in Section 2.4.

FRTP forming processes generally follow a distinct thermal cycle [96]. A preform is heated in a ‘preheat’ stage to melt the polymer matrix (above T_m for a semi-crystalline polymer (Section 2.2.2)), conventionally with a conductive (tool), convective (oven) or radiative (infrared lamp) process [97]. Induction heating is another possibility for melting the polymer matrix if conductive fibres are used, or with the presence of a susceptor if not [98, 99], although this method is currently less common. Infrared (IR) radiative heating is the most commonly used technique, as although contact heating is efficient, it is largely impractical (clamping the heater to the workpiece) [100]. Furthermore, convective heating is an inefficient form of heating due to the slow heat-up times, despite the resultant uniform temperature distribution throughout the thermoplastic composite laminate [101]. The IR heating method is considered a very effective mode that exhibit fast heat-up times, flexibility and high levels of energy efficiency [96].

An IR heating array generally consists of a group of infrared lamps, each made up of a coiled filament inside a tubular enclosure. These tubes are then mounted below reflectors to increase the heat flux efficiency. The significant parameters in the IR heating process include the (i) heater power, (ii) distance between the lamps and the laminate, (iii) laminate thickness, (iv) heater to laminate size ratio, and (v) single or double-sided heating as documented by Sweeney *et al.* [97] and illustrated in Figure 2.7. However, FRTP sheet heating is a complex nonlinear heat transfer process with other variables such as sheet colour, thermal conductivity, surrounding environmental

temperature and air velocity also significantly affecting the heating of the laminate [102].

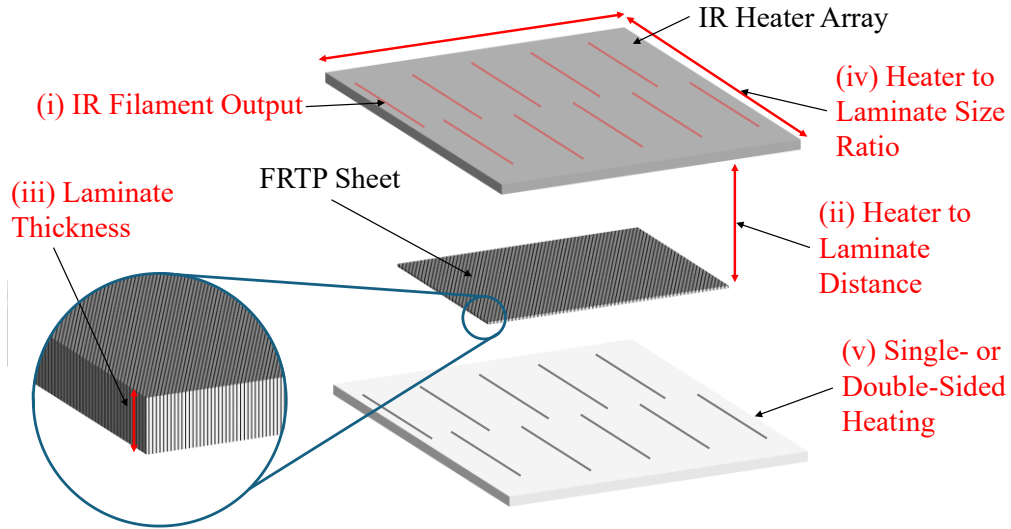


Figure 2.7: Significant parameters in the IR heating process.

Once sheet heating is achieved, forming can then be completed by imposing a positive pressure on the 2D preform (through a matched-tool, diaphragm etc.) to allow it to conform to the shape of a mould [100]. Finally, the finished FRTP part must be cooled below the recrystallisation temperature, T_c (for semi-crystalline polymers), for dimensional stability to be achieved before it can be demoulded [103]. Figure 2.8 illustrates this thermal profile, in this case for a matched-tool routine, redrawn from Reynolds *et al.* [104]. It should be noted the schematic is not-to-scale (NTS), and the preheating does not necessarily have to be conducted at the same location as the forming.

Both the draping and consolidation of the 2D preform dictate the success of the forming step. In this work, pre-impregnated organosheets were utilised owing to the increased handleability, ease of heating and assured consolidation compared to equivalent commingled fabrics [105-107]. Therefore, this work generally focuses on the drapability of each FRTP preform, hereon in denoted ‘laminate’, and the various defects that can occur during forming. These defects are analysed in Section 2.6.

The works of Okine [108] and Tomas [109] present in-depth overviews of the key forming methods that are applicable for use with FRTP laminates, which generally fall into two categories: consolidation between matched-tools, or where consolidation is

provided with a diaphragm or film [110]. Matched-tool processes include conventional matched-tool forming, rubber stamp forming and hydroforming. On the other hand, there is diaphragm forming (single and double), along with vacuum forming. These two forming categories are outlined below.

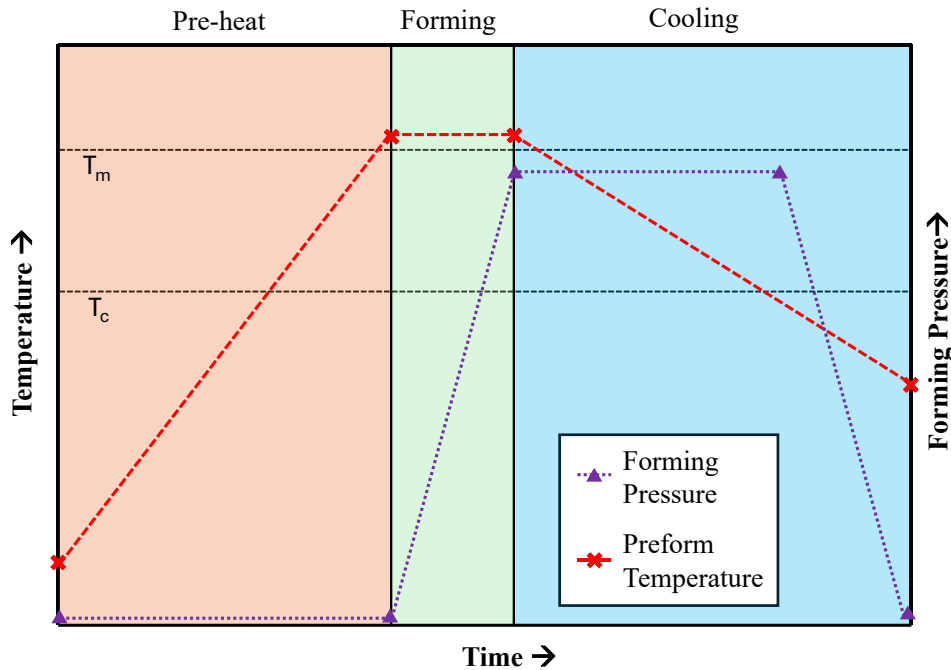


Figure 2.8: Thermal and pressure cycles of an FRTP preform during a representative matched-tool forming process, redrawn from Reynolds *et al.* [104].

2.3.1 Matched-Tool Processes

The matched-tool process, originating from the deep-drawing of sheet metal, involves pressing a molten FRTP laminate into shape at high pressure between a male and female tool [111]. Figure 2.9 illustrates this process for a carbon fibre reinforced thermoplastic (CFRTP) laminate. Here, the laminate is heated externally before being transferred to the press tool, pressed, cooled and de-moulded [112], as per the thermal profile illustrated in Figure 2.8. Conventional matched-tool forming utilised two metallic moulds to achieve mould conformity, requiring a high level of machining precision to ensure an even consolidation pressure acts over the entire FRTP laminate [108].

When used with a pre-consolidated FRTP organosheet, matched-tool processing is exceptionally quick as there is no need to wait for the resin to flow to achieve complete

part consolidation (as would be the case with a comingled fabric) [109]. Thus, the cooling procedure can commence immediately after tool-closure, sometimes at a lower temperature than the recrystallisation temperature T_c to reduce cooling time [113]. Furthermore, the high forming pressure generally eliminates the formation of ‘bridging’ (Section 2.6.2), and produces a FRTP component with two ‘A’ sides [114].

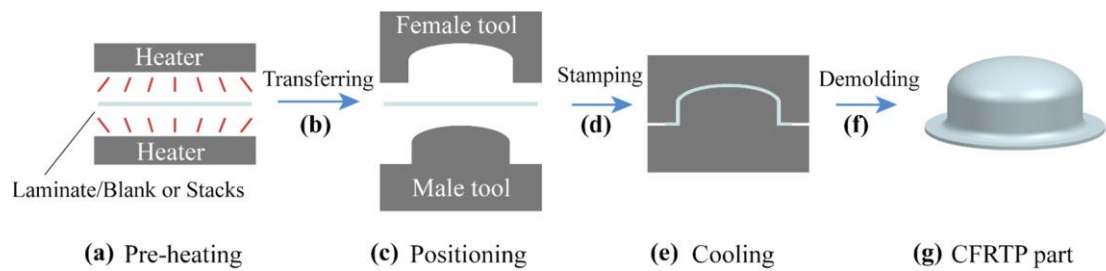


Figure 2.9: Matched-tool process for a CFRTP laminate [112].

The process does, however, have a few drawbacks. The manufactured parts must be free of undercuts and typically require a minimum draft angle of 2° to ensure a seamless interaction between the top and bottom tools [115]. The high forming force can lead to over-shearing (Section 2.4.1), resulting in wrinkles consolidated within the final component, severely degrading its mechanical performance [116]. Moreover, while it is a quick process, the matched-tool process is only suitable for producing a large quantity of parts per year considering the high cost associated with producing the tools to a high tolerance, including associated heating/cooling channels ($\sim 30,000$ parts per annum (PPA) [117]). The maximum part size is also generally constrained by the difficulty with producing these tools in large sizes. This means that the process cannot be used for structures such as wind turbine blades and aerospace wing spars [112]. Finally, it is difficult to control, with precision, the fibre displacements due to the localised loading imposed by the rigid tool [108].

In some cases, the male tool can be replaced with an elastomeric tool (rubber-stamp forming) which reduces cost and accommodates FRTP thickness variations with its inherent compliance. This does, however, increase the associated cooling times and generally reduces the tool lifespan [118]. Hydroforming, the other variant of the matched-tool process, replaces the male tool with a flexible diaphragm encompassing a hydraulic reservoir. A piston is used to pressurise the fluid, thus deforming the flexible diaphragm and laminate to the rigid tool surface with a uniform hydrostatic

pressure [110]. Once again, this process enacts an even pressure distribution on the FRTP laminate but is generally limited to lower temperatures due to the thermal constraint of the deformable diaphragm.

Regarding FRTP matched-tool processes, with the conventional stamping process often denoted ‘thermostamping’ or ‘hot stamp forming’, the process parameters are widely acknowledged as crucial factors influencing the final quality of the formed part. The most extensively studied parameters include preheating temperatures [119, 120], transfer time [113, 119], tool geometry [111, 120], tool temperature [113, 119, 120], boundary conditions [113, 121, 122], stamping speed [111, 123], stamping pressure [111, 113, 119], and cooling rate [119].

2.3.2 Diaphragm Processes

The diaphragm forming process involves one or more highly extensible diaphragms constraining a molten FRTP laminate, forcing it to conform to a tool geometry [124]. The process was initially developed exclusively for thermoplastic composites and has commonly been used for this purpose in previous works [16, 109, 124, 125]. There are two diaphragm forming techniques: Single Diaphragm Forming (SDF) and Double Diaphragm Forming (DDF). In DDF, the fabric plies are enclosed between two flexible diaphragms, allowing the entire ply stack to be shaped in a single operation. In contrast, SDF operates similarly but lacks the lower diaphragm in contact with the tool. This absence provides greater flexibility for sequentially forming multilayered preforms but increases the likelihood of defects due to the reduced constraint provided by the lower diaphragm [32].

A key advantage of diaphragm forming compared to other forming methods is its relatively low capital cost [126]. The necessary equipment, such as vacuum pumps and associated rigs, is significantly more affordable than press tools or in-autoclave systems. Furthermore, diaphragm forming is highly adaptable to a wide range of component sizes with minimal cost variation, making it a versatile choice for producing FRTP parts [35, 43, 127]. Due to the limited forming forces, however, the diaphragm forming process may have difficulty with producing parts that consist of a high level of geometric complexity [109]. Owing to the temperature requirement of FRTP laminates, only diaphragm materials rated up to an adequate temperature can be

selected [108]. Moreover, the setup time regarding layup of the diaphragms and laminate does increase the typical forming time for each part [13]. The process is therefore more suitable for low-to-mid scale production runs, those in lower quantities than can be viably produced using equivalent matched-tool methods (Section 2.3.1) [128].

This work focuses on the DDF process in-particular due to the low cost and versatility of the forming operation when compared to matched-tool methods. Furthermore, the constraint provided by the lower diaphragm was beneficial for FRTP heating and transportation, with the advantage of interfacial shear-slip reducing wrinkling (Section 2.6.1) on the formed component [129]. In this process, a FRTP laminate is placed between both diaphragms which are clamped at the edges by a picture frame [124]. Air is subsequently evacuated from in-between these diaphragms to provide clamping force, with the laminate then heated to the forming temperature. This heating can either be completed in-situ with infrared heaters, or elsewhere in a convective oven before being transported to the forming apparatus. Once the FRTP is in a molten state, air is removed from between the lower diaphragm and tool, with the subsequent pressure differential forcing the diaphragms and laminate to conform to the geometry of a tool [16]. Finally, after forming, once the FRTP has cooled below the crystallisation temperature, the part can be de-moulded. Figure 2.10 illustrates the two key operations in the DDF process, namely, the preheat and pressurisation, followed by the forming.

A range of previous literature exists for analysing the influence of different FRTP DDF process conditions, including: laminate temperature (and temperature rate) [16, 124, 125, 130-133], forming pressure (and pressure rate) [16, 124, 125, 130, 133-136], laminate shape [16, 50, 137] and fibre layup [16, 35, 50, 131, 134, 135]. The diaphragm material is often what constrains the maximum allowable forming temperature, so a range of studies have also been conducted evaluating the performance of different polymeric [124, 131, 138] and elastomer [139] films.

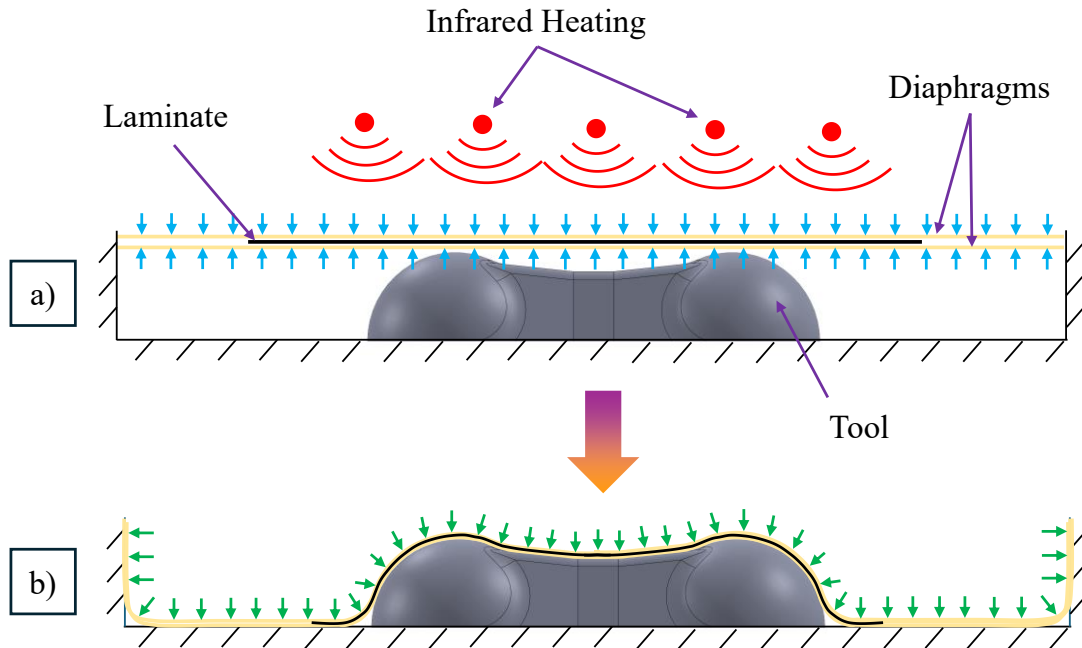


Figure 2.10: DDF process for FRTP laminates a) preheating and diaphragm pressurisation, b) thermoforming via air evacuation between the tool and lower diaphragm.

2.4 Fabric Forming Mechanisms

For the forming techniques outlined in Section 2.3 to function correctly, a range of different mechanisms must take place to allow mould conformity to be achieved. These mechanisms differ significantly than those found in isotropic sheet forming processes, such as sheet metal forming, due to the inextensible nature of the reinforcing fibres [62]. This means that continuous fibre reinforced composite laminates cannot stretch into shape and must instead draw into the tool and deform without significant in-plane strain in the fibre directions. The key deformation processes for this to occur are in-plane (trellis) shear, in-plane elongation (owing to in-plane tension) and out-of-plane bending [140]. Furthermore surface interactions, either between individual plies or between the laminate and the tool, manifest themselves in the form of frictional forces that also influence the deformation of the FRTP laminate. Figure 2.11 illustrates these key deformation mechanisms for a typical matched-tool forming operation (Section 2.3.1) [62, 141]. Laminate compaction is considered as a thermal property with deconsolidation in Section 2.6.3. These individual deformation mechanisms are outlined below, noting that they have a highly viscoelastic response due to the molten nature of the resin.

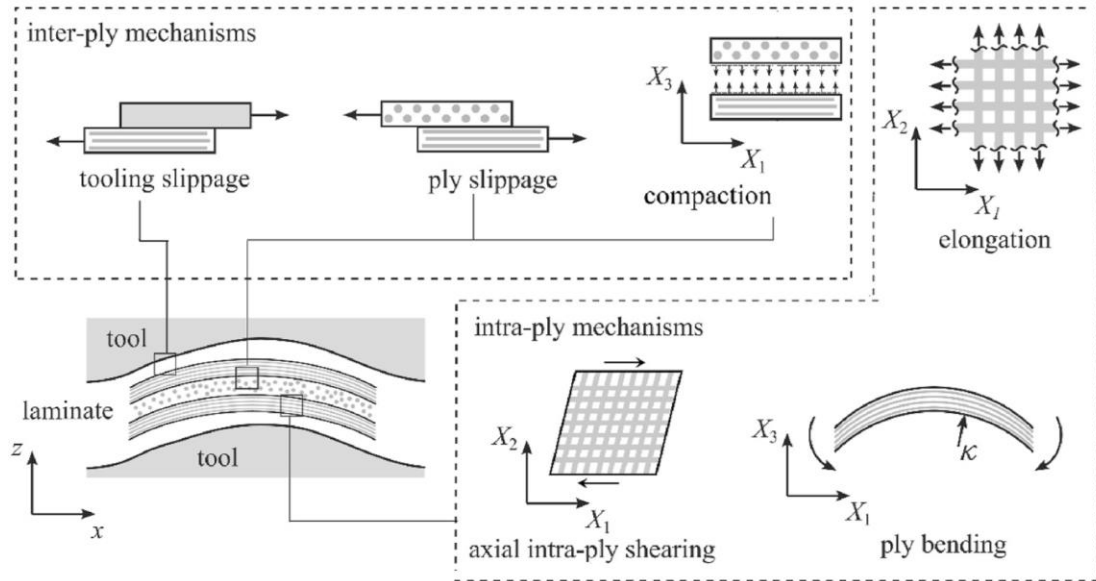


Figure 2.11: Deformation mechanisms involved with a matched-tool forming operation [62, 141].

2.4.1 In-Plane Shear

In-plane (intra-ply) shear is recognised as the dominant mode of deformation for shaping regions of a part where three-dimensional deformation of the fabric is required, such as at corners or over spherical regions [118]. This type of deformation describes a change in fibre orientation resulting from the rotation of tows at their crossover points. The degree of in-plane shear is measured by the shear angle, defined as the localised angle between the warp and weft tows [142]. The shear modulus of a fabric, G , is substantially lower than its tensile modulus, E , due to the minimal resistance provided by inter-yarn friction at the crossover points [143].

Figure 2.12a illustrates the typical shear moment *versus* shear angle response of a woven (plain weave) glass fibre fabric with three distinct regions indicated, typical of many woven fabrics [144]. At low shear strain (Region 1), the fabric exhibits minimal shear resistance, primarily determined by the weak frictional forces within the tows [145]. At this point, steady-state rotation of the yarns occurs, as per Figure 2.12b, with no shearing inside each tow [146]. As the tows begin to make partial contact, the filaments reorganise and compact, leading to an increase in the observed shear moment (Region 2) [65, 147]. When the shear angle reaches a critical value, referred to as the locking angle, the tows become fully compressed laterally, resulting in a sharp rise in

the fabrics in-plane shear moment (Region 3) [143]. Figure 2.12c illustrates a fully-laterally-compressed tow. Wrinkles often occur at this point [65].

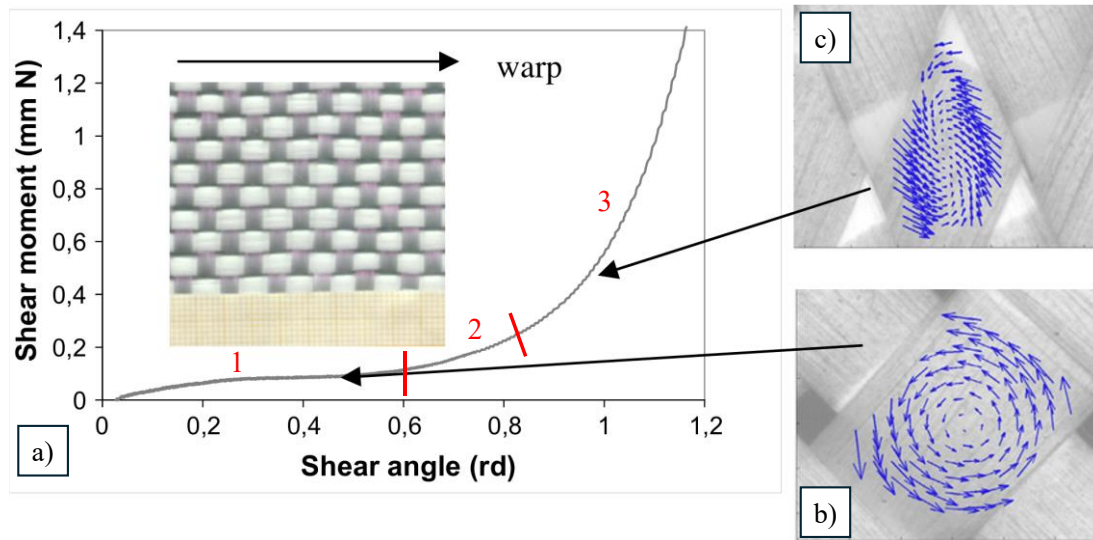


Figure 2.12: a) Shear moment *versus* shear angle for a woven (plain weave) fabric, b) steady-state yarn rotation, c) maximum yarn compaction attained at the fibre locking angle [144].

Regarding FRTP laminates specifically, the three-phase response illustrated in Figure 2.12 still applies, since it is the fibres that constrain the kinematics of shear deformation [148]. The matrix, does however, have a significant impact on the forces required for this shear deformation to take place [149]. This is because, as highlighted above, it is the friction between individual tows, followed by tow compression, that dictate the forces required for shearing. Since the presence of a molten matrix influences both of these properties, it therefore impacts the global shear behaviour [149]. In previous literature it was found that both higher temperatures and lower shear-rates reduce the forces and shear moments required for a given level of shear deformation [150-159]. This is due to the increased resin viscosity at lower temperatures, inhibiting the rotation of individual tows. While the resin viscosity actually decreases at higher shear-rates due to the ‘shear-thinning’ effect, the ‘elastic’ characteristics of the viscoelastic resin become increasingly significant, resulting in this aforementioned increase in shear force [160].

2.4.2 In-Plane Tension

In-plane tension refers to that parallel to the tow direction, leading to tow redistribution and de-crimping [161]. The axial tensile stiffness in each fibre direction is typically

much greater than the stiffness associated with other deformation modes, such as bending and shear [143]. Although the formability of a fabric is not directly influenced by the axial elongation of the fibres, many studies report that the tensile loads applied along the fibre directions contribute substantially to the strain energy during forming [59, 161]. Areas of high tensile stress have been shown to correlate with fabric bridging [50].

The tensile behaviour of woven fabrics arises from the structural deformation associated with straightening the undulating tows, resulting in a small amount of in-plane strain [143, 162]. Figure 2.13a illustrates the influence of in-plane tensile forces on the fabric geometry [143]. The ‘de-crimping’ often results in a nonlinear force-strain relationship in the warp or weft directions under small loads, as per Figure 2.13b [59, 144]. This depends on the degree of initial tow crimp; higher crimp levels require greater tensile strains to eliminate the undulation. Once the tows are fully stretched at larger strains, the modulus becomes linear, as also visible on Figure 2.13b [144]. Additionally, the tensile behaviour is influenced in a biaxial manner, as the crimp in the tows decreases when the transverse yarns straighten [162]. In woven fabrics, in-plane tension within the tows can induce transverse compression on adjacent tows, thereby increasing the frictional forces between fibres. Consequently, the fabric demonstrates greater in-plane shear resistance (Section 2.4.1) when the tows are under tension [163]. In terms of compression, fabric materials generally exhibit very low resistance, such that a compressive force often leads to fibre buckling [164].

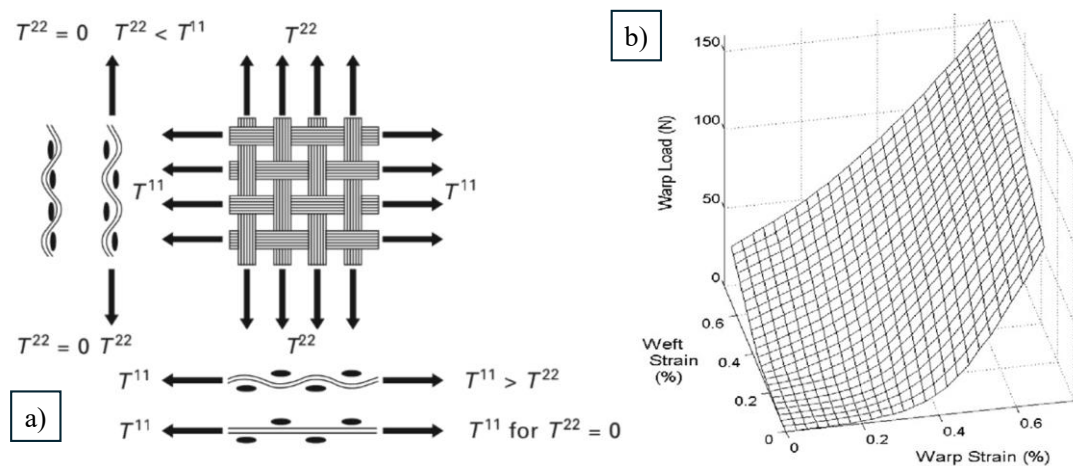


Figure 2.13: a) Influence of in-plane tension on fabric geometry [143], b) force *versus* (bi-directional) strain of a woven fabric [144].

2.4.3 Out-of-Plane Bending

The out-of-plane bending behaviour of fabrics is a crucial deformation mechanism for shaping curved geometries without causing fibre damage [165]. The bending stiffness of a fabric material is much lower than the high in-plane stiffness due to the relative sliding of tows [166, 167]. Because of this, it was originally overlooked as being an important deformation to consider during fabric forming [143, 161]. It has been shown, however, that fabric bending stiffness is highly influential on wrinkle formation (Section 2.6.1) [168]. Due to the symmetry of a balanced woven fabric about this mid-plane, the bending stiffness does not exhibit directionality, as per in Figure 2.14 [46].

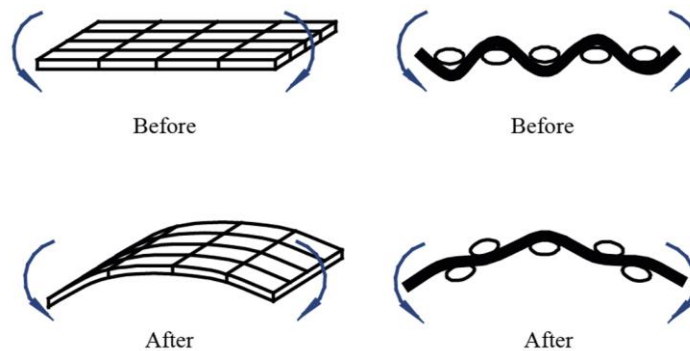


Figure 2.14: Out-of-plane bending mechanism for a balanced woven fabric [46].

Due to the vast discrepancy between the bending and in-plane stiffness, the traditional Bernoulli-Euler beam theory is inadequate for accurately describing the bending behaviour of woven fabrics [169]. This is compounded by the nonlinear bending stiffness that is often exhibited upon analysis of fabric bending behaviour [44, 170-173]. Typically, fabrics demonstrate a high bending stiffness at very small curvatures, however as the degree of bend increases, a significant nonlinear drop in fabric bending stiffness is common due to tow slippage. Figure 2.15a illustrates this nonlinearity, noting that the bending moment is the integral of the bending stiffness, hence verifying the aforementioned drop in bending stiffness with increased curvature [170, 171].

Regarding multi-ply bending, woven fabrics do not simply exhibit a proportional relationship between the number of fabric plies and the overall bending stiffness. This was illustrated by Liang *et al.* [174], where a significant ‘friction moment’ was defined as the difference between the actual multi-ply bending stiffness, and simple

interpolation from single-ply data (Figure 2.15b). This shows that inter-ply friction (Section 2.4.4) is intrinsic to a multi-ply laminates out-of-plane bending behaviour [175]. Hysteresis has also been shown to occur upon un-loading of fabrics due to the dissipation of energy through friction between individual fibres and tows [176, 177]. This only influences repeated loading and unloading behaviour, and so does not influence conventional monotonic forming techniques (Section 2.3) [178].

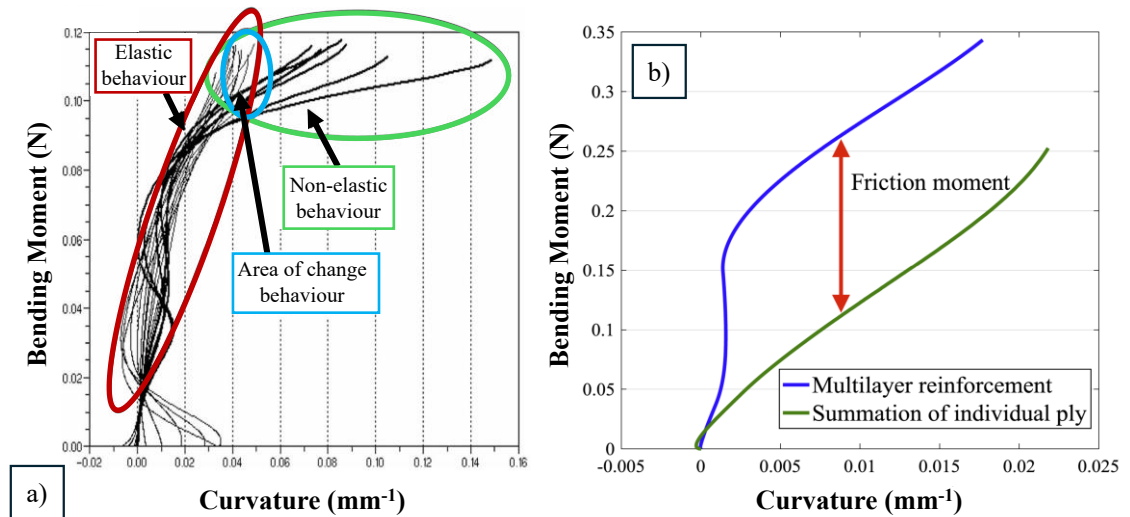


Figure 2.15: a) Typical nonlinear bending curves for a woven fabric [171], b) difference between the experimental bending moment of a multi-ply fabric and to the sum of the individual parts [174].

Regarding FRTPs specifically, the same nonlinear behaviour is reported as per dry fabrics due to the high stiffness of the fibres compared to the matrix, thus constraining the kinematic response [179]. The viscoelastic matrix does, however, dominate the *magnitude* of the forces governing the bending response [180]. It has been shown that the bending of an FRTP laminate is heavily influenced by laminate temperature [180-187], where an increase in temperature reduces the bending stiffness. Furthermore, an increased bending rate has also been shown to increase a laminate's bending stiffness [179, 180, 183, 184, 188].

2.4.4 Friction

Friction behaviour is a crucial mechanism in any forming process, by virtue of the inextensible fibres necessitating a large degree of material draw-in for mould conformity to be achieved [142]. This draw-in process inevitably involves a frictive

interaction between the laminate and tool (or diaphragm in the DDF process), denoted ‘tool-ply slip’, opposing the relative motion of the laminate. Furthermore, for multiply laminates, the process of laminate out-of-plane bending (Section 2.5.3) involves slippage between individual plies, denoted ‘inter-ply slip’, to significantly reduce the bending stiffness and allow draping to occur [175]. Both these interactions, specifically regarding the frictional forces associated with them, play a key part in the FRTP forming process.

Unlike the other detailed deformation mechanisms, namely; in-plane shear (Section 2.4.1), in-plane tension (Section 2.4.2) and out-of-plane bending (Section 2.4.3), the friction behaviour for FRTPs does not follow the behaviour that would be experienced by dry fabrics [148, 189]. For all other mechanisms, the rigid fibres dictate the kinematics of each deformation process, with the molten thermoplastic resin, in the case of in-plane shear and out-of-plane bending, influencing just the magnitude of the forces associated with the respective deformation [179]. Friction, however, is an interaction between two separate entities, therefore meaning that the kinematics of the frictional process are not constrained by the fibres. It is therefore important to consider only FRTP frictional processes relevant to this work and not those associated with dry or commingled fabrics that exhibit inherently different characteristics.

For FRTPs, it is often assumed that the interface (either tool-ply or inter-ply) consists of a thin resin-rich layer, such that the fibre properties have little influence on the friction forces. Assuming that this viscous layer is what governs the respective friction coefficients [142], the Stribeck curve, illustrated in Figure 2.16, provides a good approximation of the interfacial behaviour, as shown by Chow [190]. The curve illustrates how the laminate coefficient of friction, μ , is dependent on the matrix viscosity, η , sliding velocity, v , and sliding pressure, P . These variables can be related to each other with the Hersey number, H , where [191]:

$$H = \frac{\eta v}{P} \quad (2.1)$$

The Stribeck curve illustrates three distinct lubrication regimes [192, 193]. Under very high pressures or low slip rates and viscosities, the boundary lubrication regime is observed. In this regime, the resin film provides minimal support, leading to significant frictional forces due to direct interactions between the tool surface and the fabric

reinforcement. As the mixed lubrication regime is approached, an increasing proportion of the load is borne by the resin. This results in a marked reduction in the coefficient of friction as tool-ply interactions become less prominent. At sufficiently high Hersey numbers, the lubrication transitions to the hydrodynamic regime, where the applied load is entirely supported by the hydrodynamic pressure within the resin film separating two interfaces. Regarding FRTPs, both tool-ply and inter-ply behaviour have been shown to exist in the hydrodynamic regime [194-197], with little-to-no contact made between the reinforcement and the adjacent tool/reinforcement layer. A limited number of studies suggest that the mixed-lubrication regime can also apply if the normal pressure is sufficiently high [157, 198, 199].

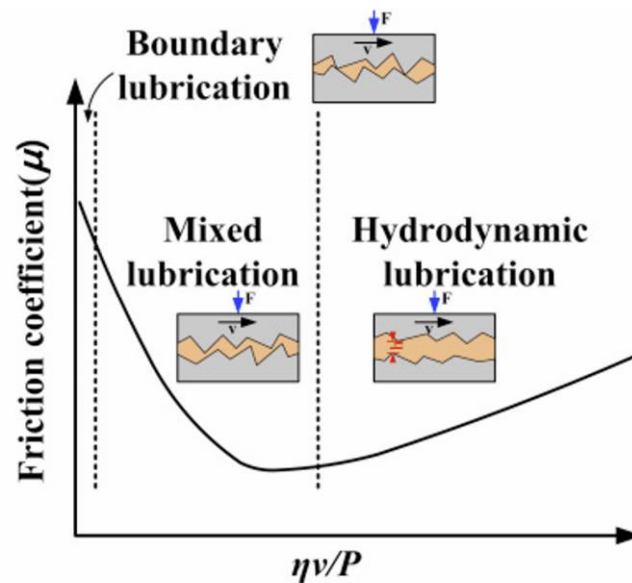


Figure 2.16: Variation in coefficient of friction with Hersey number, known as the Stribeck curve [199].

Considering the Hersey-number-dependent layer between both tool-ply and inter-ply interfaces, several factors influence the coefficient of friction (CoF), including: normal pressure [194, 195, 200-205], draw velocity [194, 195, 200-205], tool material [194], tool temperature [194, 195, 200-205], fabric temperature before forming [198, 200, 205], fabric orientation [194, 198, 200, 205-207] and cooling conditions [157]. Of these different factors, pressure, velocity and temperature characteristics are the most influential [198, 200, 205]. With the predominant mode of friction in previous works is shown to be that within the hydrodynamic regime [194-197], an increase in laminate

temperature and pressure usually results in a drop in the CoF, with a reduction in slip-rate also resulting in a fall in the CoF [196, 208].

Force *versus* displacement data produced by constant displacement rate tests (Section 2.5.4) typically follow a generic form. This can be characterised by an initial peak force that rapidly falls to a lower steady-state value, irrespective of the material under consideration [189, 206]. Thus, two friction coefficients can usually be determined corresponding to a peak (static) and steady-state (dynamic) response. Possible reasons for the initial static peak were investigated by Pierik *et al.* [209], who detailed that nonlinear viscoelastic behaviour and a slip relaxation effect leading to wall slip were possibilities. This static behaviour is, however, often neglected when it comes to implementation within numerical models (Section 2.7) [209]. It is not clear how valid this assumption is, especially considering that the slip-distances involved with typical inter-ply interfaces are small [189, 210].

2.5 Fabric Behaviour Characterisation

In Section 2.4, the different deformation mechanisms that allow a FRTP laminate to conform to a mould geometry (with the processes outlined in Section 2.3) were introduced. These mechanisms play a significant part in the draping process, including the prediction of forming-induced defects, as discussed in Section 2.6 [161]. It is therefore crucial that accurate characterisation exercises are conducted to acquire material data, specific to an FRTP laminate [141]. Only a small sample of these test methods have been standardised, thus necessitating careful consideration of the experimental material data [163].

These data can be subsequently used within numerical models to predict the forming behaviour of a FRTP laminate, as opposed to costly trial-and-error methods [141, 165]. Furthermore, with a range of FRTP mechanical properties known after completion of such numerical models, such as fibre angles, degree of crystallinity and cooling rates, these can be used downstream for other purposes such as structural analyses of the final part, warping predictions and so on.

In this section, characterisation exercises applicable to the four key deformation mechanisms outlined in Section 2.4, namely, in-plane shear, in-plane tension, out-of-plane bending and friction (tool-ply and inter-ply), are outlined with a specific focus on FRTP characterisation.

2.5.1 In-Plane Shear

The two most common approaches adopted to evaluate FRTP laminate intra-ply shearing are the picture frame test (PFT) and bias extension test (BET) [155].

The PFT describes the in-plane shearing of a laminate when a tensile force is applied across its opposing corners after being mounted within a bespoke frame. The frame itself is supported at its lower vertex, with the upper vertex connected to a universal testing machine to drive the 4-bar linkage displacing it into a rhomboid, as per Figure 2.17a [150-156, 211]. With the cruciform shaped laminate mounted such that the primary tows are aligned with the frame edge, this motion results in in-plane shearing. For FRTPs, the frame is usually mounted inside an environmental chamber such that a pre-defined laminate temperature can be obtained. The crosshead force is measured using a load cell, while its displacement is captured by a displacement sensor. The shear deformation of the fabric specimen is determined by analysing the changes in the picture frame geometry through trigonometric relationships; achieved using either the crosshead displacement data or by optically assessing the yarn orientation [163]. Multiple runs of the PFT without a specimen are necessary to measure the crosshead force, which accounts for the weight and inertia of the frame during testing. This force must be subtracted from the crosshead force recorded with loaded samples to determine the shear force [212]. Finally, a normalisation procedure must follow to eliminate the influence of specimen dimensions on the recorded force response [163, 213, 214].

On the contrary, the BET involves clamping a rectangular piece of woven or cross-ply material with the yarns originally oriented at $\pm 45^\circ$ to the applied tensile force [155, 156, 158, 159, 163, 215-218]. As per the PFT, the whole fixture is mounted within a universal testing machine, with an environmental chamber commonly used to heat the FRTP specimen. The fibrous nature of a woven FRTP laminate leads to three distinct shear zones during the bias extension test: A, B and C [155], as illustrated in Figure

2.27b. Zone A consists of a region of undeformed material, hence the shear angle, $\gamma = 0$. Zone C is the region of particular interest, where pure-shear is enacted on the specimen due to both weft and warp yarns having free ends. Zone B is a region in which one yarn direction is clamped at its end, therefore exhibiting a shear strain approximately half that of zone C. An aspect ratio of at least 2.5 is recommended in the literature [218, 219] to increase the homogeneity of the distribution of shear deformation in the sample. Unlike the PFT, simple trigonometric relations cannot be used to determine the instantaneous shear angle due to the inhomogeneous deformation field. Instead, the shear angle in zone C can be determined optically, or using pre-determined shear angle relations (*versus* axial displacement) such as that by Lebrun *et al.* [156].

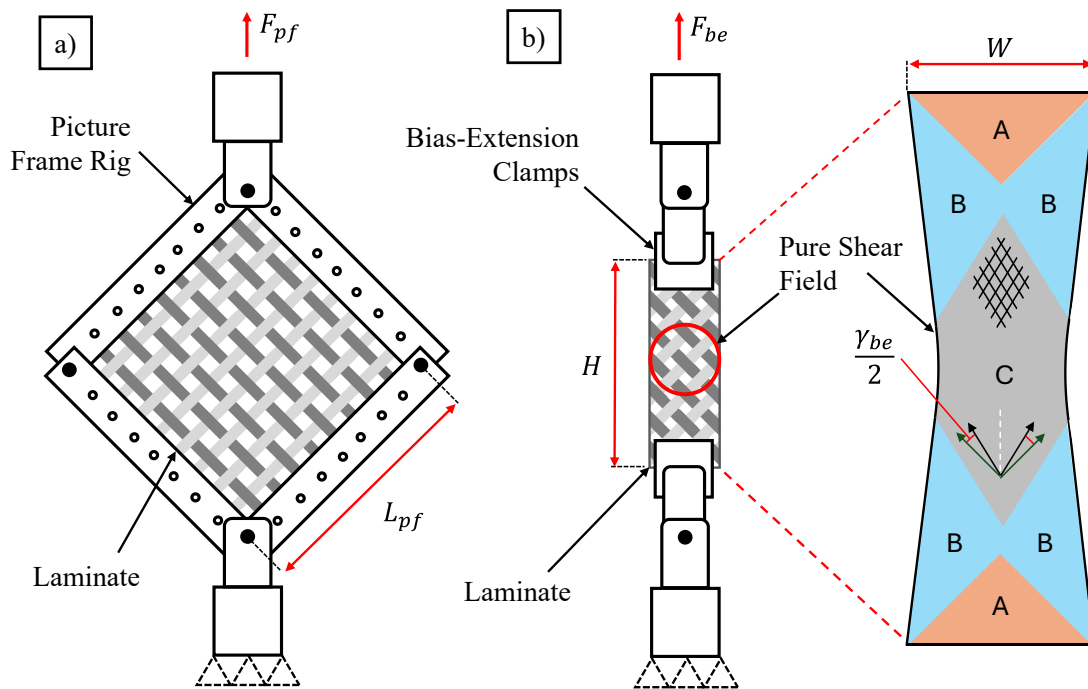


Figure 2.17: a) PFT apparatus, b) BET apparatus and three individual shear zones.

Both methods are capable at conducting FRTP intra-ply shear characterisation, however they both have inherent characteristics that influence their applicability based upon the shear kinematics involved [155, 163]. In the PFT, the shear field is homogeneous, plus the inexpensive trigonometric analysis simplifies the calculation of an accurate instantaneous shear angle. However, the PFT inadvertently introduces tension in the yarns which can affect the cross-head force during the test, thus resulting in reduced repeatability [220]. To address this, it is crucial to ensure precise alignment

of the specimen within the rig and to apply suitable clamping conditions at the boundaries [213]. Moreover, specifically related to FRTPs, the PFT can be susceptible to the heat transfer associated with the clamps that may exhibit a cooler temperature than the rest of the chamber (when using an environmental chamber [156, 211]). Furthermore, since PFT specimens are generally larger, maintaining an even temperature over the entire specimen is not trivial [150].

These issues are generally mitigated with the BET, since the clamped edges (at region A) do not deform, such that the effect of heat transfer into the clamps is minimal [155]. Furthermore, the specimens are skinnier than the PFT samples, and without the need for a custom made 4-bar linkage, can generally be of any size (obeying the aspect-ratio requirements and the unit cell size). This makes it easier to achieve uniform sample heating. Another advantage related to the clamping is that since the sheared region is away from the clamps, specimen alignment is less significant in the BET than the PFT [221]. This can often lead to improved specimen repeatability owing to a reduction in the error associated with the clamping operation. The disadvantages of the BET revolve around the inhomogeneous shear angles over the specimen, complicating the procedure of accurate shear angle calculation [222]. Furthermore, in the area of pure-shear (region C), the yarns are free at both ends, resulting in a degree of intra-ply slip where tow displacement occurs alongside the initial tow rotation [155]. This can significantly reduce the accuracy of results, typically after a shear angle of approximately 45° is exceeded. Finally, it has also been shown that wrinkling and initial specimen shear can significantly degrade the test accuracy [223, 224].

2.5.2 In-Plane Tension

Tensile testing of composite fabrics is typically performed under either uniaxial (see ASTM D5034 [225]) or biaxial loading conditions [226]. In a uniaxial tensile test, fabric samples, aligned with one of the tow directions, are clamped at both ends. A displacement is applied to the sample, commonly using a universal testing machine, and the corresponding load is measured. Similarly, a biaxial test involves clamping both tow directions at both ends such that all reinforcement is constrained. Figure 2.18 illustrates a biaxial tensile test, in this case for a dry NCF material [176].

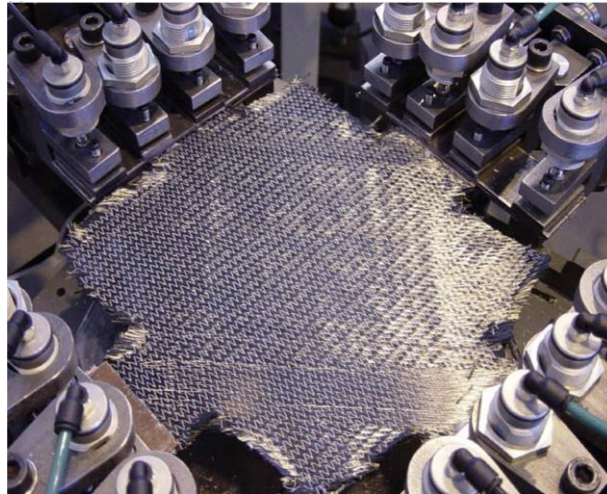


Figure 2.18: In-plane biaxial tensile testing of a dry NCF material [176].

Biaxial testing is particularly advantageous for woven fabrics as the nonlinear stiffening caused by yarn de-crimping under uniaxial loading can influence the tensile behaviour in the secondary fibre direction (Section 2.4.2) [162, 227]. Tensile loads are applied simultaneously in both directions, and the fabric's response is recorded to develop a “tension surface” that characterises its behaviour. To comprehensively understand the material's response under tensile loading, the ratio of the applied loads can be varied, allowing for the evaluation of any asymmetry in the fabric architecture. Figure 2.13b illustrates one of these tension surfaces [144].

For FRTPs, burn-off operations can be completed to remove the resin entirely (since the molten matrix has little influence on the in-plane tensile properties) to complete the testing, or, as per the work of Dangora *et al.* [185] heating elements can be used to heat the matrix up to the desired testing temperature.

2.5.3 Out-of-Plane Bending

The aim of an out-of-plane bending test for a woven fibre reinforced material is to determine the relationship between the curvature and bending moment [228]. These tests can be categorised into four different methods [161]: Peirce cantilever tests [186, 229] (see BS EN ISO 9073-7:1998 [230], ISO 4604:2011 [231], ASTM D1388-18 [232]), extended cantilever bending tests [171, 172, 185, 186, 233-235], Kawabata bending tests [176, 181-183, 236] and three-point-bending tests [179, 184, 187, 237, 238]. Figure 2.19 illustrates these four testing techniques, with their principal of

operation outlined in detail below. The choice between individual methods depends on the type of fibrous material being used, the accuracy of results required and the experimental efficiency desired.

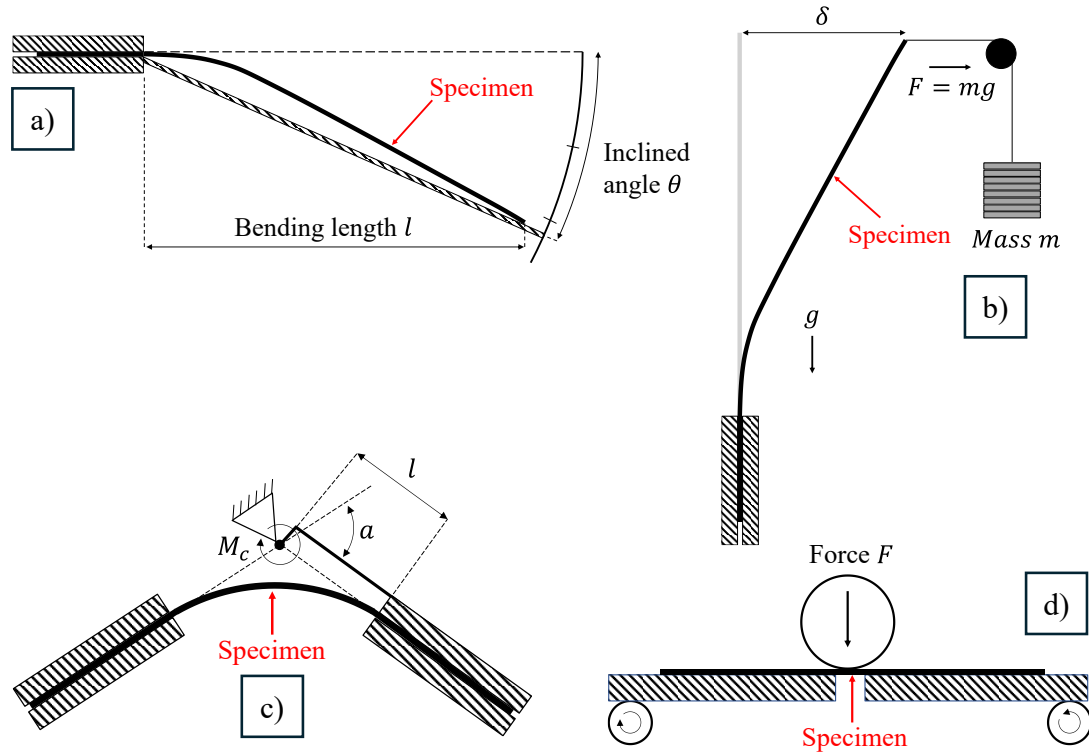


Figure 2.19: Different tests for out-of-plane bending characterisation. a) Peirce cantilever bending tests, b) Extended cantilever bending tests, c) Kawabata bending tests, d) Three-point-bending tests.

The cantilever bending test is arguably the simplest of all the bending tests and is widely used for characterising the bending behaviour of cloths and fabrics. Figure 2.19a illustrates a typical setup for the conventional cantilever test. In this method, the fabric specimen bends under its own weight and has its overhang length adjusted until its tip reaches a predefined deflection angle relative to the platform [229]. The bending stiffness is calculated based on the specimen overhang and the measured deflection angle. While straightforward to perform, this method provides only a single, constant value for bending stiffness, representing the fabrics overall bending behaviour. Some modifications have been made to capture nonlinear material behaviour, such as by Clapp *et al.* [239] who optically monitored the bending profile, followed by numerical analysis to obtain the bending moment and curvature at discrete points along it. Furthermore, as per the extended cantilever tests (Figure 2.19b), it was proposed that

the specimen be mounted vertically with weights to induce the bending force [233]. The benefit of this method was elimination of twist and greater control of the specimen bending. While these advancements have improved the cantilever test, the accuracy is heavily dependent on that of the optical measurement, which may induce a significant parallax error. 3D scanning of the cantilever profiles is one way to improve the resolution of the bending profile and eliminate twist from the acquired results [170]. For FRTPs, the cantilever test is more rare due to the heating requirement and the lack of precise control on the laminate bending profile. Only Liang *et al.* [186] have attempted to use this method for temperature-dependent bending analysis, where the cantilever apparatus was placed within an environmental chamber. The authors did not attempt, however, to analyse the rate-dependent properties of the FRTP due to the constraints imposed by the cantilever method.

The Kawabata bending test, part of the Kawabata Evaluation System (KES), is the most commonly used technique for characterising the bending behaviour of FRTPs specifically. As depicted in Figure 2.19c, the specimen is secured between a fixed clamp and a movable clamp. The movable clamp follows a circular path, inducing a constant curvature along the length of the specimen [236]. Since the sample is exposed to homogeneous curvature, the bending moment-curvature relationship can be interpreted directly [171, 176]. Furthermore, since the curvature is controlled in this test, the curvature-rate can also be controlled, one of the variables that influences an FRTP's bending stiffness (Section 2.4.3) [181, 182]. Sachs *et al.* [183] manufactured a fixture such that the test could be conducted within a rheometer, allowing for the viscoelastic bending behaviour of an FRTP to be acquired. This does, however, necessitate the acquisition or manufacture of a non-standard clamping arrangement.

The three-point bending test, as illustrated in Figure 2.19d, describes a composite specimen supported at two points while a load is applied at the midpoint. It is commonly used for thick fabric reinforcements of prepregs with a relatively high bending stiffness, or for assessing the structural performance and failure behaviour of composite laminates under flexural loads [184, 238]. It is less applicable to thin or unreinforced composite layups as it is easily influenced by gravity loading. Therefore, it is not considered in this work.

2.5.4 Friction

As detailed in Section 2.4.4, the mechanisms of friction for FRTPs are very different to those of dry fabrics due to the interfacial layer of viscous matrix that drives the friction characteristics between two bodies. In contrast, the characterisation techniques that can be employed for friction are generally compatible with both dry fabrics and FRTPs, so long as the heating requirement for FRTPs is fulfilled. Furthermore, both tool-ply and inter-ply friction characterisation can be conducted using identical techniques, so long as the material is changed such as to replicate the interface in question. The aim of friction testing (both inter-ply and tool-ply) is to determine the CoF, μ , between two surfaces, since the CoF is directly proportional to the tangential (frictional) force, F_T , using the following equation:

$$F_T = \mu \cdot F_N \quad (2.2)$$

Where F_N is the normal force.

Published works concerning FRTP friction characterisation are almost exclusively limited to the use of different variants of the pull-out friction test. Other methods such as the friction sled test [194] and rheometer [202, 240] have also been used, but are not considered in this work as it is difficult to replicate real-world forming conditions with these methods. The pull-out test used in previous literature and described below is based upon ASTM Standard D 1894 [241], however this standard details tests conducted at laboratory conditions and is therefore modified for FRTP friction characterisation. In the pull-out test, a laminate (inter-ply) or tool material (tool-ply) specimen is sandwiched between two other laminate plies, held together by a controlled normal pressure [195]. The sandwiched specimen is then ‘pulled-out’ from between the two adjacent laminates, with the measured force corresponding to the tool-ply or inter-ply frictional force. Considering FRTPs, this test was first outlined by Scherer and Friedrich [207], but has since been utilised in a large array of works [157, 194, 195, 197, 201, 203, 206, 208, 209, 242-244]. Commonly, heating is achieved by heating the platens that apply the normal pressure, however it is also applicable to conduct the test within an environmental chamber. Figure 2.20 illustrates a schematic of the apparatus for a typical (tool-ply) pull-out test [195].

During the pull-out test, the contact area decreases as the movable specimen is pulled out from between the fixed laminates, resulting in an increase in contact pressure [244]. This must therefore be accounted for either during the test by reducing the clamping force, or during post-processing, however the latter method induces errors due to the pressure-dependent CoF attributed to FRTPs. Wilks [245] proposed an evolution of the pull-out test, namely the pull-through test, to eliminate the change in contact area during the test. This alternative technique has also been used extensively for FRTP friction characterisation [198, 200, 204, 205, 218]. In this test, the specimen being pulled through is lengthened such that it extends beyond the opposite edge of the friction apparatus. This means excess material enters the pressure-plates just as material is pulled-out at the front edge. The drawback with using this method, however, is edge effects associated with the leading edge of the pull-through apparatus. Furthermore, care is required to ensure the excess material is heated adequately before entering between the pressure plates.

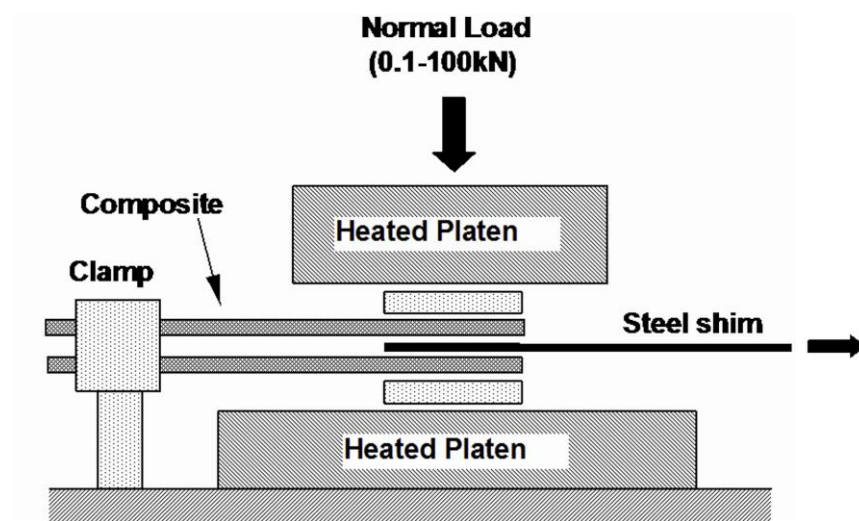


Figure 2.20: Typical apparatus for a (tool-ply) pull-out friction test [195].

2.6 FRTP Forming Defects

Defects arise during forming operations by virtue of the large deformations occurring, coupled with various constraints imposed by the process and the material type [246]. The forces and constraints associated with different forming processes (Section 2.3) are different, meaning the growth and type of defects varies considerably between each [50]. Since this work is focussed on diaphragm forming, which represents lower

forming forces than that of matched-tool equivalents [35], only defects specific to diaphragm forming are considered. Due to the lack of a rigid out-of-plane constraint in the diaphragm forming process, out-of-plane (macroscale) defects, namely; wrinkling and bridging, dominate [41, 133, 247]. Furthermore, since this work concerns pre-impregnated FRTP organosheets, deconsolidation can also occur [248]. All these defects can have a significant impact on the quality, both in terms of aesthetics and performance, of the final component [249]. Wrinkling, for example, can lead to a considerable reduction (up to 40% [250]) in the localised strength of a composite part due to the out-of-plane fibre direction, no longer acting in a load-bearing manner [250]. These defects are intrinsically linked to deformation mechanisms outlined in Section 2.4, and are analysed in-turn in this section.

2.6.1 Wrinkling

Arguably the most common macroscale defect present, not just in the diaphragm forming process, but all fabric forming processes, is out-of-plane wrinkling [251]. Sjölander *et al.* [252] proposed that wrinkling can arise either from global in-plane compressive stress applied to the entire laminate or from a single ply experiencing compression along the fibre direction, which can subsequently propagate and induce wrinkling throughout the stack. In both scenarios, compressive stress is recognised as the underlying cause of wrinkling. The onset of these stresses does not have a single definitive cause and can generally originate from two primary factors:

- Local in-plane shear and compressive stresses increase with the shear angle [117], which is frequently used as an indicator of macroscale wrinkle initiation [161]. As the localised shear force increases, these stresses are redistributed, causing the fabric to wrinkle out-of-plane in a region referred to as “over-shear”.
- High coefficients of friction, both between plies and between the tool/diaphragm and ply, have been shown to create localised compressive strains, forcing the material to bend out of plane [42, 252-254]. Reducing friction in these cases was observed to enhance the formability of the fabric.

Wrinkling of a FRTP by means of these two primary factors is illustrated in Figure 2.21.

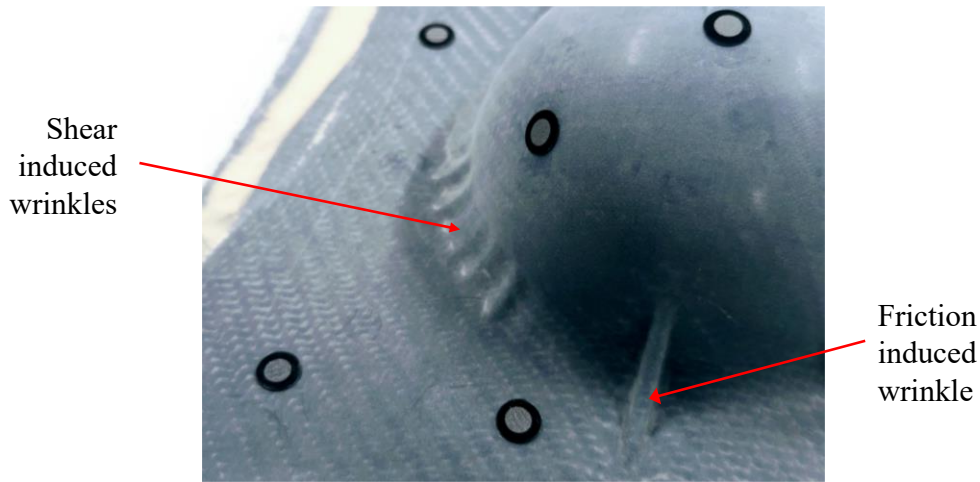


Figure 2.21: F RTP wrinkling over a double-curvature geometry.

The bending stiffness plays a critical role in determining the amplitude and wavelength of macroscale wrinkles [186]. This highlights the importance of accurate bending characterisation for predicting ply folds. Considering this, alongside the shear and friction dependent wrinkling behaviour outlined above, all three of these deformation mechanisms are coupled and require accurate characterisation for accurate wrinkling prediction. The severity of wrinkles can also be influenced by processing parameters, such as tool geometry [255, 256]. This suggests that material parameters alone, such as shear angle, may not always suffice for accurate prediction of out-of-plane wrinkles.

2.6.2 Bridging

Fabric bridging is a common phenomenon observed during the diaphragm forming process, particularly when dealing with complex geometries or sharp curvatures [41]. This is a defect specific to diaphragm forming since a rigid tool in the matched-tool process provides the forming force required to overcome it, although this can induce other defects such as fibre tearing [111]. Bridging occurs when the fabric reinforcement fails to conform fully to the tool surface, resulting in voids or gaps between the fabric and the tool [50]. This non-conformance is typically caused by insufficient slippage between the diaphragm and the laminate, or insufficient slippage between individual plies, thus increasing the stiffness of the laminate [117]. This therefore resists the bending deformation required to drape over intricate features. Bridging is therefore attributed to tension in individual fibres, as opposed to wrinkling (Section 2.6.1) which occurs as a result of compression. These tensile forces, however,

can result in compressive strains perpendicular to the bridging path [50], causing wrinkles, such that the two may be linked. Figure 2.22 illustrates a cross section of a typical bridging defect during a DDF process [257].

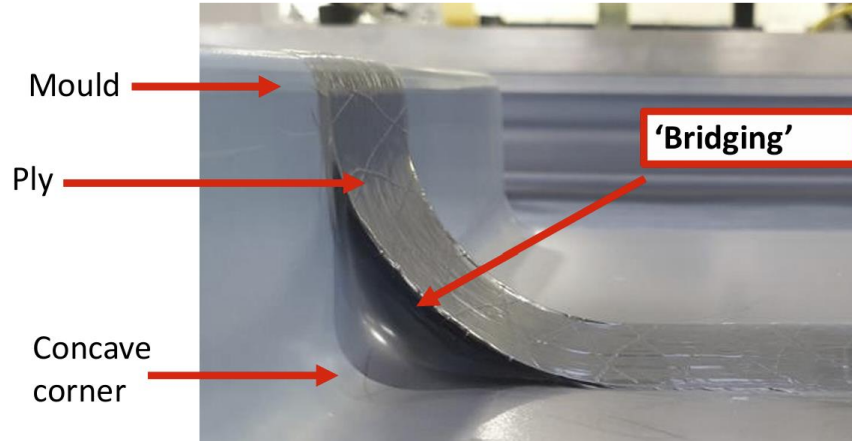


Figure 2.22: Laminite bridging cross-section at a concave tool edge [257].

Bridging is influenced by factors such as the fabrics architecture, thickness, and stiffness, as well as the forming pressure and mould complexity [50, 124, 133, 247, 256]. Since, as per the deformation modes outlined in Section 2.4, it is expected that laminate bending and frictional forces increase at lower temperatures, the degree of bridging is dependent on the forming conditions [133]. Bridging often means that the desired tool geometry has not been achieved, potentially resulting in part rejection. The mechanical performance and structural integrity of the final composite part may also be compromised with bridging. Mitigation strategies include changing the FRTP forming parameters (temperatures, speeds) [247], optimising the blank shape [50] or modifying (simplifying) the tool geometry.

2.6.3 Deconsolidation

As noted in Section 2.3, this work focuses on the use of pre-consolidated FRTP organosheets, as opposed to dry equivalents such as commingled fabrics. Because of this, a degree of concern regarding resin flow is removed during processing, since the fibres are already fully wetted out [109]. This means that during processing, time does not have to be given to allow resin flow to take place through the material, as would be the case in resin transfer moulding (RTM) for dry fabrics or processing with commingled fabrics [107]. While the sheets are pre-consolidated however, it is highly

likely that the deconsolidation phenomenon occurs after the FRTP sheet is heated above the melting temperature, as is required for forming to take place [248].

Deconsolidation refers to the formation and expansion of pores after heating a pre-consolidated FRTP laminates above the processing temperature (melt temperature for semi-crystalline polymers). This results in a physical change in the FRTP sheet geometry, usually via an increase in laminate thickness [258]. This phenomenon occurs when a pre-consolidated laminate is heated under little or no applied pressure, resulting in undesirable pores or delaminations [248]. There are many published studies that aimed to deduce the exact cause of the deconsolidation phenomenon. For woven laminates, deconsolidation has largely been attributed to the release of residual stresses (crimp relaxation) that are fixed into the laminate when it is compacted during manufacture [259-264]. A range of other studies, however, have suggested that deconsolidation is attributed to moisture-diffusion, especially for highly hygroscopic thermoplastic polymers such as polyamides [265-268]. This can also occur in thermoset composites during curing [269, 270]. It is highly likely that both the release of residual stresses and moisture-diffusion play a part in the magnitude of deconsolidation [264]. Figure 2.23 illustrates the deconsolidation of UD CF/PEEK laminates after heating, with the increase in laminate thickness and development of voids prominent [266].

Deconsolidation is important to consider; for example, numerous studies have shown that pores significantly impair a composite's mechanical properties, including shear stiffness and strength, compressive strength, transverse tensile strength, interlaminar shear strength, flexural strength, and fatigue resistance [248, 271, 272]. Henninger *et al.* [248], for example, found that for a GF/PA-12 composite sheet, an increase in void content from 1% to 12% results in approximately a 20% reduction in both the flexural strength and Young's modulus. Furthermore, deconsolidation results in areas of FRTP laminate that may not be fully wetted out, impairing both the aesthetics of the final part and potentially exposing the reinforcing fibres to environmental damage. This would not occur if the laminate were fully consolidated [273].

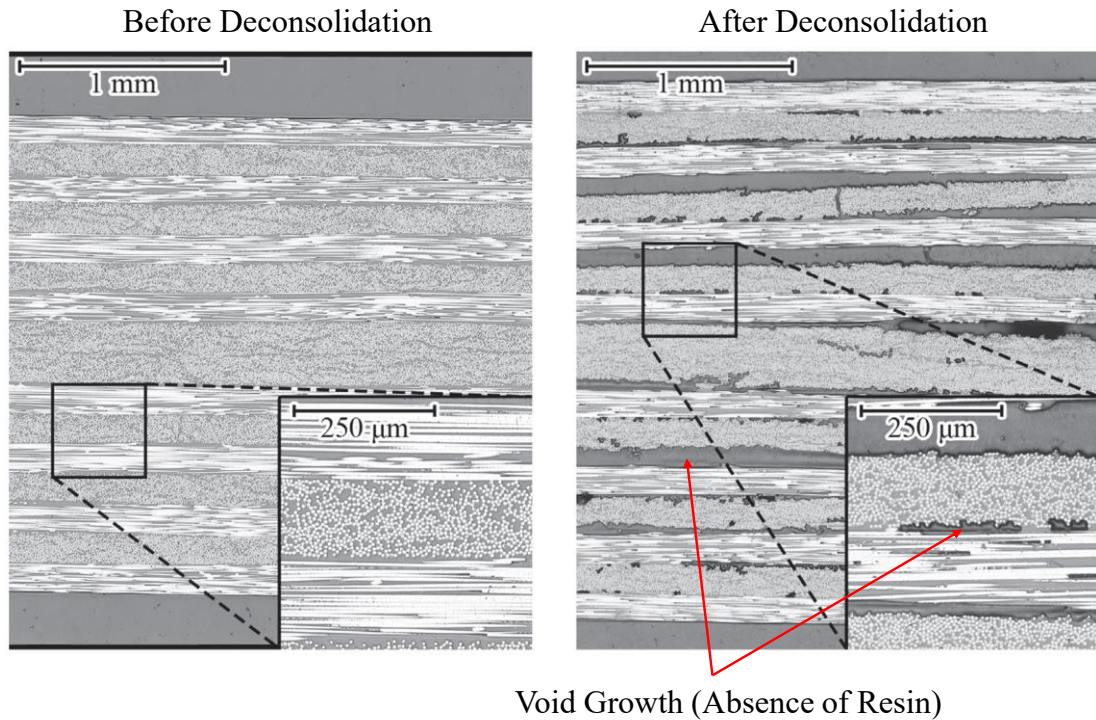


Figure 2.23: Deconsolidation of UD CF/PEEK laminates after heating [266].

The mitigation procedure for deconsolidation is a ‘reconsolidation pressure’ acting normal to the deconsolidation direction [259]. Ye *et al.* [260] determined an equation for the critical reconsolidation pressure, the pressure required for complete reconsolidation to take place. In this work, a plain-weave and 5-harness satin weave exhibited critical reconsolidation pressures of 0.28 MPa and 0.49 MPa respectively. This reconsolidation pressure can, however, cause squeezed creep flow of the matrix melt, with up to a 30% loss in localised matrix material [259]. After complete reconsolidation is achieved, further increases in compaction pressure result in squeeze-flow of resin in combination with compaction of the fibrous reinforcement [274, 275]. Due to the low forces associated with the diaphragm forming process (Section 2.3.2), this compaction and squeeze-flow behaviour is not relevant to this work. These phenomena are more commonplace with significantly (orders-of-magnitude) higher forming forces, such as those present in the matched-tool process.

2.7 Forming Simulation

Thus far in this literature review, the relevant FRTP materials and manufacturing processes have been explored along with the deformation (including characterisation)

modes for successful forming, with the subsequent defects that may occur by virtue of these deformations outlined. All of these subsections culminate in the simulation of forming to predict the behaviour of a FRTP laminate, as opposed to costly trial-and-error methods [141, 165]. Furthermore, FRTP forming simulation allows for process optimisation to be conducted, thus enhancing the specific forming process under consideration [276].

This section outlines firstly, the different approaches that can be used to simulate fabric deformation behaviour. This is followed by a specific analysis of process modelling, with matched-tool and diaphragm forming methods. Finally, the application specific for FRTPs is analysed, with the state-of-the-art in FRTP forming simulation presented, from simple isothermal models all the way through to advanced fully-coupled thermomechanical routines.

2.7.1 Simulation Approaches

Composite material forming is complicated by the heterogeneous behaviour that they exhibit [58]. Moreover, due to the expense of composite materials, trial-and-error manufacturing methods are costly and wasteful. Because of this, numerical approaches have gained popularity for predicting fabric behaviour. These numerical approaches can be broken down into two sub-categories [277]: kinematic models [278-283] and finite element models at different scales [168, 212, 284]. Both methods are outlined in detail below.

2.7.1.1 Kinematic Models

Kinematic forming simulations are based on geometrical mapping principles where the fabric is represented as a pin-jointed network of rigid bars that can deform only through shear at the crossover points [278]. Initially, two geodesic paths ('u' and 'v' yarns on Figure 2.24a) are defined as a starting framework, and the remaining yarns are then mapped onto the tool surface using 'mapping methods' [285]. A widely used mapping method is the fishnet algorithm [286], which operates very quickly but assumes yarn paths between nodes to be straight lines, leading to reduced accuracy. Figure 2.24 illustrates the kinematic draping process [280].

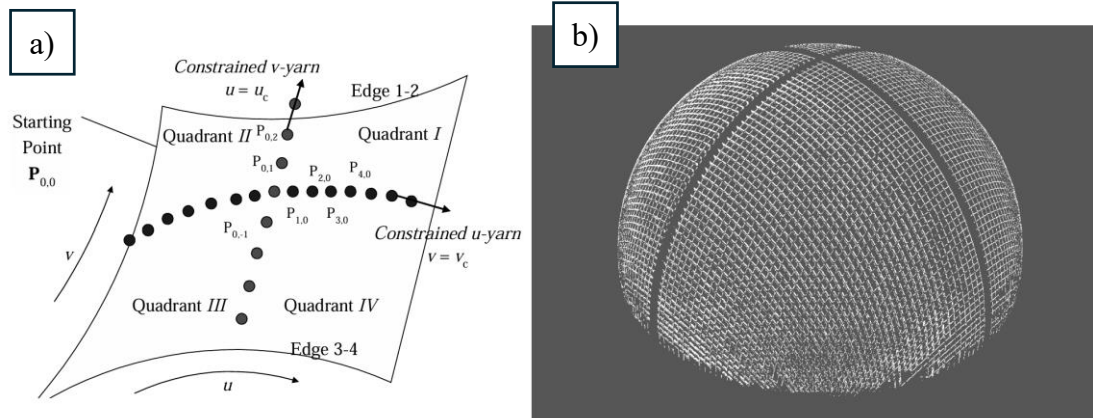


Figure 2.24: Kinematic draping algorithm. a) initial constrained yarns, b) draping over a hemispherical tool [280].

Kinematic forming simulations offer a rapid means of indicating geometric drapability but operate with a range of assumptions to simplify deformation, including [278, 287]:

1. Inextensible fibres
2. Free rotation between warp and weft yarns
3. No tool-fabric sliding
4. Forming loads and boundary conditions neglected
5. No material properties assigned (such as bending stiffness)

These analyses assess the formability of fabrics relative to a specific tool geometry by comparing the local shear angle to the experimentally determined shear locking angle. They are considered a relatively inexpensive method for modelling fabric draping behaviour [58]. However, they do not account for the precise shape of defects or the forming loads required to deform the fabric. Additionally, with material properties and frictional forces disregarded, this can further reduce the accuracy of predicted shear angles, especially in multi-layered fabric plies [65]. Due to the limited accuracy of kinematic approaches when compared to finite element methods (Section 2.7.1.2), this method is not pursued further in this work.

2.7.1.2 Finite Element Models

With advancements in commercial computational power, the adoption of three-dimensional finite element (FE) models for simulating fabric draping and forming processes has become increasingly prevalent. FE methods offer a numerical approach

to solving physical problems by incorporating governing equations, such as equilibrium, constitutive relationships, and boundary conditions [59]. Although more computationally intensive compared to kinematic approaches, FE models offer the advantage of accounting for nonlinear effects arising from the anisotropic nature of fabrics. They can be used to simulate the tools, interactions, and frictional forces between components, as well as the mechanical behaviour of composites during the forming process [37].

FE simulations help determine the conditions that enable successful forming while also identifying potential defects, including wrinkles (Section 2.6.1) [284]. Moreover, FE methods provide detailed insights into the fibre orientation within the formed component, critical for understanding and optimising its mechanical performance [284]. The precision of these simulations largely depends on the accurate characterisation of the material behaviour and the boundary conditions involved in the forming process [288].

2.7.1.2.1 *Implicit versus Explicit FE Methods*

Fabric forming, being a quasi-static process, can be modelled using either implicit or explicit FE methods [218]. Implicit methods solve a system of nonlinear equations through direct integration, considering the entire time step at once [289]. This approach allows for larger time increments since it is not constrained by stability limits. However, implicit simulations can be computationally intensive due to the iterative solution process. Moreover, the complexities of fabric forming, such as large deformations, significant sliding, and frequent changes in contact conditions, often result in convergence challenges [290]. These issues are further compounded by the formation of wrinkles and fabric buckling, which make achieving equilibrium difficult [289]. Consequently, while implicit methods are effective for many scenarios, they are less suited to handling the complexities of fabric forming simulations [37].

In contrast, explicit finite element analyses use a forward Euler integration scheme to determine the deformation state at the end of a time increment by integrating the acceleration from the start of the increment [291, 292]. Unlike implicit methods, explicit solvers do not require iterative calculations to achieve force equilibrium within each time step, relying instead on an extrapolation-based approach. This characteristic

makes explicit methods less prone to convergence issues caused by contact changes or wrinkling instabilities [168]. While explicit methods are generally less precise and require small time increments (and therefore long solve times) for stability, their simplified and robust contact formulations allow them to handle scenarios where implicit solvers might fail to converge. This makes them particularly suitable for addressing the challenges of fabric forming simulations [37].

2.7.1.2.2 *FE Modelling Scales*

As illustrated in Figure 2.2, fibre reinforced materials exhibit a multi-scale, such that they can be analysed in the micro-, meso- or macroscopic regimes. The same multi-scale applies to FE models, which are denoted: continuous, discrete, semi-discrete or mesoscale models. While microscopic models constructed at the fibre-level do exist [293-295], the computational expense of such routines becomes great even for very small subjects, meaning their implementation remains impractical [37]. These models are therefore not discussed in this work. Figure 2.25 presents an overview of the key modelling scales [37], which are analysed in-turn below.

(1) Meso-scale methods

Mesoscale FE models [296-305] are widely used for simulating the behaviour of fabrics at the mesoscopic level, focusing on individual yarns and their interactions within the fabric structure [298]. These models operate in a detailed manner where yarn geometries are modelled explicitly using continuum elements, as per Figure 2.25c. This approach captures the discrete nature of yarns and allows for a detailed analysis of phenomena such as inter-ply sliding, yarn deformation, and contact interactions between yarns [299]. Mesoscale geometries can be created through various methods, including manual modelling of each yarn, reconstruction from CT scan data [298], or procedural generation using tools like TexGen [66]. These models are particularly effective for predicting material behaviours such as permeability [300, 306]. They are not usually used to simulate an entire forming process, however, due to the computational expense of modelling the complex inter-yarn interactions [307].

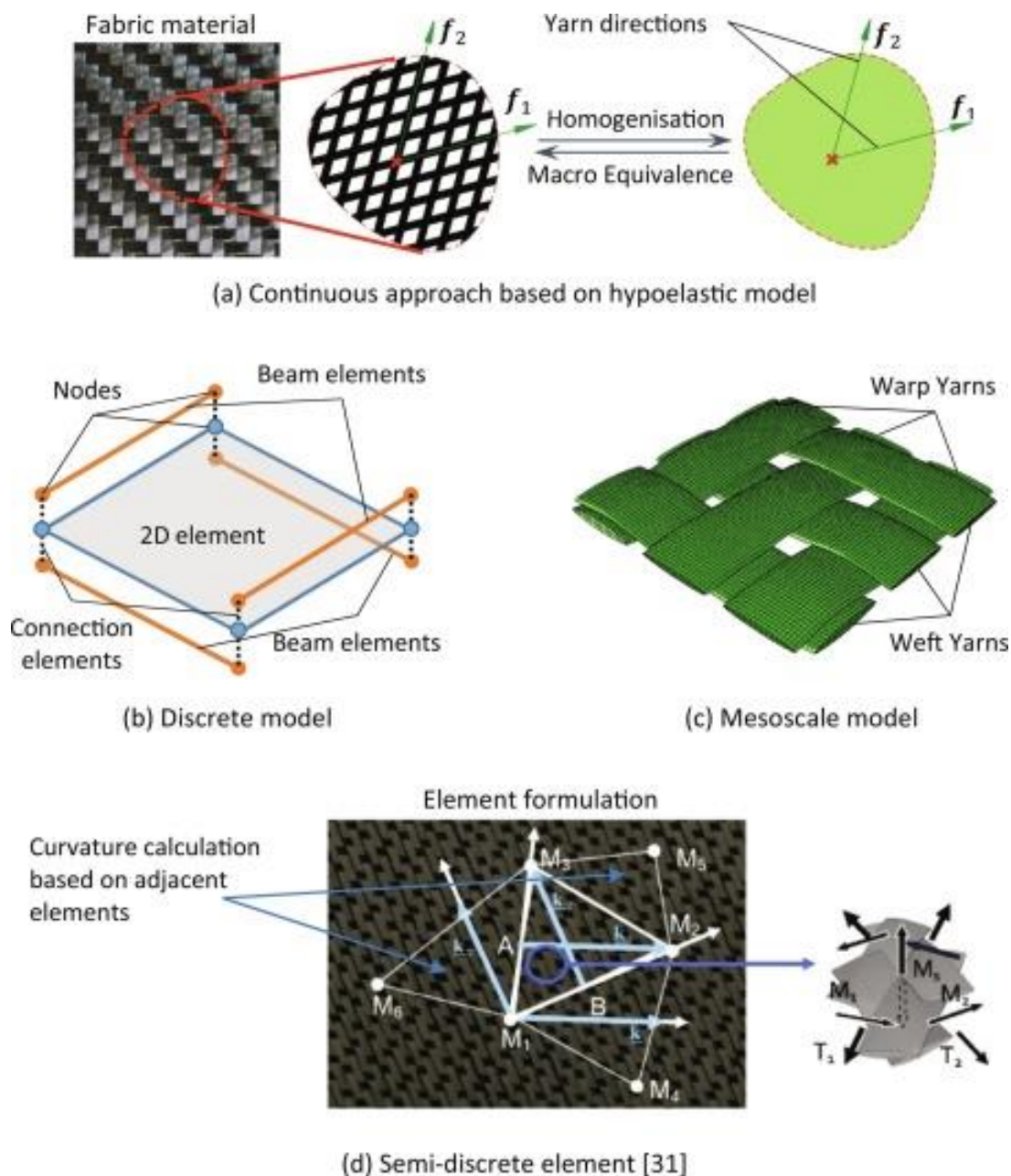


Figure 2.25: Schematics of various FE modelling techniques [37].

(2) Discrete methods

Discrete finite element models [284, 308-313] are also used for simulating fabric behaviour at the mesoscopic level, operating in essence as a larger version of a meso-scale method. In these models, rather than modelling the geometry of a yarn with continuum elements, yarns are represented explicitly using 1D elements, such as beams, trusses, or springs [311]. These are often combined with 2D elements like membranes or shells to account for the fabrics overall geometry, as per Figure 2.25b. Discrete models do not assume material homogeneity or continuity making them ideal

for studying complex fabric behaviour, including: wrinkling, shearing, and tension, without the requirement to model intricate inter-yarn interactions [309]. Yarn orientations update automatically during deformation through the rotation of the 1D elements [284], providing a realistic representation of the fabrics response under various loading conditions. However, the large number of degrees of freedom (DoF) significantly raises computational costs, often limiting the use of discrete models to small fabric subdomains [287, 312].

(3) Semi-discrete methods

Semi-discrete finite element models [59, 168, 314, 315] offer a hybrid approach to simulating fabric behaviour by combining aspects of both discrete and continuum modelling techniques. This method, originally proposed by Boisse *et al.* [59], still simulates fabric behaviour at the mesoscopic level (yarns or woven cells), however these components are modelled using finite elements that fix the kinematics in these discrete components as a function of the nodal displacement [168]. As per Figure 2.25d, the yarn directions are therefore not necessarily aligned with the edges of the element, key for simultaneous multi-layer fabric forming. These methods are more computationally efficient than standard discrete models due to them having fewer DoF [315]. Only the significant mechanical properties of the element at meso-scale are taken into account [315]. The drawback of this method is that it relies on specialised element formulations that are not typically available in standard commercial FE software packages [37].

(4) Continuous methods

The continuous FE modelling approach (Figure 2.25a) [284, 313, 316-324] treats the material as a homogenised continuum, representing its behaviour using membrane, shell, or solid elements. Unlike discrete or mesoscale models that focus on individual yarns or unit cells, the continuous approach assumes that the fabrics mechanical properties, such as tensile stiffness, shear behaviour, and bending resistance, are uniformly distributed throughout the material. Material behaviour is typically captured using constitutive models that approximate the anisotropic and nonlinear characteristics of fabrics, characterised by experimental deformation behaviour (Section 2.5) [324]. This method is computationally efficient and well-suited for

simulating large-scale fabric deformation, such as draping, without the need to resolve individual yarn interactions [37]. Furthermore, it can be easily implemented in classic FE codes without the necessity of modifying element formulations [325]. While continuous models are effective for analysing global deformation patterns and structural behaviour, they are limited in their ability to capture local phenomena such as inter-yarn sliding, with meso-scale interactions such as crimp and yarn compaction generally not included [312]. Table 2.2 illustrates the advantages and disadvantages associated with the different modelling techniques [37].

Although significant work has been done in the field of fabric modelling, no widely accepted model currently exists that accurately captures all aspects of the mechanical behaviour of fabrics [307]. In this work, a continuous approach is adopted due to the ability for these models to predict large-scale draping behaviour, implemented within classical FE codes, which represent the most popular method for modelling composite reinforcement [312]. These continuous approaches necessitate tracking of the non-orthogonal material directions during forming for the constitutive models to function correctly. This can be accomplished by utilising either hypoelastic or hyperelastic formulations [312], which are outlined below (Section 2.7.1.2.3), with a specific focus on FRTPs.

Table 2.2: Advantages and disadvantages of different fabric modelling approaches [37].

Modelling approach	Advantages	Disadvantages
Continuous approach	<ul style="list-style-type: none"> • Small number of DOFs • Applicable to classical FE model 	<ul style="list-style-type: none"> • Requirement for specialised constitutive model • Cannot model deformation characteristics or defects at mesoscale
Discrete or mesoscopic model	<ul style="list-style-type: none"> • Close to the natural architecture of fabrics. • Can model the interaction between yarns and stitches • Can model occurrence of mesoscale defects 	<ul style="list-style-type: none"> • Large number of DOFs • Limited to small structures • Needs specialised homogenisation procedure to determine material parameters in numerical model
Semi-discrete element	<ul style="list-style-type: none"> • Small number of DOFs • Applicable to classical FE model 	<ul style="list-style-type: none"> • Needs specialised element formulation • Not readily available in commercial FE codes

2.7.1.2.3 *Continuous FE Method Formulations*

One of the earliest continuum models for the forming of FRTP preregs was introduced by Rogers [326], building on Spencer's [327, 328] work on anisotropic materials and later expanded by Johnson [148]. This model assumes the fibres, whether unidirectional or bidirectional, to be inextensible, and treats the prepreg as an idealised fibre-reinforced material. This model has been the focus of several studies [152, 153, 316, 329, 330]. However, the inextensibility constraint can cause numerical challenges when implemented in FE codes [331]. In recent years, modified versions of this theory have been developed to address these limitations, incorporating more advanced and sophisticated methodologies.

(1) Hypoelastic Formulations

The hypoelastic formulation [321-325, 332-334] has been proposed for materials undergoing large strains without the necessity of a strain energy density function [312]. In this approach, the stress-strain relationship is formulated incrementally, meaning the objective stress rate at a given point is determined based on the current strain rate and a material stiffness tensor [322, 335]. The hypoelastic model allows the material stiffness to evolve dynamically with deformation, enabling the tracking of changing non-orthogonal fibre directions [336]. This is particularly suitable for fabric forming processes where large deformations exist. A limitation of this method, however, is that an incorrect definition of the hypoelastic relations can result in unrealistic material behaviour [335]. Furthermore, the closed loop loading path is not recoverable [112]. Commercial finite element simulation programs typically employ a rate-based constitutive equation or hypoelastic formulation by default, specifically in user-defined routines such as UMAT or VUMAT in Abaqus [332].

A fundamental non-orthogonal model for fabrics, based on a homogenisation technique, was proposed by Yu *et al.* [321] in order to model the behaviour of thermoplastic composites. To validate the model, it was implemented in an explicit dynamic FE code and evaluated through tests including in-plane simple shear, pure-shear, uniaxial tension, and the draping behaviour of woven composites. This model was then implemented by Yu *et al.* [337] to model the hydroforming of an FRTP laminate, taking into account the wrinkling caused by the undulation geometry of the

woven structure and its shear stiffness. After adapting the model to include the out-of-plane rigidity [166] and further applying it to NCFs [333], the approach was used by Harrison *et al.* [334] to predict the forming behaviour of a viscous textile composite sheet. This was done by combining the rate-independent constitutive equations [333] with a temperature dependent unit cell energy model [338]. The shear and tensile behaviour was captured sufficiently to model both the PFT and complex forming routines accurately.

Peng and Cao [339] proposed a dual homogenisation approach using the finite element method to predict the nonlinear elastic behaviour of textile composites. This work focused on a constitutive model to characterise the non-orthogonal material behaviour under ‘large deformations’, an approach also implemented by Xue *et al.* [322]. This method was used by Cao *et al.* [340] in what is one of the first attempts at modelling non-isothermal FRTP forming behaviour (Section 2.7.3.2). Xue *et al.* [341] conducted a mechanical analysis of a unit cell to identify the parameters of this non-orthogonal material law, with this knowledge used by Peng and Cao [323] to devise another constitutive law, introducing the convected coordinate system. This was later expanded by Badel *et al.* [325] who raised concerns about directly defining the constitutive relation of fabrics within the Green-Naghdi (GN) frame, as this approach can result in spurious stresses during large shear deformations of an element. To address this issue, stresses are instead computed using the constitutive relation defined in the fibre-parallel frames and subsequently transformed back into the GN frame. This transformation ensures an objective derivative and avoids inaccuracies during stress updates. It has since been validated by simulating a fabric forming process over a hemispherical [325] and double-dome tool [324] geometry.

(2) Hyperelastic Formulations

The hyperelastic continuous model [238, 335, 342-347] is generally used to describe the mechanical behaviour of materials that undergo large elastic deformations. In this framework, the stress-strain relationship is derived from a strain energy density function, where it is typically assumed that each strain mode contributes independently to the overall strain energy potential [312, 335]. Initial hyperelastic formulations were based on that for dry fabrics, such as that by Aimene *et al.* [342]. The authors introduced a hyperelastic invariants model that considered two tensile and one shear

deformation energy component for textile reinforcement under large strains. Building on this approach, Peng *et al.* [348] developed a hyperelastic constitutive model incorporating fibre stretching and yarn cross-over shear strain energies, subsequently applied to analyse the behaviour of dry fabric under large deformations. Both Gong *et al.* [343] and Guzman-Maldonado *et al.* [215] utilised this approach for FRTPs, specifically for modelling FRTP material behaviour during thermoforming. Hyperelastic behaviour was linked to the elongation of dry reinforcements in the warp and weft directions, while in-plane shear deformation described using a nonlinear visco-hyperelastic model based on the generalised Maxwell rheological framework.

2.7.2 Process Modelling

The simulation approaches outlined in detail in Section 2.7.1.2.3 are modelled in the form of a dynamic process, such as to simulate the forming process of a particular fabric material. This section therefore outlines the nature of these forming models in terms of the simulation tools available, the appropriate element formulations and finally a brief description of the forming models themselves, as per the processes outlined in Section 2.3.

2.7.2.1 Finite Element Simulation Tools

While FE modelling has become an indispensable tool in composite forming research, the selection of an appropriate FE platform can significantly influence both the scope and applicability of the work. Commercial general-purpose FE codes such as Abaqus and LS-DYNA are widely used across a range of engineering disciplines and are valued for their robust nonlinear analysis capabilities, flexible solver architectures (implicit and explicit), and ability to implement user-defined material models through subroutines (e.g., UMAT/VUMAT in Abaqus or MAT_ keywords in LS-DYNA). These tools support complex contact interactions, large deformations, and advanced constitutive behaviour, making them well-suited to simulate forming processes where significant sliding, wrinkling, and anisotropy are present. In contrast, dedicated forming software packages such as AniForm (implicit solver) and PAM-Form (explicit solver) are purpose-built for modelling composite forming processes, offering simplified workflows with pre-defined forming material models and user interfaces tailored to draping, stamping, and consolidation simulations.

These tools reduce the barrier to entry for composite-specific applications but are often constrained in terms of extensibility and control over the simulation framework. Notably, all previous studies modelling the Double Diaphragm Forming (DDF) process have relied on commercial general-purpose FE platforms rather than these specialist tools, highlighting the relevance of this approach. In this work, Abaqus (commercial FE package) is therefore implemented such as to ensure the highest level of control over the FE formulation was attainable.

2.7.2.2 Element Formulation

Full-scale forming processes, such as DDF or matched-tool forming, are typically simulated as a continuum (Section 2.7.1.2.2) using membrane elements, shell elements, or a combination of both [37]. Membrane elements are less computationally demanding than shell elements since they usually feature only translational degrees of freedom at each node without rotational DoF considered [254]. This has made them a popular choice owing to the complex demands of a forming simulation [144, 349, 350]. However, their main limitation is the inability to account for the bending stiffness of fabric plies [165]. Consequently, while they effectively capture shear behaviour which is helpful in identifying potential defect areas, they fall short in accurately predicting the shape and size of wrinkles [144]. On the other hand, shell elements provide a better capability to predict wrinkling defects by accounting for bending stiffness as they consider the through-thickness stress gradient [333]. This results in more precise estimates of wrinkle amplitude and length [186] and improved tool bridging predictions [43]. However, shell models tend to be more computationally intensive than membrane models. A small number of recent studies, specifically for FRTP forming simulation, have used solid elements to model the matrix material superimposed with shell elements to model the behaviour of the reinforcing fibres [216, 351]. The computational expense associated with these models is large, however.

In early studies, numerical simulations of fabrics primarily focused on tensile and in-plane shear behaviours, as the relatively low out-of-plane flexural bending stiffness (due to fibre sliding) was considered negligible [112]. However, later findings revealed that the bending stiffness significantly influences the number and size of wrinkles during fabric forming [144, 186, 188]. In commercial FE software, the bending stiffness of standard shell elements is usually derived from the axial moduli [44]. This

approach typically results in an overestimation of the fabric bending stiffness, leading to unrealistic predictions of forming-induced wrinkles [188]. To address this issue, various methods have been proposed to decouple the bending behaviour of fabrics from their axial moduli [352, 353].

Nishi *et al.* [354] for example, introduced a numerical modelling approach consisting of an offset shell and interposed membrane element, as per Figure 2.26 [287].

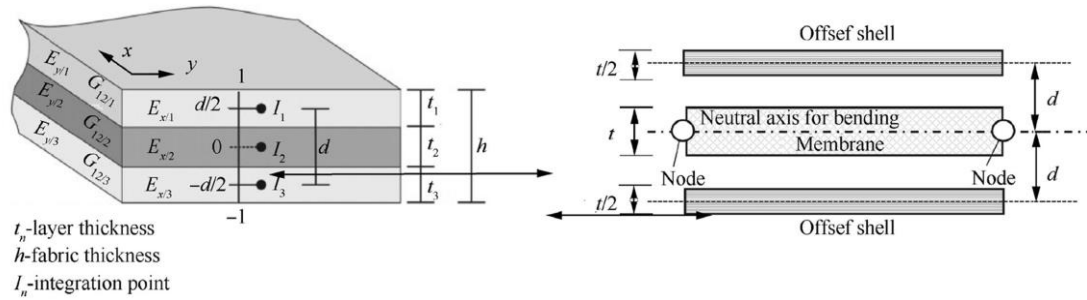


Figure 2.26: Tri-element model to decouple membrane and out-of-plane behaviour [287].

This proposed macroscopic modelling technique effectively accounts for both the in-plane material properties using the membrane element and out-of-plane properties with the shell elements. Alternative methods include the use of hybrid meshes that combine membrane and beam/shell elements [188, 349, 353], as well as custom-designed semi-discrete shell elements which incorporate bending stiffness [168, 315]. Another approach, presented by Yu *et al.* [170], defined individual properties to different integration points through the thickness of a shell element, thus achieving equivalent membrane and out-of-plane decoupling.

Regarding the in-plane properties, shear and tensile behaviour also require consideration if the model is to function correctly [144]. These properties, as well as the friction behaviour, are documented in Section 2.4 as the main mechanisms that dictate forming behaviour [140]. This is illustrated in Figure 2.27, which compares fabric draping over a hemisphere (a) with different input cases considered: (b) just tensile behaviour, (c) tensile and shear behaviour, (d) tensile, shear and bending behaviour included [144]. An isotropic laminate is included for reference (e). Only after tensile, shear and bending properties are included does the formed geometry start to replicate what would be expected in an experimental study. This again highlights

the importance of including laminate bending stiffness for accurate wrinkling predictions. For FRTPs, these properties are viscoelastically coupled.

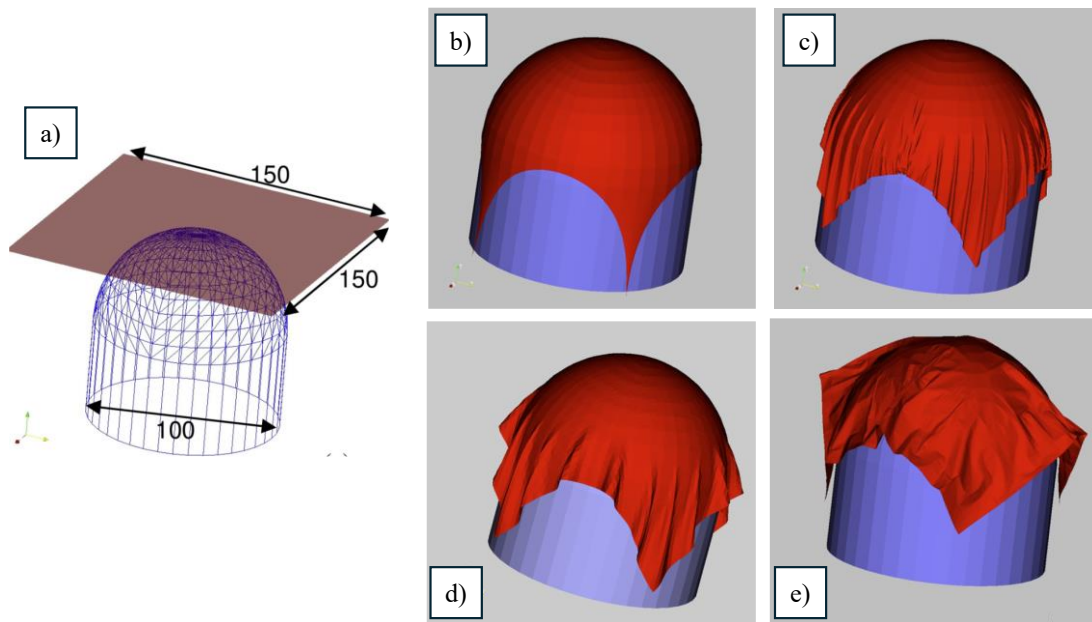


Figure 2.27: a) Draping on a hemispherical geometry including fabric. b) Tensile behaviour, c) tensile and shear behaviour, d) tensile, shear and bending behaviour. e) isotropic laminate [144].

2.7.2.3 Forming Processes

As addressed in Section 2.3, the key forming processes associated with this work are the matched-tool process and the DDF process. FRTP matched-tool simulations (outlined in detail in Section 2.7.3) generally consist of a laminate (formulated as per Section 2.7.2.2) moulded using rigid (assumed undeformable and isothermal) tooling [112].

Recent works on diaphragm forming simulation are solely based on dry fabrics or epoxy-prepregs, such as the work by Leutz *et al.* [355], Margossian *et al.* [356], Chen *et al.* [37, 50], Yu *et al.* [40-43] and Lawrence *et al.* [175] for dry NCFs, Sorrentino *et al.* [357] and Sjölander *et al.* [252] for UD epoxy-prepregs and Thompson *et al.* [254], Miris *et al.* [358] (dry) and Alshahrani [247] (epoxy-prepreg) for woven fabrics. In these models, while the laminate is typically modelled the same as per that of matched-die processes, special considerations have to be given to both the diaphragm behaviour and the diaphragm interactions. Diaphragm behaviour, due to its potential for large

deformation, is typically modelled using a hyperelastic formulation for the strain energy density function (Section 2.7.1.2.3), in the form of a Mooney-Rivlin [247, 252], Ogden [50, 254, 358], Marlow [43] or alternative hyperelastic [357, 359] model. Furthermore, as opposed to the tool-ply friction that must be accounted for in a conventional matched-tool process, both diaphragm-tool and diaphragm-laminate friction must be considered in diaphragm forming simulations [50]. Finally, it is important to consider the diaphragm pressure gradient (in DDF), meaning the spatial- and time-dependent variation in pressure transmitted from the diaphragms to the blank. This gradient controls the distribution of normal forces across the tool-laminate and diaphragm-laminate interfaces, and thereby dictates the level of interfacial friction and the resulting forming behaviour [48].

2.7.3 FRTP Forming Simulation

The quantity of previous literature regarding complete FRTP forming simulation is not exhaustive. Some of these models were outlined in Section 2.7.1.2.3, often used for validation of the relevant constitutive models. This section details the FRTP forming simulation models published to date, as opposed to the individual deformation constitutive models. These models are broken down into two classes: isothermal and non-isothermal forming simulations. Isothermal forming simulation is by far the most common in previous literature, where transient thermal effects are not considered during the course of a simulation. This was generally accepted for thermostamping processes as it was assumed that the speed of the process would negate any issues regarding laminate cool-down [112]. This assumption has since been questioned [159], however, such that fully-coupled non-isothermal simulations now represent the state-of-the-art in FRTP thermomechanical modelling. Forming simulation for commingled fabrics in the cold state, such as that by Garnish *et al.* [360], Jauffres *et al.* [309, 361] and Peng *et al.* [362] are not considered in this section since the material deformation behaviour is not temperature dependent, with heating completed after the forming step. Works that consider other defects (not laminate formability), such as creep [363] or spring-back [364, 365], are also not presented. Furthermore, the reader is referred to the works of Bussetta *et al.* [58], Chen *et al.* [112] and Gong *et al.* [141] for a detailed analyses of FRTP thermoforming simulation, the latter two with a particular focus on hot-stamp forming.

2.7.3.1 Isothermal Forming Simulation

Willems *et al.* [366] used a discrete hypoelastic formulation combined with truss elements to model the thermostamping of a FRTP fabric over a double dome geometry. In this work, material shear behaviour was characterised at a fixed temperature, and the model ran isothermally assuming this temperature was constant through the test. A reasonable agreement between experimental and simulated shear angles was presented. The same procedure was implemented by Harrison *et al.* [121], including analysis of different tool-ply friction coefficients, illustrating good agreement between experimental and simulated shear and localised defects. Dangora *et al.* [185] implemented a thermally-coupled tensile, bending and shear model into a discrete hypoelastic FE model, showing a good agreement between experimental and simulated hemispherical thermostamping defects. These works only tested a singular thermoforming condition (one defined temperature and rate).

Recently, Lv *et al.* [367] used a continuous hypoelastic model to include temperature-dependent friction, bending and shear behaviour, with the authors validating the model with a hemispherical punch simulation. They showed that friction behaviour of FRTPs does demonstrate a degree of directionality, and including an inter-ply friction model significantly increases the accuracy of simulations with regard to wrinkle development in a multi-ply laminate. Deng *et al.* [351] altered the hypoelastic model to include solid elements to represent the matrix, again illustrating the influence of temperature on shear behaviour in a hemispherical stamping operation, although with constant bending and friction behaviour. This method allows for characterisation of the fibre and matrix properties to be conducted separately, leading to a big reduction in the expense of FRTP behaviour characterisation. Building on the work of Badel *et al.* [325], Machado *et al.* [219] developed a shear angle rate-dependent constitutive model for GF/PP organosheets, representing the shear stiffness using a cubic polynomial. The shear stiffness was modified by a shifting factor, in the form of an overstress law similar to that proposed by Cowper and Symonds [368], to include the rate-dependency, as calculated using the BET (Section 2.5.1). This shear stiffness was implemented within a hypoelastic model, allowing for accurate prediction of laminate shear angles in a thermostamping operation. Neglecting bending stiffness and frictional behaviour meant that accurate wrinkling prediction was not possible.

Ten Thije *et al.* [350] characterised the friction and shear properties of a pre-consolidated FRTP laminate at a single temperature, but multiple rates, and implemented these within an updated Lagrangian FE model. The authors, as per Lv *et al.* [367], showed that inter-ply friction behaviour significantly influences the wrinkling behaviour in a hemispherical thermostamping routine. However, comparisons with experimental studies showed poor correlation due to the neglect of bending properties by virtue of the membrane element formulation. This model was then adapted by Ten Thije *et al.* [369] with shell elements to include a decoupled bending stiffness, although assumed constant in this case. Good agreement in measured shear angles was illustrated between simulated and experimental thermo-stamp forming with a moderately accurate wrinkling prediction. This model was also utilised by Haanappel *et al.* [218] to include rate-dependency in the hypoelastic constitutive equations, simulating the matched-tool stamping of both woven and UD FRTP laminates, with good wrinkling prediction achieved for a singular thermoforming condition. The authors showed wrinkling prediction is sensitive to laminate bending stiffness, which was approximated in the model.

Gong *et al.* [343], in contrast, used a hyperelastic constitutive formulation to model an isothermal double-dome matched tool process with good shear prediction. Similar work was presented by Abbassi *et al.* [370] for a hemisphere geometry. Ziegs *et al.* [371] adapted this hyperelastic model, including temperature-dependent shear and bending characterisation, illustrating the influence of temperature on laminate shear and wrinkle development in a complex part geometry. Gong *et al.* [372] used an alternative formulation, using a similar laminated approach as per Deng *et al.* [351], to also model temperature and rate-dependent shear and bending behaviour. With the inclusion of viscoelastic matrix characterisation, they were able to model a hot-stamping process at different temperatures, with good agreement in wrinkle prediction between simulation and experiment. Guzman-Maldonado *et al.* [215] used a conventional shell hyperelastic constitutive model including the temperature- and rate-dependent shear behaviour of a woven Glass/PA66 composite. The authors showed how wrinkle development in a cylindrical punch model is heavily dependent on both the forming temperature and rate, as per Figure 2.28, where the latter was neglected in the previous studies. The authors, however, did not include viscoelastic bending or friction properties in the model.

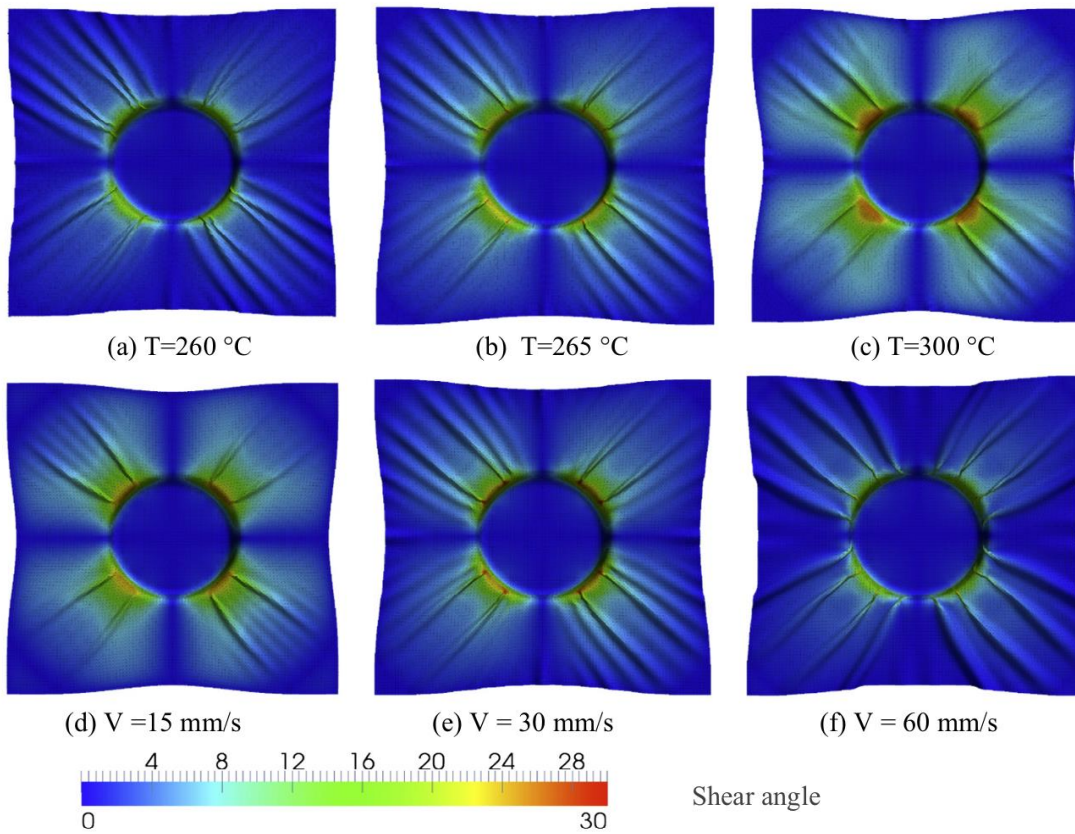


Figure 2.28: Influence of a-c) laminate temperature, d-f) forming rate, on shear angles and therefore wrinkle development in a hemispherical thermostamping simulation [215].

Dörr *et al.* [373] also simulated an isothermal hot-stamp forming exercise, although including viscoelastic bending and friction properties alongside the viscoelastic shear. A generalised Maxwell and Voigt-Kelvin approach was used (as per the work of Dörr *et al.* [188]) for the viscoelastic deformation behaviour, implemented with hyperelastic constitutive laws. Forming simulation of a complex part was completed at different temperatures to illustrate the influence of laminate temperature on wrinkle development, with a high level of agreement between experiment and simulated geometries. The wrinkle pattern was well captured with the inclusion of viscoelastic bending properties.

Wang *et al.* [374] used an alternative semi-discrete approach to model the thermostamping of a woven FRTP laminate, including temperature- and rate-dependent shear and friction properties. The authors also including the experimentally calculated in-plane and through-thickness thermal inhomogeneity, although this was assumed constant (isothermal). Figure 2.29a illustrates these distributions, which were implemented as predefined fields within the numerical model. Good agreement was

shown between experimental and simulated shear and wrinkling behaviour, with the authors noting the importance of including thermal distributions with regard to forming behaviour. Liang *et al.* [186] adapted the model by including a temperature-dependent bending formulation, but used a constant CoF. As per Haanapel *et al.* [218], they conducted a sensitivity analysis illustrating how wrinkle development increases significantly with a reduction in FRTP bending stiffness. Chen *et al.* [216] implemented a similar semi-discrete approach with solid-shell elements (as per Deng *et al.* [351]) to model woven CF/PPS laminates with the consideration of viscoelastic tension, in-plane shear and frictional behaviour. The authors again illustrated the benefits of modelling the fibre and reinforcement separately with regard to material characterisation, and novel cohesive elements were used to model the initial peak in inter-ply friction behaviour (Section 2.4.4). Xiong *et al.* [375] furthered this work (with solid-shell elements) to model through thickness stresses, and therefore time-dependent consolidation, during a double-dome hot-stamping operation. Figure 2.29b illustrates the level of consolidation, D_n , on a scale from maximum deconsolidation (0) to full consolidation (1), as a function of the dwell time, t . The variation with time was attributed to resin-squeeze flow and was well captured with the solid-shell model.

Table 2.3 (Page 72) presents an overview of the isothermal works presented in this section. The model scale and formulations are tabulated, as per Section 2.7.1.2.3. All the cited works are in reference to a thermostamping operation, however the specific geometry is also tabulated. The simulation type has been broken down into: ‘constant conditions’ (only one temperature or rate condition explored) and variable (multiple temperature/rate conditions). It should be noted that some of the works defined in ‘constant conditions’ still include rate-dependent forming behaviour, but the published thermoforming operation is only conducted at one speed. Finally, the viscoelastic mechanisms that have been included are outlined. This does not mean that the other mechanisms have been neglected entirely, for example bending stiffness is often assumed to be linear.

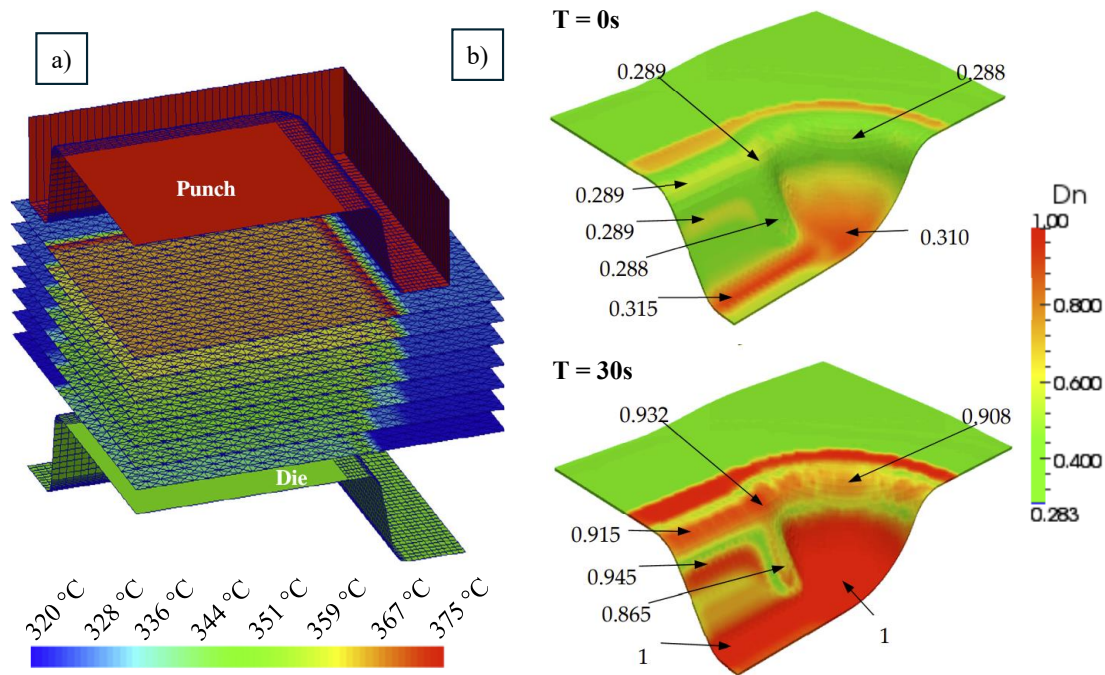


Figure 2.29: a) Through-thickness thermal distributions modelled as inputs for an isothermal thermostamping operation of a multi-ply laminate [374], b) consolidation during a forming routine as a function of dwell time [375].

2.7.3.2 Non-Isothermal Forming Simulation

Although isothermal condition simulations have offered valuable insights into the FRTP forming process, thermoforming processes are inherently non-isothermal, adding further complexity to both the phenomena and their analysis [343, 372]. Temperature gradients arise within the laminates following the heating phase [101, 376-378] and, most notably, upon contact with the tools [379]. This is due to the high production efficiency demands of the thermostamping process in industrial applications, where the initial temperatures of components such as the punching tool and blank holder are typically set lower than that of the blank [380]. Laminate-tool contact leads to a rapid cooling of the laminate surface, while the inner plies cool at a slower rate due to the laminates low thermal conductivity in the thickness direction [374]. The cooling conditions, which are jointly affected by the transfer time and the die temperature, inevitably affect the drapability of an FRTP laminate [363]. Therefore, the assumption of isothermal laminates may not be valid [159].

The first non-isothermal thermomechanical simulations were based on ‘bi-phase’ homogenisation models, where a viscous shell element formulation is implemented (solid fibres and viscous matrix). Hsiao and Kikuchi [320] used a kinematic approximation for the element fibre directions to calculate the deformed shapes along with the laminate temperature losses in a thermostamping operation. The implicit model was based on a viscosity model (tabulated in a database) for shear and bending behaviour, with constant frictional properties for model stability. The stresses in a formed part were attained, although accurate defect prediction was not assessed. Luca *et al.* [276] used a similar bi-phase model although with an explicit integration scheme, thus allowing for viscoelastic friction dependency to be modelled, although laminate bending stiffness was assumed constant. The authors showed satisfactory agreement in defect prediction between experimental and simulated hot-stamp forming operations. The influence of different temperatures and/or forming rates was not explored. Nishi *et al.* [381], more recently, used a similar formulation to model a non-isothermal FRTP stamping process with viscoelastic shear modelled, illustrating good shear angle prediction. This approach is however time-consuming and computationally costly for complex fibre architectures and forming processes, making it impractical for optimisation [340].

Cao *et al.* [340] implemented a hypoelastic constitutive law (Section 2.7.1.2.3), such as to model anisotropic material behaviour with large deformations in a conventional FE package (Abaqus). The authors used a simple two-phase non-isothermal approach, with material shear behaviour characterised at two discrete temperatures. The forming model then operated where the material properties could flip between two states, dependent on the binary state of contact between the blank and the tool. The authors illustrated that considering non-isothermal temperatures influences the shear distribution and punching force in a hemisphere thermo-stamp forming exercise. This simple non-isothermal method was also implemented by Lee *et al.* [382] (with an advanced hypoelastic constitutive law [323]) for a non-isothermal forming simulation, incorporating a nonlinear friction model, and including the influence of tension on shear behaviour. The authors also illustrated how a non-isothermal model dramatically changes the punch loading history in a hot-stamping routine. Defects were not considered in both these studies. Alternatively, Ramirez *et al.* [383] used a hyperelastic approach to model a stamp process, including non-isothermal behaviour and a viscous

shear and bending model, showing good agreement between simulated and experimental thermoforming, at constant test conditions.

Machado *et al.* [159] extended the work from a previous isothermal study [219] to also include temperature-dependent shear behaviour using an Arrhenius-type scaling factor. The authors implemented this shear model in a hypoelastic continuum model for a non-isothermal hemisphere hot-stamping process. Convective and tool-ply heat transfer was implemented in the coupled thermomechanical model, although in-plane conductivity and radiative cooling were ignored. The simulation results indicated that, under the isothermal forming model, a decrease in forming speed led to an increase in the maximum shear angle. However, the thermal transient forming model exhibited the opposite trend due to the cooling influence of the tool, as per Figure 2.30.

The work of Machado *et al.* [159] highlights the importance of including non-isothermal behaviour in forming simulations. The authors did not consider viscoelastic bending behaviour (which was not decoupled from the in-plane behaviour) or frictional behaviour, only focussing on the laminate shear distribution (not defects). Chen *et al.* [380] used a similar hypoelastic non-isothermal model, although included viscoelastic bending stiffness to evaluate hemispherical punch forming with different tool temperatures. The influence of the hemispherical punch temperature on forming behaviour was marginal, however the blank holder temperature had a big impact on wrinkle development in the formed part. This illustrates a degree of geometry-dependence with regard to non-isothermal forming sensitivity.

Guzman-Maldonado *et al.* [345] furthered the isothermal study conducted by the authors [215] by including transient thermal effects in a thermostamping operation, including viscoelastic bending and shear behaviour. These behaviours were implemented within a hyperelastic formulation, with in-plane, through thickness and tool-laminate conductivity all characterised and implemented within the model, although ignoring convective and radiative cooling. Figure 2.31 illustrates how the laminate temperature changes significantly after contact with the colder tool, which therefore has a significant impact on forming behaviour. The authors showed good agreement in terms of both shear angle and wrinkle development between simulation and experimental thermoforming trials.

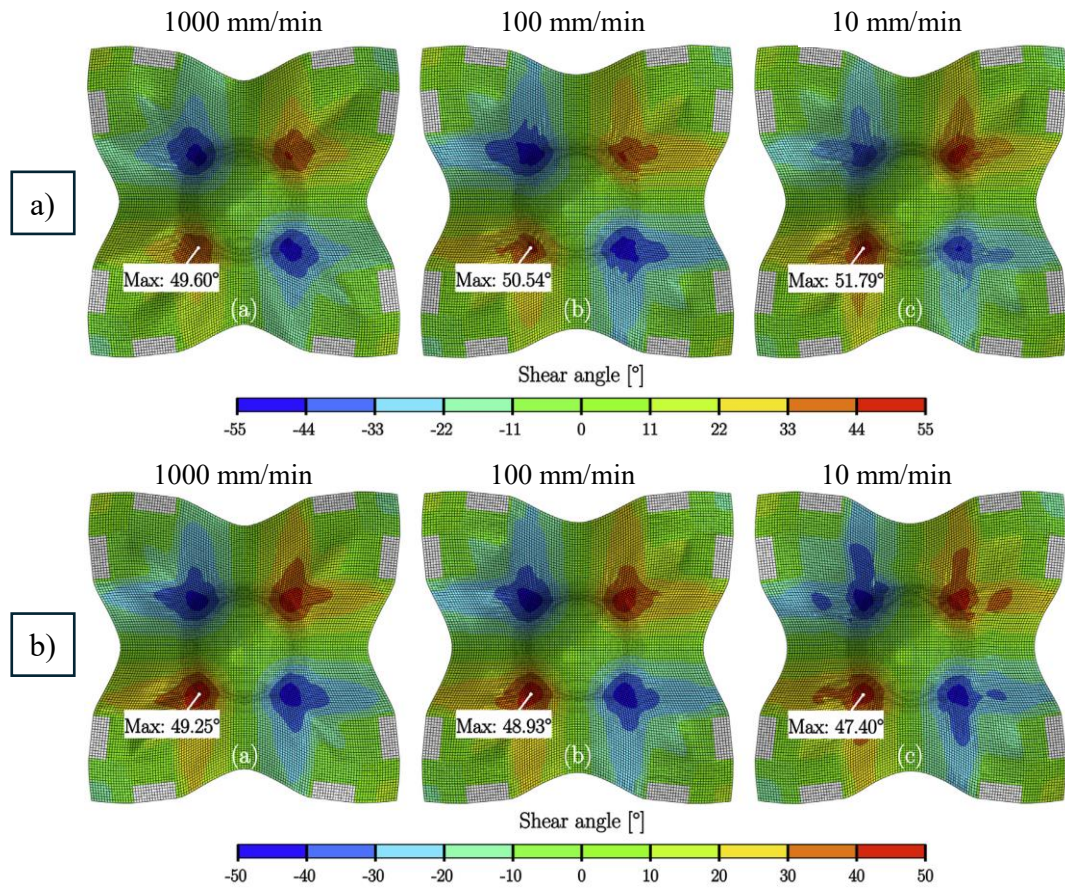


Figure 2.30: Thermostamping simulation at different forming rates: a) isothermal, b) non-isothermal [159].

Dörr *et al.* [379] also built on the work of their previous isothermal study [373] by including transient thermal effects (tool-ply conduction, intra-ply conduction, convection and radiation) in their hyperelastic model that is viscoelastically coupled with shear, bending, and friction behaviour. Furthermore, this work is among the few other studies that consider temperatures below the crystallisation temperature of the semi-crystalline polymer. To this end, temperature-rate-dependent crystallisation has been modelled (see the work of Kugele *et al.* [89]), along with the crystallisation exotherm. Furthermore, a rule of mixtures approach is adopted to implement the three aforementioned deformations in both their molten and solid states. This work therefore represents the most advanced thermomechanical simulation model published to date. The authors modelled a thermostamping operation, and showed that a non-isothermal model better replicates the experimental defects (wrinkling) in an intricate part geometry, compared to a similar isothermal model, as per Figure 2.32. This once again demonstrates the necessity for non-isothermal simulations.

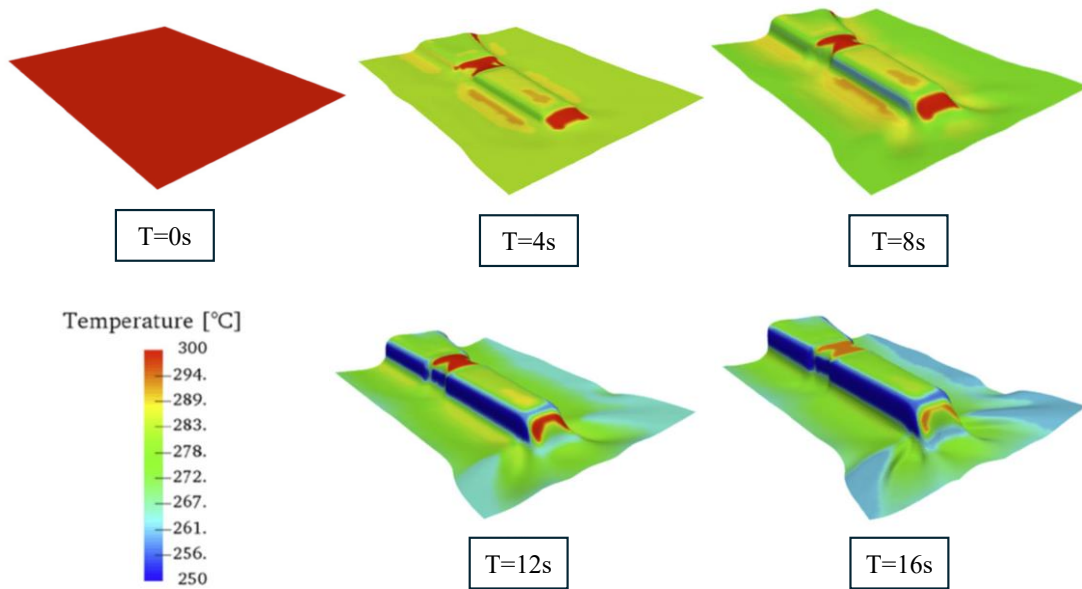


Figure 2.31: Non-isothermal thermostamping simulation illustrating the cooling effect of the tool (250 °C) on the laminate temperature profile (initially 300 °C) [345].

The non-isothermal studies outlined in this section are also summarised in Table 2.3, with the same headings as those for the isothermal works as detailed in Section 2.7.3.1.

Other notable works include that by Baumard [376] who investigated a nonlinear thermal profile, attributed to the irradiance of IR lamps, at the start of a stamp forming process. The authors did not consider the influence of temperature on the FRTP material properties, however. Moreover, Fan *et al.* [384] conducted a study analysing the interfacial heat transfer coefficient between a FRTP blank and a stamp tool. While the authors did not introduce viscoelastic material behaviour into the model, they did analyse how both the tool and blank temperatures change during a hot-stamp forming. This compares to all other works that assume an isothermal tool during the process due to its thermal mass. illustrates this temperature evolution during the thermoforming process. Finally, a non-isothermal semi-discrete model was implemented by Boisse [385] for non-isothermal hot stamping of a double-dome geometry with viscoelastic shear and bending behaviour included, although this model was not validated with experimental thermoforming operations.

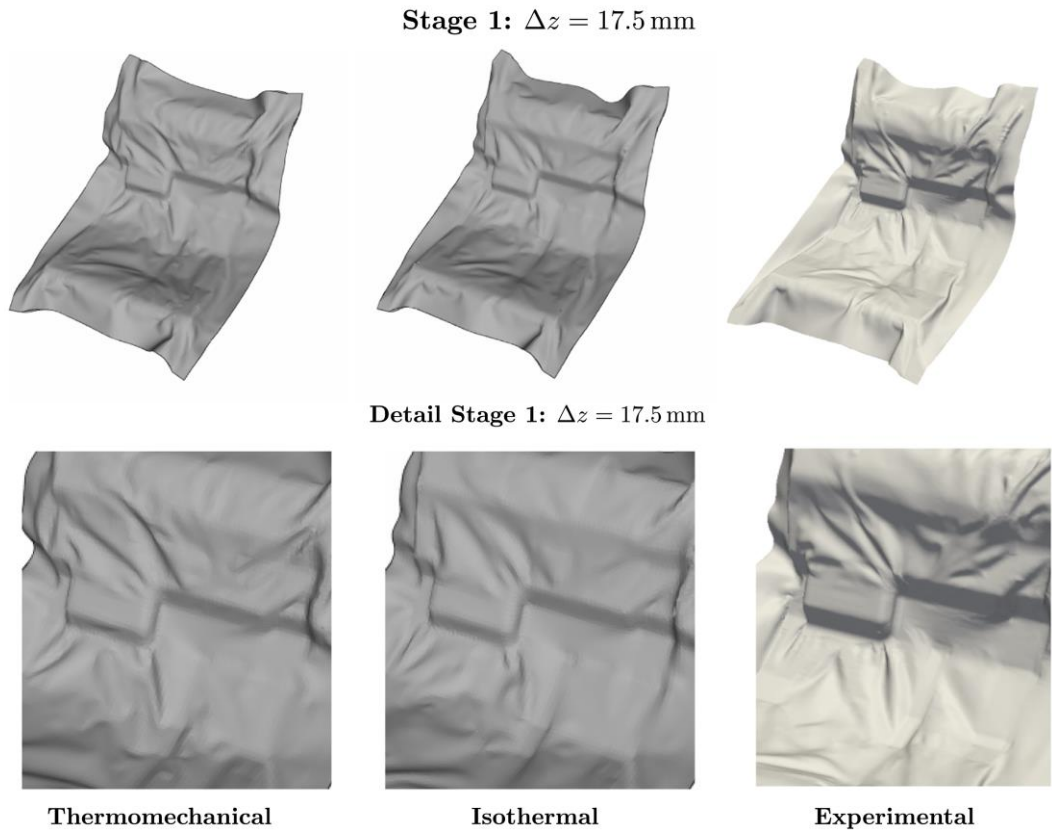


Figure 2.32: Comparison in wrinkling prediction between simulated isothermal, non-isothermal and experimental FRTP thermostamping profiles of a complex geometry [379].

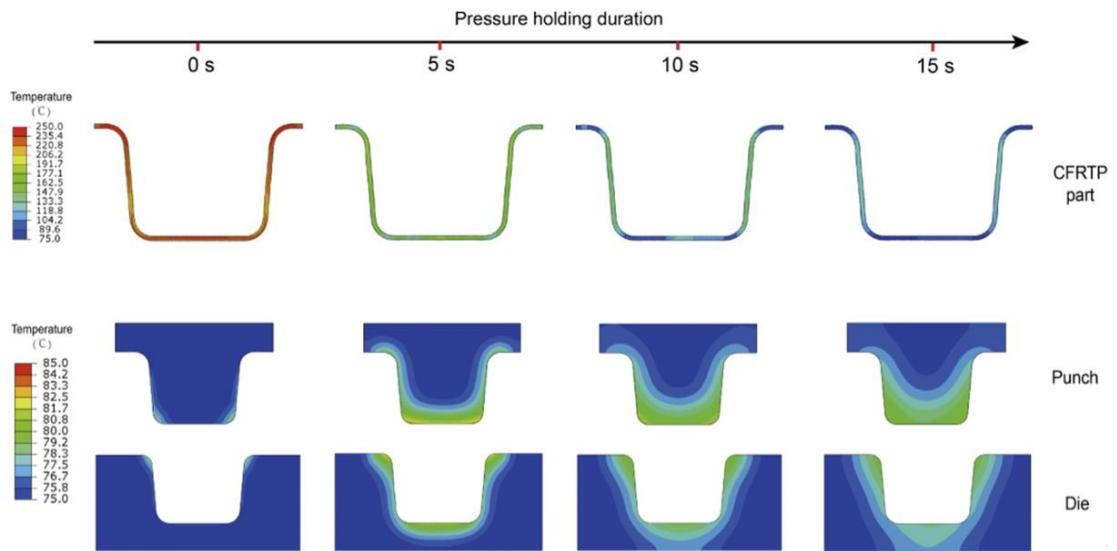


Figure 2.33: Non-isothermal thermostamping operation illustrating laminate and tool temperature distributions after forming.

Table 2.3: Summary of FRTP thermoforming simulations published to date.

		Isothermal	Non-Isothermal
Model Scale	Discrete	[121, 185, 366]	[383]
	Semi-discrete	[186, 216, 374, 375]	
	Continuous	[215, 218, 219, 343, 350, 351, 367, 369-373]	[159, 276, 320, 340, 345, 379-382]
Model Formulation	Hypoelastic	[121, 185, 218, 219, 350, 351, 366, 367, 369]	[159, 340, 380, 382]
	Hyperelastic	[215, 343, 370-373]	[345, 379, 383]
	Other	[186, 216, 374, 375]	[219, 320, 381]
Geometry	Double Dome	[121, 216, 343, 366, 375]	[219, 382]
	Hemisphere	[185, 186, 215, 219, 350, 351, 367, 370]	[159, 340, 380]
	Other	[218, 369, 371-374]	[320, 345, 379, 381, 383]
Simulation Type	Constant Conditions	[121, 185, 218, 219, 343, 350, 366, 369, 370, 374, 375]	[276, 320, 340, 345, 379, 381-383]
	Variable Temperature*	[186, 216, 351, 367, 371-373]	[380]
	Variable Rate		[159]
	Variable Rate and Temperature	[215]	
Viscoelastic Mechanisms	Shear	[121, 215, 219, 343, 351, 366, 370]	[159, 340, 381]
	Shear + Bending	[185, 186, 371, 372, 375]	[320, 345, 380]
	Shear + Friction	[216, 218, 350, 369, 374]	[276, 382, 383]
	Shear + Bending + Friction	[367, 373]	[379]

*Variable temperature for a non-isothermal model refers to whether alternative tool/initial laminate temperatures were explored.

2.7.3.3 Proposed Modelling Framework

In this work, a non-isothermal, continuum-based thermomechanical model was developed, informed by the progression of state-of-the-art approaches outlined in the literature. The continuous approach is particularly advantageous when implementing temperature- and rate-dependent mechanisms across multiple deformation modes. It simplifies material calibration and model setup and is readily compatible with commercial finite element software. In this study, a hypoelastic constitutive law, similar to that used by Machado *et al.* [159], was adopted to describe the in-plane temperature- and rate-dependent shear behaviour of the laminate. This formulation was selected due to its robust performance under large deformations, its efficiency in explicit dynamic solvers, and its compatibility with temperature-dependent input data. To accurately capture out-of-plane and interfacial mechanics, bending and

friction behaviour were also independently characterised over a range of temperatures and strain rates and implemented using rate- and temperature-sensitive analytical models.

Non-isothermal modelling has increasingly been defined as the state of the art for simulating FRTP thermoforming processes, as it captures the transient temperature gradients and heat transfer effects that strongly influence material behaviour during forming. The mechanical model in this work is therefore coupled with a fully transient thermal simulation, including laminate–tool contact heat transfer and intra-ply conduction, in accordance with best practices identified in recent forming studies [345, 346]. Very few published non-isothermal models incorporate all three critical deformation mechanisms: in-plane shear, inter-ply/slip friction, and out-of-plane bending, within a single framework. This lack of comprehensive treatment is a key limitation identified in Table 2.3, where most non-isothermal models neglect at least one of these mechanisms, reducing their predictive accuracy in scenarios prone to wrinkling and other localised deformation.

Shell elements were chosen over membrane elements to enable direct modelling of bending stiffness, which is critical for capturing wrinkling behaviour, a known limitation of membrane-only models [144, 165]. However, as identified in the literature [44, 188], standard shell formulations overestimate bending stiffness due to their dependence on axial moduli. To address this, a method similar to Yu *et al.* [45] is used to decouple membrane and bending behaviours in which through-thickness integration points are assigned different properties. This allows both membrane and out-of-plane deformation modes to be tuned independently and enables realistic wrinkle prediction while maintaining computational efficiency within the Abaqus framework.

Altogether, the modelling framework developed in this study offers a significant advancement by incorporating all three dominant deformation modes within a fully-thermally-coupled, non-isothermal, shell element continuum model, implemented entirely within a commercial finite element environment (Abaqus/Explicit). This balances fidelity with accessibility, ensuring the method is both research-robust and industrially transferable, while directly addressing the current gaps in the FRTP forming literature.

2.8 Chapter Conclusions

This literature review has provided an overview on the current knowledge in FRTP thermoforming. This has entailed analysis of material selection (fibres, architectures, matrix materials), the forming processes that convert flat 2D laminates into 3D components, the deformation mechanisms and associated characterisation exercises that allow mould conformity to be achieved, and defects associated with FRTP forming. These sections have then been brought together by analysis of fabric forming simulations, investigating the modelling techniques and constitutive laws that have been developed for accurate FRTP modelling, through to an overview of all FRTP thermomechanical models presented to date.

It has been explained that the development of simulation tools is critical to increase the uptake of FRTPs in industry, owing to a reduction in costly trial-and-error techniques, and allowing for process optimisation. While there has evidently been a heavy emphasis on producing FRTP forming simulations over the last two decades, with over 30 individual works cited, a clear gap in literature exists. Current FRTP thermomechanical models (both isothermal and non-isothermal) are solely limited to matched-tool forming routines. These are almost exclusively for thermostamping operations with rigid tools, although two hydroforming models also exist.

As detailed in Section 2.3, while matched-tool operations are suitable for manufacturing parts in a high volume, it is not a cost effective technique for FRTP component manufacturing in low-to-mid level volumes (under ~30,000 ppa [117]). Furthermore, the maximum part size is also constrained by the difficulty in producing matched-tools in large sizes. Diaphragm forming has been identified as a viable alternative. This is due to the lower costs associated with tooling, that itself requires lower geometrical accuracy and strength, plus the larger (in principal) sizes that can be formed using this technique. As detailed in Section 2.3.2, successful SDF and DDF has already been completed for FRTPs with a range of studies attempting to optimise the process. However, as of writing, there are no published works regarding the simulation of the FRTP diaphragm forming process, with all current diaphragm forming simulations concerned with dry or epoxy-prepreg fabrics.

This therefore underpins the aim of this work presented in Section 1.2: to produce a bespoke, fully-coupled FRTP thermomechanical simulation for defect prediction and optimisation of the DDF process.

As per Section 2.7.3, a comparison between isothermal and non-isothermal simulations was introduced, with the latter currently regarded as the state-of-the-art regarding thermoforming simulation due to the modelling of transient effects expected during FRTP processing. Therefore, this work endeavours to consider these transient effects, in a fully-coupled non-isothermal simulation (Objective #3). As per the majority of previous works, another objective (#1) is that of validating the numerical model with an experimental study. Due to the limited forming forces associated with the DDF process, it is expected that material (both laminate and diaphragm) deformation behaviour must be characterised with a high level of accuracy. Referring to Table 2.3, only one published non-isothermal study considers shear, bending and frictional behaviour. An objective (#2) of this work is to also include these three mechanisms such that forming behaviour is characterised as accurately as possible.

A final objective of this study (#4) is to apply the validated simulation model toward a targeted optimisation of the FRTP DDF process, focusing specifically on the influence of transient thermal conditions on forming performance. While the preceding objectives centre around forming prediction through material characterisation and simulation, this optimisation effort is motivated by the need to reduce demoulding times and energy consumption. This is critical to the economic feasibility of FRTP production in low- to mid-volume applications. In manufacturing, even a reduction of a few seconds per part can translate into significant increases in throughput, improved cost-efficiency, and reduced environmental impact; particularly when scaling up to thousands of parts per year.

DDF is particularly well-suited to such optimisation because it already offers lower tooling costs and flexibility in forming larger or more complex geometries. However, the absence of process simulation tools has prevented systematic studies of how thermal transients influence forming rate, laminate temperature evolution, and eventual part quality. By integrating these effects within a fully-coupled, non-isothermal simulation framework, this work demonstrates a pathway toward more

energy- and time-efficient forming cycles, contributing both scientifically and practically to the wider adoption of FRTPs.

The workflow of this project, along with the aim and objectives highlighted in this chapter, can be visualised in Figure 1.2.

Chapter 3.

Experimental Double Diaphragm Forming

3.1 Introduction

The first objective that had to be met to produce an accurate FRTP DDF simulation for process prediction and optimisation was conducting an experimental DDF study. This allowed for an understanding of how FRTP DDF can be achieved in the real-world, before attempting to replicate this process in a numerical model. Furthermore, conducting experimental FRTP DDF trials provided the foundations for validation of the numerical forming simulation after its production.

The purpose of this chapter is therefore to conduct successful DDF utilising carbon fibre reinforced PA6, identified in the literature review as an ideal FRTP for this purpose (Section 2.2.2). This includes the selection of materials for successful forming, building of a functional FRTP DDF rig (including commissioning and validation) and finally conducting forming at a range of different processing parameters.

3.2 FRTP Selection and Property Validation

For all the work conducted, CF/PA6 laminates were acquired from Bond Laminates GmbH, denoted ‘Tepex Dynalite 202-C200(1)/50%’. Only single-ply 2x2 twill-weave laminates were acquired for the purposes of this work. Firstly, this allowed for streamlining of the material characterisation process (Chapter 4) since inter-ply effects could subsequently be neglected. Secondly, conducting numerical simulations (Chapter 6) with a fully-coupled thermomechanical model already required significant computational resource even for just a single-ply. Due to constraints imposed by this model, it was not possible to model multiple plies due to the associated (approximately linear) increase in solve time with ply-number due to the rise in the number of model elements. Finally, it was found by the author in a previous study [386] that in a multi-ply stack it is the coldest ply that largely dictates the forming behaviour. This means that, assuming a cooler tool, it is the ply making tool-contact that is most influential. Since, with just a single-ply, it is this ply that is in contact with the tool, the outcomes from this work are transferable to that of a multi-ply stack. Each laminate exhibited a fibre volume fraction of 51 wt%. The material properties, as provided by the manufacturer [387], are tabulated in Table 3.1, however the laminate properties were subsequently validated experimentally (see below).

Table 3.1: CF/PA6 material properties as provided by the manufacturer, with laminate properties determined from subsequent validation.

Element	Property	Value
Reinforcement	Fibre	Carbon fibre (CF)
	Fabric	Woven 2x2 twill
	Areal weight	200 g/m ²
	Yarn	3K
Matrix	Polymer	Polyamide 6 (PA6)
Laminate	Density*	1450 kg/m ³
	Fibre content*	48.9 wt%
	Nominal thickness per layer*	0.23 mm
	Melt Temperature*	223 °C
	Crystallisation Onset @ -10 °Cmin ⁻¹ *	194 °C

* Value deduced by validation exercise.

3.2.1 Laminate Thickness Validation

Initially, the individual ply thickness was validated by measuring five, 40 x 40 mm CF/PA6 specimens five times with a micrometer and taking an average. An average single-ply laminate thickness of 0.23 mm \pm 8% was recorded, as opposed to the 0.22 mm thickness quoted in the datasheet. For this reason, going forwards, a single-ply thickness of 0.23 mm is assumed, more accurately replicating the in-house CF/PA6 laminates. The significant variability was also noted.

3.2.2 Laminate Density Validation

The laminate density was validated by weighing five, 40 x 40 mm samples of single-ply CF/PA6 using a microbalance. The sample mass was then divided by the sample volume, utilising the nominal thickness from Table 3.1. The calculated density was 1450 \pm 7 kg/cm³, within 1% of the quoted datasheet value [387].

3.2.3 Laminate Volume Fraction Validation

The laminate volume fraction was validated by conducting a resin burn-off test. For this test, five, 40 x 40 mm, single-ply CF/PA6 samples were weighed with a microbalance, before being placed in a furnace. The samples were heated to 530 °C and held at this temperature for one hour, after which they were removed from the

furnace and cooled naturally. The samples, for which the resin had been burnt-off, were then weighed a second time. This yielded the mass of just the fibres from each specimen. The specimen fibre volume fraction could then be calculated with:

$$\phi_{vf} = \frac{m_{fibres}}{m_{lam}} \quad (3.1)$$

Where m_{fibres} is the fibre mass (after burn-off) and m_{lam} is the laminate mass (before burn-off). From this work, the volume fraction was found to be equal to 48.9 ± 1.2 wt%, within 4% of the quoted datasheet value [387].

3.2.4 Laminate Thermal Response

Finally, the thermal response of the CF/PA6 laminate was validated. The objective of this exercise was to not only assess the quoted melt temperature of 220 °C from the material datasheet [387], but also identify an approximate recrystallisation temperature. It was important to identify the recrystallisation temperature in this study as it was expected that FRTP thermoforming would not be possible upon the occurrence of crystallisation. The crystallisation onset point therefore defined a lower bound for which thermoforming could take place.

The thermal response of a representative CF/PA6 laminate was evaluated using differential scanning calorimetry (DSC). A 30 mg sample of the chosen FRTP was heated at 10 °C /min from 50 °C up to a maximum of 300 °C, at which point it was cooled at the same rate back down to 50 °C. The results from the DSC testing are illustrated in Figure 3.1 with positive heat flow being in the exothermic direction. It can be extrapolated from this figure that the sample was fully melted at approximately 223 °C, and for a cooling rate of 10 °C /min, the onset of crystallisation was approximately 194 °C.

The results from the laminate thickness, density, volume fraction and thermal analysis studies are included in Table 3.1 which is referred to hereon in for the material properties of CF/PA6.

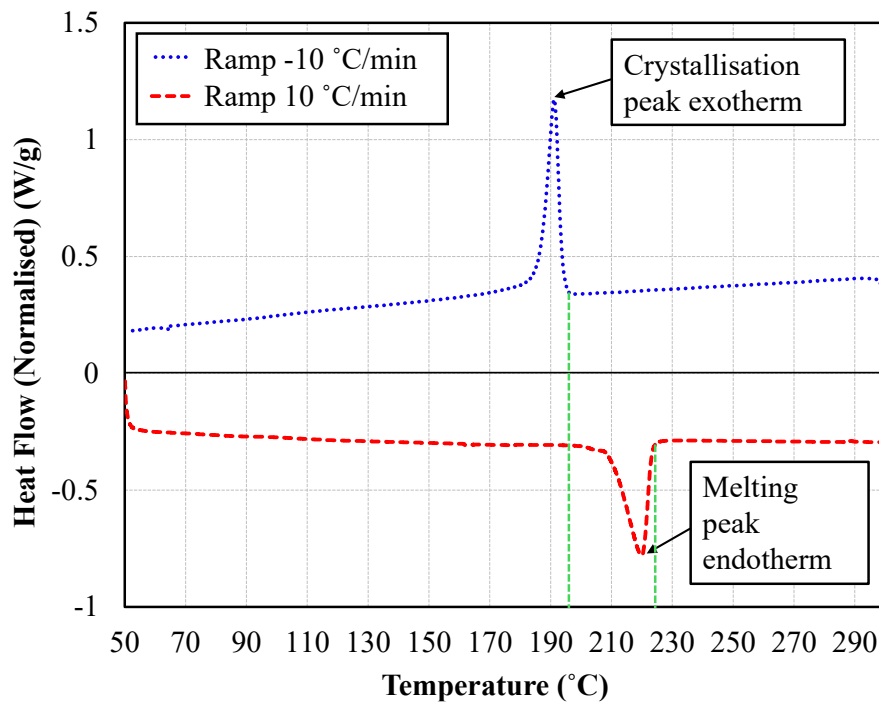


Figure 3.1: Heat flow *versus* temperature of CF/PA6 sample undergoing differential scanning calorimetry

3.3 Apparatus Production

To conduct experimental DDF with FRTPs, a vacuum chamber was required to house a tool geometry and locate the diaphragms (and therefore laminate) in position for forming to take place. Due to the requirement of heating the laminate over 223 °C (for complete melting, as per Figure 3.1), it was envisaged that the laminate would initially need to lie flat, not in contact with the tool. The DDF rig therefore resembled an open ‘box’ structure, produced using aluminium strut profiles. The high sidewalls of this structure supported the diaphragm and laminate above the tool prior to forming. The base and sides were sealed with silicone glue, capable of withstanding the high temperatures expected during the forming process. Figure 3.2 illustrates the different components of the DDF rig. An overall assembly photo is included in Appendix A - Figure A.1 to aid identification of the various components.

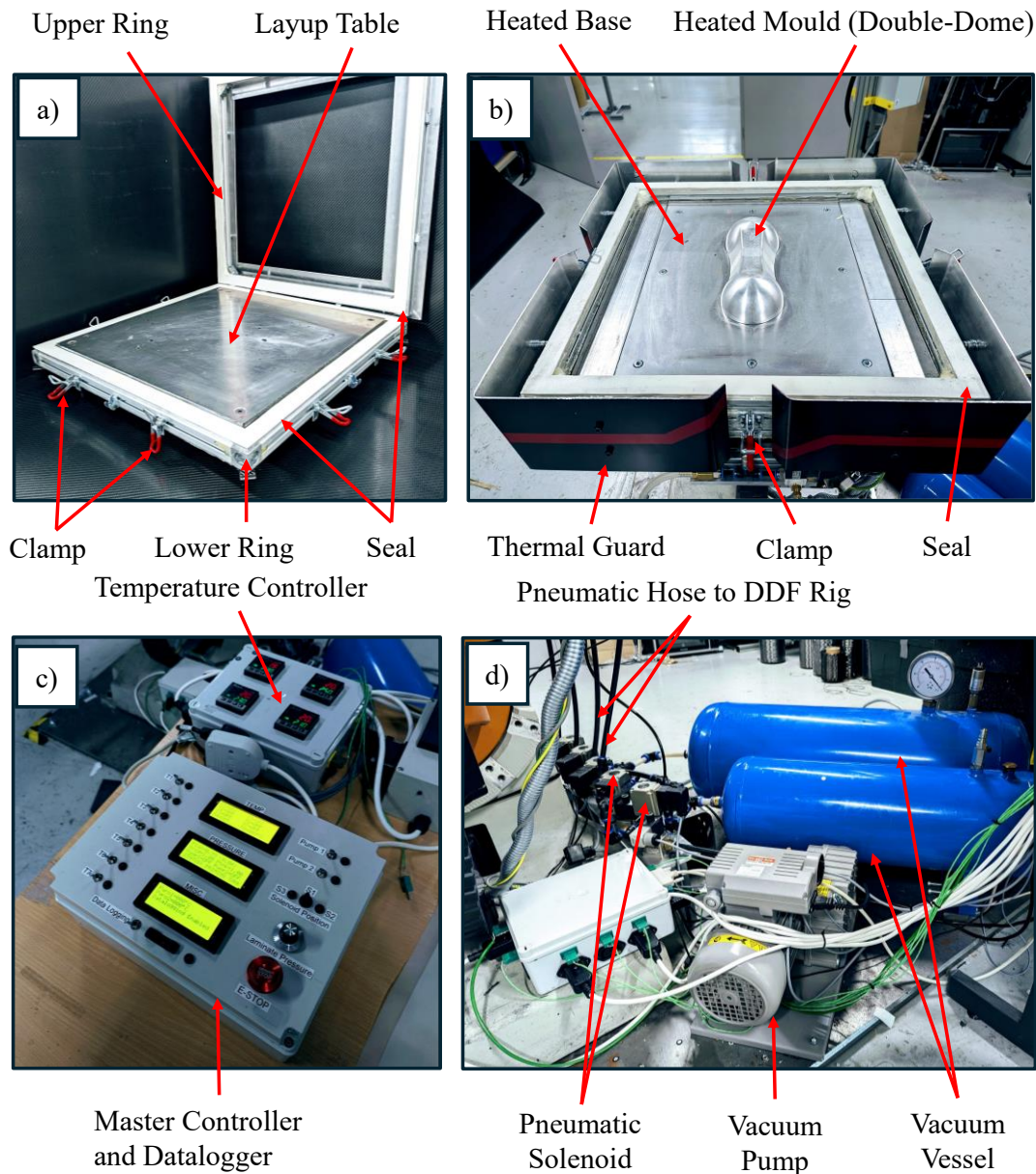


Figure 3.2: a) DDF rig, b) diaphragm layup table, c) master pneumatic and thermal control system, d) pneumatic components.

The upper section of the DDF rig could be removed and subsequently separated into an upper and lower ring (Figure 3.2a). Silicone foam seals were glued to these rings such that when clamped together, an air-tight seal was obtained. This allowed for clamping of two diaphragms. This process was conducted on a custom diaphragm layup table that kept the diaphragms, breather, and laminate, flat during the positioning process. Once this procedure was completed, the whole dual-ring setup (complete with diaphragms and laminate) could then be repositioned and clamped onto the DDF rig (Figure 3.2b), which had a second air-tight silicone foam seal.

Inside the DDF rig (Figure 3.2b), a mould was located. For the purposes of this work, a variant of the double-dome geometry, also utilised in several previous works (Section 2.7.3), was used. The double-dome itself is a good benchmark geometry that tests fibre composite forming behaviour in a range of different ways. Figure 3.3 illustrates the double-dome geometry used in this work, which also features a cambered central section.

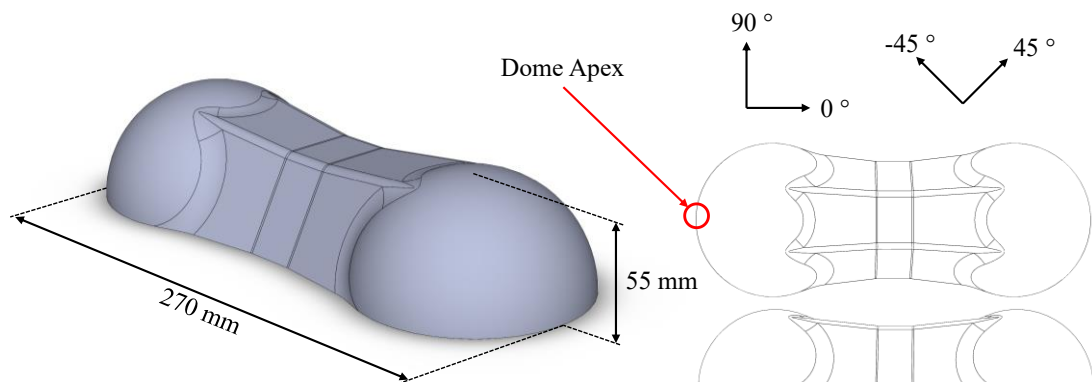


Figure 3.3: Double-dome benchmark mould used in this work.

Due to the high laminate temperature during forming, the double-dome geometry was manufactured from aluminium (polished finish), capable of withstanding the high temperatures. It was predicted, however, that a cold aluminium mould would be problematic during forming. This is by virtue of the high conductivity between the laminate and the tool potentially leading to over-cooling of the FRTP laminate, thus resulting in incomplete forming. Therefore, the mould was fitted with ten 200W heating elements allowing for complete heating of the geometry. This mould was fitted to an aluminium base (polished finish), equipped within four 300W heating pads, once again to prevent specimen cooling. Together, these are denoted the ‘tool’. A 1 mm gap was fixed between the mould and base for the purposes of airflow. All heating elements were equipped with an associated thermocouple, such that PID control for different pre-defined tool temperatures could be achieved with a thermal controller (Figure 3.2c). This also allowed for mould cooling post-forming such that the component could be demoulded. With the mould and base present inside the DDF rig, the inner working dimensions were 530 x 530 x 65 mm (not including the double-dome).

The bottom of the DDF rig was equipped with pneumatic connections such that a vacuum could be pulled within the apparatus. These vacuum connections were connected directly to a vacuum pump, and two pressure vessels (75L total volume) certified for vacuum storage (Figure 3.2d). Four vacuum solenoids were then used to initiate removal of air from the DDF rig, either using just the pump or utilising the pre-charged vacuum pressure vessels. The idea was to allow for two different forming rates since the use of vacuum pressure vessels provided a quick removal of air from the apparatus. When neither the pump nor vacuum pressure vessel were engaged, the DDF rig vented to atmosphere such as to mitigate issues regarding leaking of the vacuum solenoids. Pressure sensors were also equipped to the DDF rig and pressure vessels, with the pressure logged over time by the datalogger (Figure 3.2c). Since in the DDF process, it is also required to pull a vacuum from between the two diaphragms, in each case the upper diaphragm was equipped with a vacuum port. This inter-diaphragm vacuum would then be pulled using a secondary vacuum pump, again equipped with pressure sensors for monitoring.

Figure 3.4 illustrates the setup process for FRTP DDF, which follows:

1. Layup of the laminate and breather above the lower diaphragm layer on the layup table, with the lower clamping ring in place. The blank location was measured in each case to ensure it would be aligned fully with the tool.
2. Positioning of the upper diaphragm, complete with vacuum port, over the layup table and clamping with the upper ring.
3. Transportation of the complete dual-ring setup, complete with diaphragms, breather and laminate, to the DDF rig and clamped in place. A vacuum is then pulled between the two diaphragm layers.
4. Heating of the specimen via an 8kW Hereaus infrared heater panel (four filaments) supported over the DDF former (via an integrated pneumatic strut frame), itself equipped with a pyrometer for closed-loop control of the laminate temperature.

In this example case, silicone diaphragms are illustrated, which was the chosen material for the FRTP DDF process. This is due to the high temperature resistance of silicone elastomers, coupled with the low temperature-dependency exhibited by these materials [388]. This compares to high temperature polymeric films that exhibit a high

degree of material temperature-dependency. This results in a failed DDF operation, since the diaphragm temperature in contact with the laminate is much higher than the surrounding diaphragm material. This means that all strain initially takes place just around the circumference of the laminate, leading to a breach of the diaphragm bag. This can be seen in Appendix A - Figure A.2, where a fluoropolymer diaphragm bag [389] was tested.

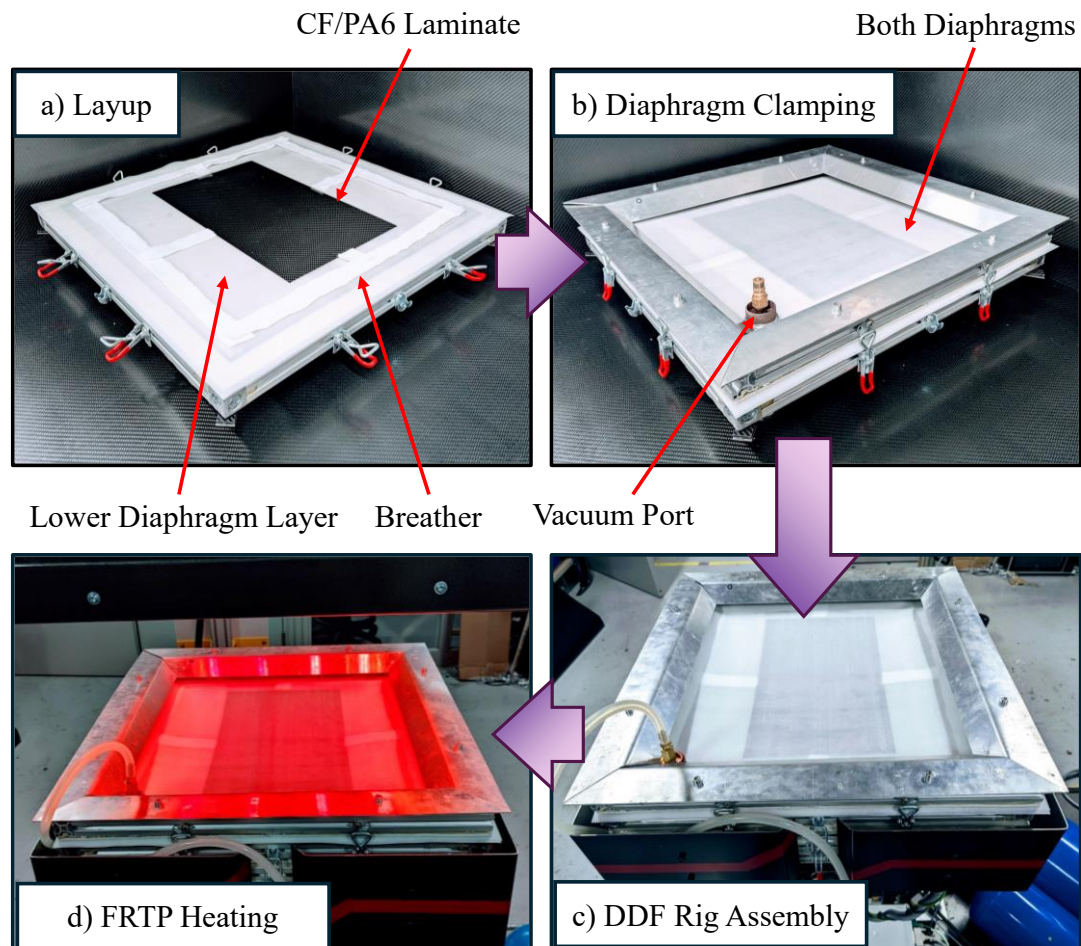


Figure 3.4: Setup process for the experimental FRTP DDF process: a) layup process, b) clamping of diaphragms, c) assembly of enclosed DDF rig, d) specimen heating.

Another advantage of using silicone diaphragms is their robust reusability across multiple forming trials, which offered both practical and economic benefits throughout the experimental campaign. Unlike high-temperature polymeric films that plastically deform after a single use, the selected silicone elastomer demonstrated excellent elastic recovery even after repeated exposure to elevated temperatures and large deformations. This meant that the same diaphragm sheets could be reused for several forming cycles without significant changes to their mechanical response. As a result, the need to

produce or replace diaphragms after each trial was eliminated, significantly reducing material costs and streamlining the experimental workflow. This reusability also helped maintain consistency between trials by avoiding variability introduced by diaphragm replacement, such as slight differences in sheet thickness and surface finish.

In this work, 1 mm thick, 40 gp shore hardness silicone sheet was obtained from Silex UK Ltd [390]. The sheet has a quoted maximum temperature of 250 °C, and maximum strain of 500%, sufficient for the purposes of this work. The continuous silicone roll was cut into 600 x 600 mm sheets to fit the diaphragm clamping rings illustrated in Figure 3.2a.

Owing to the reusable nature of the silicone diaphragms, it was imperative to ensure that the diaphragm mechanical response was identical between repeated forming trials. Therefore, to enhance performance stability, each diaphragm was pre-conditioned by rolling (pre-compressing) it three times in both principal directions. This technique was implemented to remove any strain-history-dependent stiffness and ensure that the diaphragm exhibited a consistent mechanical response from the outset. The strain-history response as well as the elastic behaviour is subsequently evaluated in Chapter 5 of this work, validating the reuse of silicone diaphragms and the pre-straining method to remove the history dependence. This method proved critical in preserving diaphragm performance over time and ensuring reliable, repeatable forming results under identical processing conditions.

3.4 FRTP Experimental DDF Forming Trial

This section outlines the process that was followed to complete successful isothermal DDF with CF/PA6 laminates. Initially, a forming trial was attempted to optimise the experimental DDF process and validate the various mechanical and thermal processes during its operation. Isothermal thermoforming denotes the fact that the laminate temperature is kept approximately constant during the forming process, utilising an overhead IR heater and a heated tool and base. The aim of this was to eliminate transient thermal effects from the forming operation, thus simplifying the procedure.

For the purposes of this work, the forming trial was completed with a CF/PA6 laminate at one temperature (250 °C) and one test rate (slow via the direct withdrawal of air using a vacuum pump). These are hereon in denoted the ‘reference conditions’. The CF/PA6 laminate was cut using a Bullmer X-CUT ply cutter, with fibres oriented in the 0/90° direction (refer to Figure 3.3), measuring 400 x 240 mm. This was sufficient to fully encapsulate the double-dome during the forming process. The setup process detailed in Figure 3.4 was subsequently implemented to instigate the DDF process.

3.4.1 Setup Optimisation

An issue was identified upon heating of the FRTP laminate (Figure 3.4d), resulting in wrinkles occurring in both diaphragms, along with significant ‘drooping’ behaviour. This resulted in both the diaphragms and laminate making tool-contact, before the forming operation was initiated. Figure 3.5a illustrates these phenomena, showing a laminate after heating to 250 °C.

This behaviour was considered unacceptable. Firstly, wrinkles occurring in both diaphragms (especially the lower diaphragm) influenced the forming behaviour, leading to wrinkles in the final cooled part. Furthermore the ‘drooping’ of the diaphragm bag meant that, with the laminate in a warped condition, significant in-plane thermal distributions could be expected. This also resulted in premature tool-contact being made.

This behaviour was attributed to the large degree of thermal expansion occurring within the silicone diaphragms. While it was not possible to remove thermal expansion from the silicone, a novel way to inhibit both the wrinkling and ‘drooping’ behaviour was identified. The layup table was fitted with thermal pads and an associated thermal control unit, as illustrated in Figure 3.5b. The entire layup table could then be heated, prior to the diaphragm clamping process illustrated in Figure 3.4b, allowing the diaphragms to expand in-situ. Since it was undesirable to melt the laminate, the layup table was maintained at a constant 200 °C. After a 5-minute dwell period, the diaphragms were clamped as per Figure 3.4b, with the rest of the setup process remaining the same. This process therefore effectively pre-stretched the diaphragms, locking them in place in an already expanded condition. While forming was completed at a maximum laminate temperature of 250 °C, the diaphragm material away from the

laminates were significantly cooler, meaning that only minimal further expansion was possible above the new 200 °C baseline. This tension eliminated the occurrence of both wrinkles and ‘drooping’ of the diaphragm from the FRTP DDF process.

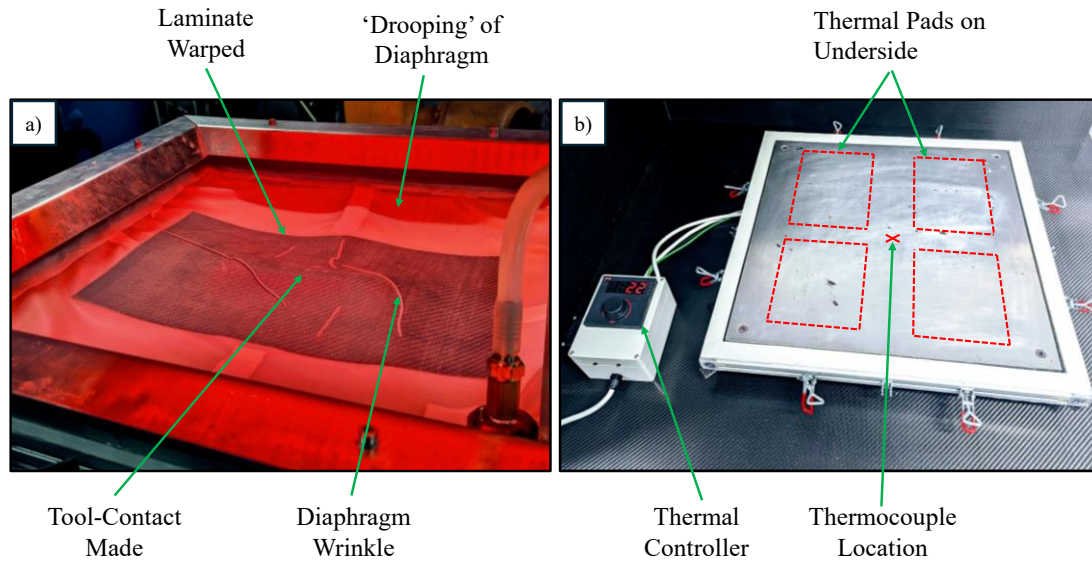


Figure 3.5: a) Defects caused by silicone thermal expansion, b) layout table equipped with heating system.

3.4.2 Thermoforming

To monitor the diaphragm behaviour during the initial trial, specifically the diaphragm strain, a 10 x 10 mm grid was applied to the upper diaphragm prior to the setup process. This also allowed for tracking of the relative movement between the diaphragm and the laminate during the forming process. Section 3.4.3.3 details the analysis of this monitoring exercise.

Forming was undertaken following the procedure illustrated in Figure 3.4, with the aforementioned heating of the layout table (Section 3.4.1) to hold the diaphragms in tension at the start of the forming process. Figure 3.6 shows ‘freeze-frames’ from four different stages of the forming operation, for the 1-ply trial laminate at reference conditions (250 °C, slow formed, 0/90° orientation).

The isothermal forming was successful; significant mould conformity was achieved for the laminate at reference conditions. A large degree of relative slip between the diaphragms and laminate was evident with the black perimeter line illustrating the initial laminate position compared to the perimeter of the formed part. Furthermore,

'bridging' behaviour was noted around the base of the tool, attributed to the 1 mm thick silicone diaphragms used in this study.

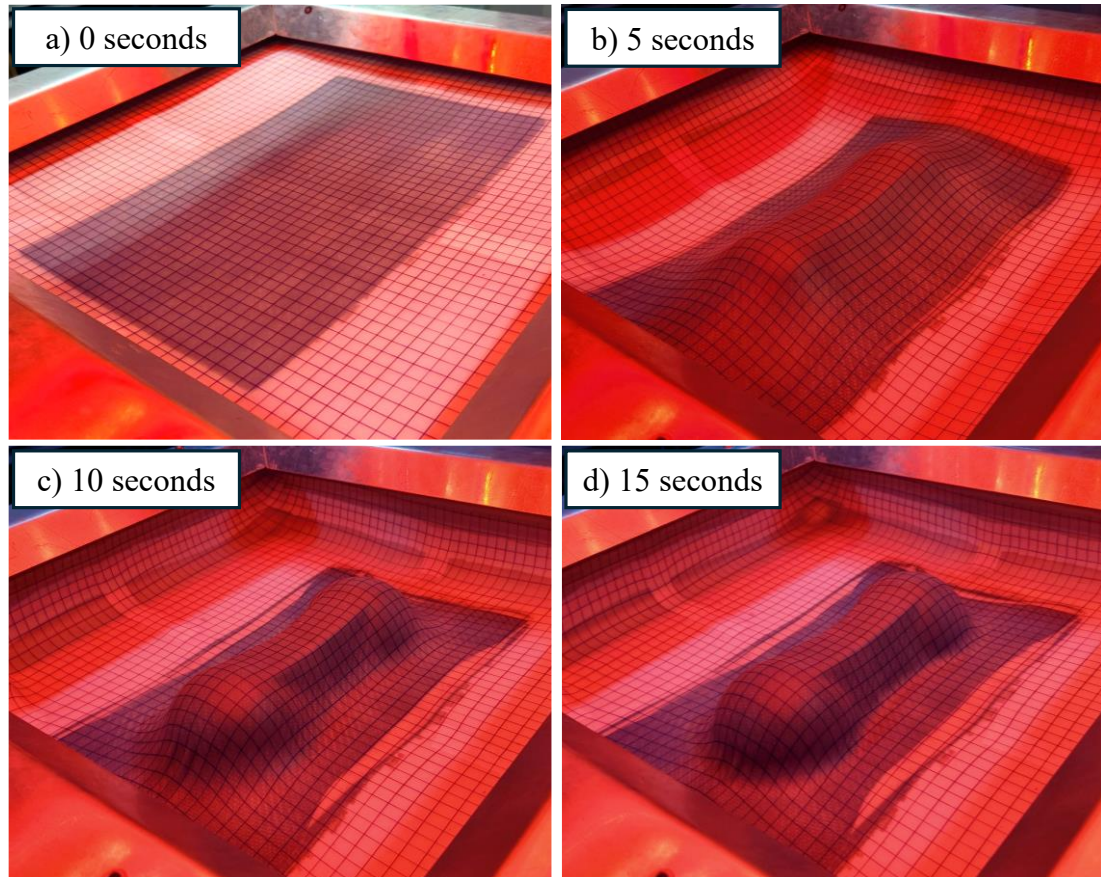


Figure 3.6: 'Freeze-frames' taken at different periods during the DDF process for the reference FRTP laminate.

To quantify the forming quality of each laminate, three individual quantitative forming behaviours were analysed:

Variable 1. Wrinkling behaviour (Section 2.6.1)

Variable 2. Bridging behaviour (Section 2.6.2)

Variable 3. Shear behaviour

Analysis of these three variables was considered sufficient to quantify the formability of each laminate, at a specific test condition. To obtain these variables, the laminate was scanned in-situ once forming was complete. In-situ scanning was prudent due to the warping behaviour that was obvious after cooling and removal from the tool. A Creaform Handyscan3D 700 white light scanner was used to scan the geometry of the final form, after the application of positioning targets to aid the scanning process. The

scanning process generated a point cloud, with a 0.5 mm resolution, which was subsequently meshed to create a surface replicating the FRTP form. Figure 3.7a illustrates the raw output from the reference laminate scan. Since this was an in-situ scan, it was the top of the upper diaphragm that was scanned in this process. This was not an issue as diaphragm-laminate contact was maintained, such that the laminate form was identical to that of the top diaphragm, offset by the diaphragm thickness.

From the raw scan, it was possible to observe the location and quantity of wrinkling (variable 1). In the case of the reference laminate, small wrinkling existed at the upper/lower apexes of both hemispheres (refer to Figure 3.3). It was expected that the severity of these wrinkles would change depending on the test conditions.

To quantify the size of these identified wrinkles (variable 1) and furthermore quantify the bridging behaviour (variable 2), the double-dome tool geometry was also scanned using the white light scanner. It was then possible to compare the point clouds from both the double-dome tool geometry and the laminate scan (top surface of the diaphragm). This process was completed using MATLAB, following the same procedure outlined by Lawrence [391], although for woven fabrics as opposed to NCFs.

The initial step involved aligning the two individual point clouds to a common coordinate system. This was achieved using a least squares minimisation algorithm via Iterative Closest Point (ICP) registration. This algorithm iteratively refines the transformation (translation and rotation) applied to the laminate point cloud to minimise the straight-line distance to the tool point cloud, thus compensating for any relative displacement or rotation during scanning. Following alignment, the minimum distance from each point on the laminate surface to the closest point on the tool surface was computed by identifying the nearest neighbours in the large point set.

The resulting distance values represent the local offset between the laminate and the tool surfaces. Wrinkle amplitude was then quantified as the spatial variation in this offset, with larger deviations corresponding to pronounced wrinkles or out-of-plane deformations. Similarly, bridging behaviour was inferred by analysing regions where the laminate–tool offset increased, indicating gaps or lifted areas between the laminate and tool surface. This methodology provides a robust and quantitative approach to characterising wrinkle severity and bridging phenomena in thermoformed laminates.

Due to the scanning of the upper diaphragm surface, it was required to subtract the upper diaphragm and laminate thickness from this value to determine a final bridging value. The minimum amount of bridging possible was therefore 1mm, or the thickness of the lower diaphragm. The reduction in diaphragm thickness owing to the biaxial strain was considered negligible in this study. Figure 3.7b illustrates the output from this process for the forming trial, with the tool-laminate offset illustrated by colour.

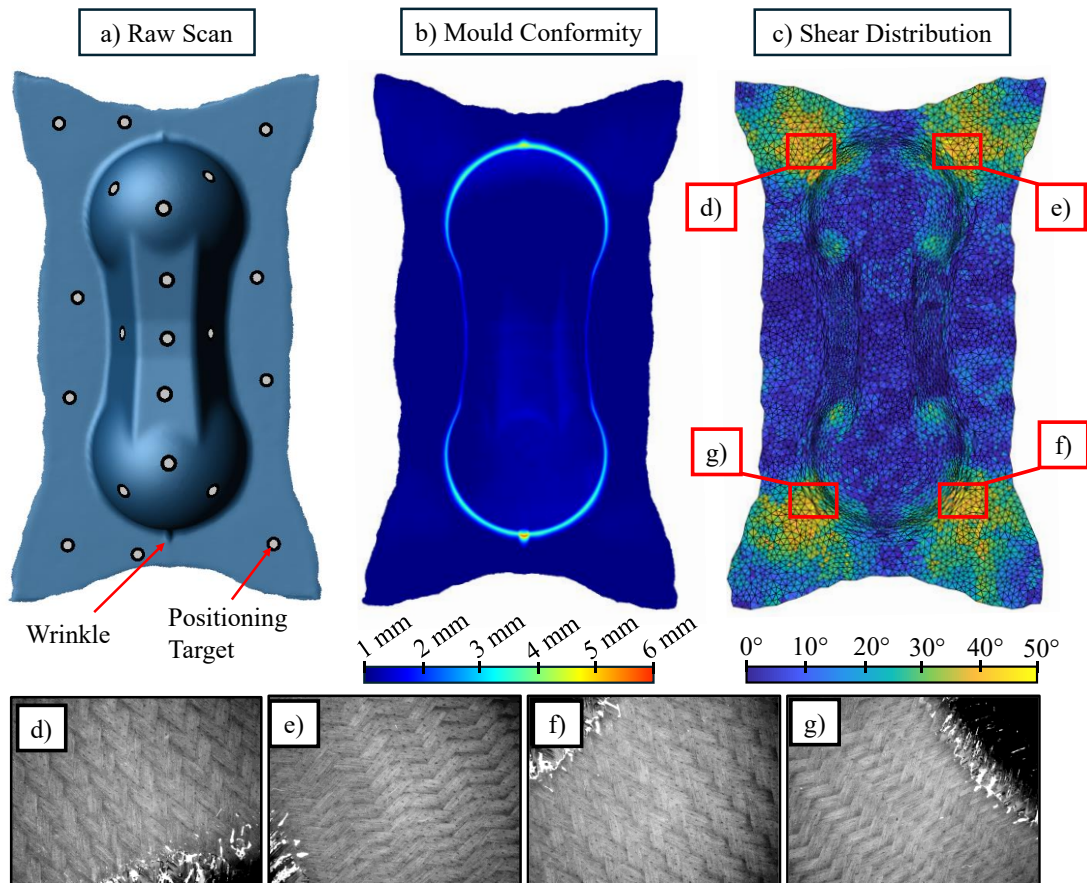


Figure 3.7: Scans of reference laminate post-forming: a) raw scan, b) mould conformity plot, c) shear angle distribution plot, d-g), images taken at locations of maximum shear.

The maximum bridging was taken as the maximum laminate-tool distance, excluding areas defined as wrinkling. Due to the symmetrical nature of the double-dome geometry, four maxima were taken, one from each quartile, to obtain an average maxima for bridging behaviour. For the rest of this work, the average value of maximum bridging between the four quartiles of the double-dome is simply denoted ‘maximum bridging’ for concision. In the case of the reference laminate, this maximum bridging was 3.8 mm. Due to the resolution of the point cloud and accuracy regarding the point-cloud alignment algorithm, this value is accurate within ± 0.25 mm.

For wrinkling, the wrinkle amplitude was taken as the maximum tool-laminate offset at the centre of the wrinkle. Furthermore, a maximum wrinkle length could be determined. For simplicity, in this study, this was defined as the straight-line distance between both ends of the wrinkle (defined as points >2 mm of tool-laminate offset). In the case of the reference laminate, the maximum wrinkle amplitude and length were 5.3 mm and 10.1 mm respectively.

It was not possible to assess the laminate shear distribution (variable 3) using the white-light scanner and point cloud since this only depicts geometry, with no information provided regarding the fibre angles. For this purpose, the trial laminate was demoulded after scanning had been completed and once the laminate temperature had dropped below the recrystallisation temperature (Table 3.1). This was achieved by switching off the tool and base heaters immediately after the completion of forming.

A Hexagon Apodius Arm was subsequently used to scan the trial laminate and obtain a point cloud, which was then then meshed with 3 mm triangular elements. The arm was then equipped with a 3D vision sensor, such that the laminate could be photographed, with each element assigned a corresponding vector for the direction of the warp and weft yarn directions respectively. This data was exported into MATLAB, where spurious data values were identified and removed. Figure 3.7c illustrates the results from this, clearly showing the shear angle distribution over the double-dome part. While the scan was considered beneficial for identifying the areas of high shear, the process was laborious due to the time associated with using the 3D vision sensor, along with the post-processing. Since all laminates oriented in the same manner exhibit a similar shear angle distribution (regardless of test conditions), the 2D vision sensor was equipped going forwards in this work to only image the four areas of maximum shear. Figure 3.7d-g illustrates the photographs of these maximum shear regions. The Apodius Explorer 2D software calculated an average shear value automatically from these images, and an average was then calculated using the four maxima. Therefore, for the reference laminate, the maximum shear angle (quadrant average) was 49.2° .

3.4.3 Forming Validation

As part of the initial forming trial, a series of validation exercises were conducted to monitor the DDF process during its operation. These data were subsequently used in

the associated DDF simulation (Chapter 6), such that the simulation closely resembled the experimental forming conditions. The exercises that were conducted were: laminate thermal validation, pressure (both inter-diaphragm and diaphragm-tool) validation and diaphragm strain validation. These are outlined in the subsections below.

3.4.3.1 Laminate Thermal Validation

While, as discussed in Section 3.3, a pyrometer was equipped to the overhead Hereaus IR heater panel to achieve PID thermal control, this only provides a point temperature reading at the centre of the laminate. It was therefore decided that before the forming was completed, as detailed in Section 3.4.2, a thermal validation study would be conducted to evaluate the thermal profile of the entire laminate. For this purpose, an RS730 IR camera was mounted above the DDF rig allowing for real-time feedback of the laminate temperature. It was not possible to use the camera during the isothermal forming process since the heater remained above the specimen, thus blocking the camera view. Instead, the laminate was prepared and heated (as per Figure 3.4) to a set temperature, with the IR heater then quickly removed. The laminate temperature could then be recorded as a pre-requisite operation, prior to forming.

For this exercise, a pyrometer set temperature of 250 °C was chosen, which resembled the maximum achievable temperature due to the thermal limitation associated with the silicone [390]. Since this was the maximum temperature, it also provided the maximum in-plane temperature discrepancies. Once the set temperature had been reached, a 5-minute dwell period followed to ensure thermal equilibrium was met. Moreover, both the tool and base temperatures were set to 250 °C to replicate real forming conditions. Figure 3.8 illustrates the IR image taken immediately after removal of the IR lamp, thus revealing the laminate thermal profile at the beginning of a subsequent forming operation. This was conducted three times, with similar results captured for each (± 1 °C). Therefore, the results from just one run are illustrated.

As expected, the temperature of the laminate far exceeded that of the surrounding diaphragm due to the higher absorptivity of the material (validated in Section 7.6). While this forming was considered isothermal, meaning constant temperature, there were still thermal discrepancies that existed across the laminate. Two distinct ‘hot spots’ were identified: at both edges, running parallel with the long edge of the

specimen. These were caused by the spectral distribution of the individual emitters within the IR unit. While the maximum laminate temperature was 250 °C, the bulk laminate temperature (average taken from a 10 x 10 mm mesh) was approximately 242 °C. A small drop in laminate temperature was expected due to the removal of the IR heater, explaining the lower centre temperature (246°C) than recorded by the pyrometer. Furthermore, the top and bottom edges of the laminate appeared to be slightly colder than the rest of the laminate, with a minimum laminate temperature of 232 °C. It is highly likely that this was caused by a degree of under-sizing of the overhead IR lamp, coupled with edge effects associated with the sides of the DDF rig. It was assumed in this work that there a negligible through-thickness temperature gradient owing to the thin single-ply laminate used in this study, with this assumption validated in Section 7.6.

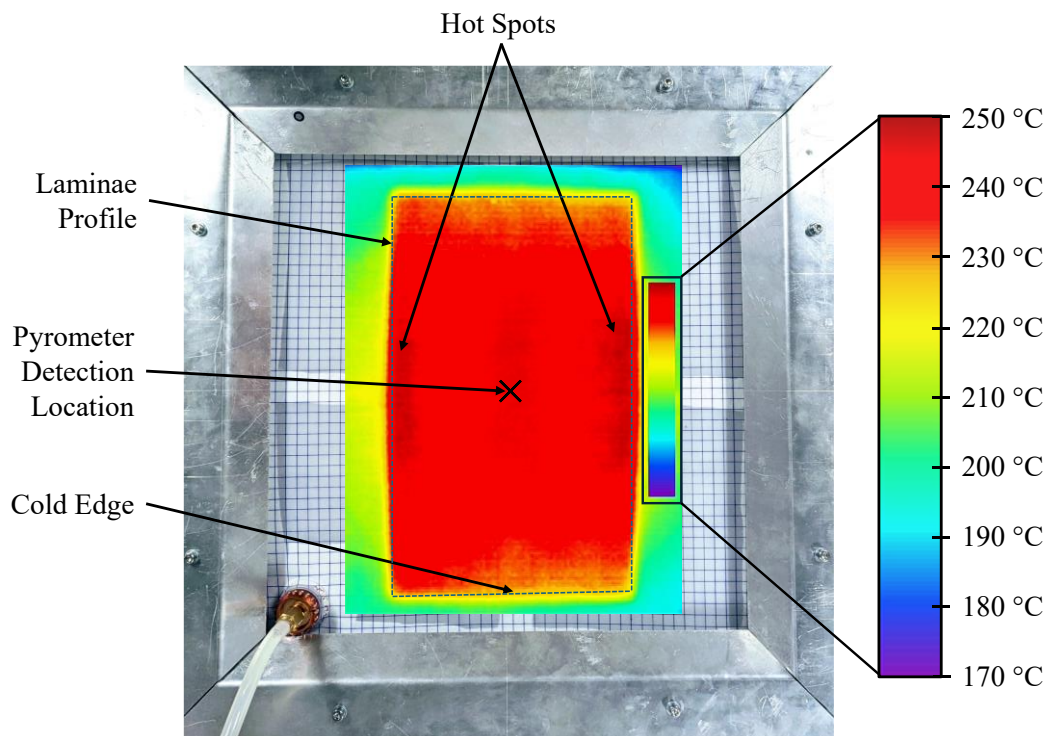


Figure 3.8: In-plane thermal distribution of the laminate before the commencement of the forming (IR Image superimposed over top-down photograph).

The diaphragm temperature was significantly lower than that of the laminate due to the low IR absorption capabilities of silicone, with this further decreasing towards the frame edges as the associated IR view factor decreased. The breather cloth was seen

to exhibit little influence on the thermal distribution, once again due to the cloth exhibiting low IR absorption capabilities.

These results illustrate that a maximum thermal variation of 18 °C exists over the entirety of the laminate. For the remainder of this work, however, the laminate temperature is referred to as the maximum temperature (assumed to be 250 °C in this case). The isothermal simulation (Chapter 6), however, utilises the bulk laminate temperature for a more accurate depiction of laminate temperature.

3.4.3.2 Pressure Validation

Both the diaphragm-rig and inter-diaphragm pressure were monitored during the forming routine since these variables considerably influence the manner to which forming is completed. These variables are assessed in-turn below.

1) Diaphragm-rig pressure validation

The main driver for the FRTP DDF operation is the reduction of air pressure below the bottom diaphragm. For the simulation to accurately recreate real-world forming conditions, the pressure-data for was recorded using a Festo pressure sensor and stored in the associated datalogging unit (Figure 3.2c). Figure 3.9a illustrates the diaphragm-rig pressure for the trial thermoforming operation.

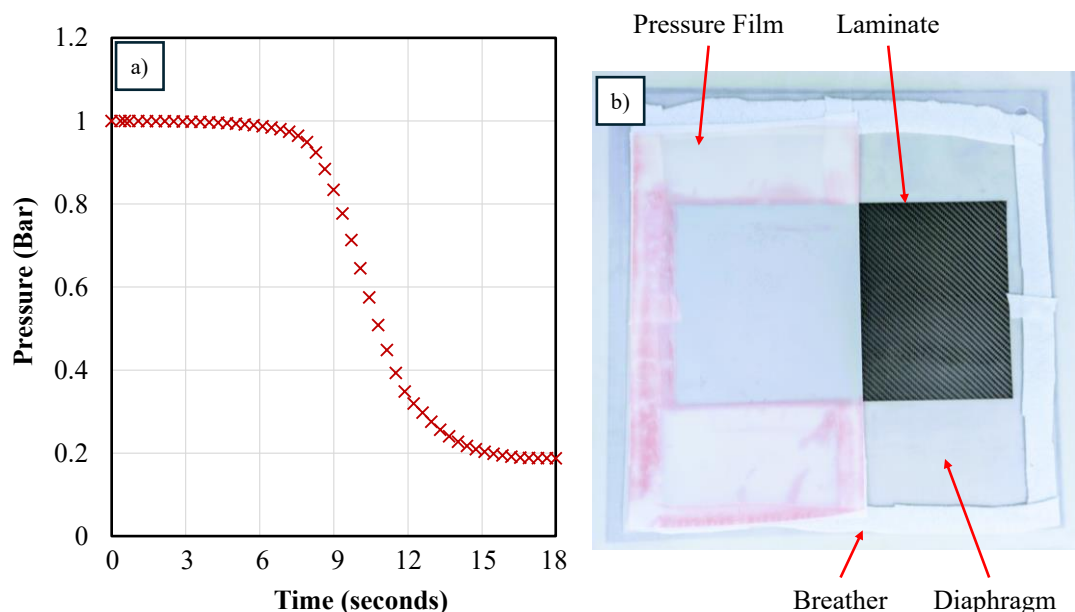


Figure 3.9: a) Diaphragm-rig pressure validation, b) inter-diaphragm pressure validation.

The dynamic pressure curve can be broken down into three distinct sections. Initially, a very gradual decrease in pressure was present for 7-8 seconds. This is due to the considerable quantity of air (approximately 25 litres) that existed within the DDF apparatus, by virtue of the high side walls, to maintain diaphragm-tool separation at the commencement of the forming routine. During this period, this quantity of air was removed from the chamber, however the subsequent deformation of the diaphragms means that only a small pressure reduction was recorded. Once diaphragm-tool contact was made, since a large proportion of air has been removed from the chamber at this point, the pressure started to decrease considerably. This is due to the limiting degree for subsequent diaphragm deformation. This considerable reduction in pressure lasted for approximately 4 seconds, before the third and final stage of the pressure curve where an equilibrium value was slowly achieved, after approximately 18 seconds in this case. Due to air leakage with the DDF rig and associated pneumatic components, the minimum achievable pressure was 0.18 bar. This was not considered to be a hindrance to successful DDF forming, however, since any subsequent pressure reduction below this value was expected to yield only marginal improvements in mould conformity. This is due to the corresponding increase in friction between the laminate and the diaphragm at the latter stages of the forming operation. For tests conducted with a high forming rate, it was assumed that the profile remained consistent with that illustrated in Figure 3.9a, but over a shorter (3 second) timespan.

2) Inter-diaphragm pressure validation

While, as described in Section 3.3, a vacuum was pulled between the two diaphragms before forming was completed, it was assumed unlikely that the pressure distribution between the diaphragms would be homogeneous. This is due to the solid organosheet that was not expected to allow vacuum propagation. Therefore, similar to the thermal validation exercise (Section 3.4.3.1), an inter-diaphragm pressure validation exercise was conducted as a pre-requisite to the forming operation described in Section 3.4.2.

For this exercise, a layer of Fujifilm Prescale film [392] was placed over half of the laminate and diaphragm (in between both diaphragms), during the layup process (Figure 3.4a). The setup was then clamped and affixed to the forming rig as per Figure 3.4b & Figure 3.4c. It should be noted that for this validation exercise, both the preheating (Section 3.4.1) and the in-situ heating (Figure 3.4d) were not completed

due to the low thermal tolerance of the Prescale film. This was not considered an issue however, as the bulk pressure distribution was assumed to remain relatively consistent, regardless of laminate temperature. Once the inter-diaphragm vacuum was pulled, the setup was left to dwell for 5 minutes, allowing the Prescale film to record the pressure distribution. The rig was then disassembled to evaluate the pressure distribution. Figure 3.9b illustrates the results from this validation exercise.

As expected, the vacuum distribution between the two diaphragms was not uniform. Unlike what would be expected with a dry fabric, the impregnated FRTP sheet did not permit airflow, meaning that no vacuum was pulled over the entirety of the laminate. Instead, a vacuum was pulled around the edge of the laminate, where a small degree of diaphragm bridging would be expected. Furthermore, areas where there was no breather generally exhibited no vacuum pressure. This meant that vacuum was limited to just the breather and the perimeter of the laminate. This work validates the use of breather, as it was considered important to remove as much air as possible from between the diaphragms at the start of the process.

This validation exercise illustrates that at the start of the forming process the laminate experiences little pressure, apart from around the edges. It was not possible in this work to evaluate the inter-diaphragm pressure *during* the forming process, due to the thermal requirement of the CF/PA6 laminates. Since the two diaphragms would be largely affixed to one another due to the removal of air, however, it is a fair assumption to make that the inter-diaphragm pressure matched that of the diaphragm-rig pressure. This is because as the lower diaphragm is pulled down towards tool, the upper diaphragm is forced to follow due to the little air between the two diaphragms. Any inter-diaphragm spacing that occurred would quickly be eliminated since this would allow for vacuum propagation. With this assumption, in effect, the diaphragm-rig pressure acts on the upper diaphragm as much as it does on the lower diaphragm. The inter-diaphragm pressure is therefore assumed to also replicate Figure 3.9a.

3.4.3.3 Diaphragm Strain Validation

The final validation exercise to analyse the DDF process described in Section 3.4.2 was analysis of the diaphragm strain, after forming completed. This was considered necessary since it was inevitable that diaphragm behaviour would also require

characterisation (Chapter 5) for implementation within the simulation routine (Chapter 6). Therefore, understanding the extent to which the diaphragm deforms was important to meet the objectives of this work.

As already noted in Section 3.4.2, for the DDF forming trial, a 10 mm x 10 mm grid was applied to the upper diaphragm prior to forming. After the completion of forming, the localised diaphragm strain could be analysed by measuring the distance between adjacent lines. Figure 3.10a illustrates a plan view of the diaphragm post-forming.

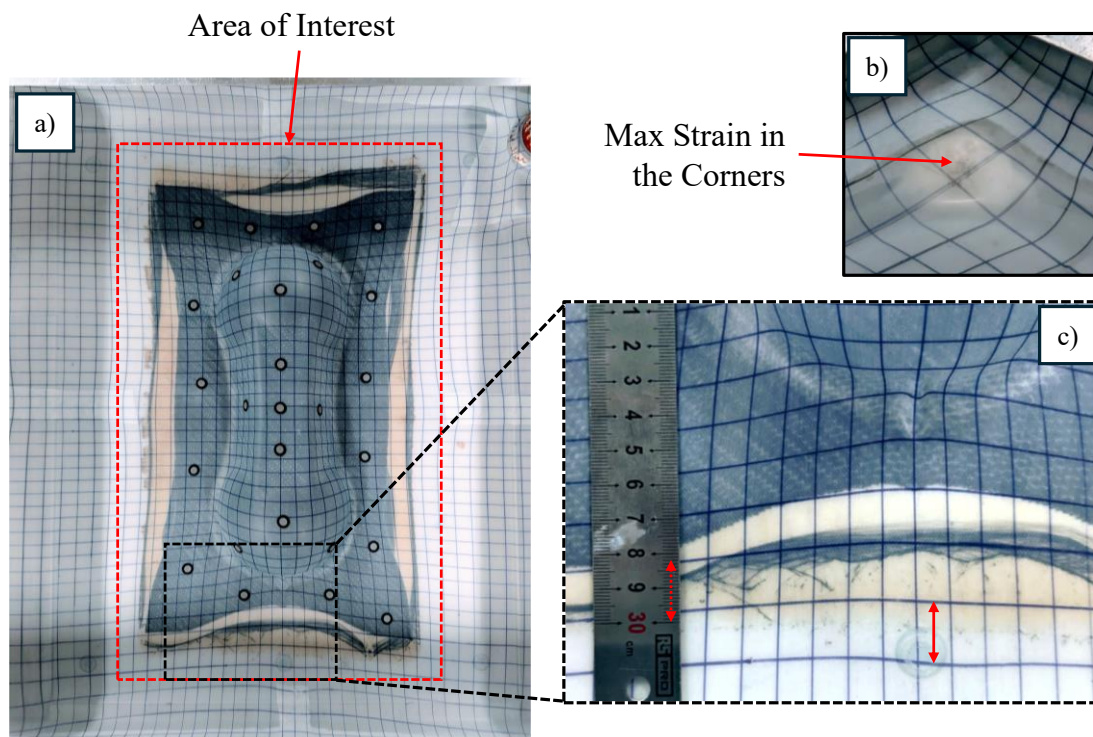


Figure 3.10: Diaphragm strain validation, a) Plan view of entire laminate, b) Maximum strain at DDF rig corners, c) Maximum strain within the designated 'area of interest'.

The maximum strain was identified in the corners of the forming rig, with up to 110% strain (biaxially) present at the acute location between adjacent sides and the base (Figure 3.10b). This area was however not considered relevant with regards to the formability of the laminate. This is because of the large proximity between the laminate and the DDF rig corners. Instead, it was proposed that the 'area of interest' (AOI), regarding the strain of the diaphragm that is expected to influence the forming behaviour, was a region offset approximately 25 mm around the perimeter of the laminate (at the beginning of the forming operation). The strain of diaphragm material within this area is expected to contribute to the laminate formability.

Therefore, neglecting the strain outside of the area of interest, the maximum diaphragm strain was identified as being at the short edges of the specimen. This was likely caused by the small laminate-side distance at these points, meaning more localised strain was required to achieve mould conformity. Figure 3.10c illustrates how the strain was measured. The maximum engineering strain, as defined within the area relevant to laminate formability, was approximately 80%. This was also considered a peak strain, slightly higher than that of surrounding diaphragm material due to the breather fabric at this location, although this breather-related increase was considered marginal. Most of the diaphragm exhibited strain lower than 50% and it was assumed the lower diaphragm also exhibited a similar strain distribution owing to the high inter-diaphragm friction. The minor strain was present at the centre of the tool, where negligible strain was witnessed.

The results from this test indicate that diaphragm behaviour characterisation (Chapter 5) is relevant up to approximately 80%. Since much of the diaphragm lies at a much lower strain than this, prominence to lower strains was considered to be a high priority.

3.5 FRTP Experimental DDF Results

With the FRTP DDF process completed (Section 3.4.2), including refinement (Section 3.4.1) and validation (Section 3.4.3), the DDF rig could be used to conduct the rest of the isothermal forming required in this study. DDF was therefore completed at different test conditions and with different laminate properties to evaluate forming behaviour over a wide forming window. The three different variables identified to test laminate forming behaviour were temperature, forming rate and ply orientation. The state of these variables is illustrated below, where, for the purposes of this study, mutual exclusivity was assumed between different variables such as to significantly reduce the number of test conditions/laminate properties. The reference conditions (fixed when changing other variables) are highlighted in bold:

1. Four different (maximum) laminate temperatures: 200 °C, 210 °C, 230 °C and **250 °C**.
2. Two different forming durations (with different rates): **18s** and 3s (without and with the vacuum pressure vessel).

3. Two different laminate orientations: $0/90^\circ$ & $-45/45^\circ$ (refer to Figure 3.3).

Initially, three tests were undertaken at identical conditions in a repeatability study. This repeatability study was conducted at 230°C (an approximate mid-point temperature between the maximum and minimum temperatures), at all other reference conditions (18s forming time, $0/90^\circ$ orientation). This number of repeats was chosen due to the symmetrical nature of the double-dome geometry (Figure 3.3), meaning that each test could be considered to be two different analyses, one for each of the domes. This allowed for not only analysis of the repeatability between different tests, where small changes in experimental setup and heating can occur, but also the intra-test repeatability under theoretically identical conditions. Due to the considerable time and material resource required for the tests, this also streamlined the forming procedure. Figure 3.11 illustrates the three forms, conducted at identical conditions, as part of the repeatability study. This therefore represents 6 individual dome geometries.

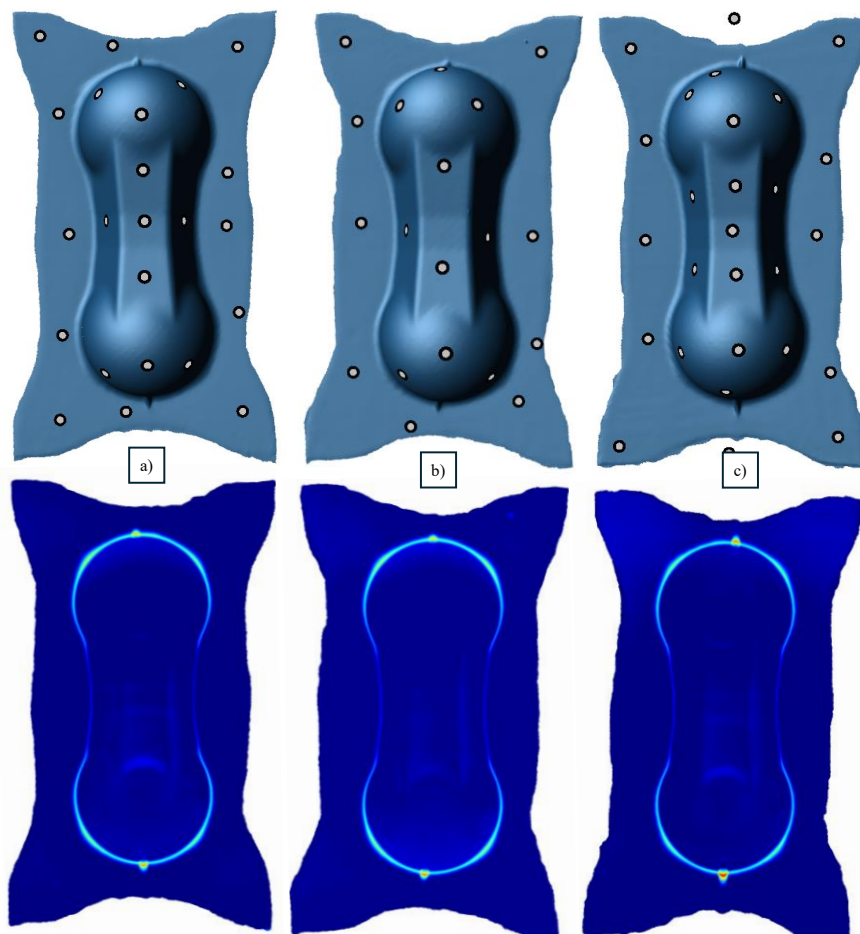


Figure 3.11: Comparison between double-dome forming geometry of three laminates (a, b ,c) conducted at identical forming conditions (230°C , 18s forming time, $0/90^\circ$ orientation).

Generally, the amount of mould conformity achieved between the 6 different domes (three double-domes) was high. The difference between the maximum and minimum dome bridging was less than 0.5 mm, with an average value of 4.1 mm. For each dome, a small wrinkle was present at the top/bottom apex, however a degree of variability existed regarding the wrinkle amplitude (1.4 mm variation) and length (6.7mm variation). Furthermore, a slight amount of lateral variability (displacement) occurred between the wrinkles. This was not surprising, due to the inherent instability of wrinkles, meaning that even small changes can influence their development. This is illustrated well when comparing adjacent wrinkles on each double-dome, where even though each is theoretically exposed to the same forming conditions, small variations in wrinkle growth still existed.

Regarding laminate shear, the average (quartile) maximum shear between the three double-domes lay between 48.2° and 48.6° , indicating a high level of repeatability between tests. This was to be expected since bridging and shear behaviour are intrinsically linked. The high repeatability indicates that experimental conditions were repeatable and further that it is feasible to reuse the silicone diaphragms after first use. This is owing to the pre-conditioning (rolling) that was completed at the outset.

For the remaining tests, it was decided that two repeats would once again be conducted for each. This allowed for an accurate calculation of the maximum bridging and shear behaviour, along with a good estimation of the location and quantity of wrinkles, and an approximation of the wrinkle amplitude and length. For concision, however, the median value for maximum bridging between repeats is used to determine which is illustrated in this work, which also replicated the median value for maximum shear in almost all cases. This also allowed for more a more concise comparison between experimental and simulated forming behaviour in Chapter 6.

3.5.1 Variable Forming Temperature

The raw FRTP DDF scans for $0/90^\circ$ laminates, undergoing a slow (18s) forming operation, at different temperatures, are illustrated in Figure 3.12. As expected, laminate temperature has a significant impact on the forming behaviour. To quantify the difference in forming behaviour between different temperatures, the laminates

were scanned (as per Figure 3.7b), to determine the laminate-tool offset. Figure 3.13 illustrates these data, for the four experimented temperatures.

Regarding bridging (mould conformity), decreasing the laminate temperature resulted in a significant increase in maximum bridging, especially on the approach to crystallisation onset (210 °C and 200 °C). Even at higher temperatures, however, bridging was influenced by laminate temperature, with maximum bridging values of 3.7 mm and 4.1 mm for 250 °C and 230 °C laminates respectively. This increases to 5.4 mm and 7.8 mm for 210 °C and 200 °C laminates respectively. A likely cause of this was the increase in coefficient of friction and/or shear force as the temperature decreases, resulting in a reduced degree of mould conformity.

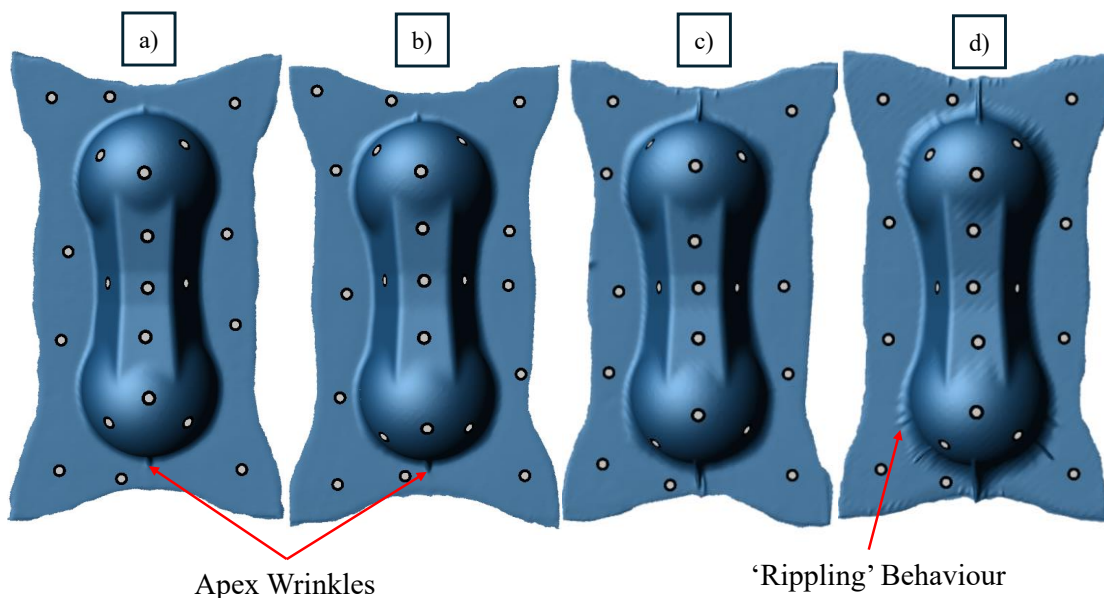


Figure 3.12: F RTP DDF forming for CF/PA6 laminate at different temperatures: a) 250 °C, b) 230 °C, c) 210 °C, d) 200 °C.

All laminates exhibited a wrinkle at the top/bottom apex of each dome, which again increased in severity as temperature decreased. There was, however, only a negligible difference in wrinkling amplitude and length between laminates at 250 °C and 230 °C. This indicates that potentially a wrinkling minimum had been reached at these temperatures. The laminate formed at 200 °C also exhibited wrinkling in the four high-shear regions. This was predominantly visible as ‘rippling’ of the laminate (Figure 3.12d), rather than a single defined wrinkle. On half of the tested domes at this temperature, a secondary larger wrinkle did exist at this location however, and diaphragm wrinkles (not replicated in the laminate) were also present on two of the six

domes. This shows that at lower temperatures, the experimental repeatability degraded due to increased forming sensitivity. For concision, the apex wrinkle properties, along with bridging and shear behaviour, are tabulated in Table 3.2 (Section 3.5.3) for all test conditions and laminate configurations.

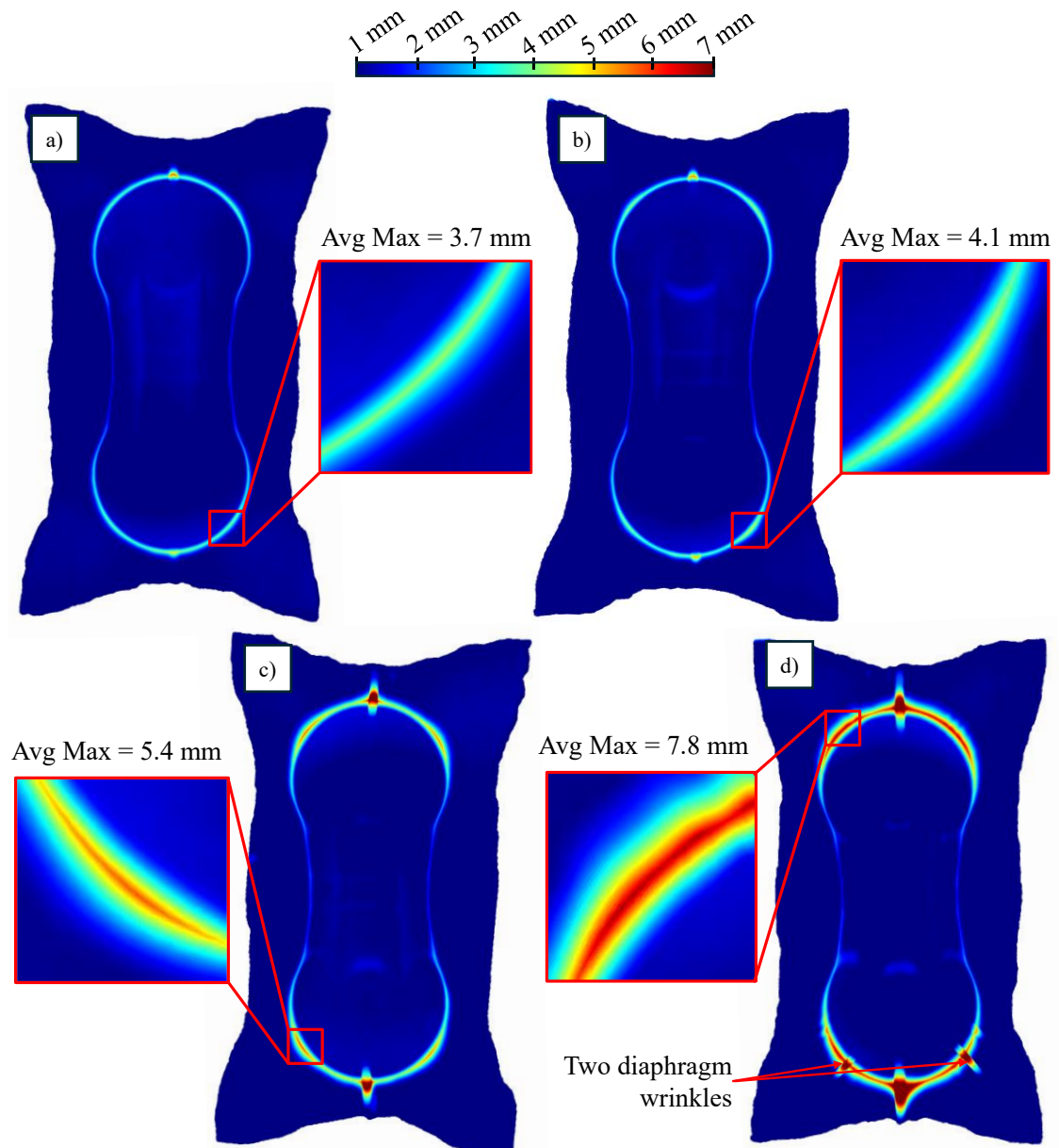


Figure 3.13: Mould conformity at different temperatures: a) 250 °C, b) 230 °C, c) 210 °C, d) 200 °C.

Finally, the maximum shear angle also reduced as the temperature reduced, due to increasing shear force at lower temperatures. Figure 3.14 illustrates the maximum shear regions on laminate at 200 °C (36.0 °) and 250 °C (49.1 °) respectively, where lines have been added to help illustrate the local fibre directions. Furthermore, the

images have been rotated such that one of the fibre directions lies horizontal, aiding the identification of changing shear angles. The other temperatures have been omitted due to the marginal differences witnessed. Due to the difficulty illustrating the changing shear angle between different test conditions clearly, for the remainder of this section these photographs are not included. Instead, the maximum shear angle in each case is tabulated in Table 3.2.

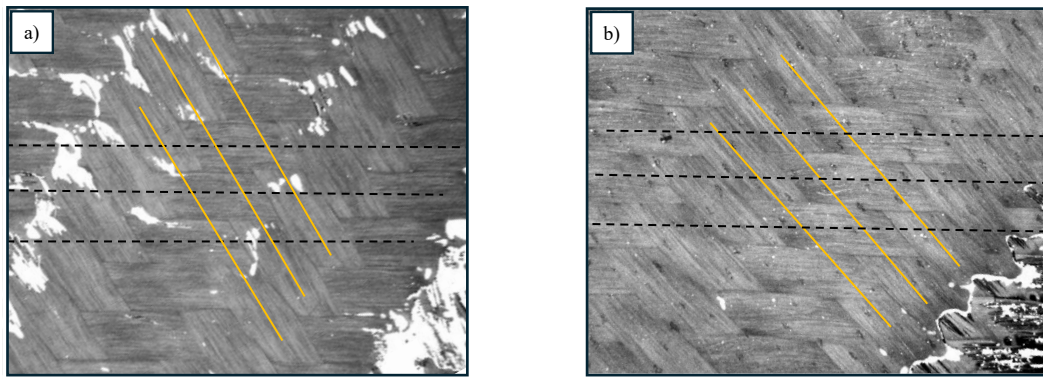


Figure 3.14: Influence of temperature on maximum observed shear angle: a) 200 °C, b) 250 °C.

3.5.2 Variable Forming Rate

The raw FRTP DDF scans for 0/90° laminates, undergoing forming at 250 °C, at two rates (18 second and 3 second forming durations) are illustrated in Figure 3.15. Similarly to the influence of temperature on forming behaviour, the rate at which forming is conducted was seemingly influential. Figure 3.16 illustrates the quantified mould conformity between both test rates.

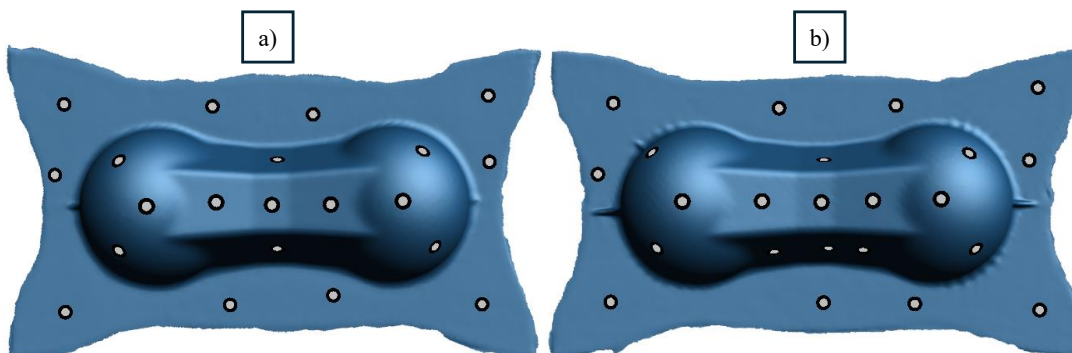


Figure 3.15: FRTP DDF forming for CF/PA6 laminates at different forming rates: a) slow (18 second duration), b) fast (3 second duration).

The biggest difference between forming at the two different rates appears to be the formation of wrinkling. The wrinkles that naturally occur at the top/bottom apex of each dome are considerably greater in length (2.6x) and amplitude (1.6x) when forming at high speed. Furthermore, wrinkling appears to exist at all of the four high-shear regions, again denoted as ‘rippling’ behaviour, as opposed to a singular clearly defined wrinkle. This is the same as that identified on laminates formed at 200 °C (Figure 3.12d), which was believed to be due to the viscoelastic nature of the laminate that exhibits a higher shear force at higher rates. This is emphasised by the small decrease in maximum shear angle at higher forming rates (48.7°), compared to lower rates (49.1 °), highlighting that the shear capability is reduced at higher forming speeds.

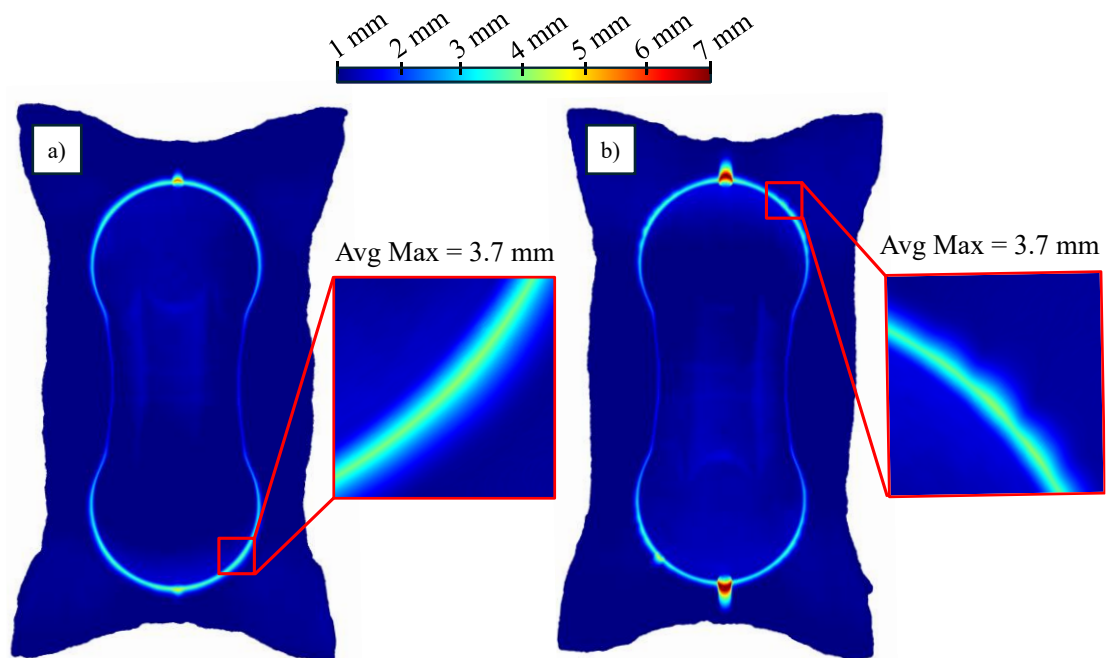


Figure 3.16: Mould conformity at different forming rates: a) slow (18 second duration), b) fast (3 second duration).

The bridging behaviour, however, was not significantly impacted between different rates. Due to the ‘ripple’ pattern present in all four of the high shear regions for the laminates formed at high speed, identifying an accurate value for bridging was difficult, however it was approximately 3.8 mm, almost identical to that formed at slower speeds. This implies that while an increase in shear force exists at higher rates (increasing wrinkling potential), the increase in friction behaviour is less prominent. Forming at higher rates may also lead to momentary higher forming pressures through the use of vacuum vessels, which may also explain the low bridging witnessed. Finally, a slight

inertia effect may also be present when forming at a higher rate due to the increased momentum of the laminate and diaphragms. The quantitative analysis of bridging, wrinkling and shear behaviour at the alternative forming rate is tabulated in Table 3.2.

3.5.3 Variable Laminate Orientation

The raw FRTP DDF scans for different laminate orientations are illustrated in Figure 3.17. This includes the reference laminate scan from Figure 3.11, and a laminate formed with $-45/45^\circ$ fibre direction. Furthermore, Figure 3.18 illustrates the mould conformity plots for the different laminate configurations.

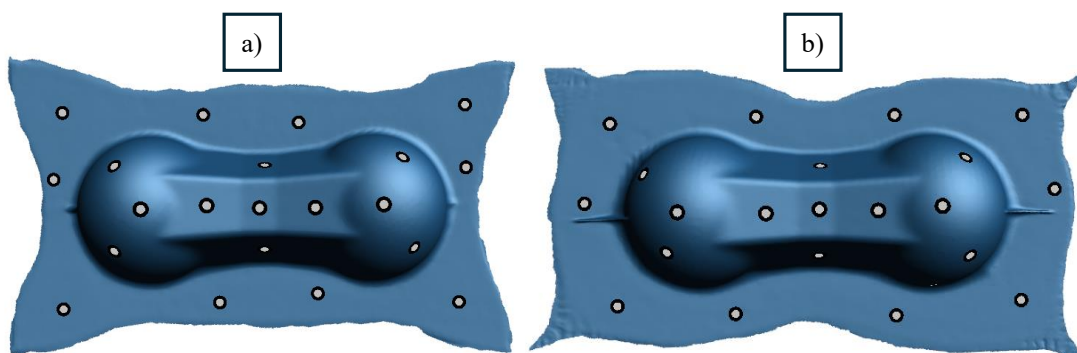


Figure 3.17: FRTP DDF forming for different laminate orientations: a) $0/90^\circ$, b) $-45/45^\circ$.

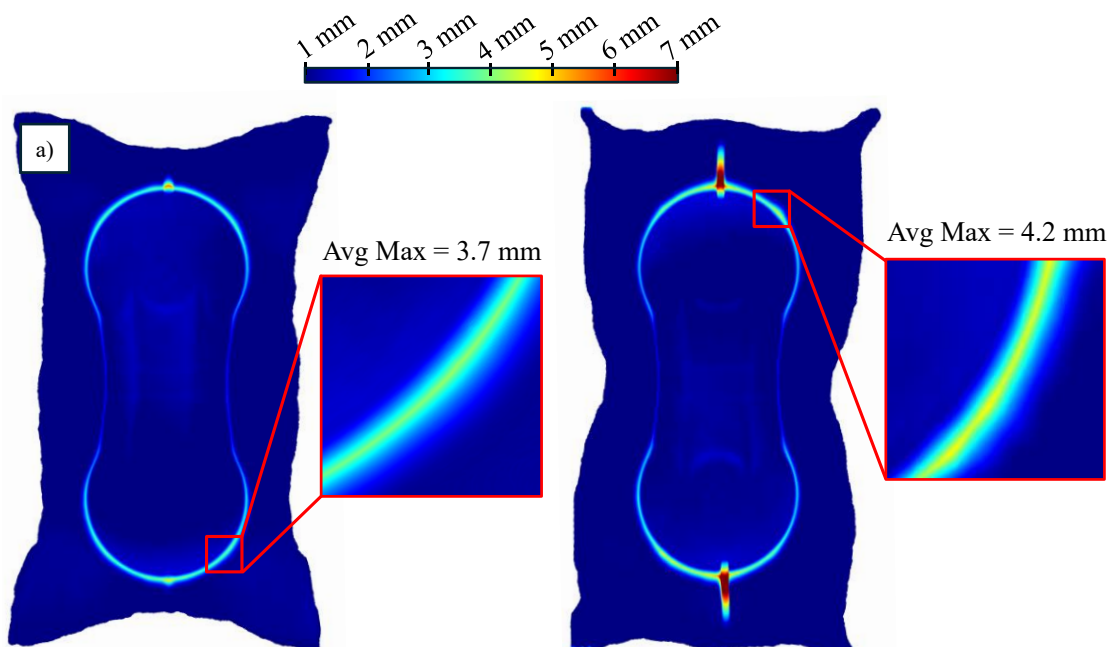


Figure 3.18: Mould conformity for different laminate orientations: a) $0/90^\circ$, b) $-45/45^\circ$

The laminate exhibiting an alternative orientation clearly deforms in a different manner to that of the conventional orientation, resulting in areas of high-shear at the dome apexes and a vastly different exterior laminate profile. For the purposes of this study, it was not considered beneficial to directly compare the forming behaviour between the 0/90 ° and -45/45° forms due to the different nature of forming behaviour exhibited between the two laminates. Instead, the results from the -45/45° form, illustrated in Figure 3.17b and Figure 3.18b, are used solely within Chapter 6 to validate the isothermal thermomechanical simulation with an alternative fibre orientation. The various forming properties for this alternative direction are, however, tabulated in Table 3.2.

Table 3.2: Quantified forming behaviour from the experimental DDF study.

Dependent Variable	Bridging (Average Quartile Maxima)	Shear Angle (Average Quartile Maxima)	Average Apex Wrinkle Size	Average Apex Wrinkle Amplitude
REF	3.7 mm	49.1 °	9.2 mm	5.0 mm
230 °C	4.1 mm	48.4 °	9.9 mm	5.4 mm
210 °C	5.4 mm	46.6 °	32 mm	8.7 mm
200 °C	7.8 mm	36.0 °	54 mm	11 mm
Fast	3.8 mm	48.7 °	24 mm	7.9 mm
-45/45	4.2 mm	51.9 ° *	56 mm	7.5 mm

*Maximum shear for alternative fibre direction taken from dome apex (refer to Figure 3.3)

3.6 Chapter Conclusions

In this chapter, successful FRTP DDF operations were completed over a double-dome reference geometry. This included initial validation of the chosen material (CF/PA6) properties, such as the thermal behaviour (melting/recrystallisation) to inform the processing parameters for the DDF operations. A DDF rig was subsequently produced, complete with double-dome mould geometry, and tested to ensure that the DDF operation was successful at a reference condition. It was found that preheating the diaphragm material to 200 °C was necessary to omit issues regarding thermal expansion. This testing procedure also included an array of validation exercises in

which the laminate temperature, pressure and diaphragm strain were all evaluated to inform the thermomechanical simulation presented later in this work (Chapter 6). An in-plane thermal distribution of 18 °C was noted due to the radiance of the IR emitters, and the laminate was seen to exhibit little vacuum due to the solid organosheet inhibiting vacuum propagation. The maximum diaphragm strain within the area of interest was measured at 80%, important for subsequent diaphragm characterisation exercises (Chapter 5).

The DDF process was then completed at different temperatures, rates and laminate orientations to evaluate forming behaviour over a range of processing conditions. Bridging, wrinkling and shearing were quantified in each case in an attempt to draw comparisons between CF/PA6 DDF behaviour at different conditions. These results are tabulated in Table 3.2.

Both reducing laminate temperature and increasing forming rate reduce the formability of a single-ply CF/PA6 laminate. Forming at 200 °C resulted in increased bridging of 110% compared to that at 250 °C, along with 13 ° less in-plane shear and an increase in apex wrinkle length from 9.2 mm to 54 mm. Moreover, high-rate forming resulted in a 58% increase in wrinkle amplitude. Experimental repeatability was high (less than 8% deviation in bridging) at high temperatures but degraded at lower temperatures due to increased forming sensitivity. Furthermore, the instability of wrinkles was highlighted, with variations even occurring intra-test between two domes of the symmetrical geometry. It was clear, however, that forming at a low temperature or at a high rate resulted in areas of concern at the high shear regions, where ‘rippling’ behaviour was prominent. Conducting DDF with a different ply-orientation resulted in a laminate exhibiting a significantly different deformation profile when compared to the standard 0/90 ° tests.

These experimental forming operations are utilised in Chapter 6 to validate the numerical DDF model.

Chapter 4.

Laminate Thermomechanical Characterisation

4.1 Introduction

In the previous chapter, the successful double diaphragm forming of CF/PA6 laminates was completed, over a double-dome tool geometry, for a range of laminate configurations (different forming rates, temperatures and orientations). From this exercise, and as detailed within the literature review (Section 2.4), it was clear that a range of different forming mechanisms act simultaneously, thus allowing tool conformity to be achieved. These mechanisms are also what determine the extent of defects that occur within the formed part, such as the wrinkling and bridging behaviour (Section 2.6).

To realise the aim of accurate thermomechanical simulation for the prediction of forming behaviour (including defects) in the DDF process, it was pivotal that these different deformation mechanisms were characterised effectively for implementation within a numerical model. Due to the nature of the limited (1 bar maximum) forming force associated with the DDF process, especially when compared to matched-tool processes, it is particularly important that the forces associated with each deformation mechanism were accurately modelled. For FRTPs, these individual mechanisms are also viscoelastically coupled in nature.

The objective of this chapter is therefore to complete the characterisation of the main deformation mechanisms, both intra-ply and interactional behaviour, associated with laminate heating and forming behaviour: deconsolidation, intra-ply shear, diaphragm-ply friction and out-of-plane bending (Figure 2.11). It should be noted that inter-ply friction characterisation is out of the scope of this work due to the single-ply nature of the DDF experimental studies in Chapter 3. The subsequent input for a thermomechanical simulation routine is considered throughout this chapter.

4.2 Methodology

This section details the methodology that was followed for accurate CF/PA6 mechanical characterisation. The CF/PA6 material properties are tabulated in Table 3.1 and apply throughout this methodology. As noted in Section 2.2.2, PA6 is porous and susceptible to water absorption. To ensure that the results throughout this work

were consistent with one another, all specimens were dried in an oven at 70 °C for 24 hours prior to testing as recommended by the manufacturer [393]. This ensured that they all exhibited approximately equal dryness throughout.

4.2.1 Deconsolidation

As described in Section 2.6.3, arguably the first deformation mechanism to take place during FRTP thermoforming is deconsolidation. This occurs immediately after the melting point is exceeded, often before forming has taken place. Since deconsolidation is generally considered detrimental, it was beneficial to analyse CF/PA6 deconsolidation behaviour to ensure that full consolidation was achieved during the DDF process.

Firstly, the magnitude of deconsolidation was analysed for a single-ply CF/PA6 laminate. For this study, 35 x 35 mm consolidated samples of CF/PA6 were waterjet cut and subsequently placed in an Anton Paar MCR 302e parallel-plate rheometer. For each sample, the rheometer was heated at 10 °C/min from room temperature up to 230 °C while a compressive force of 0.1N was maintained by the apparatus for the entirety of the experiment. The rheometer displacement was tracked over time to measure the deconsolidation for each laminate. After 240 °C had been achieved, the laminate was subsequently cooled at -10 °C/min, with the compressive force maintained, to evaluate its cooling behaviour. Four repeats were undertaken. Figure 4.1 illustrates the experimental apparatus.

A second experiment followed, to not only establish the maximum deconsolidation behaviour upon heating, but also the reconsolidation behaviour *versus* applied pressure. For this, identical samples as above were heated and held at 240 °C, before being compressed at 1 N/min with the crosshead displacement tracked over time. As before, four repeats were undertaken. To calculate the applied normal pressure, P_n , the parallel plate diameter, δ_{pp} (25 mm in this case) along with the normal force, F_n , were used:

$$P_n = \frac{4F_n}{\pi\delta_{pp}^2} \quad (4.1)$$

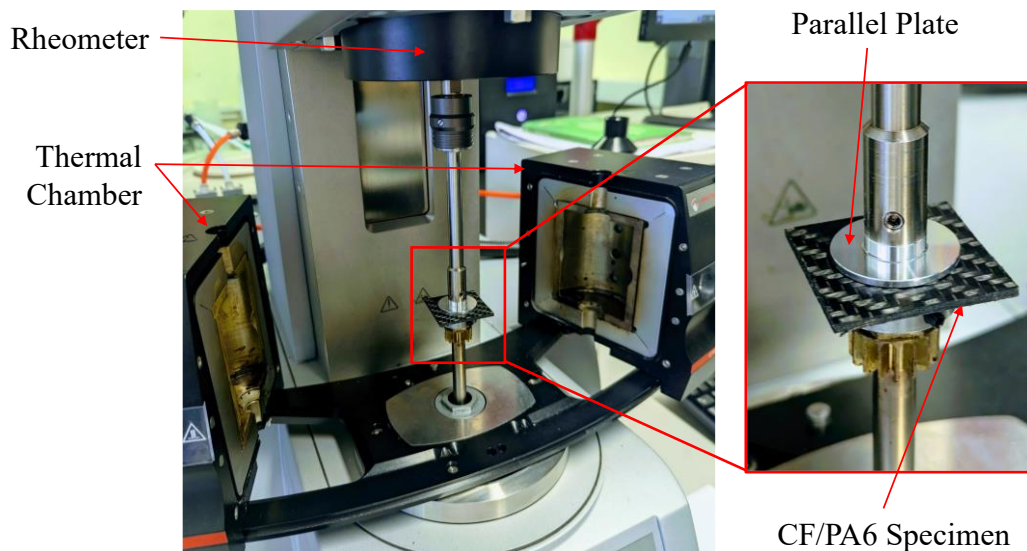


Figure 4.1: Rheometer experimental setup for deconsolidation analysis.

4.2.2 Intra-ply shear

This section details the methodology for the characterisation of intra-ply shear behaviour.

4.2.2.1 Experimental Setup

Both the PFT and the BET were used in this work package to characterise the intra-ply shear behaviour of CF/PA6. This is due to the relative drawbacks of each method described in Section 2.5.1, meaning that the utilisation of both methods increases the confidence in the acquired data. Figure 2.17 illustrates schematically both the PFT and the BET.

Single-ply CF/PA6 specimens were waterjet cut to achieve the required dimensions and attain the required 45° fibre angle for each test. All BET specimens measured 210 mm x 50 mm, allowing for 30 mm of clamping at each end. The test area was therefore 150 mm x 50 mm, exhibiting an aspect ratio of 3. An aspect ratio of at least 2.5 is recommended in the literature [218, 219] to increase the homogeneity of the distribution of shear deformation in the sample. For the PFT, cruciform specimens were waterjet cut to fit a picture frame rig with a side length, L_{pf} , of 145 mm. Due to a small degree of waviness in the CF/PA6 organosheet, it was difficult to cut these specimens with an exact $0/90^\circ$ fibre angle, with the implications of this considered in

the results section. Since the specimens were loaded before melting, however, there was little concern regarding enacting pre-shear before the beginning of each test.

Both the PFT and BET experiments were conducted using an Instron 5581 Universal Testing Machine, equipped with a 1 kN load cell. To achieve the desired specimen temperature, an Instron 3119-607 environmental chamber was utilised, equipped with closed-loop temperature control. The laminate temperature was validated by mounting a thermocouple to a ‘dummy’ specimen of the chosen FRTP hanging inside the test apparatus. To compensate for resin squeeze-out, specimens were clamped in place with four sprung bolts to eliminate the possibility of specimen pull-out. Furthermore, silicone sheet was placed within the clamp to provide an even distribution of the clamping force. The experimental setup for the BET is illustrated in Figure 4.2.

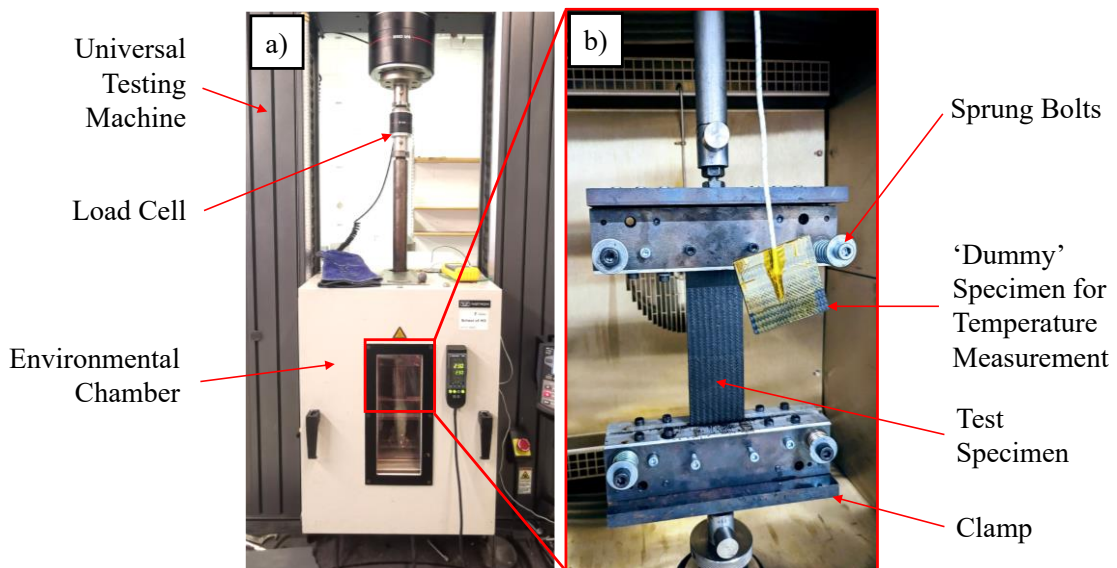


Figure 4.2: a) Universal testing machine setup, b) bias extension test apparatus.

For the BET, testing was undertaken at four different nominated temperatures (above the crystallisation onset point defined in Table 3.1) and three different test rates to evaluate viscoelastic intra-ply shear behaviour. The temperature- and rate- effects were not considered mutually exclusive, therefore meaning that 12 different shear ‘test conditions’ existed for this study. This allowed for intra-ply shear characterisation over a wide range of environmental conditions. The temperatures chosen were 210 °C, 230 °C, 250 °C and 270 °C and the three displacement rates were 20 mm/min, 100 mm/min and 500 mm/min (0.00667 Rad/s, 0.0334 Rad/s and 0.167 Rad/s shear rate), utilising the full capabilities of the universal testing machine. For the PFT, the same four

temperatures were analysed, but only two shear rates (0.00667 Rad/s and 0.0334 Rad/s) due to the physical limits of the universal testing machine. Four repeats were undertaken for each sample.

PFT and BET experiments were conducted following a prescribed thermal cycle, as depicted in Figure 4.3. Each laminate was heated through forced convection up to an initial chamber temperature of 230 °C and dwelled for 3 minutes to allow for complete specimen melting. For the two further elevated temperatures of 250 °C and 270 °C, a secondary heating phase followed, with a secondary 3 minute dwell, to achieve the desired test temperature. However, for the 210 °C tests, the initial melting phase was followed by a slow cool-down at approximately -0.03 K/s (dictated by the natural rate of the environmental chamber) until the respective temperature was reached. Once again, a secondary 3 minute dwell period was carried out after this cooling phase.

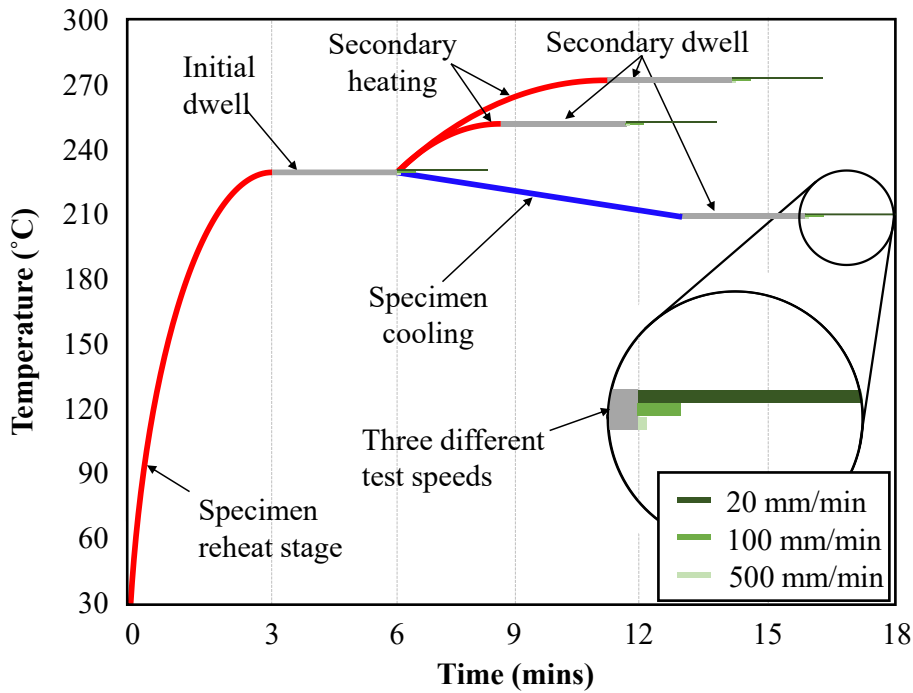


Figure 4.3: Thermal cycle for different intra-ply shear experimental test conditions.

4.2.2.2 Data Normalisation

In both cases, a data normalisation procedure was required to convert the raw axial force *versus* displacement datasets into usable shear stress *versus* shear angle curves. Regarding the PFT, this process is relatively straightforward due to the rhomboidal nature of the trellis frame enacting only pure-shear (in theory) over the entire specimen.

Harrison *et al.* [155] related the specimen shear angle, γ_{pf} , to the picture frame axial displacement, δ_{pf} , using the following equation:

$$\gamma_{pf} = \frac{\pi}{2} - 2 \cos^{-1} \left[\frac{1}{\sqrt{2}} + \frac{\delta_{pf}}{2L_{pf}} \right] \quad (4.2)$$

where L_{pf} is the side length of the picture frame, measured as the distance between the picture frame bearings. Likewise, the shear force, F_{sh} , can be subsequently calculated using:

$$F_{sh} = \frac{F - F_{frame}}{2 \cos \left[\frac{\pi}{4} - \frac{\gamma_{pf}}{2} \right]} \quad (4.3)$$

where F is the force measured by the universal testing machine and F_{frame} represents the weight and inertia influence of the frame. To obtain a value for F_{frame} , the PFT was run four times with no laminate present to obtain a ‘dry’ curve. A least-squares algorithm was used to fit a 6th order polynomial to this curve in the form of:

$$F_{frame} = u_1 \delta^6 + u_2 \delta^5 + u_3 \delta^4 + u_4 \delta^3 + u_5 \delta^2 + u_6 \delta \quad (4.4)$$

where u_{1-6} are constants, tabulated in Appendix B - Table B.2. This reduction curve is illustrated in Appendix B - Figure B.2.

In contrast, the BET normalisation procedure is influenced by the inhomogeneous deformation field (Figure 2.17b), therefore preventing simple rheological analysis. Lebrun *et al.* [156] related the vertical displacement of the BET specimen, δ_{be} , to the shear angle in zone C, γ_{be} , using the following equation:

$$\gamma_{be} = \frac{\pi}{2} - 2 \cos^{-1} \left[\frac{\delta_{be} + (H - W)}{\sqrt{2}(H - W)} \right] \quad (4.5)$$

where H is the specimen height and W is the specimen width. To ensure that shear angle was captured accurately in this work, however, a simple experimental procedure was adopted to relate the vertical displacement of the universal testing machine to the specimen shear angle. This was deemed appropriate due to the aforementioned inhomogeneity of the sample.

CF/PA6 test samples were displaced to four different extents: 10 mm, 20 mm, 30 mm and 40 mm, at 250 °C and rate of 100 mm/min, with two repeats undertaken. A Hexagon Apodius Arm, with 2D vision sensor, was used to scan the three samples and attain the weft and warp fibre angles on an elemental basis, in a global cartesian coordinate system, based upon a 3mm mesh. The scanned samples were post-processed in MATLAB® to obtain the shear angle between the two fibre directions. The scanned images and post-processed shear angles for all three samples are illustrated in Figure 4.4, a zoomed view of each specimen is included on the raw scanned images for clarity. The samples extended to 10 mm are not included on this figure for concision.

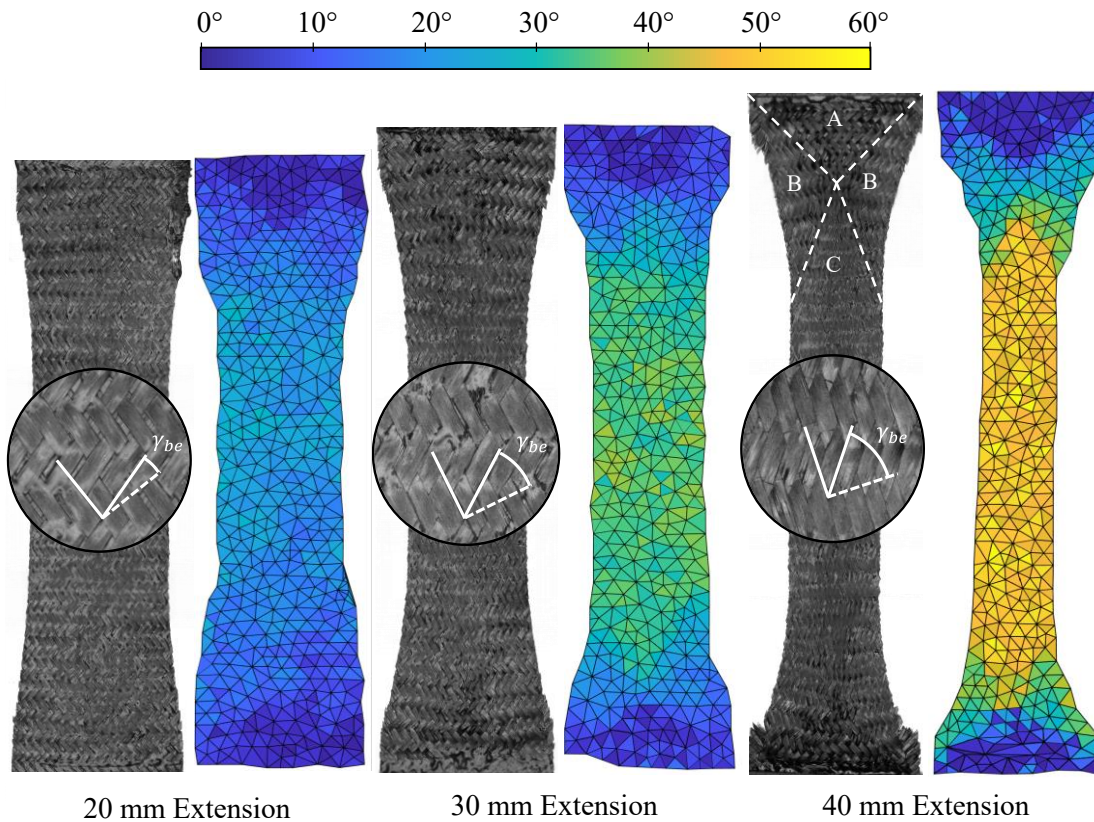


Figure 4.4: Bias extension test shear angle validation.

The samples were shown to deform correctly, with the three distinct shear regions depicted clearly on the 40 mm sample image. The average (front and rear face) shear angle in the central zone for the 10 mm, 20 mm, 30 mm and 40 mm samples was 11.2°, 23.5°, 37.8° and 50.2°, respectively, with an error of up to $\pm 4.0\%$ between repeats. Conversely, the predicted shear values, as calculated using Equation (4.5), for the four sample displacements were 12.1°, 26.1°, 43.6° and 73.7°, respectively. These results

indicate that Equation (4.5) overestimated the shear angle for the bias-extension specimens tested in this study, with a 10% error up to the onset of intra-ply slip (between 40-50°), after which the error increased up to 33%.

It was assumed that the shear angle for a given displacement was independent of laminate temperature and shear-rate for the purposes of this study. Machado *et al.* [159] illustrated that a 3° discrepancy is possible between different rates or temperatures, but this was deemed insignificant for the purposes of this work. Because of the large errors witnessed between the analytical and experimental shear angle relationships, a second-order polynomial, based upon the experimental findings, was used to more accurately portray the sample shear behaviour.

$$\gamma_{be} = m_{\gamma}\delta_{be}^2 + n_{\gamma}\delta_{be} \quad (4.6)$$

where m_{γ} and n_{γ} are constants. A least-squares algorithm was used to fit the experimental shear angles with that of the equation, with an ‘r-squared’ value of 1.00. The sample extended to 40 mm was not included for the fitting procedure to ensure fitting accuracy before the onset of intra-ply slip. The calibrated constants are tabulated in Appendix B - Table B.1, noting that they are calibrated for the shear angle in radians. Furthermore, Appendix B - Figure B.1 illustrates the fit and comparison with the analytical variation (Equation (4.5)).

Finally, a derivation by Harrison *et al.* [155], based upon a Newtonian fluid approximation, was used to estimate the laminate shear force response and eliminate the ‘softening effect’ encountered by other derivations [217]. The softening effect is a phenomenon in which the shear force with respect to the shear angle is underestimated due to the region C not only dominating the shear strain response but also the shear strain rate response. This was chosen for this work such as to eliminate the likelihood of a negative gradient in force occurring after normalisation, as illustrated by Machado *et al.* [159]. It was accepted, however, this would induce a degree of error in the final result-set. The normalised bias extension shear force could therefore be expressed as:

$$F_{sh} = \frac{\left(\frac{H}{W} - 1\right)}{\left(2\frac{H}{W} - 3 + 2X\right)} \frac{F_{ax}}{\frac{\sqrt{2}W}{2}} \quad (4.7)$$

where X, a function of the laminate dimensions, is defined as:

$$X = \frac{1}{4} \left\{ \frac{\cos^2(\gamma_{be}) \left[1 + 3\sin^2\left(\frac{\gamma_{be}}{2}\right) \right]}{\cos^2\left(\frac{\gamma_{be}}{2}\right) \left[1 + 3\sin^2(\gamma_{be}) \right]} \right\} \quad (4.8)$$

Finally, the shear stress, τ_{sh} , is defined using the following equation including the initial sample thickness, t:

$$\tau_{sh} = \frac{F_{sh}}{t} \quad (4.9)$$

These normalisation techniques allowed comparisons to be drawn between the two different test intra-ply shear experimental methods and provided shear stress *versus* shear angle curves for each dataset, paramount for input into a numerical simulation routine.

4.2.3 Diaphragm-Ply Friction

Unlike the matched-tool process where the laminate makes direct contact with the tool, in the DDF process the laminate is instead in permanent contact with the diaphragm. This therefore necessitates the accurate characterisation of this interaction, as from Figure 3.10 it appears there is a large degree of tangential displacement between the two.

The pull-through friction test, as outlined in Section 2.5.4, was used to ascertain the diaphragm-ply friction in this work. This was chosen due to the constant contact area that is exhibited during this test, maintaining a constant normal-pressure, therefore allowing for normal-pressure dependent friction behaviour to be analysed accurately. A pull-through rig was manufactured that could be mounted within a 3119-607 environmental chamber, itself equipped to a Instron 5581 Universal Testing Machine with a 1 kN load cell. Figure 4.5 illustrates the pull-through apparatus (different laminate widths owing to a setup study to find the optimal condition).

The pull-through rig comprised of two steel pressure plates with two 1 mm thick layers of silicone bonded to the clamping surface using high temperature adhesive. The steel plates were mounted facing one another using close-fit locating bolts designed to

minimise any in-plane movement, with four springs used to apply a pre-defined normal force. The use of springs was such to maintain an approximately constant pressure during the entirety of the test and maintain parallelism between the pressure plates.

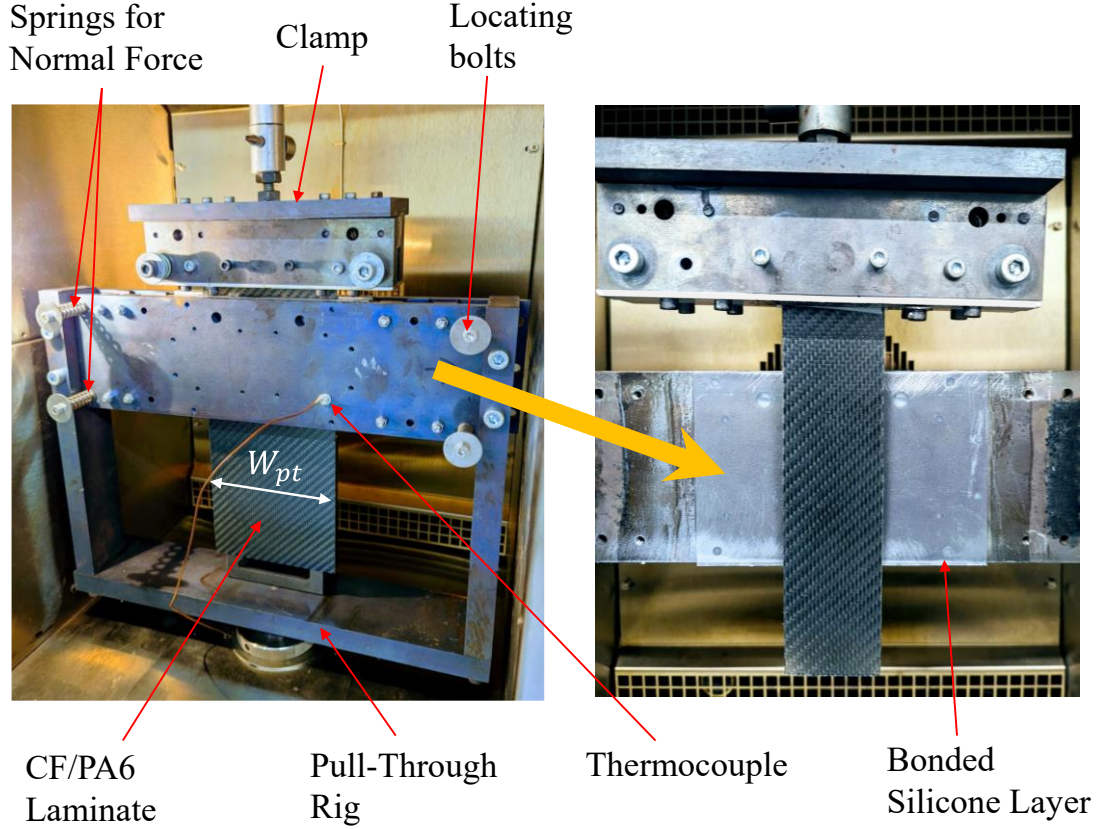


Figure 4.5: Pull-through apparatus for inter-ply friction experimentation.

The normal force, F_n , could be defined by:

$$F_n = 4 \cdot k_s \cdot x_s \quad (4.10)$$

where k_s is the spring constant and x_s is the spring compression. The spring constant was provided by the manufacturer. It would also be possible to attain the normal force by controlling the bolt torque, however this method requires that the bolt coefficient of friction be known, deemed impractical for this study. The normal pressure, P_n , was subsequently calculated using:

$$P_n = \frac{F_n}{2 \cdot W_{lam} \cdot W_s} \quad (4.11)$$

where W_{lam} and W_s are the widths of the laminate and silicone, defined as 40 mm and 80 mm respectively. In actuality the pressure was defined in this work, with Equations (4.10) and (4.11) used to define the spring compression length. The spring compression was controlled using metal shims machined to a set length. This allowed the user to screw in the locating bolts, compressing the springs up until the metal shims were lightly pinched. These shims were then removed, thus setting a pre-defined normal force. A thermocouple was mounted to the pressure plates on the pull-through rig so the temperature could be monitored during the entirety of the experiment.

A simple validation procedure was conducted to validate the pressure distribution between the two pressure plates. A 50 mm wide layer of Fujifilm Prescale Ultra Super Low film [392], along with a 50 mm wide specimen of dry TORAY T300 woven carbon fabric [394] (to replicate a molten FRTP specimen) were clamped in place. The locating bolts were subsequently tightened to apply three different test pressures (0.3 bar, 0.5 bar and 1.0 bar) to the Prescale film. Both methods of applying normal pressure were tested: using machined shims of a set length to set the spring compression (denoted ‘spring shims’), and the use of a torque wrench to tighten all four bolts equally (denoted ‘torque tightened’). Figure 4.6 illustrates the results from this simple exercise, showing that the use of machined shims to apply an even spring compression provides a more even pressure distribution than applying equal torque to each bolt. It is probable that this was due to different coefficients of friction between different bolts, a phenomenon especially likely after repeated heating and cooling.

The CF/PA6 laminates measured 40 mm x 120 mm. Diaphragm-ply friction testing was undertaken at four nominated temperatures above the crystallisation onset point (210 °C, 230 °C, 250 °C and 270 °C) and three test rates (20 mm/min, 100 mm/min and 500 mm/min). Furthermore, four different normal pressures (0.03 bar, 0.10 bar, 0.30 bar and 0.90 bar) were tested to analyse the pressure dependent friction behaviour. Contrary to the intra-ply shear tests, these variables were considered mutually exclusive for concision. This was valid owing to the Stribeck parameterisation process detailed in Section 2.4.4. Four repeats were undertaken in each case.

The thermal cycle for each test closely resembled that of the intra-ply shear testing (Figure 4.3), however extended dwell periods (10 minutes) were conducted and longer heat-up and cool-down times noted due to the thermal inertia of the pressure-plates.

The inter-ply friction coefficient, μ , can simply be deduced from the normal force and the recorded axial force:

$$\mu = \frac{F_{ax}}{2 \cdot F_n} \quad (4.12)$$

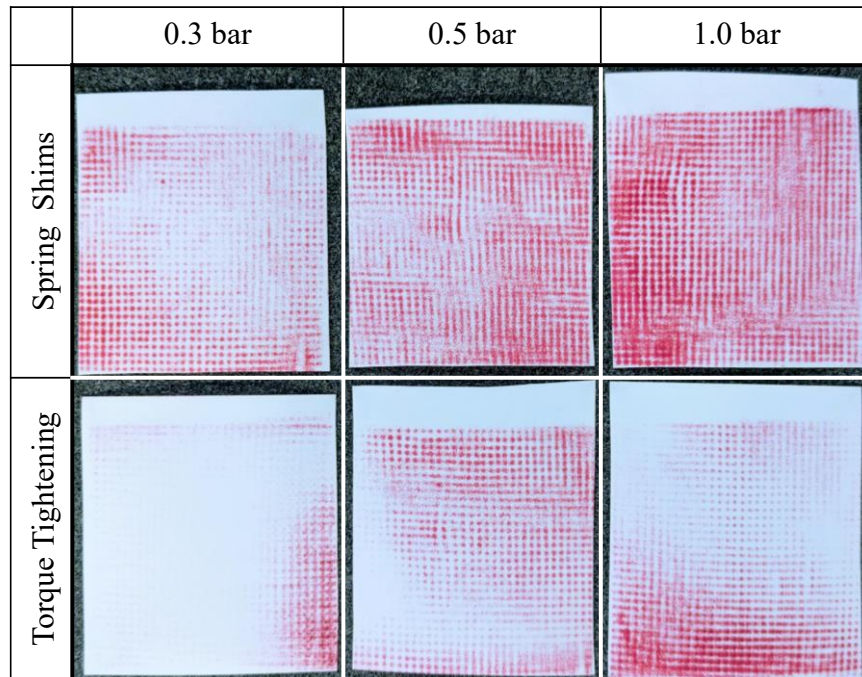


Figure 4.6: Pull-through rig pressure distribution for different pressures and different pressure application techniques.

4.2.4 Out-of-plane bending

This section details the methodology for the characterisation of out-of-plane bending behaviour.

4.2.4.1 Experimental Setup

The cantilever bending test was chosen to analyse the bending-behaviour of CF/PA6 laminates due to the simple experiment apparatus required to complete testing, as discussed in Section 2.5.3. As opposed to the only previous literature regarding FRTP bending characterisation using the cantilever test [186], it was devised that IR heating would be used to attain the desired specimen temperature, rather than convective heating in an environmental chamber. This was because the environmental chamber available did not have functionality to halt the convective fan, which was deemed to

cause severe currents within the chamber that would influence the laminate bending behaviour. Moreover, the use of an IR heater allowed for much quicker heat-up/cool-down times allowing for more streamlined testing. The IR lamp was equipped with a pyrometer, allowing non-contact thermal measurement for accurate proportional iterative derivative (PID) control of the specimen temperature.

Specimens of the chosen CF/PA6 material were cut into 30 mm wide, 150 mm long strips using a ply-cutter, exhibiting a constant fibre angle of $0/90^\circ$. A length of 10 mm was required for clamping at the cantilever point, resulting in a total bending length of 140 mm. No alternative fibre angles were experimented in this work, and it was assumed that the laminate was quasi-isotropic in the plane of the fabric.

Laminates were suspended from an aluminium support block, itself equipped with RS-PRO Mica contact heating pads to remove any concerns regarding conductive cooling from the support. Initially, laminates were maintained in a horizontal position for even heating to take place using a thermally insulative support. After the laminate had reached the desired temperature, a 3-minute dwell followed, before removal of the thermally insulative support block. This allowed the CF/PA6 specimen to bend under its own weight. The bending profile of each specimen was monitored using a high-speed camera for 600 seconds after the beginning of each test. Furthermore, the final bending profile (after 600 seconds) was scanned with a Creaform Handyscan3D 700 white light scanner to obtain the final (steady-state) bending profile. Figure 4.7 illustrates schematically the experimental apparatus.

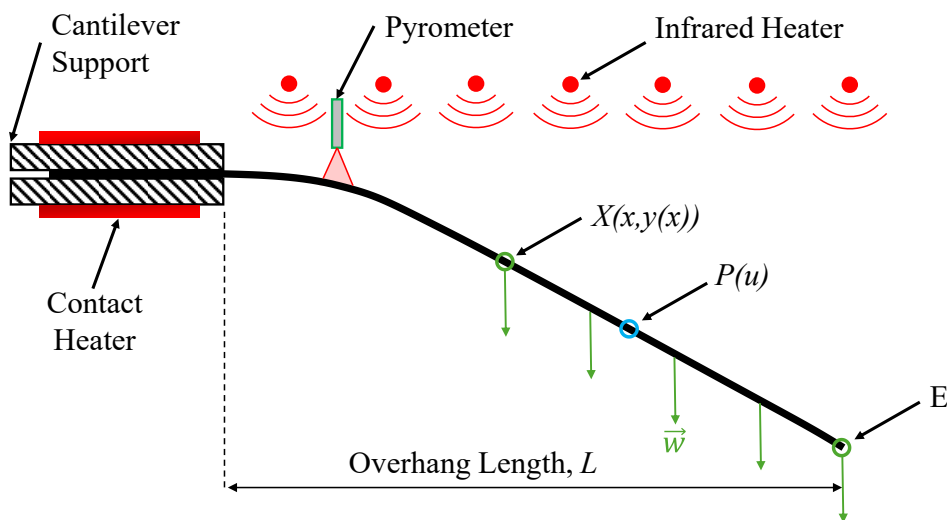


Figure 4.7: Schematic of the experimental apparatus for the cantilever bending tests.

As per the intra-ply shear (Section 4.2.2) and inter-ply friction (Section 4.2.3) tests, experiments were conducted at four test temperatures above the crystallisation onset point, 210 °C, 230 °C, 250 °C and 270 °C. Since the bending-rate was not controlled in this study, it was not possible to accurately determine its influence on bending behaviour. The thermal history for these tests is well represented by that of the intra-ply shear studies (Figure 4.3), however in this case, much quicker heat-up and cool-down times were present due to the radiative heating. Four repeats at each test temperature were undertaken.

4.2.4.2 Data Normalisation

The normalisation procedure implemented in this work is closely aligned to that presented in the work of Yu *et al.* [170]. Initially, a Levenberg–Marquardt algorithm was used to fit a 6th order polynomial to each scanned bending profile using MATLAB. This was done for both visible edges of the specimen, with an average taken to eliminate twist from the results. Following this, the bending moment, M , at any arbitrary point, $X(x,y(x))$, down the specimen could be defined as:

$$M = \int_s^L \vec{XP} \cdot \vec{w} du \quad (4.13)$$

where s is the curvilinear abscissa of Point X , L is the overhang length, \vec{w} is the specific weight of the laminate and u is the Frenet's coordinate of point P moving along the segment between point X and point E, as also illustrated in Figure 4.7. The bending moment was subsequently normalised (M_n):

$$M_n = \frac{M}{W_b} \quad (4.14)$$

where W_b represents the width of the bending samples. Furthermore, the curvature, at any arbitrary point down the specimen, could also be defined:

$$k = \frac{y_b''}{(1 + y_b'^2)^{\frac{3}{2}}} \quad (4.15)$$

Where y'_b and y''_b are the first and second derivatives, respectively, of the fitted 6th order deflection curve. Using equations (4.13)-(4.15), the relationship between normalised bending moment and curvature could be defined for each individual test.

4.3 Deconsolidation Characterisation Results

This section details the results from both the deconsolidation and subsequent reconsolidation validation studies

4.3.1 Laminate Deconsolidation

An example CF/PA6 laminate thickness *versus* temperature plot, as measured by the rheometer, is illustrated in Figure 4.8. During the initial heat-up phase and before melting, the sample thickness was seen to increase at an approximately linear rate, owing to the thermal expansion of the CF/PA6 laminate. Upon the occurrence of melting, a dramatic increase in specimen thickness was recorded by the rheometer, owing to laminate deconsolidation. After deconsolidation was complete, once melting was completed (> 223 °C, Table 3.1), the linear thickness increase returned. Upon cooling, the laminate contracted, owing to the thermal contraction. It was at this point that the laminate deconsolidation was quantified, as simply the relative increase in laminate thickness, defined as a percentage increase:

$$\rho = \frac{t_{final}}{t_{initial}} - 1 \quad (4.16)$$

where ρ is the deconsolidation, t_{final} is the final laminate thickness and $t_{initial}$ the initial thickness. This method assumes that no significant crystallisation shrinkage takes place. This process was repeated four times, such that an average value of single-ply CF/PA6 deconsolidation was calculated as $9.10\% \pm 0.17\%$.

Figure 4.9 presents a visual comparison between a consolidated and deconsolidated laminate, with the deconsolidated variant clearly exhibiting dry spots, owing to the ‘de-crimping’ effect.

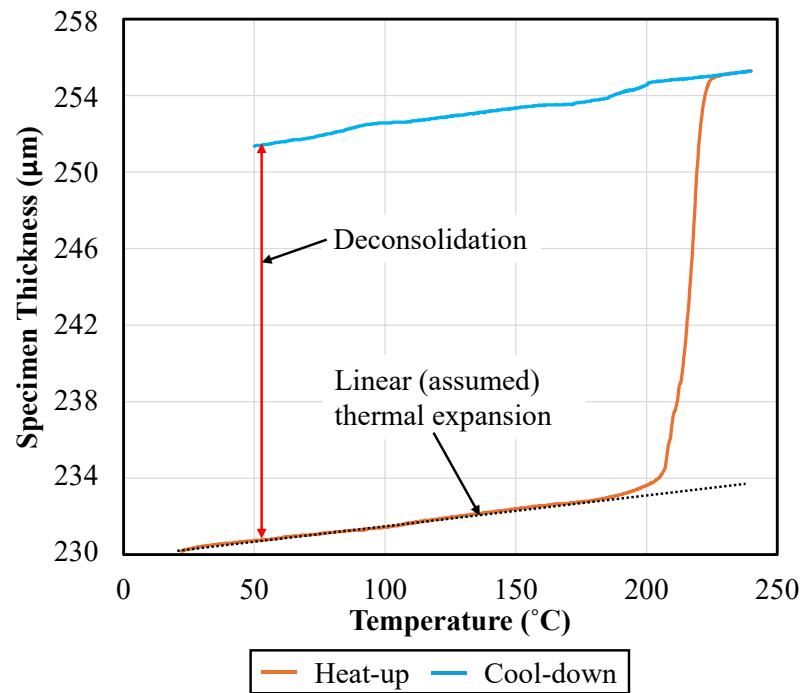


Figure 4.8: Thickness *versus* temperature plot for a CF/PA6 laminate, illustrating deconsolidation behaviour.

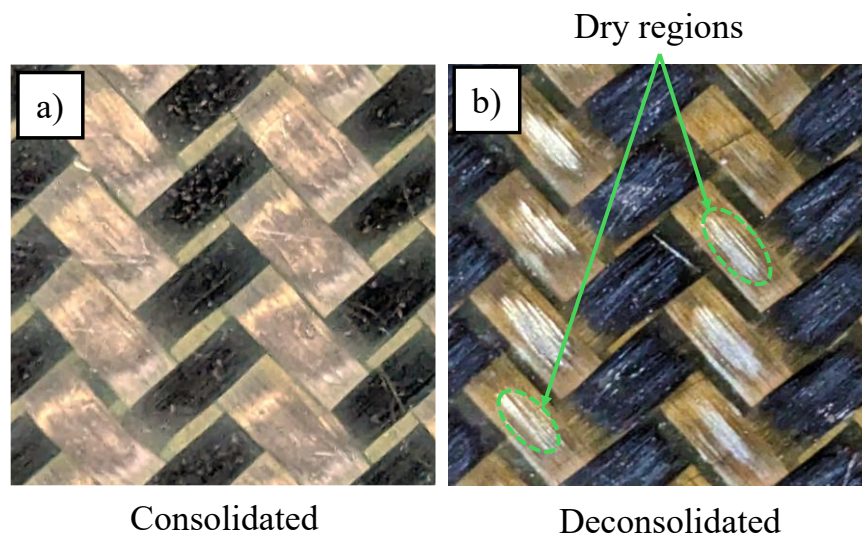


Figure 4.9: Visual comparison between laminates: a) consolidated, b) deconsolidated.

4.3.2 Laminate Reconsolidation

It was important to not only determine the maximum deconsolidation upon heating with no compaction, but the reconsolidation behaviour of the laminate on the occurrence of normal pressure. This was especially prudent for this study concerning DDF, where it was found in Section 3.4.3.2 that the laminate compaction pressure

increases throughout the forming routine, thus resulting in changing levels of laminate consolidation.

Figure 4.10a illustrates the outcomes from the reconsolidation tests, where an average curve between the five tests (repeats) is plotted. In the figure, the specimen thickness is normalised by the consolidated laminate thickness, accounting for the linear thermal expansion, yielding the total deconsolidation. Using the figure, the critical reconsolidation pressure can be determined as approximately 0.4 ± 0.02 bar, although it is assumed in this study that there is no viscoelastic effect on this value or the reconsolidation profile. Since the total deconsolidation tends towards a negative value, there was clearly a degree of resin squeeze-flow during these reconsolidation tests, however this was not deemed to significantly impact the reconsolidation pressure. This work shows that the DDF process does impart enough pressure on the laminate to achieve full-reconsolidation at the end of the process.

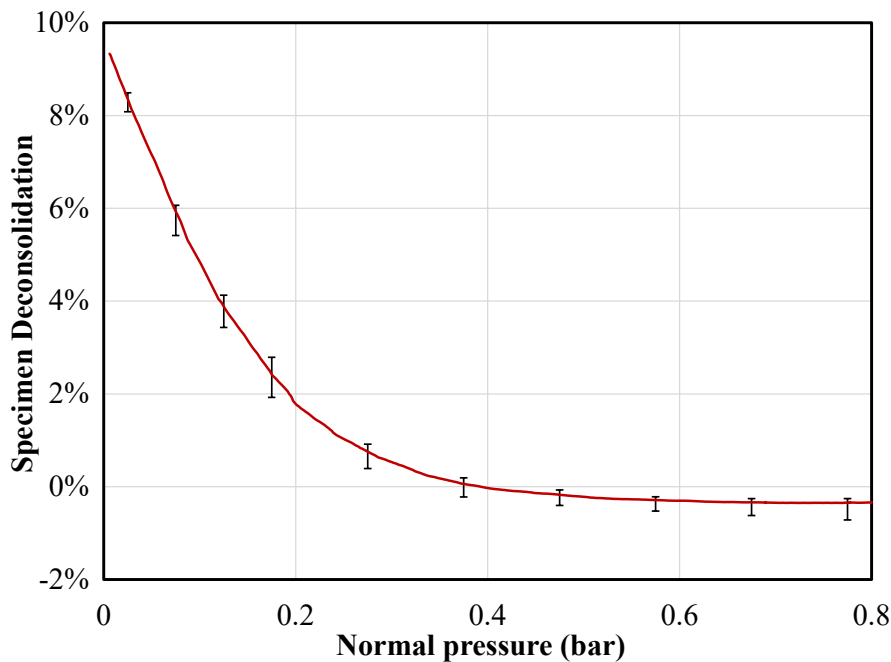


Figure 4.10: Reconsolidation behaviour with increasing normal pressure

4.4 Intra-ply Shear Characterisation Results

This section details the results from the intra-ply shear characterisation experimental studies. This includes the full array of BET results, subsequently compared with those

from the PFT. This is then followed by a parameterisation procedure to provide an intra-ply shear input for a numerical routine.

4.4.1 Bias Extension Test Results

The output from the bias extension tests for each individual shear test condition was a force *versus* displacement curve, as recorded by the testing machine. Shear stress *versus* shear angle curves were obtained utilising Equations (4.6)-(4.9). The inclusion of four repeats meant that five datasets were produced for each respective laminate test condition. An example of the five normalised force *versus* shear angle datasets, for CF/PA6 laminates at 230 °C and 100 mm/min, are illustrated in Figure 4.11.

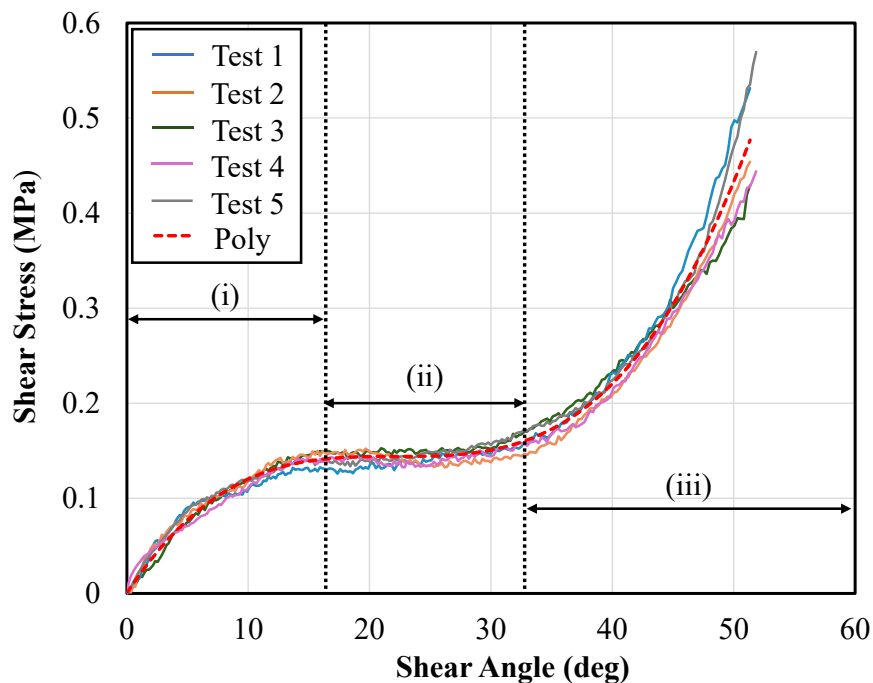


Figure 4.11: Shear stress *versus* shear angle result-set for the BET conducted on CF/PA6 laminates at 230 °C and 100 mm/min.

Each curve is broken down into three distinct sections: an initial realignment of fibre yarns at low forces resulting in a steep initial gradient in force response (i), a steady-state section of laminate shearing (ii), and a steep upturn in recorded force as the laminate approaches its locking angle (iii). The noise associated with each result-set was caused by the air circulation within the environmental chamber, coupled with small oscillations in the clamping arrangement.

To combine the five datasets, a 5th order polynomial was fitted using a Levenberg–Marquardt algorithm, resulting in a combined polynomial in the form of:

$$\tau_{sh} = a_1\gamma^5 + a_2\gamma^4 + a_3\gamma^3 + a_4\gamma^2 + a_5\gamma \quad (4.17)$$

Where $a_{1...5}$ are constants specific to each condition, calibrated for the shear angle in radians (rad). This polynomial is also illustrated in Figure 4.11, denoted ‘poly’.

Figure 4.12 subsequently illustrates the combined polynomial for CF/PA6 laminates at each tested condition. The figure is split into the four test temperatures, with the three rates compared.

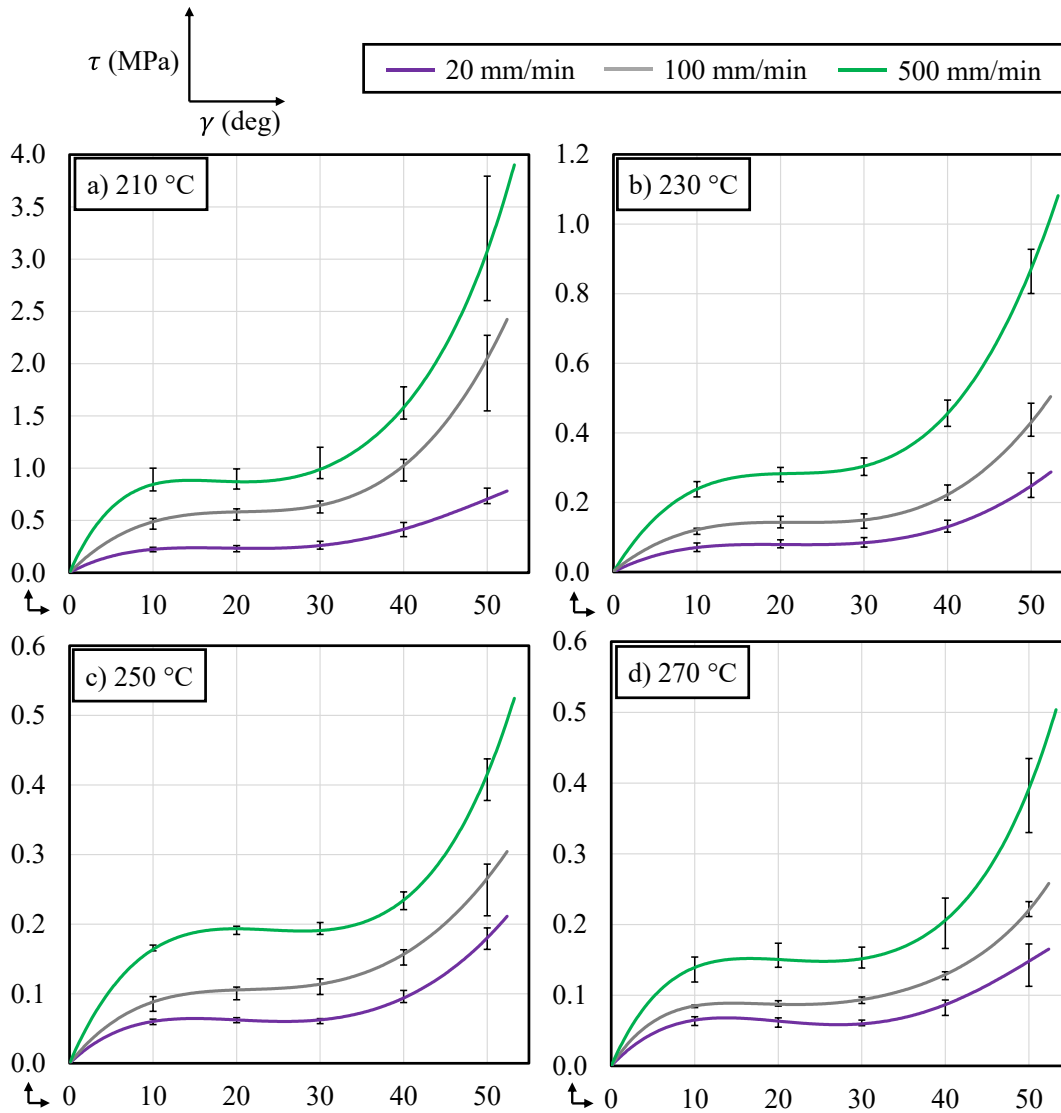


Figure 4.12: Shear stress *versus* shear angle BET results after the polynomial-fitting process, for CF/PA6 laminates at different rates, at a) 210 °C, b) 230 °C, c) 250 °C, d) 270 °C.

As expected, increasing the displacement rate (and therefore shear rate) resulted in an increased shear stress due to the viscoelastic matrix. It is also possible to interpolate from the figure that reducing the temperature also increased the required shear stress due to increasing resin viscosity. Appendix B - Figure B.3 illustrates the same data as that in Figure 4.12, however arranged with each graph representing a constant rate, therefore highlighting this effect.

Experimental repeatability was generally high at lower shear angles, with a maximum recorded deviation of approximately $\pm 15\%$ during the 'steady-state' region. It was believed these errors were caused by a small degree specimen rotation within the clamps, marginal temperature differences between tests and small amounts of specimen fibre misalignment (due to waviness in the organosheet). The error increased (up to $\pm 32\%$ deviation) after a shear angle of 45° as the material underwent intra-ply slip. An exception to this was the data for laminates at 210°C which exhibited steady-state errors up to $\pm 22\%$. Error bars have been included on Figure 4.12 to illustrate this.

4.4.2 Picture Frame Test Results

The results from the PFT exhibited a similar form to those illustrated in Figure 4.12. Figure 4.13 compares the results from the PFT and BET at the three PFT test temperatures and two test rates. It should be noted that the displacement rate is converted into a shear rate for consistency between test methods.

Generally, there is reasonable agreement between the two test methods, especially at lower shear angles. In most cases, the BET results began to track lower than the PFT results after 45° , which was assumed to be caused by intra-ply slip. Acquiring PFT results was beneficial as it allows for the characterisation of shear behaviour at high shear angles, however from Figure 3.7c it appears that shearing during the DDF process is generally limited to $<50^\circ$. The experimental repeatability of the BET was much greater than that of the PFT in these tests. It was concluded that this was caused by non-perfect specimen alignment within the clamps. This resulted in in-plane tensions applied to the specimen, which has previously been shown to influence the PFT results [213]. This was not necessarily an error associated with mounting the specimen in the clamps, but an error associated with non-orthogonal fibres within the consolidated FRTP organosheet from manufacture. Overall, the conformity between

both tests illustrates that both can be considered viable, however the improved reliability of the BET makes it a more attractive test method in this work. Only the BET is considered hereon in.

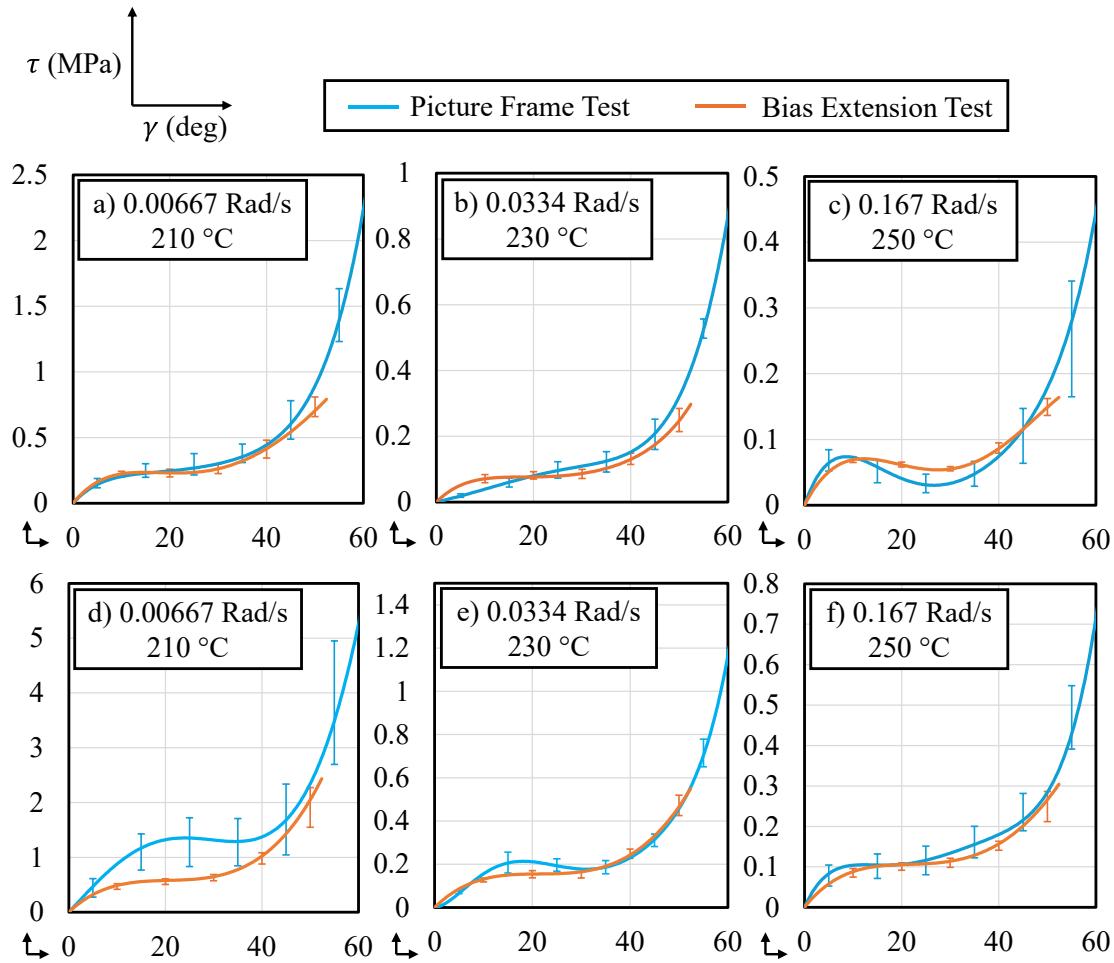


Figure 4.13: Comparison between the experimental results from the picture frame test and the bias extension test at different conditions.

4.4.3 Data Parameterisation

As part of the data analysis procedure, it was important to parameterise the shear stress *versus* shear angle BET results presented in Figure 4.12. The method followed in this work effectively follows that outlined by Machado *et al.* [159], who produced a viscoelastic intra-ply shear relationship for implementation within a hypoelastic numerical model. Initially, the polynomial functions for each curve (Equation (4.17)) were combined to produce a mean polynomial, representing the average curve ‘shape’. It was then possible to refit this new combined polynomial to each individual curve by multiplying it by a shifting factor, *S*. Each curve therefore represented:

$$\tau_{sh} = S \cdot [s_1\gamma^5 + s_2\gamma^4 + s_3\gamma^3 + s_4\gamma^2 + s_5\gamma] \quad (4.18)$$

where $s_{1...5}$ are constants, tabulated in Appendix B - Table B.1. Note that the shifting factor, S , is denoted the ‘shear factor’ for the remainder of this section. The shear factor was calculated utilising a least-squares fitting procedure for each test condition. This fitting procedure was completed only for data $<45^\circ$ shear angle to eliminate any errors associated with intra-ply slip. Appendix B - Table B.2 illustrates the calculated shear factor values for each of the 12 test conditions. The lowest recorded ‘r-squared’ value from this process was 0.913. For complete exposure, Appendix B - Figure B.4 illustrates the data from Figure 4.12 and the respective combined polynomial fit (Equation (4.18)) for each. In almost all cases, the curve fits within the experimental error of that respective BET.

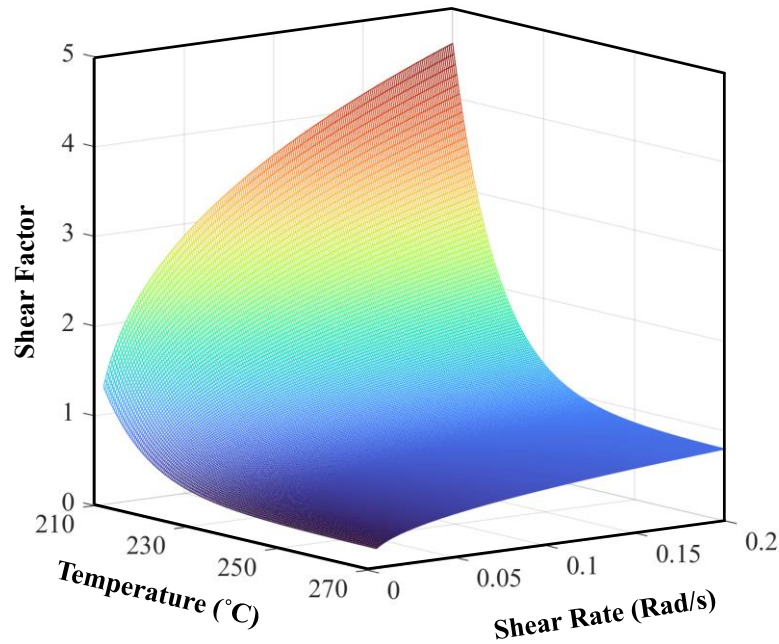


Figure 4.14: Shear factor *versus* laminate temperature and shear-rate for CF/PA6 laminates.

While the shear factor, S , reasonably well represents the complete dataset, its value has no physical meaning. It was instead desired that its relation to both temperature and shear rate be determined such as to provide an input for a numerical model. For this purpose, the work of Machado *et al.* [159] was again used, in which the authors used an overstress law and an Arrhenius-type relationship for the rate- and temperature-dependencies respectively. The shear factor therefore represented:

$$S = \left[\frac{\dot{\gamma}}{D_s} \right]^{\left(\frac{1}{P_s} \right)} \cdot \left[\exp \left(A_s \cdot \frac{T - T_s}{T_s} \right) + b_s \right] \quad (4.19)$$

where $\dot{\gamma}$ is the shear rate, and D_s , P_s , T_s , A_s and b_s are constants. Note that the second-order exponential term, b_s , was not utilised in the work of Machado *et al.* [159] but was included here due to a significant improvement in fitting accuracy.

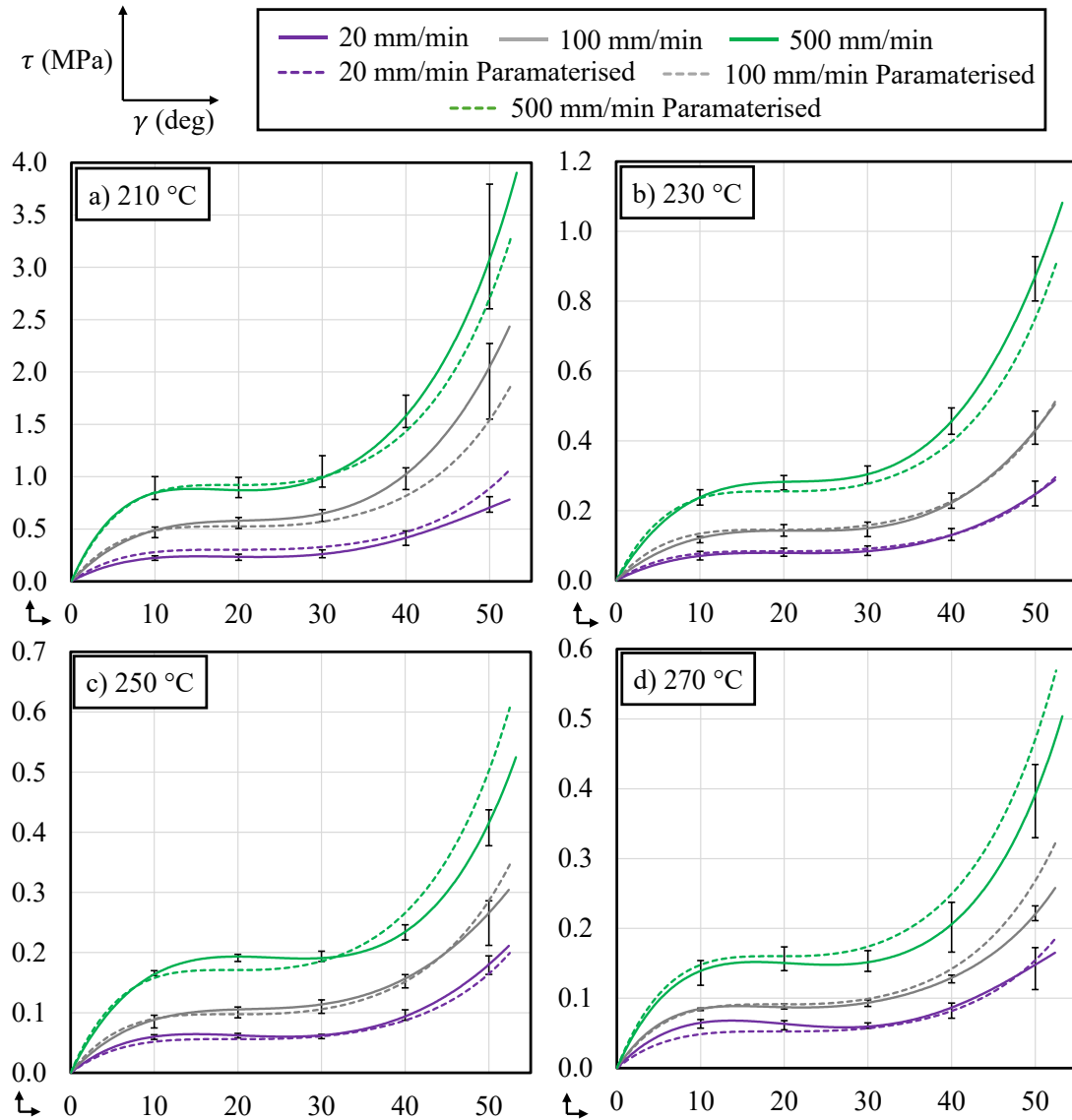


Figure 4.15: Experimental *versus* parameterised shear stress *versus* shear angle datasets for CF/PA6 laminates at a) 210 °C, b) 230 °C, c) 250 °C, d) 270 °C.

Figure 4.14 illustrates Equation (4.19) graphically, having completed a fitting procedure with the shear factor values (Appendix B- Table B.2), minimising the sum

of the squared residuals. An ‘r-squared’ value of 0.839 was recorded. The final calibrated constants are tabulated in Appendix B - Table B.1.

Finally, it was reasonable to compare the initial experimental results (Figure 4.12), to the calibrated parameterised results. Figure 4.15 illustrates these data. The parameterised results represent the following form (combining Equation (4.18) and (4.19)):

$$\tau_{sh} = \left[\frac{\dot{\gamma}}{D_s} \right]^{\left(\frac{1}{P_s} \right)} \cdot \left[\exp \left(A_s \cdot \frac{T - T_s}{T_s} \right) + b_s \right] \cdot [s_1 \gamma^5 + s_2 \gamma^4 + s_3 \gamma^3 + s_4 \gamma^2 + s_5 \gamma] \quad (4.20)$$

4.5 Diaphragm-Ply Friction Characterisation Results

This section details the results from the diaphragm-ply friction tests described in Section 4.2.3.

4.5.1 Pull-through Test Results

A typical force *versus* displacement dataset is illustrated in Figure 4.16, in this case for laminates (4 repeats) at 230 °C, 100 mm/min displacement and 0.1 bar pressure. Similar to the behaviour that was witnessed in previous works (refer to Section 2.4.4), the curves can be split into two distinct sections: firstly an initial peak force is overcome to initiate the sliding behaviour, which represents a cohesive element of the friction behaviour. After the force is overcome, the force decreases in an exponential fashion such that a ‘steady-state’ force is met, usually after 5-10 mm of displacement. Two coefficient of friction values can therefore be obtained from these curves, usually denoted the ‘static’ (initial peak) and ‘dynamic’ (steady-state) values. The raw results from experiments at all other test conditions can be viewed in Appendix B - Figure B.5.

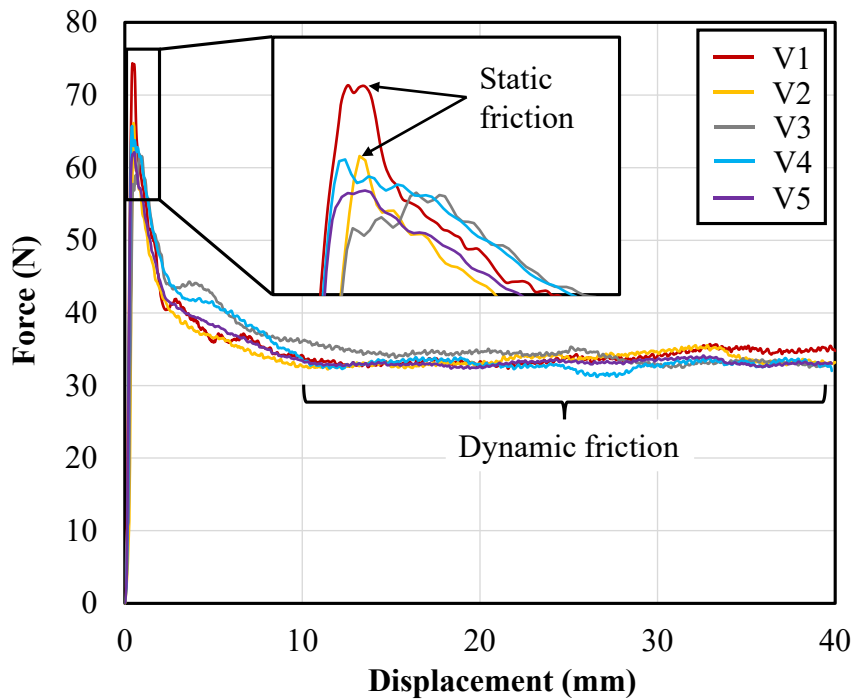


Figure 4.16: Force *versus* displacement diaphragm-ply friction experimental results for laminates at 230 °C, 100 mm/min and 0.1 bar normal pressure

In this work, an average static force was taken as the mean peak force from the 5 different repeats. For the dynamic force value, an average was acquired from all results between 10-20 mm of displacement, for each repeat. It was decided to only use this window because this ensured a steady-state condition had been met, but also didn't account for variation at high displacement levels. This was especially prudent in the case of laminates tested at 210 °C, which exhibited a gradual drop in the steady-state force over the test (Appendix B - Figure B.5a). Furthermore, referring to Figure 3.10, it appears that 20 mm is approximately the maximum diaphragm-ply slip distance applicable for double-dome geometry forming.

Figure 4.17 illustrates the mean static and dynamic force values for the three different studies: variable rate, variable temperature and variable normal pressure. Furthermore, the static values are displayed as a percentile increase when compared to the dynamic values.

Assuming a fully hydrodynamic boundary, as per a Stribeck analysis, the friction forces increase with a faster displacement rate and reduction in specimen temperature. Furthermore, the friction force increases with normal pressure as would be expected due to the relationship between normal force and friction force (Equation (4.12)). It

was also noted that generally the static force was 90-120% higher than the dynamic force. An exception to this was with the variable pressure studies, indicating that normal pressure has a considerable influence on the static CoF. This could be due to the pressure influencing the resin layer thickness, thus changing the force required to overcome the initial cohesion.

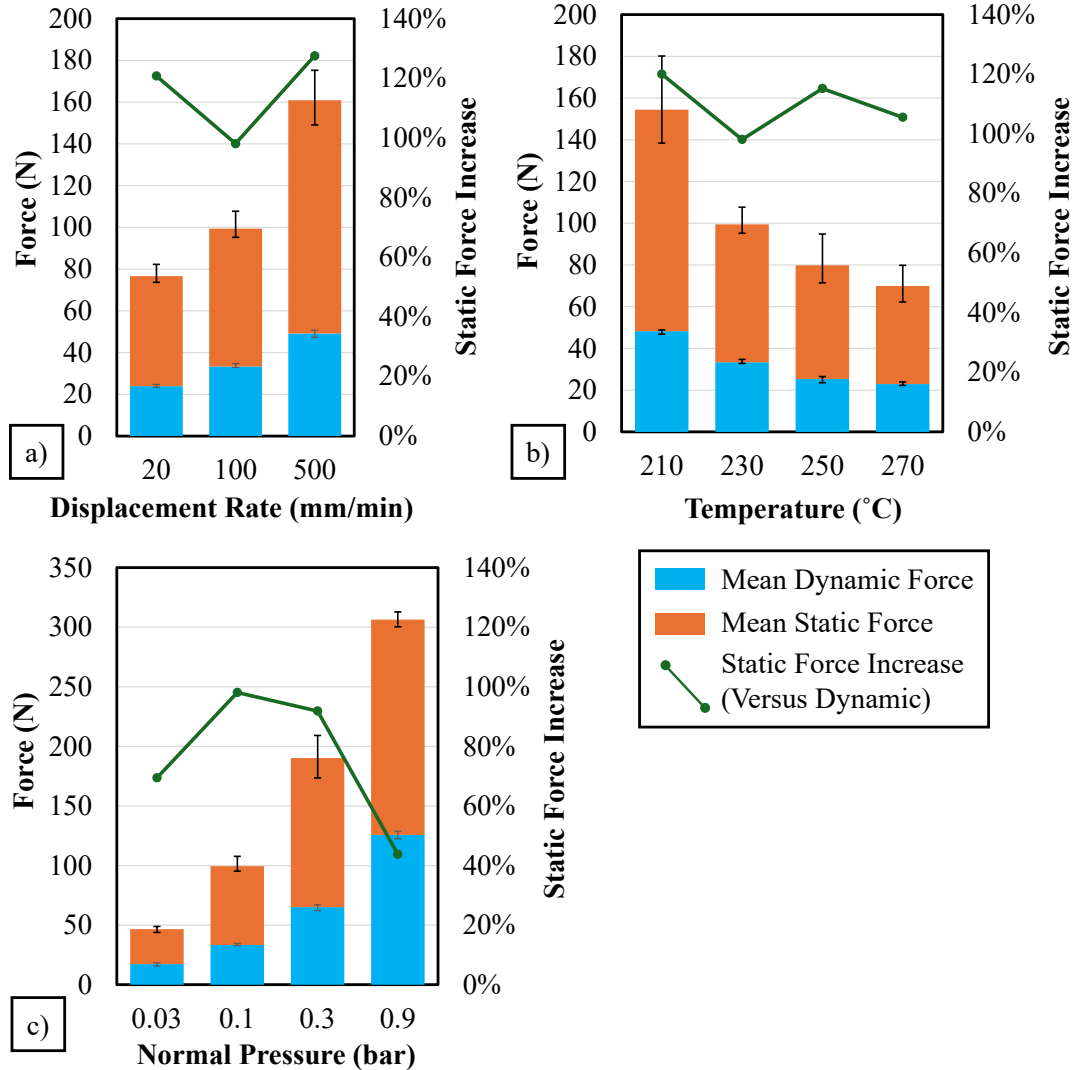


Figure 4.17: Dynamic and static force values (including comparison) for diaphragm-ply friction studies at: a) variable rates, b) variable temperatures, c) variable normal pressures.

A mean experimental deviation of approximately $\pm 15\%$ was present for the dynamic values, compared to $\pm 35\%$ for the stiction values. This is not unexpected since the sensitivity of static values is generally considered greater than that for dynamic values [395]. An exception regarding the experimental error was for tests conducted at 0.03 bar that contained considerable noise (Appendix B - Figure B.5f). This was because at

this pressure the normal force was very low, thus allowing movement in the pressure-plates to occur. This caused small oscillations in the contact area and therefore the applied normal pressure. This may have also caused the anomalous result regarding the low static force at 0.03 bar.

4.5.2 Data Parameterisation

Equation (4.12) was implemented with the mean force values to obtain mean CoF values. Generally in literature, it is the dynamic coefficient that is considered of most interest with little attention given to the static values [209]. This assumption was questioned, however, since much of the laminate is likely to undergo less than 10 mm of tangential displacement (relative to the diaphragm) in the DDF process. It was therefore decided that both the static and dynamic values would be considered in this work to improve the accuracy of the material input data.

As detailed in Section 2.4.4, a Stribeck curve is commonly used to parameterise thermoplastic laminate friction behaviour, which is usually assumed to lie within the hydrodynamic region. The same approach was therefore implemented in this work. For a Stribeck analysis, the CoF is plotted against the Hersey number (Equation (2.1)), itself proportional to the diaphragm-ply displacement rate, normal pressure and resin viscosity. While the former two variables were defined as part of the methodology, the viscosity of the PA6 resin was unknown.

Due to the practical limitations of this work, and due to the abundance of data regarding PA6 that is widely available, it was decided that 3rd party data would be utilised to characterise the viscosity profile of the resin. This viscous behaviour is, in its own right, dependent on both the laminate temperature and the shear rate, with thermoplastic matrices often exhibiting a degree of ‘shear thinning’ behaviour. To complicate the process of gathering this data, it has been shown that the moisture content also influences the viscosity of the PA6 resin [396], due to the water absorption characteristics outlined in Section 2.2.2. Therefore, to assess the variation in literature, viscosity curves (varying shear rates) were acquired for PA6, at 250 °C, from five sources [397-401]. These data are illustrated in Figure 4.18. While variation in data does exist, owing to an array of different variables, there is a clear trend in shear thinning behaviour. Moreover, the ‘zero shear-rate’ viscosity appears to be almost

constant between the different experiments, having plateaued at a low shear rate. These data therefore form the basis of the viscosity parameterisation present in this work.

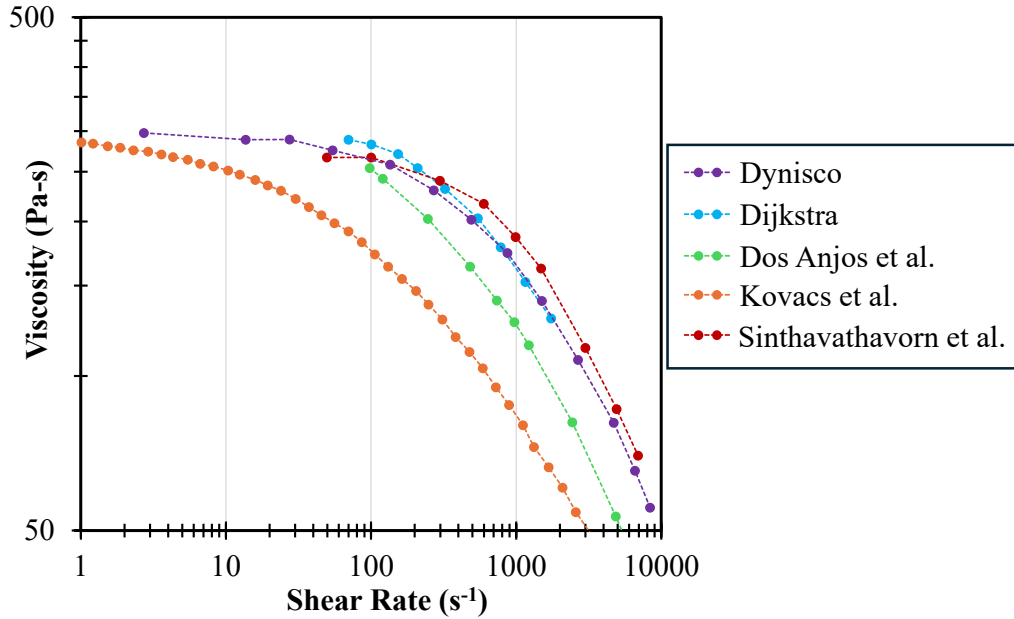


Figure 4.18: PA6 viscosity *versus* shear rate, at 250 °C, from a range of third-party sources.

A Carreau-Yasuda model formulation was utilised to model the viscosity of PA6, which is generally recognised for its ability to describe viscosity across a wide range of shear rates [402]. This makes it suitable for modelling the flow behaviour of various thermoplastic materials during processing:

$$\eta(\dot{\gamma}, T) = \eta_0(T) \cdot [1 + (\lambda\dot{\gamma})^a]^{\frac{n-1}{a}} \quad (4.21)$$

where η is the resin viscosity, η_0 is the ‘zero shear viscosity’ (temperature dependent), $\dot{\gamma}$ is the shear rate and λ (characteristic time constant), a (parameter that controls the width of the transition between Newtonian and shear-thinning regimes) and n (flow behaviour index) are constants, determined below. The zero-shear viscosity is highly temperature-dependent and often follows an Arrhenius relationship for polymers like PA6 [403]:

$$\eta_0 = \eta_{0ref} \cdot \exp\left(\frac{E_a}{R} \cdot \left(\frac{1}{T} - \frac{1}{T_{ref}}\right)\right) \quad (4.22)$$

where η_{0ref} is the zero-rate viscosity at temperature T_{ref} , T is the temperature, E_a is the activation energy of PA6 and R is the universal gas constant. From Figure 4.18, η_{0ref} was averaged from the two datasets that capture the low shear-rate behaviour ([399, 400]), for a value of 291 Pa-s (at 250 °C). Furthermore, the universal gas constant can be assumed to be 8.314 J/Kg-Mol. The activation energy of PA6 is again variable, and only the work of Kovacs [400] illustrates the viscosity curves of PA6 at different temperatures. Utilising this work, two forms of Equation (4.22) could be generated, one for each temperature and viscosity, and solved simultaneously for the activation energy. Following this process, the activation energy of PA6 was deduced as 60.5 kJ/mol. This value was checked against other works to ensure it was within appropriate bounds, such as that of Abacha [404] who derived a PA6 activation energy value of 54.28 kJ/mol.

Therefore, combining Equations (4.21) and (4.22), the viscosity of PA6 is equal to:

$$\eta(\dot{\gamma}, T) = \eta_{0ref} \cdot \exp\left(\frac{E_a}{R} \cdot \left(\frac{1}{T} - \frac{1}{T_{ref}}\right)\right) \cdot [1 + (\lambda\dot{\gamma})^a]^{\frac{n-1}{a}} \quad (4.23)$$

The third-party data illustrated in Figure 4.18 could then be fitted in a least-squares fitting procedure to this equation in an iterative process to determine the values of λ , a and n . This was completed without the data of Kovacs [400] included due to the discrepancy between this dataset and the others. Figure 4.19 illustrates the outcome of this study, where the viscosity curve from this work has been superimposed on the third-party experimental data. The Carreau-Yasuda model appears to produce a good fit for the resin viscosity against the different 3rd party datasets, with an ‘r-squared’ value of 0.895. The calibrated constants are tabulated in Appendix B - Table B.1.

With an equation for the resin viscosity, Equation (2.1) was implemented to determine the Hersey number for each of the friction tests, as a function of the test conditions. It should be noted that the shear rate, utilised in Equation (4.23), can be deduced from the slip-rate, $\dot{\delta}$, and the thickness of the interfacial film that is undergoing shear, t_{itf} :

$$\dot{\gamma} = \frac{\dot{\delta}}{t_{itf}} \quad (4.24)$$

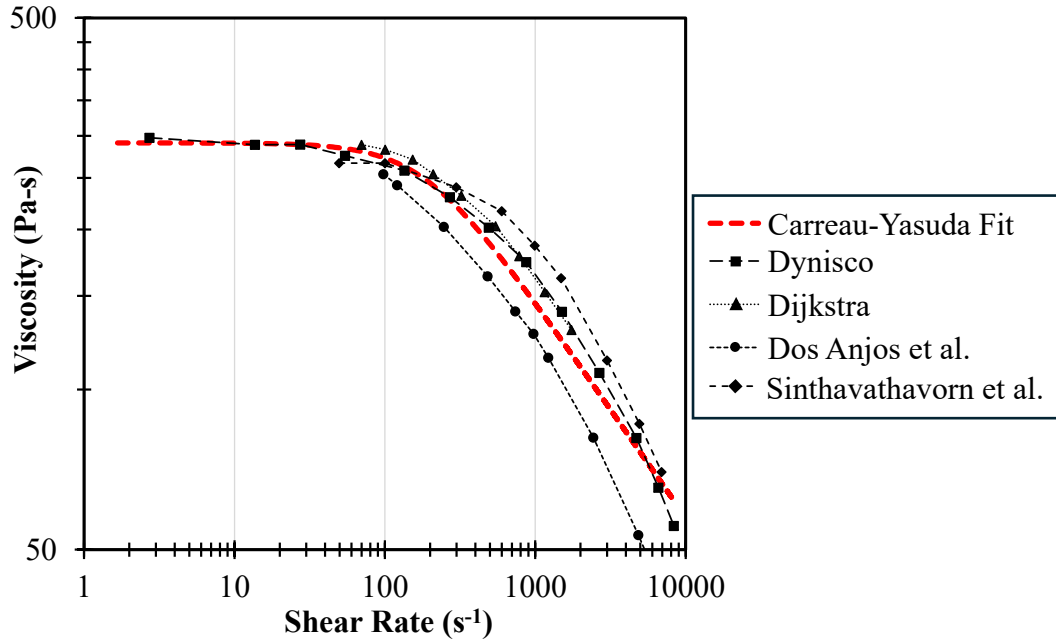


Figure 4.19: Carreau-Yasuda model (viscosity *versus* shear rate) compared to 3rd party sources.

Defining the interfacial film thickness is not trivial, so a value of 2.5 μm was used in this work, as per Pierik *et al.* [209]. Therefore, using Equations (2.1), (4.23) and (4.24), the Hersey number was calculated for each test, and subsequently plotted against the calculated CoF values, as per Figure 4.20. This was completed for both the static and dynamic cases, including the experimental error.

Finally, a logarithmic relationship was defined using a least-squares algorithm to define the CoF, μ , as a function of the Hersey number, H , in the form of:

$$\mu_s = n_s \ln(H) + m_s \quad (4.25)$$

$$\mu_d = n_d \ln(H) + m_d \quad (4.26)$$

Where subscripts s & d refer to the static and dynamic curves, respectively, and n and m are constants, tabulated in Appendix B - Table B.1. Upon analysing the constants, in both cases the static constants were approximately 2.10 (± 0.01) times greater than that of the dynamic constants. Therefore, for simplicity, Equation (4.25) was neglected, meaning only one Stribeck curve was required for the diaphragm-laminate friction behaviour. Thus, the new equation for the static CoF was:

$$\mu_s = 2.10\mu_d \quad (4.27)$$

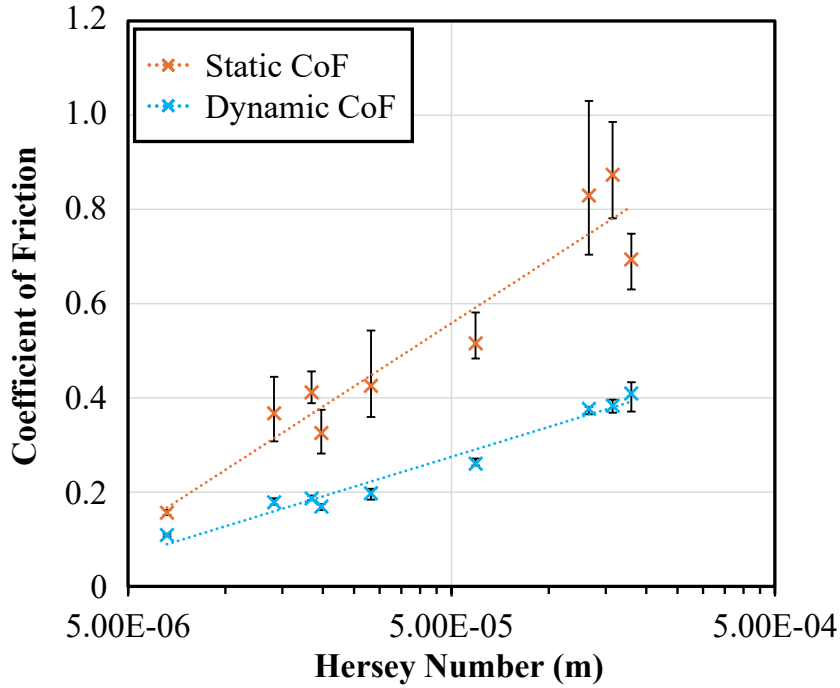


Figure 4.20: Coefficient of friction (static and dynamic) *versus* Hersey number for all pull-through tests, including experimental error.

The dynamic curve exhibited an ‘r-squared’ value of 0.978 and the goodness of fit indicates that the Stribeck analysis allows for a good approximation of the friction behaviour for the diaphragm-ply interaction. Due to its linearly increasing (linear on a log-scale) nature, it can be concluded that the friction behaviour does appear to act predominantly within the hydrodynamic regime. The implementation of these CoF relationships within a numerical model is discussed in Section 6.2.2.2, utilising the following equation for concision (combining equations (4.23), (4.24) and (4.26)):

$$\mu_d = n_d \ln \left(\frac{\left[\eta_{0ref} \cdot \exp \left(\frac{E_a}{R} \cdot \left(\frac{1}{T} - \frac{1}{T_{ref}} \right) \right) \cdot \left[1 + \left(\frac{\lambda \dot{\delta}}{t_{itf}} \right)^a \right]^{\frac{n-1}{a}} \right] \dot{\delta}}{P} \right) + m_d \quad (4.28)$$

With the inputs: T (temperature), $\dot{\delta}$ (slip-rate) and P (normal pressure).

4.6 Out-of-plane Bending Characterisation Results

This section details the results from the out-of-plane bending experiments described in Section 4.2.4.

4.6.1 Experimental Results

The bending profiles for CF/PA6 laminates, as recorded by the high-speed camera, at the four different experimental temperatures and two superimposed times, are illustrated in Figure 4.21.

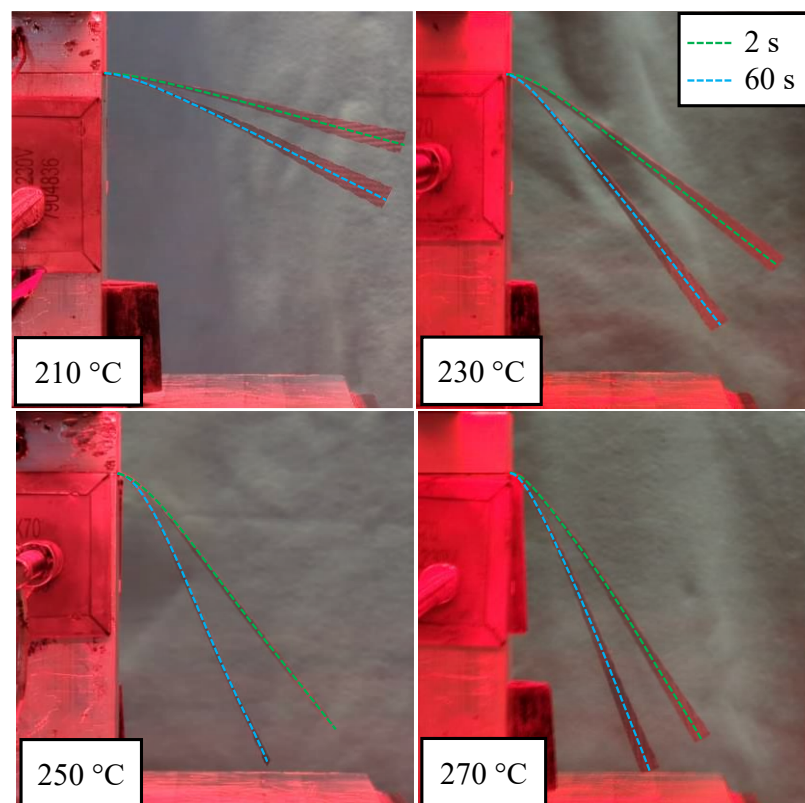


Figure 4.21: Bending profiles for CF/PA6 laminates at four different temperatures and at two different elapsed times.

From Figure 4.21, it can be seen that increasing laminate temperature leads to a decrease in the bending stiffness by virtue of the reduction in resin viscosity. Furthermore, the figure shows that a considerable variation in bending profile is witnessed over time. While CF/PA6 is likely to exhibit rate-dependent bending behaviour, this change in profile was more likely considered to be a ‘relaxation’ effect

due to the unconstrained nature of the cantilever bending test. This compares to both the intra-ply shear (Section 4.4) and diaphragm-ply slip (Section 4.5) studies in which the laminate motion was heavily constrained. Since the rate of bending cannot be controlled using the cantilever bending test, the influence of bending rate on CF/PA6 bending stiffness is neglected in this study. Furthermore, while the laminate thickness increases due to deconsolidation (Figure 4.8), this was neglected in this study.

As mentioned in the methodology (Section 4.2.4.1), the profile of each laminate was obtained from a 3D scan and averaged between the front and rear sides, such as to eliminate laminate twist, a phenomenon visible in most tests (Figure 4.21). Figure 4.22a illustrates the average (between front & rear face) bending profile for CF/PA6 laminates at 230 °C, after 600 seconds (steady-state condition), with 5 individual tests included. A moderate variation in profile was noted between individual tests, attributed to the unconstrained nature of the cantilever test, small temperature fluctuations with the IR apparatus, movement of the sample due to convective currents and the small sample size (30 mm wide) used to increase thermal homogeneity.

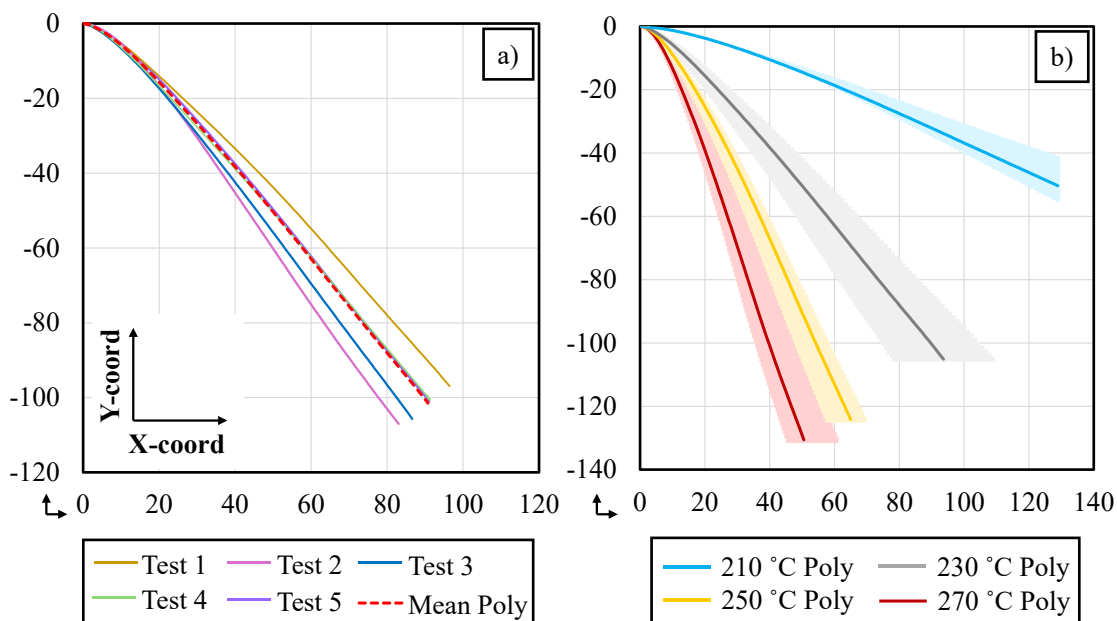


Figure 4.22: Bending profile for a) Repeated tests at 230 °C after 600 seconds (steady-state),
b) Average polynomial for the four tested temperature after 600 seconds (steady-state).

Similar to the method of combining intra-ply shear repeats (Equation (4.18)), an average bending profile was obtained by combining the five steady-state bending curves. This was done by resampling the data (using linear interpolation), such that

each profile was represented by 200 data points, thus allowing for them to be averaged for each x-displacement value. After the average bending profile had been obtained, it was pertinent to fit a 6th order polynomial, so the data was parameterised in a numerically-efficient manner. The polynomial was constrained such that the gradient at the origin was 0, as should be the case for a perfectly cantilevered specimen. The average bending profile of each test condition therefore represented:

$$y_b = b_1x_b^6 + b_2x_b^5 + b_3x_b^4 + b_4x_b^3 + b_5x_b^2 \quad (4.29)$$

where x_b and y_b are the coordinates that replicate the bending profile, and $b_{1...5}$ are constants specific to each test condition. The minimum ‘r-squared’ value for this operation was 0.996. The average bending polynomial for the 230 °C laminate is also included on Figure 4.22a, denoted ‘mean poly’. The mean bending polynomial for each test condition in the steady-state is illustrated in Figure 4.22b, with the experimental variation shaded. As can also be interpolated from Figure 4.21, an increase in laminate temperature leads to a decrease in laminate bending stiffness.

With the mean polynomial (Equation (4.29)) for each test condition obtained, Equations (4.13)-(4.15) were implemented to obtain the laminate bending moment and curvature from the bending profile. Figure 4.23a illustrates the raw bending moment *versus* curvature output from these equations, for the mean 230 °C polynomial.

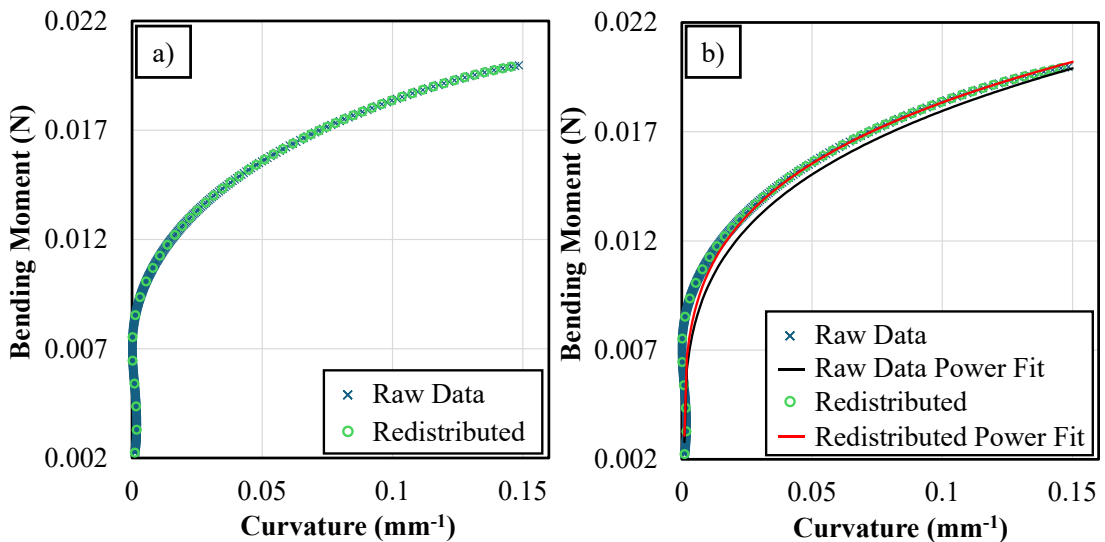


Figure 4.23: Bending moment *versus* curvature for 230 °C CF/PA6 laminates (mean polynomial): a) raw and redistributed datasets, b) power curve fitting.

It was desirable to fit a curve to these data such as to relate the two variables in a numerically efficient manner. It is apparent from the bending profiles (Figure 4.21), however, that the majority of the bending occurred directly at the cantilever support. A considerable length of the specimen is seen to exhibit little to no curvature. Because of this, the bulk of all data points in Figure 4.23a are situated in the region of low curvature. This is problematic for the intention of defining a curve fit between the two variables, since any curve is heavily skewed to fit the low-curvature section. To mitigate this issue, the data was resampled. The resampled (denoted ‘redistributed’) data points for the mean polynomial at 230 °C are also illustrated on Figure 4.23a.

To create a bending moment *versus* curvature relationship for each dataset, a 1st order power relationship was fitted to the redistributed data points such that the bending moment *versus* curvature relationship could be defined as:

$$M_n = p_b \cdot k^{q_b} \quad (4.30)$$

where p_b and q_b are constants specific to each test condition. A Levenberg-Marquardt algorithm was implemented to obtain the value of these constants, with a minimum ‘r-squared’ value of greater than 0.95 in each case, apart from for the curve at 210 °C (0.91). This was caused by the lower curvature of the 210 °C laminate, increasing the absolute experimental error in this case.

The power-fit for the mean 230 °C polynomial, with redistributed data points, is illustrated in Figure 4.23b. For comparative purposes, a power-fit for the raw data points (not redistributed) is also included in the figure, showing the importance of the distribution exercise for accurate curve fitting at high curvatures. The values for the associated constants, for each test condition, are tabulated in Appendix B - Table B.3

Figure 4.24 illustrates the four bending moment *versus* curvature power-laws obtained after the implementation of Equation (4.30), compared to the redistributed experimental data. From these curves, it was possible to quantify a maximum deviation in the experimental curvature, from the mean, of $\pm 23\%$. Furthermore, apart from the 210 °C data, the power-fit lay within the experimental error of the redistributed data in each case. The experimental uncertainty is therefore higher than that associated with the curve fitting exercise.

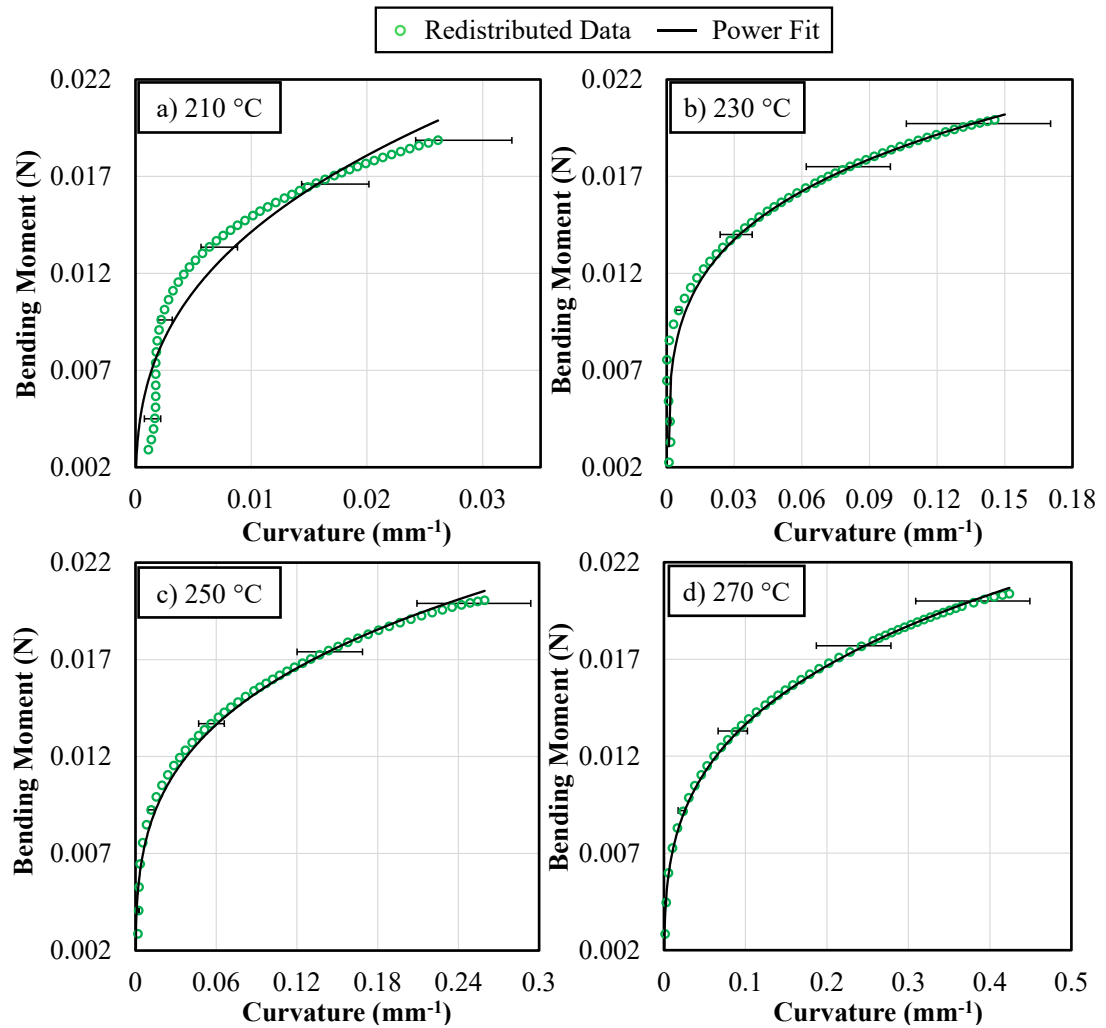


Figure 4.24: Bending moment *versus* curvature power fit and redistributed experimental data (mean polynomial) at the four tested temperatures.

Figure 4.25 compares directly between the bending moment *versus* curvature curves for each temperature. An increased laminate temperature increases the laminate curvature for a given bending moment. This figure illustrates that while the experimental error associated with the FRTP cantilever test was considerable, the error is still small enough to confidently differentiate between the individual test conditions.

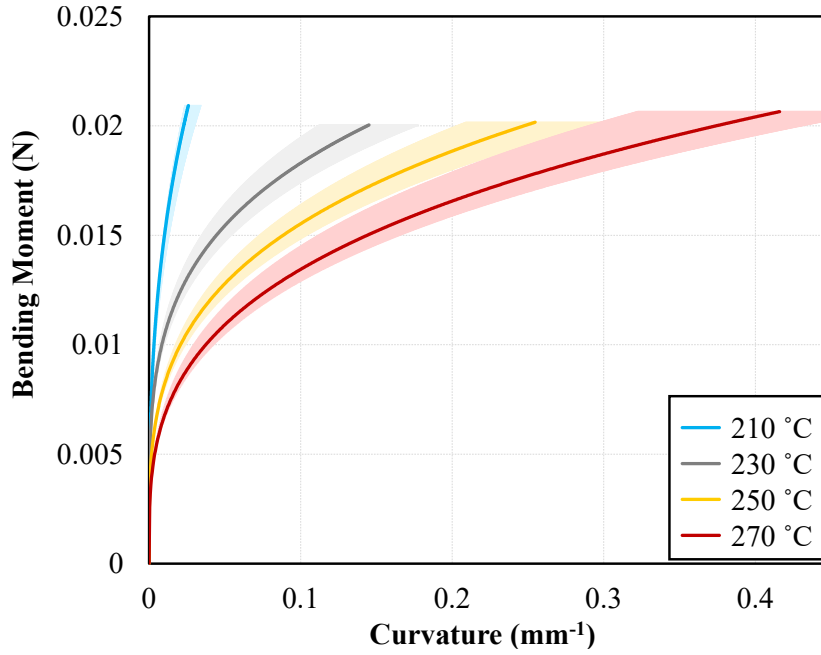


Figure 4.25: Bending moment *versus* curvature power fit and associated experimental error for CF/PA6 laminates at four tested temperatures.

4.6.2 Data Parameterisation

As per the characterisation of intra-ply shear (Section 4.4.3), it was necessary to parameterise the bending moment *versus* curvature curves illustrated in Figure 4.25, such as to provide a convenient input for a numerical routine. For reference, this process is closely aligned to that outlined in Section 4.4.3. For this process, Equation (4.30) was modified such that a single ‘bending factor’ was used to represent the power curves in each case. This was deemed possible due to the similarity in the values of q_b for each test temperature, as can be seen in Appendix B - Table B.3. Therefore, each curve therefore represented:

$$M_n = B \cdot P_b \cdot k^{Q_b} \quad (4.31)$$

where B represents the bending factor, and P_b & Q_b fixed constants. It should be noted that the value of P_b was calibrated such that the value of the bending factor was greater than 1 in each case (simplifying the following mathematical procedure). A Levenberg-Marquardt algorithm was used to fit this to each individual redistributed result set, such that the values of the bending factor (Appendix B – Table B.3) and fixed constants (Appendix B - Table B.1) were defined. The curves associated with this procedure are

illustrated for completeness in Appendix B - Figure B.6. The mean 'r-squared' value associated with this procedure was 0.947.

Finally, to provide a numerically efficient input for a numerical routine, the values of the bending factor were related to their respective temperatures. This was again achieved with an Arrhenius type (exponential relationship), as per the temperature dependent intra-ply shear behaviour (Section 4.2.2.2). Figure 4.26 illustrates this, where the bending factor is plotted against temperature. The bending factor therefore represented:

$$B = \exp\left(r_b \cdot \frac{T - T_b}{T_b}\right) + 1 \quad (4.32)$$

where r_b and T_b are constants. These constants were calibrated using a Levenberg-Marquardt algorithm, thus resulting in an 'r-squared' value of 0.996, and are tabulated in Appendix B - Table B.1.

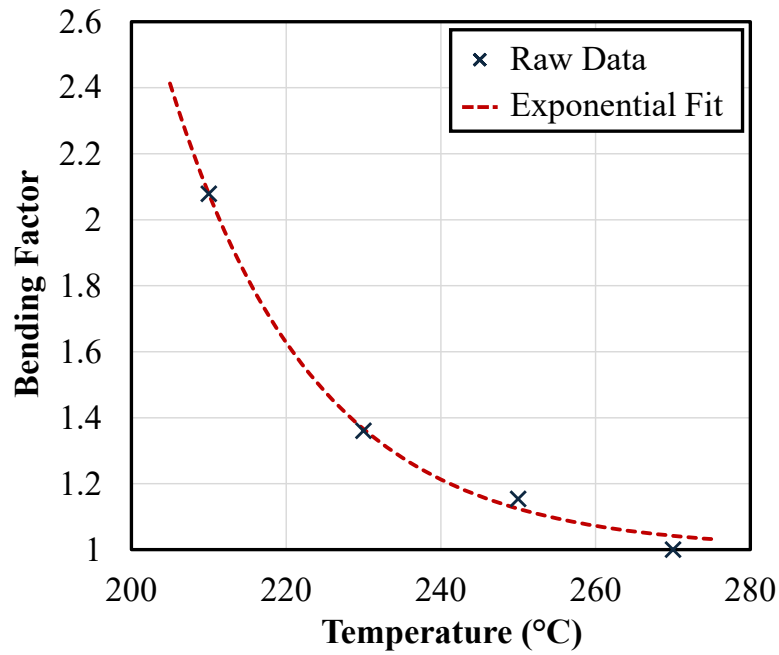


Figure 4.26: Bending factor *versus* temperature, including the associated exponential fit.

Finally, combining Equations (4.31) and (4.32) allows the bending moment to be defined directly as a function of curvature and laminate temperature:

$$M_n = P_b \cdot \left[\exp\left(r_b \cdot \frac{T - T_b}{T_b}\right) + 1 \right] \cdot k^{Q_b} \quad (4.33)$$

Figure 4.27 illustrates this parameterised fit for each test condition, compared to the original power fit (Figure 4.24) and the redistributed experimental data. The mean 'r-squared' value for the parameterised fit, *versus* the experimental fit (redistributed), was 0.939. For the majority of each curve, the parameterised fit fell within the experimental error.

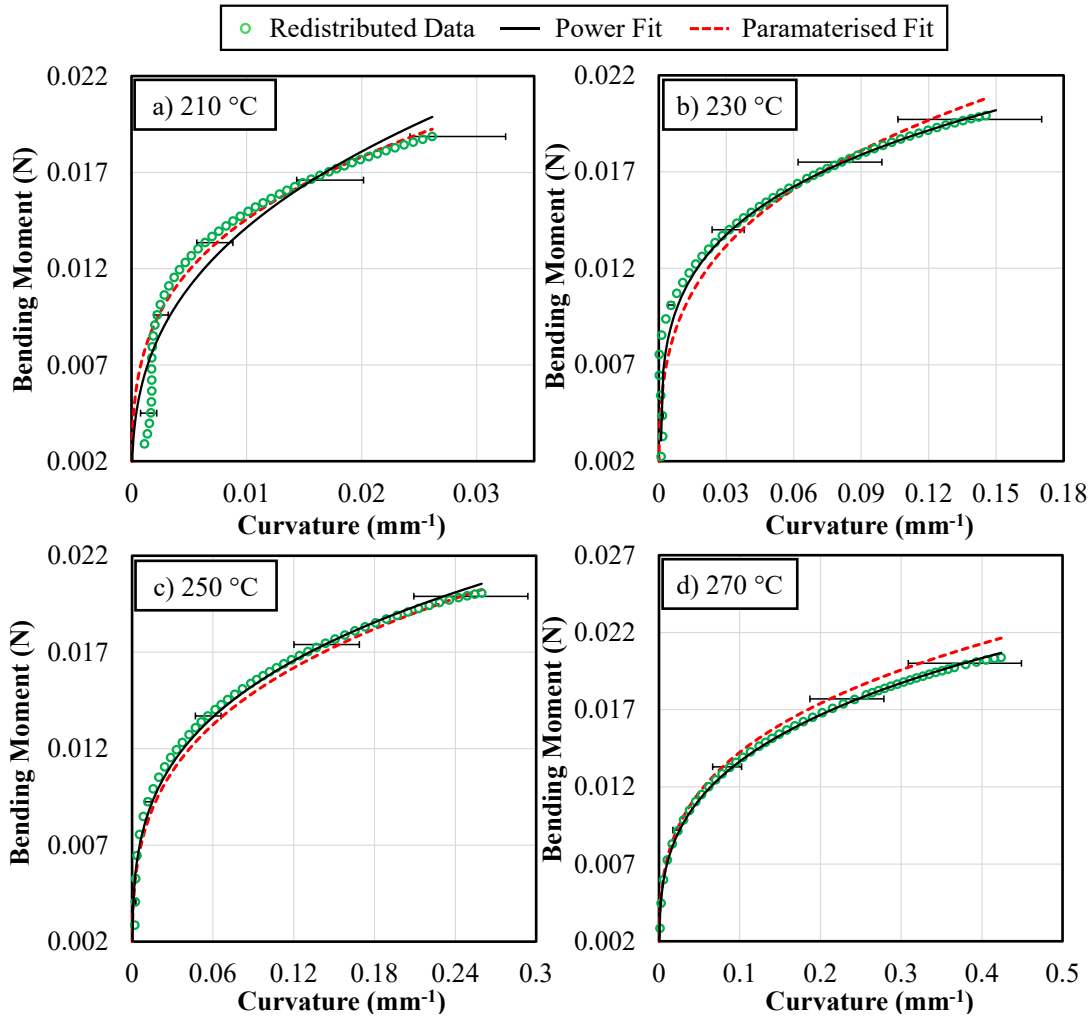


Figure 4.27: Final parameterised fit for bending moment *versus* curvature, illustrated at different experimental temperatures: a) 210 °C, b) 230 °C, c) 250 °C, d) 270 °C.

Finally, in a numerical routine, it is generally the bending *stiffness* that is implemented, as opposed to the bending moment. The bending stiffness, B , can be defined as the first differential (with respect to the curvature) of the bending moment:

$$B = P_b \cdot Q_b \cdot \left[\exp \left(r_b \cdot \frac{T - T_b}{T_b} \right) + 1 \right] \cdot k^{Q_b - 1} \quad (4.34)$$

Which can further be visualised as per Figure 4.28. As is typical for fabrics, the bending stiffness decreases with increased curvature as the fabric deforms through methods such as yarn slippage, shear and local buckling. In this work, a power relationship was used for the bending moment (Equation (4.33)), which results in the bending stiffness tending to infinity at low curvatures. This is not accurate in reality, such that the equation is not valid for very low curvatures ($<0.001 \text{ mm}^{-1}$). This is taken into consideration during the numerical modelling (Chapter 6).

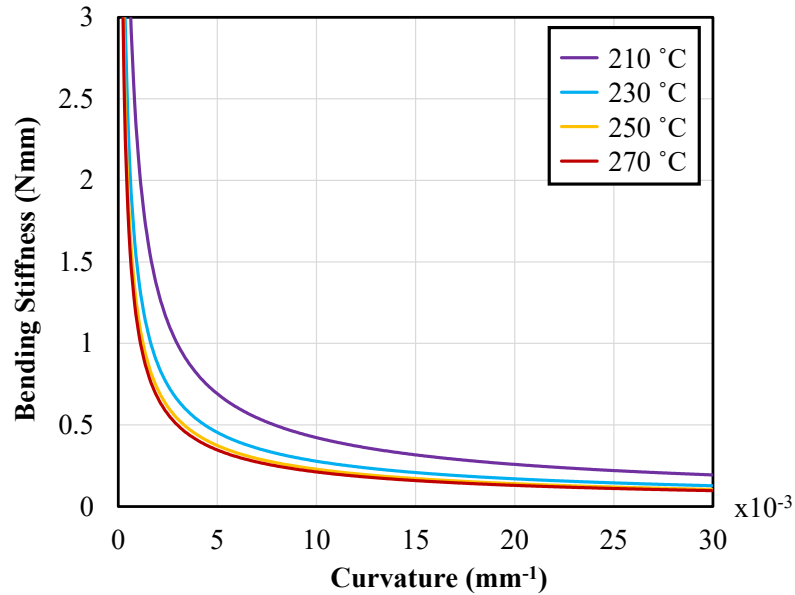


Figure 4.28: Bending stiffness versus curvature for different laminate temperatures, as would be used as an input for a simulation routine.

$$B = P_b \cdot Q_b \cdot \left[\exp \left(r_b \cdot \frac{T - T_b}{T_b} \right) + 1 \right] \cdot k^{Q_b - 1}$$

4.7 Chapter Conclusions

In this chapter, the key mechanisms associated with the thermoforming of FRTPs have been characterised, with the main objective of defining the inputs for an accurate forming simulation to be produced. Inter-ply shear, diaphragm-ply friction and out-of-

plane bending are the three primary deformation mechanisms explored, with viscoelasticity considered in each section. This includes both the rate- and temperature-dependency of all three mechanisms, although rate-dependent bending behaviour was not considered due to the limitations of the cantilever bending test. Furthermore, laminate deconsolidation, a phenomenon occurring upon heating with no normal pressure, was also characterised: with a deconsolidation of 9% and critical reconsolidation pressure of 0.4 bar noted. This means that all laminate macroscale deformation mechanisms that occur during processing have been captured in this work.

In each case, a decrease in laminate temperature or increase in the deformation rate both contribute to increased deformation forces associated with the respective primary mechanism. This therefore results in higher forming forces, if this work is to be considered regarding a forming process. This validates the differences in FRTP DDF behaviour of different laminate temperatures illustrated in Section 2.5. Pressure dependency was also considered as part of the diaphragm-ply friction characterisation, utilising a Stribeck analysis, with an increase in pressure resulting in a reduced CoF. In the intra-ply shear study, the high experimental variation ($\pm 45\%$) associated with the PFT showed that the BET is more suitable for shear analysis of FRTP organosheets.

For each deformation mechanism, a normalisation and parameterisation procedure was adopted such that a numerically efficient input for a simulation routine was produced. Equations (4.20), (4.28) and (4.34) are the outcomes from this exercise, in which the intra-ply shear, diaphragm-ply friction and out-of-plane bending mechanisms are all characterised with a single equation. These values had respective 'r-squared' values of 0.839, 0.978 and 0.939 respectively.

Chapter 5.

Diaphragm Thermomechanical Characterisation

5.1 Introduction

A unique characteristic of the DDF process is that it is not just the laminate that undergoes considerable deformation during the forming process, but the flexible diaphragms as well. This was clearly illustrated in Figure 3.10, where diaphragm strains of up to 80% were noted (within a defined area of interest) during the forming operation. Therefore, it is not only necessary to characterise the thermomechanical behaviour of the laminate, as per Chapter 4, but also the thermomechanical behaviour of the silicone diaphragms.

Regarding the silicone diaphragm, the deformation behaviour concerned the tensile/compressive behaviour of the hyperelastic material. This also includes the material behaviour after repeated loadings, owing to the reusable nature of the silicone diaphragms described in Chapter 3. Furthermore, the diaphragm interactions also required consideration; specifically the friction behaviour between the diaphragm and the tool/base. It was not necessary in this work to evaluate the thermal behaviour of the silicone. This is because the effects of thermal expansion had largely been mitigated with preheating of the silicone diaphragms (Section 3.4.1) and the material operates below its degradation temperature.

The objective of this chapter is therefore to characterise both the hyperelastic membrane behaviour and diaphragm-tool interaction, thus providing the inputs for a full FRTP DDF simulation to be produced.

5.2 Methodology

This section outlines the methodology behind characterisation of the silicone's hyperelastic behaviour and tool-diaphragm interaction.

5.2.1 Hyperelastic Characterisation

Silicone can be defined as a hyperelastic material, since it is a material that behaves in a nonlinear fashion and can comfortably exhibit strains of greater than 100%. This behaviour is difficult to characterise using a standard Young's modulus and Poisson's ratio technique implemented with conventional isotropic solids. Instead, the material

behaviour is typically characterised by modelling the strain energy density function for the respective material [405]. Abaqus has an inbuilt hyperelastic material editor, such that the implementation of such behaviour can be achieved within a numerical model.

An in-house characterisation procedure was adopted in this work due to the variable properties that silicone can exhibit, itself comprising of fillers and produced in a manner that is highly influential on its elastic behaviour.

To ensure that the strain energy density function of the silicone diaphragm was defined accurately, the three commonly-used tests to evaluate material deformation behaviour were implemented, namely, uniaxial, biaxial and pure-shear tests [406]. Figure 5.1 illustrates a schematic of each individual test. The reason that multiple test methods are used is to evaluate material behaviour under different deformation modes. For example, uniaxial testing gives a primary insight into the stiffness and stretch behaviour along one axis, which helps estimate parameters like the Young's modulus or the initial stiffness in one direction. However, uniaxial data alone cannot capture the full response of the material in multi-axial loading conditions, unlike the biaxial test, that is considered to more accurately recreate real-world conditions. Furthermore, the pure-shear test is sensitive to the material's resistance to shape change, essential for identifying the materials response to non-axial stresses. Due to the multiple parameters present within hyperelastic models (Ogden [407], Mooney-Rivlin [408] etc.), utilising these three test methods allows for more accurate and robust parameter fitting across all deformation modes, leading to a more reliable and predictive material model.

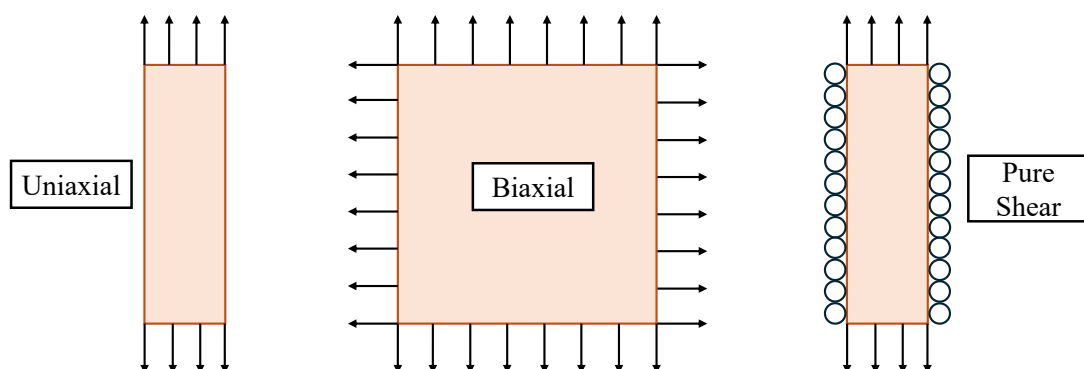


Figure 5.1: Commonly used test methods to evaluate hyperelastic material behaviour.

All testing in this work was conducted using the Silex 40 Shore hardness, 1 mm thick, silicone sheet [390], defined in Chapter 3 for the experimental DDF. For each test, the material thickness was measured 6 times along the sample width, in the respective loading condition, utilising a micrometer. An average value was then used, with a maximum single-specimen thickness deviation of 2.5%. The reduction in thickness owing to the force of the measurement gauge was deemed negligible for this study. In each case the force, F , versus displacement, ΔL , was measured, such that the sample stress, σ , and strain, ε , could be calculated (although a video extensometer was utilised with the uniaxial tests for a more accurate strain measurement):

$$\sigma = \frac{F}{W \cdot t} \quad (5.1)$$

$$\varepsilon = \frac{\Delta L}{L} \quad (5.2)$$

where L , W & t denote the sample length, width and (average) thickness in the loading direction, respectively.

5.2.2 Uniaxial Testing

The uniaxial test was used to evaluate the silicone sensitivity to a number of different deformation variables. This ensured a reliable strain energy density function could be formulated in a timely manner. Variables deemed to have little influence on the deformation behaviour could subsequently be neglected for the other two, more arduous test methods (biaxial, pure-shear).

Uniaxial testing was conducted using a Tinius Olsen 10ST testing machine, equipped with a 5 kN load cell. Samples were cut into 10 mm wide strips using a punch and marked with two 5 mm diameter spots, 25 mm apart, so the strain could be monitored accurately using a video extensometer. Each sample was scanned at 2000DPI prior to testing to validate the width measurement. The samples were then located within the universal testing machine with a uniaxial length of 120 mm. In the case of the samples tested at temperature, a Tinius Olsen environmental chamber was equipped, with closed-loop PID control, such as to achieve the desired specimen temperature. As per previous work utilising an environmental chamber (Section 4.2.2), a ‘dummy’ silicone

specimen was located within to ensure an accurate temperature value was attained. The following variables were tested to evaluate the material sensitivity:

- Two shear-rates: 0.01s^{-1} & 0.1s^{-1}
- Three test temperatures: $20\text{ }^{\circ}\text{C}$ (ambient), $100\text{ }^{\circ}\text{C}$ & $200\text{ }^{\circ}\text{C}$
- Two material directions: Longitudinal (silicone roll direction) & transverse
- Three cyclic loadings (evaluated in a continuous fashion)

The silicone was strained up to 100%, enough to capture the material behaviour within the expected strain window of the DDF experiments (Section 3.4.3.3). Four repeats were undertaken for each sample configuration. Figure 5.2 illustrates one of the samples located within the universal testing machine for tests conducted at ambient temperature conditions.

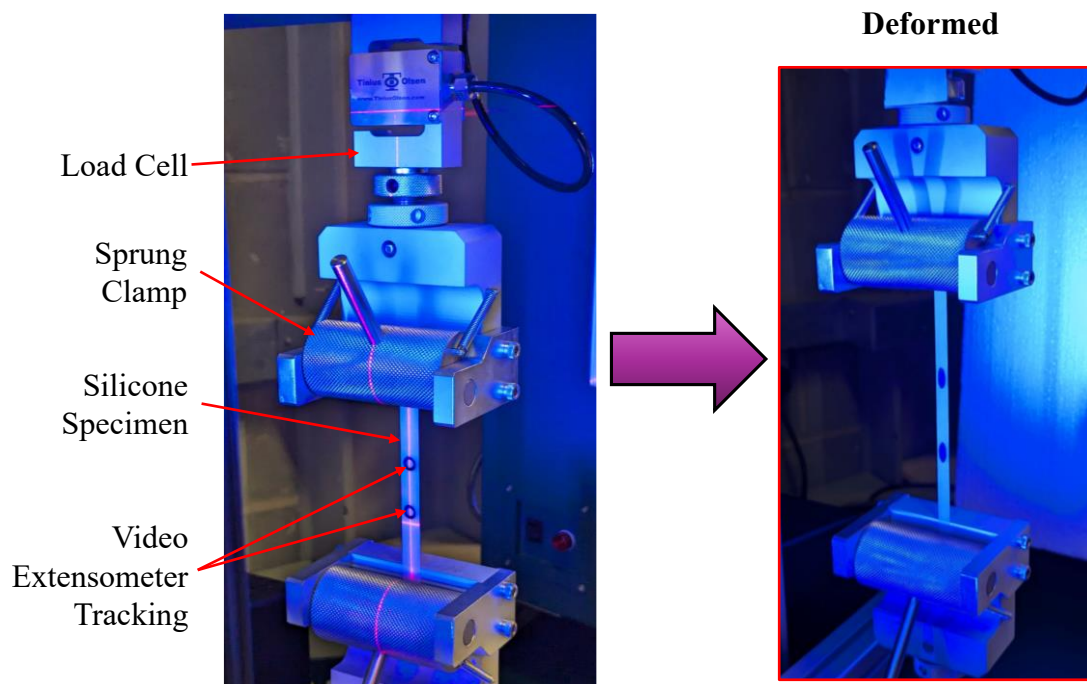


Figure 5.2: Experimental apparatus for the uniaxial testing.

Given that the silicone diaphragms were reused across multiple experimental forming trials, it was essential to ensure that they exhibited consistent and repeatable mechanical behaviour regardless of prior loading history. Repeated use introduces cyclic history-dependent effects, such as stiffening and plastic deformation, which could compromise the accuracy and comparability of forming results. To mitigate this, a dedicated study was conducted to investigate the influence of pre-compression on

the stress–strain response of the silicone material and to evaluate whether mechanical pre-conditioning could reduce such history-dependent behaviour.

Therefore in a further study, samples were rolled three times in both directions with a Vevor Rb 610 steel roller (set to 0.2 mm roller separation), and left to dwell for 10 minutes to allow for any viscoelastic recovery to take place. After this, the sample thickness and width were measured once again. These pre-rolled samples were then tested in the same manner as defined above, with the stress *versus* strain response (calculated with Equations (5.1) & (5.2)) utilising the recovered sample thickness and width.

5.2.2.1 Biaxial and Pure-Shear Testing

Both the biaxial and pure-shear tests were conducted utilising a custom biaxial tensile tester at The University of Nottingham. For these tests, 80 x 80 mm samples of silicone were cut and mounted within the testing machine utilising pneumatic clamps. The clamping area measured approximately 72.5 x 72.5 mm but was checked for each individual test. The clamps allowed for unconstrained lateral displacement and controlled axial displacement, with the force measured in both specimen directions. For the biaxial tests, all four clamps were engaged for controlled axial displacement. However, with the pure-shear tests, two of the clamps were constrained such as to maintain a constant specimen width. Figure 5.3a illustrates the experimental apparatus for both tests, with the individual constraints for the biaxial and pure-shear tests shown in Figure 5.3b and Figure 5.3c respectively.

For the tests conducted at temperature, an overhead heater blower was supported over the specimen. Prior to these tests, a validation procedure was conducted to correlate the actual specimen temperature with the indicated (thermocouple) temperature, measured slightly above the specimen. The maximum attainable specimen temperature with the heater blower was 100 °C in these tests, compared to the uniaxial tests that could be conducted at 200 °C. As per the uniaxial tests, however, specimens were strained up to 100% for both test methods. Furthermore, the influence of pre-conditioning was explored by pre-rolling samples and conducting identical biaxial and pure-shear tests. Three repeats were undertaken for each test condition, owing to the high specimen repeatability witnessed in the uniaxial tests.

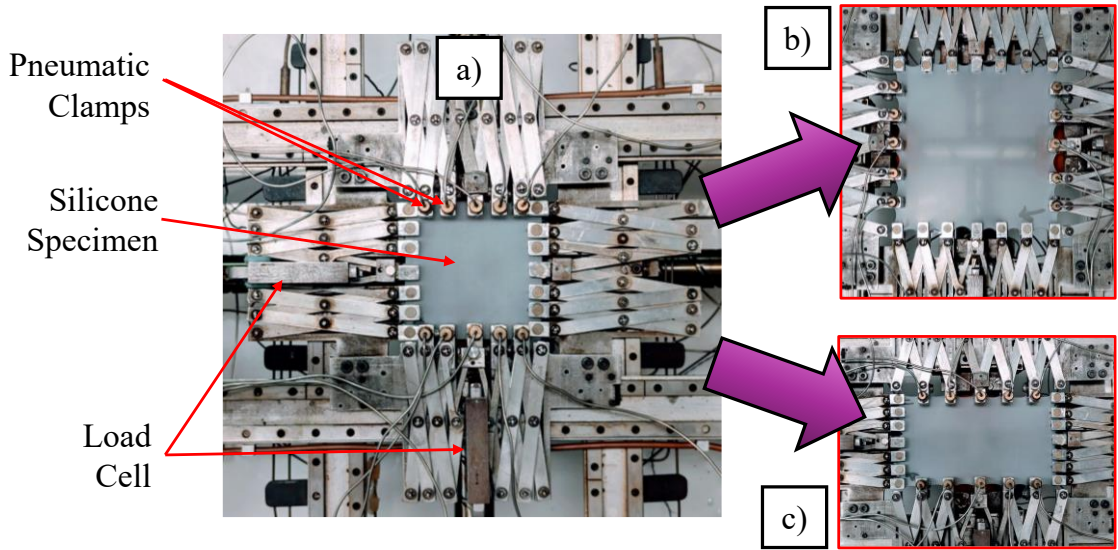


Figure 5.3: a) Overall experimental apparatus for: b) biaxial tests, c) pure-shear tests.

5.2.2.2 Strain Energy Density Function

In this work, an Ogden model [407] was used to model the hyperelastic material behaviour, using the uniaxial, biaxial and pure-shear test data. This follows the work of Yamashita [409] who showed that an Ogden model is capable of modelling the hyperelastic behaviour of silicone with a good degree of accuracy.

The Ogden strain energy function, W , can be defined as:

$$W = \sum_{i=1}^N \frac{u_i}{\alpha_i} [\lambda_1^{\alpha_i} + \lambda_2^{\alpha_i} + \lambda_3^{\alpha_i} - 3] \quad (5.3)$$

where λ_n represents the principal stretch in the n^{th} direction, N represents the model order, and u_i and α_i are calibrated Ogden material parameters (to be determined). The principal stretch can be defined simply utilising the principal strain:

$$\lambda_n = 1 + \varepsilon_n \quad (5.4)$$

The overall model stress is defined as the derivative of the strain energy function with respect to each principal stretch, such that the Cauchy stress is defined as:

$$\sigma_n = \lambda_n \frac{\partial W}{\partial \lambda_n} \quad (5.5)$$

Therefore, for each test type, the corresponding principal stretches can be substituted into this formula for the calculation of the Cauchy stress.

For uniaxial tension and/or compression, the principal stretches are:

$$\lambda_1 = \lambda, \quad \lambda_2 = \lambda_3 = \lambda^{-\frac{1}{2}} \quad (5.6)$$

such that the uniaxial stress is:

$$\sigma_{11} = \lambda \frac{\partial W}{\partial \lambda} = \sum_{i=1}^N \frac{u_i}{\alpha_i} \left[\lambda^{(\alpha_i-1)} - \frac{1}{2} \lambda^{(\frac{\alpha_i}{2}-1)} \right] \quad (5.7)$$

For biaxial tension, the principal stretches are:

$$\lambda_1 = \lambda_2 = \lambda, \quad \lambda_3 = \lambda^{-2} \quad (5.8)$$

such that the biaxial stress is:

$$\sigma_{11} = \lambda \frac{\partial W}{\partial \lambda} = \sum_{i=1}^N \frac{u_i}{\alpha_i} \left[\lambda^{(\alpha_i-1)} - \lambda^{-(2\alpha_i+1)} \right] \quad (5.9)$$

For pure-shear, the principal stretches are:

$$\lambda_1 = \lambda, \quad \lambda_2 = 1, \quad \lambda_3 = \lambda^{-1} \quad (5.10)$$

such that the pure-shear stress is:

$$\sigma_{11} = \lambda \frac{\partial W}{\partial \lambda} = \sum_{i=1}^N \frac{u_i}{\alpha_i} \left[\lambda^{(\alpha_i-1)} - \lambda^{-(\alpha_i+1)} \right] \quad (5.11)$$

Assuming that silicone behaves as an incompressible material, the following relationship applies:

$$\lambda_1 \cdot \lambda_2 \cdot \lambda_3 = 1 \quad (5.12)$$

Therefore, the results from the experimental uniaxial, biaxial and pure-shear tests are compared with equations (5.7), (5.9) & (5.11) using a nonlinear least squares method to establish the values of u_i and α_i in an iterative manner. Abaqus features an inbuilt tool for this process, although the work of Twizell *et al.* [410] provides a detailed explanation regarding the operation of this least-squares algorithm.

5.2.3 Friction Characterisation

It was assumed for this work that the friction forces between the diaphragm and the tool/base were not negligible and would influence the laminate forming behaviour. Therefore, experimental pull-through tests were conducted to evaluate this friction behaviour. For concision, the reader is referred to Section 4.2.3 for a detailed analysis of the pull-through friction test, also utilised in this study.

For characterisation of the diaphragm-tool friction behaviour, the laminate within the universal testing machine was replaced with a 40 x 200 mm aluminium plate, 3 mm in thickness. Aluminium was chosen such as to replicate the aluminium tool and base that make up the experimental DDF former (Figure 3.2b). The aluminium plate itself was polished with fine-grit emery paper prior to mounting within the test machine, thus replicating the surface conditions of the polished tool/base. Figure 5.4b illustrates the experimental apparatus for the diaphragm-tool friction test.

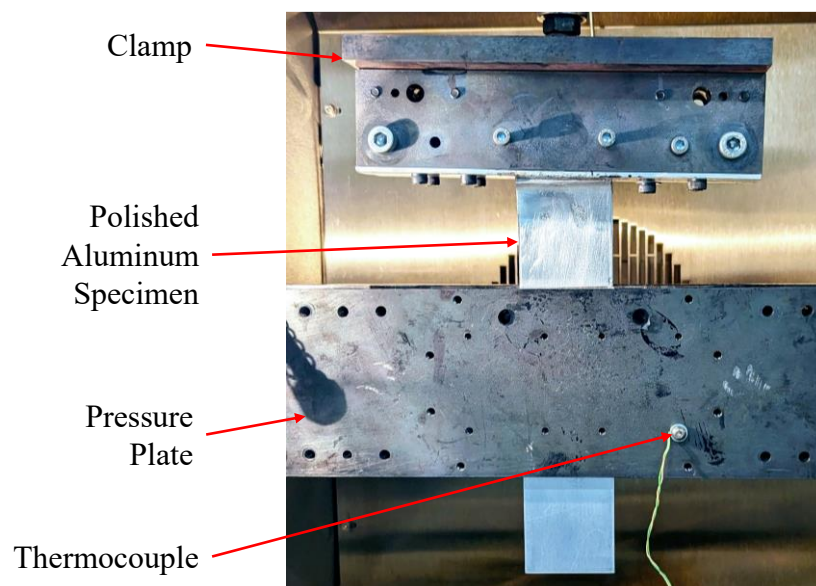


Figure 5.4: Pull-through experimental apparatus for diaphragm-tool friction tests.

Friction tests were also conducted at 230 °C, 100 mm/min and 0.1 bar pressure (four repeats), however it is assumed that there would be no rate, temperature or pressure influence on the CoF in this case. Therefore, the calculated CoF (Equation (4.12)) was a standalone value in this study. Considering the specimen dimensions (80 mm silicone width), a normal force of 32N was required to exert the desired 0.1 bar pressure.

5.3 Results

This section details the results from all three diaphragm characterisation exercises outlined in Section 5.2.

5.3.1 Hyperelastic Characterisation Results

In this work, the uniaxial tests were used to evaluate material sensitivity to a number of different processing parameters. Therefore, in this section, the results from this individual test are presented first, followed by those from the biaxial and pure-shear tests.

5.3.1.1 Uniaxial Testing Results

Uniaxial tests were conducted utilising the method outlined in Section 5.2.2. The force *versus* displacement output was converted into stress *versus* strain utilising Equations (5.1) & (5.2). Initially, the influence of cyclic loading was considered to understand if, irrespective of the test conditions (rate, temperature etc), it was considerable. For this test, a silicone specimen was stretched (and then relaxed) four consecutive times to analyse this behaviour. This was conducted at the reference conditions of 0.01s^{-1} , ambient temperature (20 °C), and with the laminate oriented in the silicone roll-direction (longitudinal). Figure 5.5a illustrates the result from this cyclic loading exercise.

There was clearly a significant reduction in the stiffness of the silicone upon repeated loading, especially between the first and second loading. A further small reduction in stiffness was present between the second and third loading, but then the stiffness appeared to plateau with subsequent loadings. It is also clear that a degree of plastic strain remained within the specimen after initial loading, with the strain only

recovering back to approximately 7%. Therefore, both the initial loading and the loading after repeated strains are considered in this work. This is especially prudent due to the reusable nature of the silicone diaphragms. Since the difference between the third and fourth loading was negligible, the third loading (up to equal strain) represented a stable cyclic loading curve. For all uniaxial results going forward, stress *versus* strain curves from both the first and third loadings are presented.

Figure 5.5b illustrates the results from the five tests (four repeats), conducted at reference conditions (0.01s^{-1} , $20\text{ }^\circ\text{C}$, longitudinal direction), with just the first and third loading curves illustrated. A high level of repeatability was witnessed between tests, quantified with a standard deviation of 3.2%. Each sample was resampled using linear interpolation (over 500 points) and then summated to produce an average first and third loading curve. This method is utilised hereon in to combine the repeated datasets.

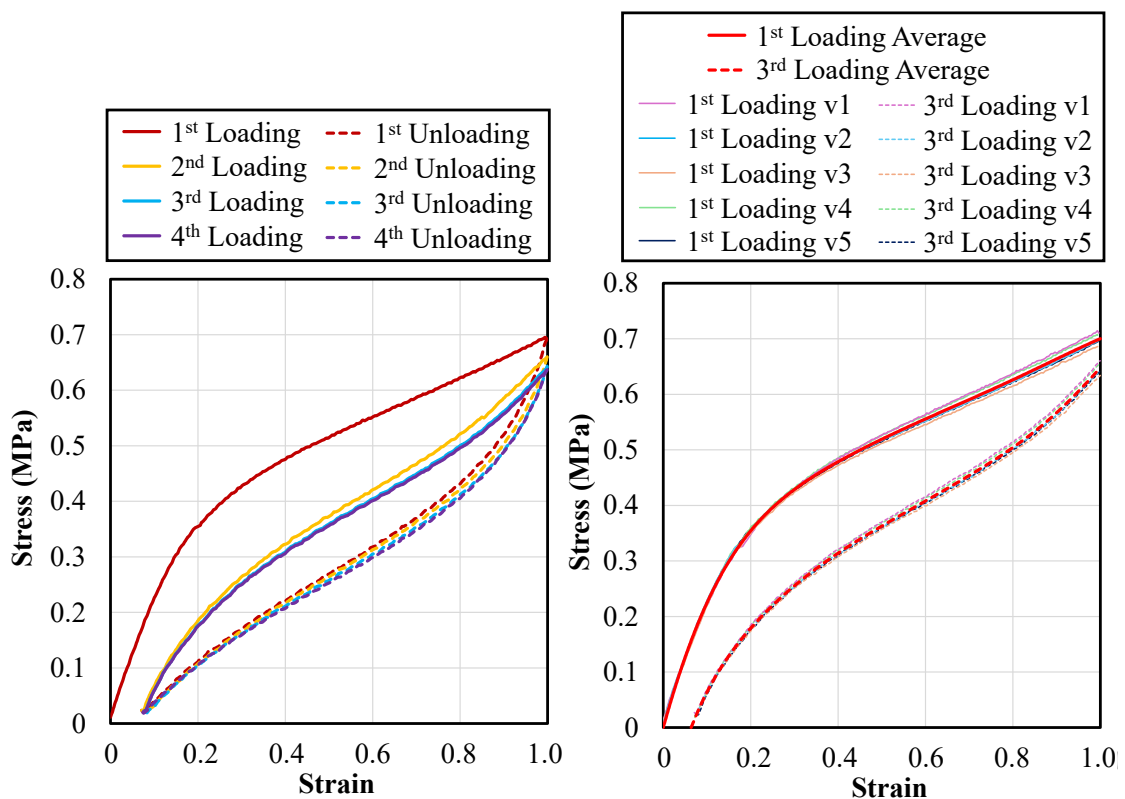


Figure 5.5: a) Stress *versus* strain curves for silicone after four repeated loadings, b) stress *versus* strain curves for five tests after the first and third loading, including the calculated average curve.

Having determined that a high level of repeatability exists, alongside a large influence of cyclic loading (up to three cycles), the influence of the other tested experimental

variables could be explored. These were namely; temperature, rate and sample directionality, with mutually exclusivity assumed between the three. In each case, the results were compared to the reference results (0.01s^{-1} , $20\text{ }^{\circ}\text{C}$, longitudinal direction), with the average curves presented for both the first and third loading condition. This also allowed for an analysis of whether the large influence of repeated loading (Figure 5.5a) was dependent on other experimental test conditions. Figure 5.6a illustrated the average stress *versus* strain curves (first and third loadings) from experiments conducted at different strain-rates ($\dot{\epsilon}$), Figure 5.6b for different silicone orientations and Figure 5.6c for different temperatures. Due to the high level of sample repeatability (Figure 5.5b), error bars have been omitted from the figure for clarity.

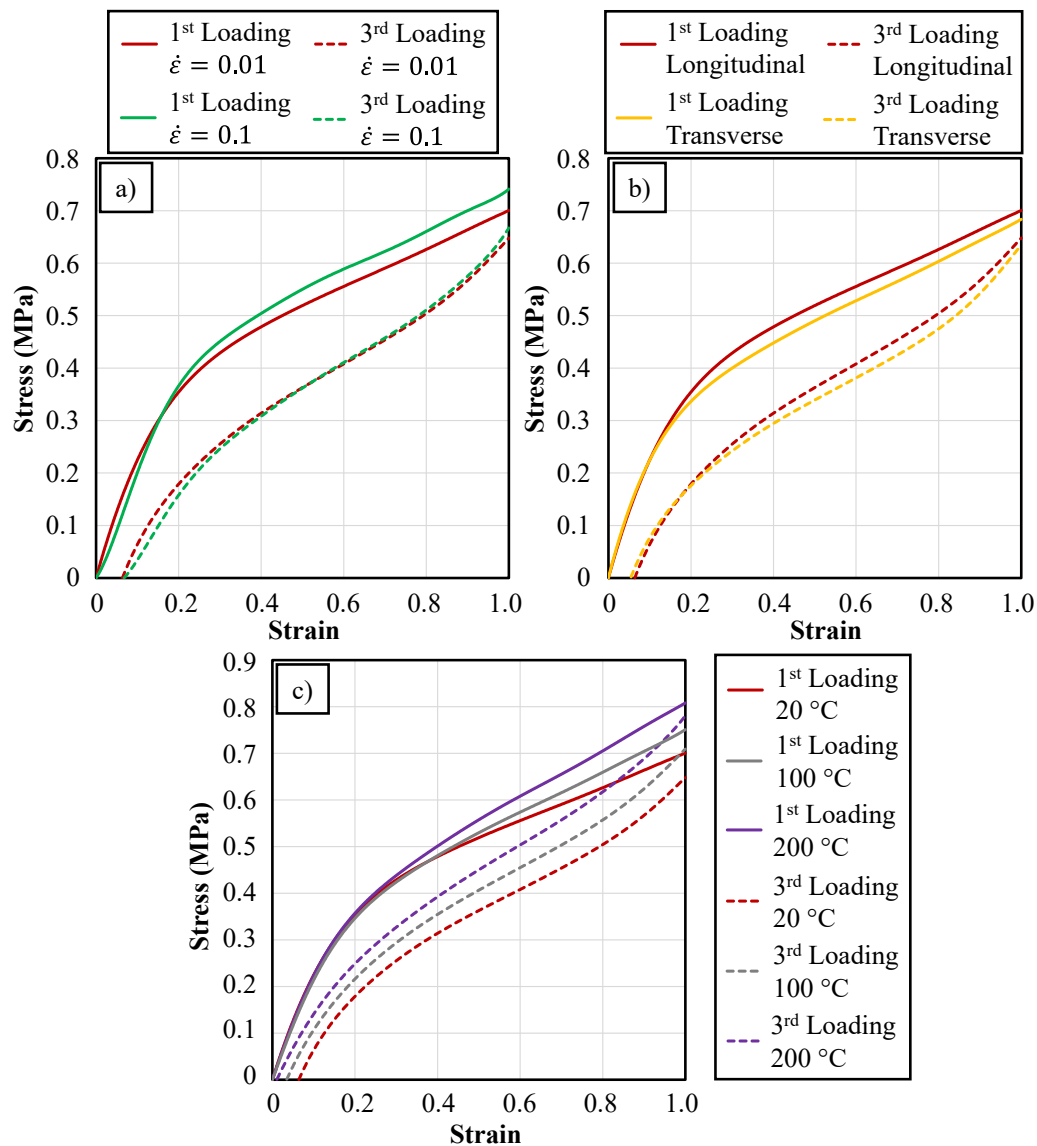


Figure 5.6: Average stress *versus* strain curves for the first and third loading of silicone samples at a) different strain-rates, b) different orientations, c) different temperatures.

The influence of both strain-rate and silicone directionality (Figure 5.6a & Figure 5.6b) were considered small, especially in the case of the third cyclic loading. A maximum difference in stiffness of 6% was noted between both the two tested strain-rates and the two tested directions. Therefore, consideration of the strain rate and/or sample anisotropy was not necessary in this work. Regarding the anisotropy, this assumption was further validated naturally with the biaxial test (Section 5.3.1.2). Furthermore, the difference between the first and third loading was also seemingly independent of both strain-rate and direction.

Figure 5.6c illustrates, however, that temperature is influential on the stiffness of the silicone specimen. An up to 20% increase in stiffness was noted for tests at 200 °C to tests at ambient conditions (20 °C). This was especially obvious for the tests conducted after the third cyclic loading due to an apparent reduction in plastic strain at higher temperatures. Tests conducted at 200 °C exhibited a residual plastic strain of approximately 1%, compared to 7% for those at room temperature. It was also noted that the absolute difference between the first and third cyclic loading shrank as the temperature increased. These observations allude to the fact that the degree of strain-history that exists within the silicone specimen is reduced at temperature.

Due to the considerable influence of temperature on both the absolute stiffness and the strain-history, it was necessary to consider the influence of temperature for the remainder of the hyperelastic characterisation exercise, alongside the influence of cyclic-loading.

While it was possible to account for the influence of silicone temperature within a strain energy density function, accounting for the influence of cyclic loading remained problematic. This is because the absolute difference between all repeated loadings illustrated in Figure 5.5a was specific to the degree of strain that was experienced in previous loadings. This means that all the cyclic stress strain curves could only be applied if the strain that was experienced in the previous loading was known. A simple test was devised to illustrate this phenomenon, known as the Mullins effect, in which a silicone specimen was extended 5 consecutive times but to different strains of 20%, 40%, 60%, 80% and finally 100%. Figure 5.7 illustrates the results from this test, including the first loading curve (Figure 5.5b) at reference conditions.

For every subsequent loading, the stiffness is lower than that of the previous loading due to the higher extent of strain that was experienced. The degree of plastic strain also increased with every subsequent loading. This was problematic since the diaphragms were reused in the experimental work, meaning that without pre-conditioning the diaphragm performance would be dependent on the diaphragm strain-history. Moreover, this highlights the difficulty with fitting a single curve in the case of repeated loadings due to the strain-history dependence. Due to the complexity associated with including this behaviour within a hyperelastic model, an attempt was made to remove the history-dependence by pre-straining the silicone material. It was hypothesised that simply running them through some compression rollers would have the desired effect (as detailed in Section 5.2.2).

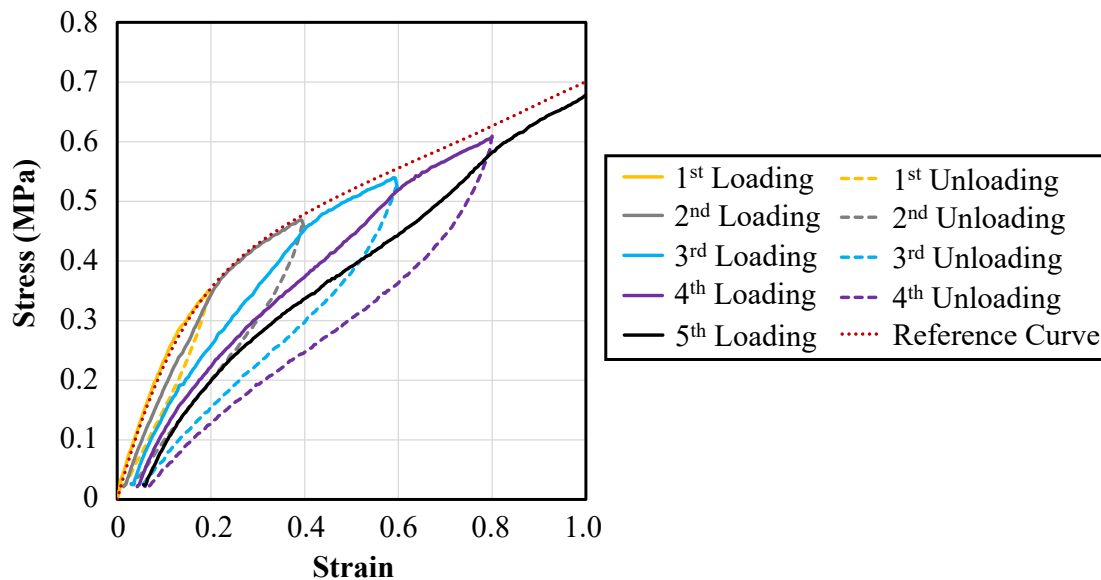


Figure 5.7: Stress *versus* strain response of silicone laminate under cyclic loading with increasing strain increments.

Pre-rolled specimens (after a 10 minute post-roll dwell) were tested at different temperatures (owing to the findings from Figure 5.6c), along with the first and third cyclic loading once again illustrated in each case. Figure 5.8b illustrates the results from uniaxial silicone testing after pre-rolling, for two different temperatures, compared to the reference case. The results at 100 °C are omitted for clarity, but can be found on Figure 5.10c.

The results illustrate that pre-rolling the silicone had the desired effect, with the difference between first and third loadings reduced considerably compared to unrolled

samples. The pre-rolled sample at 20 °C behaved significantly less stiff than the unrolled equivalent, even on the first loading. As per Figure 5.6c, temperature increased the laminate stiffness, and almost entirely eliminated the degree of plastic strain exhibited between loadings. The pre-rolled case at temperature therefore represented an ideal case, in which the influence of repeated loadings was largely removed, with negligible plastic strain present.

Since the silicone behaviour was no longer highly dependent on the strain-history after rolling, implementation within a numerical model was simplified considerably. For the remainder of the hyperelastic characterisation, the implications of sample pre-rolling are considered as opposed to the cyclic loading, since Figure 5.8b illustrates that the influence of repeated strain is largely removed.

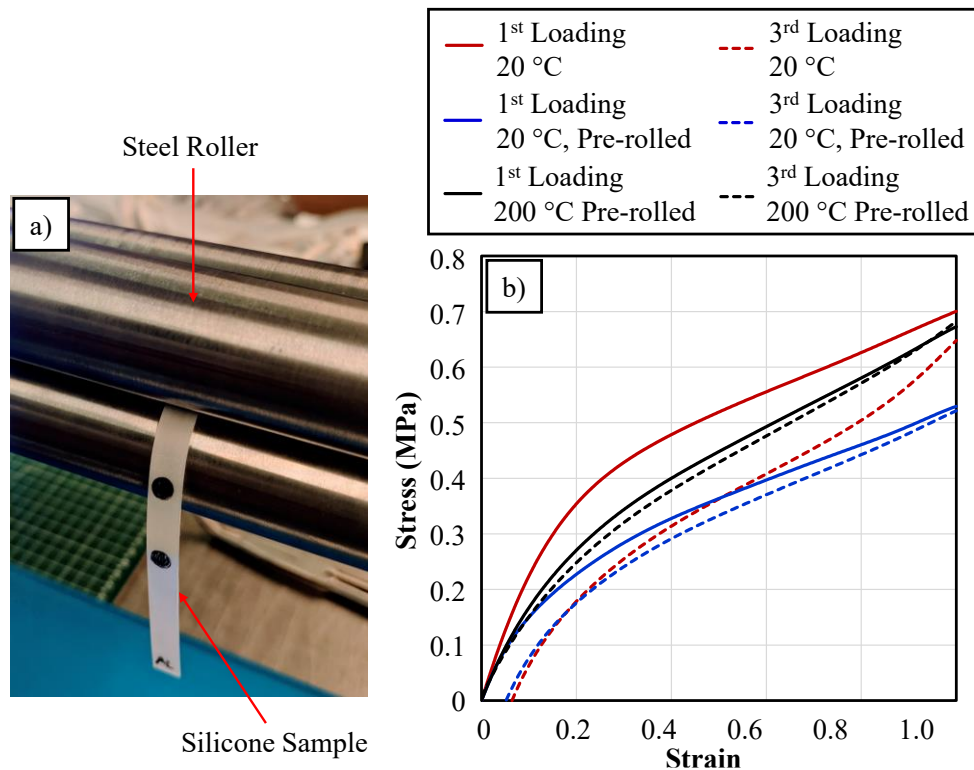


Figure 5.8: a) Pre-rolling of silicone specimens for uniaxial testing, b) average stress *versus* strain curves for pre-rolled silicone samples at different temperatures, compared to the reference case.

5.3.1.2 Biaxial and Pure-Shear Testing Results

Biaxial and pure-shear tests were conducted utilising the method outlined in Section 5.2.2.1, and once again the force *versus* displacement output was converted into stress

versus strain utilising Equations (5.1) & (5.2). Figure 5.9a illustrates the results (all repeats) from pure-shear tests conducted on neat (non-rolled) silicone samples, at ambient temperature conditions (20 °C). As per the uniaxial tests, the repeatability between samples was high (standard deviation of 4.6%), thus validating the implementation of only three repeats for these tests. An average curve was once again generated by resampling the data over 500 points and averaging between repeats.

In contrast, Figure 5.9b illustrates results from the biaxial tests at ambient temperature conditions (20 °C), although only one of the repeats is included for concision. The stress in both sample axes is plotted for both tests, yielding the four curves. A small degree of anisotropy was noted, with the longitudinal direction appearing slightly stiffer (up to 7%) than the transverse direction. This matches the uniaxial results illustrated in Figure 5.6b, in which the longitudinal tests were once again up to 7% stiffer than the transverse tests. For numerical simplicity, this degree of anisotropy was considered negligible. Therefore, for each biaxial test, the force in both directions was resampled and averaged, before being averaged with the other repeats.

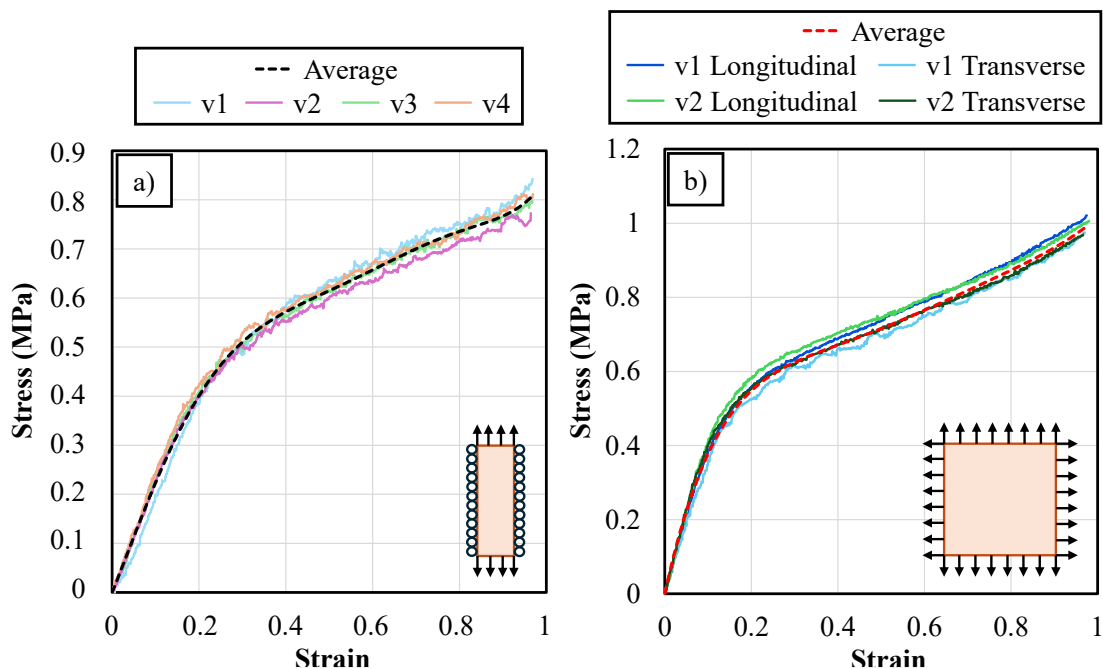


Figure 5.9: Stress *versus* strain average curves for a) pure-shear tests with all repeats, b) biaxial tests with one repeat.

Figure 5.10a illustrates the average curves from the remaining biaxial tests, and Figure 5.10b the average curves for the remaining pure-shear tests. For comparison, Figure

5.10c is included which shows the results from the uniaxial tests at temperature and with a pre-roll (room temperature and 200 °C results from Figure 5.8b).

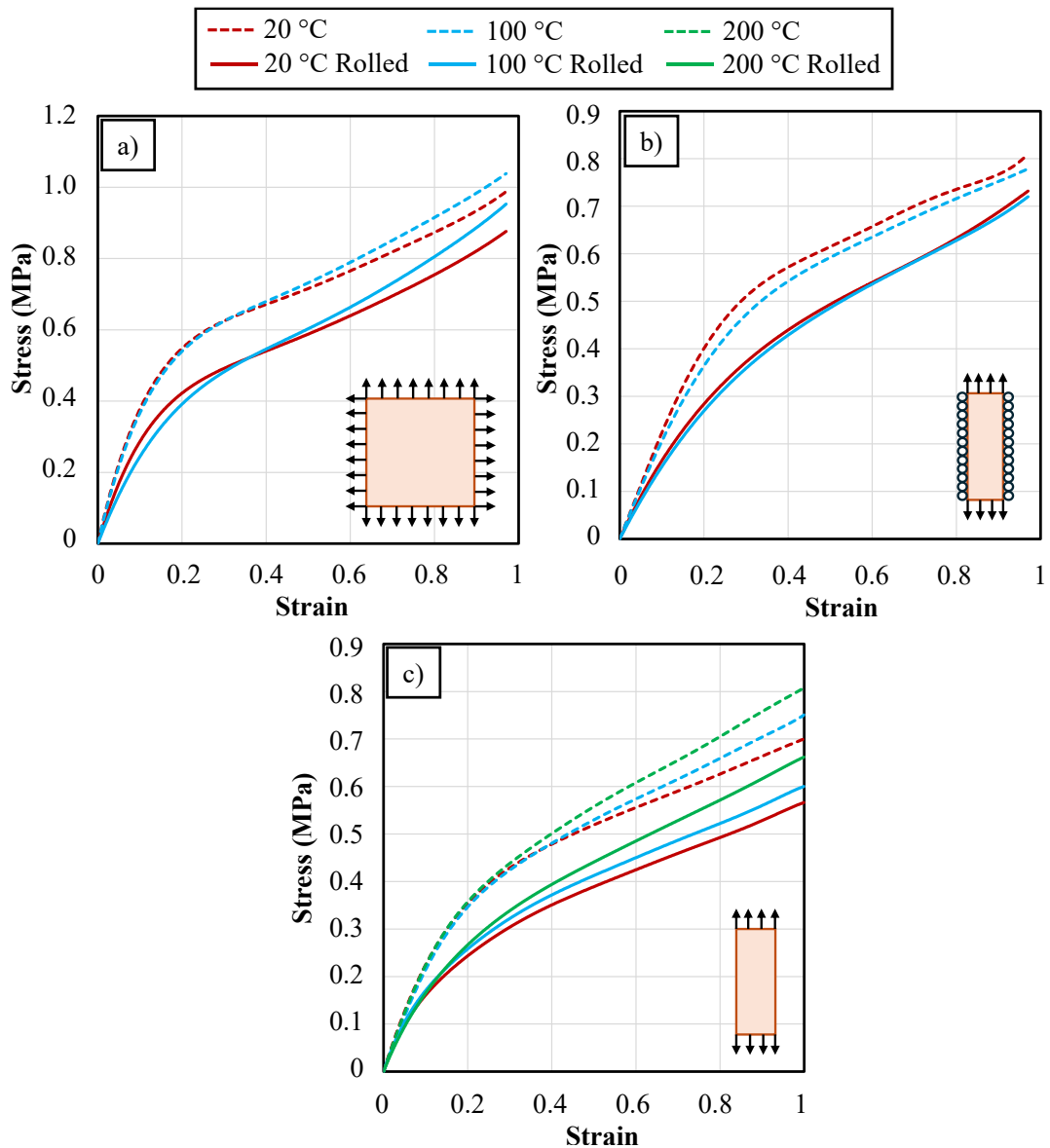


Figure 5.10: Stress *versus* strain curves for silicone specimens at different temperatures, neat & pre-rolled, for a) biaxial tests, b) pure-shear tests, c) uniaxial tests.

Comparing between all three test methods, the influence of the pre-roll was very similar in each case, with a maximum reduction in specimen stiffness of 25%, regardless of deformation mechanism. Tests conducted at temperature, however, did not appear to yield the same noticeable increase in stiffness as per the uniaxial tests illustrated in Figure 5.6c. This is likely due to 100 °C temperature limit in the biaxial and pure-shear tests. In the case of the biaxial tests, little difference was witnessed between the two temperatures until after a strain of 40% was reached. After which a

maximum stiffness increase of 6% was recorded. For the pure-shear results, however, no difference was found in the stress *versus* strain response for specimens at different temperatures after pre-rolling. It is therefore apparent that the influence of temperature in these tests is no greater, if not smaller, than the uniaxial tests. It would be expected that if tests were conducted at 200 °C, however, a further small increase in stiffness would be exhibited.

Considering these results, in this work the influence of temperature was therefore neglected for the creation of a strain energy density function, thus simplifying its formulation. The results at 100 °C were instead utilised, minimising the induced error.

5.3.1.3 Strain Energy Density Function

As outlined in Section 5.2.2.2, the strain energy function was to be fitted to uniaxial, biaxial and pure-shear stress *versus* strain curves (up to 80% strain) for pre-rolled test specimens at 100 °C, using the inbuilt Abaqus evaluation tool. A 6th order Ogden model was implemented, chosen to maximise the accuracy of the fitting process. Furthermore, the Abaqus stability criterion indicated that with a 6th order model, the hyperelastic behaviour was stable at all strains, for each deformation mechanism. This therefore meant that the strain energy function consisted of 12 fitting parameters (tabulated in Appendix C - Table C-1). Figure 5.11 illustrates the comparison between the (pre-rolled, 100 °C) experimental results and the Ogden strain energy function stress *versus* strain curves for all three test conditions.

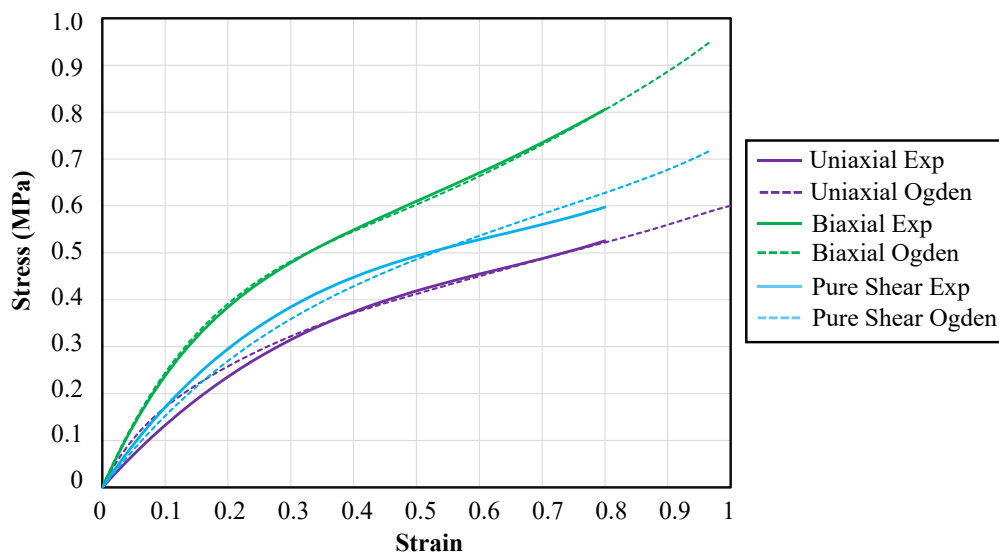


Figure 5.11: Experimental and Ogden strain energy function stress *versus* strain curves.

The correlation between the experimental results and the strain energy function was high, with a total root-mean-squared-error (RMSE) for this fitting process of 4.97%.

5.3.2 Diaphragm-Tool Friction Characterisation Results

Diaphragm-tool friction tests were conducted in accordance with the methodology outlined in section 5.2.3. Figure 5.12 illustrates the force *versus* displacement output for all tests (including repeats), as recorded by the universal testing machine.

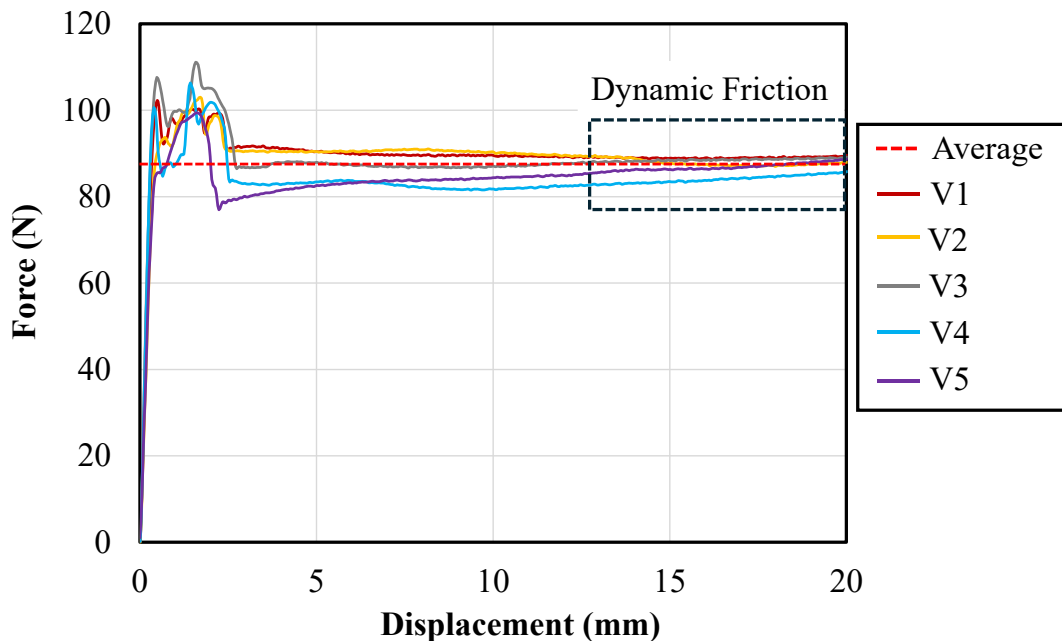


Figure 5.12: Force *versus* displacement output for the diaphragm-tool friction tests.

The diaphragm-tool tests, in contrast to the diaphragm-laminate tests (Figure 4.16) only exhibited a small static peak when compared to the steady-state dynamic force. Since this interface was dry, the interfacial mechanism was completely different to the hydrodynamic boundary layer, thus resulting in a drastically different force response. The results under 3 mm displacement appeared noisy, potentially caused by a small degree of stick-slip behaviour at the onset of displacement.

The diaphragm-tool CoF was obtained by determining an average friction value from all five tests (Equation (4.12)). This was completed between 10-20 mm displacement such as to not include noise at the early stages of slip. The diaphragm-tool CoF at reference conditions, denoted μ_{DT} , was therefore equal to 0.878, assumed to exhibit no temperature, rate or normal-pressure dependency.

5.4 Chapter Conclusions

In this chapter, the silicone diaphragms were characterised to determine the inputs required for a functional FRTP DDF simulation to be produced. This included the hyperelastic (tensile/compressive) behaviour and the interaction between silicone and the tool.

The uniaxial, biaxial and pure-shear tests were utilised to characterise the hyperelastic silicone behaviour. The testing procedure indicated that silicone is relatively independent (within 6%) of directionality and strain rate, however dependent on temperature and loading history through the Mullins effect. A novel technique was implemented to remove the influence of loading history; samples were pre-compacted by 80% through a set of rollers, resulting in a sample approximately 25% less stiff and exhibiting little strain-history. For simplicity, the influence of temperature was neglected since both the biaxial and pure-shear tests indicated its influence was not considerable. The results at 100 °C were used to reduce the error (assuming a 200 °C diaphragm temperature in a forming operation) to less than 10%. Furthermore, samples tested at temperature appeared to exhibit less plastic strain (1%) than those at room temperature (7%).

The uniaxial, biaxial and pure-shear data (at 100 °C, after pre-rolling) were implemented within a 6th order Ogden strain energy function using the inbuilt Abaqus hyperelastic tool. This resulted in a RMSE of 4.97% between the experimental and strain energy function stress/strain curves.

The diaphragm-tool friction behaviour was analysed using pull-through tests. The CoF was found to be much higher than the diaphragm-laminate counterpart due to the dry nature of this interface and also exhibited little ‘static’ behaviour. Moreover, it was assumed to not exhibit any rate-, temperature- or normal pressure- dependency.

Chapter 6.

Isothermal Thermomechanical Simulation

6.1 Introduction

This chapter introduces the numerical modelling and simulation of FRTP forming, as dictated by the material input data gathered in Chapter 4 (laminates) and Chapter 5 (diaphragm). This includes an in-depth analysis of the hypoelastic model developed to predict fabric forming behaviour, following the hypoelastic formulation outlined by Badel *et al.* [325] and Khan *et al.* [324] and then re-implemented by Yu *et al.* [45] and Chen [46]. It also incorporates the method for decoupling membrane and out-of-plane behaviour, and implementation of the intra-ply behaviour mechanisms (shear and bending) as part of the material subroutine, with their associated viscoelastic coupling.

The simulation is utilised to validate all the material inputs, with models produced within Abaqus to replicate the characterisation exercises that were outlined in the previous chapters. This work ensures that the numerical model captures the material behaviour with a sufficient level of accuracy. A full DDF thermomechanical model is subsequently constructed. Since no transient thermal properties have been analysed thus far, the simulation in this chapter operates in an isothermal manner.

The DDF thermomechanical model is validated against the isothermal experimental DDF forming conducted in Chapter 3, specifically regarding mould conformity and defect prediction. This is completed for different temperatures, rates and laminate orientations, thus providing an exact replica of the experimental tests. The objective of this chapter is therefore to assess whether an FRTP DDF simulation can accurately model laminate behaviour at a range of forming conditions.

6.2 Methodology

This section outlines the methodology behind constructing an operational thermomechanical simulation for the DDF process, with a focus on the general algorithm for stress computation implemented within Abaqus. This is followed by validation of the material inputs (Chapters 4 & 5) to ensure that they are of sufficient accuracy. Finally, the production and implementation of a thermomechanical DDF model is outlined, validated using the experimental forming conducted in Chapter 3.

6.2.1 Algorithm for Stress Computation

The premise behind all the work presented in this chapter is the creation of a functional thermomechanical simulation that accurately models fabric forming behaviour; with the end objective of accurately modelling the DDF process for thermoplastic composite laminates. While the viscoelastically-coupled nature of FRTPs requires an extensive degree of alteration from typical dry fabric forming models, these conventional routines can still be used as the backbone for which the numerical model operates due to the kinematic draping behaviour of all continuous fibre reinforced materials. This work therefore closely follows the hypoelastic formulation outlined in detail by Badel *et al.* [325] and Khan *et al.* [324]. For full transparency, the hypoelastic formulation is included in Appendix D for the reader's perusal. A schematic of this formulation is illustrated in Figure 6.1 (red-dashed box), similar to that illustrated by Khan *et al.* [324], which was reimplemented by Yu *et al.* [45] and Chen [46] and then used in this work.

As per equations (D.14) & (D.15), the Cauchy constitutive tensor, comprising of the fibre Young's modulus and fibre shear modulus values, must be defined for the calculation of the fibre stress increment for each element. These values determine the in-plane membrane & out-of-plane bending properties (E_{fi} , E_{fj}) and the in-plane shear properties ($G_{ij}(\gamma)$) of the fibrous laminate. This means that they are required to be updated on a constant basis such that the deformation behaviour (characterised in Chapter 4) is captured accurately within the numerical model.

For the in-plane shear properties, the shear modulus, $G_{ij}(\gamma)$, can be modified easily using Equation (D.16), such that the shear force is directly proportional to the shear modulus. The combined shear force equation, Equation (4.20), can therefore be implemented directly within the VFABRIC subroutine, with all variables defined on an element-by-element basis (shear angle, shear angle rate, temperature).

For the in-plane membrane and out-of-plane bending properties, however the definition of a single elemental value for the Young's Modulus in the fibre directions (E_{fi} , E_{fj}) is not trivial. As mentioned in the literature review (Section 2.7.2.2), fibrous materials often exhibit a nonlinear bending stiffness due to fibre slippage and tow buckling. It is therefore necessary to decouple the membrane and bending behaviours

of fabric material, thus allowing each to be analysed individually. The process for decoupling these behaviours is also outlined by Yu *et al.* [45]. This is detailed in Appendix D for full transparency, along with the method for calculating the elemental curvature; needed as input for the calculation of the bending stiffness (Equation (4.34)).

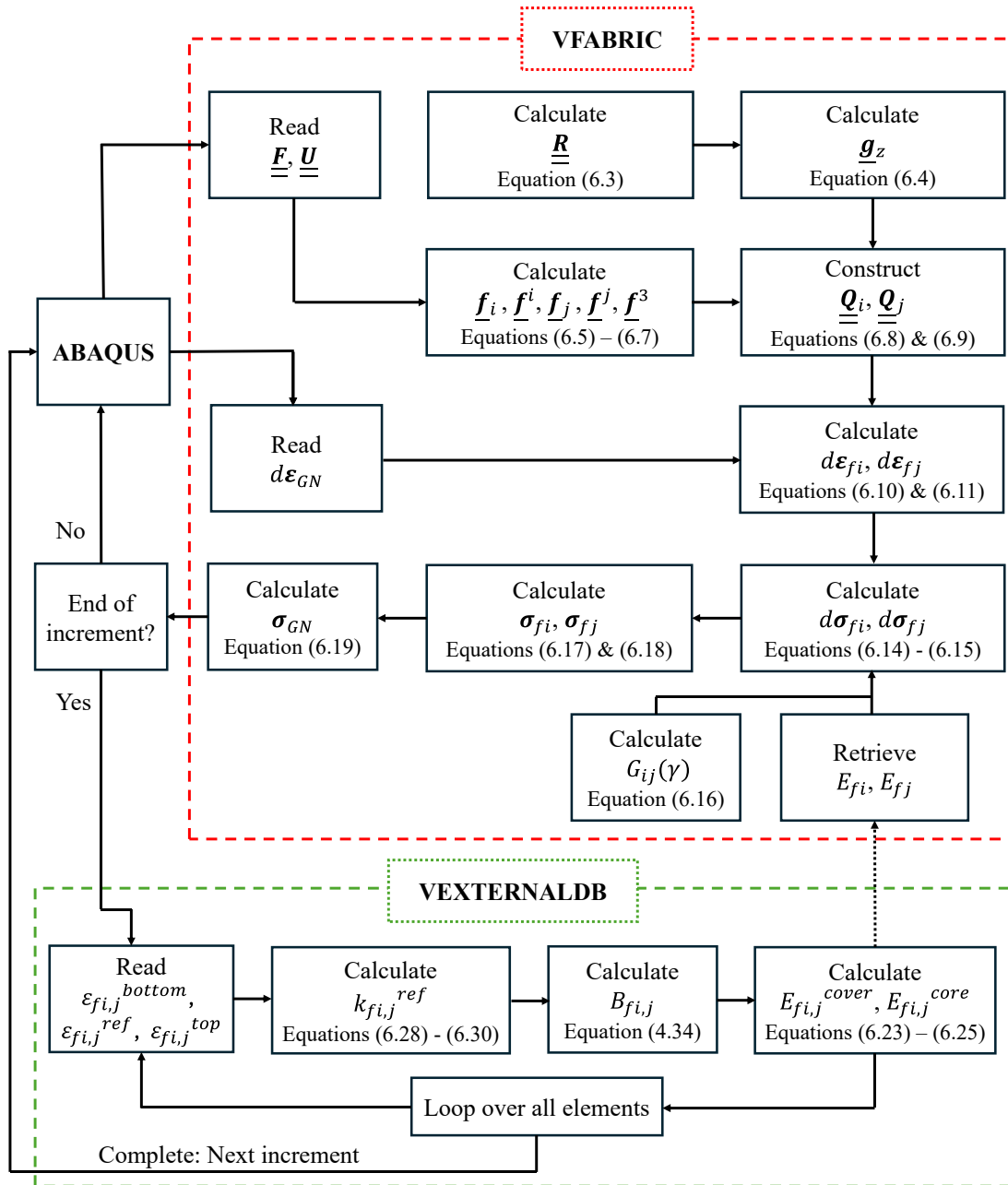


Figure 6.1: Algorithm for the stress computation of fibrous textiles, implemented within VFABRIC and VEXTERNALDB subroutines. Modified from Khan *et al.* [324], reimplemented by Yu *et al.* [45] and Chen [45].

In order to implement the curvature within the equation for bending stiffness (Equation (4.34)), Equations (D.28) & (D.29) show that the strains at different integration point (through the shell element thickness) are required. The standard operation of the VFABRIC subroutine, however, does not allow the user to obtain material point information for adjacent integration points. Therefore, as per Yu *et al.* [45] and Chen [46], a secondary user subroutine, VEXTERNALDB, was utilised as an external database to store material point information between increments. The curvature for each element was subsequently calculated within this subroutine before being passed back into VFABRIC subroutine when called upon. Figure 6.1 also illustrates the operation of the external database (green-dashed box) and how it feeds input data into the VFABRIC routine after every increment.

6.2.2 CF/PA6 Material Input Validation

With the algorithm for stress computation defined it was possible to validate the material behaviour, characterised in Chapter 4, for seamless implementation within a numerical model. The two intra-laminate deformation mechanisms that were characterised; inter-ply shear and out-of-plane bending behaviour, as well as the diaphragm-ply interaction, are analysed sequentially in this subsection.

For all of these models, Abaqus/Explicit 2022 is used as the solver for the numerical problem, with the VFABRIC and VEXTERNALDB subroutines outlined in Section 6.2.1 implemented within. The coupled temperature-displacement step was utilised to enable a temperature DoF within the analysis. In each case the FRTP laminate is modelled using linear thermally-coupled quadrilateral shell elements (S4RT), as is appropriate since the thickness of each laminate is much smaller than its in-plane dimensions. The default hourglassing controls (relax stiffness) were used within the mesh. The numerical models were all solved using the ADA high performance computer (HPC) at The University of Nottingham, with 48 cores, double-precision (analysis & packager) and full nodal output precision.

The single-ply deformable laminate utilised in each case was 0.23 mm in thickness, as per Table 3.1. A core thickness, h_{core} of 0.21 mm was utilised with cover thicknesses of 0.01 mm, such as to make up the total laminate thickness as per the decoupling of membrane and bending behaviour described in Section 0. Moreover, the density of

CF/PA6, ρ_{lam} , tabulated in Table 3.1, was implemented within the model. Transverse shear stiffness values of 500 Nm^{-1} , 500 Nm^{-1} and 0 Nm^{-1} were assigned in the K11, K22 and K12 directions respectively, as recommended in the Abaqus User's Manual [411]. A mass scaling value of 50 was applied to each model for stability and reduced run time, deemed acceptable since the kinetic energy contributed to less than 10% of the total model energy in each case, as recommended in the Abaqus User's Manual [411]. An in-plane Young's modulus ($E_{fi,j}^{lam}$) value of 3 GPa was selected, and this was assumed to be linear (due to low in-plane stresses associated with the DDF process). While this is two orders of magnitude lower than the Young's modulus of the actual CF/PA6 laminate (approximately 300 GPa), this does not influence the fabric deformation behaviour as axial strain in the fibre direction was less than 1% in each case, as recommended by Harrison *et al.* [412]. Furthermore, utilising a lower value for the Young's modulus significantly reduces the solver time, as larger time-increments can be used. This is because the speed of propagation of stress waves through the shell elements (c_d), a key factor in the maximum time-increment that can be used for stability, is influenced by the magnitude of the Young's modulus (assumed Poisson's ratio of zero):

$$: \quad c_d = \sqrt{\frac{E_{fi,j}^{lam}}{\rho_{lam}}} \quad (6.1)$$

6.2.2.1 Intra-Ply Shear Input Validation

This section describes the implementation of viscoelastic intra-ply shear behaviour within an Abaqus/Explicit BET model.

6.2.2.1.1 Intra-Ply Shear Behaviour Implementation

As outlined in Section 0, the intra-ply shear behaviour is easily implemented in the VFABRIC subroutine through the use of Equation (D.16), with the shear force defined by Equation (4.20). The incremental temperature is a standard variable called by the VFABRIC subroutine such that value is known at each integration point. The shear angle at the end of the increment, γ^{n+1} , is defined as the summation of the shear angle at the start of the increment, γ^n and the incremental shear angle, $d\gamma$, itself defined using sum of shear strain components calculated using Equations (D.10) & (D.11):

$$d\gamma = d\varepsilon_{12}^{fi} + d\varepsilon_{12}^{fj} \quad (6.2)$$

such that (as per Equations (D.17) & (D.18)):

$$\gamma^{n+1} = \gamma^n + d\gamma \quad (6.3)$$

The implementation of shear-rate within the overall intra-ply shear equation, however, is not trivial. While an instantaneous shear angle rate can be calculated easily using the incremental shear angle and the increment duration, such a method was found to result in severe discontinuities in the stress field. This is because with the stress waves moving through the model, the shear angle rate fluctuates dramatically when concerning the extremely small increment times associated with an Explicit solver. Therefore, implementing a highly variable shear angle-rate within Equation (4.20) resulted in a unstable model, producing inaccurate results or even failing to solve entirely.

A novel technique was therefore devised for the calculation of the shear angle rate. The total simulation step time was split into a number of increment ‘blocks’. These blocks are simply a group of increments (as opposed to element blocks used to pass information into the VFABRIC subroutine) and are counted in every pass of the subroutine. To ensure that no (significant) jumps in shear angle-rate existed, the instantaneous shear angle-rate was to be calculated as a rule of mixtures, regarding the current increment block time, between the shear angle rate at the start and finish of the previous increment block. The shear angle-rate at the end of the previous increment block, $\dot{\gamma}_N$, simply represents:

$$\dot{\gamma}_N = \frac{(\gamma_N - \gamma_{N-1})}{\tau_{inc}} \quad (6.4)$$

where γ_{N-1} and γ_N represent the shear angle at the start and end of the previous increment block, respectively, and τ_{inc} represents the total time duration of each increment block. Considering that the shear angle-rate at the start of the previous increment block, $\dot{\gamma}_{N-1}$, would have been calculated in the same manner, the instantaneous shear angle rate, $\dot{\gamma}_n$, therefore represents:

$$\dot{\gamma}_n = \dot{\gamma}_N \cdot \left(\frac{\tau_n}{\tau_{inc}} \right) + \dot{\gamma}_{N-1} \cdot \left(1 - \frac{\tau_n}{\tau_{inc}} \right) \quad (6.5)$$

Where τ_n represents the time within the current increment block. Figure 6.2 is included to illustrate this process schematically.

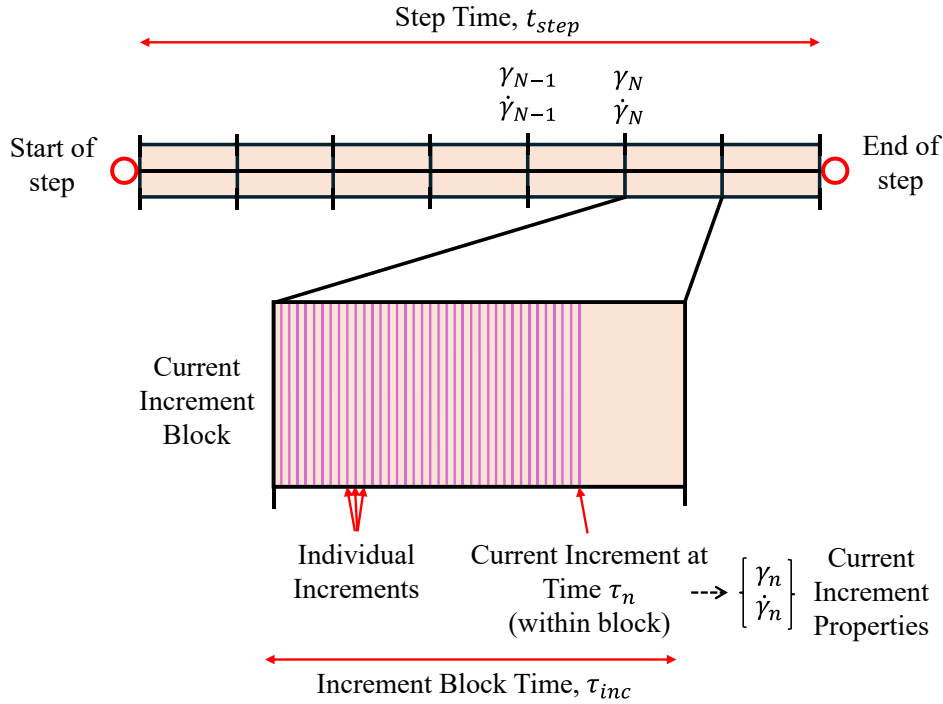


Figure 6.2: Schematic of the process for the calculation of the shear angle-rate.

With this procedure, the calculated shear angle-rate lags behind the actual shear angle-rate by the increment block time τ_{inc} . It was, however, feasible to keep the increment block time much smaller than the total step time by using a large number of blocks. This meant that any error associated with this lag was negligible. This technique ensured a smooth variation in shear angle-rate.

6.2.2.1.2 BET Finite Element Model

A scale model of the BET was produced within Abaqus/CAE. The model itself was to the same dimensions as the experimental BET samples, therefore 150 mm x 50 mm, meshed at 45 ° with 2480 elements (1.25 mm characteristic length) to ensure that the mesh and fibre directions were collinear. Due to this meshing sequence, S3RT triangular elements were also necessary around the edge of the laminate.

The BET laminate was supported at the base with the encastre boundary condition, such that all DoF were constrained. The top edge of the laminate was constrained with a ‘coupling’; fixing all nodes to one central point, subsequently used to both displace the top of the specimen and record the total shear force. This central coupling was set to extend vertically by 40 mm, as per the experimental tests, however a step time of just 0.5 seconds was selected within Abaqus/CAE. It is commonplace to use shorter step times than real life conditions within an explicit numerical package to significantly reduce the run time, so long as the user ensures that there are no anomalous inertial effects taking place during deformation (ensuring the kinetic energy remains less than 10% of the total energy). This process is complicated slightly for FRTPs due to the rate-dependent behaviour, which therefore also required scaling:

$$\dot{\gamma}_{scaled} = \frac{\dot{\gamma} \cdot t_{step}}{t_{exp}} \quad (6.6)$$

where $\dot{\gamma}_{scaled}$, the scaled shear angle rate, is a function of the step time implemented within Abaqus, t_{step} , the experimental test time, t_{exp} , and the actual shear angle-rate. The experimental test time is equal to:

$$t_{exp} = \frac{\delta_{max}}{\dot{\theta}} \quad (6.7)$$

where δ_{max} is the maximum axial displacement, and $\dot{\theta}$, in the case of intra-ply shear, represents the three experimental test rates – 20 mm/min, 100 mm/min & 500 mm/min respectively. The four test temperatures from the experimental tests; 210 °C, 230 °C, 250 °C, & 270 °C were also assigned to the CF/PA6 laminate as boundary conditions.

6.2.2.2 Diaphragm-Ply Friction Input Validation

This section describes the implementation of the diaphragm-ply friction equation (Equation (4.28)) within an Abaqus/Explicit model.

6.2.2.2.1 Inter-ply Friction Behaviour Implementation

The inter-ply friction behaviour captured in Section 4.5 was shown to be temperature, slip-rate and normal-pressure dependent. It was therefore necessary to implement this friction behaviour within a VFRICION subroutine to ensure it was modelled

adequately. Temperature, slip-rate and normal-pressure are standard variables called by the VFRICITION routine at the start of the increment for each element. The tangential frictive force (applied against the direction of movement), $F_{tangent}$, can be calculated using the CoF as:

$$F_{tangent} = -\mu_{total} \cdot F_n \quad (6.8)$$

where F_n represents the normal force and μ_{total} the final CoF value (see below).

In Section 4.5, a considerable static force was seen to be present upon the initiation of slip, which then gradually reduced down to a ‘dynamic’ friction value after approximately 5-10 mm of slip. It was considered necessary to include this static effect within the inter-ply friction model such that this behaviour was captured. Equation (4.27) shows that this static force is approximately 2.1 times higher than that of the dynamic force, and this was assumed to be irrespective of temperature, slip-rate and pressure.

It can be assumed in this work that the static force applies immediately upon the initiation of a tangential force, with zero slip. The small displacement for each maximum force illustrated in Appendix B - Figure B.5 can be attributed to a degree of backlash in the diaphragm-ply friction apparatus. Generally, after approximately 10 mm of displacement, the dynamic coefficient of friction was met after an exponential decay in the frictive force. Therefore, a simple exponential function was used to model the relative CoF (relative to the dynamic value), μ_{s_rel} , during this static phase:

$$\mu_{s_rel} = 1.1 \cdot [\exp(-A_\mu \cdot \delta) + 1] \quad (6.9)$$

where A_μ was calibrated to equal approximately 0.5 using a trial-and-error method, and δ represents the instantaneous slip distance. Figure 6.3 illustrates the operation of this equation graphically. Therefore, the final friction coefficient, μ_{total} , including the dynamic and static slip can be represented by (μ defined by Equation (4.28)):

$$\mu_{total} = \mu \cdot \mu_{s_rel} \quad (6.10)$$

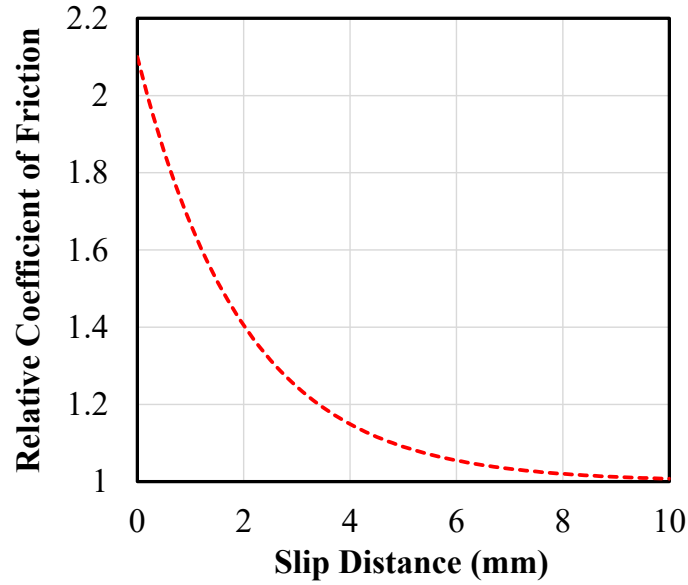


Figure 6.3: Relative coefficient of friction *versus* slip distance.

Equation (6.8) was subsequently implemented within a VFRICITION subroutine. This applies to diaphragm-ply interfaces that begin in contact. In the pull-through model, however, the elements associated with the laminate that lie below the silicone are not initially in contact. With no modification, as soon as contact is made, Abaqus sets the distance δ_{slip} to zero, causing a localised increase in the friction coefficient. To combat this, for nodes that were not initially in contact, δ_{slip} was assigned an arbitrary value > 10 mm. Furthermore, it is assumed that the laminate does not stop moving after the initial displacement, meaning the cohesive contact does not re-form during the process. For model stability, rather than an instantaneous speed (calculated at each increment), the average speed over 10000 increments was used, equating to approximately 0.01 seconds.

6.2.2.2.2 Diaphragm-Ply Friction Finite Element Model

A scale model of the experimental pull-through test was produced within Abaqus/CAE. The silicone was meshed with 660 R3D4 3-D bilinear rigid quadrilateral elements each (approx. 3 mm characteristic length), used to reduce run time and neglect any deformation of the pressure plates. These were then constrained in each DoF apart from that in the out-of-plane direction. Four static forces, calculated using a rearranged form of Equation (4.11), resembling the four experimental pressures (0.03 bar, 0.1 bar, 0.3 bar, 0.9 bar), were applied to both of these rigid parts (opposing each other). The

CF/PA6 laminate consisted of 880 S4RT elements (approx. 3 mm characteristic length) and was located in-between the two rigid silicone bodies, constrained in all directions apart from the vertical. After the normal force was applied (step 1), the pull-through laminate was raised by 40 mm as per the experimental tests (step 2), however with a step time of 0.5 seconds.

As per the calculation of the shear angle rate (Section 6.2.2.1.1), it was not feasible to calculate an instantaneous slip-rate due to the propagation of stress waves through the laminate, resulting in severe discontinuities regarding slip rate. The same procedure illustrated in Figure 6.2 was therefore implemented, with the instantaneous slip rate calculated using a rule of mixtures approach regarding the current increment block time, between the slip rate at the beginning ($\dot{\delta}_{N-1}$) and end ($\dot{\delta}_N$) of the previous increment block respectively. The slip rate, $\dot{\delta}_n$, therefore represented:

$$\dot{\delta}_n = \dot{\delta}_N \cdot \left(\frac{\tau_n}{\tau_{inc}} \right) + \dot{\delta}_{N-1} \cdot \left(1 - \frac{\tau_n}{\tau_{inc}} \right) \quad (6.11)$$

For the purposes of this work, the slip rate was defined in mm/min. Once again, while this results in a small lag in the slip-rate, keeping the increment block time small made this error negligible. Due to the short numerical step time, the slip-rate was scaled using the same method outlined in Section 6.2.2.1.1. The scaled slip-rate, $\dot{\delta}_{scaled}$, therefore represented a modified form of Equation (6.6):

$$\dot{\delta}_{scaled} = \frac{\dot{\delta} \cdot t_{step}}{t_{exp}} \quad (6.12)$$

Where t_{exp} is calculated with Equation (6.7), with the three experimental slip rates of 20 mm/min, 100 mm/min and 500 mm/min.

As per the Abaqus BET model, all nodes at the top of the pull-through laminate were coupled, with the vertical displacement applied to the single coupling node. This also allowed the total normal force to be recorded. The general contact algorithm was used to define contact between the two faces of the pull-through laminate and the respective sides of the fixed laminates, with the VFICTION subroutine assigned. Finally, the temperature of all laminates was assigned using a thermal boundary condition, with four temperatures tested (210 °C, 230 °C, 250 °C, 270 °C).

6.2.2.3 Out-of-Plane Bending Input Validation

The process of decoupling the membrane and bending behaviour has already been described in Appendix D. Therefore, implementing the out-of-plane bending behaviour was simply achieved by including the equation within the VFABRIC subroutine, and using the curvature data stored in the VEXTERNALDB subroutine from the previous increment.

A scale model of the experimental cantilever bending test was produced within Abaqus/CAE. The model consisted of a rectangular (30 mm x 140 mm) profile meshed with 400 S4RT elements (1 mm characteristic length). The rectangular profile was constrained at one end using the encastre boundary condition, simulating perfect cantilever behaviour. A gravity load was applied to the centre of the specimen with acceleration due to gravity, g , given the value -9.81 m/s^2 . A step time of 5 seconds was set to allow the laminate to achieve a steady-state condition. For this, a degree of Rayleigh damping was required to stop the laminate from oscillating continuously. An alpha value of 1.00 was used to allow steady-state conditions to be met but also not considerably influence the final bending profile. Mass scaling was removed for this model due to its high sensitivity to inertial effects. The four experimental temperatures, 210 °C, 230 °C, 250 °C and 270 °C, were applied to the model via a thermal boundary condition.

6.2.2.4 Diaphragm Hyperelastic Validation

To validate the functionality of the Ogden strain energy density function with the calculated material constants (Section 5.3.1.3), an Abaqus model was created replicating each test method. The diaphragm is modelled as an isotropic medium; hence, the stress computation algorithm outlined in Figure 6.1 was not required for these hyperelastic validation models. Instead, the diaphragms were modelled using homogeneous plane-strain shell sections, with the hyperelastic material defined by implementing the predefined Ogden coefficients within the inbuilt hyperelastic material editor. The diaphragm density was assigned a value of 1100 Kg m^{-3} [390].

The uniaxial FE model consisted of 300 S4R elements (characteristic length of 2 mm) replicating the shape of the experimental test specimens (120 x 10 mm). The shell section was constrained at the base with an encastre boundary condition, and displaced

from the top up to 100% strain over a step time of 1 second. The reaction force could then be compared to the experimental uniaxial results.

The biaxial and pure-shear FE models consisted of 1225 S4R elements (characteristic length of 2 mm) replicating the shape of the experimental test specimens (70 x 70 mm). For the pure-shear model, once again an encastre boundary condition was implemented at the base of the specimen. Furthermore, displacement boundary conditions were applied to the specimen edges to apply the constant-width constraint. The shell section was displaced from the top edge up to 100% strain. The biaxial model, in contrast, used displacement boundary conditions on all edges, with two edges supported (perpendicular to the edge direction) and two edges extended (perpendicular to the edge direction) up to 100% strain. All sides were unconstrained in the direction parallel to that respective edge. As per the uniaxial model, a 1 second step time applied for both, with the reaction forces tracked on the respective displaced edges.

6.2.3 Isothermal DDF Thermomechanical Model

This subsection details the construction of the complete isothermal FRTP DDF simulation within Abaqus/Explicit 2022. The model forms the core of this work, with the FRTP material inputs (Chapter 4) and the diaphragm material inputs (Chapter 5) implemented in a complete numerical forming model and validated against the results from the experimental DDF rig (Chapter 3). As per the numerical validation exercise (Section 6.2.2), the algorithm for stress computation (Figure 6.1) details the operation of the material model, including the associated VFABRIC and VEXTERNALDB subroutines. Furthermore, the shear, bending and friction behaviour were implemented exactly as validated in Section 6.2.2. Due to the isothermal nature of this model, all transient heat transfer processes were neglected.

6.2.3.1 Part Geometry and Mesh

The finite element model for the DDF simulation was constructed to replicate the experimental forming apparatus illustrated in Figure 3.2b.

The base and the sides of the DDF were considered undeformable for numerical simplicity. Both parts were constructed using R3D4 rigid elements, with a mesh size of 10 mm. The double-dome geometry (Figure 3.3) was also meshed utilising R3D4

elements, however a considerable amount of mesh refinement was enforced to accurately capture the geometry.

Both the silicone diaphragms and the FRTP laminate itself were considered deformable. The diaphragm were modelled as 530 x 530 mm sections, and meshed utilising S4RT elements. Shell elements were chosen due to the thickness of the silicone diaphragms used in this study, which were considered to exhibit a significant bending stiffness. The FRTP laminate was as a 400 x 240 mm section, once again meshed utilising S4RT shell elements. The laminate and the centre of the diaphragm (projecting from the laminate) were meshed with an element size of 2 mm, which was deemed to be a good compromise between simulation accuracy and computational expense. The meshes of both the diaphragm and laminate were therefore uniform, aiding the initial contact stabilisation. To provide a small reduction in computational expense, the diaphragm extremities (not initially in contact with the laminate) were meshed with a gradually increasing mesh size up to the edges. This was valid since the diaphragm deformation behaviour far away from the laminate was not of interest in this study.

The laminate therefore consisted of 24000 S4RT elements, and each diaphragm with 68800 S4RT elements. In both cases, it was found that conventional hour-glass controls were not sufficient to stop hourglassing from occurring (resulting in an excessive rotation error within Abaqus). This was probably due to the high levels of deformation, and the lack of considerable mass scaling and/or damping applied to the model. An increased hourglass scaling factor of 3 was used for both the displacement and rotational hourglass controls, as opposed to the default value of 1. This was still within acceptable limits defined in supporting literature [411].

The four sides were located vertically at the four edges of the base, with the double-dome geometry in the centre such that it sat 1 mm proud of the base, as to replicate the experimental DDF former. The diaphragms were located above the double-dome geometry with a 10 mm (minimum) gap and the laminate sat in the centre between. Figure 6.4 is included, illustrating schematically the FE model with associated boundary conditions.

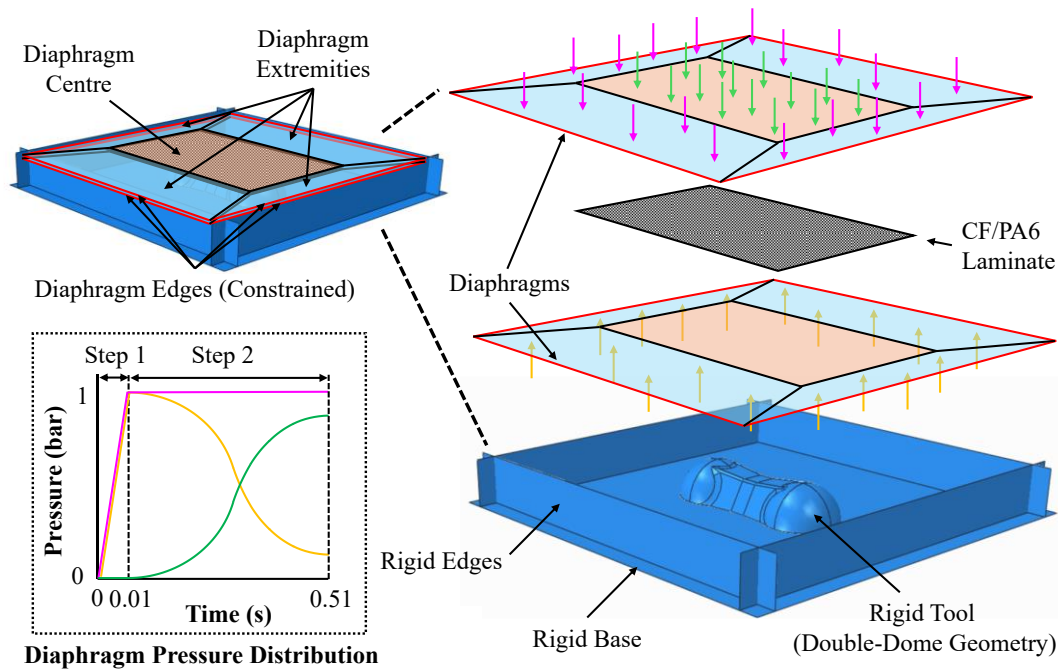


Figure 6.4: Schematic of Abaqus numerical model for FRTP DDF simulation.

6.2.3.2 Material and Section Controls

The laminate and diaphragms were modelled as per the general methods described Section 6.2.2. The thermal expansion of silicone was assumed to be negligible, since as per the method outlined in Section 3.4.1, the preheating process aimed to reduce its influence on the forming behaviour. Finally, since the double-dome geometry, base and sides were all undeformable, they were not assigned material or section properties.

6.2.3.3 Contact Definition

The general contact algorithm was utilised to track contact between individual (defined) surfaces. Individual properties were assigned to the individual contact pairs, specifically controlling the normal behaviour (hard contact) and the tangential behaviour, with friction coefficients from Sections 4.5 and 5.3.2 defined respectively. Since this was an isothermal simulation, no thermal conductance was applied to any of the contact interfaces.

6.2.3.4 Step Properties

As per the characterisation validation exercises (Section 6.2.2), a shorter step time than that of the real life experiment was used to considerably reduce the number of

increments required the FE model to solve. In this work, two (dynamic, temperature-dependent, explicit) steps were required to model the DDF process: pressurisation of the diaphragms, and subsequent forming over the tool. A step time of 0.01 seconds was applied for the diaphragm pressurisation since very little dynamic behaviour existed. This was followed by a 0.5 second step time for the actual forming. This compared to a 18 second forming time for slow experimental DDF and a 3 second forming time for the fast experimental DDF (Section 3.4.3.2). Therefore, rate-dependent properties (shear, friction) were once again scaled utilising Equations (6.6) & (6.12).

Unlike for the characterisation exercises, no mass scaling was applied to the Abaqus DDF model. This was because even a small amount of mass scaling was deemed to significantly influence the inertia of the deformable bodies. This was an issue in the case of modelling rate-dependent behaviour where accurate dynamic modelling was required. Furthermore, it was found to be beneficial to use a fixed user-defined time increment, rather than allow Abaqus to calculate the time increment. This was because the FE model would often underestimate the allowable time-step, resulting in a severe increase in run time. For the purposes of this isothermal model, the time increment was fixed at 3E-7 seconds.

6.2.3.5 Boundary Conditions

Boundary conditions were applied to all undeformable bodies (base, sides, double-dome geometry) to prevent motion. Furthermore, the four edges of each diaphragm were constrained in the same manner (with the encastre condition) to replicate the clamping present in the experimental apparatus.

Pressure boundary conditions were imposed over both steps to apply the correct diaphragm pressure (step 1) and then commence forming (step 2). It was found in the experimental DDF forming that the simply applying a vacuum between the diaphragms did not hold the specimen under 1 bar pressure, as would be the case for a dry fabric. This is since air cannot propagate through the thermoplastic-infused laminate (Section 3.4.3.2). The 1 bar pressure was found to only exist around the edge of the diaphragm and with the presence of breather. Therefore, in step 1, 100,000 Pa pressure (1 bar) was applied to the extremities of both diaphragms, in opposing

directions, to simulate this behaviour in step 1. This boundary condition was applied using a smooth-step amplitude to eliminate the possibility of discontinuities in the pressure field.

To simulate the forming behaviour experienced during the experimental DDF routine, it was necessary to replicate a vacuum being pulled from under the bottom diaphragm. For the diaphragm extremities, this process is achieved in a trivial manner; by simply reducing the upwards pressure on the bottom diaphragm, resulting in a net pressure downwards, allowing for forming to take place. Since the centre of the diaphragm was currently at 0 bar pressure, however, it was instead required to exert a positive pressure on the top diaphragm, in the centre, to replicate this behaviour. This allowed for the increase of laminate pressure during the forming process to be achieved. The removal of pressure from the bottom diaphragm extremities was completed using the pressure data illustrated in Figure 3.9a, although the time was scaled such that the step time of 0.5 seconds matched the duration of the pressure amplitude. Similarly, the pressure was applied to the centre of the top diaphragm using the inverse of this pressure curve, starting from 0 bar and increasing. Figure 6.4 illustrates these pressure boundary conditions including a NTS pressure distribution plot.

6.2.3.6 Model Implementation

The DDF model was run using the ADA high performance computer (HPC) at the University of Nottingham with 48 cores, double-precision (analysis & packager) and full nodal output precision. To validate its accuracy, it was compared to the experimental results illustrated in Section 3.5.

The four experimental temperatures were to be evaluated within the model. As illustrated in Figure 3.8, however, significant in-plane thermal distributions existed away from the point temperature reading of the pyrometer. Owing to this, a 'bulk' temperature was defined in order to more accurately replicate the temperature of the entire laminate. The bulk temperature was calculated using the IR scan, with point data acquired in the 2D-plane on a 10 x10 mm basis. An average value was then calculated from all these data points for the bulk temperature. In the case of the laminate with a centre temperature of 250 °C, the calculated bulk temperature was 246 °C. This value was calibrated to account for the drop in temperature associated with the removal of

the IR heater to capture Figure 3.8. This difference between the centre and bulk temperatures (2%) was then applied for all other temperatures with linear scaling assumed, resulting in bulk temperatures of 226 °C, 207 °C and 197 °C respectively. These are the temperatures that were implemented within the model as boundary conditions, however for simplicity these models are still denoted by their centre temperature (200 °C, 210 °C, 230 °C and 250 °C).

Furthermore, the two different experimental rates were tested by simply modifying the rate-dependent scaling factors in equations (6.6) & (6.12). The two experimented orientations; 0/90° & ±45° were also tested. Three individual properties were chosen such as to evaluate the accuracy of the simulation, which replicates the experimental analysis in Chapter 3:

- Forming behaviour with analysis of the shear angles
- Mould conformity by analysis of bridging behaviour
- Defect presence with the occurrence of wrinkles

6.3 Numerical Validation Results

Regarding the results from the input validation exercises, for the intra-ply shear and diaphragm-ply friction models, the Abaqus-calculated reaction forces are compared to the experimental forces as recorded by the universal testing machine. For the out-of-plane bending model, the steady-state Abaqus bending profile was compared to that of the experimental profiles since no forces were recorded.

6.3.1 Intra-ply Shear Input Validation

Initially the Abaqus shear angles were compared to the experimental shear angles (Equation (4.6)). Figure 6.5a illustrates this comparison, with the average shear angle from the central ‘pure-shear’ region acquired from Abaqus. The analytical shear angle equation from Lebrun *et al.* [156] has also been included (Equation (4.5)). Like the comparison with the analytical shear angles (Section 4.2.2), the experimental shear angles during the BET are lower than those recorded in Abaqus.

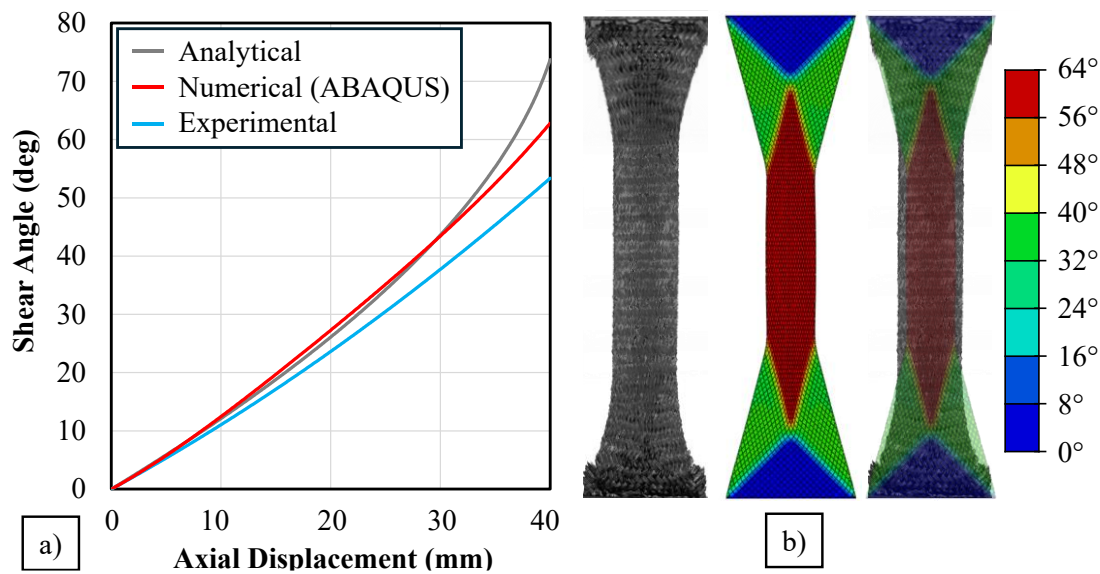


Figure 6.5: a) Shear angle *versus* axial displacement for the experimental tests, Abaqus numerical model and analytical equation, b) Profile of experimental and Abaqus BET samples, including superimposed image of the two.

Figure 6.5b both the scanned experimental profile and the Abaqus numerical model output. A superposition has also been included highlighting the difference between the two. Since the spine of the experimental specimen is wider than that of the Abaqus model specimen, the shear angle is lower in this region. A reason for this is potentially intra-ply slip, as mentioned in Section 4.2.2, that would not be captured in a numerical model. Furthermore, a small degree of rotation within the clamping apparatus may cause this phenomenon, as explored by Maldonado *et al.* [215] who used ‘T’ sections to help remedy this issue. In this work, the discrepancy was not considered an issue since it was assumed that the shear force, per respective shear angle, would approximately correlate between the two tests.

Figure 6.6 illustrates a comparison between the axial reaction force and shear angle for both the experimental (exp) and Abaqus numerical (num) studies, for all experimental test conditions. The shear angle was used rather than the axial displacement due to the shear angle discrepancy illustrated in Figure 6.5. A small amount of oscillatory noise was present in the 210 °C samples at $<5^\circ$ shear angle, however this was not deemed to influence the accuracy of the model results.

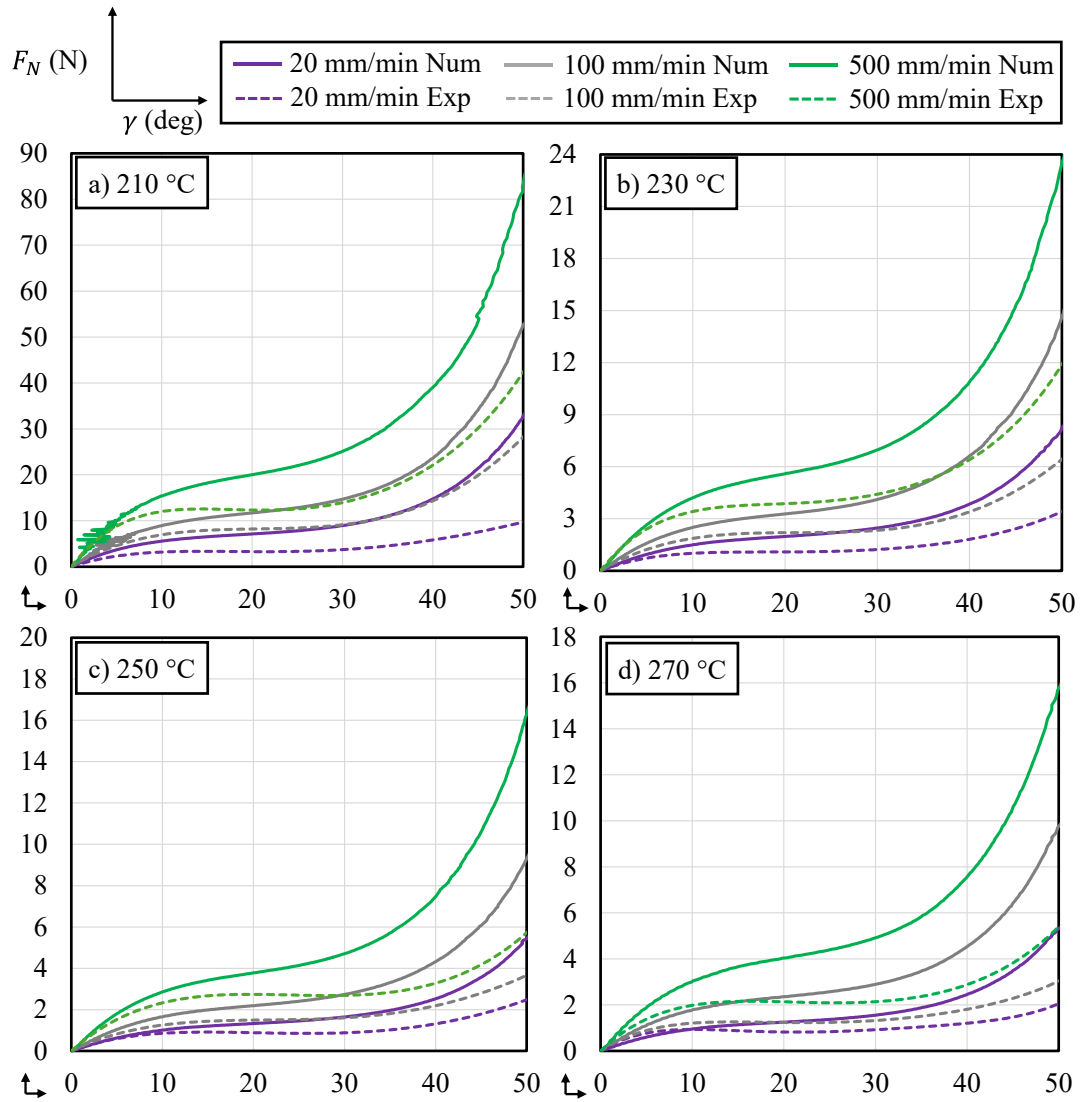


Figure 6.6: Comparison between experimental and numerical axial reaction forces from the BET at different test conditions: a) 210 °C, b) 230 °C, c) 250 °C, d) 270 °C.

In each case, the Abaqus numerical model was seen to considerably overestimate the reaction force required for laminate shearing, although the relative difference between curves for different shear-rates (and temperatures) did appear to be approximately accurate. This shows that while the viscoelastic relationship (Equation (4.19)) appeared to function correctly, the actual shear curve (Equation (4.18)) did not happen to represent the shear behaviour when implemented in a numerical model.

It was hypothesised that the reason for this overestimation was owing to the normalisation procedure outlined in Section 4.2.2. In this work, a rate-dependent normalisation model was utilised, which as explained by Machado *et al.* [159], introduces a degree of error into the result-set. To validate this theory, it was possible

to compare between the rate-dependent normalisation method used in this work (Equation (4.6)), and a rate-independent normalisation model proposed by Cao *et al.* [163] (the iterative shear force term is neglected for simplicity):

$$F_{sh_ind} = \frac{1}{(2H - 3W) \cos \gamma} \left(\left(\frac{H}{W} - 1 \right) F \left(\cos \frac{\gamma}{2} - \sin \frac{\gamma}{2} \right) \right) \quad (6.13)$$

Thus, a relative comparison between the two normalisation techniques, F_{rel} , represented:

$$F_{rel} = \frac{F_{sh}}{F_{sh_ind}} \quad (6.14)$$

where F_{sh} is the original normalised shear force calculated using Equation (4.7). This equation was implemented using the specimen dimensions used in this work for shear angles from 0-50°. Figure 6.7a illustrates the results from this exercise, where a second-order polynomial was fitted with a least-squares algorithm to parameterise the relative difference between normalisation techniques.

To confirm that it was indeed the normalisation procedure that caused the discrepancy in results, the curves from Figure 6.6b were all divided by the aforementioned second-order polynomial for the relative normalised force, effectively producing a result-set utilising the normalisation procedure outlined by Cao *et al* [163]. Figure 6.7b illustrates these results (only 230 °C). Utilising a rate-independent normalisation model vastly reduces the error between the simulated and experimental force outputs. Furthermore, this again verifies that the viscoelastic model (Equation (4.21)) operates with a high level of accuracy.

Even with the error illustrated in Figure 6.6, it was decided that the rate-dependent normalisation procedure was more suitable in this study. Firstly, this is due to model stability. As detailed by Machado *et al.* [159], the softening-effect can occur for viscous materials during the BET if the rate-independent model is used. This can result in convergence issues within a numerical model as the force required for shear decreases (or remains constant) with increasing shear angle in the ‘steady-state’ region. Secondly, it is highly likely that in-plane tension results in an increase in shear force, not accounted for in this work [413]. Thirdly, as observed by the author in a previous

study [414], it is also likely that a normal pressure increases the shear resistance of a laminate owing to laminate consolidation and the reduced ability of resin squeeze-flow from between yarns. Fourthly, the rate-dependent procedure is utilised within thermoforming numerical models before [159], demonstrating a good correlation in shear behaviour between simulation and experiment. Therefore, while it appears that the shear force is overestimated, it is likely that both the BET and the PFT results represent an underestimation in shear force. Considering all these factors, the original normalisation procedure was upheld.

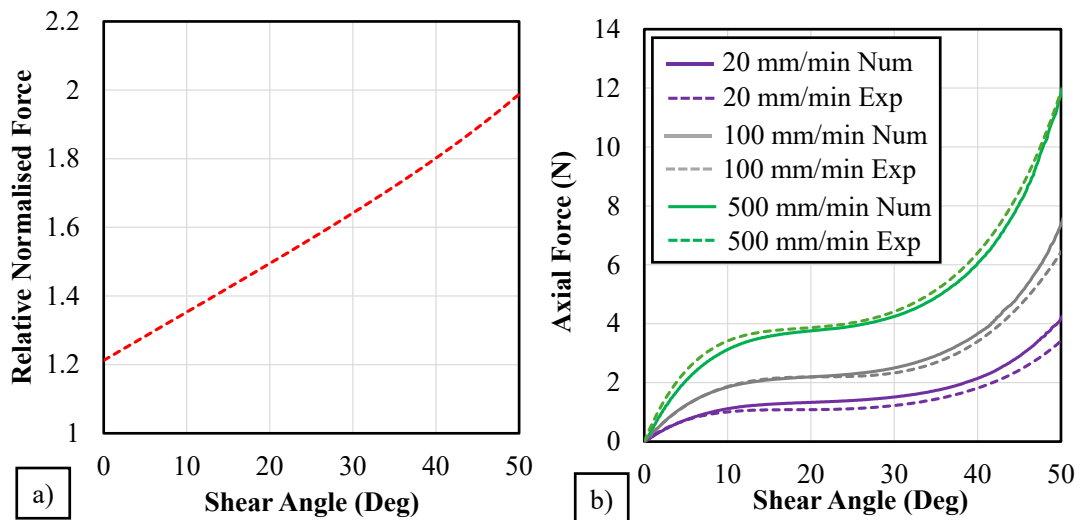


Figure 6.7: a) Relative normalised force comparison between the rate-dependent and rate-independent techniques, b) modified force *versus* shear angle curves (experimental *versus* numerical at 230 °C) accounting for the difference between normalisation techniques.

6.3.2 Diaphragm-ply Friction Input Validation

Figure 6.8 illustrates a comparison between the Abaqus diaphragm-ply friction force output, *versus* the experimental data (five repeats), at the four selected test conditions, based on Equation (4.28).

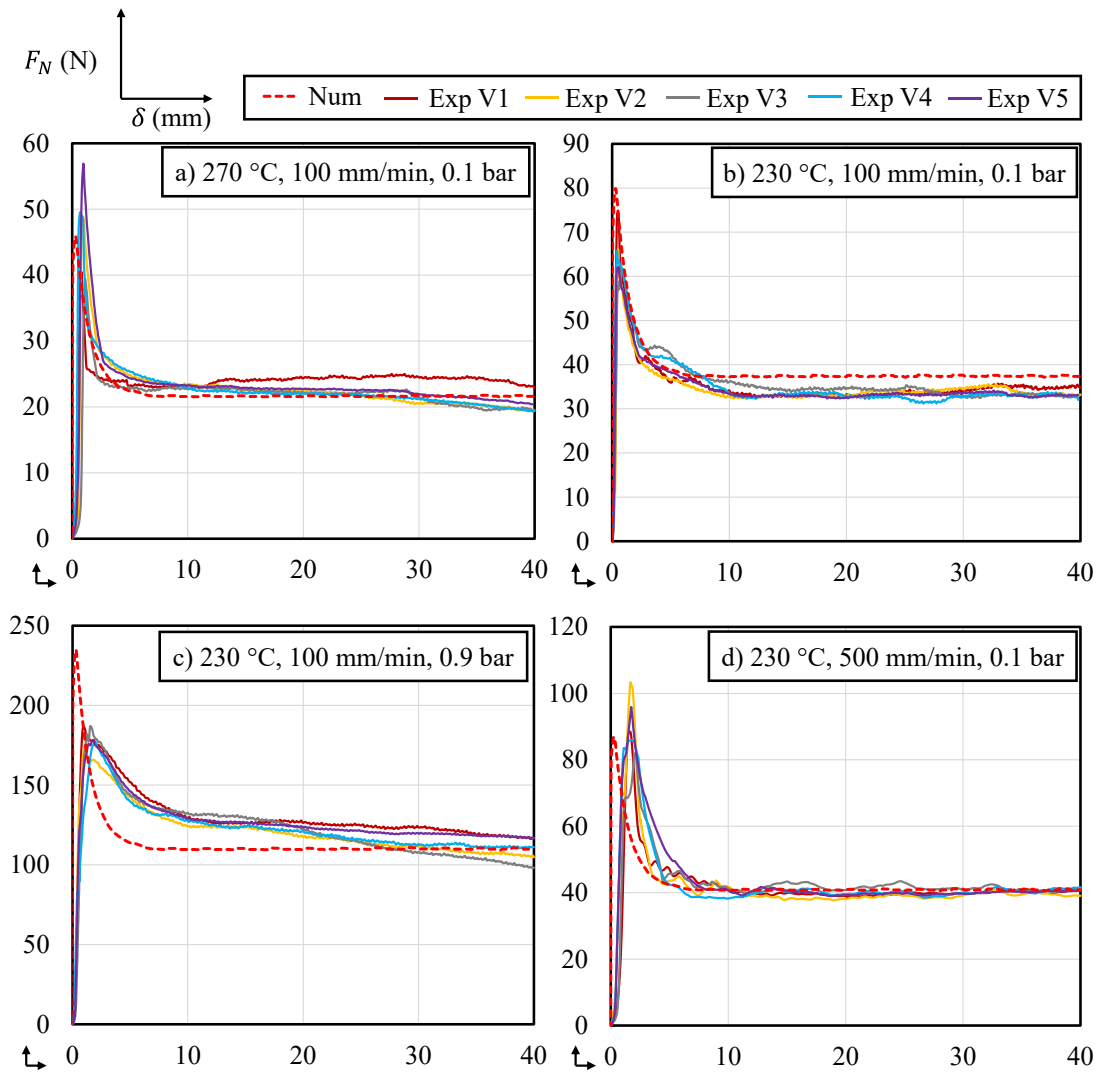


Figure 6.8: Numerical (num) *versus* experimental (exp) repeats of the force *versus* displacement output from the respective inter-ply friction tests at different test conditions.

The Abaqus numerical model well represented the experimental dynamic friction force at each test condition with a maximum error of 16%, which is based on the CoF-to-Hersey number fit illustrated in Figure 4.20. Furthermore, including a term for the relative CoF for the static friction allowed the simulation to predict the initial cohesive behaviour with a good level of accuracy. The only outlier were the results at 0.9 bar where experimental results seemed to exhibit a smaller static peak. This was not considered problematic in this study since it was expected that most of the diaphragm-ply slip occurred at lower pressures, owing to the pressure distribution illustrated in Figure 3.9a. From these results it was deemed that the diaphragm-ply friction behaviour was captured within Abaqus with a sufficient level of accuracy.

6.3.3 Out-of-plane Bending Input Validation

Figure 6.9 illustrates the results from the numerical (Abaqus) cantilever bending test, compared to the experimental results, at the four experimental test temperatures. The experimental error is included (shaded). On initial inspection, it appears that the correlation between numerical and experimental results is relatively high, with the reduction in bending stiffness for laminates at higher temperatures well predicted within the numerical model. The numerical model at 210 °C well predicts the experimental bending profile. It can be seen on the exploded view, however, that there is a reasonably large discrepancy between experimental and analytical profiles, for the high temperature (≥ 230 °C) tests, specifically in the high-curvature region.

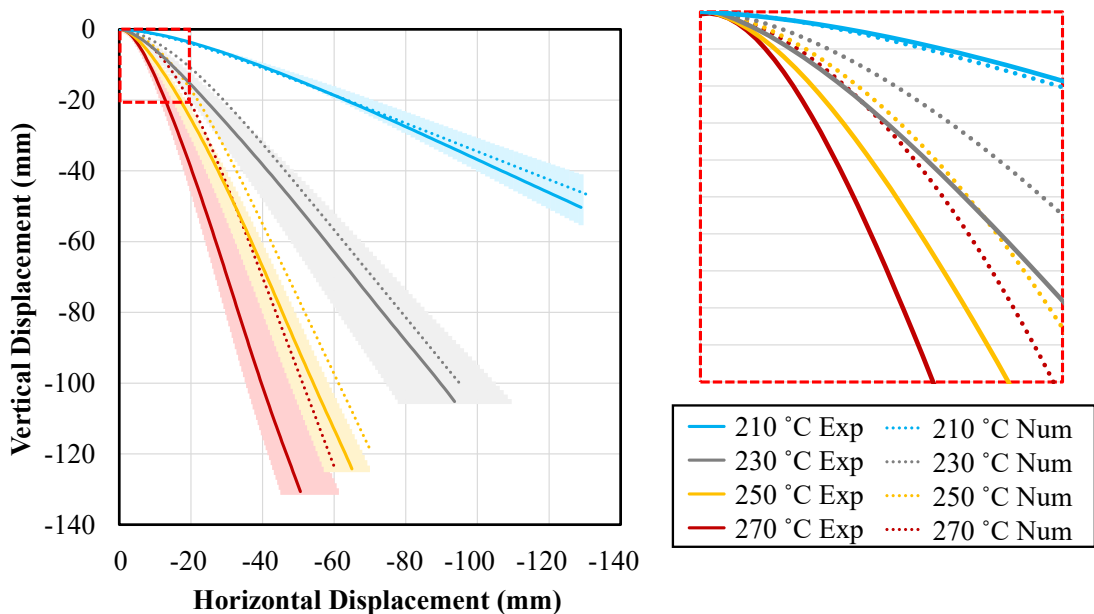


Figure 6.9: Numerical (Abaqus) *versus* experimental (error shaded) bending profiles for CF/PA6 cantilever tests at different temperatures.

It was thought that this error originated from the experimental tests or via the assumption of an un-coupled bending stiffness. This theory was backed-up upon a more detailed comparison between the bending profiles of laminates at 250 °C, as per Figure 6.10. It appears that the experimental sample undergoes a degree of buckling on one of the edges. This results in an almost immediate straightening-out of the specimen, since the buckling eliminated the requirement for bending to take place. Upon inspection, it was evident that all laminates at temperatures ≥ 230 °C exhibited this behaviour, with one edge seemingly buckling at the cantilever support. It should

be noted that the buckling experienced in the experimental tests is not behaviour that would be expected in real-world thermoforming conditions.

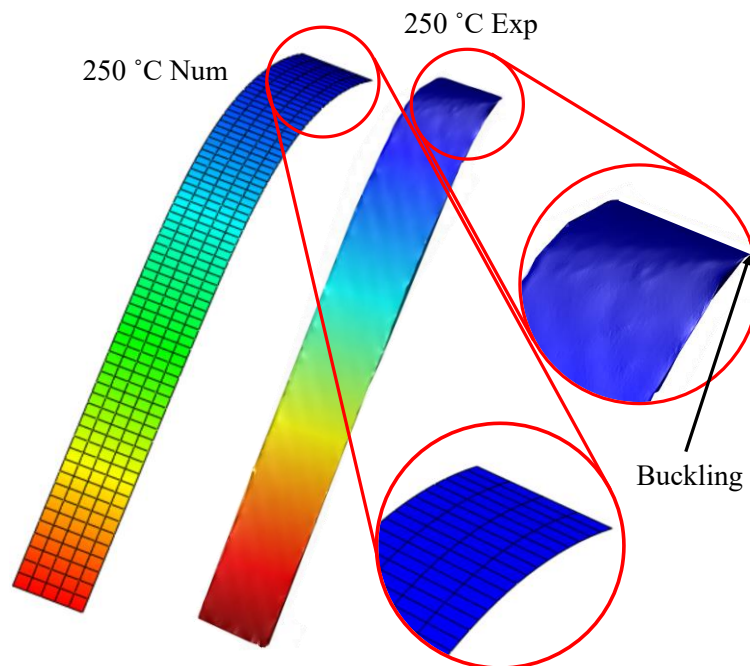


Figure 6.10: Visual comparison between numerical (Abaqus) and experiment cantilever bend test specimens.

It was believed that this was a property of the specific laminate tested, potentially due to the low ply thickness (0.23 mm). The only other published work for the cantilever bending of FRTPs did not exhibit this behaviour [186], but this was for thicker 5-harness laminates. Since the Abaqus model did not predict such behaviour, this explains why it appeared to underestimate the laminate curvature. In actuality, the accuracy of the bending numerical model cannot be assessed accurately with Figure 6.10. It was shown in previous work, however, that model sensitivity to bending stiffness is low, with a factor of two difference resulting in no difference to model wrinkle prediction [186].

Therefore, it was considered necessary to ensure that the parameterised bending stiffness within this work lay within an acceptable range, allowing for sufficient defect prediction within a forming model. For this process, a model of the PFT was produced within Abaqus, which was then used to compare wrinkling profiles with the experimental profiles from the PFT work presented in Section 4.4.2.

The PFT sample was modelled as a cruciform to the same dimensions as the clamped area of the experimental samples, with a side length of 145 mm. The sample was meshed with 8833 S4RT elements (characteristic length of approximately 1 mm). The cruciform was located within a rigid body frame to replicate the PFT apparatus, itself meshed with 1164 R3D4 elements. The exterior nodes of the fabric were tied to the interior nodes of the frame. The corners of adjacent frames were constrained to one another using a coupling constraint, with the rotational DoFs unconstrained. Furthermore, the bottom of the frame was displacement-constrained, once again allowing for rotation. The frame was displaced vertically (from the top coupling) by 81 mm, as per the experimental tests. Once again, a step time of 0.5 seconds was assigned to the model, with Equation (6.6) used to scale the associated rate-dependent variables to the quicker model speed. A temperature of 250 °C was assigned as a boundary condition. To evaluate the model sensitivity, the model bending stiffness (Equation (4.34)) was modified by multiplying it by a given factor. For the purposes of this work, factors of 1x, 5x and 0.2x were selected.

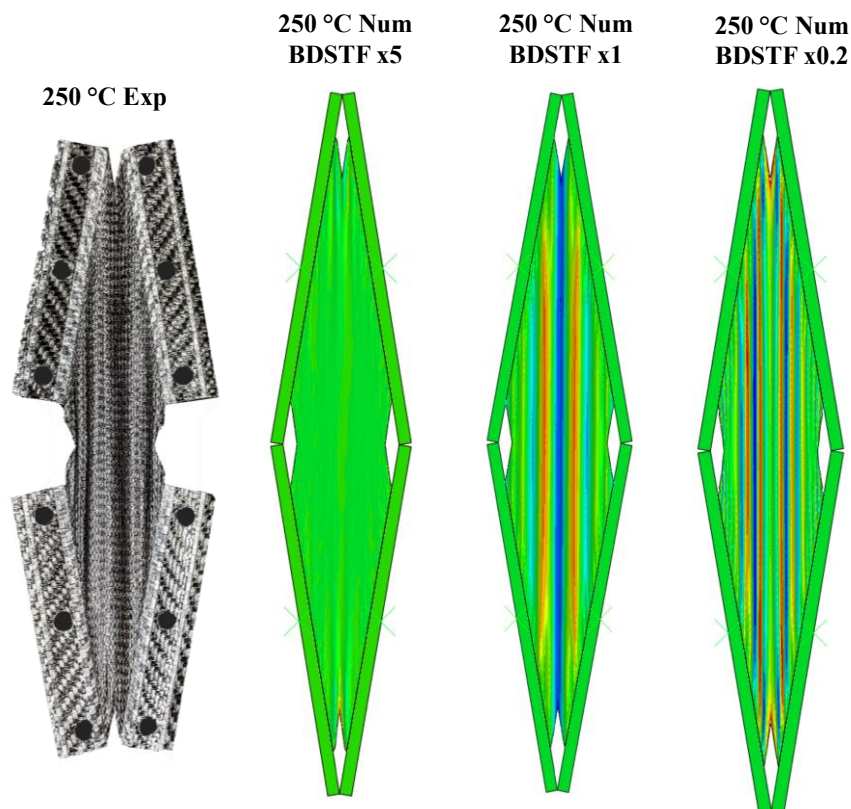


Figure 6.11: Comparison between experimental and numerical (Abaqus) PFT profiles, including a sensitivity analysis of the PFT model to changes in bending stiffness (BDSTF).

Figure 6.11 illustrates the three numerical PFT models with different bending stiffness inputs, compared to that of an experimental sample. The nominal bending stiffness input (1x) produces the most accurate wrinkle profile, with the 5x test resulting in no wrinkling behaviour, and the 0.2x test resulting in a large number of small-amplitude wrinkles. Thus, it was concluded that while the accuracy of the bending stiffness calculated in this work could not be attained exactly (due to buckling behaviour illustrated in Figure 6.10), the bending profile does lie within bounds to predict wrinkling behaviour with a sufficient degree of accuracy. For further validation, factors of 2x and 0.5x were also run, but demonstrated negligible change in bending behaviour from the nominal value (as per the work of Liang *et al.* [186]). Considering these results, the characterised bending behaviour was deemed acceptable.

6.3.4 Diaphragm Input Validation Results

Figure 6.12 illustrates the results of the hyperelastic model validation exercise. The calculated Ogden model well predicts the hyperelastic behaviour of the silicone elastomer for each deformation mode. For the remainder of this work, the 6th order Ogden strain energy function is used to model the silicone with the coefficients tabulated in Appendix C - Table C-1.

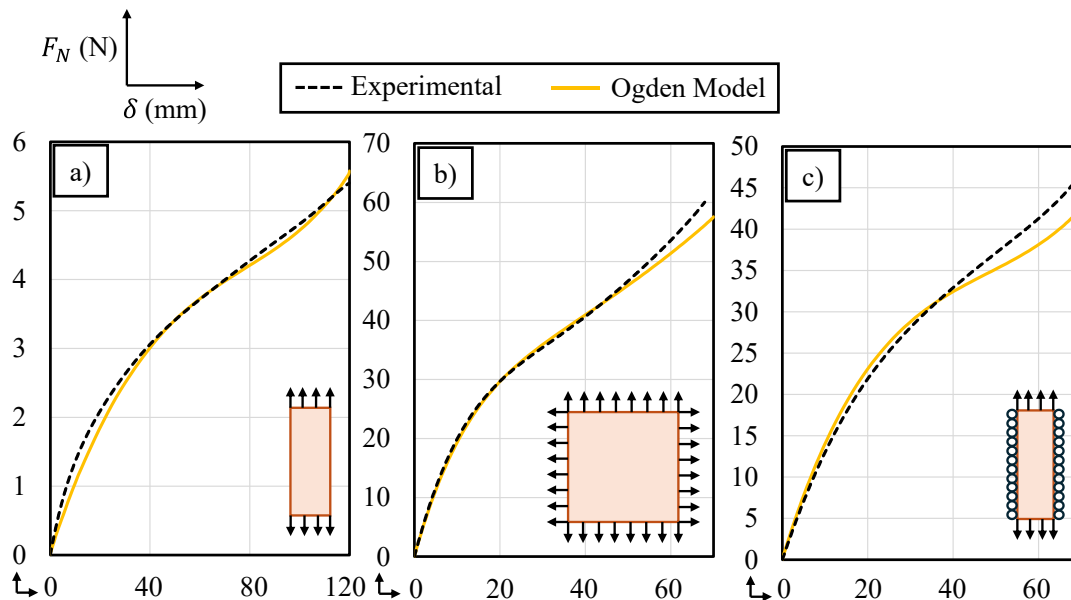


Figure 6.12: Validation of the Ogden strain energy function by comparing force *versus* displacement data to experimental results, for all three test methods.

6.4 DDF Thermomechanical Simulation Results

This section details the results from the isothermal DDF thermomechanical simulation which was outlined in Section 6.2.3. Within this section, the simulation results are compared with the experimental DDF thermoforming results illustrated in Section 3.5 such that the simulation accuracy was evaluated. Initially, the general operation of the simulation is validated, regarding the dynamic movement of the laminate and diaphragms, the diaphragm strain, and finally the shear and external edge profiles. This is followed by a structured analysis where the temperature-, rate- and directionality-dependent studies are conducted sequentially to assess the performance of the simulation at various isothermal conditions.

6.4.1 Initial Model Validation

The simulation was compared on a dynamic basis to Figure 3.6, illustrating how the changing pressure differential enacts a force that enables the FRTP laminate to conform to the double-dome geometry. As noted in Section 6.2.2.1.2, the total simulation time was scaled to 0.5 seconds in the model to reduce the computational time. With the actual forming time of 18 seconds, the simulation time was therefore scaled by a factor of 36 to resemble that of the real-world forming operation.

Figure 6.13 illustrates the simulation, at reference conditions (250 °C, 18-second forming operation, 0/90 ° layup, as per those detailed in Section 3.4) at four individual step times, with the experimental equivalents from Figure 3.6 superimposed. The upper diaphragm is hidden for clarity, and the laminate is coloured green to aid its identification. Overall, a strong correlation existed between the simulated and experimental thermoforming operations. There was potentially a slight delay that can be noticed at the 5 second mark in the simulation, compared to experiment, although this appears to amount to less than 1 second, or <6%. This was attributed to a slight inertia effect with the simulation running with a 0.5 second step time, although since no mass scaling was used, it was considered to be within tolerance.

Since this diaphragm-tool and inter-diaphragm pressure profiles are defined as boundary conditions, there was no need to validate these in this section, as was conducted for the experimental studies in Section 3.4.3.2. Furthermore, since the

simulation was operating in an isothermal manner, there was also no requirement to validate the thermal profile. It was considered prudent, however, to validate the simulated diaphragm strain and compare it to the experimental study of Section 3.4.3.3. Figure 6.14 therefore illustrates the model logarithmic strain at the end of the (reference condition) forming operation.

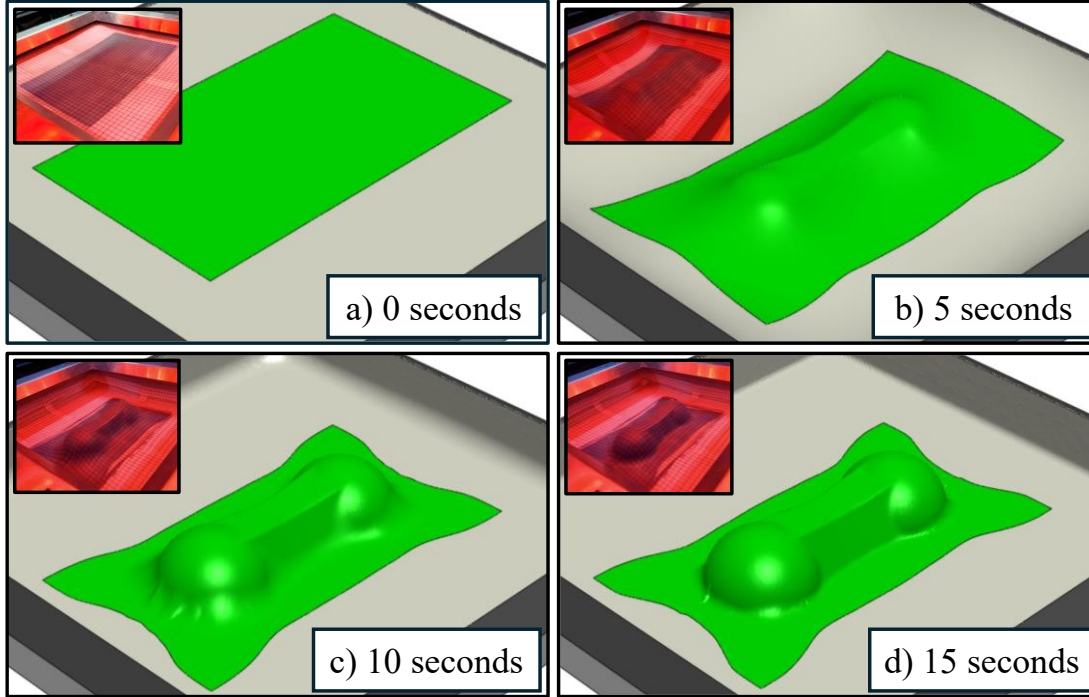


Figure 6.13: 'Freeze-frames' taken at four defined (scaled) times during the numerical FRTP DDF operation. The experimental profiles have been included for comparative purposes.

Since logarithmic strain (LE) was used for the output, it was required that this be converted into engineering strain which represents the simple change-in-length strain measured in Figure 3.10. This can be completed using the following equation:

$$\varepsilon_{eng} = \exp(\varepsilon_{true}) - 1 \quad (6.15)$$

where ε_{eng} and ε_{true} are the engineering and true strains, respectively.

From Figure 6.14, the maximum logarithmic strain was identified at the same regions as found for the experimental study. At these regions, the maximum logarithmic strain value was 0.550. Utilising Equation (6.15), this gives an engineering strain value of 0.733. This can be compared directly to the experimental value of approximately 0.8. It is likely that the small discrepancy between values is associated with the

assumptions made in Chapter 5 regarding the behaviour of the diaphragm, both in terms of thermal expansion and hyperelastic behaviour. Furthermore, a small, localised bolt hole in the experimental apparatus (see 3.10c) appears to have included localised strain behaviour. This strain profile was therefore considered to be a good correlation between experimental and numerical studies.

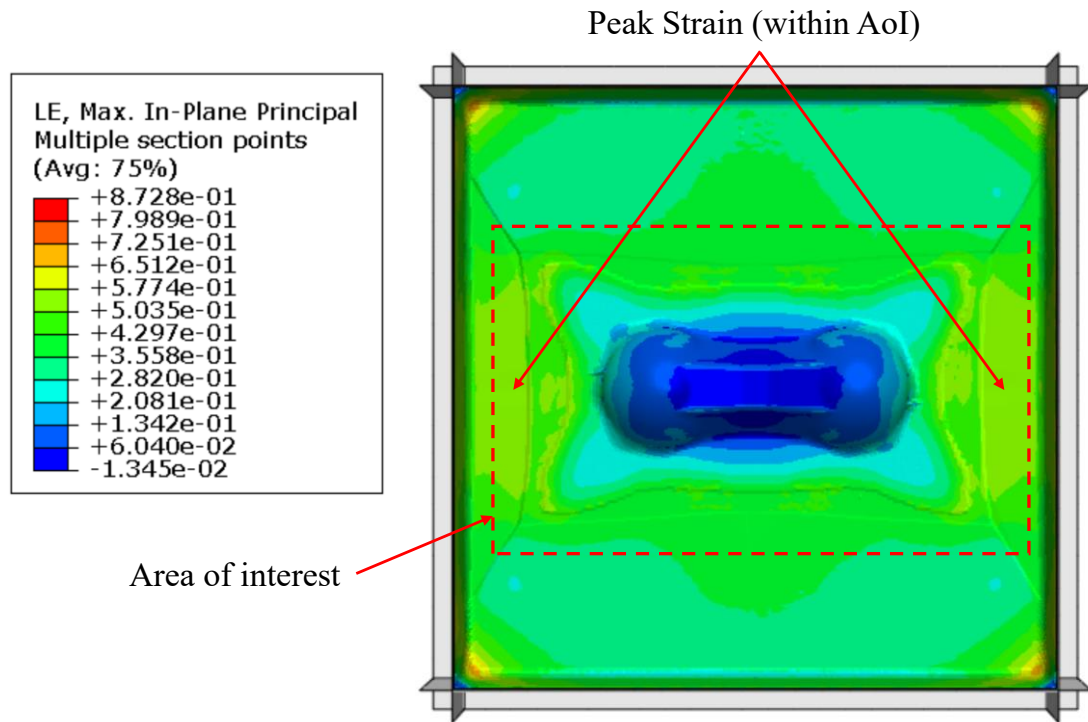


Figure 6.14: Diaphragm logarithmic strain (LE) at the end of the forming operation at reference conditions. The area of interest was defined in Section 3.4.3.3.

For every experimental thermoforming operation, the maximum shear angle from all four quadrants was recorded using a 2D scanner. Thus, only on one occasion (illustrated in Figure 3.7c) was the shear profile of the entire laminate mapped, owing to the expense associated with this exercise. While the maximum experimental and numerical shear angles are compared later in this Section, it was also possible to compare between the shear angle profiles of both the experimental and numerical studies. Figure 6.15a and Figure 6.15b therefore illustrates this comparison, again for the laminate at reference conditions. SDV21 refers to the shear angle, measured in degrees.

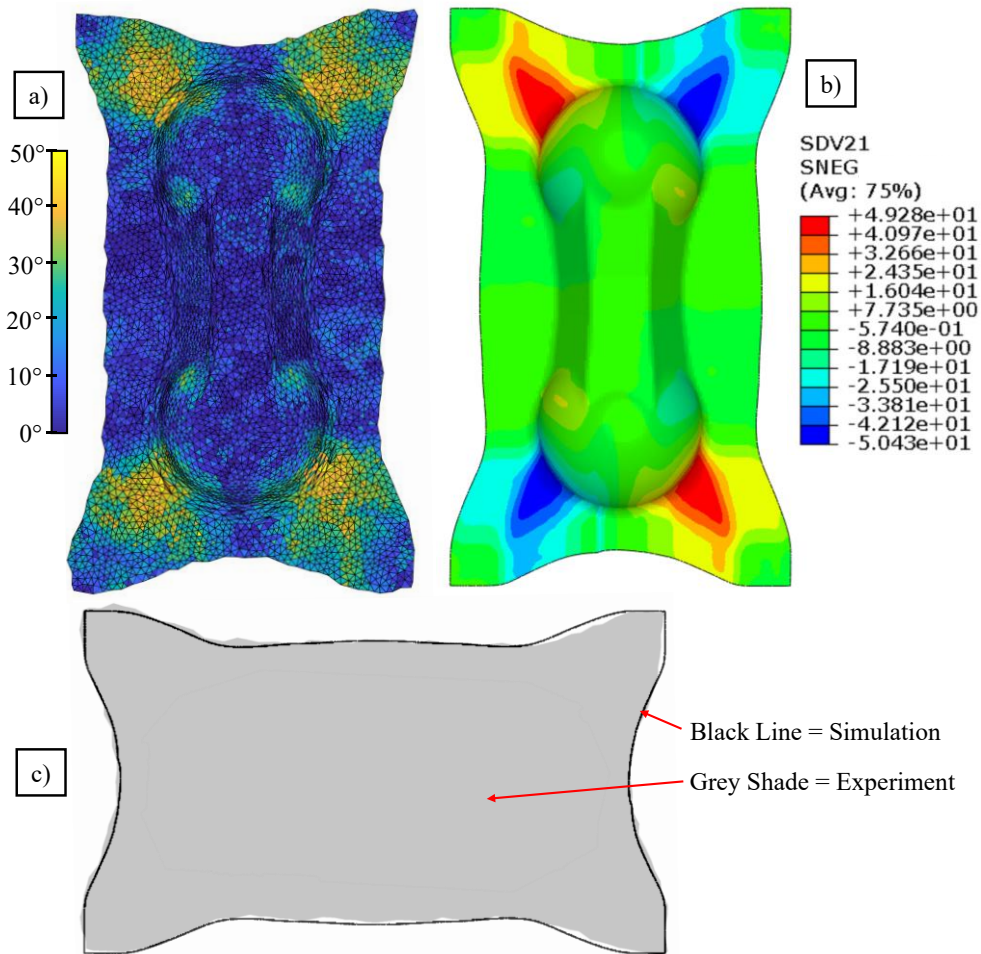


Figure 6.15: a) experimental shear profile, b) numerical shear profile, c) combined external profile comparison.

A strong agreement in the shear profiles between the experimental and simulated FRTP laminate is present, with the four high shear regions predicted correctly and limited shear at the laminate corners. Furthermore, a small degree of shear was correctly predicted on the inside surfaces of both domes, with the rest of the form largely shear-free. An exact comparison in maximum shear behaviour is presented later in this section.

This procedure also allowed for a comparison of the perimeter profile of the simulated and experimental thermoforming procedure. This was not possible for the other scans since they were completed in-situ, such that determining the exact laminate profile was difficult owing to the thickness of the diaphragms, and the resolution of the Creaform Handyscan3D 700 scanner. The shear angle scan illustrated in Figure 6.15a was however completed as a post-process, meaning that the exact laminate geometry was

scanned. Figure 6.15c therefore illustrates a comparison between the simulation (black line) and experimental (grey shade) forming profiles. A good correlation is present between the two profiles. The mesh size for the experimental scan is 3 mm in this case, resulting in the small edge deviations visible on the grey experimental output.

6.4.2 Variable Temperatures

With the initial model validation study complete, a thorough comparison between numerical and experimental forming could be concluded, beginning with the four different simulated temperatures. Figure 6.16 illustrates this comparison, providing a visual comparison between simulation and experiment. The simulation plot is not identical to that of the experimental plot since the experimental geometry includes the upper diaphragm and the simulation does not. Therefore, an exploded view including the simulation mesh is included where the diaphragm has not been hidden, allowing for an exact comparison in wrinkle profile between simulation and experiment.

The simulation appears to predict forming behaviour with a good level of accuracy over the four different tested temperatures. In all cases the main wrinkle at the apex of the dome is predicted, with the size appearing to closely correlate with the experimental results. In the case of the laminate at 200 °C, a secondary wrinkle on the dome is also predicted, however this wrinkle was only present on half the experimental domes. The bridging witnessed on the experimental domes was higher than that of the simulated ones at this temperature (evaluated quantitatively below), however, which was a likely cause for this wrinkle not appearing on some of the experimental domes. The experimental forming operations, as noted in Section 3.5, exhibited a moderate degree of experimental variation, particularly at low temperatures.

It was noted that there was even variation in the simulated profile, with the secondary wrinkle at 200 °C not predicted in its entirety in each quadrant within the simulation. However, at this temperature the simulation does clearly identify a degree of ‘rippling’ behaviour in the high shear regions, indicating that this is an area of concern at this temperature. Another noteworthy observation includes a diaphragm wrinkle on the 200 °C profile that was not predicted in the simulation.

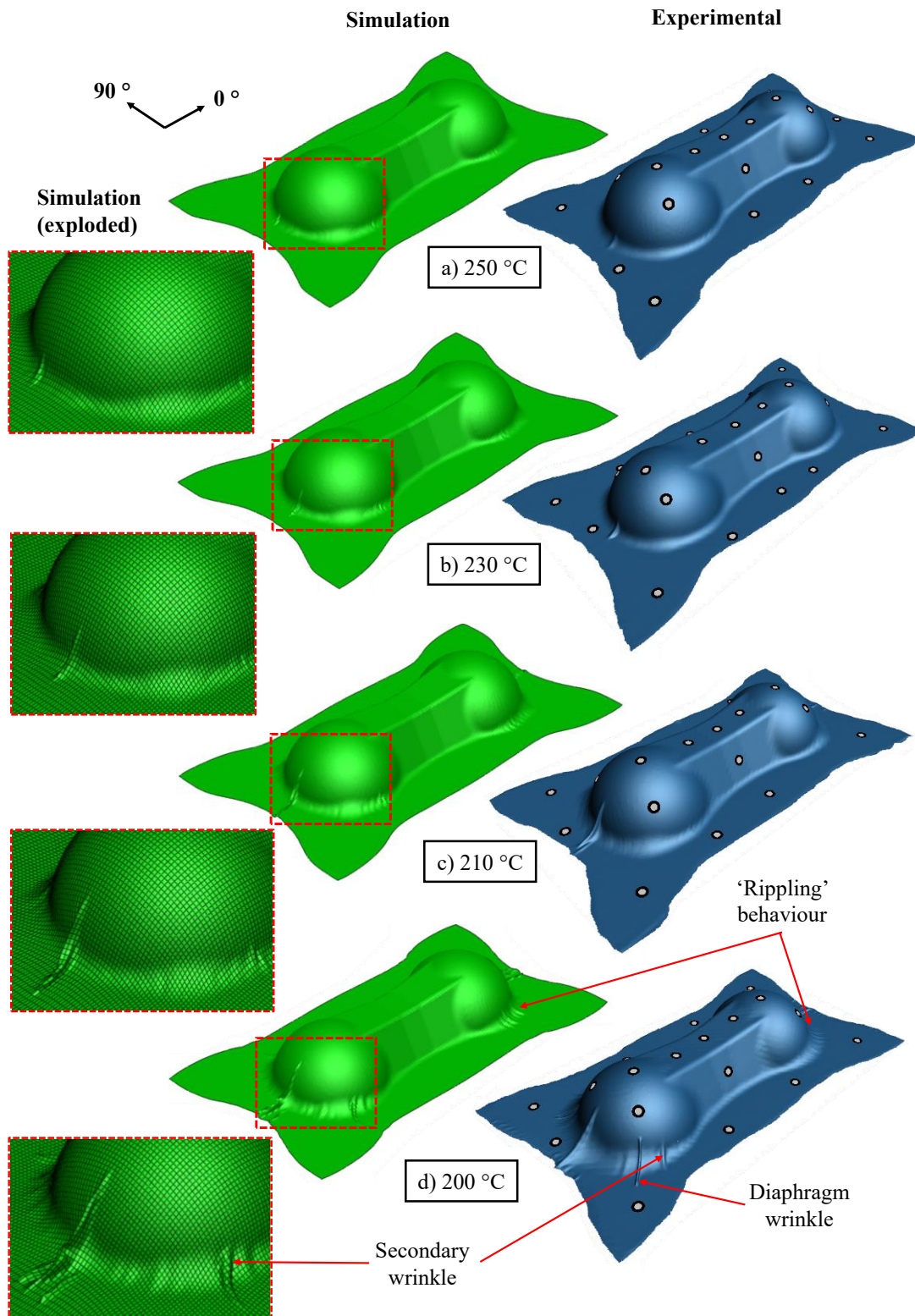


Figure 6.16: Simulated *versus* experimental forming profile of laminates at: a) 250 °C, b) 230 °C, c) 210 °C and d) 200 °C. Note the exploded view includes the diaphragm.

To allow for a quantitative analysis between simulation and experiment, the same procedure outlined in Section 3.4.2 was implemented; the simulated laminate profile

was compared to that of the tool, allowing for an exact value for bridging and wrinkling behaviour (experimental scans from Section 3.5.1). Figure 6.17 illustrates this quantitative comparison between experiment and simulation. The results from this study are subsequently illustrated in Figure 6.18, representing the apex wrinkle amplitude, wrinkle length, maximum bridging distance and maximum shear angle respectively, between simulation and experiment, including experimental error. The horizontal axis represents the different independent variables, such that 250 °C, 230 °C, 210 °C and 200 °C are relevant to this section. While quantifying the various forming defects was relatively simple, defining what the acceptable limits are regarding the differences between simulated and experimental results was not so. In this work, it was decided that the acceptable limits in all four cases would be defined by the experimental error associated with the three repeated tests conducted.

Regarding the apex wrinkle, wrinkle behaviour is well captured in the simulation for different temperatures (Figure 6.18a and Figure 6.18b). The apex wrinkle predictions (amplitude and length) lay within the experimental error in each case, with wrinkle amplitudes all captured within 1.4 mm, and lengths within 6 mm. Furthermore, regarding bridging (Figure 6.18c), at 210 °C, 230 °C and 250 °C the bridging value lay within 0.5 mm of the experimental value, although the two higher temperatures were outside the experimental repeatability. A possible reason for this is neglecting further silicone thermal expansion after the 200 °C preheat stage. A smaller mesh size may also result in a slight reduction in bridging behaviour. At the lowest temperature of 200 °C, a larger discrepancy in bridging behaviour of 3.2 mm was noted. A similar discrepancy exists with the behaviour of shear angle prediction (Figure 6.18d), where for the cases at 210 °C, 230 °C and 250 °C the simulated shear angles lay within 1° of the experimental value, in each case lower than the experimental error. Again, at 200 °C, a larger discrepancy of 6° was witnessed. The shear image plots from all simulations are included in Appendix A - Figure D.3.

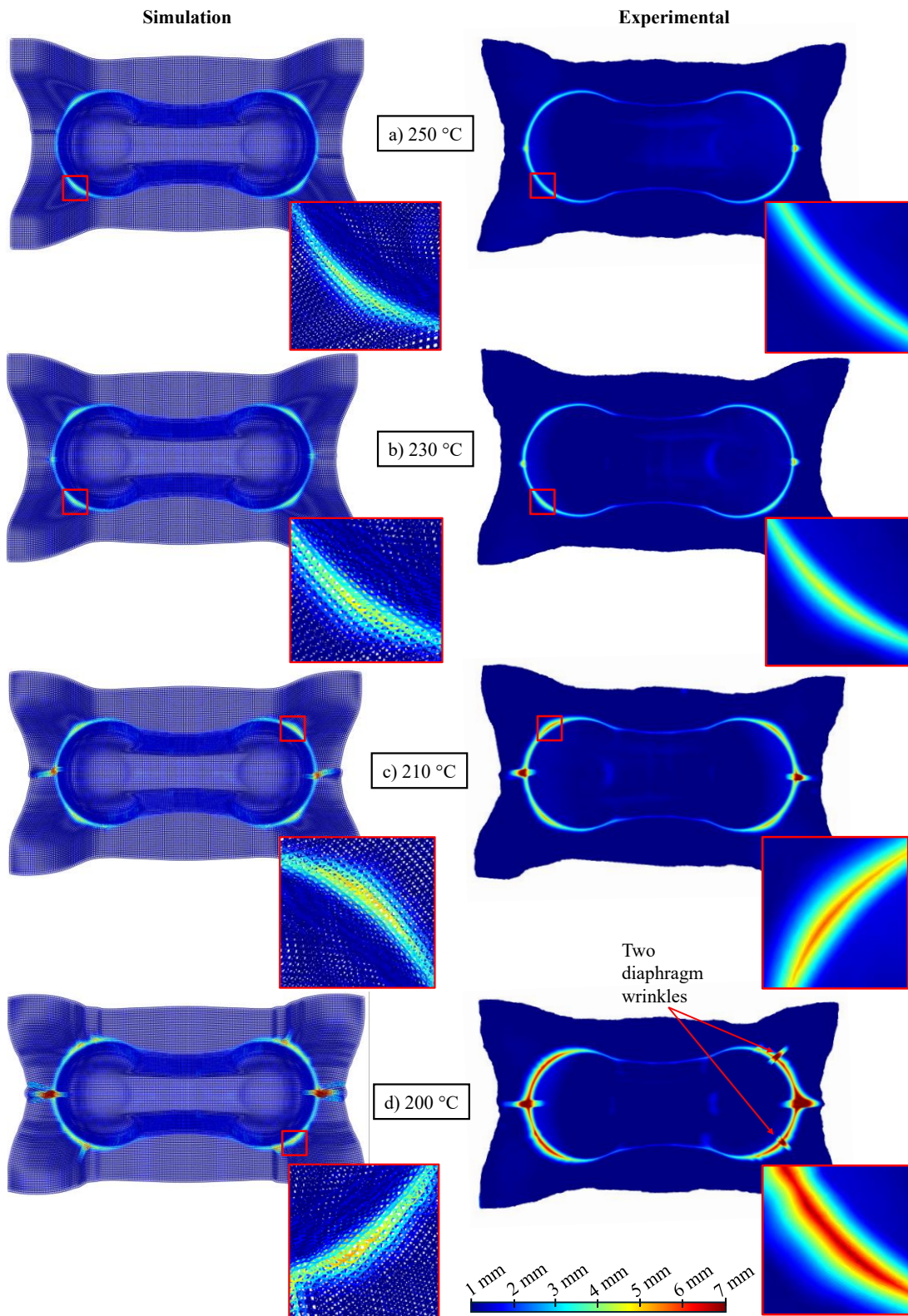


Figure 6.17: Simulated and experimental mould conformity plots, highlighting the extent of both wrinkling and bridging behaviour, for four different temperatures: a) 250 °C, b) 230 °C, c) 210 °C and d) 200 °C.

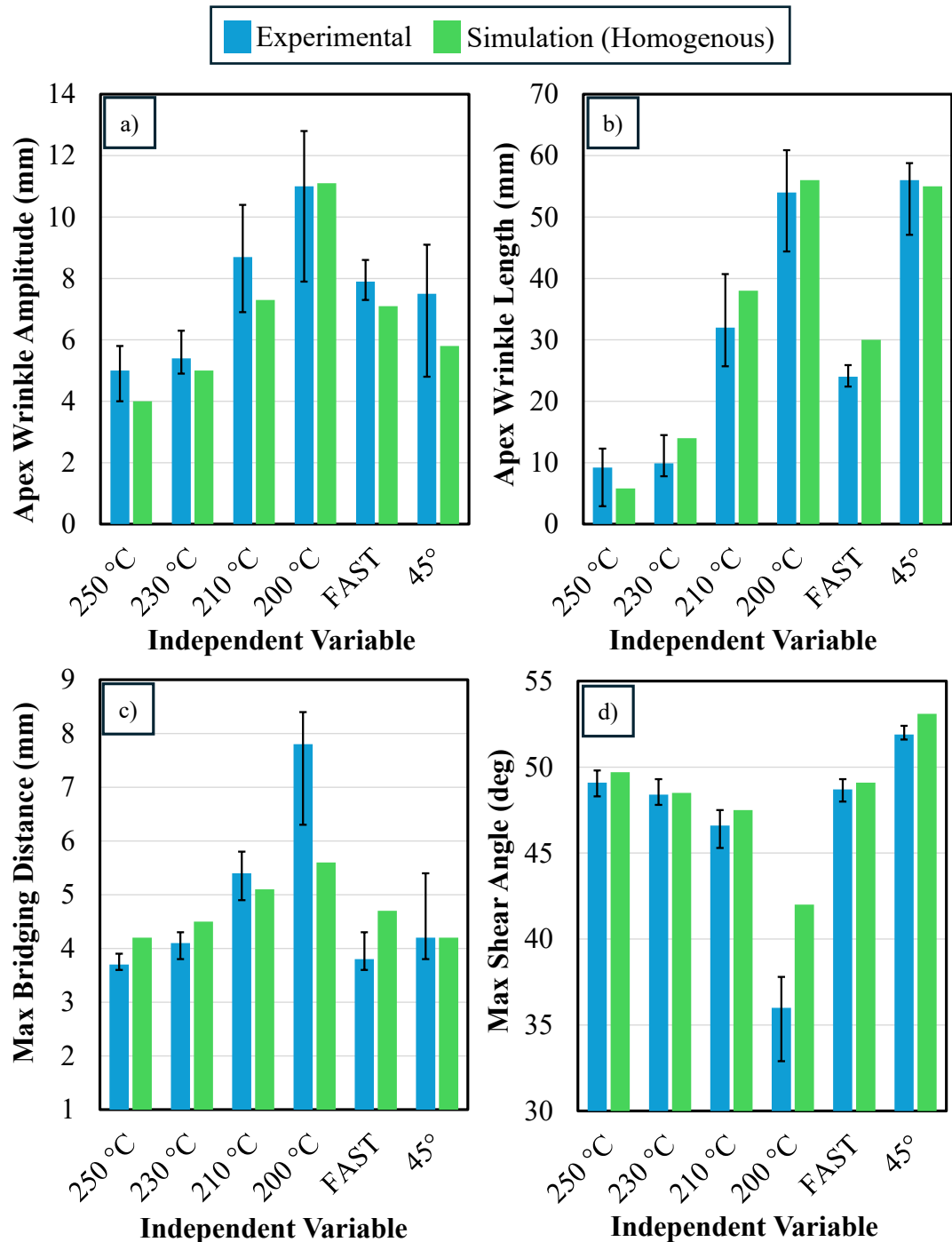


Figure 6.18: Quantitative simulation vs experimental results, including experimental error, for the six individual independent variables (four temperatures, alternative rate, alternative orientation): a) Apex wrinkle amplitude, b) Apex wrinkle length, c) Maximum bridging distance, d) maximum shear angle. Maximum values denote an average maximum from the four quarters of the double-dome geometry.

Two possible hypotheses were considered to explain the overestimation in simulated shear and behaviour underestimation in simulated bridging behaviour for the 200 °C

case. Firstly, since material data was only collected down to 210 °C, the result at 200 °C requires extrapolation of all material data, likely to result in a degree of error. Secondly, as illustrated in Figure 3.8, the experimental forming operation operated with significant in-plane temperature distributions owing to the radiance of the IR lamps and rig edge effects. To combat these distributions, a ‘bulk’ temperature value was used in the simulations to approximate the temperature of the entire sheet. For the higher temperature results, this does not appear to have significantly degraded the simulation accuracy. The 200 °C forming operation is unique however, as it is highly likely that the cooler short-edges of the experimental specimen were approaching, or undergoing crystallisation, as per Figure 6.19.

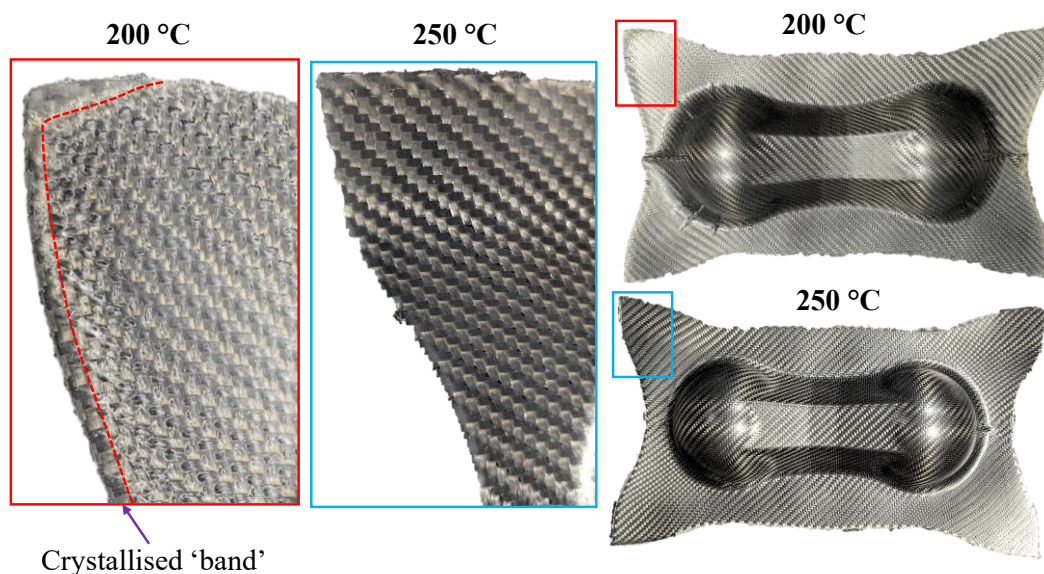


Figure 6.19: Edge-effects owing to the in-plane temperature distribution during the FRTP DDF process, resulting in crystallisation for the 200 °C laminate (250 °C laminate included for reference).

It was expected that the laminate shear response upon crystallisation increased dramatically, an effect not currently captured in the simulation. Therefore, even a short band of crystallised material would significantly inhibit the shearing operation, reducing material draw-in and increase bridging. There is a marked difference in appearance of the 200 °C laminate within 5mm of the short-edge compared to the rest of the laminate. For comparison, the laminate formed at 250 °C, has also been included in the figure, which did not exhibit this phenomenon. Furthermore, laminate shearing was extremely marginal ($<5^\circ$) in this area. This compares to the simulated shear angle

plot (Figure D.3a), which demonstrated shear up to 18° on this edge. This is therefore considered in Section 6.4.4.

6.4.3 Variable Rate and Orientation

This section follows the previous, with analysis of the alternative forming rate and orientation within the simulation, compared to the experimental results illustrated in Section 3.5.2 and Section 3.5.3. Figure 6.20 illustrates this comparison. As previous, the overall simulation plot represents just the laminate, whereas the exploded view includes the diaphragm and mesh.

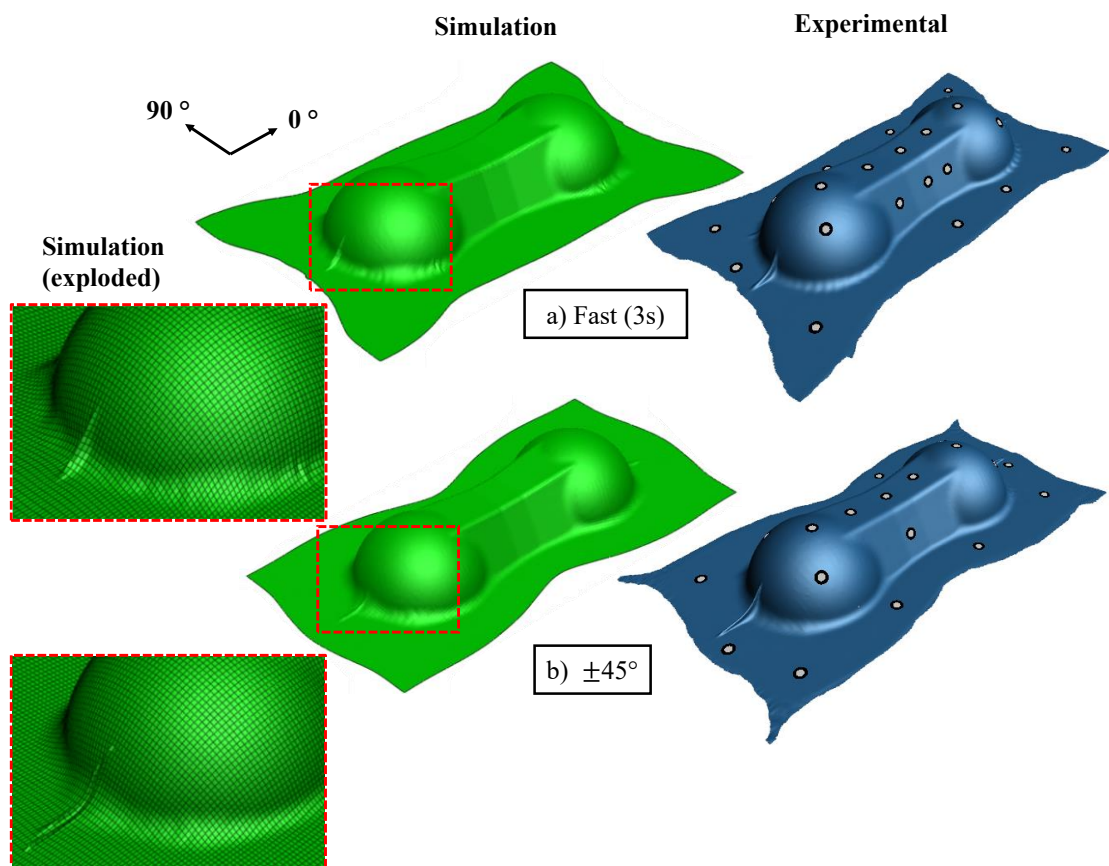


Figure 6.20: Simulated *versus* experimental forming profile of laminates at: a) alternative (3-second) rate, b) alternative ($\pm 45^\circ$) orientation. Note the exploded view includes the diaphragm, similar to the experimental scan, allowing for a like-for-like comparison.

Similar to the variable-temperature results presented in Section 6.4.2, the simulation appeared to predict the apex wrinkle with a good level of accuracy for both an alternative rate and alternative orientation. The high-speed simulation result also correctly predicted the occurrence of ‘rippling’ in the high sheared regions, although

bridging in these areas was lower in the experimental result. The forming at an alternative orientation resulted in a correct prediction of the laminate profile, noting that the four ‘spiked’ edges of the experimental form were caused by ‘laddering’ of the woven fabric. Furthermore, the simulation correctly predicted that the wrinkle on the laminate was much smaller than that of the diaphragm for this alternative orientation, which is seen clearly by comparing the overall and exploded simulation views. Figure 6.21 is included to show the experimental equivalent of this, clearly showing a small wrinkle amplitude in the alternative direction case, compared to the scan (Figure 6.20b) which includes the diaphragm. For comparative purposes, an image of the high-rate laminate apex wrinkle is included, which exhibits a much greater amplitude and much more closely correlates with the scan illustrated in Figure 6.20b.

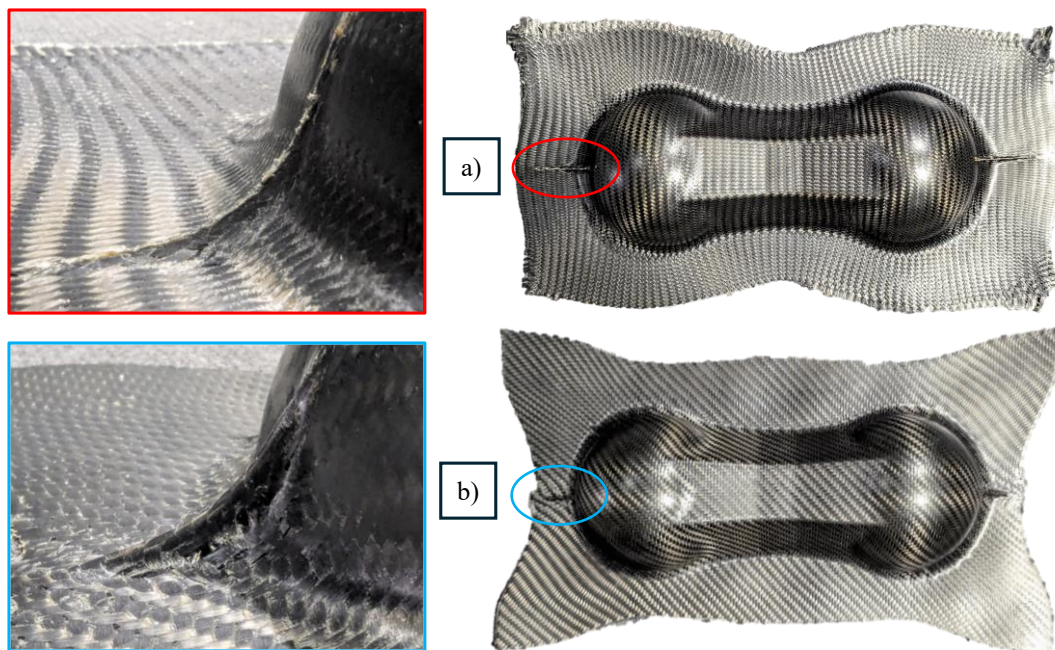


Figure 6.21: Wrinkle amplitude for forming at: a) alternative ($\pm 45^\circ$) orientation, b) alternative (3 second) rate.

A quantitative analysis was again conducted to analyse mould conformity and wrinkling behaviour, as per Figure 6.22. The outcomes from this study are also presented in Figure 6.18, with the ‘fast’ and ‘45°’ datasets relevant to this subsection. As before, the experimental repeatability is utilised to define the acceptable limits regarding simulation accuracy.

Regarding the high-speed forming simulation, the apex wrinkle amplitude (Figure 6.18a) and length (Figure 6.18b) were predicted within 0.8 mm and 1 mm respectively, although both marginally outside of the experimental accuracy; noting that experimental repeatability was very high in this case. As per the other high temperature results illustrated in Section 6.4.2, bridging (Figure 6.18c) was overestimated in the high speed simulation by 0.9 mm. As before, this may partly have been caused by thermal expansion of the silicone bag. In this case the experimental bridging was almost identical to that conducted at the same temperature, but at a slow-speed. This result is surprising, considering the findings presented in Chapter 4, where an increased slip-rate and shear-rate results in an increased CoF and shear force respectively. This indicates that the pressure distribution in the high-speed forming may not simply resemble a scaled version of that for the low-speed forming, with the vacuum tanks potentially allowing for a lower rig pressure to be achieved, not modelled in the simulation. Shear behaviour at the high forming rate was, however, well within the experimental range (Figure 6.18d).

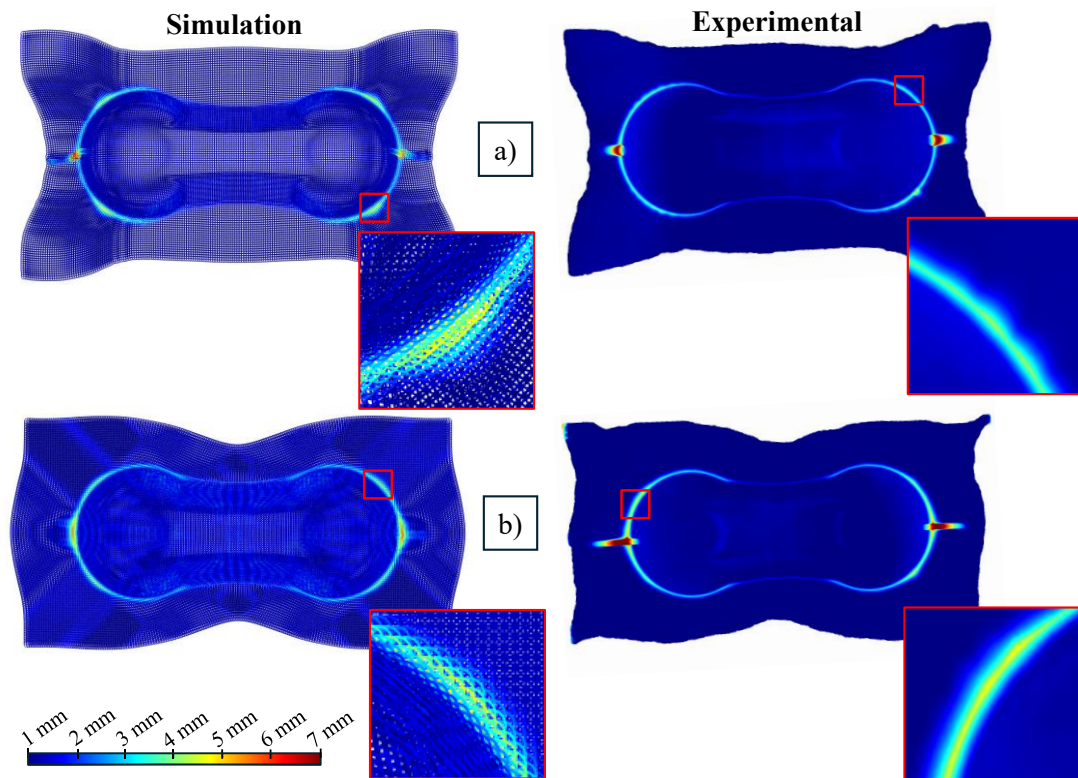


Figure 6.22: Simulated and experimental mould conformity plots, highlighting the extent of both wrinkling and bridging behaviour, for: a) alternative (3 second) rate, b) alternative ($\pm 45^\circ$) orientation.

For forming with an alternative fibre orientation, wrinkle behaviour (amplitude and length) was captured within the experimental error noting that the diaphragm wrinkle was much larger than the wrinkle in the laminate (illustrated in Figure 6.21). This meant that Figure 6.22b cannot be used to compare wrinkling behaviour visually, since the experimental scan includes the diaphragm (large wrinkle), but the numerical scan does not (small wrinkle). A secondary Abaqus output, including the diaphragm, was therefore utilised to capture the wrinkle dimensions in this case, which are presented in Figure 6.18a and Figure 6.18b. Bridging was also well captured in this case, although noting that the bridging zones were different to those with a standard laminate orientation and the large experimental error associated with this value. The simulation did appear to marginally overpredict the shear angle value (by 2.3%) compared to the experiment. In this case, the experimental error was very small since only two high-shear regions existed, both in the same direction. Thus, any differential in shear behaviour between the positive and negative direction, accounting for some of the variation in shear in the other experiments, was not present in this study.

Overall, Figure 6.18 shows that the general trend regarding wrinkle formation, bridging and shearing is captured regardless of test condition. Apart from the case at 200 °C, all simulated bridging values lay within 20% of the experimental values, and all shear values within 4%. The apex wrinkle was well predicted for all of the simulated conditions, with both amplitudes and lengths almost exclusively captured within the experimental repeatability. The only exception to this was the wrinkle length for high speed forming. Furthermore, the simulation correctly predicted other problematic areas such as the ‘rippling’ behaviour present in both high-speed and lower temperature (200 °C) tests. This also includes prediction of a bigger wrinkle on the side of the dome for the 200 °C test, although this was only present on half of the experimented domes, owing to the moderate experimental repeatability. The only large outlier in this work was therefore simulated forming at 200 °C. Therefore, the following section aims to improve simulation accuracy at lower temperatures.

6.4.4 Inhomogeneous Thermal Profile

It was hypothesised in Section 6.4.2 that the in-plane temperature distribution, illustrated in Figure 3.8, is the cause for the big discrepancy in bridging and shear behaviour between simulated and experimental thermoforming at 200 °C. This was

emphasised by analysis of the laminate edges in Figure 6.19. While at this stage it was not appropriate to consider transient thermal effects, including that of crystallisation, it was decided that this inhomogeneous thermal profile should be explored in an attempt to improve low-temperature simulation accuracy. This is similar to the standalone study by Wang *et al.* [374], who are the only authors to consider the temperature distribution before forming within a thermomechanical model, but again conduct the simulation in an isothermal manner (thermal distribution maintained constant during the test).

In this work, the thermal distribution was attained by probing values from the IR scan. Figure 6.23a illustrates this process, where the laminate temperature was probed every 10 mm in both the x- and y- directions across the laminate. This was deemed an efficient way to capture the thermal behaviour. While it would be possible to probe every single data point, this large dataset would be unwieldy. For simplicity, it was assumed that the laminate was symmetrical about the central axes, which was correct within 2 °C in all cases. These points were plotted against the datum distance, as per Figure 6.23b.

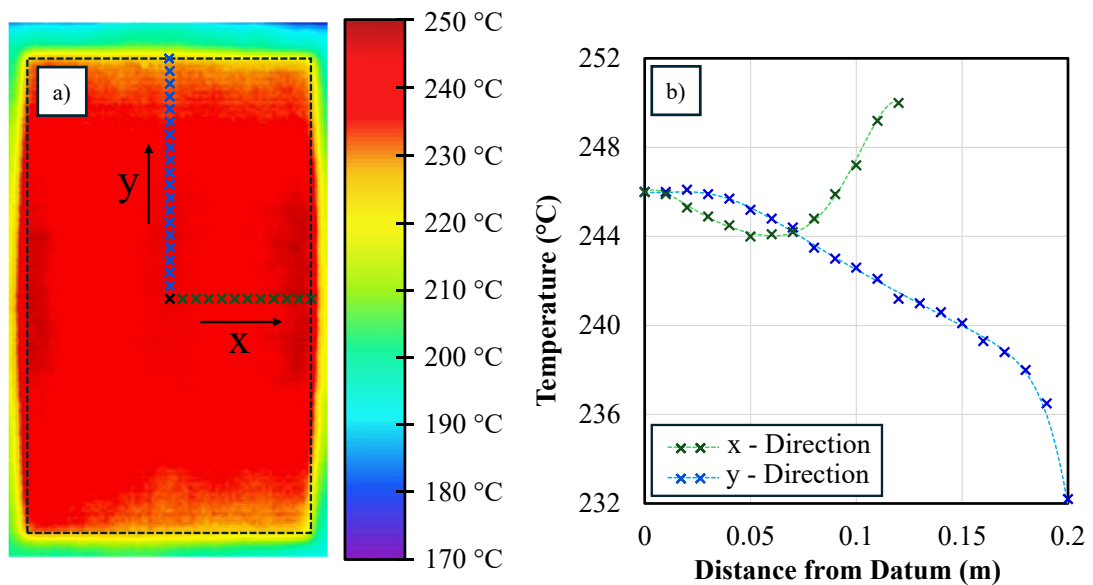


Figure 6.23: a) Probing temperature values every 10 mm in the two global laminate directions, b) Plot of laminate temperature against distance from datum (laminate centre).

A sixth and eighth order polynomial were used to parameterise the x- and y- datasets, respectively, as also illustrated in Figure 6.23b, with ‘r-squared’ values of >0.9995. This was necessary owing to the 2 mm mesh size used in the thermomechanical model,

meaning the temperature at individual nodes could be acquired. The temperature in each direction therefore represented:

$$T_x = p_1|x^6| + p_2|x^5| + p_3|x^4| + p_4|x^3| + p_5|x^2| + p_6|x| + p_7 \quad (6.16)$$

$$T_y = q_1|y^8| + q_2|y^7| + q_3|y^6| + q_4|y^5| + q_5|y^4| + q_6|y^3| + q_7|y^2| + q_8|y| + q_9 \quad (6.17)$$

Where x and y represent the relative distances from the laminate centre and p_{1-7} and q_{1-9} are constants, tabulated in Appendix A – Table D.1. These equations were then converted into a relative temperature set that allowed for the in-plane relationship to be used for multiple defined centre temperatures. This was done by dividing equations (6.16) and (6.17) by the y-intercept, such that a value of 1.00 represents the nominal value:

$$T_{Rel_x} = \frac{T_x}{p_7} \quad (6.18)$$

$$T_{Rel_y} = \frac{T_y}{q_9} \quad (6.19)$$

Therefore, the relative temperature at any point over the entire laminate could be deduced by:

$$T_{Rel} = T_{Rel_x} \cdot T_{Rel_y} \quad (6.20)$$

Since this equation operates with two directions, it can be illustrated using a 3D graph, as per Figure 6.24a. This figure only illustrates the relative temperature for a quarter of the laminate due to the aforementioned symmetry that was assumed. Equation (6.20) was subsequently implemented within Abaqus as an analytical field. This analytical field was multiplied by a boundary condition defined as T_{centre} , the temperature recorded by the pyrometer, which represents the four tested temperature in this work (250 °C, 230 °C, 210 °C and 200 °C). This enabled the calculation of the absolute temperature at each node. Figure 6.24b illustrates the in-plane thermal profile in Abaqus for a laminate at two temperatures: 250 °C and 200 °C (profile is constant but scale is different). As expected, the short-edges are the coldest areas of the profile,

with a minimum temperature of 187°C in the 200 °C centre temperature case. This is lower than the quoted crystallisation temperature (Table 3.1), which represents what is illustrated in Figure 6.19 - a small region of partially crystallised material.

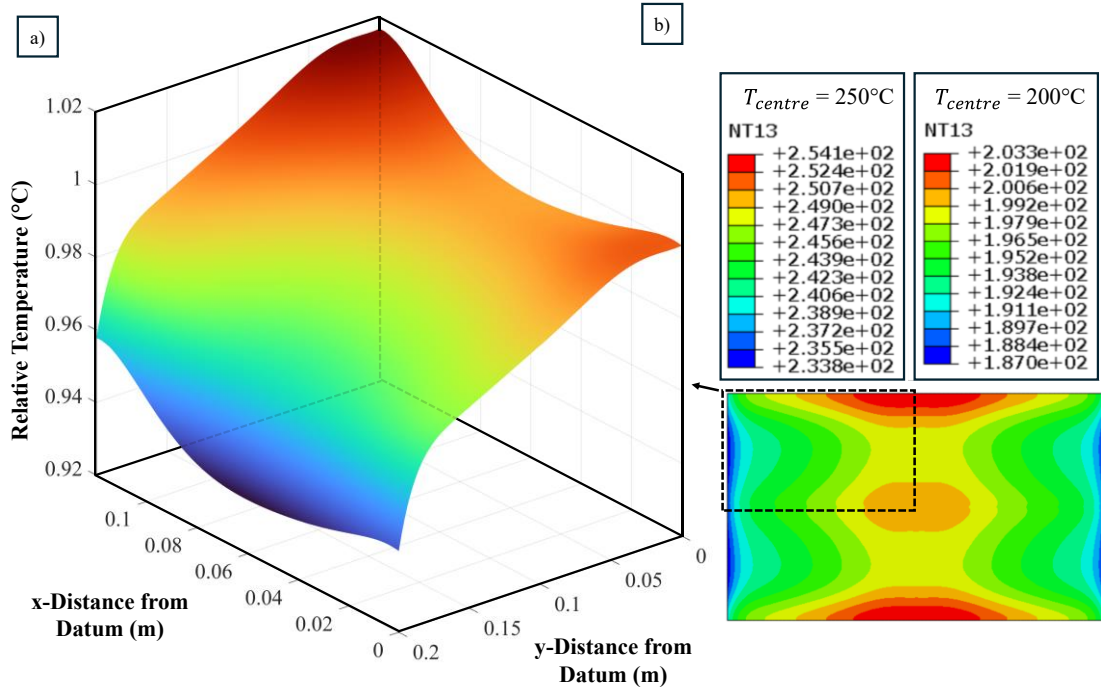


Figure 6.24: a) relative temperature as a function of laminate x- and y- distance from the centre (quarter model), b) thermal profile within Abaqus for two defined centre (pyrometer) temperatures.

In the Abaqus model, crystallisation itself was not modelled at this stage, such that the material properties (shear, bending, friction) at this lower temperature were simply extrapolated from the governing equations. This method was still expected to result in a significant effect on localised forming behaviour, even without crystallisation behaviour captured. The Abaqus thermomechanical simulation was subsequently re-run, initially for just the 200 °C centre temperature case. Figure 6.25 illustrates the Abaqus output from this study, denoted the ‘inhomogeneous temperature’ simulation, compared to the ‘homogeneous temperature’ simulation from Figure 6.16, along with the experimental scan. The nodal temperatures are output such that the inhomogeneous study is clearly identified, and the key for this profile is illustrated in Figure 6.24b.

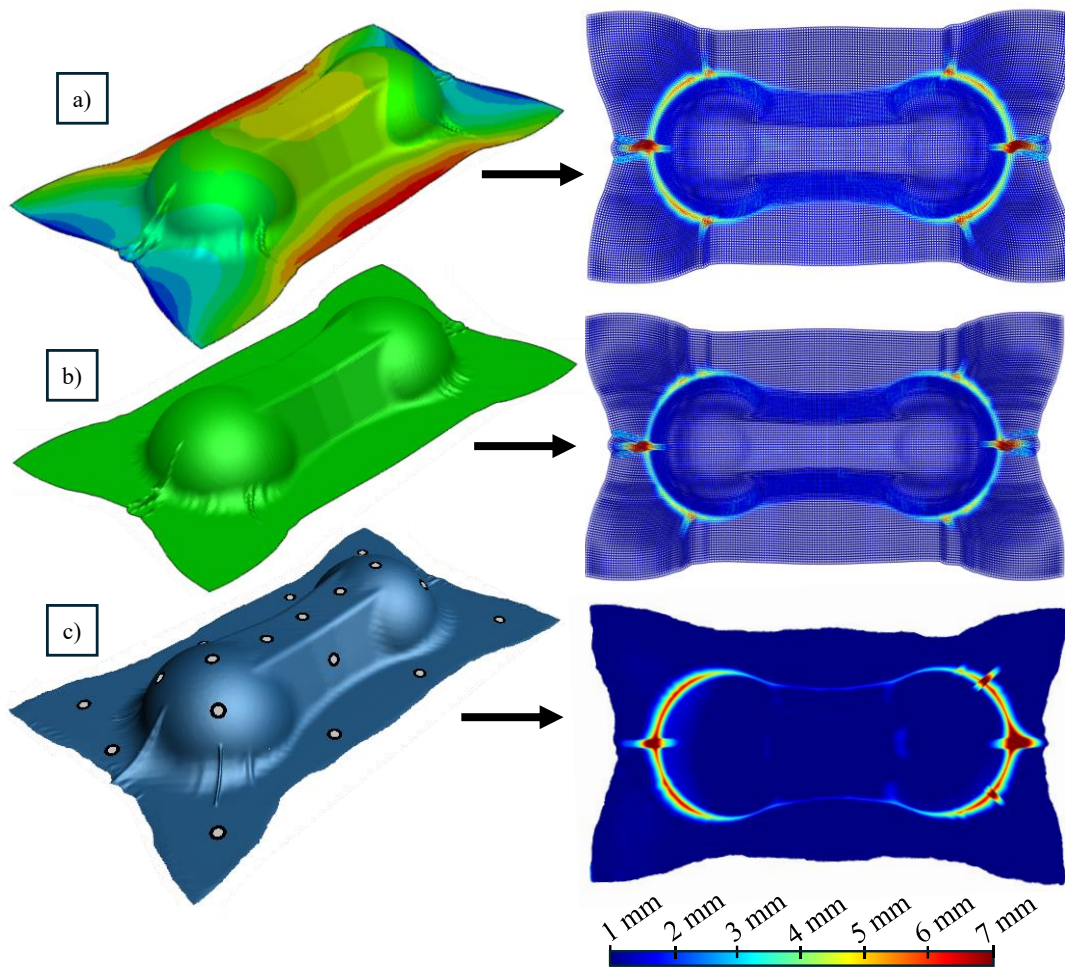


Figure 6.25: 3D scan and subsequent mould conformity plot for a laminate at 200 °C: a) inhomogeneous thermal profile, b) homogeneous (bulk) thermal profile, c) experimental result.

The main observation from Figure 6.25 can be deduced by comparing the two simulations, where it is clear that including the inhomogeneous temperature profile results in a significant increase in predicted bridging behaviour. This can also be identified on the mould conformity scans. This was caused by the cooler short-edge restricting shear movement, which can also be identified by comparing the shear output plots of the two studies (Appendix A - Figure D.3a and Appendix A - Figure D.3g). Wrinkling behaviour was marginally influenced by including the inhomogeneous profile, particularly the wrinkles on the sides of each dome, which were predicted with increased severity. As mentioned in Section 3.5.1, these were predicted on half of the experimental domes, owing to the variation in physical thermoforming results. Furthermore, in the case of the inhomogeneous study, the maximum shear angle was 4° lower than that of the homogeneous case, again more closely aligning with the 36° maximum measurement in the experimental tests.

As a comparison, the Abaqus thermomechanical simulation was again re-run with the inhomogeneous profile, but for the other centre temperatures: 210 °C, 230 °C and 250 °C. The output from the inhomogeneous 230 °C simulation is illustrated in Figure 6.26, compared to the homogeneous profile from Figure 6.16. At higher temperatures (230 °C+), almost no difference was present between the two profiles, regarding wrinkling, bridging and shear behaviour.

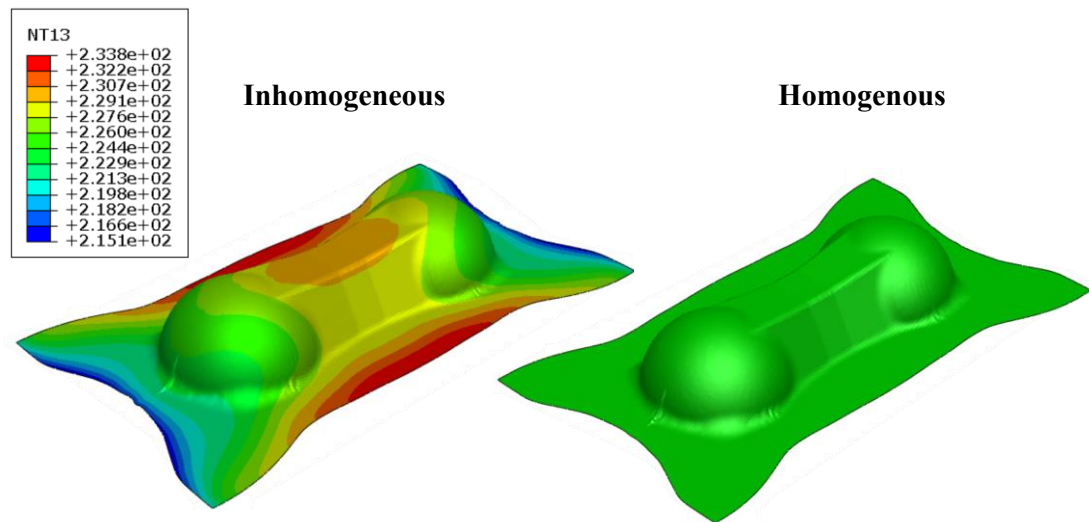


Figure 6.26: Inhomogeneous *versus* homogeneous forming simulations at 230 °C.

These results are collated in Figure 6.27, showing how the bridging and shear behaviour differs between the homogeneous and inhomogeneous thermal studies, compared to the experimental tests. As noted for the 200 °C tests, the change in apex wrinkling behaviour was marginal, however the reader is referred to Appendix A - Figure D.4 for a comparison of wrinkle amplitude and length between the two studies.

It can be concluded from these results that including an inhomogeneous profile only appears to be beneficial when forming at lower temperatures, and little difference is made to the simulated profile at higher temperatures. Including the inhomogeneous profile resulted in a significant increase in simulation accuracy for low-temperature forming, concerning bridging and shear behaviour, due to the modelled restriction of draw-in by the cooler short-edge of the laminate. Bridging was still underestimated in the model by 1.5 mm for the 200 °C case however, potentially due to the omission of crystallisation effects at this stage. It was expected that including crystallisation would have resulted in a significant reduction in localised laminate mobility, further improving the bridging and shear predictions at lower temperatures.

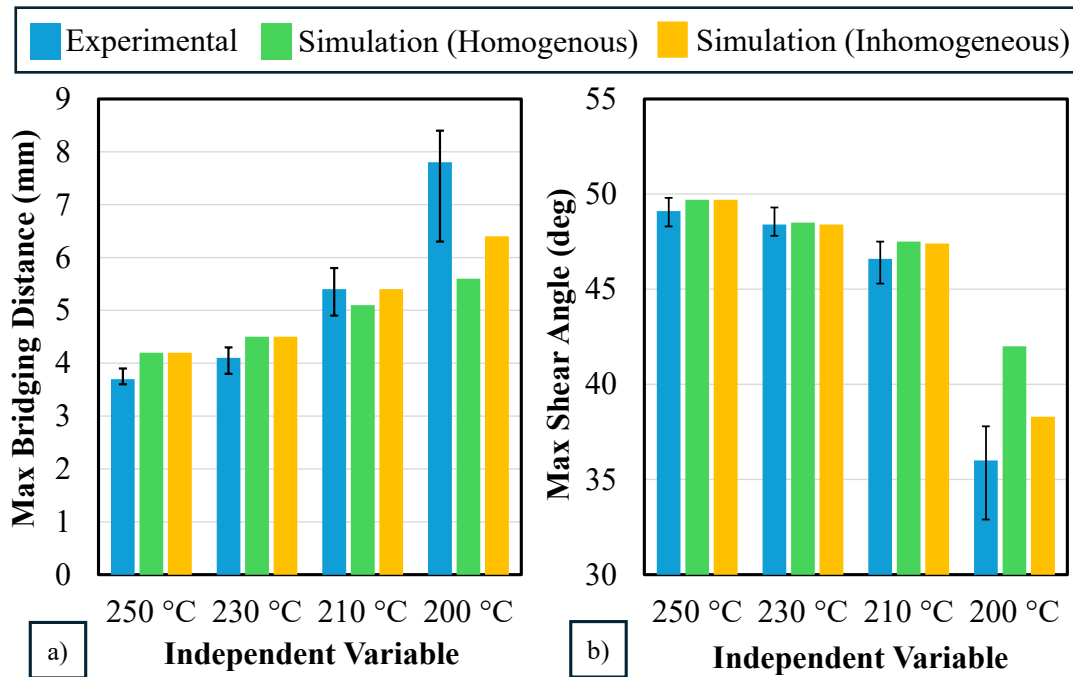


Figure 6.27: Quantitative simulation (inhomogeneous and homogeneous thermal profile) *versus* experimental results for the four tested temperatures: a) maximum bridging distance, b) maximum shear angle. Maximum values denote an average maximum from the four quarters of the double-dome geometry.

6.5 Chapter Conclusions

This chapter forms the basis for meeting the aim of this work; by producing a functional thermomechanical simulation to accurately model the FRTP DDF process, in an isothermal state, to a high level of accuracy.

After the hypoelastic model was introduced, alongside the de-coupling of membrane and bending behaviour, the characterisation exercises conducted in both Chapters 4 and 5 were subsequently modelled to validate the material inputs within a numerical routine. Viscoelastic shear behaviour was captured within the model, and although a degree of error (increasing from 20 to 100%) was introduced by virtue of the selected normalisation procedure, the BET model shows that viscoelastic shear behaviour was captured sufficiently within the simulation. Diaphragm-ply friction was captured within 18% of the experimental values in the model, owing to the errors associated with the Stribeck fitting procedure in Chapter 4. It was found that the bending

characterisation study was potentially erroneous due to buckling occurring at the cantilever support, however the model accuracy was sufficient within a set 500% range to capture wrinkle development.

These studies culminated in the creation of a full isothermal FRTP DDF model. The model was initially validated regarding its dynamic profile, diaphragm strain and initial laminate shear and perimeter profiles, with a strong correlation between simulation and experiment in each case. The maximum diaphragm strain, for example, was captured within 10% of the experimental value and the external laminate profile (at 250 °C) within 4 mm. This was followed by an in-depth study evaluating the model performance at predicting FRTP forming behaviour at a wide range of conditions including different temperatures, rates and orientations. The results found that generally the model performed well. It was able to predict the apex wrinkles for each condition generally within the experimental error, with wrinkle amplitudes all captured within 1.4 mm, and lengths within 6 mm. Furthermore, more extensive ‘rippling’ and wrinkling behaviour was correctly predicted in the case of the high-speed and 200 °C laminates. The accuracy of the model was shown to not degrade significantly with an alternative -45/45° fibre orientation or forming rate at a higher forming rate, although a small (0.9 mm) overestimation in bridging occurred in the latter case. Apart from the case at 200 °C, bridging was captured within 20% and shear within 4% of the experimental values. The small overestimation in bridging (limited to <0.5 mm) at higher temperatures was attributed to silicone thermal expansion, not captured within the model.

To improve the accuracy of the result at the lowest temperature, 200 °C, an additional study was conducted where the in-plane temperature distributions, present during the experimental thermoforming routine, were modelled within Abaqus. It was found that including these distributions significantly improves bridging and shear prediction at lower temperatures, with these errors reduced by 44% and 62% respectively. It was, however, found that including these distributions for high temperature forming made negligible difference in simulated forming behaviour, thus highlighting that a ‘bulk’ temperature is valid in these cases.

It was stated that further improvements in model accuracy at lower temperatures could be achieved by including crystallisation behaviour, which is a transient thermal

mechanism. Furthermore, for any degree of forming optimisation to be achieved (Objective #4 in this work), non-isothermal modelling would be required. Therefore, Chapter 7 considers characterising transient thermal behaviour, before re-implementation within a fully-coupled non-isothermal FRTP DDF model for process optimisation (Chapter 8).

Chapter 7.

Transient Thermal Characterisation

7.1 Introduction

The previous chapter concerning isothermal thermomechanical simulation showed that while forming behaviour is generally well captured, simulation accuracy degrades at lower temperatures due to omission of the effects of crystallisation. Furthermore, the isothermal approximation removes the possibility of laminate thermal optimisation that could streamline the forming process. Therefore, in order to develop a DDF thermomechanical simulation for the prediction and optimisation of laminate forming behaviour, it was necessary to consider transient thermal effects. To this end, it was required to characterise the non-isothermal transient thermal processes that occur within a laminate during forming.

This chapter outlines the process for which transient laminate thermal behaviour can be captured and input into a thermomechanical simulation routine. This includes transient crystallisation kinetics and heat transfer mechanisms such as convection and conduction that influence the heat flow within the laminate. A validation procedure is adopted which justifies these processes and their implementation within a numerical model proven applicable.

7.2 Methodology

It was important to consider which transient thermal processes are prominent within the FRTP thermoforming. For this, a snapshot within the FRTP forming process can be considered. Figure 7.1 illustrates a schematic of the DDF process before and after forming has been completed. The main transient heat transfer processes that occur within a laminate during thermoforming are conduction (tool-laminate and intra-laminate) and convective & radiative cooling to ambient conditions. A small amount of internal heating also acts on the laminate due to the crystallisation exotherm, with the crystallisation process itself dictating laminate mobility upon cooling. It should be noted that in contrast to the isothermal experimental thermoforming study (Chapter 3), the laminate heating was assumed to be a prerequisite process to the thermoforming operation in the non-isothermal work. This is often the case for conventional matched-tool routines (Section 2.3.1) and allows for simplification of the radiative characterisation procedure and the numerical model. While it is possible to model the

spectral distribution from the IR emitters, as per the work of Labeas [415], modelling cavity radiation within a thermomechanical model was expected to result in a significant increase in run time.

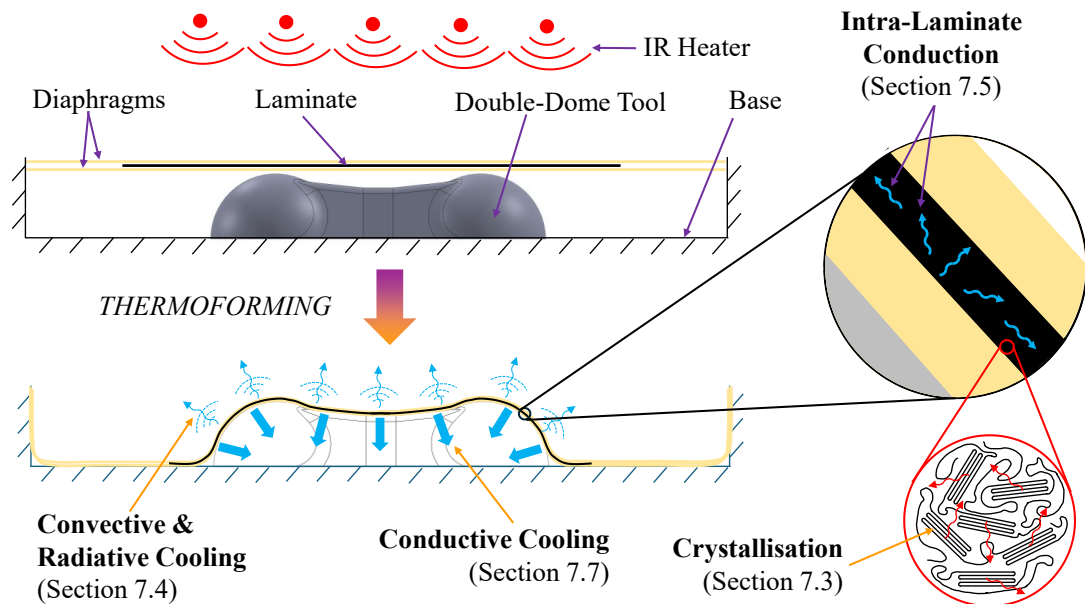


Figure 7.1: Transient thermal processes during a typical thermoforming routine.

The results presented in this chapter consider each heat transfer mechanism in-turn such that they are correctly characterised for implementation within a numerical model.

7.3 Transient Crystallisation Kinetics

This section outlines the analysis of laminate crystallisation and then uses these data to calculate the variable specific heat capacity, with the objective to characterise the crystallisation onset point and the crystallisation exotherm.

7.3.1 Cooling-Rate-dependent Crystallisation

The transient crystallisation kinetics of the CF/PA6 laminate were analysed and parameterised for input into the simulation. The kinetic behaviour informs the user of both the temperature required for melting to take place, and subsequently at what point recrystallisation (solidification) occurs. Laminate crystallinity is intrinsically linked to forming behaviour, hence its requirement as a non-isothermal simulation routine.

DSC analysis of the CF/PA6 laminate was conducted within Section 3.2.4 to attain an estimate of the laminate melting and recrystallisation point. This was subsequently used to identify appropriate temperatures for the experimental tests (Chapter 3) and thermomechanical characterisation (Chapter 4). Kugele *et al.* [89] showed, however, that the crystallisation onset point for PA6 is heavily dependent on the cooling rate using a combination of traditional DSC and Flash DSC tests (Figure 7.2). Therefore, the cooling-rate influence of laminate crystallisation was characterised in this study. This was done by utilising the data of Kugele *et al.* [89] to obtain the relative laminate crystallinity *versus* temperature at varying cooling rates.

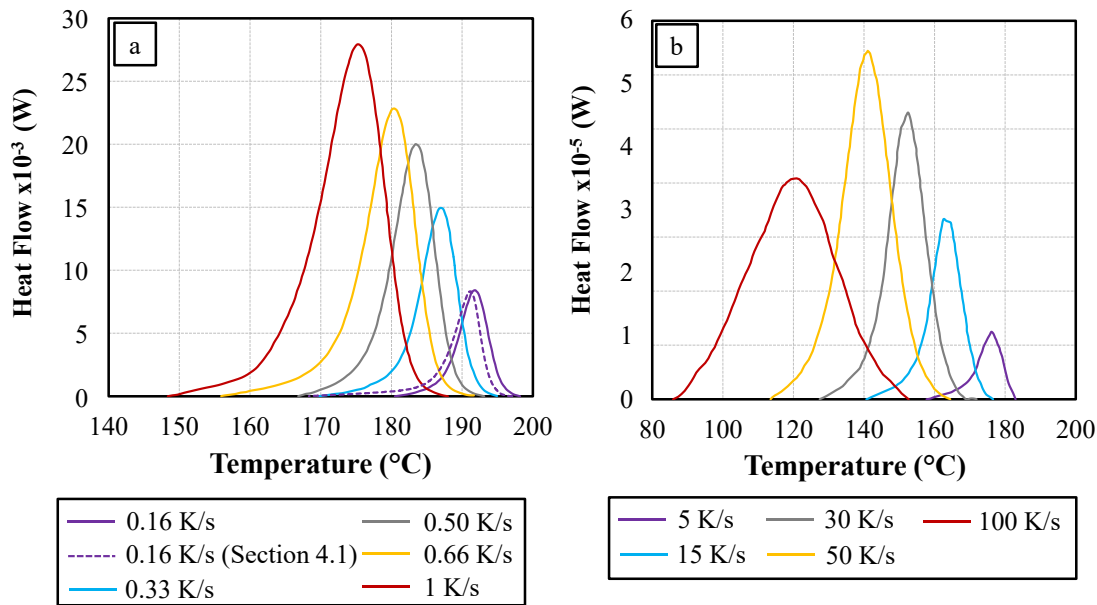


Figure 7.2: a) Standard DSC and b) Flash DSC from the work of Kugele *et al.* [89].

The experimental DSC results from Figure 3.1 have been multiplied by the sample mass and are also superimposed on this figure. A close correlation between the experimental and third-party data (0.16 °C/s) can be noted, validating the use of third-party DSC data for the CF/PA6 material used in this study. These DSC data were subsequently parameterised for input into a simulation routine. Firstly, each DSC curve was modelled using an alternative form of the Avrami equation [416], derived by Ziabicki [417, 418]:

$$Q_{cryst}(T) = K_{max} \cdot \exp\left(\frac{-4 \ln 2 (T - T_{max})^2}{D^2}\right) \quad (7.1)$$

where T is the instantaneous laminate temperature, Q_{cryst} is the absolute crystallisation heat flow (not normalised), and K_{max} , T_{max} and D are variables specific to each dataset.

The Avrami-based formulation was selected for its balance of accuracy, computational simplicity, and suitability for finite element implementation, traits that have cemented its use in modelling crystallisation kinetics of polymers [419, 420]. Unlike more complex microstructure-resolved or molecular dynamic crystallisation models, which require extensive material-specific data and are often computationally prohibitive for part-scale simulations, the Avrami approach provides a phenomenological yet reliable description of isothermal and non-isothermal crystallisation kinetics [421]. The Ziabicki-modified Avrami model in particular introduces a temperature-dependent crystallization rate constant via a Gaussian form, enabling accurate capture of transient thermal histories common in thermoforming processes [422]. Additionally, this formulation has seen widespread adoption in polymer processing simulations, particularly within semi-crystalline thermoplastic systems, due to its compatibility with DSC-derived data and its capacity to replicate both the onset and progression of crystallinity over time [89, 379]. Compared to other models such as Nakamura's extension or Scheil-type approximations, the Avrami-Ziabicki model offers a more direct route to parameterisation from experimental DSC curves without necessitating detailed nucleation or growth mechanism assumptions [422]. This makes it a pragmatic and validated choice for coupling crystallinity development with evolving thermal fields in thermomechanical simulations of FRTPs.

A Levenberg-Marquardt algorithm was used to ascertain the three variables (K_{max} , T_{max} and D) for each curve, as tabulated in Appendix E - Table E-1, with the output visualised in Figure 7.3. A minimum r^2 value of 0.968 was noted for this fitting procedure. It was observed that a very good correlation existed at each crystallisation-onset point which represents the main point of interest for this work.

To use the parameterised DSC data within a simulation routine, the relative crystallinity, $X(t)$, is often defined as a function of the absolute crystallisation enthalpy [423]. The process used by Dorr *et al.* [379] was implemented here, where:

$$X(t) = \frac{1}{\Delta H_{cryst}} H_{cryst}(t) \quad (7.2)$$

with:

$$H_{cryst}(t) = \int_{t_0}^t Q_{cryst}(T(\hat{t})) d\hat{t} \quad (7.3)$$

where ΔH_{cryst} is the absolute crystallisation enthalpy (area under each parameterised DSC curve) and t_0 is the crystallisation onset time.

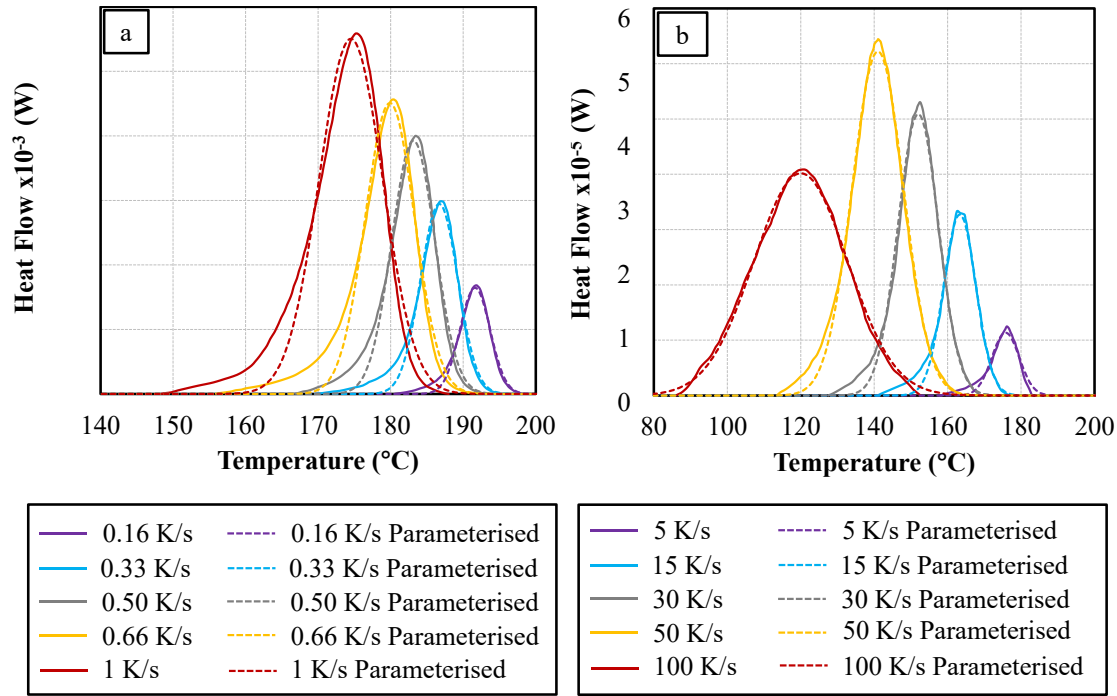


Figure 7.3: Parameterisation of DSC data for a) Standard DSC and b) Flash DSC (data from the work of Kugele *et al.* [89]).

$$X(t) = \frac{1}{\Delta H_{cryst}} H_{cryst}(t)$$

$$H_{cryst}(t) = \int_{t_0}^t Q_{cryst}(T(\hat{t})) d\hat{t}$$

Combining Equations (7.1) & (7.3) results in the following indefinite integral for the absolute crystallisation enthalpy:

$$H_{cryst}(t) = K_{max} \cdot \frac{D\sqrt{\pi}}{2\sqrt{\ln 2}} \cdot \operatorname{erf}\left(\frac{\sqrt{4 \ln 2}}{D} \cdot [T(\hat{t}) - T_{max}]\right) + C \quad (7.4)$$

where C is the constant of integration. The error function (erf) is present in this equation due to the Gaussian form of the integrand. Figure 7.4 illustrates the relative crystallinity (Equation (7.2)) for CF/PA6 laminates at 10 defined cooling rates.

While Equation (7.4) represents the absolute form of the integrated DSC curves, it is mathematically complex, especially when implemented with Equation (7.2). Furthermore, since each cooling rate had a unique value for the constants K_{max} , T_{max} and D , its implementation within a numerical model was unwieldy. To simplify this procedure, a Levenberg-Marquardt algorithm was used to fit exponential regression function to each curve in the form of:

$$X(t) = 1 - \frac{1}{1 + \exp[-C \cdot (T(\hat{t}) - T_{max})]} \quad (7.5)$$

where C is a constant specific to each cooling rate. The fitting process yielded a minimum ‘r squared’ value of 0.9999 illustrating little to no influence on the model accuracy, however providing a simpler input for numerical models. The curves calculated using this equation are also illustrated in Figure 7.4 (see ‘Parameterised’).

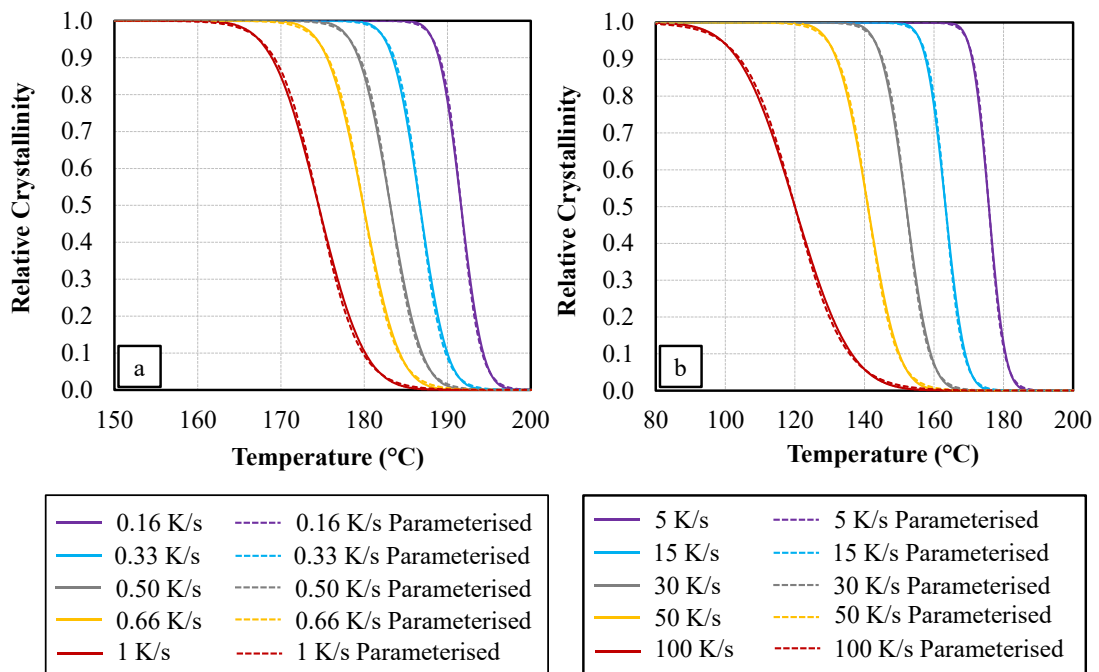


Figure 7.4: Relative crystallinity of CF/PA6 at various cooling rates as calculated using a) Standard DSC, b) Flash DSC (data from the work of Kugele *et al.* [89]).

$$X(t) = 1 - \frac{1}{1 + \exp[-C \cdot (T(\hat{t}) - T_{max})]}$$

The values for all constants used in Equation (7.5) are tabulated in Appendix E - Table E-1. For implementation within a numerical model, as per the work of Dorr *et al.* [379], linear interpolation can be used between defined cooling-rates to identify the values of these constants.

7.3.2 Specific Heat Capacity

Specific heat capacity is a physical property of the thermoplastic composite that measures the amount of heat required to change the temperature of a unit mass of the laminate by one degree Celsius. It is dependent on the molecular structure of the target specimen, with a high specific heat capacity indicating that significant energy is required to attain a change in temperature. It is a requirement for a thermally coupled simulation as it is intrinsically linked to the thermal behaviour of a FRTP composite. Moreover, it was hypothesised that considering the crystallisation exotherm within the calculation of the specific heat capacity would allow for prediction of the exotherm within a thermomechanical model.

The DSC tests conducted for the analysis of laminate crystallisation kinetics can also be used to ascertain the specific heat capacity of the CF/PA6 laminates [424]:

$$c_p = \frac{Q_{cryst}}{m \cdot \dot{T}_{cool}} \quad (7.6)$$

where c_p is the specific heat capacity (constant pressure), m is the sample mass and \dot{T}_{cool} is the cooling rate. Combining Equations (7.1) & (7.6) yields the following equation for laminate specific heat capacity:

$$c_p = \frac{K_{max} \cdot \exp\left(\frac{-4 \ln 2 (T - T_{max})^2}{D^2}\right)}{m \cdot \dot{T}_{cool}} + \frac{Q_{baseline}}{\dot{T}_{baseline_cool}} \quad (7.7)$$

in which the constants K_{max} , T_{max} and D are specific to each cooling rate and are tabulated in the Appendix E - Table E-1. The term $Q_{baseline}$ is associated with the baseline linear DSC results (with a cooling rate of $0.16 \text{ }^\circ\text{C/s}$ ($\dot{T}_{baseline_cool}$)) that were initially subtracted from the DSC curves illustrated in Figure 7.2.

As per the parameterisation of relative crystallinity (Section 7.3.1), linear interpolation of the constants can be used between the 10 defined cooling rates to ascertain the specific heat capacity over the entire cooling-rate range. The term $Q_{baseline}$ was calculated by fitting a linear polynomial to the baseline data of the experimental DSC results (Figure 3.1). Figure 7.5 illustrates this process, where a Levenberg-Marquardt algorithm was used, omitting all data points in proximity of the crystallisation exotherm. Therefore, after conversion to full SI units, the baseline DSC curve is equal to:

$$Q_{baseline} = 0.9271T + 151.8 \quad (7.8)$$

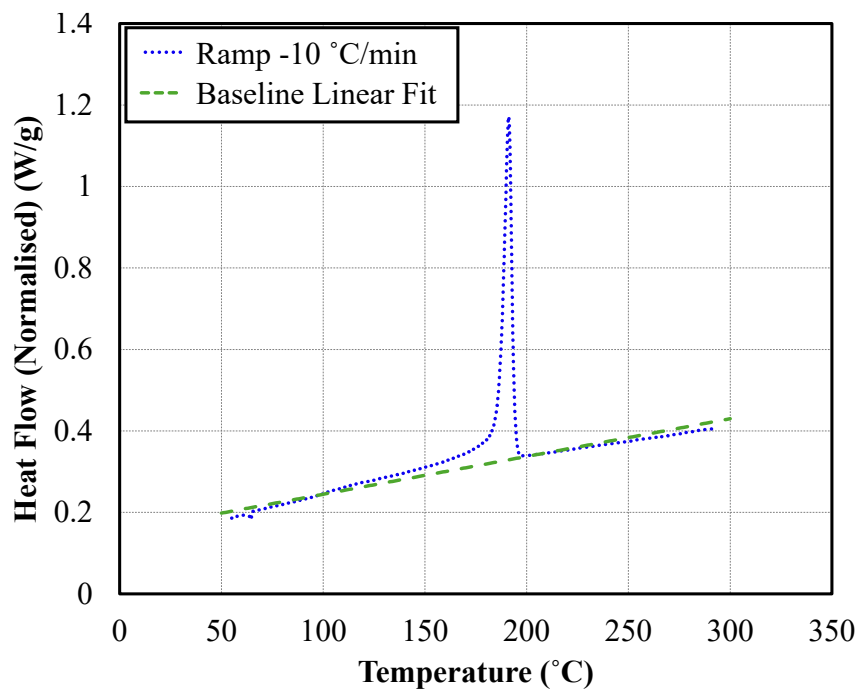


Figure 7.5: Baseline curve fitting on experimental DSC data.

Finally, using Equation (7.7), the specific heat capacity of CF/PA6 laminates at a range of different cooling rates was calculated, as per Figure 7.6.

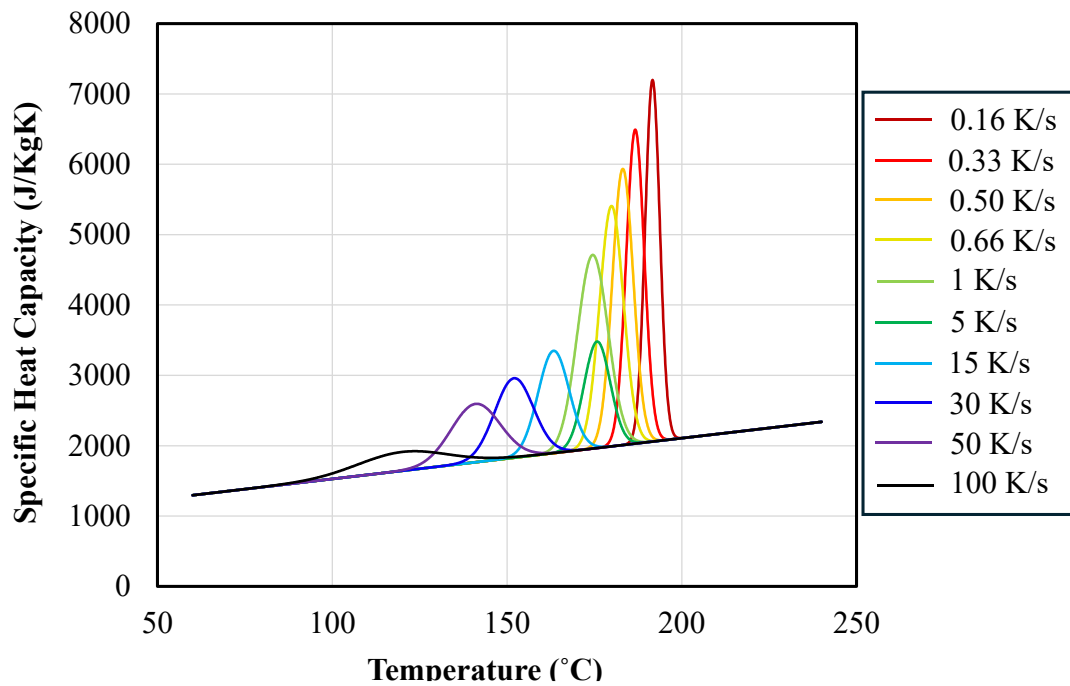


Figure 7.6: Specific heat capacity of CF/PA6 laminates at a range of cooling rates.

Higher cooling rates result in a lower absolute exotherm (area under each curve) which is also indicative of a lower degree of absolute crystallisation. Furthermore, the lower exotherm results in a smaller impediment to cooling, compared to a low cooling-rate where the exotherm is greater, further reducing the cooling speed.

The increasing specific heat capacity of the laminates during crystallisation allows a numerical model to capture the exothermic behaviour of the process which is important if the thermal-time history is to be captured accurately within a simulation routine.

7.4 Convective and Radiative Heat Transfer

Convection and radiation are the main drivers of laminate cooling before tool-contact is made, therefore accurate characterisation is necessary such that transient processes are modelled over the entirety of the forming process.

7.4.1 Convection

One of the primary methods of laminate heat-loss is the natural convection of heat from both the top and bottom surfaces of the thermoplastic composite laminate. With the FRTP at temperature, the surrounding air is heated and subsequently rises away

from the laminate, drawing more cool air in for the process to repeat (Figure 7.7). The magnitude at which the surrounding air is heated up is therefore highly dependent on the laminate temperature, with increased temperatures causing strengthened eddy currents around the laminate surface.

The amount of heat loss by virtue of convection from the surface of an object can be described using Newton's law of cooling [425]:

$$q_{convection} = hA(T_a - T_{lam}) \quad (7.9)$$

where $q_{convection}$ is the heat loss due to convection, h is the convective heat transfer coefficient, A is the characteristic length of the subject, T_{lam} is the laminate temperature and T_a is the ambient temperature. For valid functionality of these equations, the unit of temperature is Kelvin (K). Hence, it is both the convective heat transfer coefficient and the laminate temperature that dictate the speed at which heat is lost from each laminate surface. In order to compute the convective heat transfer coefficient, h , it was required that the thermal properties of air (the medium to which convection takes place) were calculated. The results presented in this chapter follow the works of Nellis *et al.* [426] and Fujii *et al.* [427].

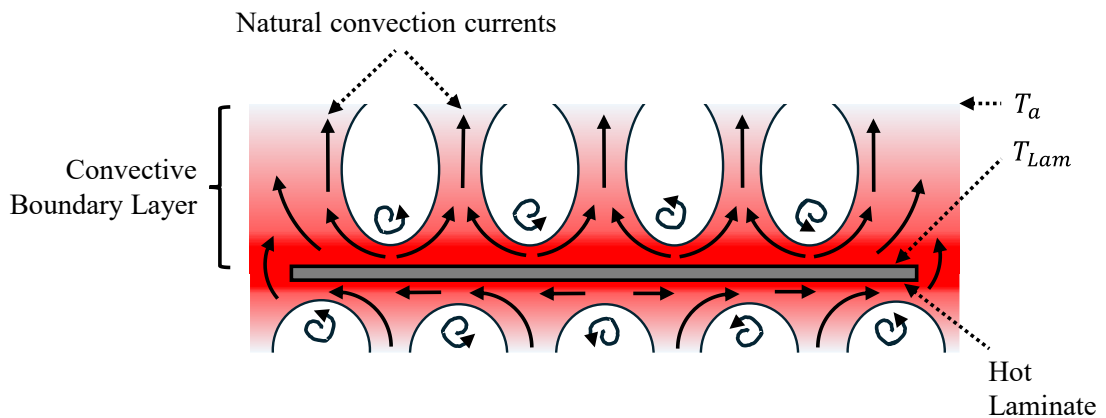


Figure 7.7: Convection currents from a hot horizontal plate.

Firstly, the film temperature can be defined as the temperature of the boundary layer (Figure 7.7), representing an average temperature between the laminate and the air:

$$T_{film} = \frac{T_{lam} + T_a}{2} \quad (7.10)$$

It is the film temperature that guides the calculation of the heat transfer coefficient, h . The density, ρ_{air} , of air can be defined using the perfect gas law [428]:

$$\rho_{air} = \rho_{amb} \cdot \frac{T_a}{T_{film}} \quad (7.11)$$

where ρ_{amb} is the air density, defined in this work as 25 °C. Next, the remaining thermal properties of air were defined. The thermal conductivity of air, k_{air} , can be deduced using the Sutherland equation [429]:

$$k_{air} = k_0 \cdot \left(\frac{T_{film}}{T_0}\right)^{\frac{3}{2}} \cdot \frac{T_0 + S_k}{T_{film} + S_k} \quad (7.12)$$

Where k_0 , S_k and T_0 are constants that can also be found in the work of White [429], and have been tabulated in Appendix E - Table E-2. The dynamic viscosity, can be deduced using an alternative form of the Sutherland equation [429]:

$$\mu_{air} = \mu_0 \cdot \left(\frac{T_{film}}{T_0}\right)^{\frac{3}{2}} \cdot \frac{T_0 + S_\mu}{T_{film} + S_\mu} \quad (7.13)$$

where μ_0 and S_μ are constants that can also be found in the work of White [429]. The specific heat capacity of air was determined experimentally by Razak [430] and parameterised using a seventh order polynomial by Mattingly [431] as follows:

$$c_{p_air} = a_0 + a_1 T_{film} + a_2 T_{film}^2 + \dots + a_7 T_{film}^7 \quad (7.14)$$

where $a_{1...7}$ are constants, also tabulated in Appendix E - Table E-2. These intrinsic properties of air (Equations (7.10) - (7.14)) are visualised in Appendix E - Figure E.1 to clearly illustrate the film temperature dependence of each.

Finally, the last intrinsic property of air to be defined, the thermal expansion coefficient, is also temperature dependent, as per [432]. In this case, only the raw data was provided with no corresponding polynomial. Therefore, for the purposes of this work, a first-order power curve was fitted to the data using a Levenberg-Marquardt algorithm, with an ‘r-squared’ value of 1.00. Figure 7.8 illustrates this power fit. The power-curve took the form of:

$$\beta_{air} = b_0 \cdot T_{film}^{b_1} \quad (7.15)$$

where b_0 and b_1 are constants, tabulated in Table C-1.

$$v_{air} = \frac{\mu_{air}}{\rho_{air}}$$

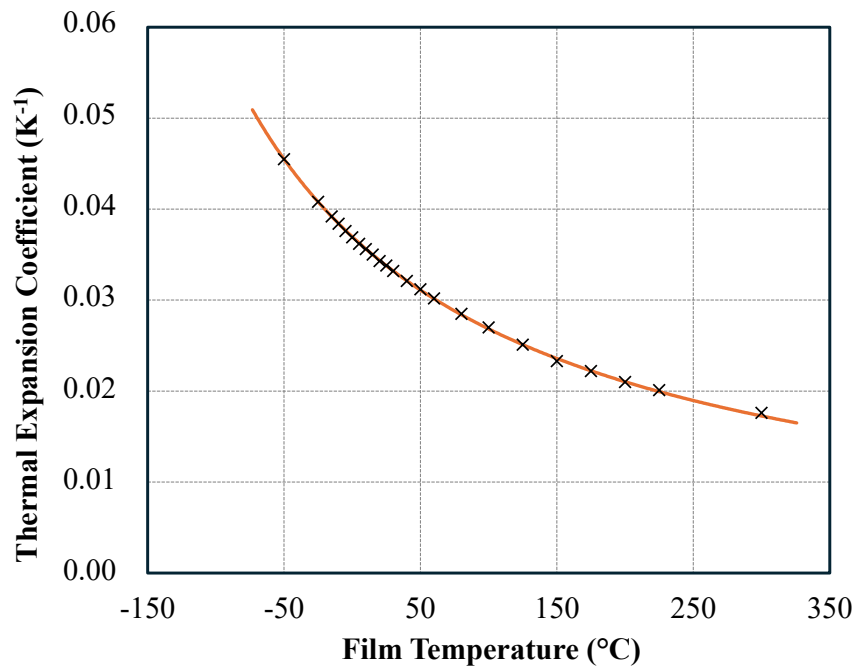


Figure 7.8: Thermal expansion coefficient *versus* temperature for air.

Utilising Equations (7.10) - (7.15), a series of other air properties could be defined that were required for the calculation of the convective heat transfer coefficient. The kinematic viscosity can be simply deduced using the dynamic viscosity from the following equation [433]:

$$v_{air} = \frac{\mu_{air}}{\rho_{air}} \quad (7.16)$$

Furthermore, the thermal diffusivity of air, a ratio between the heat conducted and the heat stored, can be calculated using the air density (Equation (7.11)), conductivity (Equation (7.12)) and specific heat capacity (Equation (7.14)) using the following relationship [434]:

$$a_{air} = \frac{k_{air}}{\rho_{air} \cdot c_{p_air}} \quad (7.17)$$

There exists a series of dimensionless numbers that describe fluid characteristics within a convective boundary layer. The Prandtl number, Pr , signifies the relative

thickness of the velocity boundary layer to that of the thermal boundary layer [435]. Utilising equations (7.16) & (7.17), it can be defined as:

$$Pr = \frac{v_{air}}{a_{air}} \quad (7.18)$$

Another dimensionless number that can be defined is the Grashof number, which describes the ratio of buoyancy forces to viscous forces within the convective boundary layer [435]. The Grashof number, Gr , can be defined using the following:

$$Gr = \frac{g\beta_{air}(T_{film} - T_a)L_c^3}{v_{air}^2} \quad (7.19)$$

where g is the acceleration due to gravity and L_c is the characteristic length of the specimen undergoing convection. For a rectangular specimen, the characteristic length can be defined as:

$$L_c = \frac{A_c}{P_c} = \frac{L_{s1} \cdot L_{s2}}{2(L_{s1} + L_{s2})} \quad (7.20)$$

where A_c is the specimen area, P_c is the specimen perimeter, and L_{s1} and L_{s2} are the rectangular side lengths.

Moreover, the Rayleigh number, Ra , is used to characterize the convective flow regime [436]. Specifically, it helps determine whether the flow will be laminar or turbulent, and how heat is transferred from the specimen to the surrounding air. The Rayleigh number is defined as the product of the Grashof number and the Prandtl number:

$$Ra = Gr \cdot Pr \quad (7.21)$$

A low Rayleigh number ($<10^3$) symbolises that the heat transfer is dominated by thermal conduction of heat from the specimen to the surrounding air that remains largely stationary. In contrast, a high Rayleigh number ($>10^6$) dictates that turbulent convective buoyancy forces govern the heat transfer process [437]. A transition region exists between the two, where laminar convection is prominent.

Combining Equations (7.16) - (7.21), the Rayleigh number can be interpolated directly from the laminate temperature. For the purposes of this heat transfer study, an initial specimen side length of 100 mm was used to reduce in-plane thermal distributions during a validation exercise detailed in Section 7.6. Moreover, acceleration due to

gravity was equal to 9.81 ms^{-2} , an ambient temperature of $25 \text{ }^\circ\text{C}$ and all thermal properties of air defined using Equations (7.10) - (7.15). Figure 7.9 therefore illustrates the range of Rayleigh number values specific to this work. It can be seen that the Rayleigh number remains almost entirely within the laminar convection region ($10^4 < Ra < 10^6$) for a rectangular specimen with side lengths of 100 mm, surrounded by air.

The Nusselt number, Nu , represents a dimensionless temperature gradient at the surface of the specimen, providing a measure of the convection taking place [437]. The work of McAdams [438] is often used for two empirical relationships for the Nusselt number, in this case for a horizontal plate. Note that the relationship to be used is dependent on the magnitude Rayleigh number:

$$Nu_{upper} = 0.54 \cdot Ra^{0.25} \quad 10^4 < Ra < 10^6 \quad (7.22)$$

(Laminar)

$$Nu_{lower} = 0.27 \cdot Ra^{0.25}$$

$$Nu_{upper} = Nu_{lower} = 0.15 \cdot Ra^{0.33} \quad 10^6 < Ra < 10^9 \quad (7.23)$$

(Turbulent)

Where Nu_{upper} and Nu_{lower} refer to the Nusselt number of the top and bottom surfaces of the specimen, respectively. Considering that the Rayleigh number remains within the laminar region, the Nusselt numbers for the top and bottom surfaces of a horizontal laminate are also plotted in Figure 7.9.

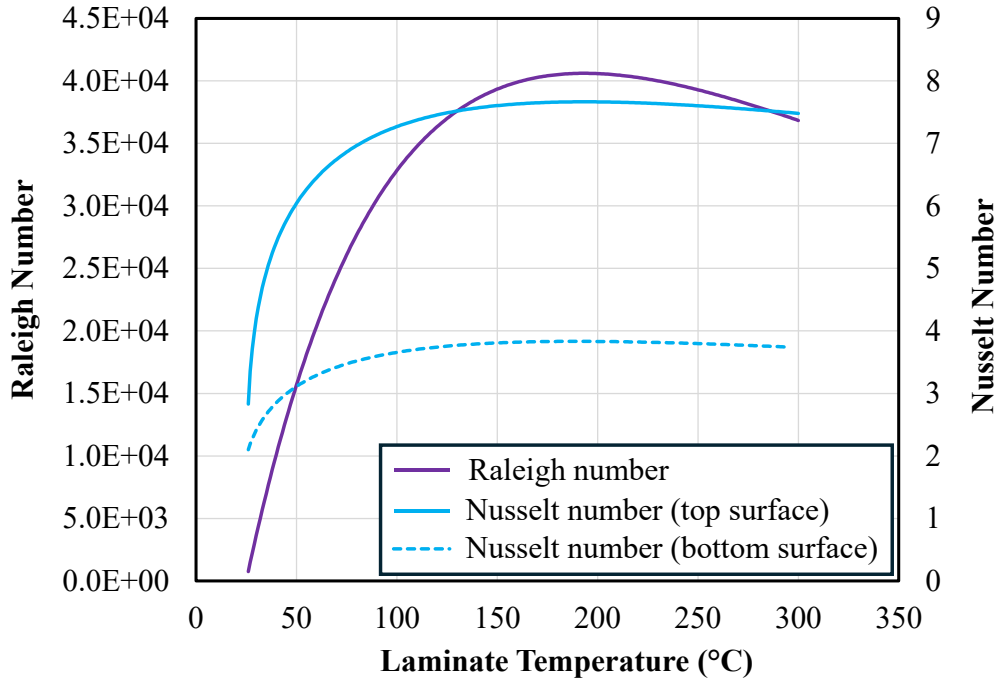


Figure 7.9: Rayleigh number and Nusselt number *versus* film temperature for a 100 mm wide laminate surrounded by air.

Finally, the average heat transfer coefficient, h , can be determined using the Nusselt number using the following relationship:

$$h = \frac{Nu \cdot k_{air}}{L_c} \quad (7.24)$$

Therefore, the convective heat transfer coefficient of a horizontal rectangular laminate with side lengths of 100 mm x 100 mm can be calculated, as illustrated in Figure 7.10.

To parameterise the calculated heat transfer coefficient at different temperatures, therefore providing a convenient input for a numerical model, a first-order power curve was fitted to the data. A Levenberg-Marquardt algorithm was used for this process, with an 'r-squared' value of 0.996. The final heat transfer coefficient for the lower, h_{lower} , and upper, h_{upper} , laminate surfaces could therefore be represented by:

$$h_{lower} = h_{l0} \cdot (T_{lam} - T_a)^{h_{l1}}, \quad h_{upper} = h_{u0} \cdot (T_{lam} - T_a)^{h_{u1}} \quad (7.25)$$

Where h_{l0} , h_{u0} , h_{l1} and h_{u1} are constants, tabulated in Appendix E - Table E-2. Using the calculated heat transfer coefficient, Newton's law of cooling (Equation (7.9)) could be used to determine the convective heat loss.

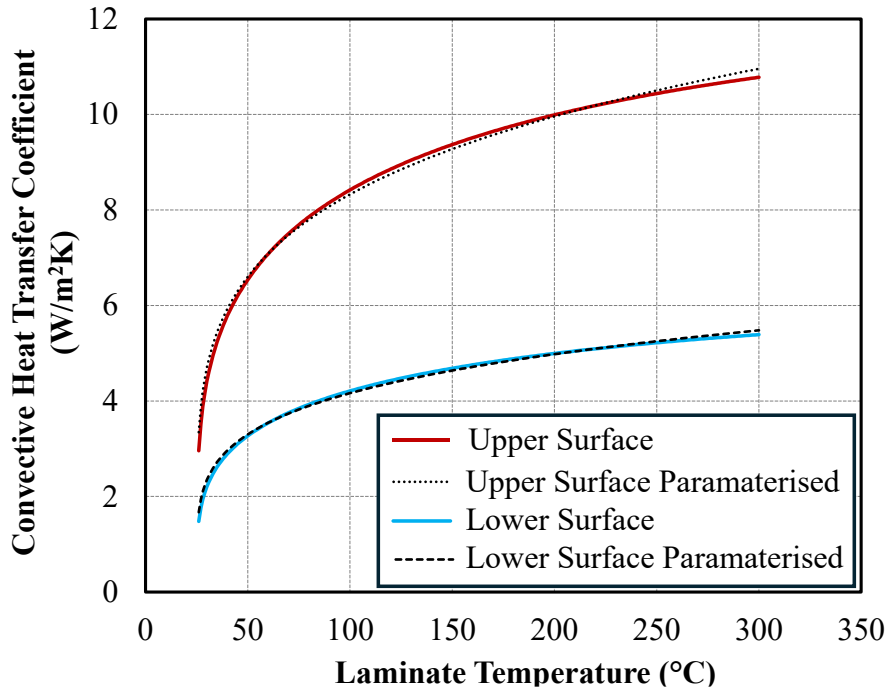


Figure 7.10: Convective heat transfer coefficient *versus* temperature for a 100 mm x 100 mm laminate in air.

7.4.2 Radiation

While radiative heating was neglected in this work (for computational simplicity), it would not be appropriate to neglect the influence of radiative cooling from the laminate surface. Similarly to convective cooling, the radiative heat flow, q_{rad} , can be represented using the Stefan-Boltzmann equation [439]:

$$q_{rad} = \varepsilon \sigma_{sb} (T_a - T_{lam})^4 \quad (7.26)$$

Where ε represents the emissivity of the laminate within the infrared spectrum, and σ_{sb} represents the Stefan-Boltzmann constant. The laminate emissivity, unlike convection that is dependent on the surrounding fluid (air), is a property associated solely with the heated substrate.

A relatively simple approach was adopted to calculate the emissivity of the CF/PA6 laminates used in this study. Four Type-K thermocouples were affixed to a small (50 x 50 mm, single-ply) test specimen using epoxy resin. The specimen was then mounted on a heated plate such that a pre-defined temperature was attained (Figure 7.11a).

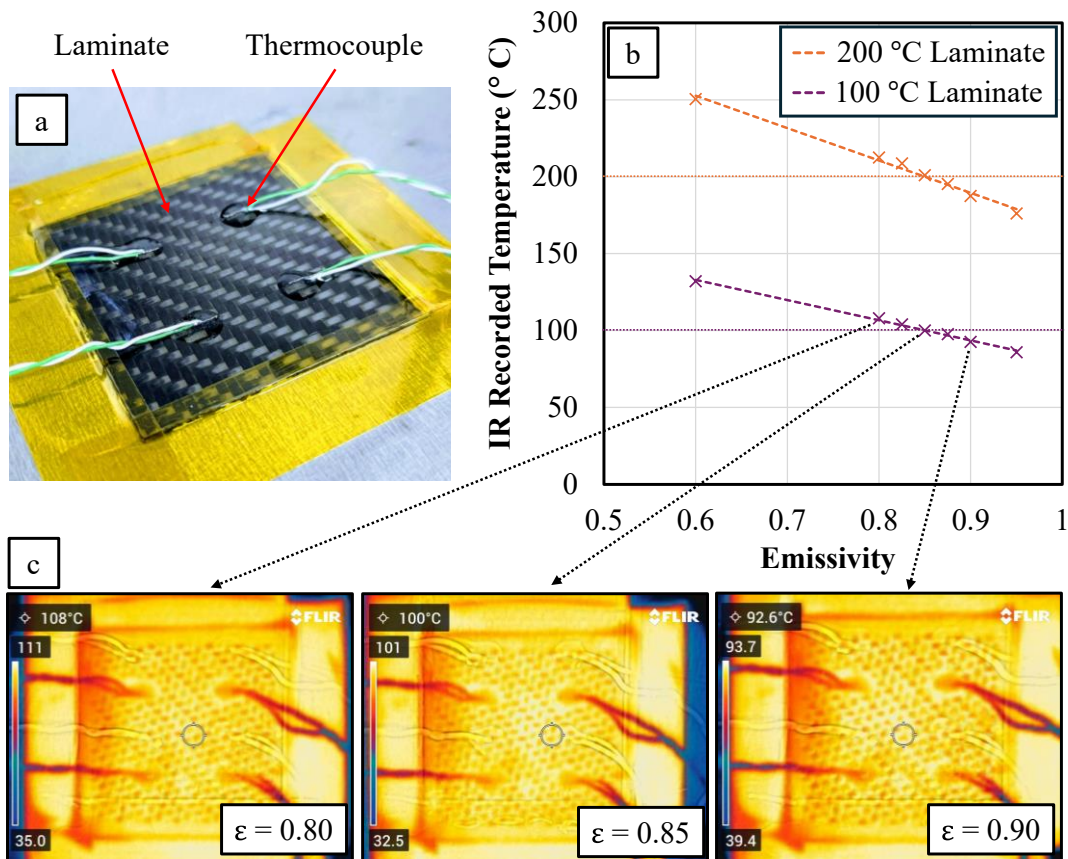


Figure 7.11: CF/PA6 emissivity calculation: a) experimental setup, b) recorded (camera) temperature *versus* emissivity, c) IR images at different emissivity values

Finally, a FLIR C5 IR camera was used to photograph the laminate at temperature, with the internal emissivity setting within the camera adjusted until it recorded the same temperature as the thermocouples. For this exercise, two different temperatures below the laminate melting temperature were selected, 100 °C and 200 °C, to evaluate the emissivity over a wide range.

Figure 7.11b illustrates the results from this study, where an emissivity value of 0.85 best matched the IR camera and thermocouple reading at both measured temperatures.

Figure 7.11c represents the IR camera output for a laminate at 100 °C, with three different selected emissivity values.

7.5 Intra-Laminate Conductivity

Intra-laminate conductivity describes the movement of thermal energy within the heated FRTP laminate. While conductivity is often considered isotropic for generic materials such as metallics, unreinforced plastics and ceramics, composite materials, by nature, exhibit anisotropic thermal conductivity. This is due to the heterogeneous structure of composites with different constituents exhibiting contrasting thermal properties. With regard to thermoforming, it is important that laminate conductivity is considered as it has a large influence on the global temperature field and therefore forming behaviour. It is required that a global conductivity tensor, K_c , be calculated for any numerical model where non-isothermal laminate behaviour is considered.

To calculate the global conductivity tensor, one must consider the thermal properties of the individual constituents and their architecture within the laminate. Due to the periodic nature of the material properties and geometry, a homogenisation technique can be employed using specific boundary conditions on a single representative volume element (RVE). For the purposes of this work, the homogenisation technique proposed by Özdemir *et al.* [440] and implemented for thermoplastic composite forming by Guzman-Maldonado *et al.* [345] was used.

Firstly, a thermal gradient is imposed at the macroscopic scale, thus resembling typical conditions that a laminate could undergo during a forming process. This thermal gradient is then transferred into the mesoscopic scale as a boundary condition. Mathematically, the average temperature gradient at the mesoscopic scale, δT_m , can be related to the macroscopic temperature gradient, δT_M , as shown in the work of Özdemir *et al.* [440], where V is the RVE volume:

$$\frac{1}{V} \int_V \delta T_m dV = \delta T_M \quad (7.27)$$

After application of this thermal boundary condition, the normalised macroscopic heat flux, q_M , can be calculated by ascertaining an average value for the normalised mesoscopic heat flux, q_m :

$$\frac{1}{V} \int_V q_m dV = q_M \quad (7.28)$$

Özdemir *et al.* [440] showed that combining Equations (7.27) and (7.28) results in equilibrium entropy between the macro- and mesoscopic scale:

$$\frac{1}{V} \int_V \delta T_m q_m dV = \delta T_M q_M \quad (7.29)$$

Finally, after numerical calculation of the macroscopic heat flux, the macroscopic conductivity can be calculated using Fourier's law for conduction, illustrated here in matrix form:

$$\begin{bmatrix} q_{M1} \\ q_{M2} \\ q_{M3} \end{bmatrix} = \begin{bmatrix} K_{11} & K_{12} & K_{13} \\ K_{21} & K_{22} & K_{23} \\ K_{31} & K_{32} & K_{33} \end{bmatrix} \cdot \begin{bmatrix} \delta T_{M1} \\ \delta T_{M2} \\ \delta T_{M3} \end{bmatrix} \quad (7.30)$$

Where δT_{M1} , δT_{M2} and δT_{M3} are three individual boundary conditions (temperature gradients) defined in each element direction, and K_{11-33} are the anisotropic conductivity components. The off-diagonal terms can be neglected within the macroscopic conductivity equation if the global principal axes are colinear with that of the RVE [441]. Therefore, Equation (7.30) becomes:

$$\begin{bmatrix} q_{M1} \\ q_{M2} \\ q_{M3} \end{bmatrix} = \begin{bmatrix} K_1 & 0 & 0 \\ 0 & K_2 & 0 \\ 0 & 0 & K_3 \end{bmatrix} \cdot \begin{bmatrix} \delta T_{M1} \\ \delta T_{M2} \\ \delta T_{M3} \end{bmatrix} \quad (7.31)$$

Where K_{1-3} are the conductivities for each principal axis. Equation (7.31) allows the global thermal conductivity tensor to be calculated for any FRTP laminate.

The homogenisation technique was implemented within an Abaqus routine so the intricate geometry of the RVE could be modelled accurately. Firstly, it was necessary to reproduce an accurate RVE of the selected woven CF/PA6 material. For this process to be conducted accurately, microscopy was used on a 4-ply sample of CF/PA6 to analyse the fabric architecture in detail. The 4-ply laminate had identical single-ply properties to that of the laminates utilised previously in this work. It was considered sufficient to solely analyse a large 2D image of the microstructure rather than acquire scanned 3D models due the repetitive nature of the internal structure that can be visualised at various points on one image. Figure 7.12 illustrates the results of this microscopy, in which the lenticular tow geometry was noted, with an average width and depth determined as 1.60 ± 0.07 mm and 0.15 ± 0.03 mm respectively.

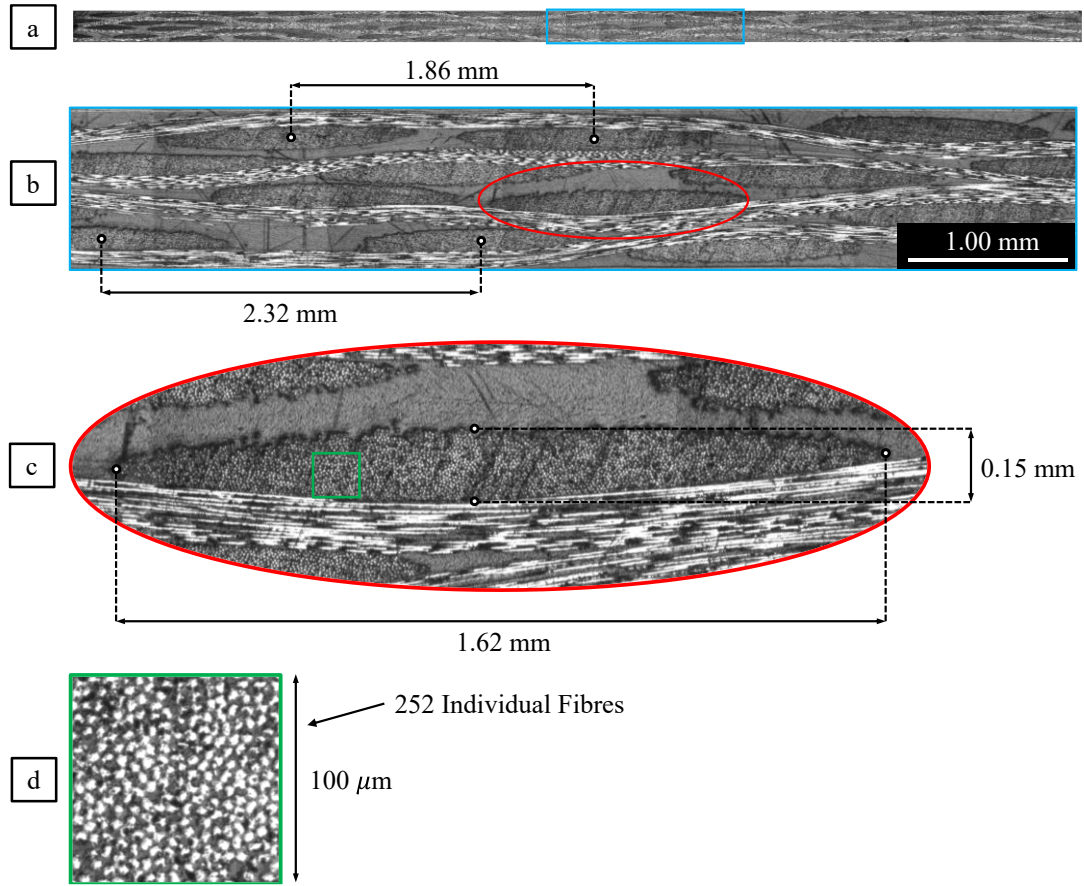


Figure 7.12: a) Analysis of fabric architecture over whole sample, b) tow spacing, c) tow dimensions, d) tow volume fraction.

Moreover, the average tow-tow separation was calculated to be 2.06 mm, although a maximum and minimum value of 1.70 mm and 2.36 mm was noted. Higher resolution microscopy of a small tow sample also allowed for the determination of the intra-tow fibre volume fraction Φ_{tow} :

$$\Phi_{tow} = \frac{4A_{sample}}{\pi n_f D_f^2} \quad (7.32)$$

where A_{sample} is the sample area, n_f if the number of fibres and D_f the nominal fibre diameter. In the representative 100 µm sample, 253 filaments were counted. Using a standard fibre diameter of 7 µm for Toray® fibres [394], this resulted in an intra-tow volume fraction of 0.584.

It was required that the conductivity of both the carbon fibre tows and the PA6 matrix be input into the numerical model for the calculation of the mesoscopic heat flux. For the PA6 matrix, the conductivity was assumed constant at 0.26 Wm⁻¹K⁻¹ (in the

melting region) as an average value from the work of Keating *et al.* [442]. While the thermal conductivity of PA6 does change with temperature [443], the temperature dependency is relatively small as can be inferred from a similar low temperature conductivity study by Kokkolaras *et al.* [444].

For the carbon fibre tows, the longitudinal conductivity, k_{lon} , can be calculated simply using the rule of mixtures and the intra-tow volume fraction (Equation (7.32)):

$$k_{lon} = \Phi_{tow} \cdot k_f + (1 - \Phi_{tow}) \cdot k_m \quad (7.33)$$

Where k_f and k_m represent the thermal conductivity for the fibres and matrix respectively. The thermal conductivity of Toray T300 carbon fibres is provided on the material datasheet [394] to be $10.8 \text{ Wm}^{-1}\text{K}^{-1}$ and assumed to be constant with temperature. Therefore, using Equation (7.33), the longitudinal conductivity was calculated as $6.42 \text{ Wm}^{-1}\text{K}^{-1}$. The calculation of tow transverse conductivity, k_{tra} , is generally more complex due to the fibre/matrix interaction that takes place. Hasselman *et al.* [445] produced an analytical equation for the transverse conductivity including the influence of this interface:

$$k_{tra} = k_m \cdot \frac{\left(\frac{k_f}{k_m} - 1 - \frac{k_f}{r_f h_c}\right) \Phi_{tow} + \left(1 + \frac{k_f}{r_f h_c} + \frac{k_f}{k_m}\right)}{\left(1 + \frac{k_f}{r_f h_c} - \frac{k_f}{k_m}\right) \Phi_{tow} + \left(1 + \frac{k_f}{r_f h_c} + \frac{k_f}{k_m}\right)} \quad (7.34)$$

Where r_f is the fibre radius and h_c is the conductance of the fibre/matrix interface. As per the work of Guzman-Maldonado *et al.* [345], full contact between the fibres and matrix was assumed ($h_c \rightarrow \infty$), such that Equation (7.34) becomes:

$$k_{tra} = k_m \cdot \frac{\left(\frac{k_f}{k_m} - 1\right) \Phi_{tow} + \left(1 + \frac{k_f}{k_m}\right)}{\left(1 - \frac{k_f}{k_m}\right) \Phi_{tow} + \left(1 + \frac{k_f}{k_m}\right)} \quad (7.35)$$

Utilising this equation, the transverse conductivity, k_{tra} , was calculated as $0.533 \text{ Wm}^{-1}\text{K}^{-1}$.

The University of Nottingham developed TexGen software [66] was used to model the RVE using the fabric architecture detailed above. A single CF/PA6 ply was modelled with four tows in both the warp and weft directions to ensure high accuracy.

Figure 7.13a illustrates the modelled TexGen architecture.

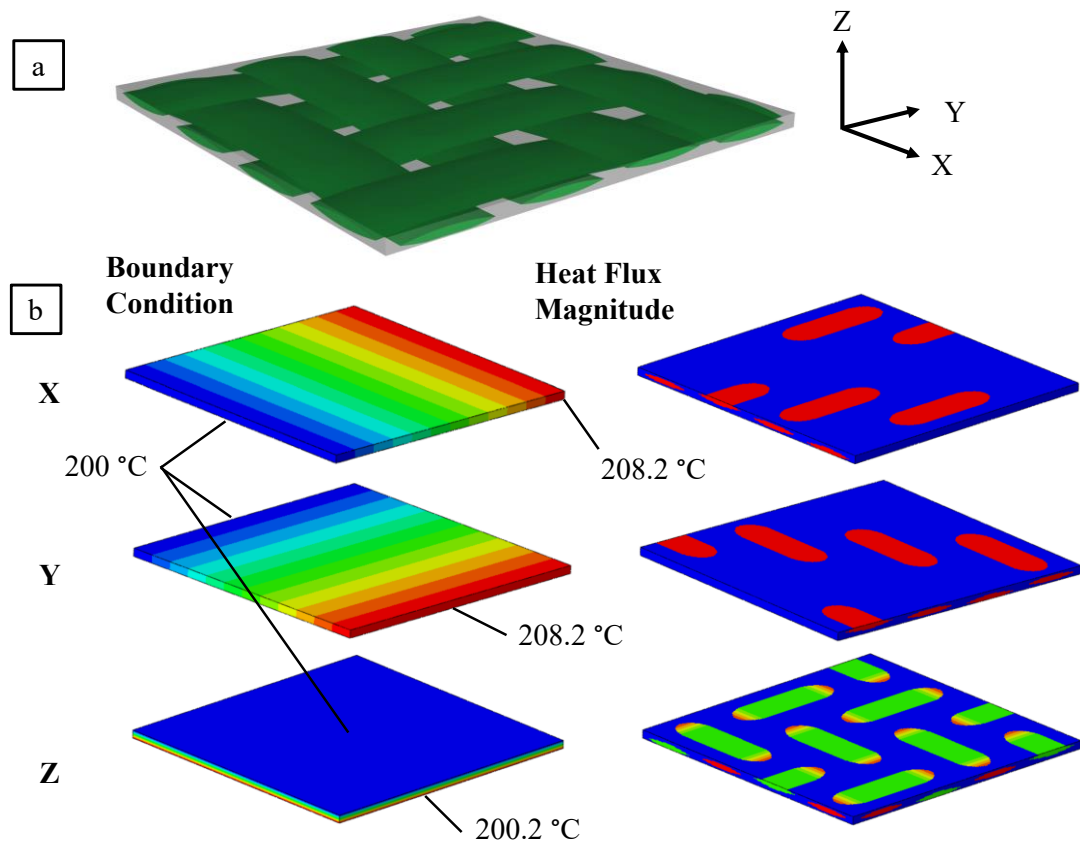


Figure 7.13: a) TexGen model of the CF/PA6 RVE b) Thermal boundary conditions and corresponding heat flux magnitudes from the Abaqus numerical model.

After creation of this RVE, TexGen creates a voxel mesh, initially with a voxel size of 23 μm (10 voxels through the laminate thickness). Each voxel has assigned a local material definition and orientation that allows Abaqus to define the correct properties to each corresponding voxel. The fibre and matrix properties calculated above were subsequently implemented within the numerical model. Furthermore, the three mesoscopic thermal boundary conditions in each direction were implemented within the model, such that the temperature gradient, δT_M , was consistent as 1°Cmm^{-1} . These three boundary conditions are illustrated in Figure 7.13b.

A steady-state implicit heat transfer analysis was then conducted for the three different boundary conditions, utilising DC3D8R elements within Abaqus/CAE. After the models had run to completion, the mesoscopic thermal heat flux (colinear with that of the prescribed boundary condition) was acquired on a voxel-by-voxel basis, and a mean value produced (as per Equation (7.29)). Finally, utilising Equation (7.31), the

macroscopic conductivity was calculated. This procedure was repeated for four different voxel sizes to analyse the model sensitivity, with the results illustrated in Figure 7.14. It can be seen that stability is achieved with a voxel size of 29 μm , with equal in-plane thermal conductivity values ($2.27 \text{ Wm}^{-1}\text{K}^{-1}$) and a much reduced out-of-plane value ($0.471 \text{ Wm}^{-1}\text{K}^{-1}$) caused by the lack of fibres running in this principal direction.

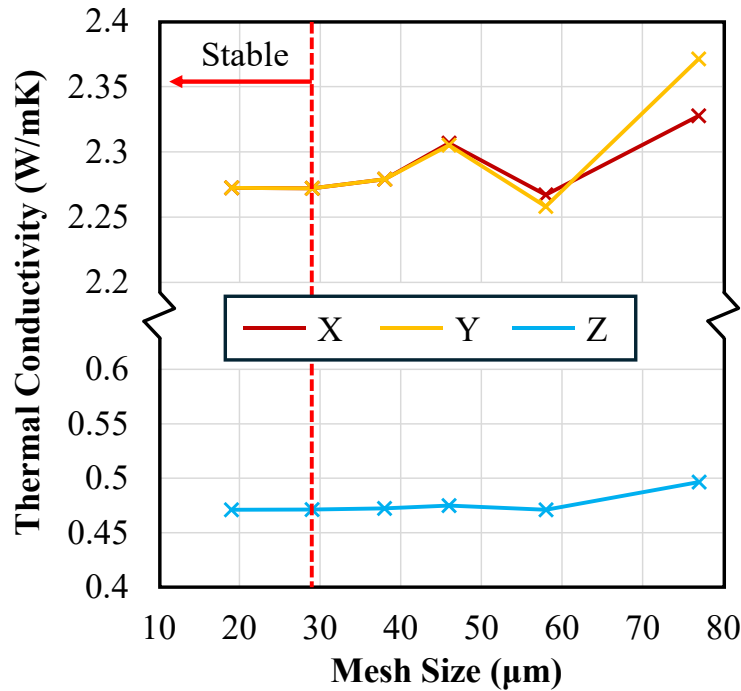


Figure 7.14: The influence of voxel size on thermal conductivity.

7.6 Heat Transfer Input Validation

To validate the crystallisation and heat transfer mechanisms explored in this chapter, a procedure was adopted such as to ensure that the outputs are suitable for use within a numerical routine. The validation procedure entailed both an experimental benchmark followed by an analytical analysis of the heat transfer mechanisms to ensure the behaviour encapsulated in the above sections was accurate to real-world thermoforming conditions. Finally, the influence of the silicone diaphragms is considered.

7.6.1 Experimental Benchmark

For the experimental study, 8-ply laminate was produced to the same 100x100 mm dimensions used during the convection study (Section 7.4.1). While this work generally concerns single-ply forming, more accurate experimental results were obtained with 8-ply laminates as thermocouples could easily be embedded within the material. This was not possible for the single-ply organosheets, meaning the goodness of the thermocouple contact became an issue. The heat transfer mechanisms associated with that of an 8-ply laminate can be considered identical to that of a single-ply however, such that these results apply to all laminate configurations.

The laminate was manually constructed with 8 single plies of CF/PA6, with thermocouples sandwiched between each ply such that the thermal response of the laminate could be tracked accordingly. It was important that the thermocouple wire was stripped prior to this process such that the wire profile within the laminate was minimised. Figure 7.15a illustrates the 7 inter-ply thermocouples before the laminate was assembled, as per Figure 7.15b. The laminate was then heated to 230 °C and compacted. The platen distance was carefully controlled using steel shims, such that the laminate thickness was controlled to 1.92 mm (as per factory-received 8-ply laminates). Figure 7.15c illustrates the finished compacted laminate with thermocouples set within the structure, with the thermocouple configuration illustrated schematically in Figure 7.15d.

After production of the representative laminate, a thermal response test was devised such that the behaviour of the laminate could be analysed. To support the laminate even once the melting temperature was reached, it was placed within two layers of A4000V fluoropolymer bagging film as produced by Airtech [389]. The bagging film itself has a maximum quoted temperature of 260 °C, allowing the test to reach the temperatures that would be expected during real-world thermoforming conditions. This film was also selected due to its thin (50 µm) structure and low thermal conductivity ($0.3 \text{ Wm}^{-1}\text{K}^{-1}$). Because the laminate thickness was much greater (40x) than that of the bag, it was assumed for this study that the film had no influence on the thermal behaviour of the laminate. The two layers of vacuum bag were secured and sealed within a custom frame. The purpose of this was to allow a vacuum to be drawn between the two layers, ensuring that no insulative air was present between the bag

and the laminate. The entire frame was then suspended underneath the 8 kW IR heater panel, equipped with PID closed loop control. All thermocouples were connected to a Pico TC-08 thermocouple datalogger so that the laminate temperature could be tracked over time, with a sampling rate of 1 hz. Figure 7.16 illustrates the experimental setup.

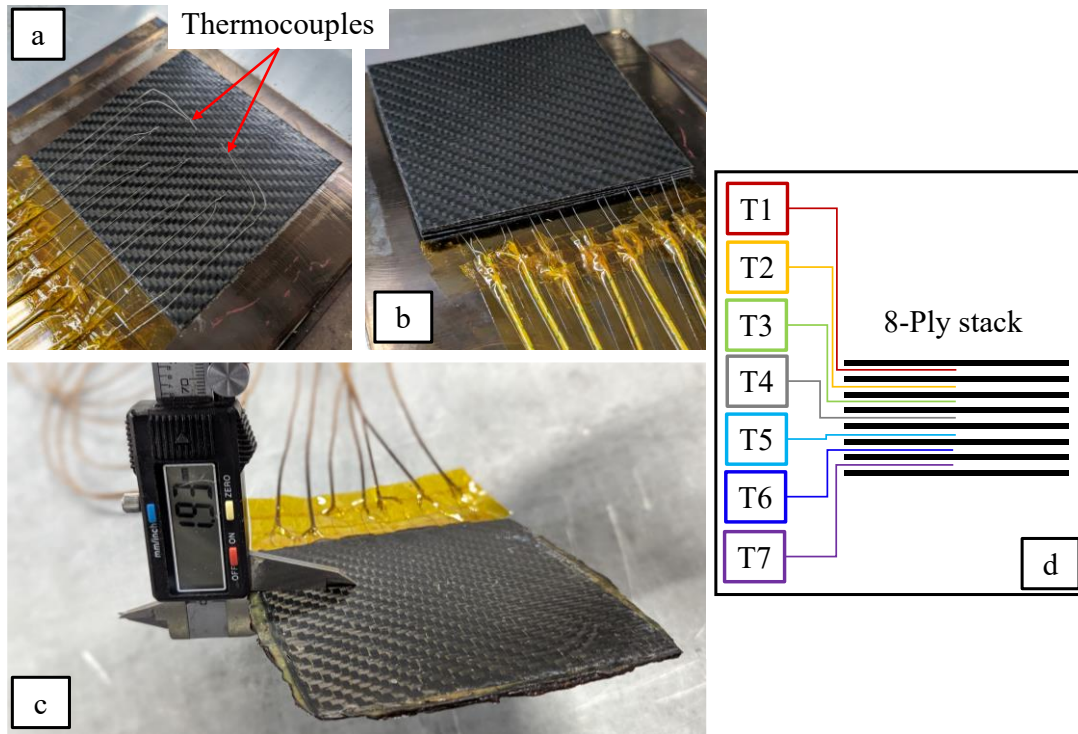


Figure 7.15: Production of CF/PA6 laminate for heat transfer validation.

An experimental test was devised to evaluate the laminate thermal behaviour. The upper laminate ply was heated up to 235 °C using the infrared heater (set using the inbuilt pyrometer and PID control). For the purposes of all heating operations, the fixed IR unit PID variables were calibrated such as to negate the possibility of an overshoot regarding the top laminate temperature, at the expense of increased heating-time. After this temperature was achieved, a 10-minute dwell was completed thus allowing the temperatures to stabilise and the thermal processes to reach a position of equilibrium. Finally, the heater was removed, allowing natural convection to cool the laminate for a further 10 minutes. The objective of this exercise was to evaluate the through-thickness thermal profile during the dwell stage, which itself is dependent on the laminate conductivity. Moreover, the convective cooling allowed for experimental analysis of the cooling curve for an 8-ply laminate at forming temperature. Figure 7.17

illustrates the thermocouple output from one of these tests, where the heat-up, dwell and cooling stages are clearly defined.

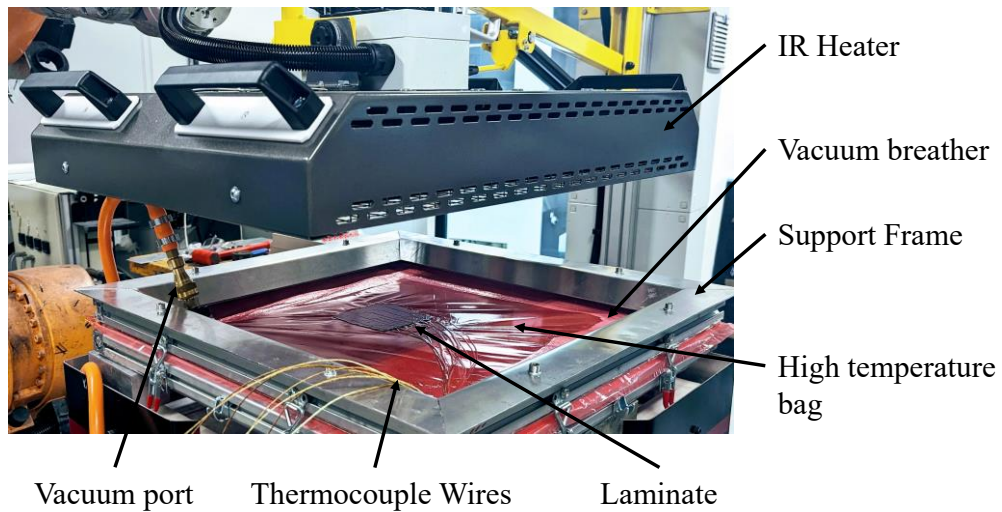


Figure 7.16: Experimental setup for the thermal validation exercise.

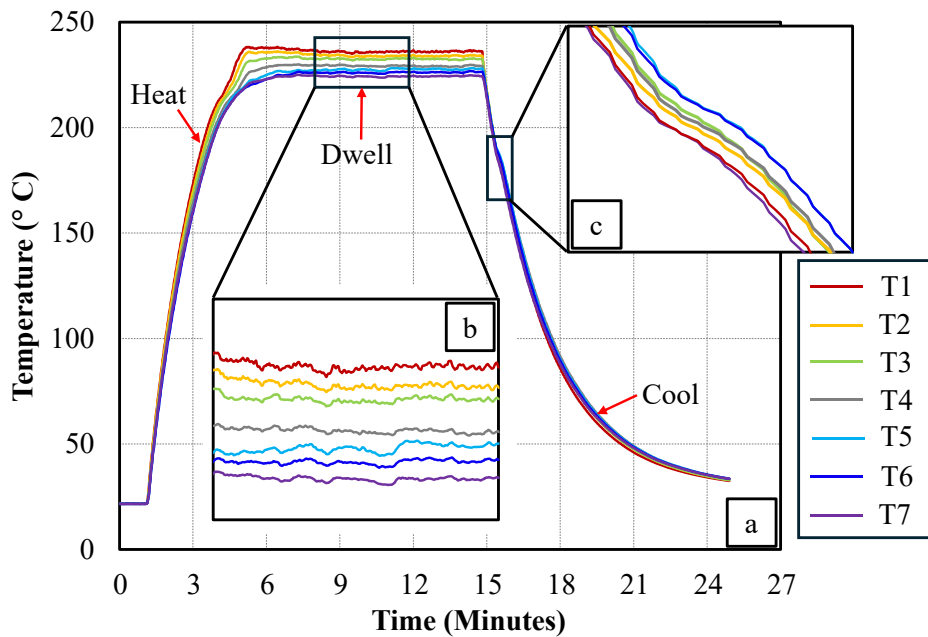


Figure 7.17: Thermal response of an 8-ply laminate subjected to three thermal regimes.

During the dwell stage, a maximum temperature was achieved at the top of the laminate (heated surface), then progressively cooling through the thickness (Figure 7.17b). The cooling rate was temperature dependent, as is to be expected from Newton’s law of cooling (Equation (7.9)) and a temperature-dependant convective heat transfer coefficient (Figure 7.10). The crystallisation exotherm can be noted

during the cool-down stage resulting in a momentary drop in cooling-rate (Figure 7.17c).

Four of these tests were conducted with the heater rotated 90° between each such as to illuminate any concerns regarding uneven thermal distributions from the emitter. The results from these tests were then averaged to provide an average dwell condition and an average cooldown slope. Figure 7.18a illustrates the average dwell condition from the four tests, highlighting up to 9 °C through thickness temperature distribution with a median laminate temperature of approximately 230 °C. These values can also be extrapolated to attain the upper and lower surface temperatures, assuming a linear thermal distribution. Figure 7.18b illustrates the average cooldown slopes from the four experiments.

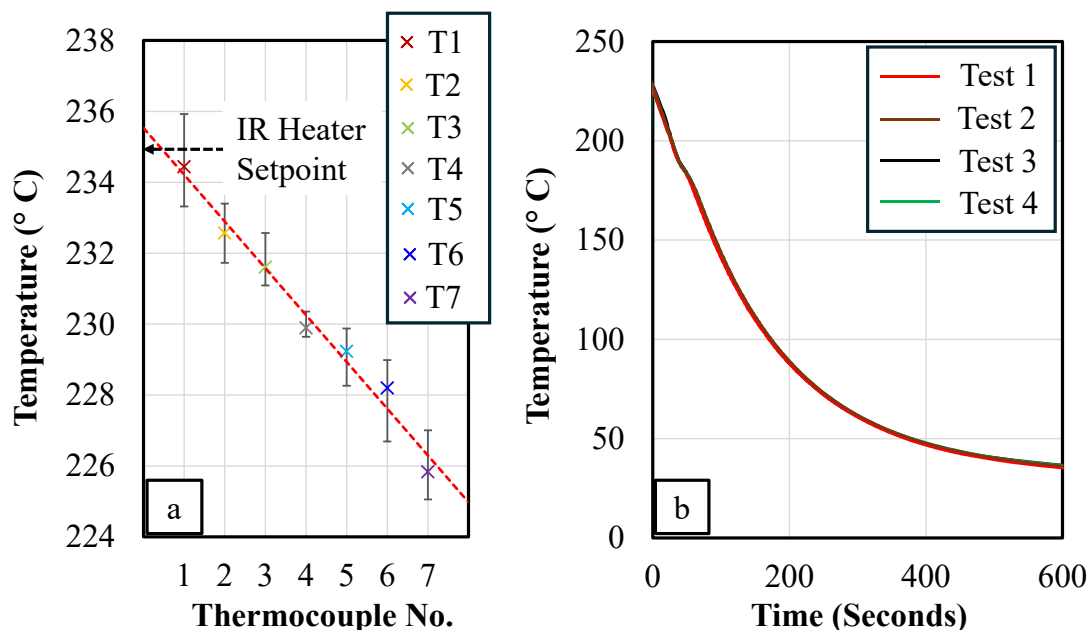


Figure 7.18: a) Through-thickness thermal profile during the dwell step, b) Cooling curves attributed to natural convection.

7.6.2 Analytical Validation

To evaluate the characterisation of dynamic thermal processes undertaken in this chapter, the experimental benchmark results (Section 7.6.1) were compared directly to that of an analytical study, validating the heat transfer mechanisms that were explored. It is possible to model the thermal processes that occur within a laminate using a 1-dimensional transient heat transfer model.

A thermal energy balance can be considered, where the laminate is split up into a number of nodes, n_x , where x is the node number, through the thickness. An energy balance can subsequently be analysed at each node, such that the increase in thermal energy is equal to the net heat inflow. For simplicity, the nodes were chosen to be coincident with each ply-ply interface, resulting in 9 nodes through the thickness of the 8-ply laminate, as illustrated in Figure 7.19.

Heat flow between adjacent nodes, Q_{cond} , can be calculated using Fourier's law for conduction [446]:

$$Q_{cond} = \frac{k \Delta T_n}{\Delta x_n} \quad (7.36)$$

where k is the out-of-plane conductivity (as calculated in Section 7.5), ΔT_n is the inter-node temperature difference and Δx_n is the slice thickness (Figure 7.19). The slice thickness is used in this case (rather than a nodal reference) to provide a dimension for the heat transfer equations. Moreover, the increase in thermal energy of the associated slice, \dot{Q} , in time δt , can be calculated using a modified form of the specific heat capacity equation (Equation (7.6)):

$$\dot{Q} = \rho c_p \Delta x_n \Delta T_t \quad (7.37)$$

where ρ , the density, and c_p the specific heat capacity, were defined in Table 3.1 and Section 7.3.2 respectively. ΔT_t represents the nodal transient temperature increase.

The energy balance for interior node n_{1-7} (nodes within the laminate structure) is simply the summation of heat flow from both adjacent nodes ($n-1$ and $n+1$) resulting in a thermal energy increase from time t^0 to t^1 (combining Equations (7.36) & (7.37)):

$$\rho c_p \Delta x_n (T_n^1 - T_n^0) = \left[\frac{k (T_{n-1}^0 - T_n^0)}{\Delta x_n} + \frac{k (T_{n+1}^0 - T_n^0)}{\Delta x_n} \right] \delta t \quad (7.38)$$

where the superscript represents the transient time step. Equation (7.38) can be simplified and rearranged such that the new transient nodal temperature, T_n^1 , is the subject:

$$T_n^1 = T_n^0 + \frac{k \delta t}{\rho c_p \Delta x_n^2} (T_{n-1}^0 - 2T_n^0 + T_{n+1}^0) \quad (7.39)$$

The energy balance for the exterior nodes n_0 and n_8 , rather than being the product of conduction from two adjacent nodes, represents the conduction from a single node and the convection and radiation to ambient conditions. It is assumed in this work that radiation and convection only apply to exterior nodes owing to the spectrally opaque nature of carbon fibres. Convective heat flow, Q_{conv} , can be represented using a 1D transient form of Newton's law of cooling (modified Equation (7.9)):

$$Q_{conv} = h\Delta T_{na}\delta t \quad (7.40)$$

where the convective heat transfer coefficient, h , was defined in Section 7.4.1, and ΔT_{na} represents the ambient-to-node temperature difference. Furthermore, radiative heat flow, Q_{rad} , can be represented using an alternative form of the Stefan-Boltzmann equation (modified Equation (7.26)):

$$Q_{rad} = \varepsilon\sigma_{sb}\Delta T_{na}^4\delta t \quad (7.41)$$

where ε represents the emissivity of the laminate within the infrared spectrum, and σ_{sb} represents the Stefan-Boltzmann constant. The energy balance for exterior nodes therefore represents a combination of the convective, conductive and radiative heat transfer, which in its simplified form represents (for node $n = 0$):

$$T_n^1 = T_n^0 + \frac{\delta t}{\rho c_p} \left[\frac{2k(T_{n+1}^0 - T_n^0)}{\Delta x_n} + h(T_{amb} - T_0^0) + \varepsilon\sigma_{sb}[(T_{amb})^4 - (T_0^0)^4] \right] \quad (7.42)$$

It should be noted that this equation does not include the influence of radiative heating from an IR emitter for the top surface, as would be the case during the dwell period. For simplicity, a heater temperature term, T_{IR} , can be added within the radiative heat transfer term resulting in a positive net radiative heat flux. This term can be calibrated during the dwell step resulting in zero net heat flux and is neglected during the cooling step ($T_{IR} = 0$).

$$T_n^1 = T_n^0 + \frac{\delta t}{\rho c_p} \left[\frac{2k(T_{n+1}^0 - T_n^0)}{\Delta x_n} + h(T_{amb} - T_0^0) + \varepsilon\sigma_{sb}[(T_{IR} - T_{amb})^4 - (T_0^0)^4] \right] \quad (7.43)$$

Equations (7.39), (7.42) and (7.43) are included on Figure 7.19 to illustrate the energy balance at each node through the 8-ply laminate. It is therefore possible with these equations at each node to step forwards in time δt in a transient heat transfer problem using the temperature values from the previous increment.

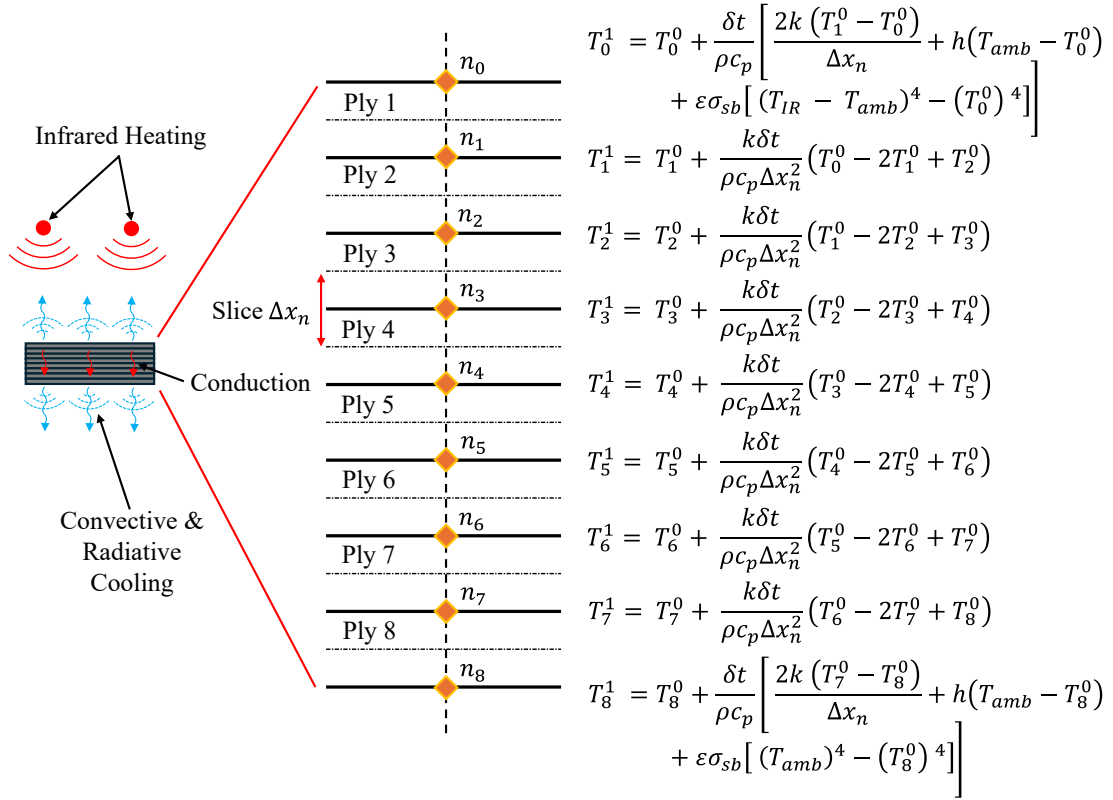


Figure 7.19: Analytical transient heat transfer analysis of an 8-ply CF/PA6 laminate.

MATLAB was employed to calculate the incremental temperatures at each node in a transient thermal study. Initially, just the cooling step was considered, with nodal temperatures fixed at 230 °C at the start of the analysis, and T_{IR} set to zero. A small time-step of 0.05 s was used to ensure model stability, and the cooling step was run for 600 seconds. All variables defined in this chapter were implemented within.

Figure 7.20a illustrates the results from the analytical study compared to those from the experimental study (Figure 7.18b). A very close agreement between the analytical and experimental results can be witnessed, with a very slight overestimation of the laminate cooling predicted in the analytical study. This can be attributed to the ‘oven effect’ that was present in the experimental study: hot air getting trapped under the lower bag therefore raising the local ambient temperature. Furthermore, since the convective heat transfer coefficient is based on analytical relations, small errors are

commonplace within its calculation. The analytical study also correctly predicts the laminate exotherm upon crystallisation owing to the inclusion of the cooling-rate dependant specific heat capacity (Equation 7.7). These results validate the convective and radiative heat transfer processes calculated in this chapter.

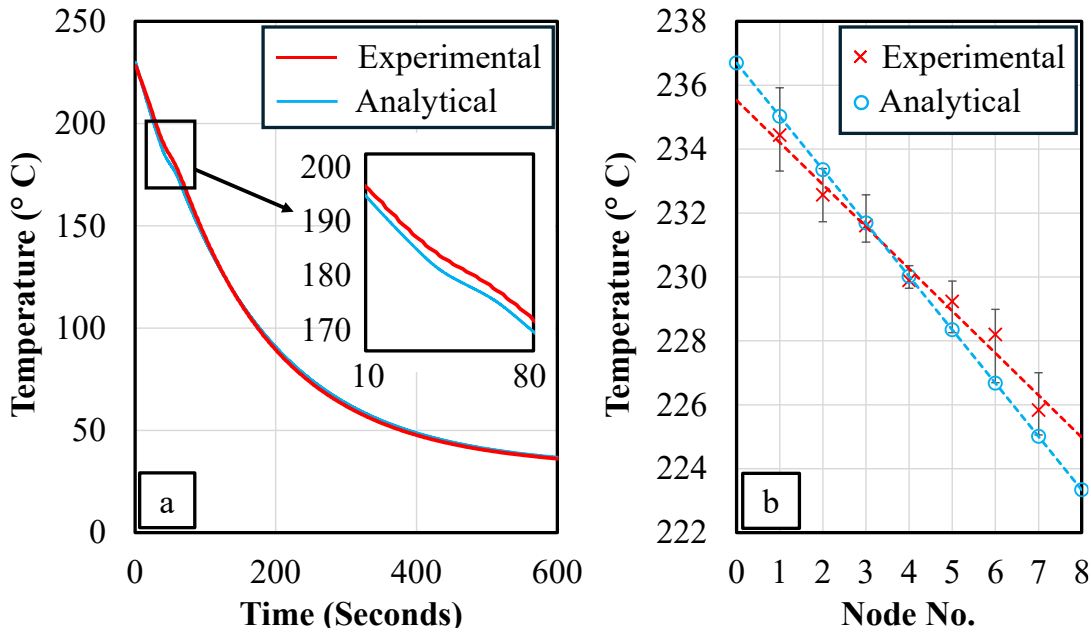


Figure 7.20: Analytical *versus* experimental results for: a) laminate cooling, b) laminate dwelling.

Following the analytical cooling study, an iterative procedure was adopted to identify the correct value of T_{IR} such that the laminate would dwell with a median temperature of 230 °C. The thermal output from the dwell study is illustrated in the Appendix E - Figure E.2, with the stabilised analytical temperatures compared to the experimental temperatures in Figure 7.20b. While a small deviation between both result sets can be noted, the results from the analytical study lie within the error-bounds of the experimental study. The analytical study therefore ensures that the conductivity values obtained within this chapter are adequate for use within a numerical model.

7.6.3 Silicone Heat Transfer

During the real-world DDF process, the silicone diaphragms are highly likely to influence the cooling behaviour. This is due to their much greater thickness than the fluoropolymer bag used in the previous study, coupled with a larger specific heat capacity and higher conductivity. The experimental study from Section 7.6.1 was

therefore repeated, this time replacing the fluoropolymer bag layers with layers of 1 mm silicone to understand how the silicone influences the laminate cooling behaviour. For the purposes of this study, only the cooling slope is of interest as the silicone diaphragms do not influence the intra-laminate conductivity. Figure 7.21a compares the cooling slope of a CF/PA6 laminate when cooled from 230 °C between the original fluoropolymer bagging (assumed negligible impact on cooling) and the silicone bag.

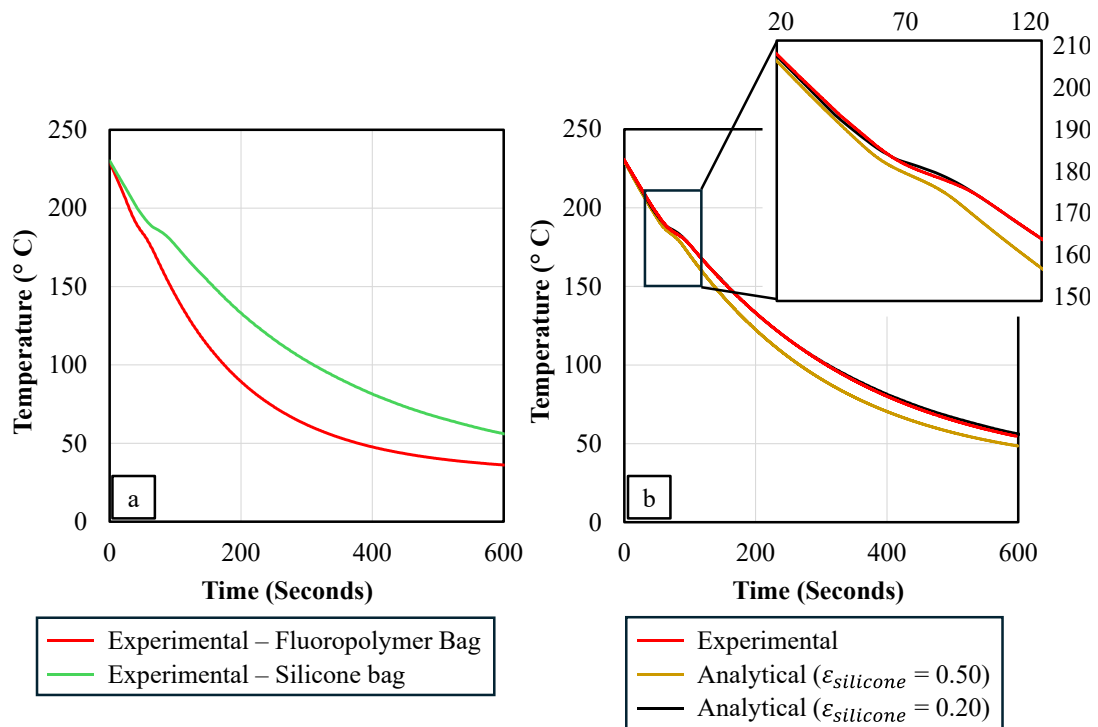


Figure 7.21: a) Cooling curve comparison between: a) different bagging materials, b) experimental and analytical studies of the silicone bag.

The silicone bag has a large influence on the cooling rate due to, but not limited to, the increase in thermal inertia. This can be visualised by analysing the instantaneous cooling-rate, as per Appendix E - Figure E.3. There is a marked decrease in the initial cooling rate for the silicone study, when compared to that of the fluoropolymer.

The analytical study from Section 7.6.2 was repeated, however this time with a larger number of nodes each side of the 9 intra-laminate nodes to replicate the silicone layers on either side. Similar principles were followed, with internal nodes solely dependent on conduction from adjacent nodes. The top and bottom laminate nodes were an exception to this, with radiative heat transfer still occurring on these nodes. This is because silicone is approximately 50% transmissive within the 300-600 K infrared

spectrum (0.1-0.5 μm), as illustrated in Appendix E - Figure E.4 [447]. This results in approximately half emitted radiation from the laminate still radiating to ambient conditions. This is a relatively complex problem, since the rest of the emitted radiation from the laminate is subsequently re-absorbed by the silicone, or reflected back to the laminate. To simplify the study, initially the laminate nodes were assigned an emissivity half that of the original study (0.425), accounting for the transmitted radiation. The silicone was assumed spectrally opaque, such that only the top and bottom nodes were assigned a radiative boundary condition. The reflectivity, R_s , transmissivity T_s , and absorptivity, A_s , can be related using the following equation [448] :

$$R_s + T_s + A_s = 1 \quad (7.44)$$

where, according to Kirchoff's law for thermal radiation, for any given wavelength [449]:

$$A_s = \varepsilon \quad (7.45)$$

Therefore, assuming zero reflectivity, the emissivity of the silicone was assumed to be 0.5 and the external silicone nodes were assigned this value. The radiation absorbed and reflected by the silicone was neglected to simplify the problem. A convective boundary condition was solely applied to the top and bottom silicone nodes, and all silicone nodes were assigned the properties of the silicone sheet [390].

Figure 7.21b illustrates the results of this analytical study. A moderate agreement between the silicone experimental and analytical studies was evident in this study. The overestimation in the cooling performance in the analytical model was likely caused by the omission of absorbed and reflected radiation within the silicone. While it is theoretically possible to account for this within numerical routines, modelling translucent materials correctly requires in-depth experimental analysis of the spectral properties [450], deemed too expensive for this piece of work. Therefore, a simple iterative procedure was adopted to minimise the residual-squared error in the analytical model by reducing the silicone emissivity, simulating the absorption of radiation, assuming absorption \gg reflection. A corrected emissivity of 0.20 was found to best correct the analytical model to recreate real-world conditions, as also illustrated on Figure 7.21b. This silicone emissivity value is therefore used hereon in.

7.7 Tool-ply Conductivity

The last transient heat transfer mechanism that required analysis was the amount of thermal conduction that occurred between the laminate and the tool, especially because it is likely that this became the dominant mode of heat loss during forming. As per Section 7.6, it was concluded that an experimental benchmark procedure could then be validated, in the case of tool-ply conductivity, with a numerical (Abaqus) study.

7.7.1 Experimental Benchmark

To ascertain the tool-ply conductivity, an experimental procedure was devised similar that used for the analytical heat transfer validation. Another 8-ply CF/PA6 laminate with through-thickness thermocouples was produced as per Section 7.6. In this study, instead of the laminate starting at the forming temperature and cooled naturally, the laminate began at room temperature, once again sandwiched between two layers of silicone to replicate real-world thermoforming conditions. This also maintained laminate consolidation and removed air from the silicone/CF/PA6 interface. The laminate and silicone were then instantaneously placed on a 100 x 100 x 80 mm aluminium block, itself at 210 °C (below the CF/PA6 melting point), thus quickly raising the laminate temperature via conduction through the silicone bag. The aluminium block was machined and polished for this study to replicate the material and surface properties of a DDF tool. The block was mounted on a heated table and equipped with a thermocouple such that its temperature could be controlled using a PID interface. The weight of the frame, bag and specimen were deemed to apply a 0.1 bar pressure between the specimen and the block. Five repeats were undertaken to validate experimental accuracy. Figure 7.22 illustrates the experimental setup.

The laminate temperature was once again tracked using the through-thickness thermocouples, connected to a Pico TC-08 thermocouple datalogger such that the laminate temperature could be tracked over time, with a sampling rate of 1 hz. The output for this study was similar to that illustrated in Figure 7.17, only that it is solely the heating stage of interest in this study, achieved via conductive rather than radiative heat transfer. A 300 second heating time was deemed sufficient to capture the laminate behaviour on heating. Figure 7.23 illustrates the heat-up curve for the CF/PA6 laminate, initially at 30 °C, with a 210 °C aluminium block. The thermocouple locations are

illustrated schematically in Figure 7.15, with T7 being the tool-side. Experimental repeats have been omitted from the figure for clarity, however, ply temperatures were within $\pm 2\%$ between each study.

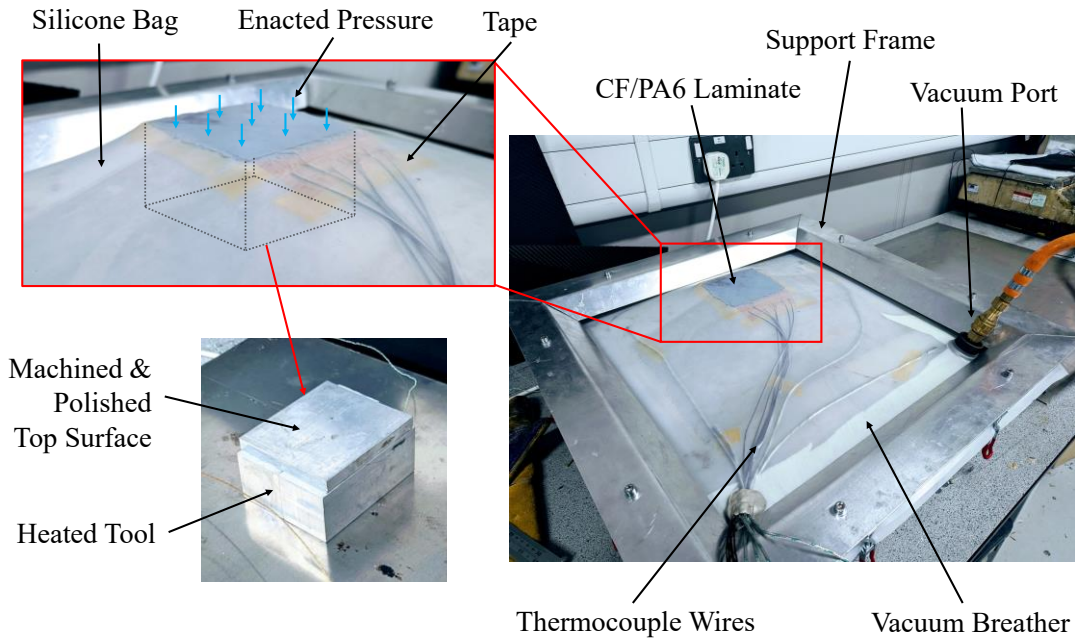


Figure 7.22: Experimental setup for tool-ply conductivity analysis.

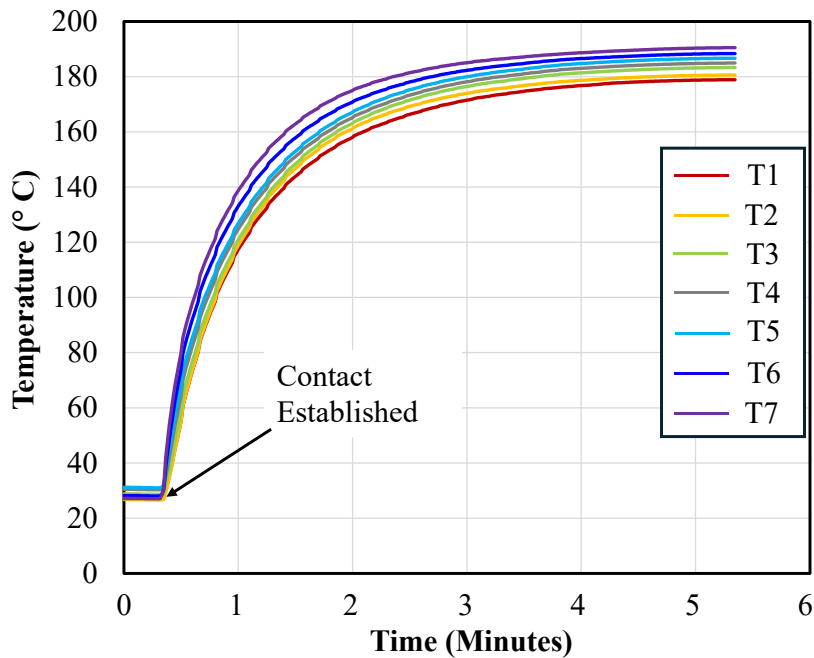


Figure 7.23: Experimental thermocouple output for the calculation of tool-ply conductivity.

7.7.2 Numerical Study

A numerical procedure was adopted to calculate a tool-ply conductivity value that can be taken forward into a fully-coupled thermomechanical simulation. This method was preferred over the analytical method utilised in Section 7.6 since the analytical model uses nodes at which perfect thermal contact is assumed, compared to numerical models where thermal contact resistance can be established.

Initially, it was necessary to ensure that an Abaqus numerical model also replicated the analytical and experimental cooling curves illustrated in Figure 7.21b. Eight plies of CF/PA6 and two layers of 1mm silicone sheet were modelled with DS4 heat transfer shell elements, with three through-thickness integration points. The thermal properties of CF/PA6 (Table 3.1) and silicone [390] were implemented within the model. A user defined field USDFLD subroutine was produced so that the cooling-rate-dependent crystallisation kinetics (Section 7.3) were also employed within the model, allowing for prediction of the laminate exotherm during cooling. Furthermore, the convective heat transfer coefficients (Section 7.4.1) and radiative emissivity values (Section 7.4.2) were assigned to the laminate and silicone respectively, noting that these values were previously validated analytically. Perfect thermal contact was assumed between individual laminate plies and the laminate/silicone interface. An initial temperature of 230 °C was assigned to the whole model. A transient thermal step was run for the same 600 s duration as per the experimental and analytical studies, with the output illustrated in Figure 7.24a. The experimental and analytical results have also been included in this figure. A very close agreement between analytical, experimental, and numerical results can be witnessed, with all curves within 1.5 °C of one another. This shows that the Abaqus numerical model was adequate for modelling laminate cooling behaviour.

This model was then adapted to replicate the tool-ply experimental apparatus, by including a 100 x 100 x 80 mm aluminium block, consisting of DC3D8R heat transfer solid elements. The tool was assigned the properties of aluminium 3rd party databases [451, 452]. The convective and radiative boundary conditions on the bottom of the laminate were not deactivated, meaning that the tool-ply conductivity was calculated as an over-estimation to account for these superficial thermal losses. This however, meant that contact tracking was not necessary when implemented within a thermomechanical model (Section 8.2.2). Initially, perfect thermal contact was

assigned between the aluminium block and silicone to evaluate the validity of this assumption. Figure 7.24b illustrates the heat up curve for nodal temperature 1-3 (NT13) of the bottommost ply – this replicates thermocouple position T7. The experimental T7 output from Figure 7.23 is also included.

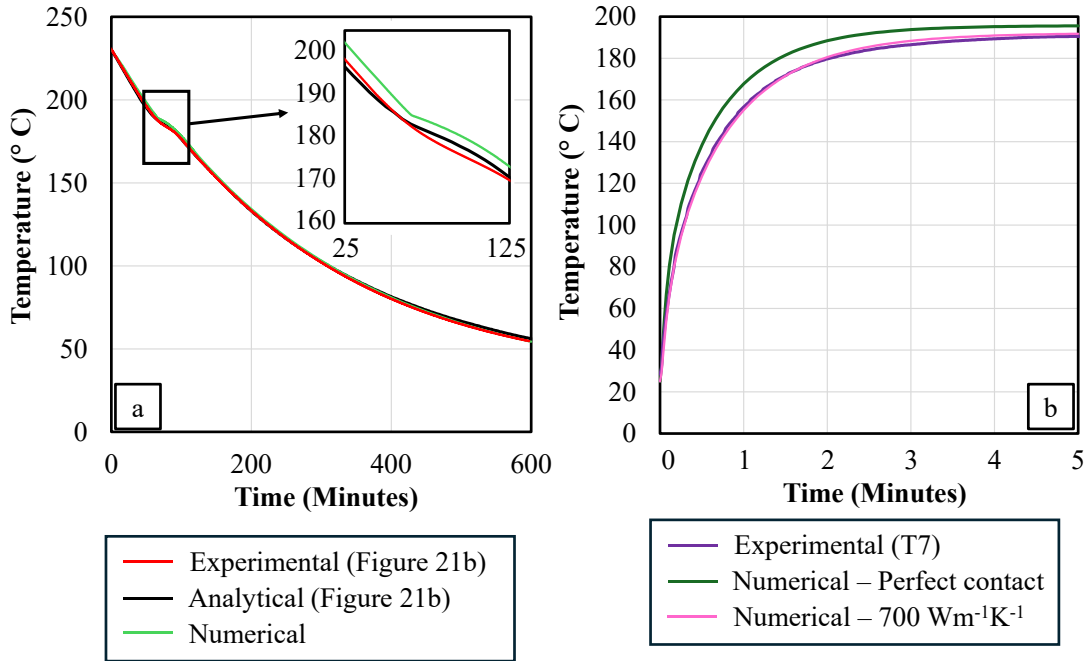


Figure 7.24: a) Validation of numerical transient heat transfer model, b) numerical *versus* Experimental tool-ply conductivity comparison, for the bottom-most thermocouple position.

The assumption of perfect thermal contact results in an overestimation of the conduction between the laminate and the tool. An iterative procedure was subsequently followed, determining that a tool-silicone interfacial conductivity of 700 Wm⁻¹K⁻¹ results in a numerical heat up curve almost identical to that of the experimental result, as also illustrated on Figure 7.24. While it is possible that this value is slightly normal-pressure dependent, the expected influence on conductivity was considered marginal.

7.8 Chapter Conclusions

In this chapter, the principal transient thermal mechanisms that act during FRTP thermoforming were characterised. An overview of the different mechanisms was presented, with heat transfer mechanisms including conduction, convection and radiation all acting upon the laminate during the forming process. Each of these

processes was analysed individually using analytical (convection), numerical (intra-ply conduction) and experimental (radiation) methods. These heat transfer mechanisms inevitably induce laminate cooling during the thermoforming process. Due to the semi-crystalline nature of the PA6 matrix, at a certain temperature, crystallisation occurs resulting in a significant increase in resin viscosity. Since this crystallisation onset point consequently has a substantial influence on laminate rigidity, the cooling-rate-dependent crystallisation behaviour of PA6 was also characterised in this chapter. This was followed by the calculation of cooling-rate-dependent specific heat capacity, with the objective to model the crystallisation exotherm.

To ensure that the results from these characterisation exercises were of sufficient accuracy to resemble conditions that would be expected during FRTP thermoforming, a validation exercise was also presented. A comparison between experimental and analytical thermal behaviour illustrated that the laminate heat transfer mechanisms were captured with a high level of accuracy. The experimental and analytical models matched within 2 °C for all tested thermal conditions and the crystallisation exotherm was predicted accurately. It was also discovered that the silicone diaphragms used during thermoforming cause a 50% reduction in laminate heat loss. Corrected silicone and laminate emissivity values of 0.2 and 0.425 were implemented within the model to account for the spectral absorption of the diaphragms. Furthermore, with the heat transfer mechanisms validated, it was possible to analyse the thermal contact between the silicone bag and the tool. It was found that assuming perfect thermal contact results in an overestimation of the heat flux between the silicone bag and the tool of approximately 35%. An interfacial conductivity value of $700 \text{ Wm}^{-1}\text{K}^{-1}$ allowed for a much better prediction of the tool-diaphragm conductivity.

These transient thermal processes can now be utilised within a fully-coupled FRTP thermoforming model, allowing for optimisation of the DDF processing conditions.

Chapter 8.

Numerical Forming Optimisation

8.1 Introduction

In the literature review (Section 2.7.3.2), fully coupled non-isothermal thermomechanical simulations were defined as the state-of-the-art regarding modelling of FRTP forming processes. These simulations not only have the capability for enhanced defect prediction [379], but also optimisation of the forming procedure regarding process conditions.

This chapter therefore is a culmination of all the work detailed thus far, specifically combining the transient thermal effects, characterised in Chapter 7, with the isothermal forming simulation produced within Chapter 6. Considering that both the operation of the isothermal simulation (including all deformation modes), and all transient thermal effects have been validated within Abaqus thus far, it was not necessary to conduct further experimental forming exercises to validate the non-isothermal forming model. Instead, this chapter uses the simulation to not only analyse the influence of non-isothermal effects, but conduct low-level optimisation of the forming process with regard to forming speed and the mould/base temperature. This is more akin with how the simulation would be used in an industry setting and is viable since confidence in both the simulation and transient thermal properties has already been established.

The implementation of transient effects within the isothermal thermomechanical model (Section 6.2.3) is therefore outlined. This also includes modification of the technique utilised for de-coupling membrane and bending behaviour, necessary for model stability. After the non-isothermal simulation was produced, it was run at different forming rates and then with different mould temperatures. Both defect initiation and demoulding time are considered in an optimisation scheme for minimising the tool temperature. Finally, this work is enhanced by considering a novel thermally-zoned tool, in an attempt to further optimise the FRTP DDF process.

8.2 Methodology

The section defines the modifications to the isothermal forming model required for a fully-coupled non-isothermal simulation to be produced. Section 6.2.1 can be referred

to for an in-depth description of the stress computation algorithm (Figure 6.1) that still applies for the non-isothermal routine.

8.2.1 Bending Behaviour Modification

In Section 0, the methodology for de-coupling bending and membrane behaviour was outlined. The Abaqus Composites Layup Toolset was utilised, splitting each shell element into three theoretical layers which were then assigned individual membrane properties (core layer) and bending properties (cover layers) to decouple the two. For this purpose, it was required that the central layer had only one integration point, such that it had no influence on laminate bending. Furthermore, the two cover layers were also assigned just one integration point for computation efficiency. This method was acceptable for an isothermal forming model.

It was however, acknowledged by Dassault Systems that only utilising one integration point per layer in a transient thermal problem leads to a numerical error, where element temperatures drain to absolute zero due to a floating-point exception within the model [453]. This has since been corrected in Abaqus 2023 onwards, although now requiring the user to utilise (at least) three integration points per composite layer, for a coupled temperature-displacement shell element. The implications are such that the initial method for de-coupling membrane behaviour is no longer valid for a fully-coupled FRTP forming model.

While other methods for de-coupling membrane and out-of-plane behaviour were considered, such as utilising a three-element model (detailed in Figure 2.26), this was considered undesirable since the model had already been validated for a single-element formulation. Furthermore, the associated increase in computational expense required for a three-element model was considered detrimental. Therefore, a novel method was utilised to still use the Abaqus Composites Layup Toolset, however including three integration points per theoretical layer, thus allowing for transient thermal effects to be implemented.

Since the core layer has to be assigned three integration points, it was not possible with the same technique to completely remove its influence from bending behaviour. However, its actual contribution to bending behaviour could be made negligible by

significantly reducing the core thickness, compared to that of the cover layers. The core layer itself governs the membrane properties of the laminate, including the tensile and shear behaviours. The axial stiffness, k_{ax} , is governed by the product of the Young's modulus, E , and the core thickness, h_{core} :

$$k_{ax} \propto E \cdot h_{core} \quad (8.1)$$

And also for the shear stiffness, k_{shear} :

$$k_{shear} \propto G \cdot h_{core} \quad (8.2)$$

Where G is the shear modulus. Therefore, in the case of the core layer, in order to significantly reduce its thickness, for example by 100x, then the assigned Young's modulus must increase by the same factor for both the axial and shear stiffnesses to remain the same.

Now, the same principle can be assigned to bending behaviour. The bending stiffness of the core layer, $k_{bending}$, is proportional to the Young's modulus and the cube of the core thickness (due to the second-moment of area):

$$k_{bending} \propto E \cdot h_{core}^3 \quad (8.3)$$

Following the approach that was utilised above, where the Young's modulus is increased by a factor of 100, and the thickness reduced by a factor of 100 (to maintain the membrane stiffnesses constant), in this case results in a 1×10^{-6} factor decrease in bending stiffness. This means that it is possible to maintain membrane properties and significantly reduce the bending properties of the core layer by simply reducing the thickness, as long as the assigned modulus is scaled accordingly. The new shell element formulation, with a small core layer, is illustrated in Figure 8.1.

Since, in this work, a rule of mixtures approach was adopted for the overall shell element modulus (Equation (D.25)), changing the layer dimensions automatically scaled both E_{fi}^{cover} and E_{fi}^{core} to represent the bending behaviour correctly, however maintaining the total modulus constant. This method provided a unique way of utilising three integration points per shell layer, allowing for the elimination of the core's bending contribution from the overall bending stiffness.

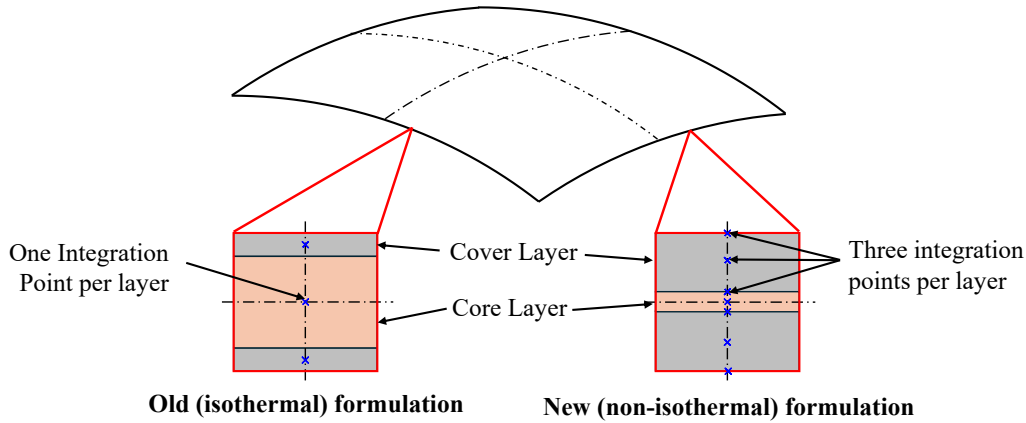


Figure 8.1: New shell element formulation utilising three integration points per layer, with a small core layer to marginalise its influence on bending behaviour.

As per Equation (D.23), it is the bending stiffness of the cover layers that is used to define the cover modulus (dependent on the core thickness). When one integration point per layer was used, the three-point Simpson approximation (applied across the full thickness with nodes at the layer centroids) provided a suitable estimate of the bending stiffness. However, after moving to three points per layer, the spacing no longer matched the assumptions of Simpson's rule, so it was necessary to revert to the conventional closed-form expression. In this case, the bending stiffness of the cover layers, B_{fi_cover} , was obtained directly from the exact integral of $E \cdot z^2$ (z is an arbitrary point) through the cover thickness, giving:

$$B_{fi_cover} = E_{fi}^{cover} \int_{z_2}^{z_1} z^2 dz = \frac{E_{fi}^{cover}}{12} [h^3 - h_{core}^3] \quad (8.4)$$

Thus, as per Appendix D, rearranging Equation (D.22) allows the cover modulus to be calculated as a function of the bending stiffness (Equation (4.34)) and element dimensions:

$$E_{fi}^{cover} = \frac{12B_{fi_cover}}{[h^3 - h_{core}^3]} \quad (8.5)$$

Once the cover modulus is known, the core modulus is calculated using Equation (D.25).

Deciding upon the correct value for h_{core} required a numerical study, trialling different values until the influence of the core layer on the bending stiffness was

sufficiently marginal. While one may expect a significant increase in run time with reducing h_{core} dimensions, Abaqus/Explicit uses the overall element dimensions (and modulus E_{fi}^{lam}) for the stress-wave propagation speed (Equation (6.1)). Therefore, reducing the core thickness had no influence on the simulation run time. It should be noted, however, that using three integration points per layer did increase the solve time as opposed to one per layer owing to the increase in the number of calculations required. With three integration points per layer, there were seven integration points through the thickness (two shared integration points between adjacent layers), compared to the original three. This resulted in 2.3x increase in run time, with simulations taking between 140-170 hours.

The method for curvature updating (Appendix D) was still valid for this alternative formulation, although now it was required that the VEXTERNALDB subroutine select the outermost integration points for the top and bottom curvatures, respectively.

For the bending formulation validation, the same model as used for validation of the cantilever bending test (Section 6.2.2.3) was utilised for this numerical study, with different values of h_{core} implemented. The results were then compared to a baseline model to understand the core's overall influence on bending behaviour.

8.2.2 Implementing Transient Thermal Effects

Implementing the transient thermal effects from Chapter 7 was trivial since most had already been validated within an Abaqus model. As per Chapter 7, the laminate was assumed to undergo preheating as a pre-requisite to the forming process. This meant that modelling of the IR lamp and solving the associated cavity radiation problem was not necessary. Therefore, cooling commenced right at the beginning of the forming routine.

As outlined in Section 6.2.2.1.2, rate-dependent properties require scaling in the DDF model due to the short model step time (0.5 seconds) compared to that of the actual forming routine (18 seconds). Generally, these scaled variables were outputs from the forming model (slip-rate/shear-rate), such that their values were scaled down to represent real-world conditions. The heat transient mechanisms defined in Chapter 7, however, are simulation inputs. This meant that the scaling applies the other way, with

properties such as conduction and convection increased in intensity by the scaling factor, thus accounting for the short step time:

$$\theta_{scaled} = \frac{\theta \cdot t_{exp}}{t_{step}} \quad (8.6)$$

where θ_{scaled} and θ are the scaled and un-scaled transient properties (defined below), t_{step} is the step time (0.5s) and t_{exp} is the experimental time (18s).

8.2.2.1 Intra-ply Conduction

Intra-ply conductivity was calculated in Section 7.5, in an orthogonal manner (K11, K22, K33). The FRTP DDF model uses a non-orthogonal stress computational algorithm, allowing for rotation of the initial orthogonal frame such that K11 and K22 remain parallel with the fibre direction. This ensures the changes regarding the global conductivity tensor, relative to the shear angle, are tracked accordingly. This was proven in the work of Guzman-Maldonado *et al.* [345]. The conductivity values of $81.72 \text{ Wm}^{-1}\text{K}^{-1}$ (K11 and K22) and $16.97 \text{ Wm}^{-1}\text{K}^{-1}$ (K33) are therefore implemented, having been scaled using Equation (6.6). Moreover, the scaled conductivity of silicone ($16.97 \text{ Wm}^{-1}\text{K}^{-1}$) [390] was assigned to the diaphragm, assuming no directionality and no temperature-dependence.

8.2.2.2 Convection and Radiation

Convection was assigned to the upper and lower laminate faces, as well as the upper and lower diaphragm faces, utilising the convective heat transfer coefficients calculated in Section 7.4.1. These coefficients were scaled (Equation (6.6)) to capture convective behaviour correctly. Sink temperatures of $25 \text{ }^\circ\text{C}$ were applied to the top and bottom surfaces respectively.

Similar to convection, radiation was applied to the top and bottom faces of both the laminate and the diaphragm. As validated in Section 7.6.3, the emissivity for the laminate and diaphragms was 0.425 and 0.20, respectively. Radiative heat transfer scaling was possible by scaling the Steffan-Boltzmann constant within Equation (6.6).

It was not necessary for the model to track contact and ‘turn-off’ convection and radiation once tool contact was made, as this was accounted for in the tool-ply

conduction study (Section 7.7). No cavity radiation approximations were conducted in the thermomechanical model.

8.2.2.3 Diaphragm-Tool Conduction

Diaphragm-tool conduction was assigned in the same manner as per Section 7.7, activating below a clearance of 100 μm . This value ($700 \text{ Wm}^{-1}\text{K}^{-1}$) was subsequently scaled using Equation (6.6). Perfect conduction was assumed between the diaphragm and the laminate and between both diaphragms.

8.2.2.4 Laminate Specific Heat Capacity

The specific heat capacity of CF/PA6 was defined in Section 7.3.2. It varied not just linearly with temperature, but included a significant spike during crystallisation, effectively modelling the exothermic crystallisation process. Due to the limitations of the Abaqus material editor, the specific heat capacity, defined by Equation (7.7), was implemented with a VUSDFLD (user defined field) subroutine. The subroutine VUSDFLD calls the temperature and cooling rate (Section 8.2.3) for every element and uses linear interpolation to define the constants K_{max} , T_{max} and D , thus calculating the specific heat capacity. Finally, the specific heat capacity of silicone [390] was assigned to the diaphragms, again assuming it to be isotropic, and not thermally coupled.

8.2.3 Crystallised Material Behaviour

Implementing crystallisation within the model was achieved by including the equation for relative crystallinity (Equation (7.5)) within the model. This equation operated simply utilising the instantaneous laminate temperature and the laminate cooling rate. As per the specific heat capacity, a VUSDFLD was used for its definition

The temperature rate, as per the outcomes of Section 6.2.2.1.1, could not be calculated on an instantaneous basis. Once again, a rule of mixtures approach regarding the current increment block time between the temperature rates at the beginning and end of the previous increment block was used (as per Figure 6.2). An increment block time of 0.01s was sufficient for eliminating sudden changes in the temperature-rate that could cause model instabilities. Equation (7.5) was implemented within the

VUSDFLD subroutine. Owing to changes in the cooling-rate, the subroutine operated with ‘memory’ and at no point allowed for a decrease in the value of the relative crystallinity.

To couple the mechanical properties of the laminate to the crystallisation state, the same procedure as that outlined by Dorr *et al.* [379] was implemented. The relative crystallinity operates as a value from 0 to 1, allowing for rule-of-mixtures approach to be adopted between uncrystallised and crystallised material states. The uncrystallised material states were characterised in Chapter 4, and represent the behaviour of the laminate when it is fully molten (above the crystallisation onset). The crystallised material states, however, represent those of a solid laminate, once crystallisation has been achieved. At any time, the material behaviour is therefore represented as:

$$\phi = (1 - X)\phi_{molten} + X\phi_{cryst} \quad (8.7)$$

Where ϕ_{molten} is the material behavioural mechanism in the molten state (Chapter 4), ϕ_{cryst} is the material behaviour in the fully crystallised state, X is the relative crystallinity and ϕ is the combined behavioural mechanism. This was applied to both intra-ply behavioural mechanisms characterised in this work: intra-ply shear and out-of-plane bending. It was therefore required that the crystallised state of both of these properties be defined.

Intra-ply shear in the cold state was assumed to be fully isotropic and depend on the shear properties of the PA6 matrix. In actuality, it is likely that the fibres increase the cold shear properties, however this effect was neglected for this work. In the cold state, PA6 has a shear modulus of approximately 1 GPa. Note that this value is much higher than that calculated for a molten material (Figure 4.12). Thus, in the case of intra-ply shear, semi-crystallised material behaviour can be modelled with:

$$G_{ij}(\gamma) = (1 - X)G_{ij}(\gamma)_{molten} + (1E9 \cdot X) \quad (8.8)$$

With $G_{ij}(\gamma)_{molten}$ defined by Equation .

Bending behaviour in the cold state was implemented by removing the de-coupling of bending behaviour defined in Section 8.2.1. That is, a fully solidified laminate exhibits a bending stiffness as per Equation (8.4), although utilising the nominal Young’s

modulus of the material as opposed to an arbitrary lower value. Therefore, to model the significant increase in bending rigidity upon cooling, the semi-crystallised behaviour can be modelled by assigning a new value for the cover modulus, E^{cover} :

$$E^{cover} = (1 - X)E_{fi}^{cover} + (E_{fi}^{all} \cdot X) \quad (8.9)$$

Where E_{fi}^{all} represents the Young's modulus of the CF/PA6 laminate, chosen to be 3 GPa for computational efficiency (Section 6.2.2).

In this study, the effects of crystallisation on diaphragm-ply friction behaviour are ignored. This is because this is likely to be a cohesive interaction which cannot be modelled by simply modifying the friction coefficient. However, the increasing CoF with decreasing temperature from Section 4.5 means that even before crystallisation has taken place, it is likely that diaphragm-ply sliding is largely inhibited within the model, replicating this cohesive contact. A contact point temperature of 190 °C, for example, with a normal pressure of 1 bar and slip rate of 500 mm/min yields an interfacial CoF (Equation (4.28)) greater than 1.00.

8.2.4 Non-Isothermal Thermomechanical Model

Having implemented the novel bending formulation (Section 8.2.1), the transient thermal properties (Section 8.2.2) and the crystallised material behaviour (Section 8.2.3), the model could then be used to capture non-isothermal FRTP DDF behaviour. The model itself functioned the same as that outlined in Section 6.2.3, although it was required that the stable-time-increment be reduced to 1.5E-7 seconds to inhibit the initiation of floating point exceptions within the solver. As before, the numerical models were all solved using the ADA high performance computer (HPC) at The University of Nottingham, with 48 cores, double-precision (analysis & packager) and full nodal output precision. All models consisted of a laminate in the conventional 0/90° fibre orientation. Furthermore, while the inhomogeneous initial laminate temperature from Section 6.4.4 was maintained, only one centre temperature (250 °C) was used in this study. This is due to the transient cooling effects meaning that it was unsuitable to begin forming with lower laminate temperatures.

Initially, the thermomechanical simulation was re-run with a tool at 250 °C, at the two different forming rates from Chapter 6. In the isothermal simulation, it was shown that

increasing the forming rate had a detrimental impact on the forming quality. In a non-isothermal model, however, a faster model allowed for less cooling, potentially leading to different conclusions regarding an ideal forming rate. This initial work package is similar to that conducted by Machado *et al.* [159], illustrated in Figure 2.30, showing how including transient thermal effects can change the outcomes regarding specific forming parameters.

Following this study, a tool temperature optimisation was conducted, with the thermomechanical simulation run with five different temperatures to illustrate how this can influence forming behaviour. The different tool temperatures selected were 220 °C, 200 °C, 180 °C, 160 °C and 140 °C. Forming below 140 °C was not possible due to the significant laminate cooling. Moreover, forming with a tool temperature above 220 °C led to a negligible difference in forming behaviour. Note that the ‘mould’ and base’ are defined separately in Figure 3.2 but are referred to collectively as the ‘tool’.

As part of this work package, forming limits were defined that describe the maximum bridging that can be considered acceptable. Bridging was singled out due to the inherent instability of wrinkles. The forming limits were arbitrary, but a maximum bridging distance of 5 mm was selected. This means that, concerning the isothermal results (Figure 6.18c), only the best formed components (at 250 °C and 230 °C) would be deemed to be of acceptable quality. This work includes analysis of the laminate cooling rate, therefore representing a low-level optimisation of the DDF process for both part quality and demoulding time. Finally, utilising the outcomes of this study, simple non-isothermal tooling is considered (different temperature for the mould and base) to further improve part quality and/or reduce demoulding time.

8.3 Results

This section details the validation of the bending behaviour validation, followed by the various outputs from the non-isothermal thermomechanical simulation.

8.3.1 Bending Validation Results

In the bending validation exercise, the original bending formulation (1 integration point per layer) was compared to that of the new formulation (3 integration points per

layer) by comparing the bending profile of a cantilever specimen, with different core thicknesses. Figure 8.2 illustrates the results from this study.

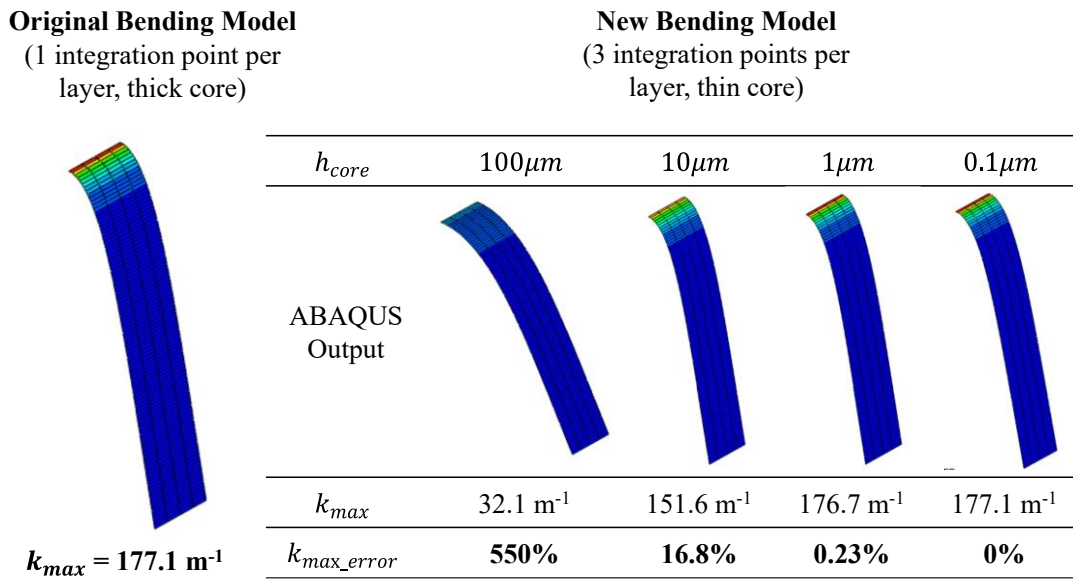


Figure 8.2: Comparison between new and old bending models.

The cantilever specimen with the original bending formulation exhibited a maximum curvature of 177.1 m^{-1} . This can be compared to the new formulation, where decreasing the core thickness in orders of magnitude led to increased curvature, and subsequently a reduced error compared to the original model. It is shown that with a core thickness of 0.1 μm there is no error between the old and new formulations, owing to the negligible influence the thin core layer has on the overall bending stiffness.

From this exercise, a core thickness of 0.1 μm is selected going forwards in this work. A series of isothermal thermomechanical simulations from Chapter 6 were re-run with the new formulation, with no changes made to the forming behaviour. As noted in Section 8.2.1, however, the run time was increased by 2.3x.

8.3.2 Non-Isothermal Thermomechanical Simulation

The non-isothermal simulation took the same form as that illustrated in Figure 6.13, only now including transient thermal effects. Figure 8.3 illustrates four individual steps during the forming process, in this case with a mould/base temperature of 140 $^{\circ}\text{C}$. As noted in Section 8.2.4, this represented the coldest mould temperature used in this study. At the beginning of the forming operation ($t=0$), the inhomogeneous in-plane

distribution from Section 6.4.4 is clearly visible, owing to the radiance of the IR emitters. Initially, cooling was dominated by convection and radiation from the laminate/diaphragm surfaces at approximately $2\text{ }^{\circ}\text{C}\text{s}^{-1}$. Once tool contact was made, however, the cooling rate increased, resulting in localised laminate cooling with the colder tool. This resulted in a peak cooling rate of $6\text{ }^{\circ}\text{C}\text{s}^{-1}$. This rapid cooling inevitably led to defects forming in the laminate which are analysed in Section 8.3.2.2. Generally, areas that experience bridging remain at a higher temperature than surrounding material due to the lack of tool contact, clearly visible on Figure 8.3c. Finally, at the end of the forming process (Figure 8.3d), the laminate represented a highly cooled state, exhibiting regions of crystallised material (see below).

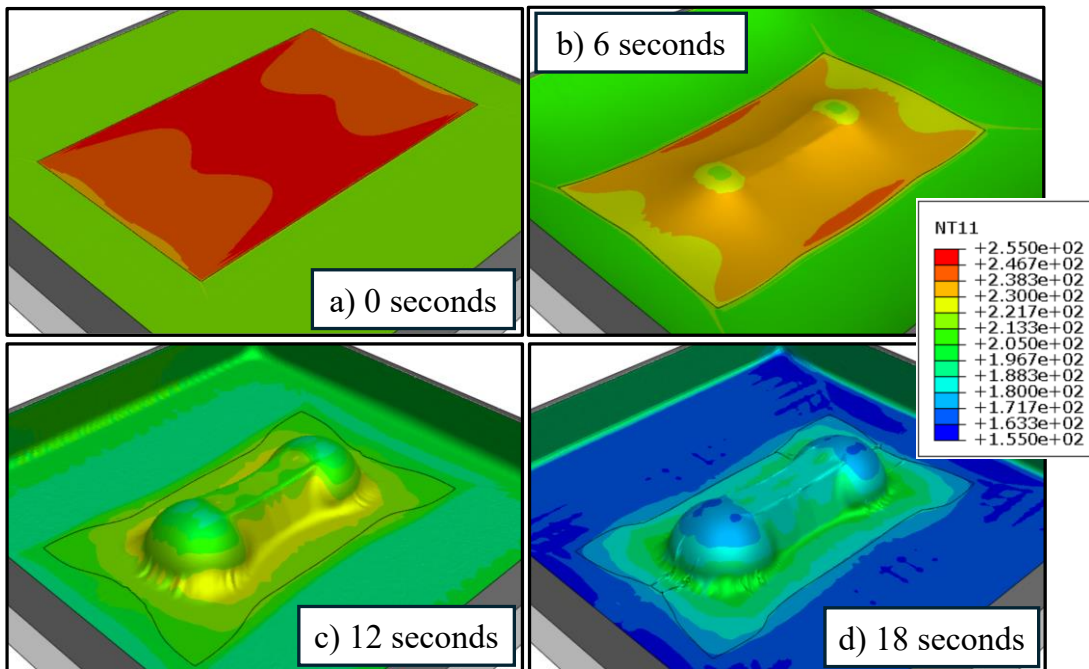


Figure 8.3: Dynamic laminate profile illustrating four ‘freeze-frames’ from the simulated forming process with a $140\text{ }^{\circ}\text{C}$ tool/base. The upper diaphragm has been omitted for clarity.

Figure 8.4a shows the thermal profile of the laminate at the end of the 18 second forming operation, and Figure 8.4b shows the relative crystallisation. The colourmap for the relative crystallisation is scaled such that a value of 0.01 (and above) is coloured red. This is because, as per Equation (8.8), even 1% crystallisation results in a shear force of $1\text{-E}7$, resulting in a significant increase in laminate rigidity. It is likely that forming is not possible after this threshold is met. It is clear that the coldest regions indicated in Figure 8.4a are those that have begun the crystallisation process in Figure 8.4b.

Figure 8.4c shows a point temperature history for the centre of the laminate, which exhibits the two cooling regimes noted above. For the remainder of this section, the laminate centre temperature is used to define an approximate maximum temperature of the double-dome geometry. As per Figure 8.4a, the two domes represent the coldest regions, with the four laminate corners also exhibiting a low temperature. Although areas of bridging represent the highest temperatures, these areas are localised; meaning that laminate rigidity is not dependent on these areas. The laminate centre temperature remains warmer due to the later tool-contact experienced by this tapered section. This point is utilised in Section 8.3.2.2 to define an approximate ‘demoulding’ time once sufficient rigidity is achieved.

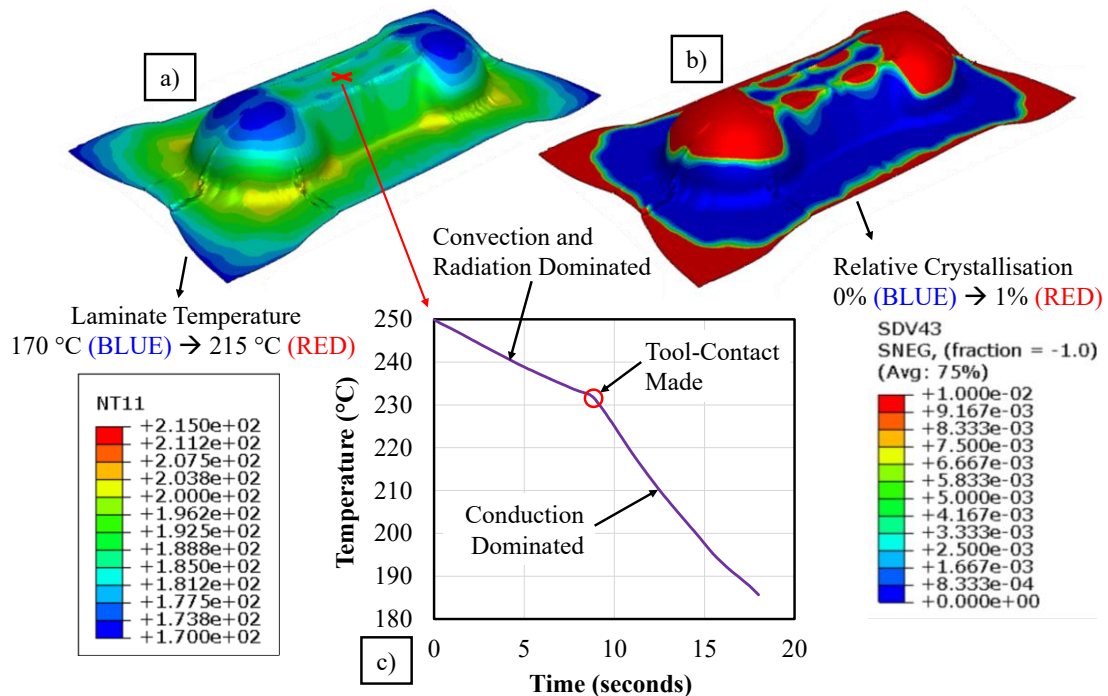


Figure 8.4: Laminate at the end of the 18 second forming process with a 140 °C tool: a) thermal profile, b) relative crystallisation, c) laminate centre thermal history.

8.3.2.1 Forming Rate Study

The first study as part of the fully-coupled non-isothermal thermomechanical simulation was analysis of the influence of rate on laminate forming behaviour. In an isothermal simulation, as per Figure 6.17a and Figure 6.22a, increasing the forming rate was shown to be detrimental to the forming process due to the viscoelastic nature of the resin. The same conclusion was not guaranteed in a fully-coupled non-isothermal model. This is because while the same rate effects still exist, laminate

cooling is significantly reduced at a higher forming rate. This reduction in cooling was expected to aid laminate mobility.

Figure 8.5 illustrates a comparison between forming rates for both the isothermal and non-isothermal studies. Subsequently, as per Chapter 3 and Chapter 6, the mould conformity was calculated and is illustrated in Figure 8.6.

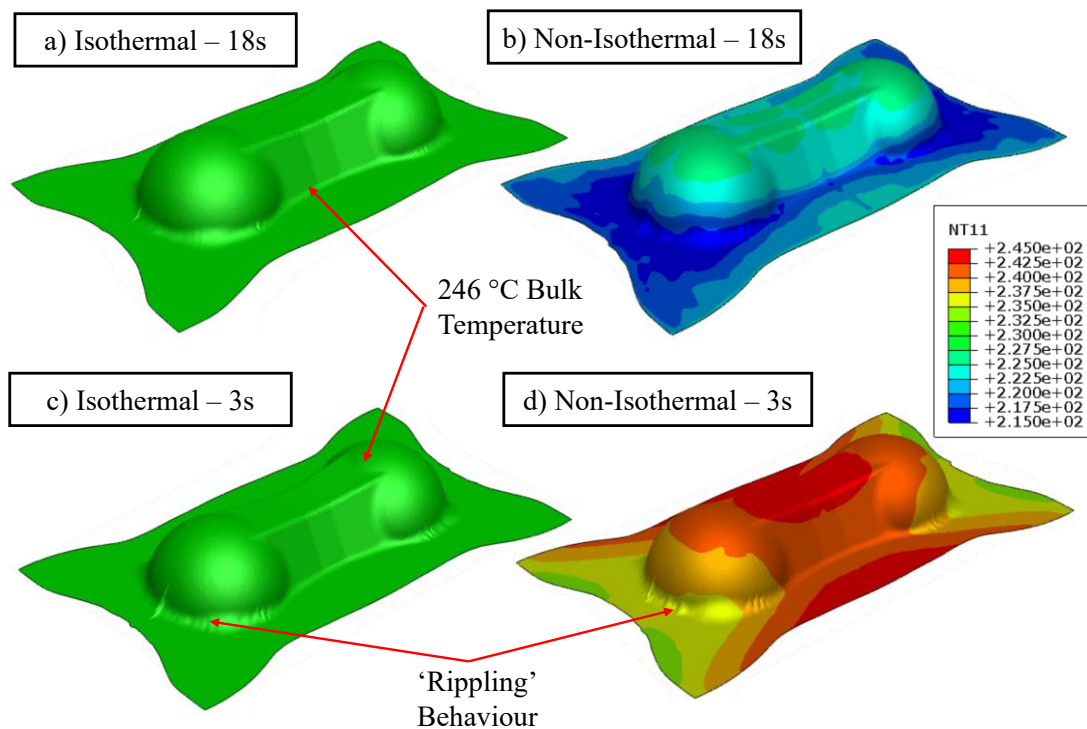


Figure 8.5: Isothermal (a, c) and non-isothermal (b, d) laminate profiles for forming at low (a, b) and high (c, d) speed. 'NT11' represents the laminate temperature.

In the isothermal studies, both bridging and wrinkling were increased in severity at higher forming rates. In the non-isothermal study, however, a marginal drop in bridging is noted (from 4.8 mm to 4.5 mm) owing to the reduced heat loss at higher forming speeds. Furthermore, there was no change in the maximum apex wrinkle amplitude between the two non-isothermal studies. A degree of 'rippling' behaviour was present in the non-isothermal study at a high forming rate, similar that in the isothermal case. In both non-isothermal cases, bridging was slightly higher than that of the isothermal case, although a small degree of this was attributed to the inclusion of the inhomogeneous thermal profile.

Overall, the difference in forming quality when including transient thermal effects is much smaller than that when they are neglected, since less heat is lost when forming

at higher speeds. Going forward in this work, while high-speed forming yields a similar forming quality to low-speed forming, the standard 18 second operation was upheld. This is due to both the ‘rippling’ behaviour that still occurred at high forming rates along with the lack of tool temperature optimisation possible with high-speed forming. The objective of this chapter was to outline the principles for optimisation, thus meaning a slower forming rate was preferred.

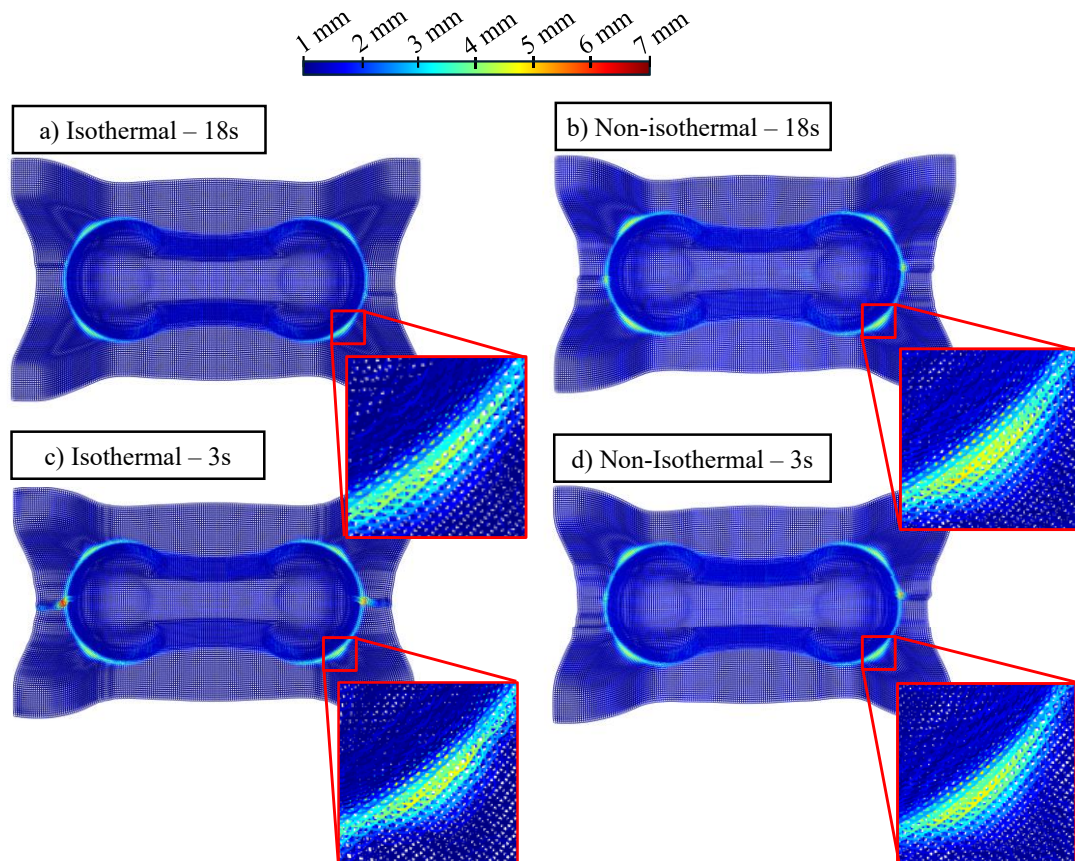


Figure 8.6: Isothermal (a, c) and non-isothermal (b, d) mould conformity plots for forming at low (a, b) and high (c, d) speed.

8.3.2.2 Tool Temperature Optimisation

The results from forming with different tool/base temperatures are illustrated in Figure 8.7, where both the Abaqus thermal output and the mould conformity plots have been included. Furthermore, the equivalent cooling-rate and relative crystallisation plots are illustrated in Appendix F - Figure F.1.

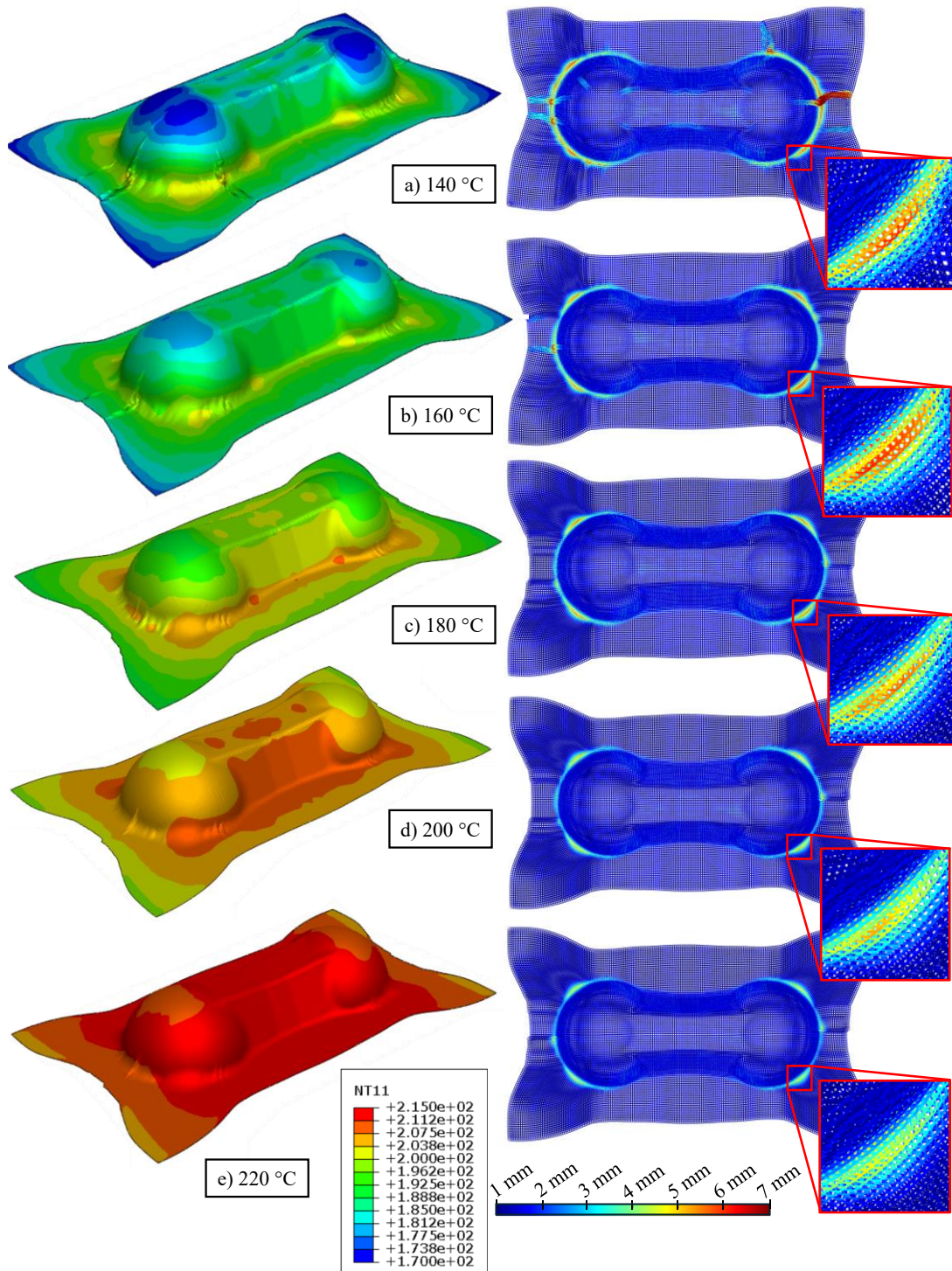


Figure 8.7: Simulated forming behaviour for a laminate with an initial centre temperature (inhomogeneous profile) of 250 °C, with different tool temperatures: a) 140 °C, b) 160 °C, c) 180 °C, d) 200 °C, e) 220 °C.

Decreasing the tool temperature led to a significant reduction in the laminate temperature at the latter stages of the forming operation. This resulted in significant wrinkling for laminates when forming over a 140 °C and 160 °C tool. Significant

‘rippling’ behaviour is also present on these forms as well as that with a 180 °C tool. Only once a tool temperature of 200 °C was met did the forming quality represent what is considered acceptable, with a single apex wrinkle in both cases (200 °C and 220 °C tool).

Regarding the mould conformity, significant bridging (greater than the 5 mm threshold defined in Section 8.2.4) was present once again until a tool temperature of 200 °C was met and exceeded. The maximum bridging in the case of the 200 °C and 220 °C tools was 5.0 mm and 4.6 mm respectively.

Both the wrinkling and bridging indicate that the minimum tool temperature resulting in acceptable forming quality was of 200 °C. The reason this minimisation exists is such as to reduce the demoulding time. Therefore, as per Figure 8.4c, the centre temperature for each laminate, which for simplicity was used to signify the laminate rigidity, was plotted against the forming time. Figure 8.8a illustrates these plots for the different tool temperatures. The cooling profile for the 18 second forming with a 250 °C tool from Section 8.3.2.1 has also been included in the figure.

In this work, due to constraints regarding the simulation time, it was not possible to model the cooling behaviour of the laminate after the 18 second forming operation was completed. Ideally, however, the simulation would continue tracking laminate temperature until full crystallisation had been achieved to obtain information regarding crystallinity and demoulding time. For simplicity, in this work, the cooling curves post tool-contact were extrapolated to approximate the cooling behaviour of each laminate. While this induces some error, the objective of this study was to highlight how tool temperature optimisation could be completed in an industry setting. Figure 8.8a therefore also includes a power-based extrapolation for each of the curves (post 10s – after tool contact is made).

As illustrated in Appendix F - Figure F.1, a lower tool temperature resulted in an increased cooling rate after tool contact was made. To determine an accurate value for the demoulding time, the relative crystallinity could be obtained from these extrapolated cooling curves. Each curve represented:

$$T = y_c \cdot t_f^{z_c} \tag{8.10}$$

where T is the laminate temperature, t_f is the forming time and y_c and z_c are constants specific to each tool/base temperature, tabulated in Appendix F - Table F-1. The cooling rate therefore represents:

$$\frac{dT}{dt_f} = y_c \cdot z_c \cdot t_f^{z_c-1} \quad (8.11)$$

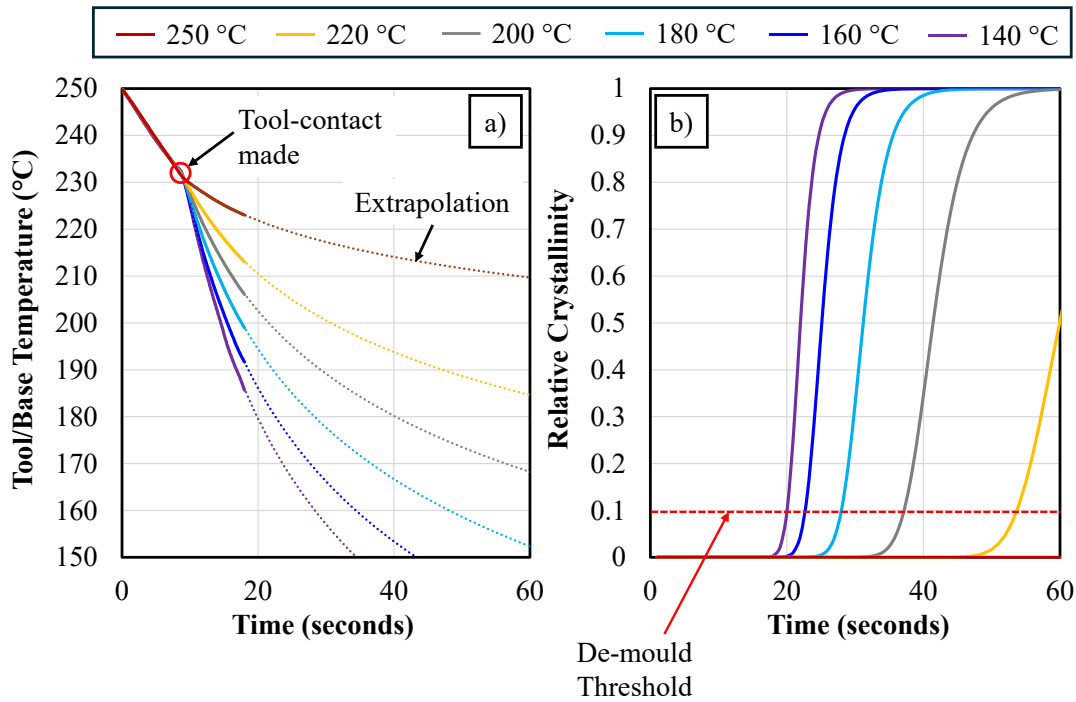


Figure 8.8: Forming with different tool temperatures: a) laminate temperature *versus* forming time, including power extrapolation, b) relative crystallinity *versus* forming time.

At any time, the relative crystallinity can be calculated utilising Equation (7.5), with the temperature and cooling rates from Equations (8.10) and (8.11) respectively. Figure 8.8b illustrates the relative crystallinity of each laminate *versus* the forming time. While (as noted above) a relative crystallinity of 0.01 was expected to result in a significant increase in laminate rigidity, it was considered unwise to de-mould exactly at this point due to potential tackiness of the matrix. Instead, a value 10x greater than this was chosen (resembling 10% crystallinity), where laminate rigidity was expected to be high. In practice, this value would require experimental calibration to ensure it is suitable. This threshold is also included on Figure 8.8b, with the intercept between each curve and this threshold representing the minimum demoulding time. These demoulding times, along with the values for laminate bridging and maximum wrinkle amplitude from Figure 8.7, are illustrated in Figure 8.9.

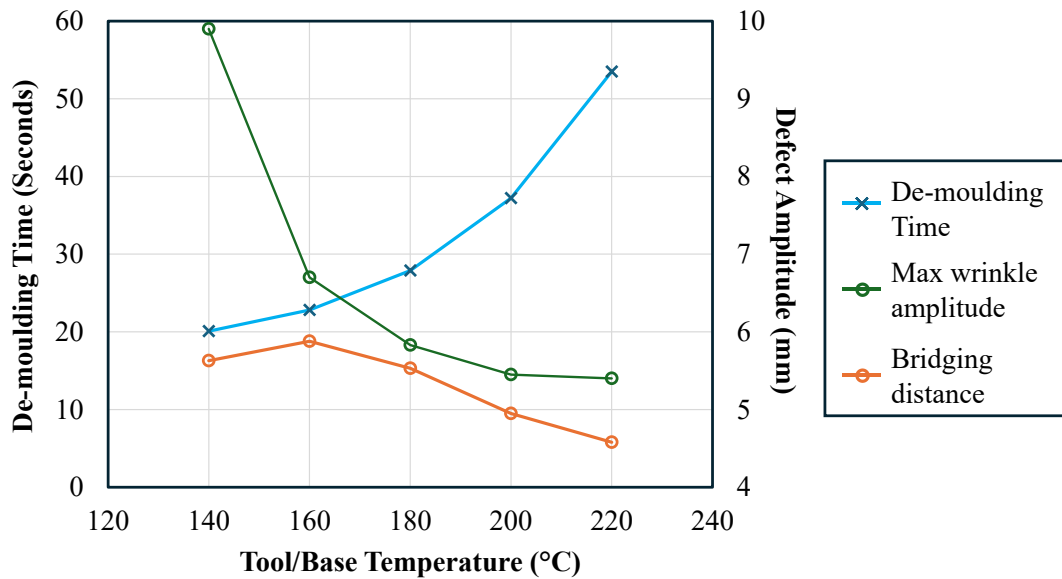


Figure 8.9: Demoulding time, wrinkle amplitude and bridging distance *versus* the model tool/base temperature.

With the maximum allowable bridging distance being 5 mm, the tool temperature at 200 °C, with a demoulding time of 38 seconds was defined as the optimal condition for forming quality and minimised processing time.

8.3.2.3 Zonal Tooling

Considering Figure 8.7, it was apparent that the problem with forming at lower temperatures was specifically related to the restriction of material draw-in as a result of the cool base temperature. This is the same outcome as that presented in Section 6.4.2, where the cold laminate extremities are what caused a significant decrease in laminate forming quality. With a double-dome geometry, however, the material that is in contact with the mould experiences little movement after mould-contact is made. The draw-in that occurs relates specifically to the base. Therefore, it was hypothesised that the tool/base temperature could be further optimised by setting each to a different temperature. This would be possible in practice since each is a different component meaning they could be thermally isolated from each other.

Figure 8.7b shows that the large majority of the double-dome geometry is well formed with a tool temperature of 160 °C with wrinkles mostly occurring around the base and bridging regions. Only with a 140 °C tool do wrinkles propagate over the double-dome itself. Therefore, a tool temperature of 160 °C was fixed with base temperatures

changed in increments of 20 °C, up to 220 °C. The simulations were subsequently re-run with these zoned tooling temperatures. Figure 8.10 illustrates the results from these forming operations.

Since the tool and base temperature are different, a different thermal profile is exhibited by the laminates where the double-dome cools considerably, but the base section remains warmer (where the base is a higher temperature). This is also highlighted in Appendix F - Figure F.2 which shows the cooling rate and relative crystallisation for each of the four tested conditions. The relative crystallinity for the top of the double-dome is identical in each case which was expected due to the constant tool temperature and low in-plane thermal conductivity.

Increasing just the base temperature up to (and above) 200 °C was sufficient to significantly reduce the amount of wrinkling present compared to the nominal case where both the mould and base are at 160 °C. A base temperature of 180 °C was also not sufficient to considerably reduce wrinkling and ‘rippling’ behaviour. The maximum bridging for a laminate with a 200 °C base was 5 mm, which also represents the threshold chosen in this study for forming quality. Furthermore, the apex wrinkle amplitude was 5.9 mm, only 0.5 mm greater than when both the tool and the base were at 200 °C. Further reductions could also be achieved with a 220 °C base (4.7 mm bridging, 5.8 mm wrinkle amplitude).

Since the mould temperature was fixed at 160 °C, the demoulding time for each of these laminates was identical at 23 seconds (Figure 8.9). While the portion of the laminate in contact with the base was considerably warmer in the case of the 200 °C and 220 °C bases, the extremities of the laminate (short-edges) were still much cooler. Therefore it was still assumed that once the double dome centre has achieved sufficient rigidity, the laminate can be demoulded safely. As noted in Section 8.3.2.2, this assumption would need to be evaluated to ensure that the laminate did not deform upon demoulding.

Forming with a 160 °C mould and 200 °C base therefore represents further optimisation in this work, resulting in acceptable forming quality (within predefined limits) and a minimised demoulding time of 23 seconds, compared to 38 seconds for a homogeneous tool temperature. Further thermal zoning is possible, such as a

different temperature of the domes compared to the central tapered section. This would likely require an intricate split tool however due to the high aluminium conductivity, out of the scope of this work where the objective was to keep the associated tooling costs low.

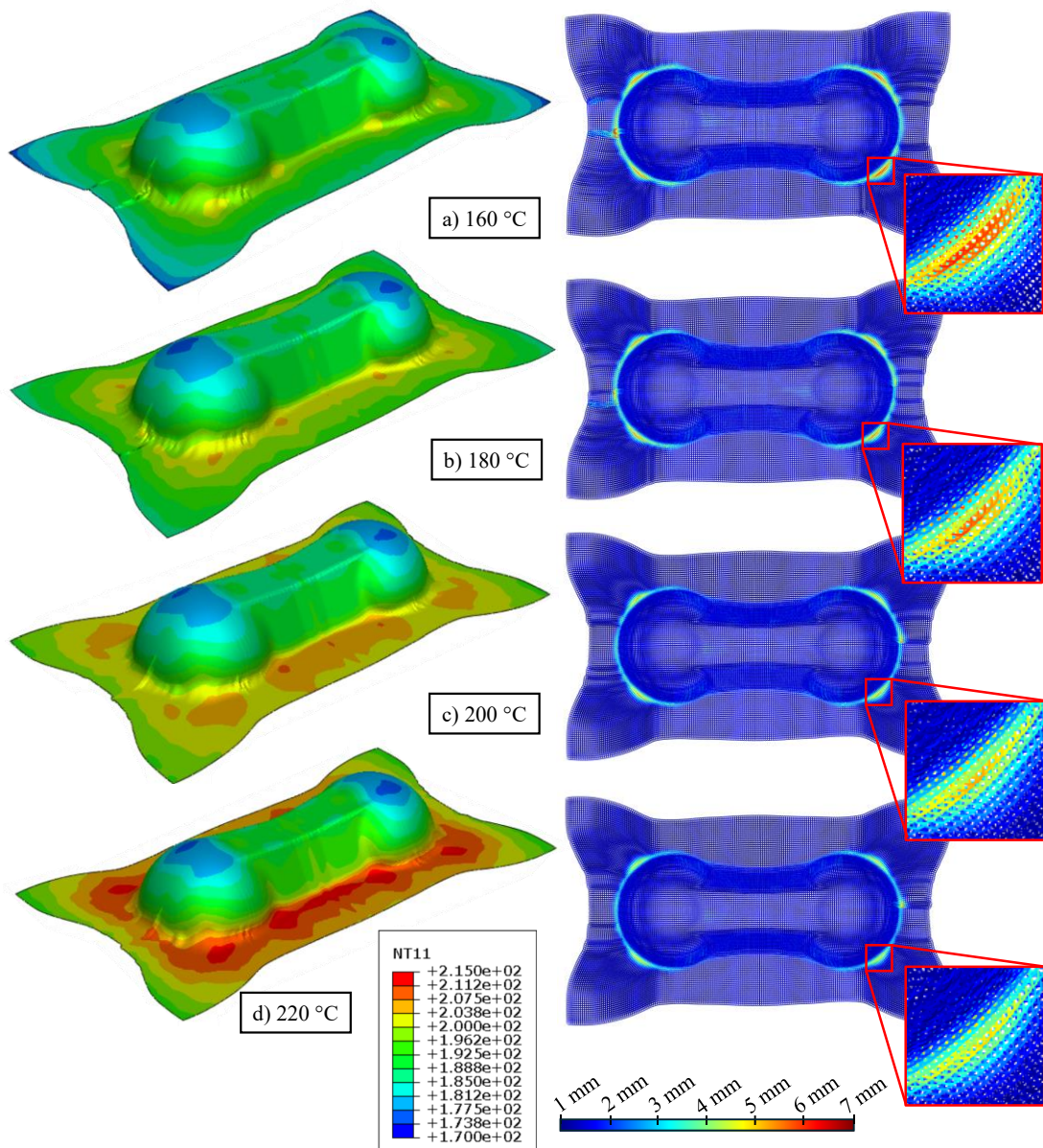


Figure 8.10: Simulated forming behaviour for a laminate with an initial centre temperature (inhomogeneous profile) of 250 °C, a constant tool temperature (160 °C) and different base temperatures: a) 160 °C, b) 180 °C, c) 200 °C, d) 220 °C.

8.4 Chapter Conclusions

In this chapter, the transient thermal effects, characterised in Chapter 7, were implemented within the numerical forming model, produced in Chapter 6, resulting in the creation of a fully-coupled non-isothermal FRTP DDF simulation. The model itself was similar to that of the isothermal variant, although an increase in the number of through-thickness integration points (from three to seven) was required to ensure model stability under transient thermal conditions. Laminate crystallisation was implemented alongside all heat transfer mechanisms allowing the model to predict the increase in laminate rigidity upon cooling, identified in Section 6.4.4 as being a severe limitation of an isothermal model for low temperature forming prediction.

Initially, the influence of forming rate was studied. As opposed to the isothermal models that indicate a noticeable increase in wrinkling and bridging for higher forming rates, the difference at a non-isothermal condition was much smaller. Bridging was reduced by 0.3 mm when forming at a higher speed owing to the reduction in laminate cooling, compared to a 0.1 mm increase in the isothermal work. No significant difference regarding the apex wrinkle was noted, although the laminate forming at high speed did exhibit 'rippling' behaviour, also witnessed on the isothermal forms. Forming at the lower speed was upheld in this work because of this outcome and to allow for tool temperature optimisation. The non-isothermal simulation was subsequently run with 5 different tool temperatures. It was found that an optimal temperature of 200 °C exists, resulting in acceptable forming quality (bridging less than 5 mm and one apex wrinkle) and minimised (38-second) combined forming and cooling time. A novel zoned tool was then introduced, where the mould was held at 160 °C and the base at 200 °C, resulting in no difference to the forming quality, but a 42% reduction in the demoulding time.

This chapter therefore represents not only an advancement in the already unique DDF simulation presented in Chapter 6, but optimisation of the forming process. As outlined in Section 1.1, it is this simulation and optimisation that will pave the way for the increased uptake of FRTPs in industry.

Chapter 9.

Conclusions

9.1 Summary of Thesis

This thesis set out to address a clear gap in the literature: the absence of a reliable forming simulation for FRTP laminates within the DDF process. While FRTP thermostamping has benefitted from decades of research and progressively sophisticated simulations, the FRTP DDF process, despite its industrial potential, lacked a predictive numerical framework. By producing a bespoke, fully-coupled thermomechanical simulation for FRTP DDF, this thesis provides not only a scientific contribution but also a practical foundation for the industrial uptake of FRTPs.

The research demonstrates that FRTP forming is not simply a thermal variant of thermoset prepreg forming. Instead, it is governed by complex couplings between viscoelastic deformation, transient heat transfer, and crystallisation kinetics. The outcomes of this thesis therefore extend beyond the DDF process: they show how FRTP materials demand a different philosophy of process simulation, one in which time-dependent thermal effects are inseparable from the mechanical response.

9.2 Reflection and Implications

This section addresses the four individual objectives (Section 1.2) and discusses the manner to which they have been addressed, the significance of these findings and the broader implications for industry, modelling, and FRTP forming.

9.2.1 Objective 1: Experimental DDF study

The experimental programme established that FRTP laminates can indeed be formed successfully with the DDF process, but only within a relatively narrow processing window. The sensitivity to forming temperature and rate was particularly striking. For example, reducing the forming temperature from 250 °C to 200 °C more than doubled bridging distances and increased wrinkle severity by several-fold. These results underline the central limitation of FRTP DDF: the material is highly formable when hot, but the onset of cooling, even by a few tens of degrees, dramatically restricts deformation. Similarly, high-rate forming resulted in a 58% increase in wrinkle amplitude under identical process conditions.

This experimental insight matters for two reasons. Firstly, it confirms that industrial DDF processes cannot rely on broad process windows; instead, precise thermal control is essential. Secondly, it provided the necessary benchmark data against which the numerical models could be validated. Without this foundation, the subsequent modelling work would have lacked credibility.

9.2.2 Objective 2: Thermomechanical Characterisation

The detailed material characterisation (Chapters 4 & 5) produced perhaps the most fundamental scientific contribution of this thesis: a quantitative description of FRTP behaviour across multiple deformation modes, consolidated into parameterised forms suitable for finite element implementation.

Crucially, the work revealed that existing characterisation methods developed for dry fabrics or thermoset prepregs are not always transferable. For example, the bias-extension test was shown to be superior to the picture-frame test for FRTP intra-ply shear, owing to clamping artefacts and thermal anomalies unique to thermoplastic organosheets. This highlights the need to adapt classical tests to the realities of FRTP processing. Furthermore, pull-through friction tests illustrated that the ply-diaphragm interface operates entirely within the hydrodynamic boundary region. Once again, this is in stark contrast to friction associated with dry fabrics which is dominated by the fibre interface as opposed to a matrix boundary layer.

The characterisation also provided practical insight into the diaphragm behaviour. It was shown that silicone diaphragms can be assumed effectively isotropic and rate-independent, means that industrial models can confidently neglect these complexities, saving both experimental effort and computational cost. The significant strain-history dependent response of silicone can also be eliminated via a novel technique of precompression. This allows for more consistent silicone diaphragm behaviour (with an approximately 25% reduction in stiffness), thus resulting in more repeatable and reliable DDF forming.

9.2.3 Objective 3: Creation of a Thermomechanical Simulation

The first version of the numerical model, an isothermal simulation, was able to replicate many key forming defects with good fidelity. Wrinkle amplitudes were

captured within 20% accuracy, bridging within 0.5 mm, and shear angles within 1° for simulations at higher temperatures ($210\text{ °C} \leq$). While shear forces were overestimated due to the chosen normalisation method, the viscoelastic trends were well reproduced with thermally coupled shear, bending and friction mechanisms.

The accuracy of the model was also shown to not degrade significantly with an alternative -45/45° fibre orientation or forming rate at a higher forming rate. The accuracy of bridging and in-plane shear predictions did, however, significantly degrade at the lowest tested temperature of 200 °C, with errors of 39% and 16% respectively. This was due to localised crystallisation effects and high forming sensitivity. Including the inhomogeneous thermal profile from the experimental study reduced these errors by 44% and 62% respectively.

The significance here lies not just in reproducing the experiments, but in showing that a DDF-specific numerical framework is viable at all. Until this work, there was no demonstration that the complex coupling between diaphragms, friction, and ply deformation could be represented numerically, especially when including a thermal-coupling for each of these elements. This provides the industry with confidence that process-specific models can be built, validated and trusted for FRTP DDF prediction.

9.2.4 Objective 4: DDF Process Conditions Optimisation

The integration of transient heat transfer and crystallisation behaviour into the forming simulation represented a step change from an isothermal approximation to a fully-coupled non-isothermal model, which the literature recognises as state-of-the-art.

The non-isothermal model was not only a technical upgrade; it fundamentally altered the interpretation of forming behaviour. For instance, whereas the isothermal model suggested high forming rates worsen wrinkling, the coupled model showed that faster forming can sometimes improve quality by reducing cooling-induced stiffening. Similarly, tool temperature studies revealed that a moderate 200 °C tool represents the optimum compromise between formability and demoulding time. Such nuanced insights are only possible when transient effects are included. This level of forming optimisation is not present in current FRTP simulation publications and advances this work to a level at which it can inspire a step change in the industry uptake of FRTPs.

The exploration of zonal tooling added an important industrial perspective. By demonstrating that a cooler mould paired with a warmer base can cut demoulding time by 42% without degrading quality, this thesis points to practical strategies for further reducing cycle time and therefore part cost, a key barrier to wider FRTP adoption.

9.3 Overall Impact and Contribution

Collectively, this thesis delivers three major contributions:

1. Experimental evidence that the DDF process is viable for FRTPs but constrained by narrow thermal process windows.
2. A validated, process-specific simulation framework capable of reproducing both forming defects and transient cooling effects, advancing beyond the capabilities of matched-tool simulations.
3. Demonstrated pathways for process optimisation, including tool temperature management and heating strategies, directly relevant to industrial practice.

These contributions shift FRTP DDF forming from an experimental curiosity toward a scientifically grounded, optimisable process. For industry, the work suggests that reliable DDF production is achievable, provided simulations are used to identify process windows and optimise forming conditions. For academia, it provides a methodological roadmap: adapt test methods for FRTPs, parameterise the results, implement them into a DDF-specific model, and validate with carefully controlled experiments.

9.4 Recommendations for Future Work

This thesis has provided the first validated simulation of FRTP DDF forming, but it should be seen as a foundation. Future work can be grouped under the four objectives of this study:

1) Experimental FRTP DDF process

Repeatability could be improved through semi-automated or robotic forming cells to reduce operator variability. Alternative heating methods (e.g., conductive or laser)

could overcome the in-plane temperature gradients seen with IR lamps. Studies on multi-ply laminates, more complex geometries, and alternative diaphragm materials (e.g., high-temperature silicones [448]) would further demonstrate industrial viability.

2) Material characterisation

This work assumed silicone was isotropic, rate-independent, and nearly temperature-insensitive. Future studies should test these assumptions and assess whether diaphragm mechanics can be exploited as a lever to improve forming outcomes.

3) Thermomechanical simulation

The current simulation is accurate but computationally expensive (>100 hours per run). Efforts should focus on improving algorithm efficiency, incorporating neglected effects (thermal expansion of silicone, realistic IR heating, coupled bending stiffness), and extending the model to multi-ply laminates. These steps would make the model more practical for industry.

4) Process optimisation

Optimisation in this work was limited to tool temperature. Expanding this to include forming rate, laminate temperature, and advanced zoned tooling would better balance quality and cycle time. Future models should also predict residual stresses and warpage after cooling, ensuring parts meet structural tolerance requirements.

9.5 Final Remarks

This thesis has shown that the challenge of FRTP DDF is not simply exceeding a laminate's melting temperature, but managing the dynamic interaction between deformation, heat transfer and crystallisation kinetics. By embedding this reality into a fully-coupled simulation, the work provides both new scientific understanding and a practical tool for process engineers.

In conclusion, the significance of this research is that it moves FRTP DDF forming from a trial-and-error practice toward a predictive, optimisable technology. This is a necessary step if FRTP composites are to fulfil their promise of faster, greener, and more recyclable structural components in aerospace, automotive, and beyond.

Appendix A.

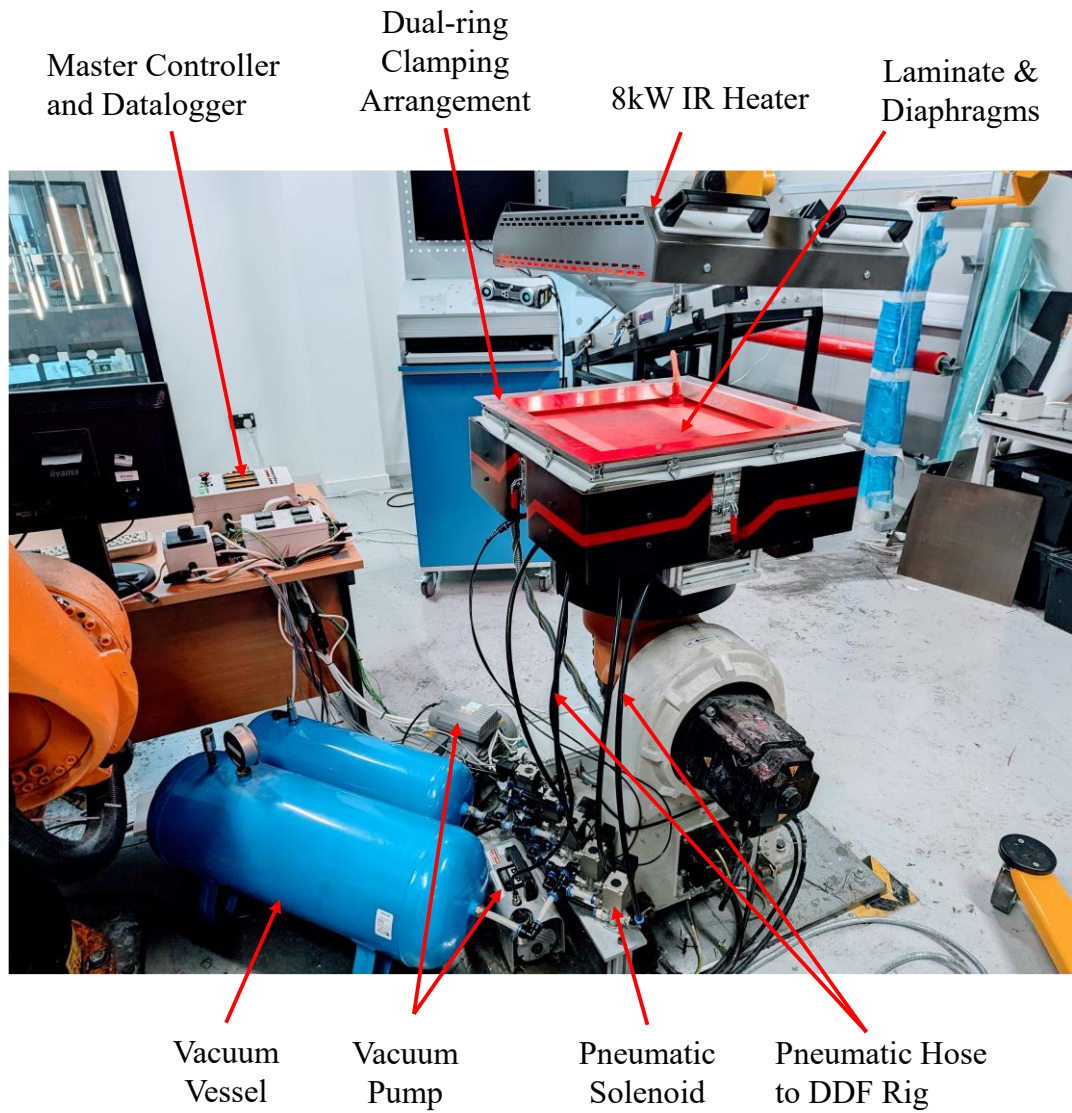


Figure A.1: All components associated with the DDF rig.

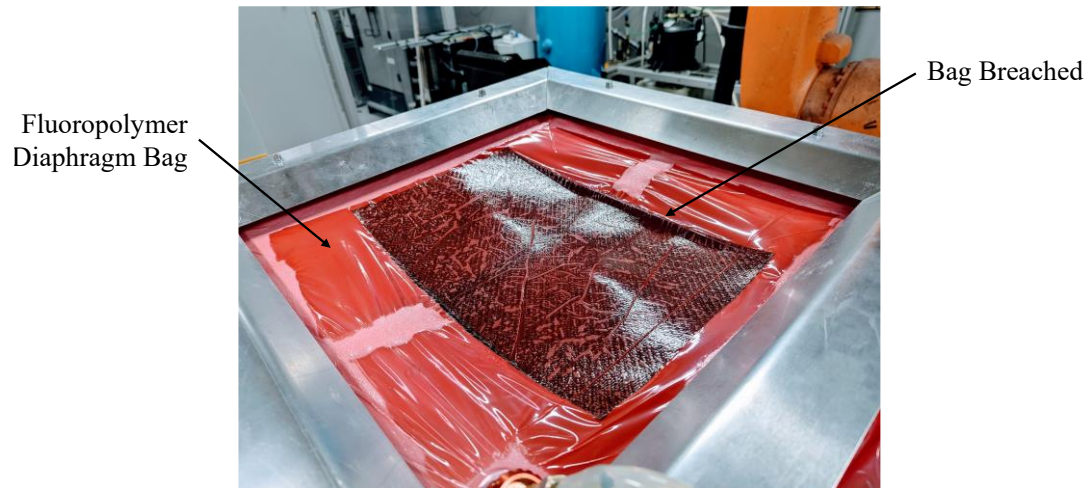


Figure A.2: Failure of a fluoropolymer diaphragm bag experienced during DDF trials.

Appendix B.

Table B.1: Values of all fixed constants in Chapter 4.

Constant	Value	Units	Constant	Value	Units
m_γ	106.0	mm^{-2}	λ	0.00538	s
n_γ	18.61	mm^{-1}	a	1.778	-
s_1	7.021	MPa	n	0.593	-
s_2	-16.90	MPa	t_{itf}	2.5	μm
s_3	18.11	MPa	E_a	60.5	$J \cdot mol^{-1}$
s_4	-9.421	MPa	R	8.314	$J \cdot mol^{-1} \cdot K^{-1}$
s_5	2.312	MPa	T_{ref}	250	K
D_s	3.670	s^{-1}	P_b	0.02662	$N \cdot m^{Q_b}$
P_s	2.929	-	Q_b	0.2897	-
A_s	-24.01	-	r_b	-11.42	-
T_s	232.6	K	T_b	211.4	K
b_s	2.142	-	u_1	8.09E-9	$N \cdot mm^6$
n_d	0.0915	m^{-1}	u_2	-1.35E-6	$N \cdot mm^5$
m_d	1.1816	-	u_3	8.16E-5	$N \cdot mm^4$
n_s	0.1934	m^{-1}	u_4	2.07E-3	$N \cdot mm^3$
m_s	2.4737	-	u_5	1.66E-2	$N \cdot mm^2$
η_0	291.0	Pa·s	u_6	3.26E-1	$N \cdot mm^{-1}$

Appendix B

Table B.2: Test conditions and shear factors for intra-ply shear characterisation.

Condition No.	Displacement Rate (mm/min)	Temperature (°C)	Single-ply shear factor
1	20	210	1.16
2	20	230	0.372
3	20	250	0.285
4	20	270	0.282
5	100	210	2.81
6	100	230	0.653
7	100	250	0.468
8	100	270	0.400
9	500	210	4.41
10	500	230	1.31
11	500	250	0.786
12	500	270	0.657

Table B.3: Temperature specific constants for the laminate bending study.

Constant	210 °C	230 °C	250 °C	270 °C
p_b (N · m ^{q_b})	0.07248	0.03169	0.02995	0.02648
q_b	0.3549	0.2371	0.2793	0.2876
B	2.078	1.361	1.154	1.00

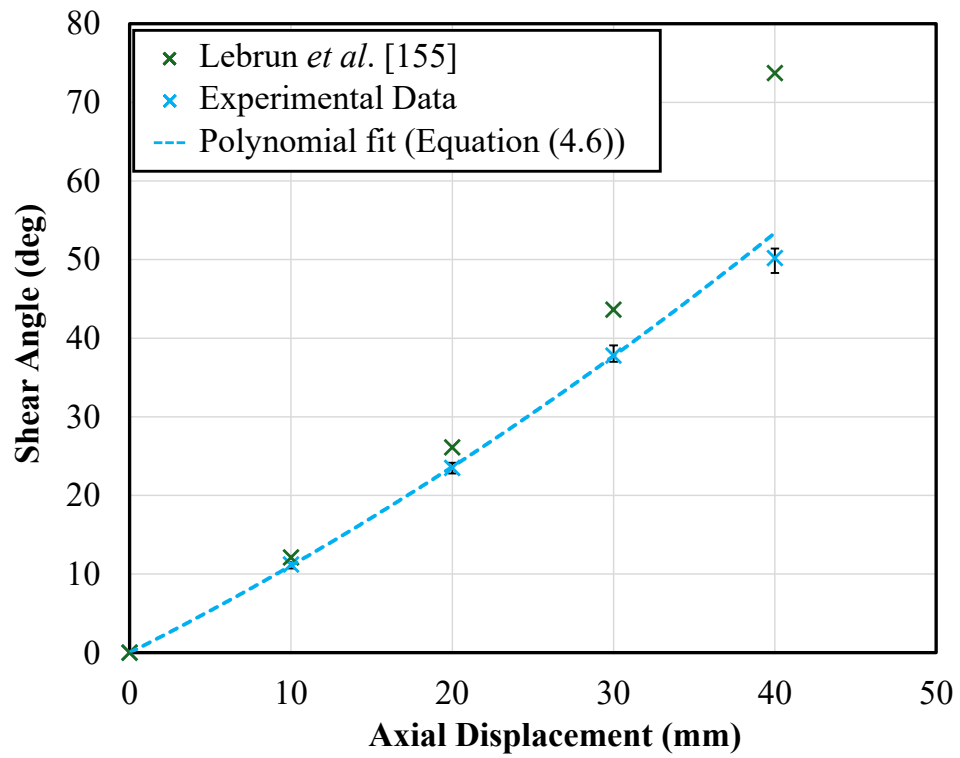


Figure B.1: Shear angle *versus* axial displacement experimental polynomial fit *versus* analytical [156].

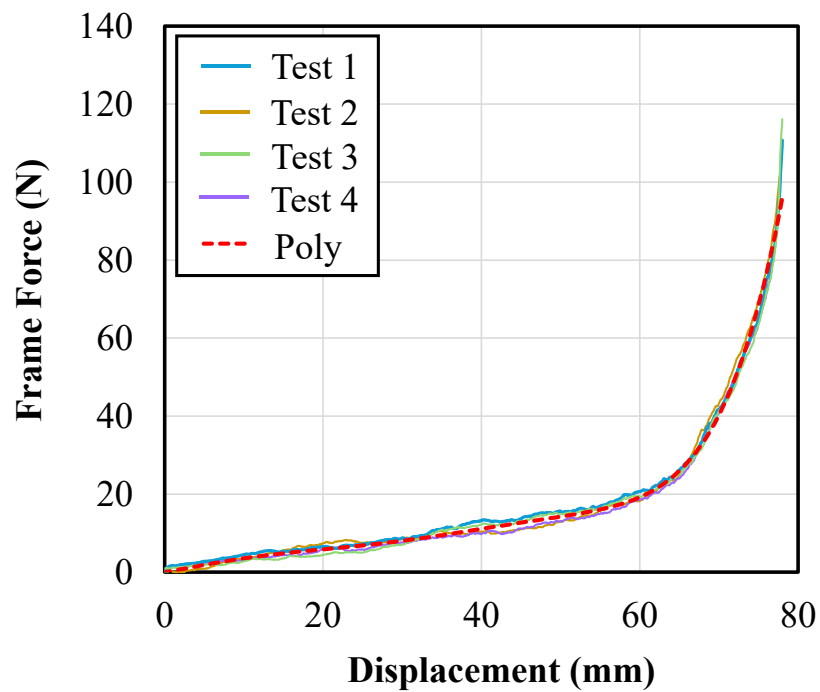


Figure B.2: PFT Frame force and combined polynomial, as subtracted from the raw PFT force results.

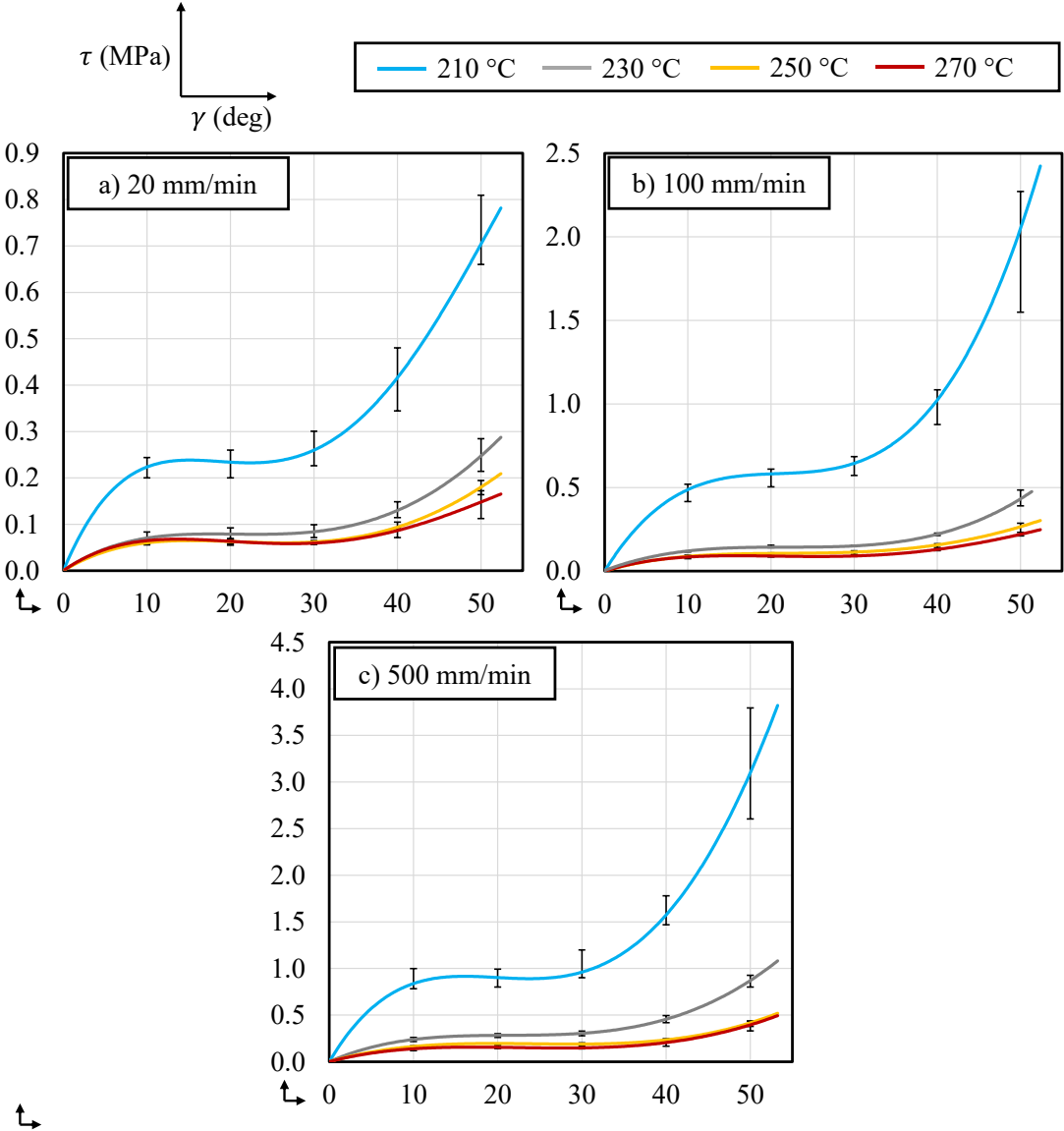


Figure B.3: Shear stress *versus* shear angle for single-ply CF/PA6 laminates at different test conditions.

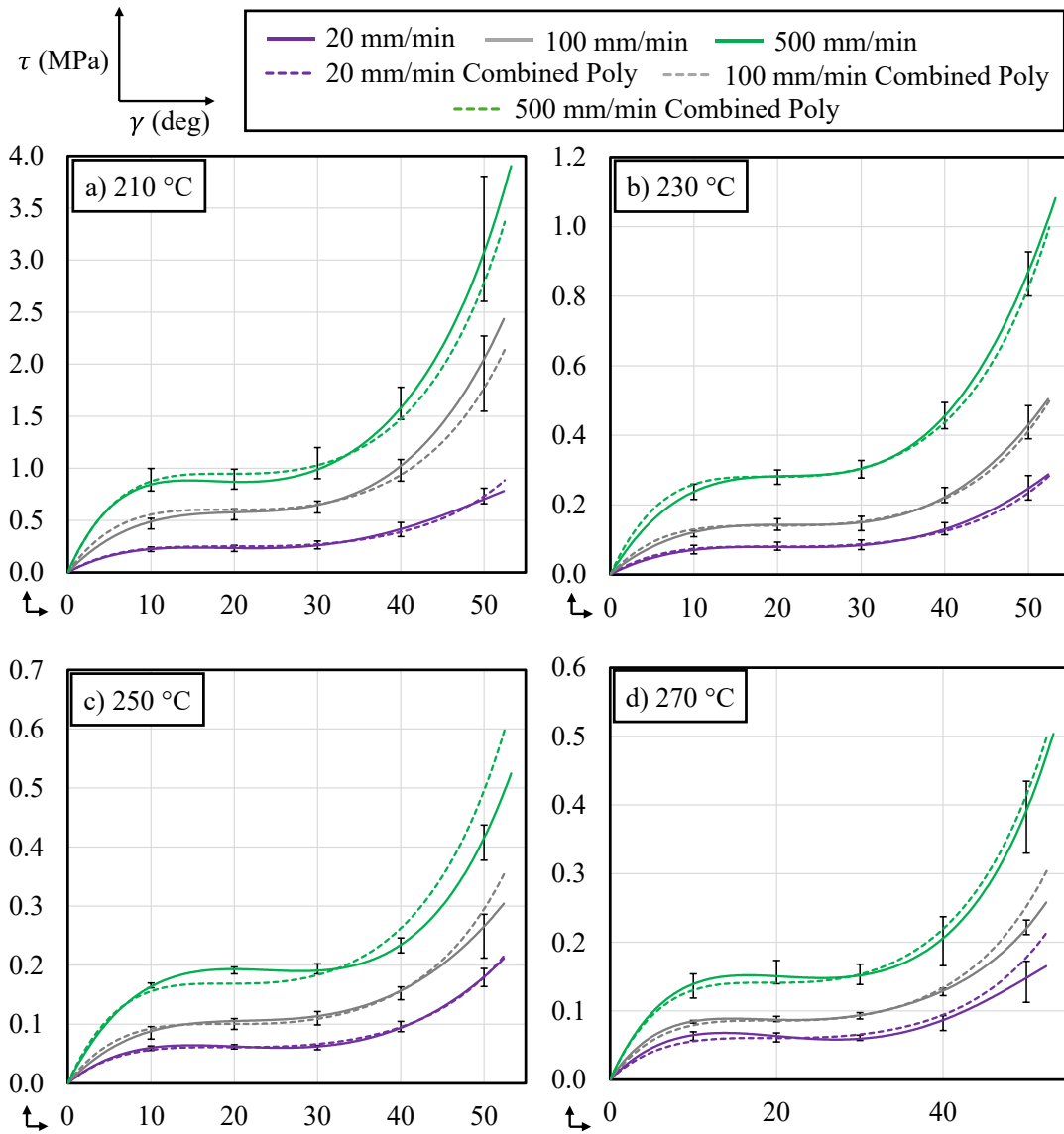


Figure B.4: Shear stress *versus* shear angle for CF/PA6 laminates - combined polynomial fitting.

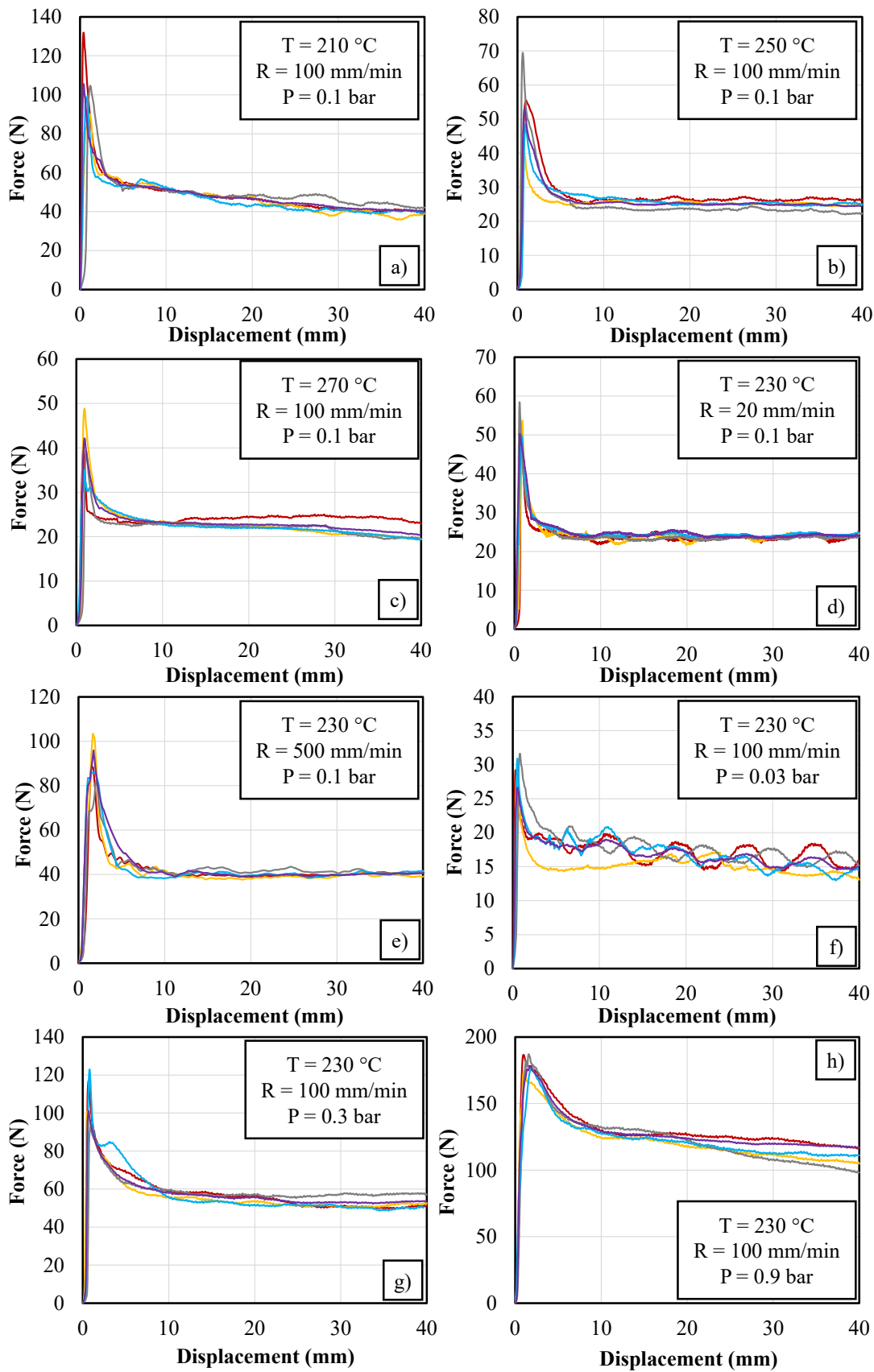


Figure B.5: Raw force *versus* displacement results for diaphragm -ply friction testing.

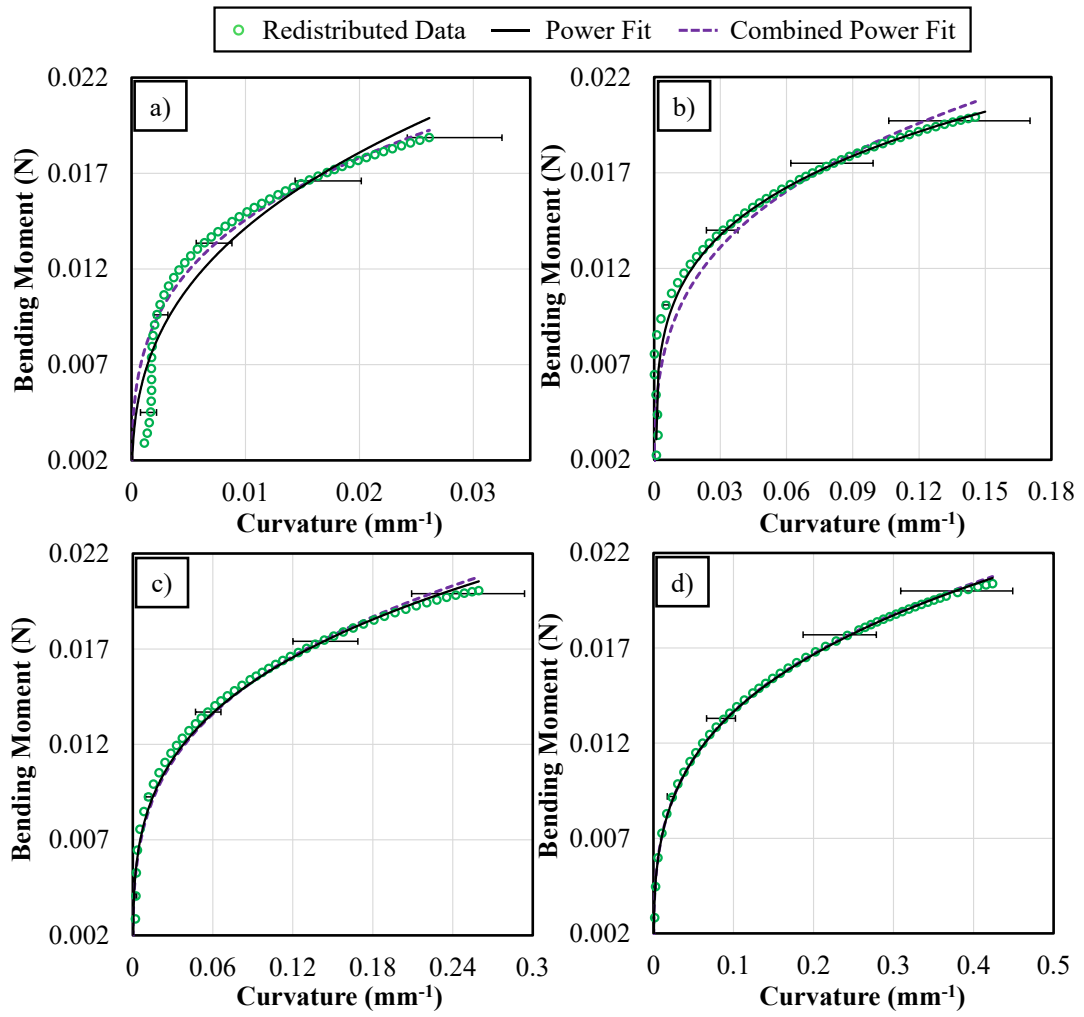


Figure B.6: Bending moment *versus* curvature for CF/PA6 laminates at different temperatures; combined power fitting.

Appendix C.

Table C-1: Ogden coefficients

Constant	Value	Units
α_1	1.915	-
α_2	3.663	-
α_3	4.680	-
α_4	0.06148	-
α_5	-1.357	-
α_6	-2.166	-
μ_1	4.899E+6	Pa
μ_2	-3.577E+6	Pa
μ_3	1.243E+6	Pa
μ_4	-3.149E+6	Pa
μ_5	1.386E+6	Pa
μ_6	-3.071E+5	Pa

Appendix D.

D.1 Hypoplastic Law

The hypoelastic law, defined in [292, 454], resembles:

$$\underline{\underline{\underline{\sigma}}}^\nabla = \underline{\underline{\underline{C}}} : \underline{\underline{\underline{D}}} \quad (\text{D.1})$$

where $\underline{\underline{\underline{\sigma}}}$ is the Euclidean tensor of the Cauchy stress, $\underline{\underline{\underline{C}}}$ is the Euclidean constitutive tensor oriented in the fibre direction, and $\underline{\underline{\underline{D}}}$ is the strain rate. Note the colon represents the tensor contraction, reducing the rank of the matrices by two. The superscript ∇ illustrates that the Euclidean tensor of Cauchy stress is an objective derivative to avoid stress change through rigid body rotations. It can further be represented mathematically as:

$$\underline{\underline{\underline{\sigma}}}^\nabla = \underline{\underline{\underline{\Phi}}} \left[\frac{\delta}{\delta t} \left(\underline{\underline{\underline{\Phi}}}^T \cdot \underline{\underline{\underline{\sigma}}} \cdot \underline{\underline{\underline{\Phi}}} \right) \right] \underline{\underline{\underline{\Phi}}}^T \quad (\text{D.2})$$

where $\underline{\underline{\underline{\Phi}}}$ is the rotation of the fibre.

To implement this hypoplastic law (Equation), the current fibre directions must be updated within the constitutive model, since the Euclidean constitutive tensor, $\underline{\underline{\underline{C}}}$, is oriented in the fibre direction. This process is not trivial, because in Abaqus/Explicit (and other commercial finite element packages) large-strain analyses are based on the Green-Naghdi rotated frame to update the Cauchy stress tensor. Therefore, the strains must be transformed from the GN axes to the current fibre axes. The rotational tensor, $\underline{\underline{\underline{R}}}$, for this operation, is obtained from the polar decomposition of the deformation gradient tensor, $\underline{\underline{\underline{F}}}$:

$$\underline{\underline{\underline{R}}} = \underline{\underline{\underline{F}}} \underline{\underline{\underline{U}}}^{-1} \quad (\text{D.3})$$

where $\underline{\underline{U}}$ is the right stretch tensor. Therefore, the GN rotated frame in the initial configuration, $\underline{\underline{g}}_z^0$, can be updated using this rotational tensor to ascertain the vectors of the updated frame, $\underline{\underline{g}}_z$, where the subscript ‘z’ represents the three vector directions (1, 2, 3):

$$\underline{\underline{g}}_z = \underline{\underline{R}} \cdot \underline{\underline{g}}_z^0 \quad (\text{D.4})$$

Both the original and updated frames are illustrated on . The fibre directions, $\underline{\underline{f}}_{i,j}$, are found using the deformation gradient tensor, $\underline{\underline{F}}$, noting that once again the superscript ‘0’ represents the initial configuration. In the following, let i and j represent the two fibre directions, where the subscript ($\underline{\underline{f}}_i$) represents the (covariant) principal fibre direction and the superscript ($\underline{\underline{f}}^i$) represents the perpendicular (contravariant) direction. $\underline{\underline{f}}_3$ represents the orthogonal normal direction:

$$\underline{\underline{f}}_i = \frac{\underline{\underline{F}} \cdot \underline{\underline{f}}_i^0}{\|\underline{\underline{F}} \cdot \underline{\underline{f}}_i^0\|} \quad (\text{D.5})$$

$$\underline{\underline{f}}^i = \frac{\underline{\underline{F}} \cdot \underline{\underline{f}}_j^0 - (\underline{\underline{F}} \cdot \underline{\underline{f}}_j^0 \cdot \underline{\underline{f}}_i) \underline{\underline{f}}_i}{\|\underline{\underline{F}} \cdot \underline{\underline{f}}_j^0 - (\underline{\underline{F}} \cdot \underline{\underline{f}}_j^0 \cdot \underline{\underline{f}}_i) \underline{\underline{f}}_i\|} \quad (\text{D.6})$$

$$\underline{\underline{f}}_3 = \underline{\underline{f}}^3 = \underline{\underline{f}}_i \times \underline{\underline{f}}^i \quad (\text{D.7})$$

Note that $\underline{\underline{g}}_1^0$ and $\underline{\underline{f}}_i^0$ (and subsequently $\underline{\underline{g}}_2^0$ and $\underline{\underline{f}}_j^0$) are assumed to begin coincident with one another, and can therefore be substituted for one another in Equations -. For concision, only the equations for the i^{th} fibre direction have been illustrated. It can be seen on that the two fibre directions, $\underline{\underline{f}}_i$ and $\underline{\underline{f}}_j$, hereby have their own respective orthogonal frames ($[\underline{\underline{f}}_i, \underline{\underline{f}}^i, \underline{\underline{f}}^3]$ and $[\underline{\underline{f}}_j, \underline{\underline{f}}^j, \underline{\underline{f}}^3]$). After deformation, it is highly unlikely that orthogonality is maintained between them.

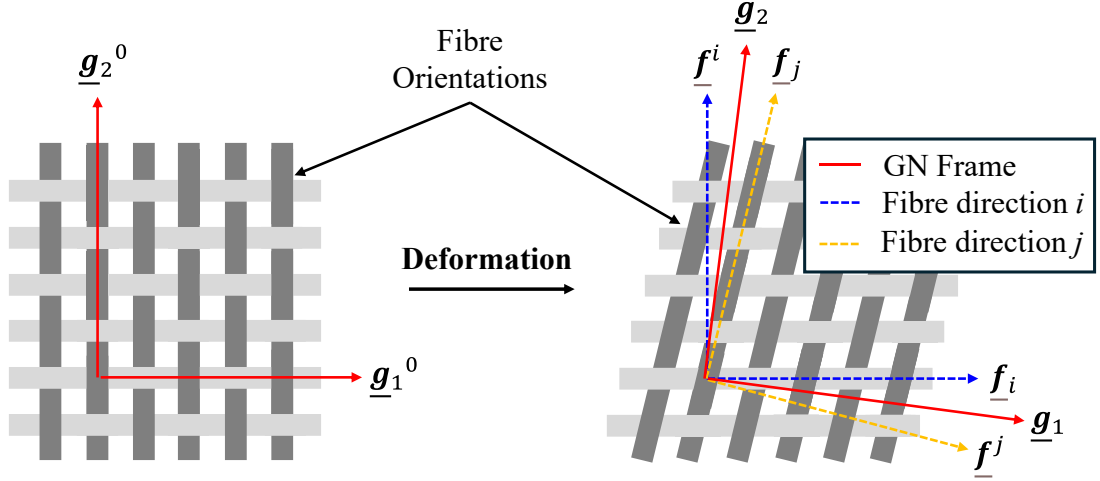


Figure D.1: Orientation of Green-Naghdi axes and fibre axes after the occurrence of deformation.

With the GN axes and fibre axes both known, the fibre strain components can be transferred between them using the following transformation matrices:

$$\underline{\underline{Q}}_i = \underline{\underline{Q}}_{i \rightarrow GN} = \begin{bmatrix} \underline{g}_1 \cdot \underline{f}_i & \underline{g}_1 \cdot \underline{f}_j & \underline{g}_1 \cdot \underline{f}^3 \\ \underline{g}_2 \cdot \underline{f}_i & \underline{g}_2 \cdot \underline{f}_j & \underline{g}_2 \cdot \underline{f}^3 \\ \underline{g}_3 \cdot \underline{f}_i & \underline{g}_3 \cdot \underline{f}_j & \underline{g}_3 \cdot \underline{f}^3 \end{bmatrix} \quad (D.8)$$

$$\underline{\underline{Q}}_j = \underline{\underline{Q}}_{j \rightarrow GN} = \begin{bmatrix} \underline{g}_1 \cdot \underline{f}^i & \underline{g}_1 \cdot \underline{f}_j & \underline{g}_1 \cdot \underline{f}^3 \\ \underline{g}_2 \cdot \underline{f}^i & \underline{g}_2 \cdot \underline{f}_j & \underline{g}_2 \cdot \underline{f}^3 \\ \underline{g}_3 \cdot \underline{f}^i & \underline{g}_3 \cdot \underline{f}_j & \underline{g}_3 \cdot \underline{f}^3 \end{bmatrix} \quad (D.9)$$

Therefore, the strain increment, $d\varepsilon$, for each fibre direction, as calculated in each increment by the FE solver, can be transferred from the GN frame (subscript ‘GN’) to the fibre frames (subscript f) using:

$$d\varepsilon_{fi} = \underline{\underline{Q}}_i^T \cdot d\varepsilon_{GN} \cdot \underline{\underline{Q}}_i \quad (D.10)$$

$$d\varepsilon_{fj} = \underline{\underline{Q}}_j^T \cdot d\varepsilon_{GN} \cdot \underline{\underline{Q}}_j \quad (D.11)$$

where T denotes the matrix transpose. The stress increment can be calculated from the aforementioned strain increments (Equations (D.10) & (D.11)) and the Cauchy constitutive tensor in the fibre directions, $\underline{C}_{fi,j}$, as per Equation :

$$d\boldsymbol{\sigma}_{fi} = \mathbf{C}_{fi} \cdot d\boldsymbol{\varepsilon}_{fi} \quad (\text{D.12})$$

$$d\boldsymbol{\sigma}_{fj} = \mathbf{C}_{fj} \cdot d\boldsymbol{\varepsilon}_{fj} \quad (\text{D.13})$$

which can be defined explicitly as (assuming only the fibre elastic modulus and shear modulus are the only non-zero values):

$$\begin{bmatrix} d\sigma_{11} \\ d\sigma_{22} \\ d\sigma_{12} \end{bmatrix}_{fi} = \begin{bmatrix} E_{fi} & 0 & 0 \\ 0 & 0 & 0 \\ 0 & 0 & G_{ij}(\gamma) \end{bmatrix} \begin{bmatrix} d\varepsilon_{11} \\ d\varepsilon_{22} \\ d\varepsilon_{12} \end{bmatrix}_{fi} \quad (\text{D.14})$$

$$\begin{bmatrix} d\sigma_{11} \\ d\sigma_{22} \\ d\sigma_{12} \end{bmatrix}_{fj} = \begin{bmatrix} 0 & 0 & 0 \\ 0 & E_{fj} & 0 \\ 0 & 0 & G_{ij}(\gamma) \end{bmatrix} \begin{bmatrix} d\varepsilon_{11} \\ d\varepsilon_{22} \\ d\varepsilon_{12} \end{bmatrix}_{fj} \quad (\text{D.15})$$

In the case analysed here, and as detailed in the work of Badel *et al.* [325], it can be assumed that the contribution of each yarn to the shear force is equal, such that the shear modulus can be calculated using the normalised shear force, F_n :

$$G_{ij}(\gamma) = \frac{F_n}{h} \quad (\text{D.16})$$

where h is the thickness of the shell element.

These stress increments may be added to the total fibre stress at the beginning of the increment, $\boldsymbol{\sigma}^n$, to calculate the final stress at the end of the increment, $\boldsymbol{\sigma}^{n+1}$, as per the incremental formulation of Hughes *et al.* [455]. This formulation is utilised in Abaqus/Explicit, represented mathematically as:

$$\boldsymbol{\sigma}_{fi}^{n+1} = \boldsymbol{\sigma}_{fi}^n + d\boldsymbol{\sigma}_{fi} \quad (\text{D.17})$$

$$\boldsymbol{\sigma}_{fj}^{n+1} = \boldsymbol{\sigma}_{fj}^n + d\boldsymbol{\sigma}_{fj} \quad (\text{D.18})$$

Finally, for implementation within Abaqus/Explicit, these stresses are transformed back into the GN frame:

$$\boldsymbol{\sigma}_{GN}^{n+1} = \left[\underline{\underline{\mathbf{Q}}}_i \cdot \boldsymbol{\sigma}_{fi}^{n+1} \cdot \underline{\underline{\mathbf{Q}}}_i^T \right] + \left[\underline{\underline{\mathbf{Q}}}_j \cdot \boldsymbol{\sigma}_{fj}^{n+1} \cdot \underline{\underline{\mathbf{Q}}}_j^T \right] \quad (\text{D.19})$$

D.2 Bending Formulation

The bending moments in each fibre direction, M_{fi} and M_{fj} , are calculated by integrating the moment from the fibre stress at each individual integration point through the shell element thickness (only equations for the i^{th} direction are illustrated for concision):

$$M_{fi} = \int_{-h/2}^{h/2} [\sigma_{fi}(z) \cdot \bar{F}_{33}^2 \cdot z] dz \quad (\text{D.20})$$

where \bar{F}_{33} represents the relative thickness change (the deformation gradient in the thickness direction) and z represents the original distance between the shell reference plane and the integration point. Shell elements are incompressible in the thickness direction, however, so the thickness change can instead be calculated using the in-plane components of the deformation gradient:

$$\bar{F}_{33} = \frac{1}{\bar{F}_{ii}\bar{F}_{jj} - \bar{F}_{ij}\bar{F}_{ji}} \quad (\text{D.21})$$

To decouple the membrane and bending behaviour within Abaqus/Explicit, the Abaqus Composite Layup Toolset was used to split each fabric shell element into three theoretical layers. The central layer was denoted the ‘core’ and the two outer layers, the ‘covers’. At the shell reference surface (through the centre of the core), $z=0$, meaning the bending moment component at this point is equal to zero (Equation). Therefore, setting the number of integration points to one for this core layer means it has no influence on the bending stiffness of the shell element. In this manner, only the cover layers influence the bending moment of the element. The core layer can subsequently be used to solely represent the membrane behaviour of the shell element. illustrates the shell element cross-section.

It is worth noting that while it is possible to assign three integration points to the cover layers, the stress/strain relationship at each point is assumed to be elastic, meaning that the use of one integration point per cover layer is sufficient. Furthermore, it is not possible in Abaqus to assign a different number of integration points to different layers of a heat transfer shell element. This also reduces the numerical

expense associated with each element and removes the inertia moment of each cover layer with respect to its centroid axis.

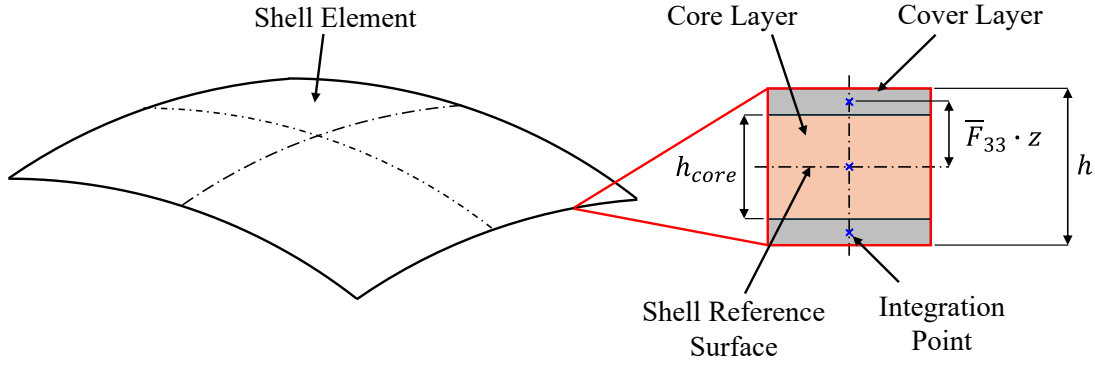


Figure D.2: Shell element cross-section illustrating the three theoretical layers.

An identical Young's modulus was therefore designated to both cover layers, denoted E_{fi}^{cover} & E_{fj}^{cover} . With the three points through the shell element thickness, a three-point Simpsons integration scheme could be implemented to calculate the laminate bending stiffness:

$$B_{fi} = \frac{E_{fi}^{cover}}{16} [h - h_{core}][h + h_{core}]^2 \quad (D.22)$$

where h_{core} is the core thickness. Rearranging Equation allowed the layer Young's modulus to be determined as a functions of the bending stiffness, as per Equation (4.34).

$$E_{fi}^{cover} = \frac{16B_{fi}}{[h - h_{core}][h + h_{core}]^2} \quad (D.23)$$

The overall laminate membrane behaviour (E_{fi}^{lam} & E_{fj}^{lam}) can be defined in a rule of mixtures approach between the stiffness of both the core layers, E_{fi}^{core} & E_{fj}^{core} , and the cover layers:

$$E_{fi}^{lam} = \left[\frac{h - h_{core}}{h} \right] E_{fi}^{cover} + \left[\frac{h_{core}}{h} \right] E_{fi}^{core} \quad (D.24)$$

However, the overall laminate modulus is defined as an input condition, meaning Equation can be rearranged for definition of the membrane (core) behaviour.

$$E_{fi}^{core} = \frac{h}{h_{core}} \left[E_{fi}^{lam} - \left[\frac{h - h_{core}}{h} \right] E_{fi}^{cover} \right] \quad (D.25)$$

Therefore, by defining the bending stiffness and laminate modulus, both the membrane and bending properties can be defined. The laminate bending stiffness itself, however, depends on the shell element curvature, necessitating its calculation after every increment.

D.3 Curvature Updating

To determine the element curvature, the Koiter-Sanders shell theory [456] was implemented to relate the fibre strains on the element surfaces (in the respective fibre direction), ε_{fi}^{top} & $\varepsilon_{fi}^{bottom}$, to the fibre strain on the element reference surface, ε_{fi}^{ref} , the curvature, κ_{fi} , and the integration point location:

$$\varepsilon_{fi}^{top} = \varepsilon_{fi}^{ref} + [\bar{F}_{33} \cdot z \cdot \kappa_{fi}^{top}] \quad (D.26)$$

$$\varepsilon_{fi}^{bottom} = \varepsilon_{fi}^{ref} + [\bar{F}_{33} \cdot z \cdot \kappa_{fi}^{bottom}] \quad (D.27)$$

such that:

$$\kappa_{fi}^{top} = \frac{\varepsilon_{fi}^{top} - \varepsilon_{fi}^{ref}}{[\bar{F}_{33} \cdot z]} \quad (D.28)$$

$$\kappa_{fi}^{bottom} = \frac{\varepsilon_{fi}^{bottom} - \varepsilon_{fi}^{ref}}{[\bar{F}_{33} \cdot z]} \quad (D.29)$$

where $\varepsilon_{fi}^{bottom}$, ε_{fi}^{ref} and ε_{fi}^{top} are defined at the 1st, 2nd and 3rd integration points through the laminate thickness, respectively. Finally, the shell element curvature (on the reference surface) is taken as an average between the two surface curvatures:

$$\kappa_{fi}^{ref} = \frac{\kappa_{fi}^{top} + \kappa_{fi}^{bottom}}{2} \quad (D.30)$$

Appendix D

Table D-1: Constants defined within Chapter 6.

Constant	Value	Units
p_1	-1.02E+8	$\text{K} \cdot \text{m}^{-6}$
p_2	3.28E+7	$\text{K} \cdot \text{m}^{-5}$
p_3	-4.02E+6	$\text{K} \cdot \text{m}^{-4}$
p_4	2.47E+5	$\text{K} \cdot \text{m}^{-3}$
p_5	-7.45E+3	$\text{K} \cdot \text{m}^{-2}$
p_6	4.76E+1	$\text{K} \cdot \text{m}^{-1}$
p_7	2.46E+2	K
q_1	-4.12E+8	$\text{K} \cdot \text{m}^{-8}$
q_2	2.37E+8	$\text{K} \cdot \text{m}^{-7}$
q_3	-4.79E+7	$\text{K} \cdot \text{m}^{-6}$
q_4	2.98E+6	$\text{K} \cdot \text{m}^{-5}$
q_5	2.49E+5	$\text{K} \cdot \text{m}^{-4}$
q_6	-4.08E+4	$\text{K} \cdot \text{m}^{-3}$
q_7	1.19E+3	$\text{K} \cdot \text{m}^{-2}$
q_8	-9.72E+0	$\text{K} \cdot \text{m}^{-1}$
q_9	2.46E+2	K ·

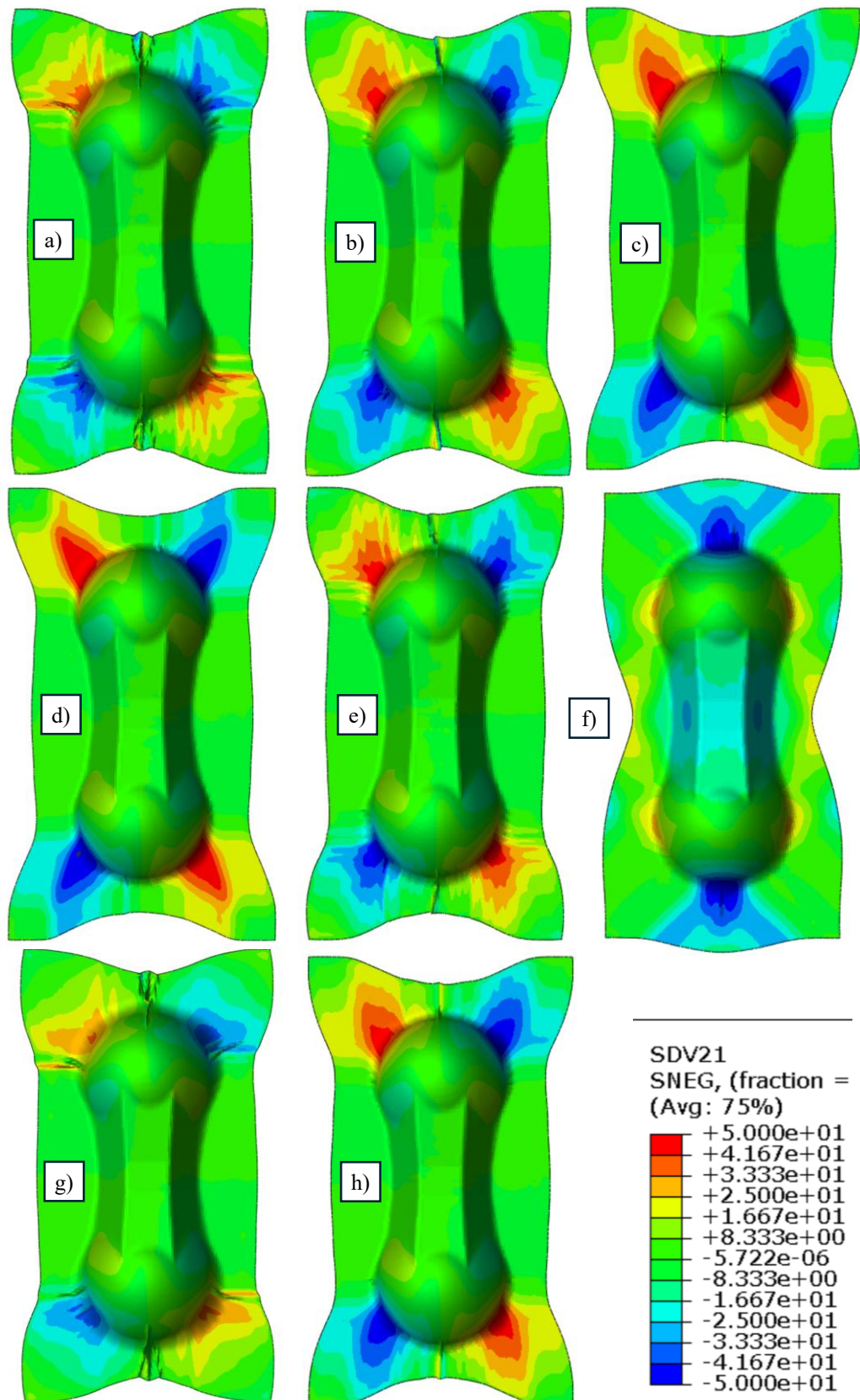


Figure D.3: Shear angle for homogeneous simulations: a) 250 °C, b) 230 °C, c) 210 °C, d) 200 °C, e) Fast (3s), f) 45°, and inhomogeneous simulations: g) 200 °C, h) 230 °C.

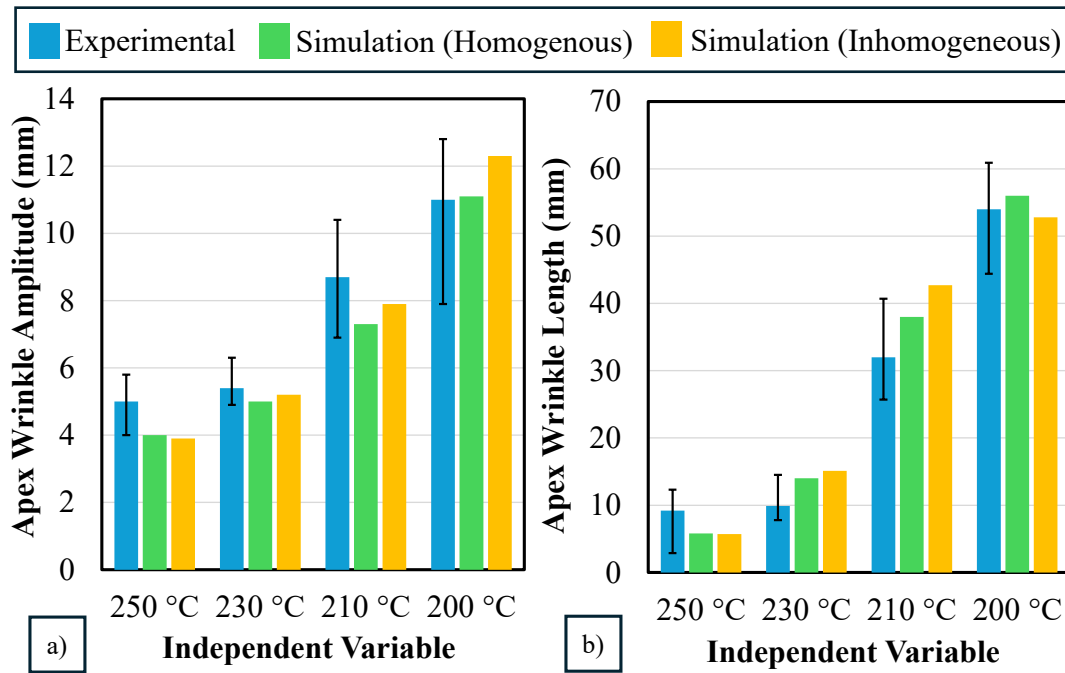


Figure D.4: Quantitative simulation (inhomogeneous and homogeneous thermal profile) *versus* experimental results for the four tested temperatures: a) apex wrinkle amplitude, b) apex wrinkle length.

Appendix E.

Table E-1: Variables associated with the DSC parameterization exercise.

Cooling Rate	D (K)	T_{max} (K)	$K_{max} \times 10^{-5}$ (W)	C (J)
0.16	4.912	191.6	820	0.8675
0.33	6.054	186.7	1470	0.7120
0.50	7.025	183.1	1960	0.6011
0.66	8.017	179.9	2250	0.5182
1.00	10.313	174.5	2750	0.4124
5.00	8.805	175.8	1.135	0.4792
15.0	10.413	163.3	3.271	0.4120
30.0	13.036	152.0	5.086	0.3244
50.0	16.512	141.1	6.219	0.2521
100.0	30.019	120.0	4.017	0.1397

Table E-2: Constants associated with convective heat transfer.

Constant	Value	Units
k_0	0.0241	W
S_k	194	K
T_0	273	K
a_0	1.04763E+3	$J \cdot kg^{-1} \cdot K^{-1}$
a_1	-3.90E-1	$J \cdot kg^{-1} \cdot K^{-2}$
a_2	8.89E-4	$J \cdot kg^{-1} \cdot K^{-3}$
a_3	-1.64E-7	$J \cdot kg^{-1} \cdot K^{-4}$
a_4	6.65E-10	$J \cdot kg^{-1} \cdot K^{-5}$
a_5	6.03E-13	$J \cdot kg^{-1} \cdot K^{-6}$
a_6	-2.07E-16	$J \cdot kg^{-1} \cdot K^{-7}$
a_7	2.59E-20	$J \cdot kg^{-1} \cdot K^{-8}$
k_μ	1.716E-5	K
S_μ	111	K
b_0	1.176	$K^{-(b_1+1)}$
b_1	-1.027	-

Appendix E

h_{l0}	1.6718	$K^{-(h_{l1}+1)}$
h_{l1}	0.2113	-
h_{u0}	3.3435	$K^{-(h_{u1}+1)}$
h_{u1}	0.2113	-

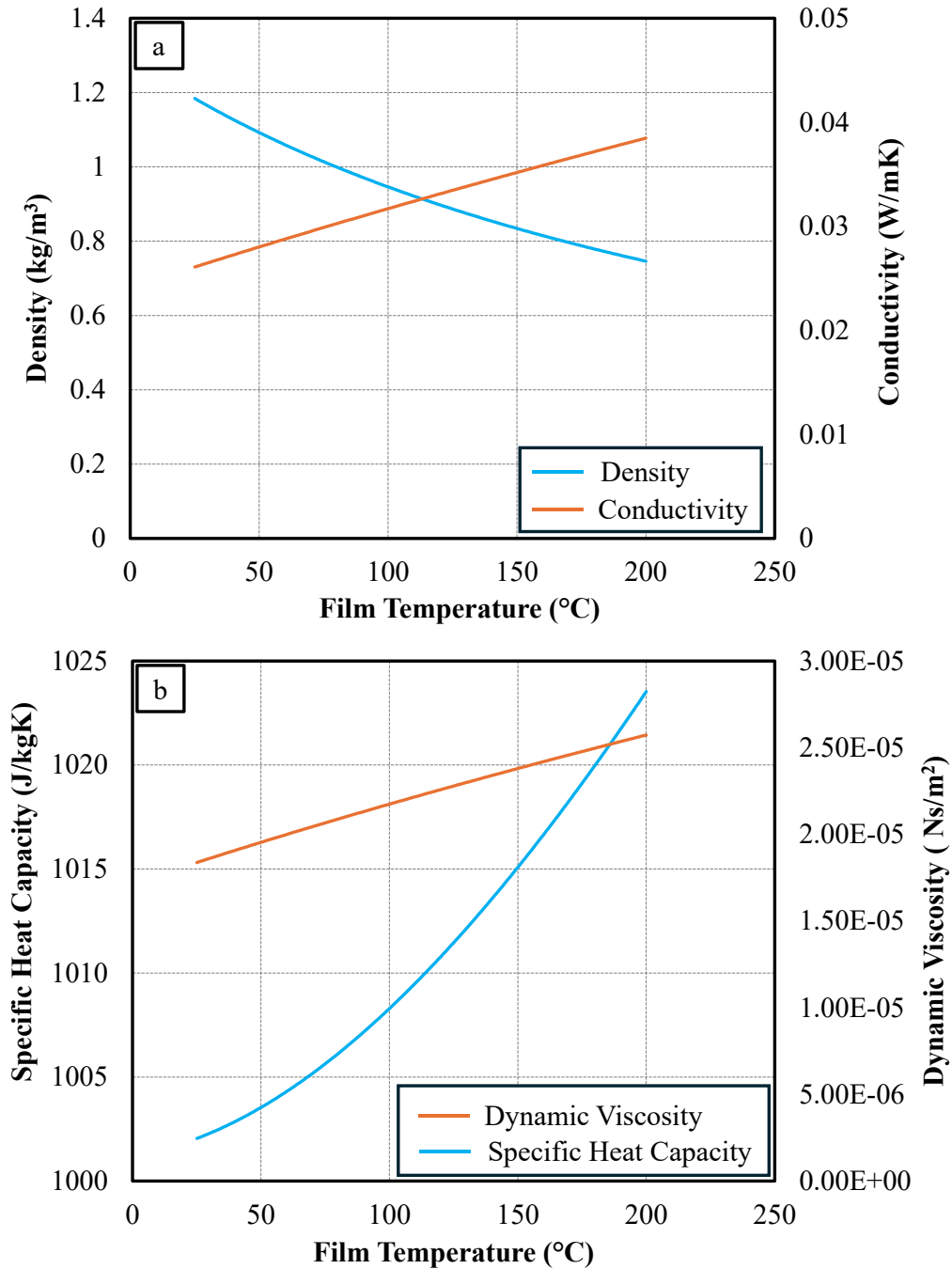


Figure E.1: Properties of air: a) density and conductivity, b) specific heat capacity (constant pressure) and dynamic viscosity.

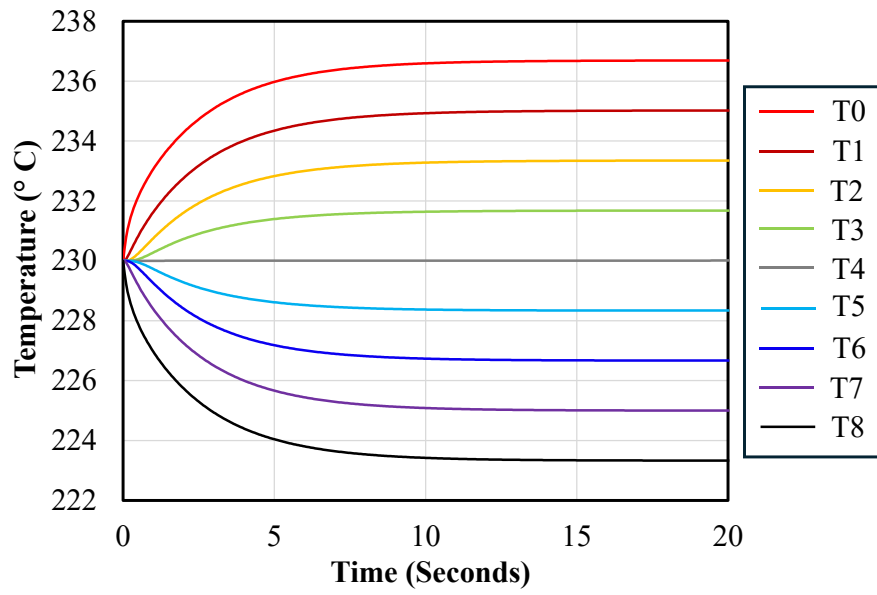


Figure E.2: Analytical dwell study to analyse through-thickness laminate conductivity.

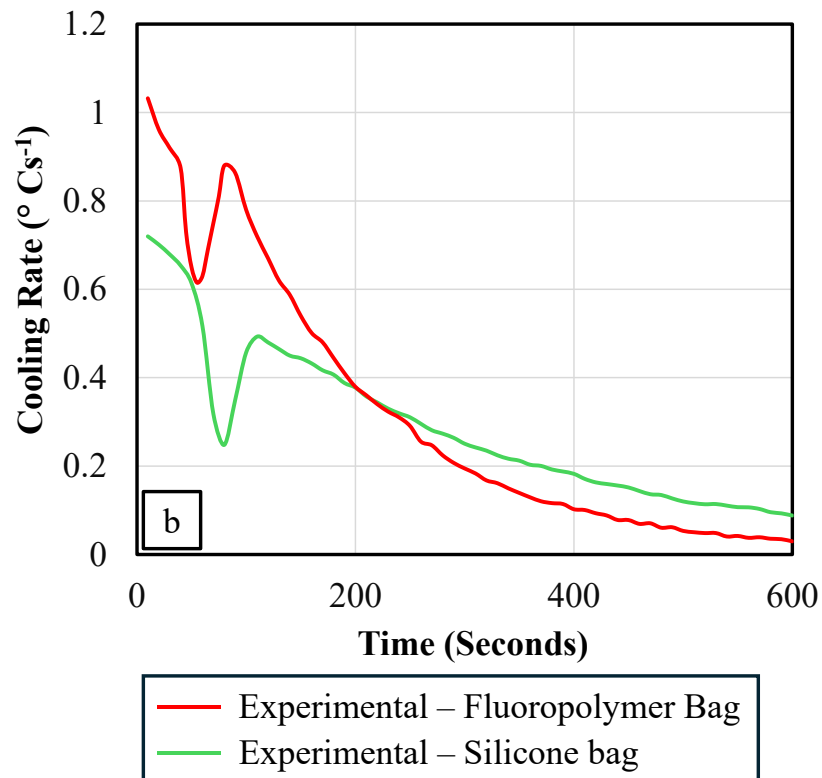


Figure E.3: Cooling rate *versus* time for different bag materials under natural cooling conditions.

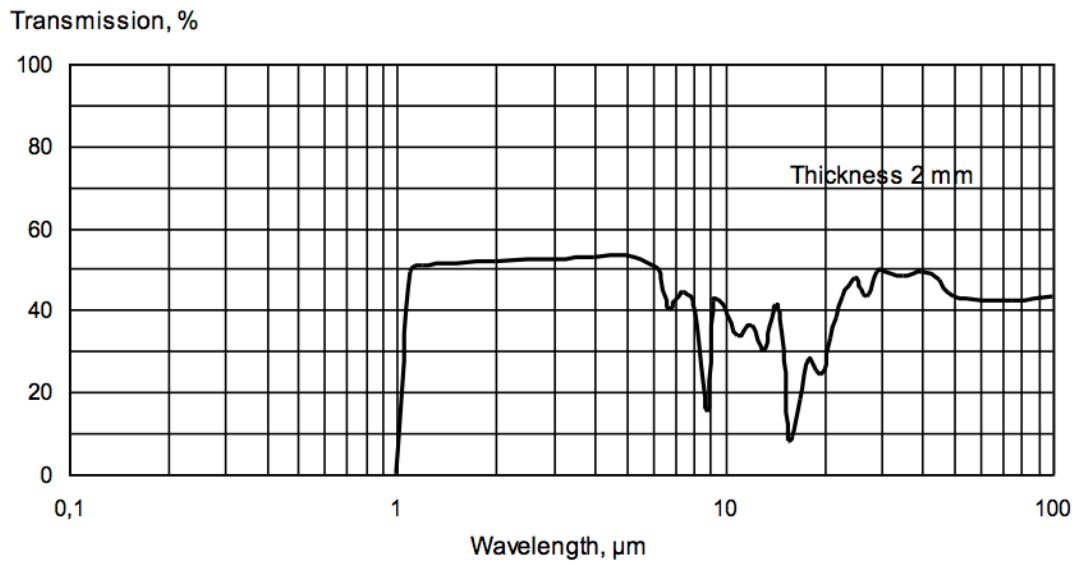


Figure E.4: Transmissivity of silicone at different wavelengths [447].

Appendix F.

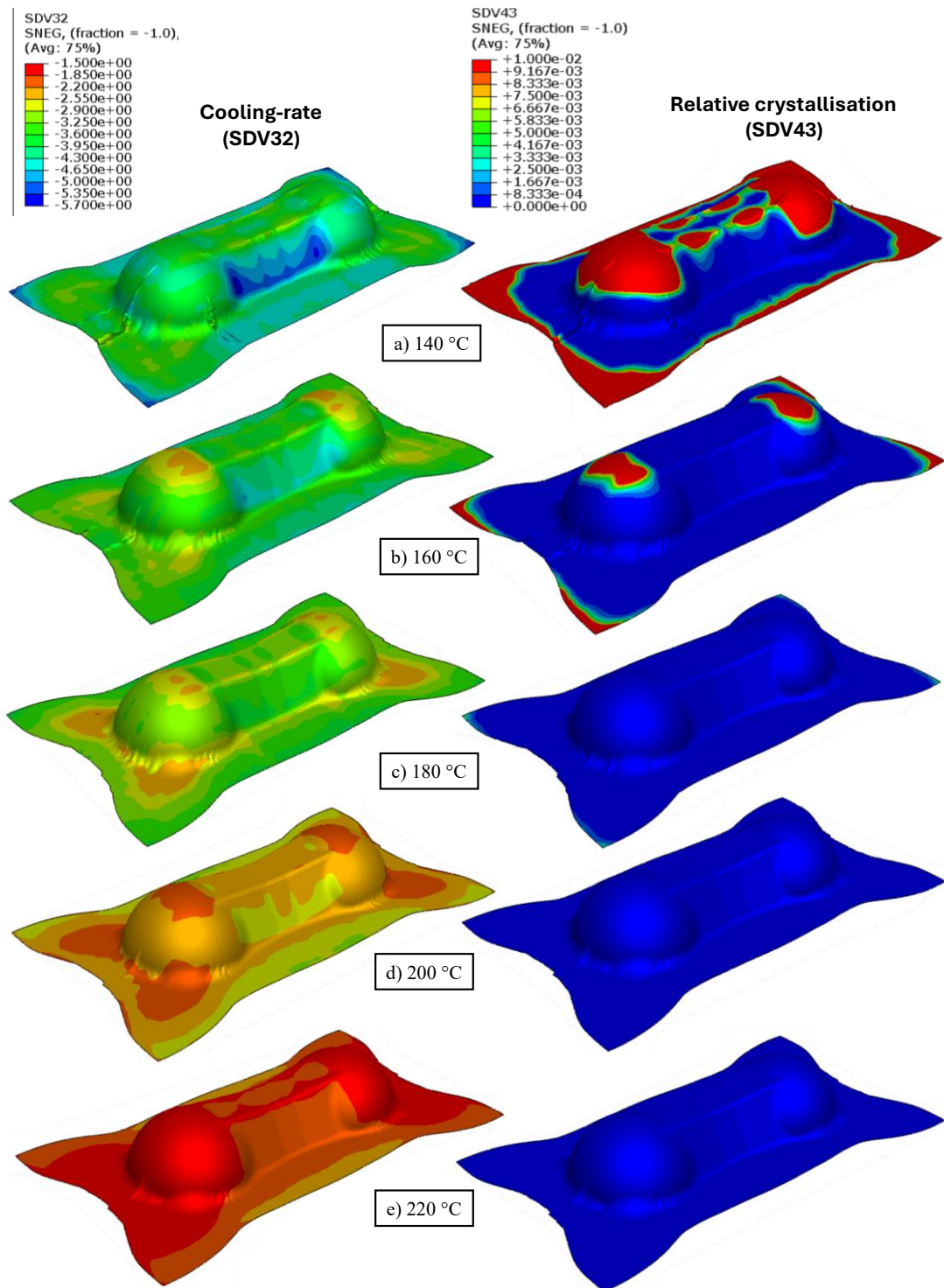


Figure F.1: Simulated forming behaviour for a laminate with an initial centre temperature of 250 °C and different tool temperatures: a) 140 °C, b) 160 °C, c) 180 °C, d) 200 °C, e) 220 °C - cooling-rate (left), relative crystallisation (right).

Appendix F

Table F-1: Constants associated with the extrapolation of laminate temperature *versus* forming times.

Tool Temperature (°C)	y_c (°C · s ^{-z_c})	z_c
140	483.82	-0.331
160	429.48	-0.279
180	378.03	-0.222
200	336.12	-0.169
220	301.01	-0.119
250	258.67	-0.051

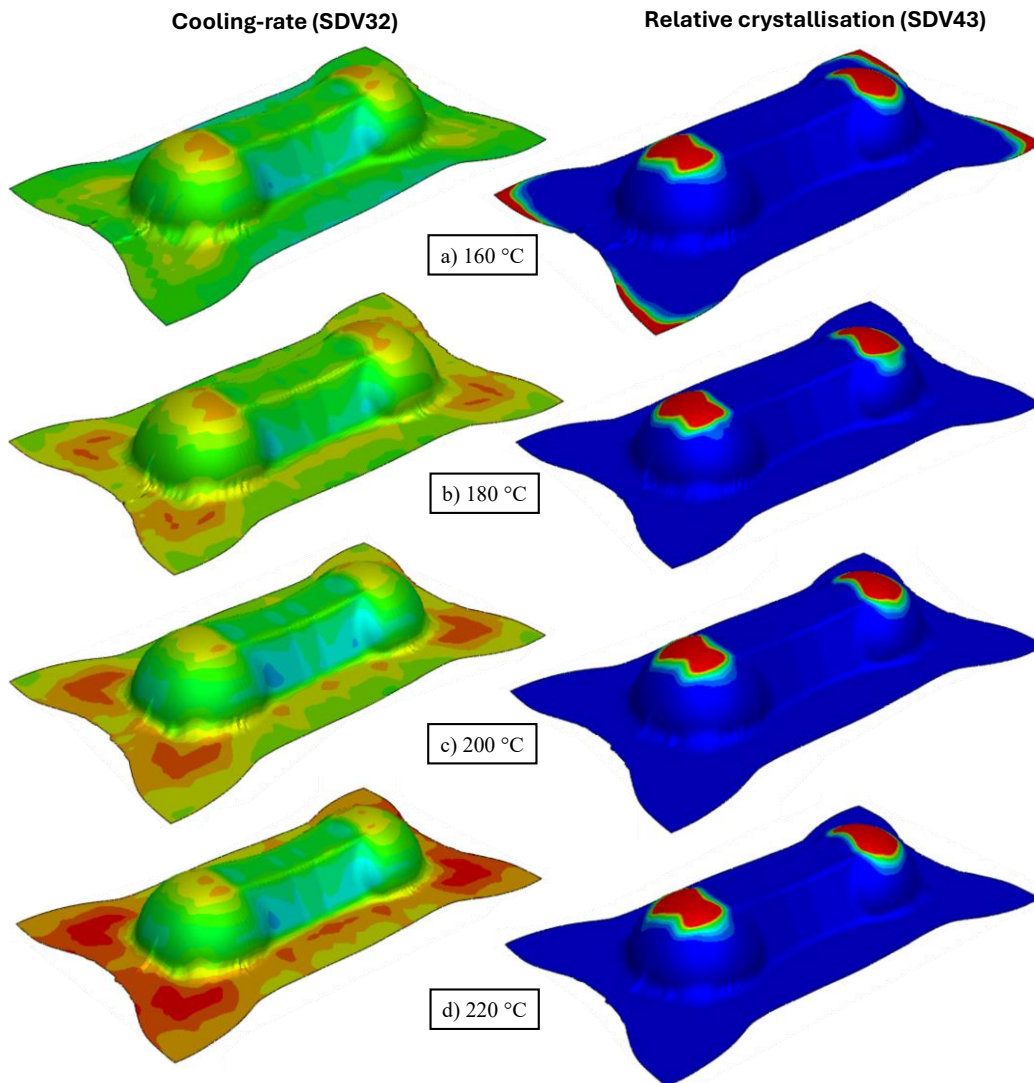


Figure F.2: Simulated forming behaviour for a laminate with an initial centre temperature of 250 °C, a constant tool temperature (160 °C) and different base temperatures: a) 140 °C, b) 160 °C, c) 180 °C, d) 200 °C, e) 220 °C - cooling-rate (left), relative crystallisation (right).

The key for this figure is included in Figure A.2.

References

- [1] Soutis C. Introduction: Engineering requirements for aerospace composite materials. *Polymer Composites in the Aerospace Industry*. (2014)
<https://doi.org/10.1016/B978-0-85709-523-7.00001-3>
- [2] Mrázová M. Advanced composite materials of the future in aerospace industry. *INCAS BULLETIN*. 5 (2013)
<https://doi.org/10.13111/2066-8201.2013.5.3.14>
- [3] N. Arnold. Carbon fiber: Using the hi-tech material in car-marking. BMW (2020).
[Accessed: 02/2025]
<https://www.bmw.com/en/performance/carbon-fiber-in-a-car.html>
- [4] L Luong. Lighter, Faster, Further Groundbreaking Advanced Composites Project. Jaguar Land Rover (2021). [Accessed: 02/2025]
<https://www.landrover.co.uk/explore-land-rover/articles/lighter-faster-further-groundbreaking-advanced-composites-project>
- [5] Toyota Industries Corporation Wins JEC Composites Innovation Awards for CFRP Recycling Technology and Recycling System. Toyota Industries Corporation (2023).
[Accessed: 02/2025]
<https://www.toyota-industries.com/news/2023/03/09/005485/index.html>
- [6] Reddy SSP, Suresh R, M.B H, Shivakumar BP. Use of composite materials and hybrid composites in wind turbine blades. *Materials Today: Proceedings*. 46 (2021)
<https://doi.org/10.1016/j.matpr.2021.02.745>
- [7] Rubino F, Nisticò A, Tucci F, Carlone P. Marine Application of Fiber Reinforced Composites: A Review. *Journal of Marine Science and Engineering*. 8 (2020)
<https://doi.org/10.3390/jmse8010026>
- [8] Overview of the global composites market 2022-2027. *JEC Observer*. (2023)
- [9] Composites Market Size And Share | Industry Report, 2030. (2023)
- [10] Transitioning to zero emission cars and vans: 2035 delivery plan. HM Government. (2024)
- [11] Electric car sales to increase to 440,000 in 2025, but still missing UK industry target. *DriveElectric* (2025). [Accessed: 02/2025]
<https://www.drive-electric.co.uk/press/electric-car-sales-to-increase-to-440000-in-2025/>

- [12] Guzman Maldonado E, Bigot N, Denis Y, Hamila N. 13 - Thermomechanical modeling and experimental characterization of continuous fiber-reinforced thermoplastic composites at forming temperatures. In: Wang P, Hamila N (Eds.). *Advanced Structural Textile Composites Forming*. Woodhead Publishing (2025). pp.355-88
- [13] Béland S. 5 – Processing of Advanced Thermoplastic Composites. In: National Research Council of Canada (Eds.). *High Performance Thermoplastic Resins and Their Composites*. Noyes Publications (1990).
- [14] Michaeli W, Koschmieder M. 2.25 - Processing Principles for Thermoplastic Polymers. In: Kelly A, Zweben C (Eds.). *Comprehensive Composite Materials*. Pergamon (2000). pp.853-72
- [15] Vieille B, Coppalle A, Le Pluart L, Schuhler E, Chaudhary A, Rijal B, Alia A, Delpouve N. Kerosene flame behaviour of C/PEKK composite laminates: Influence of exposure time and laminates lay-up on residual mechanical properties. *Composites Part B: Engineering*. 222 (2021)
<https://doi.org/10.1016/j.compositesb.2021.109046>
- [16] Friedrich K, Hou M, Krebs J. Chapter 4 - Thermoforming of continuous fibre/thermoplastic composite sheets. In: Bhattacharyya D (Eds.). *Composite Materials Series*. Elsevier (1997). pp.91-162
- [17] Thermoplastic composites gain leading edge on the A380. *CompositesWorld* (2006). [Accessed: 02/2025]
<https://www.compositesworld.com/articles/thermoplastic-composites-gain-leading-edge-on-the-a380>
- [18] Daher wins its first Boeing production contract to supply thermoplastic composite structural parts for the Boeing 787 Dreamliner. Daher (2018). [Accessed: 02/2025]
<https://www.daher.com/en/daher-wins-its-first-boeing-production-contract-to-supply-thermoplastic-composite-structural-parts-for-the-boeing-787-dreamliner/>
- [19] Thermoplastic primary aerostructures take another step forward. *CompositesWorld* (2019). [Accessed: 02/2025]
<https://www.compositesworld.com/articles/thermoplastic-primary-aerostructures-take-another-step-forward>
- [20] Thermoplastic Composites Taking-off into a Clearer Future. *Composights* (2024). [Accessed: 02/2025]

- <https://www.composights.com/article/Thermoplastic-Composites-Taking-off-into-a-Clearer-Future>
- [21] Krueger R, Bergan A. Advances in Thermoplastic Composites Over Three Decades – A Literature Review NASA. (2024)
- [22] Walker T. LANXESS helps develop first all-plastic brake pedal for battery-electric sports car. Interplas Insights (2020). [Accessed: 02/2025]
<https://interplasinsights.com/plastics-industry-news/lanxess-helps-develop-first-all-plastic-brake-pedal-for-batt/>
- [23] Mason H. Thermoplastic composites incorporated into vehicle seatback concept. CompositesWorld (2020). [Accessed: 02/2025]
<https://www.compositesworld.com/news/thermoplastic-composites-incorporated-into-vehicle-seatback-concept>
- [24] Moore S. Continuous-fiber-reinforced thermoplastic composite adopted for car engine undertrays. Plastics Today (2017). [Accessed: 02/2025]
<https://www.plasticstoday.com/automotive-mobility/continuous-fiber-reinforced-thermoplastic-composite-adopted-for-car-engine-undertrays>
- [25] Malnati P. Hybrid thermoplastics give load floor impact strength. CompositesWorld (2018). [Accessed: 02/2025]
<https://www.compositesworld.com/articles/multi-material-thermoplastics-give-load-floor-impact-strength>
- [26] Electric mountain bike frame. Composite Braiding (2024). [Accessed: 02/2025]
<https://compositebraiding.com/projects/electric-mountain-bike-frame/>
- [27] Improve Your Game. TORAY (2022). [Accessed: 02/2025]
<https://www.cf-composites.toray/markets/qol/sporting/others.html>
- [28] Case study: HP Spectre 13 Ultrabook. TORAY Performance Materials (2019). [Accessed: 02/2025]
<https://www.toraypmc.com/media/4aa07205-7b27-4445-a2a1-3234deeffa16>
- [29] Mandaoka A. Carbon Thermoplastic Composites Market Overview. Market Research Future. (2025)
- [30] Triandafilou LN. Emerging Bridge Applications. Federal Highway Administration (2011). [Accessed: 02/2025]
<https://highways.dot.gov/public-roads/julyaugust-2011/emerging-bridge-applications>
- [31] Almushaikeh AM, Alaswad SO, Alsuhybani MS, AlOtaibi BM, Alarifi IM, Alqahtani NB, Aldosari SM, Alsaleh SS, Haidyrah AS, Alolyan AA, Alshammari BA.

- Manufacturing of carbon fiber reinforced thermoplastics and its recovery of carbon fiber: A review. *Polymer Testing*. 122 (2023)
<https://doi.org/10.1016/j.polymertesting.2023.108029>
- [32] McGregor OPL, Chen S, Harper LT, Endruweit A, Warrior NA. Defect Reduction in the Double Diaphragm Forming Process. *Proceedings of ICCM21*. Xi'an, China. (2017)
- [33] Chen S, McGregor OPL, Harper LT, Endruweit A, Warrior NA. Optimisation of Double Diaphragm Forming Process Through Local Adjustment of In-Plane Constraint. *Proceedings of ICCM21*. Xi'an, China. (2017)
- [34] Create a complex composite part in under 5 minutes. Syensqo (2025). [Accessed: 08/2025]
<https://www.syensqo.com/en/chemical-categories/our-composite-materials-solutions/ddf>
- [35] Krebs J, Friedrich K, Bhattacharyya D. A direct comparison of matched-die versus diaphragm forming. *Composites Part A: Applied Science and Manufacturing*. 29 (1998)
[https://doi.org/10.1016/S1359-835X\(97\)82706-6](https://doi.org/10.1016/S1359-835X(97)82706-6)
- [36] Akkerman R, Haanappel SP, Sachs U. History and future of composites forming analysis. *IOP Conference Series: Materials Science and Engineering*. 406 (2018)
<https://doi.org/10.1088/1757-899X/406/1/012003>
- [37] Chen S, Yu F. 15 - Process simulation: Fabric forming. In: Harper L, Clifford M (Eds.). *Design and Manufacture of Structural Composites*. Woodhead Publishing (2023). pp.373-400
- [38] The Future Composites Manufacturing Research Hub. CIMComp (2020). [Accessed: 02/2025]
<https://cimcomp.ac.uk/>
- [39] Composites Research Group. The University of Nottingham (2025). [Accessed: 02/2025]
<https://www.nottingham.ac.uk/research/groups/composites-research-group/research/index.aspx>
- [40] Yu F, Chen S, Lawrence GD, Warrior NA, Harper LT. A global-to-local sub modelling approach to investigate the effect of lubrication during double diaphragm forming of multi-ply biaxial non-crimp fabric preforms. *Composites Part B: Engineering*. 254 (2023)
<https://doi.org/10.1016/j.compositesb.2023.110590>

- [41] Yu F. The prediction of wrinkle formation in non-crimp fabrics during double diaphragm forming [PhD Thesis]. Department of Mechanical Engineering: The University of Nottingham, Nottingham (2022)
- [42] Yu F, Chen S, Harper LT, Warrior NA. Investigation into the effects of inter-ply sliding during double diaphragm forming for multi-layered biaxial non-crimp fabrics. *Composites Part A: Applied Science and Manufacturing*. 150 (2021)
<https://doi.org/10.1016/j.compositesa.2021.106611>
- [43] Yu F, Chen S, Harper LT, Warrior NA. Double diaphragm forming simulation using a global-to-local modelling strategy for detailed defect detection in large structures. *Composites Part A: Applied Science and Manufacturing*. 147 (2021)
<https://doi.org/10.1016/j.compositesa.2021.106457>
- [44] Yu F, Chen S, Harper LT, Warrior NA. Simulating the effect of fabric bending stiffness on the wrinkling behaviour of biaxial fabrics during preforming. *Composites Part A: Applied Science and Manufacturing*. 143 (2021)
<https://doi.org/10.1016/j.compositesa.2021.106308>
- [45] Yu F, Chen S, Viisainen JV, Sutcliffe MPF, Harper LT, Warrior NA. A macroscale finite element approach for simulating the bending behaviour of biaxial fabrics. *Composites Science and Technology*. 191 (2020)
<https://doi.org/10.1016/j.compscitech.2020.108078>
- [46] Chen S. Fabric forming simulation and process optimisation for composites [PhD Thesis]. Department of Engineering: The University of Nottingham, Nottingham (2016)
- [47] Chen S. Forming simulations of multi-layered woven preforms assembled with stitch yarns. *Proceedings of ECCM16*. Seville, Spain. (2014)
- [48] Codolini A, Chen S, Lawrence GD, Harper LT, Sutcliffe MPF. Characterisation of process-induced variability in wrinkle defects during double diaphragm forming of non-crimp fabric. *Composites Part B: Engineering*. 281 (2024)
<https://doi.org/10.1016/j.compositesb.2024.111549>
- [49] Chen S, McGregor OPL, Harper LT, Endruweit A, Warrior NA. Defect formation during preforming of a bi-axial non-crimp fabric with a pillar stitch pattern. *Composites Part A: Applied Science and Manufacturing*. 91 (2016)
<https://doi.org/10.1016/j.compositesa.2016.09.016>

- [50] Chen S, McGregor OPL, Endruweit A, Elsmore MT, De Focatiis DSA, Harper LT, Warrior NA. Double diaphragm forming simulation for complex composite structures. *Composites Part A: Applied Science and Manufacturing*. 95 (2017)
<https://doi.org/10.1016/j.compositesa.2017.01.017>
- [51] Giurgiutiu V. Chapter 1 - Introduction. In: Giurgiutiu V (Eds.). *Structural Health Monitoring of Aerospace Composites*. Academic Press (2016). pp.1-23
- [52] Mohammed TW, Taha DY, Abdul-Ilah RR. Evaluation of Composite Material used in the Wings of Typical Airplane based on Stress Analysis. *European journal of engineering and technology research*. 3 (2018)
<https://doi.org/10.24018/ejeng.2018.3.11.921>
- [53] Campbell FC. *Structural Composite Materials*. 1st ed. ASM International, Ohio, USA (2010)
- [54] Harris B. *Engineering Composite Materials*. 1st ed. Institute of Materials, London, UK (1999)
- [55] Chawla KK. *Composite Materials: Science and Engineering*. 3rd ed. Springer, New York, USA (2013)
- [56] Mallick P. *Fiber-Reinforced Composites: Materials, Manufacturing, And Design*. 3rd ed. CRC Press, Boca Raton, USA (2007)
- [57] Long AC. *Design and Manufacture of Textile Composites*. 1st ed. Woodhead Publishing, Cambridge, England (2005)
- [58] Bussetta P, Correia N. Numerical forming of continuous fibre reinforced composite material: A review. *Composites Part A: Applied Science and Manufacturing*. 113 (2018)
<https://doi.org/10.1016/j.compositesa.2018.07.010>
- [59] Boisse P, Borr M, Buet K, Cherouat A. Finite element simulations of textile composite forming including the biaxial fabric behaviour. *Composites Part B: Engineering*. 28 (1997)
[https://doi.org/10.1016/S1359-8368\(96\)00067-4](https://doi.org/10.1016/S1359-8368(96)00067-4)
- [60] Lomov S, Ignaas V, Robitaille F. 1 - Manufacturing and internal geometry of textiles. In: Long A (Eds.). *Design and Manufacture of Textile Composites*. Woodhead Publishing (2005). pp.1-61
- [61] Lomov SV. *Non-crimp fabric composites: Manufacturing, properties and applications*. 1st ed. Woodhead Publishing, Cambridge, UK (2011)

-
- [62] Akkerman R, Haanappel SP. 6 - Thermoplastic composites manufacturing by thermoforming. In: Boisse P (Eds.). *Advances in Composites Manufacturing and Process Design*. Woodhead Publishing (2015). pp.111-29
- [63] Harrison P, Wiggers J, Long A, Rudd C. A Constitutive Model Based on Meso and Micro Kinematics for Woven and Stitched Dry Fabrics. *Proceedings of ICCM13*. San Diego, USA. (2003)
- [64] Farboodmanesh S, Chen J, Tao Z, Mead J, Zhang H. 3 - Base fabrics and their interaction in coated fabrics. In: Smith WC (Eds.). *Smart Textile Coatings and Laminates*. Woodhead Publishing (2010). pp.42-94
- [65] Prodromou AG, Chen J. On the relationship between shear angle and wrinkling of textile composite preforms. *Composites Part A: Applied Science and Manufacturing*. 28 (1997)
[https://doi.org/10.1016/S1359-835X\(96\)00150-9](https://doi.org/10.1016/S1359-835X(96)00150-9)
- [66] Long AC, Brown LP. 8 - Modelling the geometry of textile reinforcements for composites: TexGen. In: Boisse P (Eds.). *Composite Reinforcements for Optimum Performance*. Woodhead Publishing (2011). pp.239-64
- [67] Maragoni L, Modenato G, De Rossi N, Vescovi L, Quaresimin M. Effect of fibre waviness on the compressive fatigue behavior of woven carbon/epoxy laminates. *Composites Part B: Engineering*. 199 (2020)
<https://doi.org/10.1016/j.compositesb.2020.108282>
- [68] Hearle JWS. 11 - Mechanical properties of textile reinforcements for composites. In: Boisse P (Eds.). *Advances in Composites Manufacturing and Process Design*. Woodhead Publishing (2015). pp.231-51
- [69] Potter K, Khan B, Wisnom M, Bell T, Stevens J. Variability, fibre waviness and misalignment in the determination of the properties of composite materials and structures. *Composites Part A: Applied Science and Manufacturing*. 39 (2008)
<https://doi.org/10.1016/j.compositesa.2008.04.016>
- [70] Rolfes R, Ernst G, Hartung D, Teßmer J. Strength of Textile Composites — A Voxel Based Continuum Damage Mechanics Approach. *Proceedings of 3rd European Conference on Computational Mechanics*. Lisbon, Portugal. (2006)
- [71] Kari S, Kumar M, Jones A, Warrior NA, Long A. Effect of yarn cross-sectional shapes and crimp on the mechanical properties of 3D woven composites. *Proceedings of ICCM17*. Edinburgh, Scotland. (2009)
-

- [72] Weeton JW, Peters DM, Thomas KL. *Engineers' Guide to Composite Materials*. 1st ed. American Society for Metals, Ohio, USA (1987)
- [73] Huang S, Fu Q, Yan L, Kasal B. Characterization of interfacial properties between fibre and polymer matrix in composite materials – A critical review. *Journal of Materials Research and Technology*. 13 (2021)
<https://doi.org/10.1016/j.jmrt.2021.05.076>
- [74] Mohammed L, Ansari MNM, Pua G, Jawaid M, Islam MS. A Review on Natural Fiber Reinforced Polymer Composite and Its Applications. *International Journal of Polymer Science*. 2015 (2015)
<https://doi.org/10.1155/2015/243947>
- [75] Park S-J, Seo M-K. Chapter 6 - Element and Processing. In: Park S-J, Seo M-K (Eds.). *Interface Science and Technology*. Elsevier (2011). pp.431-99
- [76] Biron M. Chapter 1 - Outline of the actual situation of plastics compared to conventional materials. In: Biron M (Eds.). *Thermosets and Composites*. Elsevier Science (2004). pp.1-30
- [77] Tarafdar A, Jia C, Hu W, Hosein ID, Fu K, Wang Y. Three-dimensional modeling of frontal polymerization for rapid, efficient, and uniform thermoset composites manufacturing. *Composites Part B: Engineering*. 266 (2023)
<https://doi.org/10.1016/j.compositesb.2023.111029>
- [78] Vanclooster K. *Forming of multilayers fabric reinforced thermoplastic composites [PhD Thesis]*. Faculty of Engineering Technology: KU Leuven, Leuven, Belgium (2009)
- [79] Rodriguez F, Cohen C, Ober CK, Archer LA. *Principles of polymer systems*. 6th ed. CRC Press, Boca Raton, USA (2014)
- [80] Oladele IO, Okoro CJ, Taiwo AS, Onuh LN, Agbeboh NI, Balogun OP, Olubambi PA, Lephuthing SS. Modern Trends in Recycling Waste Thermoplastics and Their Prospective Applications: A Review. *Journal of Composites Science*. 7 (2023)
<https://doi.org/10.3390/jcs7050198>
- [81] Mark JE. *Physical properties of polymers handbook*. 2nd ed. Springer, New York, USA (2007)
- [82] Kumar A, Gupta RK. *Fundamentals of Polymer Engineering, Revised and Expanded*. 2nd ed. CRC Press, Boca Raton, USA (2003)
- [83] Rubinstein M, Colby RH. *Polymer Physics*. 1st ed. Oxford University Press, Oxford (2003)

-
- [84] Vanclooster K, Lomov SV, Verpoest I. Experimental validation of forming simulations of fabric reinforced polymers using an unsymmetrical mould configuration. *Composites Part A: Applied Science and Manufacturing*. 40 (2009)
<https://doi.org/10.1016/j.compositesa.2009.02.005>
- [85] Kim JM, Locker R, Rutledge GC. Plastic Deformation of Semicrystalline Polyethylene under Extension, Compression, and Shear Using Molecular Dynamics Simulation. *Macromolecules*. 47 (2014)
<https://doi.org/10.1021/ma402297a>
- [86] Mirkhalaf M, Vadizadeh R. Micro-mechanical modeling of semi-crystalline polymers: A review. *International Journal of Solids and Structures*. 290 (2024)
<https://doi.org/10.1016/j.ijsolstr.2024.112691>
- [87] Yoshida T, Nakane T, Uchida M, Kaneko Y. Mechanical modeling and testing of different polyamides considering molecular chain structure, crystallinity, and large strains. *International Journal of Solids and Structures*. 239-240 (2022)
<https://doi.org/10.1016/j.ijsolstr.2021.111419>
- [88] Beck KR, Korsmeyer R, Kunz RJ. An overview of the glass transition temperature of synthetic polymers. *Journal of Chemical Education*. 61 (1984)
<https://doi.org/10.1021/ed061p668>
- [89] Kugele D, Dörr D, Wittemann F, Hangs B, Rausch J, Kärger L, Henning F. Modeling of the non-isothermal crystallization kinetics of polyamide 6 composites during thermoforming. . *Proceedings of ESAFORM 2017*. Dublin, Ireland. (2017)
- [90] Strong AB. *Plastics: Materials and Processing*. 3rd ed. Pearson Prentice Hall, New Jersey, USA (2006)
- [91] Greene JP. 7 - Commodity Plastics. In: Greene JP (Eds.). *Automotive Plastics and Composites*. William Andrew Publishing (2021). pp.83-105
- [92] Osswald T, Menges G. *Material Science of Polymers for Engineers*. 3rd ed. Hanser Publications, Ohio, USA (2012)
- [93] Ghosh P. *Polymer Science and Technology: Plastics, Rubbers, Blends and Composites*. 2nd ed. Tata McGraw-Hill Publishing, New Delhi, India (2001)
- [94] Pruitt LA. 1.23 - Load-Bearing Medical Polymers (Non-Degradable). In: Ducheyne P (Eds.). *Comprehensive Biomaterials II*. Elsevier (2017). pp.507-15
- [95] Zakaria Z, Ahmad Tarmizi Z, Jawaid M, Hassan A. Effect of degree of deacetylation of chitosan on thermal stability and compatibility of chitosan-polyamide blend. *Bioresources*. 7 (2012)
-

- <https://doi.org/10.15376/biores.7.4.5568-5580>
- [96] Florian J. Practical Thermoforming: Principles and Applications. 1st ed. CRC Press, Boca Raton, USA (1987)
- [97] Sweeney GJ, Monaghan PF, Brogan MT, Cassidy SF. Reduction of infra-red heating cycle time in processing of thermoplastic composites using computer modelling. *Composites Manufacturing*. 6 (1995)
[https://doi.org/10.1016/0956-7143\(95\)95018-T](https://doi.org/10.1016/0956-7143(95)95018-T)
- [98] Rudolf R, Mitschang P, Neitzel M. Induction heating of continuous carbon-fibre-reinforced thermoplastics. *Composites Part A: Applied Science and Manufacturing*. 31 (2000)
[https://doi.org/10.1016/S1359-835X\(00\)00094-4](https://doi.org/10.1016/S1359-835X(00)00094-4)
- [99] Harrison P, Campbell I, Guliyev E, McLelland B, Gomes R, Curado-Correia N, McGookin E, Mulvihill DM. Induction melt thermoforming of advanced multi-axial thermoplastic composite laminates. *Journal of Manufacturing Processes*. 60 (2020)
<https://doi.org/10.1016/j.jmapro.2020.10.026>
- [100] Throne JL. Technology of thermoforming 1st ed. Hanser Publications, Munich, Germany (1996)
- [101] Cunningham JE, Monaghan PF, Brogan MT, Cassidy SF. Modelling of pre-heating of flat panels prior to press forming. *Composites Part A: Applied Science and Manufacturing*. 28 (1997)
[https://doi.org/10.1016/S1359-835X\(96\)00089-9](https://doi.org/10.1016/S1359-835X(96)00089-9)
- [102] Khan SA, Girard P, Bhuiyan N, Thomson V. Improved mathematical modeling for the sheet reheat phase during thermoforming. *Polymer Engineering & Science*. 52 (2012)
<https://doi.org/10.1002/pen.22125>
- [103] Sonmez F, Eyol E. Optimal post-manufacturing cooling paths for thermoplastic composites. *Composites Part A: Applied Science and Manufacturing*. 33 (2002)
[https://doi.org/10.1016/S1359-835X\(01\)00133-6](https://doi.org/10.1016/S1359-835X(01)00133-6)
- [104] Reynolds N, Awang-Ngah S, Williams G, Hughes DJ. Direct Processing of Structural Thermoplastic Composites Using Rapid Isothermal Stamp Forming. *Applied Composite Materials*. 27 (2020)
<https://doi.org/10.1007/s10443-020-09797-4>
- [105] Svensson, Shishoo R, Gilchrist M. Manufacturing of Thermoplastic Composites from Commingled Yarns-A Review. *Journal of Thermoplastic Composite Materials*. 11 (1998)
-

- <https://doi.org/10.1177/089270579801100102>
- [106] Rath J-E, Graupner R, Schüppstuhl T. Processing Strategies for Dieless Forming of Fiber-Reinforced Plastic Composites. *Machines*. 11 (2023)
<https://doi.org/10.3390/machines11030365>
- [107] Vaidya UK, Chawla KK. Processing of fibre reinforced thermoplastic composites. *International Materials Reviews*. 53 (2008)
<https://doi.org/10.1179/174328008X325223>
- [108] Okine RK. Analysis of forming parts from advanced thermoplastic composite sheet materials. *Journal of Thermoplastic Composite Materials*. 25 (1989)
<https://doi.org/10.1177/089270578900200104>
- [109] Tomas, ström B. Chapter 2 Thermoplastic composite sheet forming: Materials and manufacturing techniques. In: Bhattacharyya D (Eds.). *Composite Materials Series*. Elsevier (1997). pp.27-73
- [110] Wakeman M, Cain TA, Rudd C, Brooks R, Long A. Compression moulding of glass and polypropylene composites for optimised macro- and micro-mechanical properties - 1 Commingled glass and polypropylene. *Composites Science and Technology*. 58 (1998)
[https://doi.org/10.1016/S0266-3538\(98\)00011-6](https://doi.org/10.1016/S0266-3538(98)00011-6)
- [111] Hou M. Stamp forming of continuous glass fibre reinforced polypropylene. *Composites Part A: Applied Science and Manufacturing*. 28 (1997)
[https://doi.org/10.1016/S1359-835X\(97\)00013-4](https://doi.org/10.1016/S1359-835X(97)00013-4)
- [112] Chen H, Li S, Wang J, Ding A. A focused review on the thermo-stamping process and simulation progresses of continuous fibre reinforced thermoplastic composites. *Composites Part B: Engineering*. 224 (2021)
<https://doi.org/10.1016/j.compositesb.2021.109196>
- [113] Schug A, Winkelbauer J, Hinterhölzl R, Drechsler K. Thermoforming of glass fibre reinforced polypropylene: A study on the influence of different process parameters. *Proceedings of ESAFORM 2017*. Dublin, Ireland. (2017)
- [114] Kc B, Pervaiz M, Faruk O, Tjong J, Sain M. Green Composite Manufacturing via Compression Molding and Thermoforming. In: Salit MS, Jawaid M, Yusoff NB, Hoque ME (Eds.). *Manufacturing of Natural Fibre Reinforced Polymer Composites*. Springer International Publishing (2015). pp.45-63
- [115] Ma C-M, Wang T-H, Yu C-T, Cheng B-W. Two-dimensional Stamp Forming Analysis for Thermoplastic Composites. *Journal of Applied Sciences*. 13 (2013)
-

- <https://doi.org/10.3923/jas.2013.1461.1466>
- [116] Smith R. Composite defects and their detection. *Materials Science and Engineering*. 3 (2009)
<https://research-information.bris.ac.uk/en/publications/composite-defects-and-their-detection-article-63653>
- [117] Chen S, Harper L. 5 - Two-dimensional to three-dimensional dry fibre preforming. In: Harper L, Clifford M (Eds.). *Design and Manufacture of Structural Composites*. Woodhead Publishing (2023). pp.101-23
- [118] Robroek L. The development of rubber forming as a rapid thermoforming technique for continuous fibre reinforced thermoplastic composites: Quality control by process control [PhD Thesis]. Structures and Materials Lab: Technische Univ. Delft, Delft (1994)
- [119] Lessard H, Lebrun G, Benkaddour A, Pham X-T. Influence of process parameters on the thermostamping of a [0/90]₁₂ carbon/polyether ether ketone laminate. *Composites Part A: Applied Science and Manufacturing*. 70 (2015)
<https://doi.org/10.1016/j.compositesa.2014.12.009>
- [120] McCool R, Murphy A, Wilson R, Jiang Z, Price M, Butterfield J, Hornsby P. Thermoforming carbon fibre-reinforced thermoplastic composites. *Proceedings of the Institution of Mechanical Engineers, Part L: Journal of Materials: Design and Applications*. 226 (2012)
<https://doi.org/10.1177/1464420712437318>
- [121] Harrison P, Gomes R, Curado-Correia N. Press forming a 0/90 cross-ply advanced thermoplastic composite using the double-dome benchmark geometry. *Composites Part A: Applied Science and Manufacturing*. 54 (2013)
<https://doi.org/10.1016/j.compositesa.2013.06.014>
- [122] Benkaddour A, Lebrun G, Laberge-Lebel L. Thermostamping of [0/90] carbon/peek laminates: Influence of support configuration and demolding temperature on part consolidation. *Polymer Composites*. 39 (2018)
<https://doi.org/10.1002/pc.24354>
- [123] Poppe C, Joppich T, Dörr D, Kärger L, Henning F. Modeling and validation of gripper induced membrane forces in finite element forming simulation of continuously reinforced composites. *ESAFORM 2017*. ed. Dublin, Ireland. (2017).
- [124] Bersee HEN, Beukers A. Diaphragm forming of continuous fibre reinforced thermoplastics: influence of temperature, pressure and forming velocity on the forming

- of Upilex-R® diaphragms. *Composites Part A: Applied Science and Manufacturing*. 33 (2002)
[https://doi.org/10.1016/S1359-835X\(02\)00037-4](https://doi.org/10.1016/S1359-835X(02)00037-4)
- [125] Pantelakis SG, Baxevani EA. Optimization of the diaphragm forming process with regard to product quality and cost. *Composites - Part A: Applied Science and Manufacturing*. 33 (2002)
[https://doi.org/10.1016/S1359-835X\(01\)00147-6](https://doi.org/10.1016/S1359-835X(01)00147-6)
- [126] Bersee HEN, Lindstedt S, Niño G, Beukers A. Diaphragm forming of thermoset composites. *Proceedings of ICCM13*. Beijing, China. (2007)
- [127] Langlois G. Diaphragm forming : innovation and application to ocean engineering [Masters Thesis]. Dept. of Ocean Engineering: Massachusetts Institute of Technology, Massachusetts (2007)
- [128] O'Bradaigh C, Pipes B, Mallon P. Issues in diaphragm forming of advanced thermoplastic composites. *Polymer Composites*. 12 (1991)
<https://doi.org/10.1002/pc.750120406>
- [129] Bersee HEN. Diaphragm forming of continuous fibre reinforced thermoplastics. Process analysis and development. [PhD Thesis]. Faculty of Mechanical Engineering: TU Delft, Delft, Netherlands (1997)
- [130] Bian XX, Gu YZ, Sun J, Li M, Liu WP, Zhang ZG. Effects of processing parameters on the forming quality of C-shaped thermosetting composite laminates in hot diaphragm forming process. *Applied Composite Materials*. 20 (2013)
<https://doi.org/10.1007/s10443-012-9310-7>
- [131] Delaloye S, Niedermeier M. Optimization of the diaphragm forming process for continuous fibre-reinforced advanced thermoplastic composites. *Composites Manufacturing*. 6 (1995)
[https://doi.org/10.1016/0956-7143\(95\)95004-I](https://doi.org/10.1016/0956-7143(95)95004-I)
- [132] Sun J, Gu Y, Li M, Ma X, Zhang Z. Effect of forming temperature on the quality of hot diaphragm formed C-shaped thermosetting composite laminates. *Journal of Reinforced Plastics and Composites*. 31 (2012)
<https://doi.org/10.1177/0731684412453778>
- [133] Alshahrani H, Hojjati M. Optimum processing parameters for hot drape forming of out-of-autoclave prepreg over complex shape using a double diaphragm technique. *Proceedings of ICCM International Conferences on Composite Materials*. (2015)

- [134] Mallon PJ, O'Bradaigh CM. Development of a pilot autoclave for polymeric diaphragm forming of continuous fibre-reinforced thermoplastics. *Composites*. 19 (1988)
[https://doi.org/10.1016/0010-4361\(88\)90542-3](https://doi.org/10.1016/0010-4361(88)90542-3)
- [135] Keane MA, Mulhern MB, Mallon PJ. Investigation of the effects of varying the processing parameters in diaphragm forming of advanced thermoplastic composite laminates. *Composites Manufacturing*. 6 (1995)
[https://doi.org/10.1016/0956-7143\(95\)95005-J](https://doi.org/10.1016/0956-7143(95)95005-J)
- [136] Alshahrani H, Hojjati M. Influence of double-diaphragm vacuum compaction on deformation during forming of composite prepregs. *Journal of Science: Advanced Materials and Devices*. 1 (2016)
<https://doi.org/10.1016/j.jsamd.2016.09.003>
- [137] McGuinness GB, ÓBrádaigh CM. Effect of preform shape on buckling of quasi-isotropic thermoplastic composite laminates during sheet forming. *Composites Manufacturing*. 6 (1995)
[https://doi.org/10.1016/0956-7143\(95\)95020-Y](https://doi.org/10.1016/0956-7143(95)95020-Y)
- [138] Monaghan MR, Mallon PJ. High temperature mechanical characterisation of polyimide diaphragm forming films. *Composites Part A: Applied Science and Manufacturing*. 29 (1998)
[https://doi.org/10.1016/S1359-835X\(97\)00086-9](https://doi.org/10.1016/S1359-835X(97)00086-9)
- [139] Hopmann C, Michaeli EHW, Schöldgen R. Advanced Diaphragm Forming Process for high temperature applications. *Proceedings of International SAMPE Technical Conference*. (2011)
- [140] Kouwonou K, Pham X-T, Lebrun G. Modeling and characterization of thermoplastic composites peek/carbon. *Proceedings of ICCM14*. Montreal. (2013)
- [141] Gong Y, Song Z, Ning H, Hu N, Peng X, Wu X, Zou R, Liu F, Weng S, Liu Q. A comprehensive review of characterization and simulation methods for thermo-stamping of 2D woven fabric reinforced thermoplastics. *Composites Part B: Engineering*. 203 (2020)
<https://doi.org/10.1016/j.compositesb.2020.108462>
- [142] Murtagh AM, Mallon PJ. Chapter 5 Characterisation of shearing and frictional behaviour during sheet forming. In: Bhattacharyya D (Eds.). *Composite Materials Series*. Elsevier (1997). pp.163-216

- [143] Long AC, Boisse P, Robitaille F. 2 - Mechanical analysis of textiles. In: Long AC (Eds.). Design and Manufacture of Textile Composites. Woodhead Publishing (2005). pp.62-109
- [144] Boisse P, Hamila N, Vidal-Sallé E, Dumont F. Simulation of wrinkling during textile composite reinforcement forming. Influence of tensile, in-plane shear and bending stiffnesses. Composites Science and Technology. 71 (2011)
<https://doi.org/10.1016/j.compscitech.2011.01.011>
- [145] Skelton J. Fundamentals of Fabric Shear. Textile Research Journal. 46 (1976)
<https://doi.org/10.1177/004051757604601202>
- [146] Zouari B, Daniel J-L, Boisse P. A woven reinforcement forming simulation method. Influence of the shear stiffness. Computers & Structures. 84 (2006)
<https://doi.org/10.1016/j.compstruc.2005.09.031>
- [147] Zhu B, Yu TX, Tao XM. An experimental study of in-plane large shear deformation of woven fabric composite. Composites Science and Technology. 67 (2007)
<https://doi.org/10.1016/j.compscitech.2006.08.011>
- [148] Johnson AF. Rheological model for the forming of fabric-reinforced thermoplastic sheets. Composites Manufacturing. 6 (1995)
[https://doi.org/10.1016/0956-7143\(95\)95006-K](https://doi.org/10.1016/0956-7143(95)95006-K)
- [149] Bersee HEN, Robroek LMJ. The role of the thermoplastic matrix in forming processes of composite materials. Composites Manufacturing. 2 (1991)
[https://doi.org/10.1016/0956-7143\(91\)90143-5](https://doi.org/10.1016/0956-7143(91)90143-5)
- [150] Dangora LM, Hansen CJ, Mitchell CJ, Sherwood JA, Parker JC. Challenges associated with shear characterization of a cross-ply thermoplastic lamina using picture frame tests. Composites Part A: Applied Science and Manufacturing. 78 (2015)
<https://doi.org/10.1016/j.compositesa.2015.08.015>
- [151] Mattner T, Wrensch M, Drummer D. Shear behavior of woven and non-crimp fabric based thermoplastic composites at near-processing conditions. Composites Part B: Engineering. 185 (2020)
<https://doi.org/10.1016/j.compositesb.2020.107761>
- [152] McGuinness GB, ÓBrádaigh CM. Characterisation of thermoplastic composite melts in rhombus-shear: The picture-frame experiment. Composites Part A: Applied Science and Manufacturing. 29 (1998)
[https://doi.org/10.1016/S1359-835X\(97\)00061-4](https://doi.org/10.1016/S1359-835X(97)00061-4)

- [153] McGuinness GB, ÓBrádaigh CM. Development of rheological models for forming flows and picture-frame shear testing of fabric reinforced thermoplastic sheets. *Journal of Non-Newtonian Fluid Mechanics*. 73 (1997)
[https://doi.org/10.1016/S0377-0257\(97\)00040-2](https://doi.org/10.1016/S0377-0257(97)00040-2)
- [154] Jauffres D, Morris C, Sherwood J, Chen J. Simulation of the thermostamping of woven composites: Determination of the tensile and in-plane shearing behaviors. *International Journal of Material Forming*. 2 (2009)
10.1007/s12289-009-0590-x
- [155] Harrison P, Clifford MJ, Long AC. Shear characterisation of viscous woven textile composites: A comparison between picture frame and bias extension experiments. *Composites Science and Technology*. 64 (2004)
<https://doi.org/10.1016/j.compscitech.2003.10.015>
- [156] Lebrun G, Bureau MN, Denault J. Evaluation of bias-extension and picture-frame test methods for the measurement of intraply shear properties of PP/glass commingled fabrics. *Composite Structures*. 61 (2003)
[https://doi.org/10.1016/S0263-8223\(03\)00057-6](https://doi.org/10.1016/S0263-8223(03)00057-6)
- [157] Lebrun G, Bureau MN, Denault J. Thermoforming-Stamping of Continuous Glass Fiber/Polypropylene Composites: Interlaminar and Tool-Laminate Shear Properties. *Journal of Thermoplastic Composite Materials*. 17 (2004)
<https://doi.org/10.1177/0892705704035411>
- [158] Wang P, Hamila N, Pineau P, Boisse P. Thermomechanical analysis of thermoplastic composite prepregs using bias-extension test. *Journal of Thermoplastic Composite Materials*. 27 (2014)
<https://doi.org/10.1177/0892705712454289>
- [159] Machado M, Murenu L, Fischlschweiger M, Major Z. Analysis of the thermomechanical shear behaviour of woven-reinforced thermoplastic-matrix composites during forming. *Composites Part A: Applied Science and Manufacturing*. 86 (2016)
<https://doi.org/10.1016/j.compositesa.2016.03.032>
- [160] Martin TA, Bhattacharyya D. Squeeze flow in thermoplastic composites. In: Karger-Kocsis J (Eds.). *Polypropylene: An A-Z reference*. Springer Netherlands (1999). pp.776-82

-
- [161] Long AC, Clifford MJ. 1 - Composite forming mechanisms and materials characterisation. In: Long AC (Eds.). *Composites Forming Technologies*. Woodhead Publishing (2007). pp.1-21
- [162] Boisse P, Gasser A, Hivet G. Analyses of fabric tensile behaviour: determination of the biaxial tension–strain surfaces and their use in forming simulations. *Composites Part A: Applied Science and Manufacturing*. 32 (2001)
[https://doi.org/10.1016/S1359-835X\(01\)00039-2](https://doi.org/10.1016/S1359-835X(01)00039-2)
- [163] Cao J, Akkerman R, Boisse P, Chen J, Cheng HS, de Graaf EF, Gorczyca JL, Harrison P, Hivet G, Launay J, Lee W, Liu L, Lomov SV, Long A, de Luycker E, Morestin F, Padvoiskis J, Peng XQ, Sherwood J, Stoilova T, Tao XM, Verpoest I, Willems A, Wiggers J, Yu TX, Zhu B. Characterization of mechanical behavior of woven fabrics: Experimental methods and benchmark results. *Composites Part A: Applied Science and Manufacturing*. 39 (2008)
<https://doi.org/10.1016/j.compositesa.2008.02.016>
- [164] Potter K, Ward C. 5 - Draping processes for composites manufacture. In: Boisse P (Eds.). *Advances in Composites Manufacturing and Process Design*. Woodhead Publishing (2015). pp.93-109
- [165] Boisse P, Colmars J, Hamila N, Naouar N, Steer Q. Bending and wrinkling of composite fiber preforms and prepregs. A review and new developments in the draping simulations. *Composites Part B: Engineering*. 141 (2018)
<https://doi.org/10.1016/j.compositesb.2017.12.061>
- [166] Yu WR, Zampaloni M, Pourboghrat F, Chung K, Kang TJ. Analysis of flexible bending behavior of woven preform using non-orthogonal constitutive equation. *Composites Part A: Applied Science and Manufacturing*. 36 (2005)
<https://doi.org/10.1016/j.compositesa.2004.10.026>
- [167] Ghosh TK, Batra SK, Barker RL. The Bending Behaviour of Plain-woven Fabrics Part I: A Critical Review. *The Journal of The Textile Institute*. 81 (1990)
<https://doi.org/10.1080/00405009008658708>
- [168] Hamila N, Boisse P, Chatel S. Semi-Discrete Shell Finite Elements for Textile Composite Forming Simulation. *International Journal of Material Forming*. 2 (2009)
<https://doi.org/10.1007/s12289-009-0518-5>
- [169] Cornelissen B, Akkerman R. Analysis of yarn bending behaviour. ICCM17. ed. Edinburgh, Scotland. (2009).
-

- [170] Yu F, Chen S, Viisainen JV, Sutcliffe MPF, Harper LT, Warrior NA. A macroscale finite element approach for simulating the bending behaviour of biaxial fabrics. *Composites Science and Technology*. 191 (2020)
<https://doi.org/10.1016/j.compscitech.2020.108078>
- [171] de Bilbao E, Soulat D, Hivet G, Gasser A. Experimental Study of Bending Behaviour of Reinforcements. *Experimental Mechanics*. 50 (2010)
<https://doi.org/10.1007/s11340-009-9234-9>
- [172] Liang B, Chaudet P, Boisse P. Curvature determination in the bending test of continuous fibre reinforcements. *Strain*. 53 (2017)
<https://doi.org/10.1111/str.12213>
- [173] Broberg PH, Lindgaard E, Krogh C, Jensen SM, Trabal GG, Thai AFM, Bak BLV. One-click bending stiffness: Robust and reliable automatic calculation of moment–curvature relation in a cantilever bending test. *Composites Part B: Engineering*. 260 (2023)
<https://doi.org/10.1016/j.compositesb.2023.110763>
- [174] Liang B, Colmars J, Boisse P. A shell formulation for fibrous reinforcement forming simulations. *Composites Part A: Applied Science and Manufacturing*. 100 (2017)
<https://doi.org/10.1016/j.compositesa.2017.04.024>
- [175] Lawrence G, Chen S, Warrior N, Harper LT. Preforming of multi-ply non-crimp fabric laminates using double diaphragm forming. *Proceedings of ICCM23*. Belfast, Northern Ireland. (2023)
- [176] Lomov SV, Verpoest I, Barbarski M, Laperre J. Carbon composites based on multiaxial multiply stitched preforms. Part 2. KES-F characterisation of the deformability of the preforms at low loads. *Composites Part A: Applied Science and Manufacturing*. 34 (2003)
[https://doi.org/10.1016/S1359-835X\(03\)00025-3](https://doi.org/10.1016/S1359-835X(03)00025-3)
- [177] Ngo Ngoc C, Bruniaux P, Castelain J. Modeling friction for yarn/fabric simulation Application to bending hysteresis. *Proceedings of the 14th European Simulation Symposium*. Dresden, Germany. (2002)
- [178] Abdul Ghafour T, Colmars J, Boisse P. The importance of taking into account behavior irreversibilities when simulating the forming of textile composite reinforcements. *Composites Part A: Applied Science and Manufacturing*. 127 (2019)
<https://doi.org/10.1016/j.compositesa.2019.105641>

- [179] Martin TA, Bhattacharyya D, Collins IF. Bending of fibre-reinforced thermoplastic sheets. *Composites Manufacturing*. 6 (1995)
[https://doi.org/10.1016/0956-7143\(95\)95009-N](https://doi.org/10.1016/0956-7143(95)95009-N)
- [180] Wang J, Long AC, Clifford MJ. Experimental measurement and predictive modelling of bending behaviour for viscous unidirectional composite materials. *International Journal of Material Forming*. 3 (2010)
<https://doi.org/10.1007/s12289-009-0670-y>
- [181] Ropers S, Sachs U, Kardos M, Osswald TA. A thermo-viscoelastic approach for the characterization and modeling of the bending behavior of thermoplastic composites – Part II. *Composites Part A: Applied Science and Manufacturing*. 96 (2017)
<https://doi.org/10.1016/j.compositesa.2017.02.007>
- [182] Ropers S, Kardos M, Osswald TA. A thermo-viscoelastic approach for the characterization and modeling of the bending behavior of thermoplastic composites. *Composites Part A: Applied Science and Manufacturing*. 90 (2016)
<https://doi.org/10.1016/j.compositesa.2016.06.016>
- [183] Sachs U, Akkerman R. Viscoelastic bending model for continuous fiber-reinforced thermoplastic composites in melt. *Composites Part A: Applied Science and Manufacturing*. 100 (2017)
<https://doi.org/10.1016/j.compositesa.2017.05.032>
- [184] Margossian A, Bel S, Hinterhoelzl R. Bending characterisation of a molten unidirectional carbon fibre reinforced thermoplastic composite using a Dynamic Mechanical Analysis system. *Composites Part A: Applied Science and Manufacturing*. 77 (2015)
<https://doi.org/10.1016/j.compositesa.2015.06.015>
- [185] Dangora LM, Mitchell C, White KD, Sherwood JA, Parker JC. Characterization of temperature-dependent tensile and flexural rigidities of a cross-ply thermoplastic lamina with implementation into a forming model. *International Journal of Material Forming*. 11 (2018)
<https://doi.org/10.1007/s12289-016-1327-2>
- [186] Liang B, Hamila N, Peillon M, Boisse P. Analysis of thermoplastic prepreg bending stiffness during manufacturing and of its influence on wrinkling simulations. *Composites Part A: Applied Science and Manufacturing*. 67 (2014)
<https://doi.org/10.1016/j.compositesa.2014.08.020>

- [187] Martin TA, Mander SJ, Dykes RJ, Bhattacharyya D. Chapter 9 Bending of continuous fibre-reinforced thermoplastic sheets. In: Bhattacharyya D (Eds.). *Composite Materials Series*. Elsevier (1997). pp.371-401
- [188] Dörr D, Schirmaier FJ, Henning F, Kärger L. A viscoelastic approach for modeling bending behavior in finite element forming simulation of continuously fiber reinforced composites. *Composites Part A: Applied Science and Manufacturing*. 94 (2017)
<https://doi.org/10.1016/j.compositesa.2016.11.027>
- [189] Sachs U. Friction and bending in thermoplastic composites forming processes [PhD Thesis]. Faculty of Engineering Technology: University of Twente, Twente (2014)
- [190] Chow S. Frictional interaction between blank holder and fabric in stamping of woven thermoplastic composites [Masters Thesis]. College of Engineering: University of Massachusetts, Massachusetts (2002)
- [191] Hutchings I, Shipway P. *Tribology: Friction and wear of engineering materials*. 2nd ed. Butterworth-Heinemann, Oxford, UK (2017)
- [192] Tu C-F, Fort T. A study of fiber–capstan friction. 1. Stribeck curves. *Tribology International*. 37 (2004)
<https://doi.org/10.1016/j.triboint.2004.02.008>
- [193] Stachowiak G, Batchelor AW. *Engineering Tribology*. 4th ed. Butterworth-Heinemann, Oxford, UK (2013)
- [194] Murtagh AM, Lennon JJ, Mallon PJ. Surface friction effects related to pressforming of continuous fibre thermoplastic composites. *Composites Manufacturing*. 6 (1995)
[https://doi.org/10.1016/0956-7143\(95\)95008-M](https://doi.org/10.1016/0956-7143(95)95008-M)
- [195] Harrison P, Lin H, Ubbink M, Akkerman R, Haar K, Long A. Characterising and modelling tool-ply friction of viscous textile composites. *Proceedings of ICCM16*. Kyoto, Japan. (2007)
- [196] Akkerman R, Thijsse RHWt, Sachs U, Rooij M, Binetruy C, Boussu F. Friction in Textile Thermoplastic Composites Forming. In: Binetruy C, Boussu F (Eds.). *Recent Advances in Textile Composites*. DEStech Publications (2010). pp.271-9
- [197] Sachs U, Haanappel SP, Rietman B, Ten Thijsse R, Akkerman R. Formability of fiber-reinforced thermoplastics in hot press forming process based on friction properties. *Key Engineering Materials*. 554-557 (2013)
<https://doi.org/10.4028/www.scientific.net/KEM.554-557.501>
- [198] Gorczyca JL, Sherwood JA, Liu L, Chen J. Modeling of Friction and Shear in Thermostamping of Composites - Part I. *Journal of Composite Materials*. 38 (2004)
-

-
- <https://doi.org/10.1177/0021998304048416>
- [199] Lee J-M, Kim B-M, Lee C-J, Ko D-C. A characterisation of tool-ply friction behaviors in thermoplastic composite. *Procedia Engineering*. 207 (2017)
<https://doi.org/10.1016/j.proeng.2017.10.743>
- [200] Gorczyca-Cole JL, Sherwood JA, Chen J. A friction model for thermostamping commingled glass–polypropylene woven fabrics. *Composites Part A: Applied Science and Manufacturing*. 38 (2007)
<https://doi.org/10.1016/j.compositesa.2006.03.006>
- [201] ten Thije RHW, Akkerman R, van der Meer L, Ubbink MP. Tool-ply friction in thermoplastic composite forming. *International Journal of Material Forming*. 1 (2008)
<https://doi.org/10.1007/s12289-008-0215-9>
- [202] Lin H, Harrison P, K H, Long A, Akkerman R, Clifford M. Investigation of tool-ply friction of viscous textile composites. *Proceedings of 10th International ESAFORM Conference*. Zaragoza, Spain. (2006)
- [203] Akkerman R, Ubbink MP, Rooij MBd, Thije RHWt. Tool-Ply Friction In Composite Forming. *10th International ESAFORM Conference*. ed. Zaragoza, Spain. (2007).pp.1080-5.
- [204] Liu L, Chen J, Gorczyca JL, Sherwood JA. Modeling of Friction and Shear in Thermostamping of Composites - Part II. *Journal of Composite Materials*. 38 (2004)
<https://doi.org/10.1177/0021998304048417>
- [205] Gorczyca J, Sherwood J, Chen J. A friction model for use with a commingled fiberglass-polypropylene plain-weave fabric and the metal tool during thermostamping. *Revue Europeenne des Elements Finis*. 2005 (2012)
<https://doi.org/10.3166/reef.14.729-751>
- [206] Morris SR, Sun CT. An investigation of interply slip behaviour in AS4/PEEK at forming temperatures. *Composites Manufacturing*. 5 (1994)
[https://doi.org/10.1016/0956-7143\(94\)90136-8](https://doi.org/10.1016/0956-7143(94)90136-8)
- [207] Scherer R, Friedrich K. Inter- and intraply-slip flow processes during thermoforming of cf/pp-laminates. *Composites Manufacturing*. 2 (1991)
[https://doi.org/10.1016/0956-7143\(91\)90185-J](https://doi.org/10.1016/0956-7143(91)90185-J)
- [208] Ten Thije RHW, Akkerman R, Ubbink M, Van Der Meer L. A lubrication approach to friction in thermoplastic composites forming processes. *Composites Part A: Applied Science and Manufacturing*. 42 (2011)
<https://doi.org/10.1016/j.compositesa.2011.03.023>
-

-
- [209] Pierik R, Groupe W, Wijskamp S, Akkerman R. On the origin of start-up effects in ply-ply friction for UD fiber-reinforced thermoplastics in melt. Proceedings of ESAFORM 2021. Liège, Belgium. (2021)
- [210] Dörr D, Faisst M, Joppich T, Poppe C, Henning F, Kärger L. Modelling approach for anisotropic inter-ply slippage in finite element forming simulation of thermoplastic UD-tapes. Proceedings of ESAFORM 2018. Palermo, Italy. (2018)
- [211] Mattner T, Körbel W, Wrensch M, Drummer D. Compensation of edge effects in picture frame testing of continuous fiber reinforced thermoplastics. *Composites Part B: Engineering*. 142 (2018)
<https://doi.org/10.1016/j.compositesb.2018.01.009>
- [212] Bel S, Hamila N, Boisse P, Dumont F. Finite element model for NCF composite reinforcement preforming: Importance of inter-ply sliding. *Composites Part A: Applied Science and Manufacturing*. 43 (2012)
<https://doi.org/10.1016/j.compositesa.2012.08.005>
- [213] Launay J, Hivet G, Duong AV, Boisse P. Experimental analysis of the influence of tensions on in plane shear behaviour of woven composite reinforcements. *Composites Science and Technology*. 68 (2008)
<https://doi.org/10.1016/j.compscitech.2007.06.021>
- [214] Peng XQ, Cao J, Chen J, Xue P, Lussier DS, Liu L. Experimental and numerical analysis on normalization of picture frame tests for composite materials. *Composites Science and Technology*. 64 (2004)
[https://doi.org/10.1016/S0266-3538\(03\)00202-1](https://doi.org/10.1016/S0266-3538(03)00202-1)
- [215] Guzman-Maldonado E, Hamila N, Boisse P, Bikard J. Thermomechanical analysis, modelling and simulation of the forming of pre-impregnated thermoplastics composites. *Composites Part A: Applied Science and Manufacturing*. 78 (2015)
<https://doi.org/10.1016/j.compositesa.2015.08.017>
- [216] Chen Q, Boisse P, Park CH, Saouab A, Bréard J. Intra/inter-ply shear behaviors of continuous fiber reinforced thermoplastic composites in thermoforming processes. *Composite Structures*. 93 (2011)
<https://doi.org/10.1016/j.compstruct.2011.01.002>
- [217] Härtel F, Harrison P. Evaluation of normalisation methods for uniaxial bias extension tests on engineering fabrics. *Composites Part A: Applied Science and Manufacturing*. 67 (2014)
<https://doi.org/10.1016/j.compositesa.2014.08.011>
-

- [218] Haanappel SP, Ten Thije RHW, Sachs U, Rietman B, Akkerman R. Formability analyses of uni-directional and textile reinforced thermoplastics. *Composites Part A: Applied Science and Manufacturing*. 56 (2014)
<https://doi.org/10.1016/j.compositesa.2013.09.009>
- [219] Machado M, Fischlschweiger M, Major Z. A rate-dependent non-orthogonal constitutive model for describing shear behaviour of woven reinforced thermoplastic composites. *Composites Part A: Applied Science and Manufacturing*. 80 (2016)
<https://doi.org/10.1016/j.compositesa.2015.10.028>
- [220] Krogh C, White KD, Sabato A, Sherwood JA. Picture-frame testing of woven prepreg fabric: An investigation of sample geometry and shear angle acquisition. *International Journal of Material Forming*. 13 (2020)
<https://doi.org/10.1007/s12289-019-01499-y>
- [221] Potter K. Bias extension measurements on cross-plyed unidirectional prepreg. *Composites Part A: Applied Science and Manufacturing*. 33 (2002)
[https://doi.org/10.1016/S1359-835X\(01\)00057-4](https://doi.org/10.1016/S1359-835X(01)00057-4)
- [222] Wang J, Page JR, Paton R. Experimental investigation of the draping properties of reinforcement fabrics. *Composites Science and Technology*. 58 (1998)
[https://doi.org/10.1016/S0266-3538\(97\)00115-2](https://doi.org/10.1016/S0266-3538(97)00115-2)
- [223] Harrison P, Taylor E, Alsayednoor J. Improving the accuracy of the uniaxial bias extension test on engineering fabrics using a simple wrinkle mitigation technique. *Composites Part A: Applied Science and Manufacturing*. 108 (2018)
<https://doi.org/10.1016/j.compositesa.2018.02.025>
- [224] Alsayednoor J, Lennard F, Yu WR, Harrison P. Influence of specimen pre-shear and wrinkling on the accuracy of uniaxial bias extension test results. *Composites Part A: Applied Science and Manufacturing*. 101 (2017)
<https://doi.org/10.1016/j.compositesa.2017.06.006>
- [225] ASTM International. D5034. Standard Test Method for Breaking Strength and Elongation of Textile Fabrics (Grab Test). (2021)
- [226] David Alejandro Arellano E, Diego C, Hugo E, Ricardo R, Oliver P. Biaxial Tensile Strength Characterization of Textile Composite Materials. In: Ning H (Eds.). *Composites and Their Properties*. IntechOpen (2012). pp.269-89
- [227] Buet-Gautier K, Boisse P. Experimental analysis and modeling of biaxial mechanical behavior of woven composite reinforcements. *Experimental Mechanics*. 41 (2001)
<https://doi.org/10.1007/BF02323143>

- [228] Xie J, Guo Z, Shao M, Zhu W, Jiao W, Yang Z, Chen L. Mechanics of textiles used as composite preforms: A review. *Composite Structures*. 304 (2023)
<https://doi.org/10.1016/j.compstruct.2022.116401>
- [229] Peirce FT. 26 - The “Handle” of Cloth as a Measurable Quantity. *Journal of the Textile Institute Transactions*. 21 (1930)
<https://doi.org/10.1080/19447023008661529>
- [230] British Standard. BS EN ISO 9073-7:1998. Textiles. Test methods for nonwovens - Determination of bending length. (1998)
- [231] Standardisation IOF. ISO 4604:2011. Reinforcement fabrics — Determination of conventional flexural stiffness — Fixed-angle flexometer method. (2011)
- [232] ASTM International. D1388-18. Standard Test Method for Stiffness of Fabrics. (2018)
- [233] Dangora LM, Mitchell CJ, Sherwood JA. Predictive model for the detection of out-of-plane defects formed during textile-composite manufacture. *Composites Part A: Applied Science and Manufacturing*. 78 (2015)
<https://doi.org/10.1016/j.compositesa.2015.07.011>
- [234] Alshahrani H, Hojjati M. A new test method for the characterization of the bending behavior of textile prepregs. *Composites Part A: Applied Science and Manufacturing*. 97 (2017)
<https://doi.org/10.1016/j.compositesa.2017.02.027>
- [235] Alshahrani H, Hojjati M. Bending behavior of multilayered textile composite prepregs: Experiment and finite element modeling. *Materials & Design*. 124 (2017)
<https://doi.org/10.1016/j.matdes.2017.03.077>
- [236] Kawabata S, Gakki. NSiK. *The Standardization and Analysis of Hand Evaluation*. 2nd ed. Textile Machinery Society of Japan, Osaka, Japan (1980)
- [237] Mitchell C, Dangora L, Bielmeier C, Sherwood J. Investigation into the changes in bending stiffness of a textile reinforced composite due to in-plane fabric shear: Part 1 – Experiment. *Composites Part A: Applied Science and Manufacturing*. 85 (2016)
<https://doi.org/10.1016/j.compositesa.2016.03.008>
- [238] Charmentant A, Orliac JG, Vidal-Sallé E, Boisse P. Hyperelastic model for large deformation analyses of 3D interlock composite preforms. *Composites Science and Technology*. 72 (2012)
<https://doi.org/10.1016/j.compscitech.2012.05.006>
- [239] Clapp TG, Peng H, Ghosh TK, Eischen JW. Indirect Measurement of the Moment-Curvature Relationship for Fabrics. *Textile Research Journal*. 60 (1990)

-
- <https://doi.org/10.1177/004051759006000906>
- [240] Heyer P, Lauger J. A Flexible Platform for Tribological Measurements on a Rheometer. Proceedings of 15th International Congress on Rheology. Monterey, California. (2008)
- [241] ASTM International. Standard D - Standard test method for static and kinetic coefficients of friction of plastic film and sheeting. (1894)
- [242] Murtagh AM, Monaghan MR, Mallon PJ. Development of a Shear Deformation Apparatus to Characterize the Interply Slip Mechanism of Advanced Thermoplastic Composites. Key Engineering Materials. 86-87 (1993)
<https://doi.org/10.4028/www.scientific.net/KEM.86-87.123>
- [243] Kramer ETM, Grouve WJB, Warnet LL, Koussios S, Akkerman R. Tool-ply interaction in the formation of waviness during C/PEEK consolidation. Composites Part A: Applied Science and Manufacturing. 144 (2021)
<https://doi.org/10.1016/j.compositesa.2021.106327>
- [244] ten Thije RHW, Akkerman R. Design of an experimental setup to measure tool-ply and ply-ply friction in thermoplastic laminates. International Journal of Material Forming. 2 (2009)
<https://doi.org/10.1007/s12289-009-0638-y>
- [245] Wilks CE. Processing technologies for woven glass polypropylene composites [PhD Thesis]. Department of Engineering: The University of Nottingham, Nottingham (1999)
- [246] Sun X, Belnoue JP-H, Thompson A, Said BE, Hallett SR. Dry Textile Forming Simulations: A Benchmarking Exercise. Frontiers in Materials. 9 (2022)
<https://doi.org/10.3389/fmats.2022.831820>
- [247] Alshahrani H, Hojjati M. Experimental and numerical investigations on formability of out-of-autoclave thermoset prepreg using a double diaphragm process. Composites Part A: Applied Science and Manufacturing. 101 (2017)
<https://doi.org/10.1016/j.compositesa.2017.06.021>
- [248] Henninger F, Ye L, Friedrich K. Deconsolidation behaviour of glass fibre-polyamide 12 composite sheet material during post-processing. Plastics, Rubber and Composites Processing and Applications. 27 (1998)
- [249] D'Emilia G, Gaspari A, Natale E, Stamopoulos AG, Di Ilio A. Experimental and numerical analysis of the defects induced by the thermoforming process on woven textile thermoplastic composites. Engineering Failure Analysis. 135 (2022)
-

- <https://doi.org/10.1016/j.engfailanal.2022.106093>
- [250] Bloom LD, Wang J, Potter KD. Damage progression and defect sensitivity: An experimental study of representative wrinkles in tension. *Composites Part B: Engineering*. 45 (2013)
- <https://doi.org/10.1016/j.compositesb.2012.05.021>
- [251] Boisse P, Hamila N, Madoe A. Modelling the development of defects during composite reinforcements and prepreg forming. *Philosophical Transactions of the Royal Society A: Mathematical, Physical and Engineering Sciences*. 374 (2016)
- <https://doi.org/10.1098/rsta.2015.0269>
- [252] Sjölander J, Hallander P, Åkermo M. Forming induced wrinkling of composite laminates: A numerical study on wrinkling mechanisms. *Composites Part A: Applied Science and Manufacturing*. 81 (2016)
- <https://doi.org/10.1016/j.compositesa.2015.10.012>
- [253] Lightfoot JS, Wisnom MR, Potter K. A new mechanism for the formation of ply wrinkles due to shear between plies. *Composites Part A: Applied Science and Manufacturing*. 49 (2013)
- <https://doi.org/10.1016/j.compositesa.2013.03.002>
- [254] Thompson AJ, Belnoue JPH, Hallett SR. Modelling defect formation in textiles during the double diaphragm forming process. *Composites Part B: Engineering*. 202 (2020)
- <https://doi.org/10.1016/j.compositesb.2020.108357>
- [255] Viisainen JV, Hosseini A, Sutcliffe MPF. Experimental investigation, using 3D digital image correlation, into the effect of component geometry on the wrinkling behaviour and the wrinkling mechanisms of a biaxial NCF during preforming. *Composites Part A: Applied Science and Manufacturing*. 142 (2021)
- <https://doi.org/10.1016/j.compositesa.2020.106248>
- [256] Levy A, Hubert P. Vacuum-bagged composite laminate forming processes: Predicting thickness deviation in complex shapes. *Composites Part A: Applied Science and Manufacturing*. 126 (2019)
- <https://doi.org/10.1016/j.compositesa.2019.105568>
- [257] Mistry PJ. *Lightweighting of Railway Vehicles* [EngD Thesis]. Department of Engineering: University of Nottingham, Nottingham (2022)
- [258] Amedewovo L. *Study of Thermoplastic Matrix Composites Deconsolidation Phenomenon by Considering the Consolidation Process* [PhD Thesis]. Engineering and Systems Sciences: Nantes université, Nantes, France (2023)

- [259] Lu M, Ye L, Mai Y-W. Thermal de-consolidation of thermoplastic matrix composites—II. “Migration” of voids and “re-consolidation”. *Composites Science and Technology*. 64 (2004)
[https://doi.org/10.1016/S0266-3538\(03\)00233-1](https://doi.org/10.1016/S0266-3538(03)00233-1)
- [260] Ye L, Chen Z-R, Lu M, Hou M. De-consolidation and re-consolidation in CF/PPS thermoplastic matrix composites. *Composites Part A: Applied Science and Manufacturing*. 36 (2005)
<https://doi.org/10.1016/j.compositesa.2004.12.006>
- [261] Wolfrath J, Michaud V, Manson JAE. Deconsolidation in glass mat thermoplastic composites: Analysis of the mechanisms. *Composites Part A: Applied Science and Manufacturing*. 36 (2005)
<https://doi.org/10.1016/j.compositesa.2005.04.001>
- [262] Gutowski TG. Resin flow/fiber deformation model for composites. *SAMPE Quarterly*. 16 (1985)
- [263] Ye L, Lu M, Mai Y-W. Thermal de-consolidation of thermoplastic matrix composites—I. Growth of voids. *Composites Science and Technology*. 62 (2002)
[https://doi.org/10.1016/S0266-3538\(02\)00144-6](https://doi.org/10.1016/S0266-3538(02)00144-6)
- [264] Amedewovo L, Levy A, de Parscau du Plessix B, Aubril J, Arrive A, Orgéas L, Le Corre S. A methodology for online characterization of the deconsolidation of fiber-reinforced thermoplastic composite laminates. *Composites Part A: Applied Science and Manufacturing*. 167 (2023)
<https://doi.org/10.1016/j.compositesa.2022.107412>
- [265] Bernet N, Michaud V, Bourban PE, Manson JAE. An Impregnation Model for the Consolidation of Thermoplastic Composites Made from Commingled Yarns. *Journal of Composite Materials*. 33 (1999)
<https://doi.org/10.1177/002199839903300806>
- [266] Slange TK, Warnet LL, Groupe WJB, Akkerman R. Deconsolidation of C/PEEK blanks: on the role of prepreg, blank manufacturing method and conditioning. *Composites Part A: Applied Science and Manufacturing*. 113 (2018)
<https://doi.org/10.1016/j.compositesa.2018.06.034>
- [267] Gröschel C, Drummer D. The Influence of Moisture and Laminate Setup on the De-Consolidation Behavior of PA6/GF Thermoplastic Matrix Composites. *International Polymer Processing*. 29 (2014)
<https://doi.org/10.3139/217.2976>
-

- [268] Donadei V, Lionetto F, Wielandt M, Offringa A, Maffezzoli A. Effects of blank quality on press-formed PEKK/Carbon composite parts. *Materials*. 11 (2018)
<https://doi.org/10.3390/ma11071063>
- [269] Grunenfelder LK, Nutt SR. Void formation in composite prepregs – Effect of dissolved moisture. *Composites Science and Technology*. 70 (2010)
<https://doi.org/10.1016/j.compscitech.2010.09.009>
- [270] Anderson JP, Altan MC. Formation of voids in composite laminates: Coupled effect of moisture content and processing pressure. *Polymer Composites*. 36 (2015)
<https://doi.org/10.1002/pc.22952>
- [271] Costa ML, Almeida SFMd, Rezende MC. The influence of porosity on the interlaminar shear strength of carbon/epoxy and carbon/bismaleimide fabric laminates. *Composites Science and Technology*. 61 (2001)
[https://doi.org/10.1016/S0266-3538\(01\)00157-9](https://doi.org/10.1016/S0266-3538(01)00157-9)
- [272] Wisnom MR, Reynolds T, Gwilliam N. Reduction in interlaminar shear strength by discrete and distributed voids. *Composites Science and Technology*. 56 (1996)
[https://doi.org/10.1016/0266-3538\(95\)00128-X](https://doi.org/10.1016/0266-3538(95)00128-X)
- [273] Längauer M, Zitzenbacher G, Heupl S, Plank B, Burgstaller C, Hochenauer C. Influence of thermal deconsolidation on the anisotropic thermal conductivity of glass fiber reinforced, pre-consolidated polypropylene sheets used for thermoforming applications. *Polymer Composites*. 43 (2022)
10.1002/pc.26538
- [274] Engmann J, Servais C, Burbidge AS. Squeeze flow theory and applications to rheometry: A review. *Journal of Non-Newtonian Fluid Mechanics*. 132 (2005)
<https://doi.org/10.1016/j.jnnfm.2005.08.007>
- [275] Robitaille F, Gauvin R. Compaction of textile reinforcements for composites manufacturing. I: Review of experimental results. *Polymer Composites*. 19 (1998)
<https://doi.org/10.1002/pc.10091>
- [276] de Luca P, Lefébure P, Pickett AK. Numerical and experimental investigation of some press forming parameters of two fibre reinforced thermoplastics: APC2-AS4 and PEI-CETEX. *Composites Part A: Applied Science and Manufacturing*. 29 (1998)
[https://doi.org/10.1016/S1359-835X\(97\)00060-2](https://doi.org/10.1016/S1359-835X(97)00060-2)
- [277] Gereke T, Döbrich O, Hübner M, Cherif C. Experimental and computational composite textile reinforcement forming: A review. *Composites Part A: Applied Science and Manufacturing*. 46 (2013)

-
- 10.1016/j.compositesa.2012.10.004
- [278] Fong L, Lee LJ. Preforming Simulation of Thermoformable Fiber Mats Using Geometric Modeling Approach. *Science and Engineering Composite Materials*. 4 (1995)
- [279] Smith JR, Vaidya UK, Johnstone JK. Analytical modeling of deformed plain woven thermoplastic composites. *International Journal of Material Forming*. 7 (2014)
<https://doi.org/10.1007/s12289-013-1133-z>
- [280] Potluri P, Sharma S, Ramgulam R. Comprehensive drape modelling for moulding 3D textile preforms. *Composites Part A: Applied Science and Manufacturing*. 32 (2001)
[https://doi.org/10.1016/S1359-835X\(01\)00040-9](https://doi.org/10.1016/S1359-835X(01)00040-9)
- [281] Wang J, Paton R, Page JR. The draping of woven fabric preforms and prepregs for production of polymer composite components. *Composites Part A: Applied Science and Manufacturing*. 30 (1999)
[https://doi.org/10.1016/S1359-835X\(98\)00187-0](https://doi.org/10.1016/S1359-835X(98)00187-0)
- [282] Van Der Weeën F. Algorithms for draping fabrics on doubly-curved surfaces. *International Journal for Numerical Methods in Engineering*. 31 (1991)
<https://doi.org/10.1002/nme.1620310712>
- [283] Baillargeon Y, Vu-Khanh T. Prediction of fiber orientation and microstructure of woven fabric composites after forming. *Composite Structures*. 52 (2001)
[https://doi.org/10.1016/S0263-8223\(01\)00037-X](https://doi.org/10.1016/S0263-8223(01)00037-X)
- [284] Boisse P, Hamila N, Helenon F, Aimene Y, Mabrouki T. Draping of Textile Composite Reinforcements: Continuous and Discrete Approaches. *Advanced Composites Letters*. 16 (2019)
<https://doi.org/10.1177/096369350701600401>
- [285] Pickett A, Creech G, Luca P. Simplified and advanced simulation methods for prediction of fabric draping. *Revue Europeenne des Elements Finis*. 2005 (2012)
<https://doi.org/10.3166/reef.14.677-691>
- [286] Yang B, Jin T, Bi F, Li J. A Geometry Information Based Fishnet Algorithm for Woven Fabric Draping in Liquid Composite Molding. *Medziagotyra*. 20 (2014)
<https://doi.org/10.5755/j01.ms.20.4.6075>
- [287] Liang B, Boisse P. A review of numerical analyses and experimental characterization methods for forming of textile reinforcements. *Chinese Journal of Aeronautics*. 34 (2021)
<https://doi.org/10.1016/j.cja.2020.09.027>
-

- [288] Lin H, Wang J, Long AC, Clifford MJ, Harrison P. Predictive modelling for optimization of textile composite forming. *Composites Science and Technology*. 67 (2007)
<https://doi.org/10.1016/j.compscitech.2007.03.040>
- [289] Ó Brádaigh CM, McGuinness GB, McEntee SP. Chapter 7 Implicit finite element modelling of composites sheet forming processes. In: Bhattacharyya D (Eds.). *Composite Materials Series*. Elsevier (1997). pp.247-322
- [290] Pickett A. Review of Finite Element Simulation Methods Applied to Manufacturing and Failure Prediction in Composites Structures. *Applied Composite Materials*. 9 (2002)
<https://doi.org/10.1023/A:1012667427575>
- [291] Belytschko T, Hughes TJR. *Computational Methods for Transient Analysis*. 1st ed. North-Holland, Amsterdam, Netherlands (1983)
- [292] Belytschko T, Liu WK, Moran B, Elkhodary K. *Nonlinear Finite Elements for Continua and Structures*. 2nd ed. Wiley, Chichester, England (2013)
- [293] Durville D. Simulation of the mechanical behaviour of woven fabrics at the scale of fibers. *International Journal of Material Forming*. 3 (2010)
<https://doi.org/10.1007/s12289-009-0674-7>
- [294] Miao Y, Zhou E, Wang Y, Cheeseman BA. Mechanics of textile composites: Micro-geometry. *Composites Science and Technology*. 68 (2008)
<https://doi.org/10.1016/j.compscitech.2008.02.018>
- [295] Latil P, Orgéas L, Geindreau C, Dumont PJJ, Rolland du Roscoat S. Towards the 3D in situ characterisation of deformation micro-mechanisms within a compressed bundle of fibres. *Composites Science and Technology*. 71 (2011)
<https://doi.org/10.1016/j.compscitech.2010.12.023>
- [296] El Said B, Ivanov D, Long AC, Hallett SR. Multi-scale modelling of strongly heterogeneous 3D composite structures using spatial Voronoi tessellation. *Journal of the Mechanics and Physics of Solids*. 88 (2016)
<https://doi.org/10.1016/j.jmps.2015.12.024>
- [297] Daelemans L, Faes J, Allaoui S, Hivet G, Dierick M, Van Hoorebeke L, Van Paepegem W. Finite element simulation of the woven geometry and mechanical behaviour of a 3D woven dry fabric under tensile and shear loading using the digital element method. *Composites Science and Technology*. 137 (2016)
<https://doi.org/10.1016/j.compscitech.2016.11.003>

- [298] Naouar N, Vidal-Sallé E, Schneider J, Maire E, Boisse P. Meso-scale FE analyses of textile composite reinforcement deformation based on X-ray computed tomography. *Composite Structures*. 116 (2014)
<https://doi.org/10.1016/j.compstruct.2014.04.026>
- [299] Zheng R, Naouar N, Colmars J, Platzer A, Schäfer B, Morestin F, Kärger L, Boisse P. Mesoscopic finite element modeling of biaxial non-crimp fabric including representative stitch pattern. *Composite Structures*. 339 (2024)
<https://doi.org/10.1016/j.compstruct.2024.118126>
- [300] Sirtautas J, Pickett AK, Lépicier P. A mesoscopic model for coupled drape-infusion simulation of biaxial Non-Crimp Fabric. *Composites Part B: Engineering*. 47 (2013)
<https://doi.org/10.1016/j.compositesb.2012.09.088>
- [301] Lomov SV, Ivanov DS, Verpoest I, Zako M, Kurashiki T, Nakai H, Hirosawa S. Meso-FE modelling of textile composites: Road map, data flow and algorithms. *Composites Science and Technology*. 67 (2007)
<https://doi.org/10.1016/j.compscitech.2006.10.017>
- [302] Badel P, Vidal-Sallé E, Maire E, Boisse P. Simulation and tomography analysis of textile composite reinforcement deformation at the mesoscopic scale. *Composites Science and Technology*. 68 (2008)
<https://doi.org/10.1016/j.compscitech.2008.04.038>
- [303] Bayraktar H, Ehrlich D, Scarlat G, McClain M, Timoshchuk N, Redman C. Forming and performance analysis of a 3D woven composite curved beam through meso-scale FEA. *SAMPE Technical Conference*. ed. Seattle, Washington, USA. (2014).
- [304] Tabatabaei SA, Swolfs Y, Wu H, Lomov SV. Full-field strain measurements and meso-FE modelling of hybrid carbon/self-reinforced polypropylene. *Composite Structures*. 132 (2015)
<https://doi.org/10.1016/j.compstruct.2015.07.018>
- [305] Wang D, Naouar N, Vidal-Salle E, Boisse P. Longitudinal compression and Poisson ratio of fiber yarns in meso-scale finite element modeling of composite reinforcements. *Composites Part B: Engineering*. 141 (2018)
<https://doi.org/10.1016/j.compositesb.2017.12.042>
- [306] Zeng X, Endruweit A, Brown LP, Long AC. Numerical prediction of in-plane permeability for multilayer woven fabrics with manufacture-induced deformation. *Composites Part A: Applied Science and Manufacturing*. 77 (2015)
<https://doi.org/10.1016/j.compositesa.2015.03.027>
-

- [307] Boisse P, Hamila N, Helenon F, Hagege B, Cao J. Different approaches for woven composite reinforcement forming simulation. *International Journal of Material Forming*. 1 (2008)
<https://doi.org/10.1007/s12289-008-0002-7>
- [308] Rahali Y, Assidi M, Goda I, Zghal A, Ganghoffer JF. Computation of the effective mechanical properties including nonclassical moduli of 2.5D and 3D interlocks by micromechanical approaches. *Composites Part B: Engineering*. 98 (2016)
<https://doi.org/10.1016/j.compositesb.2016.04.066>
- [309] Jauffrès D, Sherwood JA, Morris CD, Chen J. Discrete mesoscopic modeling for the simulation of woven-fabric reinforcement forming. *International Journal of Material Forming*. 3 (2010)
<https://doi.org/10.1007/s12289-009-0646-y>
- [310] Boubaker BB, Haussy B, Ganghoffer J-F. Discrete models of fabric accounting for yarn interactions. *Revue Européenne des Éléments Finis*. 14 (2005)
<https://doi.org/10.3166/reef.14.653-675>
- [311] Ben Boubaker B, Haussy B, Ganghoffer JF. Discrete models of woven structures. Macroscopic approach. *Composites Part B: Engineering*. 38 (2007)
<https://doi.org/10.1016/j.compositesb.2006.01.007>
- [312] Boisse P, Aimène Y, Dogui A, Dridi S, Gatouillat S, Hamila N, Aurangzeb Khan M, Mabrouki T, Morestin F, Vidal-Sallé E. Hypoelastic, hyperelastic, discrete and semi-discrete approaches for textile composite reinforcement forming. *International Journal of Material Forming*. 3 (2010)
<https://doi.org/10.1007/s12289-009-0664-9>
- [313] d'Agostino MV, Giorgio I, Greco L, Madeo A, Boisse P. Continuum and discrete models for structures including (quasi-) inextensible elasticae with a view to the design and modeling of composite reinforcements. *International Journal of Solids and Structures*. 59 (2015)
<https://doi.org/10.1016/j.jjsolstr.2014.12.014>
- [314] Hamila N, Boisse P. A Meso–Macro Three Node Finite Element for Draping of Textile Composite Preforms. *Applied Composite Materials*. 14 (2007)
<https://doi.org/10.1007/s10443-007-9043-1>
- [315] Hamila N, Boisse P. Simulations of textile composite reinforcement draping using a new semi-discrete three node finite element. *Composites Part B: Engineering*. 39 (2008)

-
- <https://doi.org/10.1016/j.compositesb.2007.11.008>
- [316] Spencer AJM. Theory of fabric-reinforced viscous fluids. *Composites Part A: Applied Science and Manufacturing*. 31 (2000)
[https://doi.org/10.1016/S1359-835X\(00\)00006-3](https://doi.org/10.1016/S1359-835X(00)00006-3)
- [317] Harrison P, Yu W-R, Long AC. Rate dependent modelling of the forming behaviour of viscous textile composites. *Composites Part A: Applied Science and Manufacturing*. 42 (2011)
<https://doi.org/10.1016/j.compositesa.2011.07.026>
- [318] Kang TJ, Yu WR. Drape Simulation of Woven Fabric by Using the Finite-element Method. *The Journal of The Textile Institute*. 86 (1995)
<https://doi.org/10.1080/00405009508659040>
- [319] Dong L, Lekakou C, Bader MG. Solid-mechanics finite element simulations of the draping of fabrics: a sensitivity analysis. *Composites Part A: Applied Science and Manufacturing*. 31 (2000)
[https://doi.org/10.1016/S1359-835X\(00\)00046-4](https://doi.org/10.1016/S1359-835X(00)00046-4)
- [320] Hsiao S-W, Kikuchi N. Numerical analysis and optimal design of composite thermoforming process. *Computer Methods in Applied Mechanics and Engineering*. 177 (1999)
[https://doi.org/10.1016/S0045-7825\(98\)00273-4](https://doi.org/10.1016/S0045-7825(98)00273-4)
- [321] Yu WR, Pourboghraat F, Chung K, Zampaloni M, Kang TJ. Non-orthogonal constitutive equation for woven fabric reinforced thermoplastic composites. *Composites Part A: Applied Science and Manufacturing*. 33 (2002)
[https://doi.org/10.1016/S1359-835X\(02\)00053-2](https://doi.org/10.1016/S1359-835X(02)00053-2)
- [322] Xue P, Peng X, Cao J. A non-orthogonal constitutive model for characterizing woven composites. *Composites Part A: Applied Science and Manufacturing*. 34 (2003)
[https://doi.org/10.1016/S1359-835X\(02\)00052-0](https://doi.org/10.1016/S1359-835X(02)00052-0)
- [323] Peng XQ, Cao J. A continuum mechanics-based non-orthogonal constitutive model for woven composite fabrics. *Composites Part A: Applied Science and Manufacturing*. 36 (2005)
<https://doi.org/10.1016/j.compositesa.2004.08.008>
- [324] Khan MA, Mabrouki T, Vidal-Sallé E, Boisse P. Numerical and experimental analyses of woven composite reinforcement forming using a hypoelastic behaviour. Application to the double dome benchmark. *Journal of Materials Processing Technology*. 210 (2010)
-

-
- <https://doi.org/10.1016/j.jmatprotec.2009.09.027>
- [325] Badel P, Gauthier S, Vidal-Sallé E, Boisse P. Rate constitutive equations for computational analyses of textile composite reinforcement mechanical behaviour during forming. *Composites Part A: Applied Science and Manufacturing*. 40 (2009)
<https://doi.org/10.1016/j.compositesa.2008.04.015>
- [326] Rogers TG. Rheological characterization of anisotropic materials. *Composites*. 20 (1989)
[https://doi.org/10.1016/0010-4361\(89\)90677-0](https://doi.org/10.1016/0010-4361(89)90677-0)
- [327] Spencer AJM. *Deformations of fibre-reinforced materials*. 1st ed. Clarendon Press, Oxford, England (1972)
- [328] Spencer AJM, Hashin Z. Continuum Theory of the Mechanics of Fibre-Reinforced Composites. *Journal of Applied Mechanics*. 53 (1986)
<https://doi.org/10.1115/1.3171730>
- [329] O'Bradaigh CM, Byron Pipes R. Finite element analysis of composite sheet-forming process. *Composites Manufacturing*. 2 (1991)
[https://doi.org/10.1016/0956-7143\(91\)90135-4](https://doi.org/10.1016/0956-7143(91)90135-4)
- [330] ÓBrádaigh CM, McGuinness GB, Pipes RB. Numerical analysis of stresses and deformations in composite materials sheet forming: central indentation of a circular sheet. *Composites Manufacturing*. 4 (1993)
[https://doi.org/10.1016/0956-7143\(93\)90074-I](https://doi.org/10.1016/0956-7143(93)90074-I)
- [331] Harrison P, Clifford M. 3 - Rheological behaviour of pre-impregnated textile composites. In: Long AC (Eds.). *Design and Manufacture of Textile Composites*. Woodhead Publishing (2005). pp.110-48
- [332] Aridhi A, Arfaoui M, Mabrouki T, Naouar N, Denis Y, Zarroug M, Boisse P. Textile composite structural analysis taking into account the forming process. *Composites Part B: Engineering*. 166 (2019)
<https://doi.org/10.1016/j.compositesb.2019.02.047>
- [333] Yu W-R, Harrison P, Long A. Finite element forming simulation for non-crimp fabrics using a non-orthogonal constitutive equation. *Composites Part A: Applied Science and Manufacturing*. 36 (2005)
<https://doi.org/10.1016/j.compositesa.2005.01.007>
- [334] Harrison P, Yu W-R, Wang J, Long AC, Clifford MJ. A predictive approach to simulating the forming of viscous textile composite sheet. *Revue Européenne des Éléments Finis*. 14 (2005)
-

-
- <https://doi.org/10.3166/reef.14.613-631>
- [335] Khiêm VN, Krieger H, Itskov M, Gries T, Stapleton SE. An averaging based hyperelastic modeling and experimental analysis of non-crimp fabrics. *International Journal of Solids and Structures*. 154 (2018)
- <https://doi.org/10.1016/j.ijsolstr.2016.12.018>
- [336] Syerko E, Comas-Cardona S, Binetruy C. Models for shear properties/behavior of dry fibrous materials at various scales: a review. *International Journal of Material Forming*. 8 (2015)
- <https://doi.org/10.1007/s12289-013-1138-7>
- [337] Yu WR, Zampaloni M, Pourboghrat F, Chung K, Kang TJ. Sheet hydroforming of woven FRT composites: non-orthogonal constitutive equation considering shear stiffness and undulation of woven structure. *Composite Structures*. 61 (2003)
- [https://doi.org/10.1016/S0263-8223\(03\)00056-4](https://doi.org/10.1016/S0263-8223(03)00056-4)
- [338] Harrison P, Clifford MJ, Long AC, Rudd CD. A constituent-based predictive approach to modelling the rheology of viscous textile composites. *Composites Part A: Applied Science and Manufacturing*. 35 (2004)
- <https://doi.org/10.1016/j.compositesa.2004.01.005>
- [339] Peng X, Cao J. A dual homogenization and finite element approach for material characterization of textile composites. *Composites Part B: Engineering*. 33 (2002)
- [https://doi.org/10.1016/S1359-8368\(01\)00052-X](https://doi.org/10.1016/S1359-8368(01)00052-X)
- [340] Cao J, Xue P, Peng X, Krishnan N. An approach in modeling the temperature effect in thermo-stamping of woven composites. *Composite Structures*. 61 (2003)
- [https://doi.org/10.1016/S0263-8223\(03\)00052-7](https://doi.org/10.1016/S0263-8223(03)00052-7)
- [341] Xue P, Cao J, Chen J. Integrated micro/macro-mechanical model of woven fabric composites under large deformation. *Composite Structures*. 70 (2005)
- <https://doi.org/10.1016/j.compstruct.2004.08.013>
- [342] Aimène Y, Vidal-Sallé E, Hagége B, Sidoroff F, Boisse P. A Hyperelastic Approach for Composite Reinforcement Large Deformation Analysis. *Journal of Composite Materials*. 44 (2009)
- <https://doi.org/10.1177/0021998309345348>
- [343] Gong Y, Peng X, Yao Y, Guo Z. An anisotropic hyperelastic constitutive model for thermoplastic woven composite prepregs. *Composites Science and Technology*. 128 (2016)
- <https://doi.org/10.1016/j.compscitech.2016.03.005>
-

- [344] Charmetant A, Vidal-Sallé E, Boisse P. Hyperelastic modelling for mesoscopic analyses of composite reinforcements. *Composites Science and Technology*. 71 (2011)
<https://doi.org/10.1016/j.compscitech.2011.07.004>
- [345] Guzman-Maldonado E, Hamila N, Naouar N, Moulin G, Boisse P. Simulation of thermoplastic prepreg thermoforming based on a visco-hyperelastic model and a thermal homogenization. *Materials & design*. 93 (2016)
<https://doi.org/10.1016/j.matdes.2015.12.166>
- [346] Garcia M, Gonzalez L. Comparison of hyperelastic material models in the analysis of fabrics. *International Journal of Clothing Science and Technology*. 18 (2006)
<https://doi.org/10.1108/09556220610685249>
- [347] ten Thije RHW, Akkerman R, Huétink J. Large deformation simulation of anisotropic material using an updated Lagrangian finite element method. *Computer Methods in Applied Mechanics and Engineering*. 196 (2007)
<https://doi.org/10.1016/j.cma.2007.02.010>
- [348] Peng X, Guo Z, Du T, Yu W-R. A simple anisotropic hyperelastic constitutive model for textile fabrics with application to forming simulation. *Composites Part B: Engineering*. 52 (2013)
<https://doi.org/10.1016/j.compositesb.2013.04.014>
- [349] Harrison P. Modelling the forming mechanics of engineering fabrics using a mutually constrained pantographic beam and membrane mesh. *Composites Part A: Applied Science and Manufacturing*. 81 (2016)
<https://doi.org/10.1016/j.compositesa.2015.11.005>
- [350] Ten Thije RHW, Akkerman R. A multi-layer triangular membrane finite element for the forming simulation of laminated composites. *Composites Part A: Applied Science and Manufacturing*. 40 (2009)
<https://doi.org/10.1016/j.compositesa.2009.03.004>
- [351] Deng T, Zhang W, Jiang W, Zhou H, Huang Z, Peng X, Zhou H, Li D. A hybrid lamination model for simulation of woven fabric reinforced thermoplastic composites solid-state thermo-stamping. *Materials & Design*. 200 (2021)
<https://doi.org/10.1016/j.matdes.2020.109419>
- [352] Schäfer F, Werner HO, Henning F, Kärger L. A hyperelastic material model considering biaxial coupling of tension–compression and shear for the forming simulation of woven fabrics. *Composites Part A: Applied Science and Manufacturing*. 165 (2023)

- <https://doi.org/10.1016/j.compositesa.2022.107323>
- [353] Iwata A, Inoue T, Naouar N, Boisse P, Lomov SV. Coupled meso-macro simulation of woven fabric local deformation during draping. *Composites Part A: Applied Science and Manufacturing*. 118 (2019)
- <https://doi.org/10.1016/j.compositesa.2019.01.004>
- [354] Nishi M, Hirashima T, Kurashiki T. Textile composite reinforcement forming analysis considering out-of-plane bending stiffness and tension dependent in-plane shear behavior. ECCM16. ed. Seville, Spain. (2014).
- [355] Leutz D, Kluepfel M, Dumont F, Hinterhoelzl R, Drechsler K, Weimer C. FE-Simulation of the Diaphragm Draping Process for NCF on a Macro-Scale Level. *Proceedings of the 14TH International EASFORM Conference*. Belfast, Northern Ireland. (2011)
- [356] Margossian A, Bel S, Balvers JM, Leutz D, Freitas R, Hinterhoelzl R. Finite element forming simulation of locally stitched non-crimp fabrics. *Composites Part A: Applied Science and Manufacturing*. 61 (2014)
- <https://doi.org/10.1016/j.compositesa.2014.02.020>
- [357] Sorrentino L, Bellini C. Potentiality of Hot Drape Forming to produce complex shape parts in composite material. *The International Journal of Advanced Manufacturing Technology*. 85 (2016)
- <https://doi.org/10.1007/s00170-015-7998-x>
- [358] Miris G, Ravandi M, Cardew-Hall A, Eisenbart B, Di Pietro A. Efficient numerical analysis of in-plane compression-induced defects in thick multi-ply woven textile preforms during double diaphragm forming. *Composites Part A: Applied Science and Manufacturing*. 186 (2024)
- <https://doi.org/10.1016/j.compositesa.2024.108431>
- [359] Wang L, Peng X, Liu M. Development and application of hyperelastic model for diaphragm considering the influence of temperature. *International Journal of Computational Materials Science and Engineering*. 8 (2019)
- <https://doi.org/10.1142/S2047684119500106>
- [360] Garnich MR, Klymyshyn NA. Multiscale analysis of stamp forming of a woven composite. *Journal of Thermoplastic Composite Materials*. 26 (2013)
- <https://doi.org/10.1177/0892705711428654>
-

- [361] Jauffrès D, Morris CD, Sherwood JA, Chen J. Simulation of the thermostamping of woven composites: mesoscopic modelling using explicit fea codes. *International Journal of Material Forming*. 2 (2009)
<https://doi.org/10.1007/s12289-009-0519-4>
- [362] Peng X, Ding F. Validation of a non-orthogonal constitutive model for woven composite fabrics via hemispherical stamping simulation. *Composites Part A: Applied Science and Manufacturing*. 42 (2011)
<https://doi.org/10.1016/j.compositesa.2010.12.014>
- [363] Guo W, Zhao J, Zhao F, Liu X, Feng T, Yan H. Numerical simulation analysis of forming of continuous fiber reinforced polypropylene composites: Relaxation, creep, and hot stamping. *Journal of Thermoplastic Composite Materials*. (2023)
<https://doi.org/10.1177/08927057231218274>
- [364] Han P, Butterfield J, Buchanan S, McCool R, Jiang Z, Price M, Murphy A. The prediction of process-induced deformation in a thermoplastic composite in support of manufacturing simulation. *Proceedings of the Institution of Mechanical Engineers, Part B: Journal of Engineering Manufacture*. 227 (2013)
<https://doi.org/10.1177/0954405413488362>
- [365] Soulat D, Cheruet A, Boisse P. Simulation of continuous fibre reinforced thermoplastic forming using a shell finite element with transverse stress. *Computers & Structures*. 84 (2006)
<https://doi.org/10.1016/j.compstruc.2006.02.011>
- [366] Willems A, Lomov SV, Verpoest I, Vandepitte D, Harrison P, Yu WR. Forming simulation of a thermoplastic commingled woven textile on a double dome. *International Journal of Material Forming*. 1 (2008)
<https://doi.org/10.1007/s12289-008-0218-6>
- [367] Lv B, Zhang J, Xiao J, Wang S, Wen L, Hou X. Analyses of wrinkling mechanisms during forming of multi-layer woven fabric reinforced thermoplastic prepregs. *Composites Part A: Applied Science and Manufacturing*. 184 (2024)
<https://doi.org/10.1016/j.compositesa.2024.108240>
- [368] Cowper G, Symonds PS. Strain-Hardening and Strain-Rte Effects in the Impact Loading of Cantilever Beams. Defense Technical Information Center. (1957)
- [369] ten Thije RHW, Akkerman R. Finite Element Simulations of Laminated Composites Forming Processes. *International Journal of Material Forming*. 3 (2010)
<https://doi.org/10.1007/s12289-010-0870-5>
-

- [370] Abbassi F, Elfaleh I, Mistou S, Zghal A, Fazzini M, Djilali T. Experimental and numerical investigations of a thermoplastic composite (carbon/PPS) thermoforming. *Structural Control and Health Monitoring*. 18 (2011)
<https://doi.org/10.1002/stc.491>
- [371] Ziegs J-P, Weck D, Gude M, Kästner M. Thermo-mechanical modeling of the temperature dependent forming behavior of thermoplastic prepregs. *Engineering Reports*. 4 (2022)
<https://doi.org/10.1002/eng2.12373>
- [372] Gong Y, Xu P, Peng X, Wei R, Yao Y, Zhao K. A lamination model for forming simulation of woven fabric reinforced thermoplastic prepregs. *Composite Structures*. 196 (2018)
<https://doi.org/10.1016/j.compstruct.2018.05.004>
- [373] Dörr D, Henning F, Kärger L. Nonlinear hyperviscoelastic modelling of intra-ply deformation behaviour in finite element forming simulation of continuously fibre-reinforced thermoplastics. *Composites Part A: Applied Science and Manufacturing*. 109 (2018)
<https://doi.org/10.1016/j.compositesa.2018.03.037>
- [374] Wang P, Hamila N, Boisse P. Thermoforming simulation of multilayer composites with continuous fibres and thermoplastic matrix. *Composites Part B: Engineering*. 52 (2013)
<https://doi.org/10.1016/j.compositesb.2013.03.045>
- [375] Xiong H, Hamila N, Boisse P. Consolidation Modeling during Thermoforming of Thermoplastic Composite Prepregs. *Materials*. 12 (2019)
<https://doi.org/10.3390/ma12182853>
- [376] Baumard T, Menary GH, De Almeida O, Schmidt F, Martin P, Bikard J. Towards a Coupled Heating-Forming Simulation of the Thermoforming of Thermoplastic Composites. *The 20th International ESAFORM Conference*. ed. Dublin, Ireland. (2017).
- [377] Cunningham JE, Monaghan PF, Brogan MT. Predictions of the temperature profile within composite sheets during pre-heating. *Composites Part A: Applied Science and Manufacturing*. 29 (1998)
[https://doi.org/10.1016/S1359-835X\(97\)00031-6](https://doi.org/10.1016/S1359-835X(97)00031-6)

- [378] Schmidt FM, Le Maout Y, Monteix S. Modelling of infrared heating of thermoplastic sheet used in thermoforming process. *Journal of Materials Processing Technology*. 143-144 (2003)
[https://doi.org/10.1016/S0924-0136\(03\)00291-7](https://doi.org/10.1016/S0924-0136(03)00291-7)
- [379] Dörr D, Joppich T, Kugele D, Henning F, Kärger L. A coupled thermomechanical approach for finite element forming simulation of continuously fiber-reinforced semi-crystalline thermoplastics. *Composites Part A: Applied Science and Manufacturing*. 125 (2019)
<https://doi.org/10.1016/j.compositesa.2019.105508>
- [380] Chen H, Wang J, Colin D, Li S, Drechsler K. Temperature-Dependent modelling of tension, in-Plane shear, and bending behaviour in non-isothermal thermo-Stamping process simulation of unidirectional UHMWPE fibre reinforced thermoplastic TPU composites. *Journal of Thermoplastic Composite Materials*. 36 (2023)
<https://doi.org/10.1177/08927057221142222>
- [381] Nishi M, Kaburagi T, Kurose M, Hirashima T, Kurasiki T. Forming Simulation of Thermoplastic Pre-Impregnated Textile Composite. *International Journal of Chemical, Nuclear, Metallurgical and Materials Engineering*. 8 (2014)
<https://doi.org/10.5281/zenodo.1095434>
- [382] Lee W, Um M-K, Byun J-H, Boisse P, Cao J. Numerical study on thermo-stamping of woven fabric composites based on double-dome stretch forming. *International Journal of Material Forming*. 3 (2010)
<https://doi.org/10.1007/s12289-009-0668-5>
- [383] Berro Ramirez JP, Palaniswamy H, Roy S. Numerical modelling of thermoplastic resin behaviour for thermoforming of laminates composed of non-crimp fabrics. *Journal of Physics: Conference Series*. 1063 (2018)
<https://doi.org/10.1088/1742-6596/1063/1/012147>
- [384] Fan Y, Yang Z, Liu Y, Zhang H, Li Y. Testing and identification method for the interfacial heat transfer coefficient between CF RTP and tools under fast hot-stamping conditions. *International Journal of Heat and Mass Transfer*. 226 (2024)
<https://doi.org/10.1016/j.ijheatmasstransfer.2024.125494>
- [385] Boisse P. Simulation of Continuous Fibre Composite Forming. In: Picu C, Ganghoffer J-F (Eds.). *Mechanics of Fibrous Materials and Applications: Physical and Modeling Aspects*. Springer International Publishing (2020). pp.157-93

-
- [386] Street GE, Johnson MS. The Intra-Ply Shear Behaviour of Non-Isothermal Thermoplastic Composite Laminates. *Journal of Composites Science*. 7 (2023)
<https://doi.org/10.3390/jcs7100432>
- [387] Material Data Sheet - Tepex® dynalite 202-C200(x)/50%. Lanxess. 2025 (2022)
- [388] Cardarelli F. Polymers and Elastomers. In: Cardarelli F (Eds.). *Materials Handbook: A Concise Desktop Reference*. Springer International Publishing (2018). pp.371–93
- [389] Data Sheet A4000V. Airtech International Inc. (2020)
- [390] Technical Data Sheet - Silicone Rubber Sheeting General Purpose Solid. SILEX Ltd. (2019)
- [391] Lawrence GD. Automated forming of multi-ply non-crimp fabric structures. Department of Mechanical Engineering: The University of Nottingham, Nottingham (2024)
- [392] Pressure measurement film. Fujifilm (2024). [Accessed: 10/2024]
<https://www.fujifilm.com/uk/en/business/inspection/measurement-film/prescale>
- [393] Lanxess. Quality Performs. Information for Processors. (2023)
- [394] T300 Standard Modulus Carbon Fibre. Toray Composite Materials America Inc. (2018)
- [395] Meriam JL, Kraige LG. *Engineering Mechanics: Dynamics*. 7th ed. Wiley, Hoboken, New Jersey, USA (2012)
- [396] Jiang Z, Li C, Tian M, Zhang L, Guo Z, Jia Z, Jiang F, Jin J. Rheological properties of PA6 chips with different spinnability in high-speed spinning. *Polymer Bulletin*. 74 (2017)
<https://doi.org/10.1007/s00289-016-1865-2>
- [397] Sinthavathavorn W, Nithitanakul M, Grady B, Magaraphan R. Melt rheology and die swell of PA6/LDPE blends by using lithium ionomer as a compatibilizer. *Polymer Bulletin*. 63 (2009)
<https://doi.org/10.1007/s00289-009-0063-x>
- [398] Dijkstra D. Guidelines for rheological characterization of polyamide melts (IUPAC Technical Report). *Pure and Applied Chemistry*. 81 (2009)
<https://doi.org/10.1351/PAC-REP-08-07-22>
- [399] Dynisco. Practical Rheology - Section 3. (2021). [Accessed: 01/2025]
https://www.dynisco.com/userfiles/files/Practical_Rheology_Section_3.pdf
- [400] Kovacs J, Bercsey T. Influence of mold properties on the quality of injection molded parts. *Periodica Polytechnica, Mechanical Engineering*. 49 (2005)
-

- [401] dos Anjos E, Backes E, Marini J, Pessan L, Passador F, Montagna L. Effect of LLDPE-g-MA on the rheological, thermal, mechanical properties and morphological characteristic of PA6/LLDPE blends. *Journal of Polymer Research*. 26 (2019)
<https://doi.org/10.1007/s10965-019-1800-y>
- [402] Bird RB, Armstrong RC, Hassager O. *Dynamics of polymeric liquids*. Vol. 1: Fluid mechanics. 2nd ed. Wiley, New York, USA (1987)
- [403] Laidler KJ. The development of the Arrhenius equation. *Journal of Chemical Education*. 61 (1984)
<https://doi.org/10.1021/ed061p494>
- [404] Abacha N. Diffusion behavior of water in polyamide 6 organoclay nanocomposites. *Express Polymer Letters*. 3 (2009)
<https://doi.org/10.3144/expresspolymlett.2009.31>
- [405] Marckmann G, Verron E. Comparison of Hyperelastic Models for Rubber-Like Materials. *Rubber Chemistry and Technology*. 79 (2006)
<https://doi.org/10.5254/1.3547969>
- [406] Treloar LRG. *The Physics of Rubber Elasticity*. 3rd ed. Clarendon Press, Oxford, England (1975)
- [407] Ogden RW. *Non-linear Elastic Deformations*. 1st ed. Dover Publications, Mineola, New York, USA (1997)
- [408] Mooney M. A Theory of Large Elastic Deformation. *Journal of Applied Physics*. 11 (1940)
<https://doi.org/10.1063/1.1712836>
- [409] Yamashita Y, Uematsu H, Tanoue S. Calculation of Strain Energy Density Function Using Ogden Model and Mooney–Rivlin Model Based on Biaxial Elongation Experiments of Silicone Rubber. *Polymers*. 15 (2023)
<https://doi.org/10.3390/polym15102266>
- [410] Twizell EH, Ogden RW. Non-linear optimization of the material constants in Ogden's stress-deformation function for incompressible isotropic elastic materials. *The Journal of the Australian Mathematical Society - Series B Applied Mathematics*. 24 (1983)
<https://doi.org/10.1017/S0334270000003787>
- [411] ABAQUS (2014) *Analysis User's Manual*. Dassault Systemes Simulia, Inc. Version 6.14 (2014)

- [412] Harrison P, Alvarez MF, Anderson D. Towards comprehensive characterisation and modelling of the forming and wrinkling mechanics of engineering fabrics. *International Journal of Solids and Structures*. 154 (2018)
<https://doi.org/10.1016/j.ijsolstr.2016.11.008>
- [413] Nosrat-Nezami F, Gereke T, Eberdt C, Cherif C. Characterisation of the shear–tension coupling of carbon-fibre fabric under controlled membrane tensions for precise simulative predictions of industrial preforming processes. *Composites Part A: Applied Science and Manufacturing*. 67 (2014)
<https://doi.org/10.1016/j.compositesa.2014.08.030>
- [414] Street GE, Johnson MS. Investigating the Intra-Ply Shear Behaviour of Multi-Ply Woven Carbon Fibre Reinforced PA6 Laminates. *Proceedings of ICCM23*. Belfast, Northern Ireland. (2023)
- [415] Labeas GN, Watiti VB, Katsiropoulos CV. Thermomechanical Simulation of Infrared Heating Diaphragm Forming Process for Thermoplastic Parts. *Journal of Thermoplastic Composite Materials*. 21 (2008)
<https://doi.org/10.1177/0892705708089480>
- [416] Avrami M. Kinetics of Phase Change. I General Theory. *The Journal of Chemical Physics*. 7 (1939)
<https://doi.org/10.1063/1.1750380>
- [417] Ziabicki A. *Fundamentals of Fibre Formation: The Science of Fibre Spinning and Drawing*. 1st ed. Wiley, New York, USA (1976)
- [418] Ziabicki A. Crystallization of polymers in variable external conditions. *Colloid and Polymer Science*. 274 (1996)
<https://doi.org/10.1007/BF00665637>
- [419] Song Z, Ning H, Liu F, Hu N, Gong Y. An Improved Mampel Model of the Non-Isothermal Crystallization Kinetics of Fiber-Reinforced Thermoplastic Composites. *Materials (Basel)*. 17 (2024)
10.3390/ma17194747
- [420] Shirzad K, Viney C. A critical review on applications of the Avrami equation beyond materials science. *J R Soc Interface*. 20 (2023)
10.1098/rsif.2023.0242
- [421] Sierra J, Noriega Escobar M, Gómez JF, Pastor JM. Isothermal and non-isothermal Crystallization Kinetics for Blends of Polyamide 6 and Polypropylene. *Zeitschrift Kunststofftechnik/Journal of Plastics Technology*. (2006)
-

- [422] Kulkarni S, Reuvers M-C, Brepols T, Reese S, Johlitz M, Lion A. Characterization of crystallization kinetics in Polyamide 6 with a focus on modeling the thermoforming process: experiments, modeling, simulations. *Continuum Mechanics and Thermodynamics*. 36 (2024)
[10.1007/s00161-023-01268-y](https://doi.org/10.1007/s00161-023-01268-y)
- [423] Ozawa T. Kinetics of non-isothermal crystallization. *Polymer*. 12 (1971)
[https://doi.org/10.1016/0032-3861\(71\)90041-3](https://doi.org/10.1016/0032-3861(71)90041-3)
- [424] O'Neill MJ. Measurement of Specific Heat Functions by Differential Scanning Calorimetry. *Analytical Chemistry*. 38 (1966)
<https://doi.org/10.1021/ac60242a011>
- [425] Newton I. *The Mathematical principles of natural philosophy*, trans. 1st ed. Andrew Motte. London, (1846)
- [426] Nellis G, Klein S. *Heat transfer*. 1st ed. Cambridge university press, Cambridge (2008)
- [427] Fujii T, Imura H. Natural-convection heat transfer from a plate with arbitrary inclination. *International Journal of Heat and Mass Transfer*. 15 (1972)
[https://doi.org/10.1016/0017-9310\(72\)90118-4](https://doi.org/10.1016/0017-9310(72)90118-4)
- [428] Perry RH, Chilton CH, Kirkpatrick SD. *Perry's chemical engineers' handbook*. 4th ed. McGraw-Hill, New York (1963)
- [429] White FM. *Viscous Fluid Flow*. 3rd ed. McGraw-Hill, New York, USA (1974)
- [430] Razak A. *Industrial gas turbines: performance and operability*. 1st ed. Elsevier, Boca Raton, USA (2007)
- [431] Mattingly JD. *Elements of Propulsion: Gas Turbines and Rockets*. 2nd ed. American Institute of Aeronautics and Astronautics, Reston, Virginia, USA (2006)
- [432] Air - Density, Specific Weight and Thermal Expansion Coefficient vs. Temperature and Pressure. *The Engineering ToolBox* (2003). [Accessed: 08/2024]
https://www.engineeringtoolbox.com/air-density-specific-weight-d_600.html
- [433] Rapp B. *Microfluidics: Modeling, mechanics and mathematics*. 1st ed. Elsevier, London, UK (2016)
- [434] Mylona SK, Assael MJ, Wakeham WA. *Transport Properties of Fluids: Thermal Conductivity, Viscosity, and Diffusion Coefficient*. 1st ed. Elsevier, London, UK (1988)

- [435] Smith R, Inomata H, Peters C. Chapter 8 - Heat Transfer and Finite-Difference Methods. In: Smith R, Inomata H, Peters C (Eds.). *Supercritical Fluid Science and Technology*. Elsevier (2013). pp.557-615
- [436] Zeneli M, Nikolopoulos A, Karellas S, Nikolopoulos N. Chapter 7 - Numerical methods for solid-liquid phase-change problems. In: Datas A (Eds.). *Ultra-High Temperature Thermal Energy Storage, Transfer and Conversion*. Woodhead Publishing (2021). pp.165-99
- [437] Incropera F, DeWitt D, Bergman T, Lavine A. *Fundamentals of Heat and Mass Transfer*. 6th ed. Wiley, Hoboken, New Jersey, USA (2007)
- [438] McAdams WH. *Heat Transmission*. 3rd ed. McGraw-Hill, New York, USA (1954)
- [439] Wyatt CL. Chapter IV - Blackbody Radiation. In: Wyatt CL (Eds.). *Radiometric Calibration: Theory and Methods*. Academic Press (1978). pp.29-37
- [440] Özdemir I, Brekelmans WAM, Geers MGD. Computational homogenization for heat conduction in heterogeneous solids. *International Journal for Numerical Methods in Engineering*. 73 (2008)
<https://doi.org/10.1002/nme.2068>
- [441] Adamczyk WP, Bialecki RA, Kruczek T. Measuring thermal conductivity tensor of orthotropic solid bodies. *Measurement*. 101 (2017)
<https://doi.org/10.1016/j.measurement.2017.01.023>
- [442] Keating MY, McLaren CS. Thermal conductivity of polymer melts. *Thermochimica Acta*. 166 (1990)
[https://doi.org/10.1016/0040-6031\(90\)80170-4](https://doi.org/10.1016/0040-6031(90)80170-4)
- [443] Fuller TR, Fricke AL. Thermal conductivity of polymer melts. *Journal of Applied Polymer Science*. 15 (1971)
<https://doi.org/10.1002/app.1971.070150716>
- [444] Kokkolaras M, Audet C, Dennis JE. Mixed Variable Optimization of the Number and Composition of Heat Intercepts in a Thermal Insulation System. *Optimization and Engineering*. 2 (2001)
<https://doi.org/10.1023/A:1011860702585>
- [445] Hasselman DPH, Donaldson KY, Thomas JR. Effective Thermal Conductivity of Uniaxial Composite with Cylindrically Orthotropic Carbon Fibers and Interfacial Thermal Barrier. *Journal of Composite Materials*. 27 (1993)
<https://doi.org/10.1177/002199839302700605>
- [446] Fourier JBJ. *Théorie analytique de la chaleur*. 1st ed. Firmin Didot, Paris, France (1822)

- [447] Silicon for IR-range. Princeton Scientific Corp (2016). [Accessed: 09/2024]
<https://princetonscientific.com/materials/optical-components/silicon-ir-range/>
- [448] Çengel YA, Cimbala JM, Ghajar AJ. Fundamentals of Thermal-fluid Sciences. 6th ed. McGraw Hill, New York, USA (2021)
- [449] Kelly F. On kirchhoff's law and its generalized application to absorption and emission by cavities. Journal of Research of the National Bureau of Standards-B. Mathematics and Mathematical Physics 69b (1965)
- [450] McMahon HO. Thermal Radiation from Partially Transparent Reflecting Bodies. J Opt Soc Am. 40 (1950)
<https://doi.org/10.1364/JOSA.40.000376>
- [451] Metals, Metallic Elements and Alloys - Thermal Conductivities. The Engineering Toolbox (2020). [Accessed: 09/2024]
https://www.engineeringtoolbox.com/thermal-conductivity-metals-d_858.html
- [452] Metals - Specific Heats. The Engineering Toolbox (2020). [Accessed: 09/2024]
https://www.engineeringtoolbox.com/specific-heat-metals-d_152.html
- [453] Abaqus 2023 release available. 4RealSim (2023). [Accessed: 02/2025]
<https://www.4realsim.com/abaqus-2023-release-available/>
- [454] Xiao H, Bruhns OT, Meyers A. Hypo-Elasticity Model Based upon the Logarithmic Stress Rate. Journal of Elasticity. 47 (1997)
<https://doi.org/10.1023/A:1007356925912>
- [455] Hughes TJR, Winget J. Finite rotation effects in numerical integration of rate constitutive equations arising in large-deformation analysis. International Journal for Numerical Methods in Engineering. 15 (1980)
<https://doi.org/10.1002/nme.1620151210>
- [456] Buidiansky B, Sanders JL. On the "best" First-order Linear Shell Theory. ed. Division of Engineering and Applied Physics, Harvard University, New York, USA (1962).129-140